

# Mathematical Problems in Engineering

Theory, Methods, and Applications

---

Special Issue

Coupled Numerical Methods in Engineering Analysis

Guest Editors: Delfim Soares Jr., Otto von Estorf, Jan Sladek, and Luis Godinho



---

# **Coupled Numerical Methods in Engineering Analysis**

**Mathematical Problems in Engineering**

---

**Coupled Numerical Methods in  
Engineering Analysis**

**Guest Editors: Delfim Soares Jr., Otto von Estorf, Jan Sladek,  
and Luis Godinho**



---

**Copyright © 2011 Hindawi Publishing Corporation. All rights reserved.**

**This is an issue published in "Mathematical Problems in Engineering." All articles are open access articles distributed under the Creative Commons Attribution License, which permits unrestricted use, distribution, and reproduction in any medium, provided the original work is properly cited.**



## Editorial Board

- E. M. Abdel-Rahman, Canada  
Hamdy Nabih Agiza, Egypt  
Sebastian Anita, Romania  
W. Assawinchaichote, Thailand  
K. V. Avramov, Ukraine  
Erwei Bai, USA  
Ezzat G. Bakhoum, USA  
J. M. Balthazar, Brazil  
Shankar P. Bhattacharyya, USA  
Stefano Boccaletti, Spain  
Michael J. Brennan, UK  
John Burns, USA  
Piermarco Cannarsa, Italy  
Carlo Cattani, Italy  
Miguel Cerrolaza, Venezuela  
Michael J. Chappell, UK  
Kue-Hong Chen, Taiwan  
Kui Fu Chen, China  
Michele Chiumenti, Spain  
Jyh Horng Chou, Taiwan  
Slim Choura, Tunisia  
Biswa N. Datta, USA  
M. do R. de Pinho, Portugal  
Joao B. R. Do Val, Brazil  
Horst Ecker, Austria  
Alex Elias-Zuniga, Mexico  
Anders Eriksson, Sweden  
Qi Fan, USA  
Moez Feki, Tunisia  
Ricardo Femat, Mexico  
Rolf Findeisen, Germany  
R. A. Fontes Valente, Portugal  
Zoran Gajic, USA  
Ugo Galvanetto, Italy  
Furong Gao, Hong Kong  
Oleg V. Gendelman, Israel  
Paulo Batista Gonçalves, Brazil  
Oded Gottlieb, Israel  
Muhammad R. Hajj, USA  
Thomas Hanne, Switzerland  
Katica R. Hedrih, Serbia  
M. I. Herreros, Spain  
Wei-Chiang Hong, Taiwan  
J. Horacek, Czech Republic  
Gordon Huang, Canada  
Anuar Ishak, Malaysia  
Reza Jazar, Australia  
Zhijian Ji, China  
J. Jiang, China  
J. J. Judice, Portugal  
Tadeusz Kaczorek, Poland  
Tamas Kalmar-Nagy, USA  
Tomasz Kapitaniak, Poland  
Hamid R. Karimi, Norway  
Nikolaos Kazantzis, USA  
Jurgen Kurths, Germany  
Claude Lamarque, France  
Stefano Lenci, Italy  
Ming Li, China  
Shanling Li, Canada  
Teh-Lu Liao, Taiwan  
P. Liatsis, UK  
Jui-Sheng Lin, Taiwan  
Wanquan Liu, Australia  
Bin Liu, Australia  
Angelo Luongo, Italy  
Alexei Mailybaev, Brazil  
R. Martinez-Guerra, Mexico  
B. Maslowski, Czech Republic  
Yuri V. Mikhlin, Ukraine  
G. V. Milovanović, Serbia  
Trung Nguyen Thoi, Vietnam  
Hung Nguyen-Xuan, Vietnam  
Ben T. Nohara, Japan  
Anthony Nouy, France  
Francesco Pellicano, Italy  
F. Lobo Pereira, USA  
A. Pogromsky, The Netherlands  
Seppo Pohjolainen, Finland  
Stanislav Potapenko, Canada  
Sergio Preidikman, USA  
Serge Prudhomme, USA  
Dane Quinn, USA  
K. R. Rajagopal, USA  
Sivaguru Ravindran, USA  
G. Rega, Italy  
Pedro Ribeiro, Portugal  
J. Rodellar, Spain  
Rosana Rodríguez-López, Spain  
A. J. Rodriguez-Luis, Spain  
Rubén Ruiz García, Spain  
Miguel A. F. Sanjuán, Spain  
Ilmar Ferreira Santos, Denmark  
Nickolas S. Sapidis, Greece  
Andrey V. Savkin, Australia  
Massimo Scalia, Italy  
Alexander P. Seyranian, Russia  
Tony Sheu, Taiwan  
Zhan Shu, UK  
Christos H. Skiadas, Greece  
Davide Spinello, Canada  
Sri Sridharan, USA  
Jitao Sun, China  
Xi-Ming Sun, China  
Andrzej Swierniak, Poland  
Allen Tannenbaum, USA  
Cristian Toma, Romania  
Irina N. Trendafilova, UK  
Kuppalapalle Vajravelu, USA  
Victoria Vampa, Argentina  
Blas M. Vinagre, Spain  
Yongqi Wang, Germany  
Moran Wang, USA  
Gerhard-Wilhelm Weber, Turkey  
Peter R. Wolenski, USA  
Kwok W. Wong, HongKong  
Christine Qiong Wu, Canada  
Ligang Wu, China  
Zheng-Guang Wu, China  
Xuping Xu, USA  
Xing-Gang Yan, UK  
Jun-Juh Yan, Taiwan  
Xing-Gang Yan, UK  
Mahmoud T. Yassen, Egypt  
Mohammad I. Younis, USA  
Ion Zaballa, Spain  
Xu Zhang, China

# Contents

**Coupled Numerical Methods in Engineering Analysis**, Delfim Soares Jr., Otto von Estorf, Jan Sladek, and Luis Godinho  
Volume 2011, Article ID 436978, 4 pages

**Stress Analysis of Three-Dimensional Media Containing Localized Zone by FEM-SGBEM Coupling**, Jaroon Rungamornrat and Sakravee Sripirom  
Volume 2011, Article ID 702082, 27 pages

**Finite Element Analysis of Dam-Reservoir Interaction Using High-Order Doubly Asymptotic Open Boundary**, Yichao Gao, Feng Jin, Xiang Wang, and Jinting Wang  
Volume 2011, Article ID 210624, 23 pages

**Coupling the BEM/TBEM and the MFS for the Numerical Simulation of Wave Propagation in Heterogeneous Fluid-Solid Media**, António Tadeu and Igor Castro  
Volume 2011, Article ID 159389, 26 pages

**Dynamic Analysis of Partially Embedded Structures Considering Soil-Structure Interaction in Time Domain**, Sanaz Mahmoudpour, Reza Attarnejad, and Cambyse Behnia  
Volume 2011, Article ID 534968, 23 pages

**A New Reduced Stabilized Mixed Finite-Element Method Based on Proper Orthogonal Decomposition for the Transient Navier-Stokes Equations**, Aiwen Wang, Jian Li, Zhenhua Di, Xiangjun Tian, and Dongxiu Xie  
Volume 2011, Article ID 895386, 19 pages

**A Hybrid Analytical-Numerical Model Based on the Method of Fundamental Solutions for the Analysis of Sound Scattering by Buried Shell Structures**, L. Godinho, P. Amado-Mendes, and A. Pereira  
Volume 2011, Article ID 710623, 22 pages

**Modeling and Simulation of Fiber Orientation in Injection Molding of Polymer Composites**, Jang Min Park and Seong Jin Park  
Volume 2011, Article ID 105637, 14 pages

**A Fully Discrete Galerkin Method for a Nonlinear Space-Fractional Diffusion Equation**, Yunying Zheng and Zhengang Zhao  
Volume 2011, Article ID 171620, 20 pages

**Coupled Numerical Methods to Analyze Interacting Acoustic-Dynamic Models by Multidomain Decomposition Techniques**, Delfim Soares Jr.  
Volume 2011, Article ID 245170, 28 pages

**Interior Noise Prediction of the Automobile Based on Hybrid FE-SEA Method**, S. M. Chen, D. F. Wang, and J. M. Zan  
Volume 2011, Article ID 327170, 20 pages

**A Numerical Treatment of Nondimensional Form of Water Quality Model in a Nonuniform Flow Stream Using Saulyev Scheme**, Nopparat Pochai  
Volume 2011, Article ID 491317, 15 pages

**A Corotational Finite Element Method Combined with Floating Frame Method for Large Steady-State Deformation and Free Vibration Analysis of a Rotating-Inclined Beam**, Ming Hsu Tsai, Wen Yi Lin, Yu Chun Zhou, and Kuo Mo Hsiao  
Volume 2011, Article ID 146505, 29 pages

## *Editorial*

# **Coupled Numerical Methods in Engineering Analysis**

**Delfim Soares Jr.,<sup>1</sup> Otto von Estorff,<sup>2</sup>  
Jan Sladek,<sup>3</sup> and Luis Godinho<sup>4</sup>**

<sup>1</sup> Structural Engineering Department, Federal University of Juiz de Fora, Juiz de Fora, MG 36036-330, Brazil

<sup>2</sup> Institute of Modeling and Computation, Hamburg University of Technology, 21073 Hamburg, Germany

<sup>3</sup> Department of Mechanics, Slovak Academy of Sciences, 845 03 Bratislava, Slovakia

<sup>4</sup> CICC—Research Center in Construction Sciences, Department of Civil Engineering, University of Coimbra, 3030-788 Coimbra, Portugal

Correspondence should be addressed to Delfim Soares Jr., [delfim.soares@ufjf.edu.br](mailto:delfim.soares@ufjf.edu.br)

Received 11 December 2011; Accepted 12 December 2011

Copyright © 2011 Delfim Soares Jr. et al. This is an open access article distributed under the Creative Commons Attribution License, which permits unrestricted use, distribution, and reproduction in any medium, provided the original work is properly cited.

Complex engineering analyses usually require the use of numerical methods to provide accurate data. Although nowadays there are several powerful numerical techniques available, such as the Finite Element Method, the Finite Volume Method, the Boundary Element Method, and Meshless Methods, none of them can be considered most appropriate for all kinds of analysis, and usually the coupling of different numerical methodologies is necessary to analyze complex problems more effectively. In this context, several coupling procedures have been proposed over the last decades considering different numerical methods, in order to profit from their respective advantages. The papers selected for this special issue represent a good panel for addressing this challenging theme. Although different kinds of coupling procedures and hybrid formulations are presented here to analyze multiphysics behavior, of course, they are not an exhaustive representation of the vast area of coupled numerical methods in engineering analysis. Nonetheless, they represent the rich and many-faceted knowledge, that we have the pleasure of sharing with the readers. Therefore, we would like to thank the authors for their contributions and the reviewers for all their fundamental work on these papers.

This special issue contains twelve papers, which are organized considering firstly interface coupled analyses and, later on, domain coupled models. Considering interface

coupling procedures, initially, papers discussing fluid-solid coupled systems are presented, being, in the sequence, papers based on solid-solid coupled models enumerated. Regarding domain coupled analyses, the papers presented here are mostly related to computational fluid models. It is important to remark that several coupled numerical procedures, taking into account a vast game of numerical techniques, are discussed in this issue, highlighting the richness and variety of the theme.

In the paper entitled *"Coupled numerical methods to analyze interacting acoustic-dynamic models by multidomain decomposition techniques,"* several numerical methods, such as the Finite Difference Method, the Finite Element Method, the Boundary Element Method, and Meshless Methods, are considered to model each subdomain of the fluid-solid coupled model, and multidomain decomposition techniques are applied to deal with the coupling relations. In this case, completely independent spatial and temporal discretizations among the interacting subdomains are permitted and coupling algorithms based on explicit and implicit time-marching techniques are discussed.

In the paper entitled *"Finite element analysis of dam-reservoir interaction using high-order doubly asymptotic open boundary,"* direct and partitioned coupled methods are developed to analyze a dam-reservoir system, which is divided into the near-field, modeled by the finite element method, and the far-field, modeled by the high-order doubly asymptotic open boundary (DAOB). In the direct coupled method, a symmetric monolithic governing equation is formulated by incorporating the DAOB with the finite element equation, which is solved using standard time-integration methods. In the partitioned coupled method, the near-field finite element equation and the far-field DAOB condition are separately solved and coupling is achieved by applying the interaction force on the truncated boundary, taking into account an iteration strategy, which is employed to improve the numerical stability and accuracy of the methodology.

In the paper entitled *"Coupling the BEM/TBEM and the MFS for the numerical simulation of wave propagation in heterogeneous fluid-solid media,"* wave propagation in an elastic medium containing elastic, fluid, rigid and empty heterogeneities is simulated, taking into account frequency-domain analyses. In this case, a coupling formulation between the boundary element method (BEM)/the traction boundary element method (TBEM) and the method of fundamental solutions (MFS) is employed. Thus, the full domain is divided into subdomains, which are handled separately by the BEM/TBEM or the MFS, being the coupling enforced by applying the prescribed boundary conditions at all medium interfaces.

In the paper entitled *"A hybrid analytical-numerical model based on the method of fundamental solutions for the analysis of sound scattering by buried shell structures,"* a hybrid numerical-analytical model is proposed to address the problem of underwater sound scattering by an elastic circular shell structure that is buried in a fluid seabed, below a water waveguide. In this case, the coupling between the analytical solutions developed both for sound propagation in the waveguide and in the vicinity of the circular hollow shell is performed using the Method of Fundamental Solutions; the proposed strategy allows a compact description of the propagation medium and claims to be accurate and efficient from the computational point of view.

In the paper entitled *"Dynamic analysis of partially embedded structures considering soil-structure interaction in time domain,"* the substructure method, using the dynamic stiffness of soil, is used to analyze soil-structure systems. In this case, a time-domain coupled model based on the finite element method and on the scaled boundary finite element method is applied, where the finite element method is used to analyze the structure and the scaled boundary finite element method is applied in the analysis of the unbounded soil region.

In the paper entitled *“Stress analysis of three-dimensional media containing localized zone by FEM-SGBEM coupling,”* an efficient numerical technique for three-dimensional stress analysis of an infinite medium containing a line of singularity introduced by dislocations and cracks and a localized region exhibiting complex behaviors (e.g., material nonlinearities and material inhomogeneities) is proposed. In this case, a coupling procedure exploiting positive features of both standard finite element method (FEM) and symmetric Galerkin boundary element method (SGBEM) is considered. Thus, an infinite medium is decomposed into two subdomains such that a finite subdomain that is of small size and may contain a region exhibiting complex behavior is modeled by the FEM while the other (complement) unbounded subdomain that may contain cracks is treated by the weakly singular SGBEM.

In the paper entitled *“A corotational finite element method combined with floating frame method for large steady-state deformation and free vibration analysis of a rotating-sinclined beam,”* large steady-state deformation and infinitesimal-free vibration around the steady state deformation of a rotating-inclined Euler beam at constant angular velocity are analyzed. In this analysis, the authors take into account the corotational finite element method combined with the floating frame method.

In the paper entitled *“Interior noise prediction of the automobile based on hybrid FE-SEA method,”* a hybrid FE-SEA method (where FE stands for Finite Element and SEA stands for Statistical Energy Analysis) is employed to predict the interior noise of the automobile in the low- and middle-frequency band in the design and development stage. This is based on the prediction of parameters, which include modal density, damping loss factor and coupling loss factor, and excitations, which incorporate sound excitation of engine cabin, excitation of engine mounts, excitation of road roughness, and wind excitations.

In the paper entitled *“A new reduced stabilized mixed finite-element method based on proper orthogonal decomposition for the transient Navier-Stokes equation,”* a reduced stabilized mixed finite element (RSMFE) formulation based on proper orthogonal decomposition (POD) for the transient Navier Stokes equations is presented. In this case, by combining the POD with the SMFE formulation, a new low dimensional and highly accurate SMFE method for the transient Navier Stokes equations is obtained, which not only reduces the degrees of freedom but also circumvents the constraint of inf-sup stability condition.

In the paper entitled *“A fully discrete Galerkin method for a nonlinear space-fractional diffusion equation,”* a fully discrete scheme for a type of nonlinear space-fractional anomalous advection-diffusion equation is presented, where, in the spatial direction, the finite element method is used, whereas, in the temporal direction, the modified Crank-Nicolson approximation is employed.

In the paper entitled *“A numerical treatment of nondimensional form of water quality model in a nonuniform flow stream using Saul’yev scheme,”* mathematical models are used to simulate pollution due to sewage effluent and a finite difference scheme for solving the advection-dispersion-reaction equations (ADRE) of the uniform flow model is considered, as well as the effect of nonuniform water flows in a stream.

Finally, in the paper entitled *“Modeling and simulation of fiber orientation in injection molding of polymer composites,”* the fundamental modeling and numerical simulation for a prediction of fiber orientation during injection molding process of polymer composite is reviewed. In general, the simulation of fiber orientation involves coupled analysis of flow, temperature, moving-free surface, and fiber kinematics. Therefore, coupled numerical methods are needed to analyze these complex problems. Thus, in this last paper, several well-established methods, such as the finite-element/finite-different hybrid scheme for the Hele-Shaw

flow model and the finite element method for the general three-dimensional flow model, are reviewed.

*Delfim Soares Jr.*

*Otto von Estorff*

*Jan Sladek*

*Luis Godinho*

## *Research Article*

# **Stress Analysis of Three-Dimensional Media Containing Localized Zone by FEM-SGBEM Coupling**

**Jaroon Rungamornrat and Sakravee Sripirom**

*Department of Civil Engineering, Faculty of Engineering, Chulalongkorn University, Bangkok 10330, Thailand*

Correspondence should be addressed to Jaroon Rungamornrat, jaroon.r@chula.ac.th

Received 24 May 2011; Accepted 5 August 2011

Academic Editor: Delfim Soares Jr.

Copyright © 2011 J. Rungamornrat and S. Sripirom. This is an open access article distributed under the Creative Commons Attribution License, which permits unrestricted use, distribution, and reproduction in any medium, provided the original work is properly cited.

This paper presents an efficient numerical technique for stress analysis of three-dimensional infinite media containing cracks and localized complex regions. To enhance the computational efficiency of the boundary element methods generally found inefficient to treat nonlinearities and non-homogeneous data present within a domain and the finite element method (FEM) potentially demanding substantial computational cost in the modeling of an unbounded medium containing cracks, a coupling procedure exploiting positive features of both the FEM and a symmetric Galerkin boundary element method (SGBEM) is proposed. The former is utilized to model a finite, small part of the domain containing a complex region whereas the latter is employed to treat the remaining unbounded part possibly containing cracks. Use of boundary integral equations to form the key governing equation for the unbounded region offers essential benefits including the reduction of the spatial dimension and the corresponding discretization effort without the domain truncation. In addition, all involved boundary integral equations contain only weakly singular kernels thus allowing continuous interpolation functions to be utilized in the approximation and also easing the numerical integration. Nonlinearities and other complex behaviors within the localized regions are efficiently modeled by utilizing vast features of the FEM. A selected set of results is then reported to demonstrate the accuracy and capability of the technique.

## **1. Introduction**

A physical modeling of three-dimensional solid media by an idealized mathematical domain that occupies the full space is standard and widely used when inputs and responses of interest are only localized in a zone with its length scale much smaller than that of the body. Influence of the remote boundary of a domain on such responses is generally insignificant for this particular case and can, therefore, be discarded in the modeling without loss of accuracy of the predicted solutions. Such situations arise in various engineering applications



such as the simulation of crack growth in hydraulic fracturing process in which the fracture is generally treated as an isolated crack in an infinite medium, the evaluation and assessment of service life of large-scale structures in which the influence of embedded initial defects can be characterized by small pre-existing flaws, and the determination of effective properties of materials possessing a microstructure such as cracks, voids, inclusions, and localized inelastic zones. Unlike the stress analysis of linear elasticity problems, complexity of a mathematical model can substantially increase when an infinite body contains additionally a line of singularity and/or a localized nonlinear region. The former situation arises naturally when a surface of displacement discontinuities (e.g., cracks and dislocations) is present whereas the latter may result from applications of high-intensity loads, complex constitutive laws, containment of small defects and inhomogeneities, and localized non-mechanical effects (such as temperature change). Besides various practical applications, such present complexity renders the modeling itself theoretically and computationally challenging.

Various analytical techniques (e.g., integral transform methods, methods based on stress and displacement representations, techniques related to potential theories, etc.) have been proposed and used extensively in the stress analysis of solid media (e.g., [1–5]). However, their applications are very limited to either two-dimensional boundary value problems involving simple data or three-dimensional problems with extremely idealized settings. Such limitation becomes more apparent when complexity of involved physical phenomena increases (e.g., complexity introduced by the presence of material nonlinearities, inhomogeneities, and embedded singularities). For those particular situations, a more sophisticated mathematical model is generally required in order to accurately predict responses of interest, and, as a major consequence, an analytical or closed-form solution of the corresponding boundary value problem cannot readily be obtained and numerical techniques offer better alternatives in the solution procedure.

The finite element method (FEM) and the boundary element method (BEM) are two robust numerical techniques extensively used in the modeling of various field problems. Both techniques possess a wide range of applications, and there are various situations that favor the FEM over the BEM and vice versa. The FEM has proven to be an efficient and powerful method for modeling a broad class of problems in structural and solid mechanics (e.g., [6–8]). In principle, the basis of the FEM is sufficiently general allowing both nonlinearities and inhomogeneities present within the domain to be treated. In addition, a final system of discrete algebraic equations resulting from this method possesses, in general, desirable properties (e.g., symmetry, sparseness, positive definiteness of the coefficient matrix, etc.). Nevertheless, the conventional FEM still exhibits some major shortcomings and requires nontrivial treatments when applied to certain classes of problems. For instance, a standard discretization procedure cannot directly be applied to boundary value problems involving an infinite domain. A domain truncation supplied by a set of remote boundary conditions is commonly employed to establish an approximate domain of finite dimensions prior to the discretization. It should be noted that defining such suitable truncated surface and corresponding boundary conditions remains the key issue and it can significantly influence the quality of approximate solutions. Another limited capability of the method to attain adequately accurate results with reasonably cheap computational cost is apparent when it is applied to solve fracture problems. In the analysis, it generally requires substantially fine meshes in a region surrounding the crack front in order to accurately capture the complex (singular) field and extract essential local fracture information such as the stress intensity factors (e.g., [9–11]).

The boundary element method (BEM) has been found computationally efficient and attractive for modeling certain classes of linear boundary value problems since, for



a homogeneous domain that is free of distributed sources, the key governing equation involves only integrals on the boundary of the domain (e.g., [12–23]). As a direct consequence, the discretization effort and cost are significantly reduced, when compared to the FEM, due to the reduction of spatial dimensions of the governing equation by one. Another apparent advantage of the method is associated with its simplicity in the modeling of an infinite media. In such particular situation, the remote boundary of the domain can basically be discarded without loss via an appropriate treatment of remote conditions (e.g., [14, 17, 19, 23]). Among various strategies utilized to form the BEM, the weakly singular symmetric Galerkin boundary element method (SGBEM) has become a well-established and well-known technique and, during the past two decades, has proven robust for three-dimensional analysis of linear elasticity problems (e.g., [15, 16]), linearly elastic infinite media containing isolated cracks (e.g., [14, 19, 23]), and cracks in finite bodies (e.g., [16, 18, 20, 21, 23]). Superior features of this particular technique over other types of the BEM are due mainly to that all kernels appearing in the governing integral equations are only weakly singular of  $\mathcal{O}(1/r)$  and that a final system of linear algebraic equations resulting from the discretization possesses a symmetric coefficient matrix. The weakly singular nature not only renders all involved integrals to be interpreted in an ordinary sense and evaluated numerically using standard quadrature but also allows standard  $C^0$  interpolation functions to be employed in the approximation procedure. It has been also demonstrated that the weakly singular SGBEM along with the proper enrichment of an approximate field near the crack front yields highly accurate fracture data (e.g., mixed-mode stress intensity factors) even that relatively coarse meshes are employed in the discretization (e.g., [18, 21, 23]). While the weakly singular SGBEM has gained significant success in the analysis of linear elasticity and fracture problems, the method still contains certain unfavorable features leading to its limited capability to solve various important classes of boundary value problems. For instance, the method either becomes computationally inefficient or experiences mathematical difficulty when applied to solve problems involving nonlinearity and nonhomogeneous media. As the geometry of the domain becomes increasingly complex and its size and surface to volume ratio are relatively large (requiring a large number of elements to reasonably represent the entire boundary of the domain), the method tends to consume considerable computational resources in comparison with the standard FEM. Although the SGBEM yields a symmetric system of linear equations, the coefficient matrix is fully dense and each of its entries must be computed by means of a double surface integration.

In the past two decades, various investigators have seriously attempted to develop efficient and accurate numerical procedures for analysis of elasticity and fracture problems by exploiting positive features of both the BEM and the FEM. The fundamental idea is to decompose the entire domain into two regions and then apply the BEM to model a linearly elastic region with small surface-to-volume ratio and possibly containing the displacement discontinuities (e.g., cracks and dislocations) and the FEM to model the remaining majority of the domain possibly exhibiting complex behavior (e.g., material nonlinearity and nonhomogeneous data). The primary objective is to compromise between the requirement of computational resources and accuracy of predicted results. Within the context of linear elasticity, there have been several investigations directed towards the coupling of the conventional BEM and the standard FEM (e.g., [24–26]) and the coupling of the strongly singular SGBEM and the standard FEM (e.g., [27–30]). It should be emphasized that the former type of coupling procedure generally destroys the desirable symmetric feature of the entire system of linear algebraic equations whereas the latter type requires special numerical treatment of strongly and hyper singular integrals (e.g., [31, 32]). Extensive review

of various types of coupling between boundary integral equation methods and finite element techniques can be found in [33]. Among those existing techniques, a particular symmetric coupling strategy between the weakly singular SGBEM and the standard FEM has been found computationally efficient and has recently become an attractive alternative for performing comprehensive stress and fracture analysis. This is due primarily to (i) the symmetry feature of the SGBEM that leads to the symmetric coupling formulation and (ii) the weakly singular nature of all involved boundary integrals requiring simpler theoretical and numerical treatment in comparison with strongly singular and hypersingular integrals. Xiao [16] first presented such coupling formulation for cracks in isotropic, linearly elastic finite bodies; more precisely, a pair of weakly singular, weak-form displacement and traction integral equations was utilized along with the principle of virtual work and the proper enforcement of continuity conditions on the interface to establish the symmetric coupling formulation. Later, Frangi and Novati [34] successfully implemented Xiao's formulation to analyze cracked bodies subjected to pure traction boundary conditions. Besides its accuracy and robustness, the technique was still restricted to the conforming discretization of the interface between the two regions. Springhetti et al. [35] relaxed such limitation by allowing the weak enforcement of continuity across the interface and also generalized the technique to treat both potential and elastostatic problems. Nevertheless, their main focus is on uncracked bodies made of linearly isotropic materials. Recently, Rungamornrat and Mear [36] extended the work of Xiao [16] to enable the treatment of both material anisotropy and nonmatching interface. While this particular coupling scheme has been well-established for decades, on the basis of an extensive literature survey, applications of this technique to model a problem of an infinite space containing isolated cracks and localized complex zones have not been recognized.

In this paper, a numerical procedure based on the symmetric coupling between the weakly singular SGBEM and the standard FEM is implemented to perform three-dimensional stress analysis of an infinite medium containing displacement discontinuities and localized complex zones. Vast features of the FEM are exploited to allow the treatment of very general localized zones, for instance, those exhibiting material nonlinearity, material nonuniformity, and other types of complexity. The weakly singular SGBEM is utilized to readily and efficiently model the remaining unbounded region. A pair of weakly singular boundary integral equations proposed by Rungamornrat and Mear [22] is employed as a basis for the development of SGBEM, and this, therefore, allows the treatment of the unbounded region that is made of an anisotropic linearly elastic material and contains cracks. It is worth emphasizing that while the present study is closely related to the work of Frangi and Novati [34], Springhetti et al. [35], and Rungamornrat and Mear [36], the proposed technique offers additional crucial capabilities to treat an infinite domain, material nonlinearity in localized zones, and general material anisotropy. Following sections of this paper present basic equations and the coupling formulation, essential components for numerical implementations, numerical results and discussions, and conclusions and useful remarks.

## 2. Formulation

Consider a three-dimensional infinite medium, denoted by  $\Omega$ , containing a crack and a localized complex zone as shown schematically in Figure 1(a). The crack is represented by two geometrical coincident surfaces  $S_C^+$  and  $S_C^-$  with their unit outward normal being denoted by  $\mathbf{n}^+$  and  $\mathbf{n}^-$ , respectively, and the localized complex zone is denoted by  $\Omega^L$ . In the present study, the medium is assumed to be free of a body force and loading on its remote boundary, and both surfaces of the crack are subjected to prescribed self-equilibrated traction defined by

$\mathbf{t}_C = \mathbf{t}_C^+ = -\mathbf{t}_C^-$ . Now, let us introduce an imaginary surface  $S_I$  to decompose the body  $\Omega$  into two subdomains, an unbounded “BEM-region” denoted by  $\Omega^B$  and a finite “FEM-region” denoted by  $\Omega^F$ , as indicated in Figure 1(b). The surface  $S_I$  is selected such that the localized complex zone and the crack are embedded entirely in the FEM-region and in the BEM-region, respectively (i.e.,  $S_C^+ \cup S_C^- \subset \Omega^B$  and  $\Omega^L \subset \Omega^F$ ), and, in addition, the BEM-region must be linearly elastic. To clearly demonstrate the role of the interface between the two subregions in the formulation presented below, we define  $\{S_{BI}, \mathbf{t}_{BI}, \mathbf{u}_{BI}\}$  and  $\{S_{FI}, \mathbf{t}_{FI}, \mathbf{u}_{FI}\}$  as the interface, the unknown traction, and the unknown displacement on the interface of the BEM-region  $\Omega^B$  and the FEM-region  $\Omega^F$ , respectively. It is important to emphasize that the interfaces  $S_{BI}$  and  $S_{FI}$  are in fact identical to the imaginary surface  $S_I$ . While the formulation is presented, for brevity, only for a domain containing a single crack and a single localized complex zone, it can readily be extended to treat multiple cracks and multiple complex zones; in such particular case, multiple FEM-regions are admissible.

## 2.1. Governing Equations for $\Omega^B$

The total boundary of the BEM-region  $\Omega^B$ , denoted by  $S_B$ , consists of the reduced crack surface  $S_{BC} \equiv S_C^+$  on which the traction is fully prescribed and the interface  $S_{BI}$  where neither the traction nor the displacement is known a priori. Note again that the subscript “B” is added only to emphasize that those surfaces are associated with the BEM-region. To form a set of governing integral equations for this region, a pair of weakly singular, weak-form displacement and traction boundary integral equations developed by Rungamornrat and Mear [22] is employed. These two integral equations were derived from standard boundary integral relations for the displacement and stress along with a systematic regularization technique. The final form of completely regularized integral equations is well suited for establishing the symmetric formulation for the weakly singular SGBEM. Such pair of integral equations is given here, for convenience in further reference, by

$$\begin{aligned} \frac{1}{2} \int_{S_{BI}} \tilde{t}_k(\mathbf{y}) u_k(\mathbf{y}) dS(\mathbf{y}) &= \int_{S_{BI}} \tilde{t}_k(\mathbf{y}) \int_{S_{BI}} U_i^k(\boldsymbol{\xi} - \mathbf{y}) t_i(\boldsymbol{\xi}) dS(\boldsymbol{\xi}) dS(\mathbf{y}) \\ &+ \int_{S_{BI}} \tilde{t}_k(\mathbf{y}) \int_{S_B} G_{mj}^k(\boldsymbol{\xi} - \mathbf{y}) D_m v_j(\boldsymbol{\xi}) dS(\boldsymbol{\xi}) dS(\mathbf{y}) \\ &- \int_{S_{BI}} \tilde{t}_k(\mathbf{y}) \int_{S_B} n_i(\boldsymbol{\xi}) H_{ij}^k(\boldsymbol{\xi} - \mathbf{y}) v_j(\boldsymbol{\xi}) dS(\boldsymbol{\xi}) dS(\mathbf{y}), \end{aligned} \quad (2.1)$$

$$\begin{aligned} - \int_{S_B} c(\mathbf{y}) \tilde{v}_k(\mathbf{y}) t_k(\mathbf{y}) dS(\mathbf{y}) &= \int_{S_B} D_i \tilde{v}_k(\mathbf{y}) \int_{S_{BI}} G_{ik}^j(\boldsymbol{\xi} - \mathbf{y}) t_j(\boldsymbol{\xi}) dS(\boldsymbol{\xi}) dS(\mathbf{y}) \\ &+ \int_{S_B} D_i \tilde{v}_k(\mathbf{y}) \int_{S_B} C_{mj}^{ik}(\boldsymbol{\xi} - \mathbf{y}) D_m v_j(\boldsymbol{\xi}) dS(\boldsymbol{\xi}) dS(\mathbf{y}) \\ &+ \int_{S_B} \tilde{v}_k(\mathbf{y}) \int_{S_{BI}} n_l(\mathbf{y}) H_{lk}^j(\boldsymbol{\xi} - \mathbf{y}) t_j(\boldsymbol{\xi}) dS(\boldsymbol{\xi}) dS(\mathbf{y}), \end{aligned} \quad (2.2)$$

where  $\tilde{t}_k$  and  $\tilde{v}_k$  are sufficiently smooth test functions;  $D_m(\cdot) = n_i \varepsilon_{ism} \partial(\cdot) / \partial \xi_s$  is a surface differential operator with  $\varepsilon_{ism}$  denoting a standard alternating symbol;  $v_j(\boldsymbol{\xi}) = u_j(\boldsymbol{\xi})$  for  $\boldsymbol{\xi} \in S_{BI}$  and  $\Delta u_j(\boldsymbol{\xi})$  for  $\boldsymbol{\xi} \in S_{BC}$  with  $\Delta u_j(\boldsymbol{\xi}) = u_j^+(\boldsymbol{\xi}) - u_j^-(\boldsymbol{\xi})$  denoting the jump in

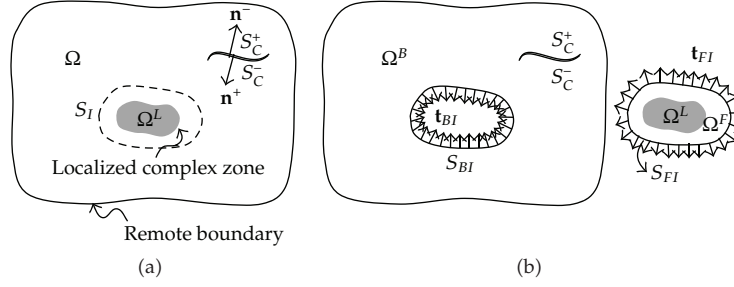


**Figure 1:** (a) Schematic of three-dimensional infinite medium containing crack and localized complex zone and (b) schematic of BEM-region  $\Omega^B$  and FEM-region  $\Omega^F$ .

the displacement across the crack surface; the geometry-dependent constant  $c(\mathbf{y})$  is defined by  $c(\mathbf{y}) = 1/2$  for  $\xi \in S_{BI}$  and 1 for  $\xi \in S_{BC}$ . All involved kernels, that is,  $H_{ij}^p(\xi - \mathbf{y})$ ,  $U_i^p(\xi - \mathbf{y})$ ,  $G_{mj}^p(\xi - \mathbf{y})$ ,  $C_{mj}^{tk}(\xi - \mathbf{y})$ , are given, for generally anisotropic materials, by

$$H_{ij}^p(\xi - \mathbf{y}) = -\frac{(\xi_i - y_i)\delta_{pj}}{4\pi r^3}, \quad (2.3)$$

$$U_i^p(\xi - \mathbf{y}) = K_{mp}^{mi}(\xi - \mathbf{y}), \quad (2.4)$$

$$G_{mj}^p(\xi - \mathbf{y}) = \varepsilon_{abm}E_{ajdc}K_{cp}^{bd}(\xi - \mathbf{y}), \quad (2.5)$$

$$C_{mj}^{tk}(\xi - \mathbf{y}) = A_{mjdn}^{tkoe}K_{dn}^{oe}(\xi - \mathbf{y}), \quad (2.6)$$

where  $\delta_{pj}$  is a standard Kronecker-delta symbol;  $E_{ijkl}$  are elastic moduli;  $A_{mjdn}^{tkoe}$  and  $K_{jl}^{ik}(\xi - \mathbf{y})$  are defined by

$$A_{mjdn}^{tkoe} = \varepsilon_{pam}\varepsilon_{pbt}\left(E_{bknd}E_{ajeo} - \frac{1}{3}E_{ajkb}E_{dneo}\right), \quad (2.7)$$

$$K_{jl}^{ik}(\xi - \mathbf{y}) = \frac{1}{8\pi^2 r} \oint_{\mathbf{z} \cdot \mathbf{r} = 0} (\mathbf{z}, \mathbf{z})_{kl}^{-1} z_i z_j ds(\mathbf{z}), \quad (2.8)$$

in which  $\mathbf{r} = \xi - \mathbf{y}$ ,  $r = \|\mathbf{r}\|$ ,  $(\mathbf{z}, \mathbf{z})_{jk} = z_i E_{ijkl} z_l$  and the closed contour integral is to be evaluated over a unit circle  $\|\mathbf{z}\| = 1$  on a plane defined by  $\mathbf{z} \cdot \mathbf{r} = 0$ . It is evident that the kernel  $H_{ij}^p(\xi - \mathbf{y})$  is given in an explicit form independent of material properties and the kernels  $n_i(\xi)H_{ij}^p(\xi - \mathbf{y})$ ,  $n_i(\mathbf{y})H_{ij}^p(\xi - \mathbf{y})$ ,  $U_i^p(\xi - \mathbf{y})$ ,  $G_{mj}^p(\xi - \mathbf{y})$ ,  $C_{mj}^{tk}(\xi - \mathbf{y})$  are singular only at  $\xi = \mathbf{y}$  of  $\mathcal{O}(1/r)$  (see details in Xiao [16] for discussion of the singularity behavior of the kernel  $H_{ij}^p(\xi - \mathbf{y})$ ). It should be remarked that for isotropic materials, the kernels  $U_i^p(\xi - \mathbf{y})$ ,  $G_{mj}^p(\xi - \mathbf{y})$ ,  $C_{mj}^{tk}(\xi - \mathbf{y})$  possess an explicit form in terms of elementary functions (see [18, 22]).

Towards obtaining a system of governing integral equations for the BEM-region  $\Omega^B$ , the weak-form boundary integral equation for the traction (2.2) is applied directly to the crack surface  $S_{BC}$  (with the test function being chosen such that  $\tilde{\mathbf{v}} = 0$  on  $S_{BI}$ ) and to

the interface  $S_{BI}$  (with the test function being chosen such that  $\tilde{\mathbf{v}} = 0$  on  $S_{BC}$ ), and the weak-form boundary integral equation for the displacement (2.1) is applied only to the interface  $S_{BI}$ . A final set of three integral equations is given concisely by

$$\begin{aligned}\mathcal{A}_{CC}(\tilde{\mathbf{v}}, \Delta \mathbf{u}) + \mathcal{B}_{IC}(\mathbf{t}_{BI}, \tilde{\mathbf{v}}) + \mathcal{A}_{CI}(\tilde{\mathbf{v}}, \mathbf{u}_{BI}) &= -2\mathcal{F}_{BC}(\tilde{\mathbf{v}}, \mathbf{t}_C), \\ \mathcal{B}_{IC}(\tilde{\mathbf{t}}_{BI}, \Delta \mathbf{u}) + \mathcal{C}_{II}(\tilde{\mathbf{t}}_{BI}, \mathbf{t}_{BI}) + \mathcal{D}_{II}(\tilde{\mathbf{t}}_{BI}, \mathbf{u}_{BI}) &= 0, \\ \mathcal{A}_{IC}(\tilde{\mathbf{u}}_{BI}, \Delta \mathbf{u}) + \mathcal{D}_{II}(\mathbf{t}_{BI}, \tilde{\mathbf{u}}_{BI}) + \mathcal{A}_{II}(\tilde{\mathbf{u}}_{BI}, \mathbf{u}_{BI}) &= -2\mathcal{F}_{BI}(\tilde{\mathbf{u}}_{BI}, \mathbf{t}_{BI}),\end{aligned}\quad (2.9)$$

where  $\{\tilde{\mathbf{u}}_{BI}, \tilde{\mathbf{t}}_{BI}\}$  are test functions defined on the interface  $S_{BI}$  and all involved bilinear integral operators are defined, with subscripts  $P, Q \in \{I, C\}$  being introduced to clearly indicate the surface of integration, by

$$\mathcal{A}_{PQ}(\mathbf{X}, \mathbf{Y}) = \int_{S_{BP}} D_i X_k(\mathbf{y}) \int_{S_{BQ}} C_{mj}^{tk}(\xi - \mathbf{y}) D_m Y_j(\xi) dS(\xi) dS(\mathbf{y}), \quad (2.10)$$

$$\begin{aligned}\mathcal{B}_{IP}(\mathbf{X}, \mathbf{Y}) &= \int_{S_{BI}} X_k(\mathbf{y}) \int_{S_{BP}} G_{mj}^k(\xi - \mathbf{y}) D_m Y_j(\xi) dS(\xi) dS(\mathbf{y}) \\ &\quad - \int_{S_{BI}} X_k(\mathbf{y}) \int_{S_{BP}} n_m(\xi) H_{mj}^k(\xi - \mathbf{y}) Y_j(\xi) dS(\xi) dS(\mathbf{y}),\end{aligned}\quad (2.11)$$

$$\mathcal{C}_{II}(\mathbf{X}, \mathbf{Y}) = \int_{S_{BI}} X_k(\mathbf{y}) \int_{S_{BI}} U_i^k(\xi - \mathbf{y}) Y_i(\xi) dS(\xi) dS(\mathbf{y}), \quad (2.12)$$

$$\mathcal{F}_{BP}(\mathbf{X}, \mathbf{Y}) = \frac{1}{2} \int_{S_{BP}} X_i(\mathbf{y}) Y_i(\mathbf{y}) dS(\mathbf{y}), \quad (2.13)$$

$$\mathcal{D}_{II}(\mathbf{X}, \mathbf{Y}) = \mathcal{B}_{II}(\mathbf{X}, \mathbf{Y}) - \mathcal{F}_{BI}(\mathbf{X}, \mathbf{Y}). \quad (2.14)$$

It should be noted that the linear operator  $\mathcal{A}_{PQ}(\mathbf{X}, \mathbf{Y})$  is in a symmetric form satisfying the condition  $\mathcal{A}_{PQ}(\mathbf{X}, \mathbf{Y}) = \mathcal{A}_{QP}(\mathbf{Y}, \mathbf{X})$ , and, as a consequence, it renders the left hand side of the system (2.9) being in a symmetric form. Although such symmetric formulation can readily be obtained, the right-hand side of (2.9) still contains the unknown traction on the interface  $\mathbf{t}_{BI}$ . The treatment of a term  $\mathcal{F}_{BI}(\tilde{\mathbf{u}}_{BI}, \mathbf{t}_{BI})$  will be addressed once the formulation for the FEM-region  $\Omega^F$  is established.

## 2.2. Governing Equations for $\Omega^F$

Let us consider, next, the FEM-region  $\Omega^F$ . For generality, the entire boundary of this particular region can be decomposed into two surfaces: the interface  $S_{FI}$  on which both the traction  $\mathbf{t}_{FI}$  and the displacement  $\mathbf{u}_{FI}$  are unknown a priori and the surface  $S_{FT}$  on which the traction  $\mathbf{t}_{FT}$  is fully prescribed. The existence of the surface  $S_{FT}$  is apparent for the case that the FEM-region contains embedded holes or voids. It is also important to emphasize that, in the development of a key governing equation for  $\Omega^F$ , the traction  $\mathbf{t}_{FI}$  is treated, in a fashion different from that for the BEM-region, as unknown data instead of the primary unknown variable. In addition, to be capable of modeling a complex localized

zone embedded within the FEM-region, a constitutive model governing the material behavior utilized in the present study is assumed to be sufficiently general allowing the treatment of material nonlinearity, anisotropy, and inhomogeneity. The treatment of such complex material models has been extensively investigated and well established within the context of nonlinear finite element methods (e.g., [6, 37, 38]), and those standard procedures also apply to the current implementation and will not be presented for brevity. Here, we only outline the key governing equation for the FEM-region and certain unknowns and necessary data connected to those for the BEM-region.

Following standard formulation of the finite element technique, the weak-form equation governing the FEM-region can readily be obtained via the principle of virtual work [6–8] and the final equation can be expressed in a concise form by

$$\mathcal{K}_{FF}(\tilde{\mathbf{u}}, \boldsymbol{\sigma}) = 2\mathfrak{F}_{FI}(\tilde{\mathbf{u}}_{FI}, \mathbf{t}_{FI}) + 2\mathfrak{F}_{FT}(\tilde{\mathbf{u}}_{FT}, \mathbf{t}_{FT}), \quad (2.15)$$

where  $\boldsymbol{\sigma}$  is a stress tensor;  $\tilde{\mathbf{u}}$  is a suitably well-behaved test function defined over the domain  $\Omega^F$ ;  $\tilde{\mathbf{u}}_{FI}$  and  $\tilde{\mathbf{u}}_{FT}$  are the restriction of  $\tilde{\mathbf{u}}$  on the interface  $S_{FI}$  and boundary  $S_{FT}$ , respectively; the integral operators are defined, with subscripts  $P \in \{I, T\}$ , by

$$\mathcal{K}_{FF}(\tilde{\mathbf{u}}, \boldsymbol{\sigma}) = \int_{\Omega^F} \tilde{\varepsilon}_{ij}(\mathbf{y}) \sigma_{ij}(\mathbf{y}) dV(\mathbf{y}), \quad (2.16)$$

$$\mathfrak{F}_{FP}(\mathbf{X}, \mathbf{Y}) = \frac{1}{2} \int_{S_{FP}} X_i(\mathbf{y}) Y_i(\mathbf{y}) dS(\mathbf{y}), \quad (2.17)$$

in which  $\tilde{\varepsilon}_{ij}(\mathbf{y})$  denotes the virtual strain tensor defined by  $\tilde{\varepsilon}_{ij}(\mathbf{y}) = (\partial \tilde{u}_i / \partial y_j + \partial \tilde{u}_j / \partial y_i) / 2$ . Note again that a function form of the stress tensor in terms of the primary unknown depends primarily on a constitutive model employed. For a special case of the FEM-region being made of a homogeneous, linearly elastic material, the stress tensor can be expressed directly and explicitly in terms of elastic constants  $E_{ijkl}$  and the strain tensor  $\boldsymbol{\varepsilon}$  (i.e.,  $\sigma_{ij} = E_{ijkl} \varepsilon_{kl}$ ), and, within the context of an infinitesimal deformation theory (i.e.,  $\varepsilon_{ij}(\mathbf{y}) = (\partial u_i / \partial y_j + \partial u_j / \partial y_i) / 2$ ), the integral operator  $\mathcal{K}_{FF}$  can be expressed directly in terms of the displacement  $\mathbf{u}$  as

$$\mathcal{K}_{FF}(\tilde{\mathbf{u}}, \mathbf{u}) = \int_{\Omega^F} \tilde{u}_{i,j}(\mathbf{y}) E_{ijkl} u_{k,l}(\mathbf{y}) dV(\mathbf{y}). \quad (2.18)$$

It should be remarked that the factor of one half in the definition (2.17) has been introduced for convenience to cast this term in a form analogous to that for  $\mathfrak{F}_{BP}$  given by (2.13), and this, as a result, leads to the factor of two appearing on the right-hand side of (2.15). It is also worth noting that the first term on the right-hand side of (2.15) still contains the unknown traction on the interface  $\mathbf{t}_{FI}$ .

### 2.3. Governing Equations for $\Omega$

A set of governing equations of the entire domain  $\Omega$  can directly be obtained by combining a set of weakly singular, weak-form boundary integral equations (2.9) and the virtual work



equation (2.15). In particular, the last equations of (2.9) and (2.15) are properly combined, and this finally leads to

$$\begin{aligned} \mathcal{A}_{CC}(\tilde{\mathbf{v}}, \Delta \mathbf{u}) + \mathcal{B}_{IC}(\mathbf{t}_{BI}, \tilde{\mathbf{v}}) + \mathcal{A}_{CI}(\tilde{\mathbf{v}}, \mathbf{u}_{BI}) &= -2\mathcal{F}_{BC}(\tilde{\mathbf{v}}, \mathbf{t}_C), \\ \mathcal{B}_{IC}(\tilde{\mathbf{t}}_{BI}, \Delta \mathbf{u}) + \mathcal{C}_{II}(\tilde{\mathbf{t}}_{BI}, \mathbf{t}_{BI}) + \mathcal{D}_{II}(\tilde{\mathbf{t}}_{BI}, \mathbf{u}_{BI}) &= 0, \\ \mathcal{A}_{IC}(\tilde{\mathbf{u}}_{BI}, \Delta \mathbf{u}) + \mathcal{D}_{II}(\mathbf{t}_{BI}, \tilde{\mathbf{u}}_{BI}) + \mathcal{A}_{II}(\tilde{\mathbf{u}}_{BI}, \mathbf{u}_{BI}) - \mathcal{K}_{FF}(\tilde{\mathbf{u}}, \sigma) &= \mathcal{E} - 2\mathcal{F}_{FT}(\tilde{\mathbf{u}}_{FT}, \mathbf{t}_{FT}), \end{aligned} \quad (2.19)$$

where  $\mathcal{E}$  is given by

$$\mathcal{E} = -2[\mathcal{F}_{BI}(\tilde{\mathbf{u}}_{BI}, \mathbf{t}_{BI}) + \mathcal{F}_{FI}(\tilde{\mathbf{u}}_{FI}, \mathbf{t}_{FI})]. \quad (2.20)$$

From the continuity of the traction and displacement across the interface of the BEM-region and FEM-region (i.e.,  $\mathbf{t}_{BI}(\mathbf{y}) + \mathbf{t}_{FI}(\mathbf{y}) = \mathbf{0}$  and  $\mathbf{u}_{BI}(\mathbf{y}) = \mathbf{u}_{FI}(\mathbf{y})$  for all  $\mathbf{y} \in S_I = S_{BI} = S_{FI}$ ), the test functions  $\tilde{\mathbf{u}}_{BI}$  and  $\tilde{\mathbf{u}}$  are chosen such that  $\tilde{\mathbf{u}}_{BI}(\mathbf{y}) = \tilde{\mathbf{u}}_{FI}(\mathbf{y})$  for all  $\mathbf{y} \in S_I = S_{BI} = S_{FI}$  and, as a direct consequence,  $\mathcal{E}$  identically vanishes. It is therefore evident that the right-hand side of (2.19) involves only prescribed boundary data, and, in addition, if the integral operator  $\mathcal{K}_{FF}$  possesses a symmetric form, (2.19) constitutes a symmetric formulation for the boundary value problem currently treated.

### 3. Numerical Implementation

This section briefly summarizes numerical procedures adopted to construct approximate solutions of a set of governing equations (2.19) and to postprocess certain quantities of interest. The discretization of the BEM-region and the FEM-region is first discussed. Then, components essential for numerical evaluation of weakly singular and nearly singular double-surface integrals, evaluations of kernels, and determination of general mixed-mode stress intensity factors are addressed. Finally, the key strategy for establishing the coupling between the in-house weakly singular SGBEM code and the reliable commercial finite element package is discussed.

#### 3.1. Discretization

Standard Galerkin strategy is adopted to construct an approximate solution of the governing equation (2.19). For the BEM-region  $\Omega^B$ , only the crack surface  $S_{BC}$  and the interface  $S_{BI}$  need to be discretized. In such discretization, standard isoparametric  $C^0$  elements (e.g., 8-node quadrilateral and 6-node triangular elements) are employed throughout except along the crack front where special 9-node crack-tip elements are employed to accurately capture the asymptotic field near the singularity zone. Shape functions of these special elements are properly enriched by square root functions, and, in addition, extra degrees of freedom are introduced along the element boundary adjacent to the crack front to directly represent the gradient of the relative crack-face displacement [18, 21, 23]. These positive features also enable the calculation of the mixed-mode stress intensity factors (i.e., mode-I, mode-II, and mode-III stress intensity factors) in an accurate and efficient manner with

use of reasonably coarse meshes. For the FEM-region  $\Omega^F$ , standard three-dimensional, isoparametric  $C^0$  elements (e.g., ten-node tetrahedral elements, fifteen-node prism elements, and twenty-node brick elements) are utilized throughout in the domain discretization.

It is important to note that the BEM-region and the FEM-region are discretized such that meshes on the interface of the two regions conform (i.e., the two discretized interfaces are geometrically identical). A simple means to generate those conforming interfaces is to mesh the FEM-region first and then use its surface mesh as the interface mesh of the BEM-region. With this strategy, all nodal points on both discretized interfaces are essentially coincident. The key advantage of using conforming meshes is that the strong continuity of the displacement, the traction, and the test functions across the interface can be enforced exactly, and, as a result, the condition  $\mathcal{E} = 0$  is also satisfied in the discretization level. It should be emphasized also that nodes on the interface of the BEM-region contain six degrees of freedom (i.e., three displacement degrees of freedom and three traction degrees of freedom) while nodes on the FEM-region contain only three displacement degrees of freedom.

### 3.2. Numerical Integration

For the FEM-region, all integrals arising from the discretization of the weak-form equation contain only regular integrands, and, as a result, they can be efficiently and accurately integrated by standard Gaussian quadrature. On the contrary, numerical evaluation of integrals arising from the discretization of the BEM-region is nontrivial since it involves the treatment of three types of double surface integrals (i.e., regular integrals, weakly singular integrals, and nearly singular integrals). The regular double surface integral arises when it involves a pair of remote outer and inner elements (i.e., the distance between any source and field points is relatively large when compared to the size of the two elements). This renders its integrand nonsingular and well-behaved and, as a result, allows the integral to be accurately and efficiently integrated by standard Gaussian quadrature.

The weakly singular double surface integral arises when the outer surface of integration is the same as the inner surface. For this particular case, the source and field points can be identical and this renders the integrand singular of order  $1/r$ . While the integral of this type exists in an ordinary sense, it was pointed out by Xiao [16] that the numerical integration by Gaussian quadrature becomes computationally inefficient and such inaccurate evaluation can significantly pollute the quality of approximate solutions. To circumvent this situation, a series of transformations such as a well-known triangular polar transformation and a logarithmic transformation is applied first both to remove the singularity and to regularize the rapid variation of the integrand. The final integral contains a nonsingular integrand well suited to be integrated by Gaussian quadrature. Details of this numerical quadrature can be found in [16, 39, 40].

The most challenging task is to compute nearly singular integrals involving relatively close or adjacent inner and outer elements. Although the integrand is not singular, it exhibits rapid variation in the zone where both source and field points are nearly identical. Such complex behavior of the integrand was found very difficult and inefficient to be treated by standard Gaussian quadrature [16]. To improve the accuracy of such quadrature, the triangular polar transformation is applied first and then a series of logarithmic transformations is adopted for both radial and angular directions to further regularize the rapid variation integrand. The resulting integral was found well-suited for being integrated by standard Gaussian quadrature [16, 40–42].



### 3.3. Evaluation of Kernels

To further reduce the computational cost required to form the coefficient matrix contributed from the BEM-region, all involved kernels  $n_i(\xi)H_{ij}^p(\xi - \mathbf{y})$ ,  $n_i(\mathbf{y})H_{ij}^p(\xi - \mathbf{y})$ ,  $U_i^p(\xi - \mathbf{y})$ ,  $G_{mj}^p(\xi - \mathbf{y})$ ,  $C_{mj}^{tk}(\xi - \mathbf{y})$  must be evaluated in an efficient manner for any pair of source and field points  $\{\xi, \mathbf{y}\}$ . For the first two kernels  $n_i(\xi)H_{ij}^p(\xi - \mathbf{y})$  and  $n_i(\mathbf{y})H_{ij}^p(\xi - \mathbf{y})$ , they only involve the calculation of a unit normal vector  $\mathbf{n}$  and the elementary function  $H_{ij}^p$ . As a result, this task can readily be achieved via a standard procedure. For the last three kernels, the computational cost is significantly different for isotropic and anisotropic materials. For isotropic materials, such kernels only involve elementary functions and can therefore be evaluated in a straightforward fashion. On the contrary, the kernels  $U_i^p(\xi - \mathbf{y})$ ,  $G_{mj}^p(\xi - \mathbf{y})$ , and  $C_{mj}^{tk}(\xi - \mathbf{y})$  for general anisotropy are expressed in terms of a line integral over a unit circle (see (2.4)–(2.6), and (2.8)). Direct evaluation of such line integral for every pair of points  $(\xi, \mathbf{y})$  arising from the numerical integration is obviously computationally expensive. To avoid this massive computation, a well-known interpolation technique (e.g., [21, 23, 36]) is adopted to approximate values of those kernels. Specifically, the interpolant of each kernel is formed based on a two-dimensional grid using standard quadratic shape functions. Values of kernels at all grid points are obtained by performing direct numerical integration of the line integral (2.8) via Gaussian quadrature and then using the relations (2.4)–(2.6). The accuracy of such approximation can readily be controlled by refining the interpolation grid.

### 3.4. Determination of Stress Intensity Factors

Stress intensity factors play an important role in linear elastic fracture mechanics in the prediction of crack growth initiation and propagation direction and also in the fatigue-life assessment. This fracture data provides a complete measure of the dominant behavior of the stress field in a local region surrounding the crack front. To obtain highly accurate stress intensity factors, we supply the developed coupling technique with two crucial components, one associated with the use of special crack-tip elements to accurately capture the near-tip field and the other corresponding to the use of an explicit formula to extract such fracture data. The latter feature is a direct consequence of the extra degrees of freedom being introduced along the crack front to represent the gradient of relative crack-face displacement. Once a discretized system of algebraic equations is solved, nodal quantities along the crack front are extracted and then postprocessed to obtain the stress intensity factors.

An explicit expression for the mixed-mode stress intensity factors in terms of nodal data along the crack front, local geometry of the crack front, and material properties can be found in the work of Li et al. [18] for cracks in isotropic media and Rungamornrat and Mear [23, 36] for cracks in general anisotropic media. In the current investigation, both formulae are implemented.

### 3.5. Coupling of SGBEM and Commercial FE Package

To further enhance the modeling capability, the weakly singular SGBEM can be coupled with a reliable commercial finite element code that supports user-defined subroutines. The key objective is to exploit available vast features of such FE package (e.g., mesh generation, user-defined elements, powerful linear and nonlinear solvers, and various material models, etc.) to treat a complex, localized FEM-region and utilize the SGBEM in-house code to supply

information associated with the majority of the domain that is unbounded and possibly contains isolated discontinuities.

In the coupling procedure, the governing equation for the BEM-region is first discretized into a system of linear algebraic equations. The corresponding coefficient matrix and the vector involving the prescribed data are constructed using the in-house code, and they can be viewed as a stiffness matrix and a load vector of a “super element” containing all degrees of freedom of the BEM-region. This piece of information is then imported into the commercial FE package via a user-defined subroutine channel and then assembled with element stiffness matrices contributed from the discretized FEM-region. Since meshes of both interfaces (one associated with the BEM-region and the other corresponding to the FEM-region) are conforming, the assembly procedure can readily be achieved by using a proper numbering strategy. Specifically, nodes on the interface of the BEM-region are named identical to nodes on the interface of the FEM-region (associated with the same displacement degrees of freedom). It is important to emphasize that all interface nodes of the BEM-region possess six degrees of freedom (i.e., three displacement degrees of freedom and three traction degrees of freedom) but there are only three (displacement) degrees of freedom per interface node of the FEM-region. To overcome such situation, each interface node of the BEM-region is fictitiously treated as double nodes where the first node is chosen to represent the displacement degrees of freedom and is numbered in the same way as its coincident interface node of the FEM-region whereas the second node is chosen with different name to represent the traction degrees of freedom. With this particular scheme, the assembling procedure follows naturally that for a standard finite element technique.

Once the coupling analysis is complete, nodal quantities associated with the BEM-region are extracted from the output file generated by the FE package and then postprocessed for quantities of interest. For instance, the displacement and stress within the BEM-region can readily be computed from the standard displacement and stress boundary integral relations [17, 22], and the stress intensity factors can be calculated using an explicit expression proposed in [18, 23].

## 4. Numerical Results and Discussion

As a means to verify both the formulation and the numerical implementations, we first carry out numerical experiments on boundary value problems in which the analytical solution exists. In the analysis, a series of meshes is adopted in order to investigate both the convergence and accuracy of the numerical solutions. Once the method is tested, it is then applied to solve more complex boundary value problems in order to demonstrate its capability and robustness. For brevity of the presentation, a selected set of results are reported and discussed as follows.

### 4.1. Isolated Spherical Void under Uniform Pressure

Consider an isolated spherical void of radius  $a$  embedded in a three-dimensional infinite medium as shown schematically in Figure 2(a). The void is subjected to uniform pressure  $\sigma_0$ . In the analysis, two constitutive models are investigated: one associated with an isotropic, linearly elastic material with Young's modulus  $E$  and Poisson ratio  $\nu = 0.3$  and the other chosen to represent an isotropic hardening material obeying  $J_2$ -flow theory of plasticity [43].

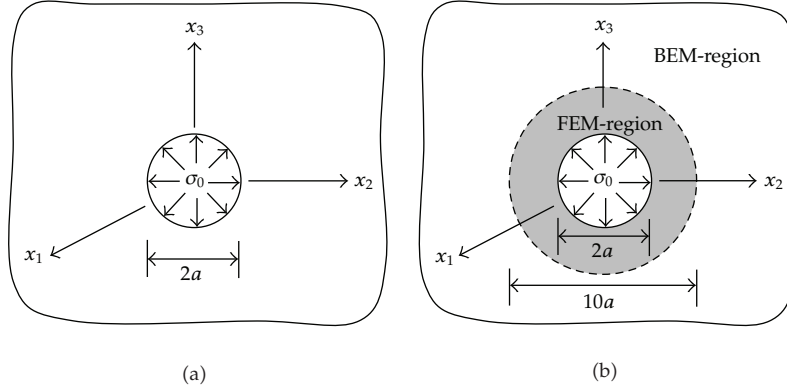


**Figure 2:** (a) Schematic of three-dimensional infinite medium containing spherical void and (b) schematic of BEM-region and FEM-region.

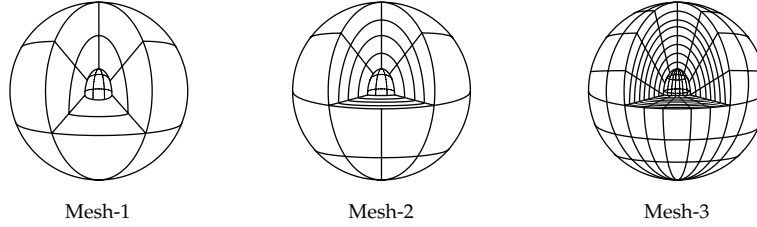


**Figure 3:** Three meshes adopted in the analysis for FEM-region; meshes for BEM-region are identical to the interface mesh of FEM-region.

For the latter material, the uniaxial stress-strain relation is assumed in a bilinear form with  $E_1$  and  $E_2$  denoting the modulus in the elastic regime and the modulus of the hardening zone, respectively, and  $\sigma_y$  and  $\varepsilon_y$  denoting the initial yielding stress and its corresponding strain, respectively.

To test the coupling technique, we first decompose the body into two regions by a fictitious spherical surface of radius  $5a$  and centered at the origin as shown by a dashed line in Figure 2(b). It is important to remark that such a surface must be chosen relatively large compared to the void to ensure that the inelastic zone that may exist (for the second constitutive model) is fully contained in the FEM-region. In the experiments, three different meshes are adopted as shown in Figure 3. Although meshes for the BEM-region are not shown, they can simply obtain from the interface meshes of the FEM-region. As clearly illustrated in the figure, mesh-1, mesh-2, and mesh-3 consist of 12, 32, 144 boundary elements and 24, 128, 1152 finite elements, respectively.

#### 4.1.1. Results for Isotropic Linearly Elastic Material

For linear elasticity, this particular boundary value problem admits the closed form solution (e.g., [44]). Since the problem is spherically symmetric, only the radial displacement  $u_r$  and the normal stress components  $\{\sigma_{rr}, \sigma_{\theta\theta}, \sigma_{\phi\phi}\}$  are nonzero and they are given explicitly by

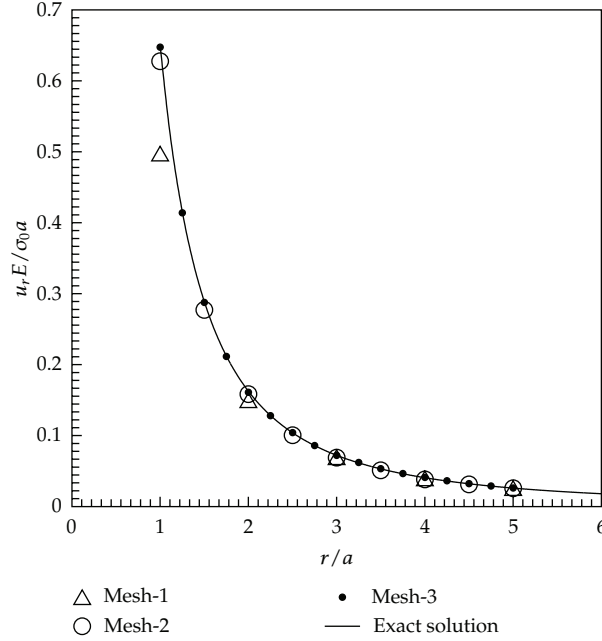


**Figure 4:** Normalized radial displacement versus normalized radial coordinate for isotropic, linearly elastic material with  $\nu = 0.3$ .

(note that these quantities are referred to a standard spherical coordinate system  $\{r, \theta, \phi\}$  with its origin located at the center of the void)

$$u_r(r) = \frac{1 + \nu}{2E} \sigma_0 \frac{a^3}{r^2}, \quad (4.1)$$

$$\sigma_{rr}(r) = -2\sigma_{\theta\theta}(r) = -2\sigma_{\phi\phi}(r) = -\sigma_0 \left(\frac{a}{r}\right)^3. \quad (4.2)$$

This analytical solution is employed as a means to validate the proposed formulation and the numerical implementation. Numerical solutions for the radial displacement obtained from the three meshes are reported and compared with the exact solution in Figure 4. As evident from this set of results, the radial displacements obtained from the mesh-2 and the mesh-3 are highly accurate with only slight difference from the exact solution while that obtained from the mesh-1 is reasonably accurate except in the region very near the surface of the void. The discrepancy of solutions observed in the mesh-1 is due to that the level of refinement is too coarse to accurately capture the geometry and responses in the local region near the surface of the void.

We further investigate the quality of numerical solutions for stresses. Since all nonzero stress components are related by (4.2), only results for the radial stress component are reported. Figure 5 shows the normalized radial stress obtained from the three meshes and the exact solution versus the normalized radial coordinate. It is observed that the mesh-3 yields results that are almost indistinguishable from the exact solution, whereas the mesh-1 and mesh-2 give accurate results for relatively large  $r$ , and the level of accuracy

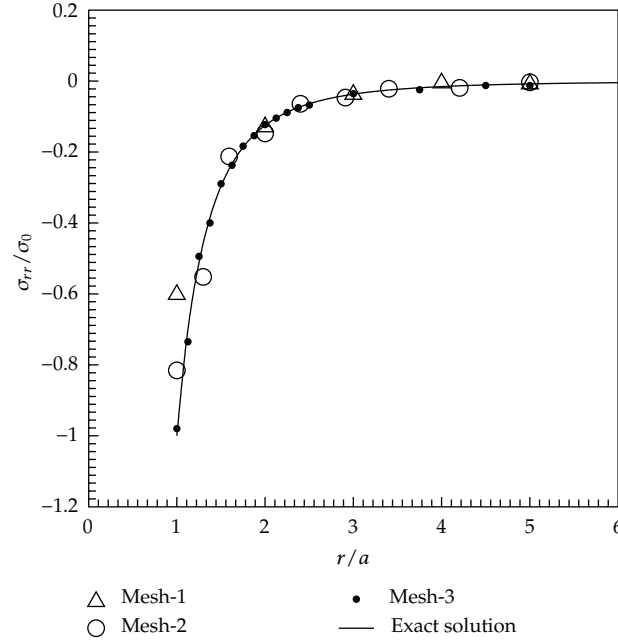


**Figure 5:** Normalized radial stress versus normalized radial coordinate for isotropic, linearly elastic material with  $\nu = 0.3$ .

decreases as the distance  $r$  approaches  $a$ . It is noted by passing that the degeneracy of the accuracy in computing stress is common in a standard, displacement-based, finite element technique.

To demonstrate the important role of the SGBEM in the treatment of an unbounded part of the domain instead of truncating the body as practically employed in the finite element modeling, we perform another FE analysis of the FEM-region alone without coupling with the BEM-region but imposing zero displacement condition at its interface. The radial displacement and the radial stress obtained for this particular case using the mesh-3 are reported along with the exact solution and those obtained from the coupling technique in Figures 6 and 7, respectively. As evident from these results, numerical solutions obtained from the FEM with a domain truncation strategy deviate from the exact solution as approaching the truncation surface while the proposed technique yields almost identical results to the exact solution. The concept of domain truncation to obtain a finite body is simple, but it still remains to choose a proper truncation surface and boundary conditions to be imposed on that surface to mimic the original boundary value problem. This coupling technique provides an alternative to treat the whole domain without any truncation and difficulty to treat the remote boundary.

#### 4.1.2. Isotropic Hardening Material

For this particular case, we focus attention to the material with no hardening modulus (i.e.,  $E_2 = 0$ ) since the corresponding boundary value problem admits the closed form solution. For a sufficiently high applied pressure  $\sigma_0$ , a layer close to the boundary of the void becomes inelastic and the size of such inelastic zone (measured by the radius  $r_0$ ) becomes larger as

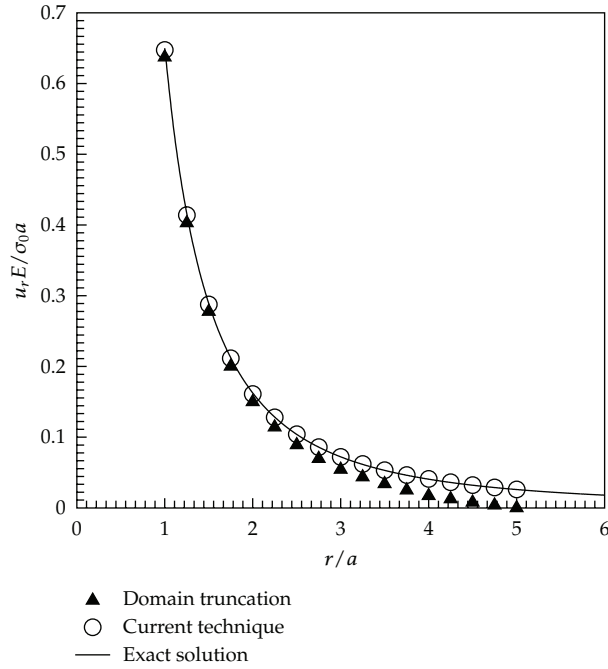


**Figure 6:** Normalized radial displacement versus normalized radial coordinate for isotropic, linearly elastic material with  $\nu = 0.3$ . Results are obtained from mesh-3 for both the coupling technique and the FEM with domain truncation.

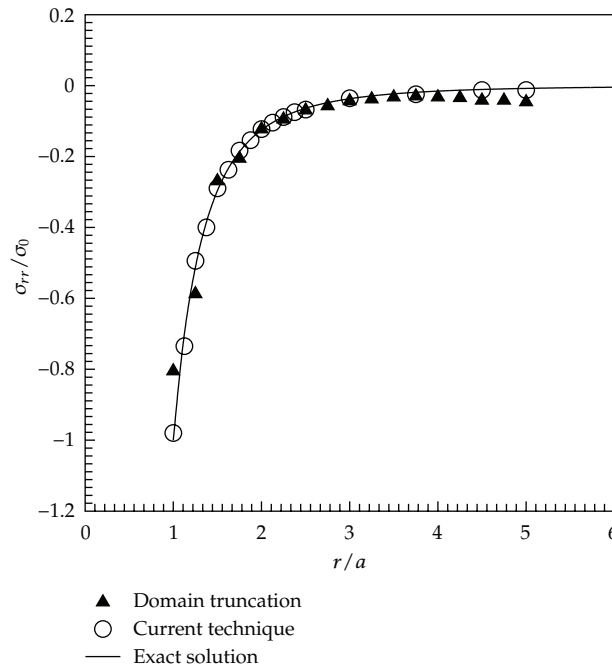


**Figure 7:** Normalized radial stress versus normalized radial coordinate for isotropic, linearly elastic material with  $\nu = 0.3$ . Results are obtained from mesh-3 for both the coupling technique and the FEM with domain truncation.

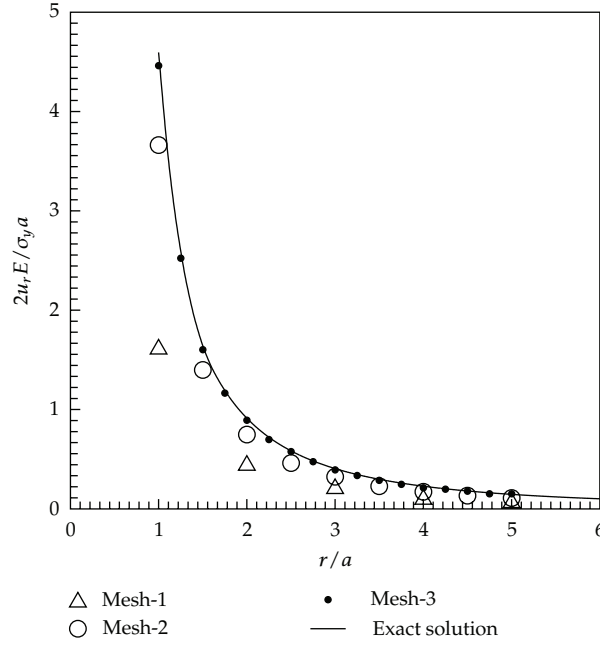


**Figure 8:** Normalized radial displacement versus normalized radial coordinate for isotropic hardening material with  $E_2 = 0$ .

$\sigma_0$  increases. By incorporating  $J_2$ -flow theory of plasticity and spherical symmetry, the radial displacement and the radial stress can be obtained exactly as given below:

$$u_r(r) = \begin{cases} \frac{1-2\nu}{E} \left\{ 2\sigma_y \ln\left(\frac{r}{a}\right) - \sigma_0 \right\} r + \frac{1-\nu}{E} \sigma_y \left( \frac{r_0^3}{r^2} \right), & r < r_0, \\ \frac{\sigma_y(1+\nu)}{3E} \left( \frac{r_0^3}{r^2} \right), & r \geq r_0, \end{cases} \quad (4.3)$$

$$\sigma_{rr}(r) = \begin{cases} 2\sigma_y \ln\left(\frac{r}{a}\right) - \sigma_0, & r < r_0, \\ -\frac{2\sigma_y}{3} \left( \frac{r_0}{r} \right)^3, & r \geq r_0, \end{cases}$$

where the Poisson ratio  $\nu$  is taken to be 0.3 and  $r_0 = ae^{((\sigma_0/2\sigma_y)-(1/3))}$  is the radius of an inelastic zone.

In the analysis, the pressure  $\sigma_0 = 1.625\sigma_y$  is chosen to ensure that the medium contains an inelastic zone; in fact, this selected applied pressure corresponds to  $r_0 = 1.615a$ . Numerical results obtained from the current technique are reported along with the exact solution in Figure 8 for the normalized radial displacement and in Figure 9 for the normalized radial stress. It can be concluded from computed solutions that they finally converge to the exact solution as the mesh is refined. In particular, results obtained from the mesh-3 are nearly indistinguishable from the benchmark solution. It should be pointed out that results obtained from the same level of mesh refinement for this particular case are less accurate than those

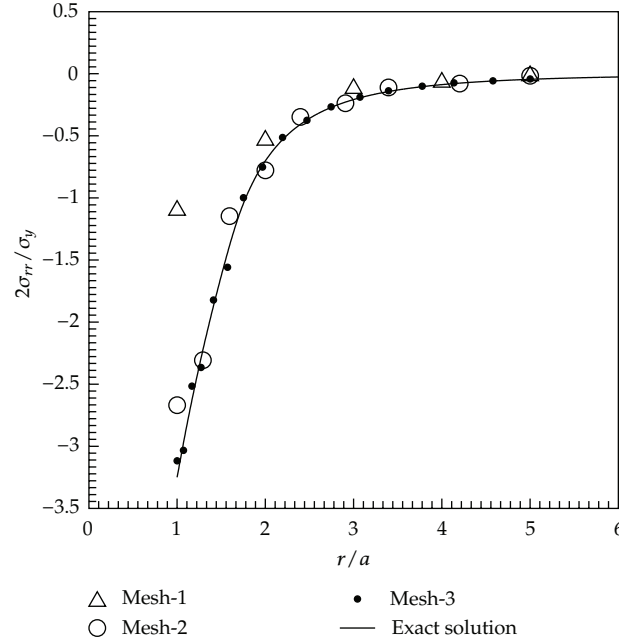


**Figure 9:** Normalized radial stress versus normalized radial coordinate for isotropic hardening material with  $E_2 = 0$ .

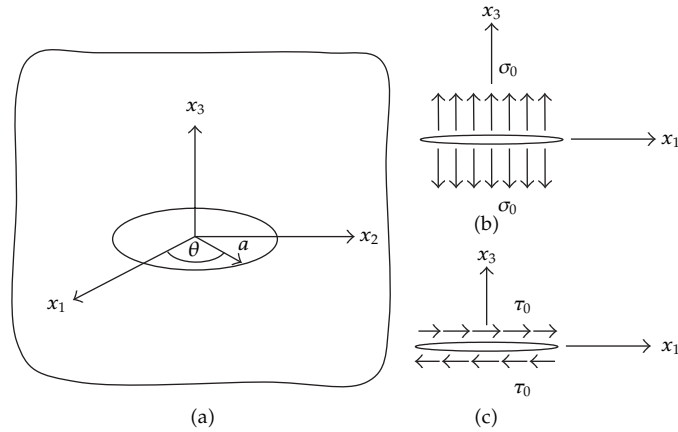


**Figure 10:** (a) Schematic of infinite medium containing penny-shaped crack, (b) crack under uniform normal traction  $\sigma_0$ , and (c) crack under uniform shear traction  $\tau_0$ .

obtained for the linear elastic case. This is due to the complexity posed by the presence of an inelastic zone near the surface of the void, and, in order to capture this behavior accurately, it requires sufficiently fine meshes.

#### 4.2. Isolated Penny-Shaped Crack in Infinite Medium

Consider, next, a penny-shaped crack of radius  $a$  which is embedded in a linearly elastic, infinite medium as shown schematically in Figure 10(a). The body is made of either an



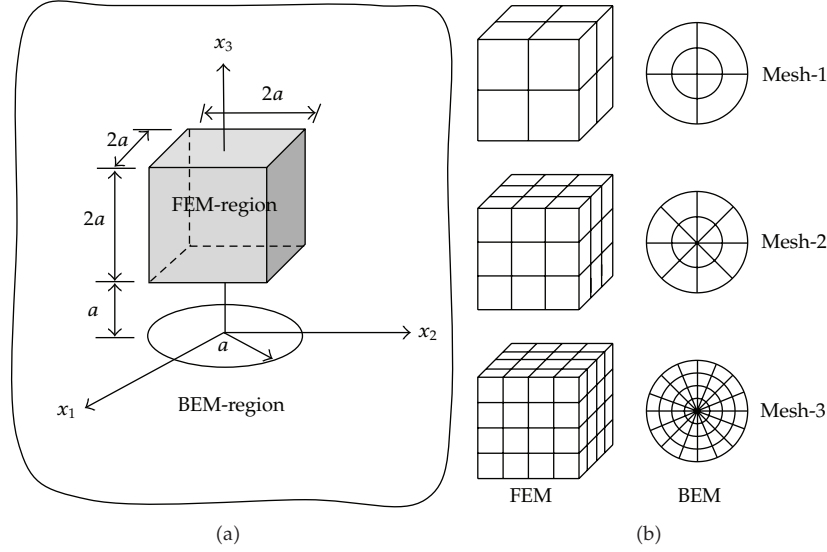


**Figure 11:** (a) Schematic of selected FEM-region and the remaining BEM-region and (b) three meshes adopted in the analysis.

**Table 1:** Nonzero elastic constants for zinc and graphite-reinforced composite (where axis of material symmetry is taken to direct along the  $x_3$ -coordinate direction).

Nonzero elastic constants	( $\times 10^6$ ) psi	
	Zinc	Graphite-reinforced composite
$E_{1111}$	16.09	14.683
$E_{1122}$	3.35	6.986
$E_{1133}$	5.01	5.689
$E_{3333}$	6.10	144.762
$E_{1313}$	3.83	4.050

isotropic material with Poisson's ratio  $\nu = 0.3$  or zinc and graphite-reinforced composite. The last two materials are transversely isotropic with the axis of material symmetry directing along the  $x_3$ -axis, and their elastic constants are given in Table 1. The crack is subjected to two types of traction boundary conditions: the uniform normal traction  $\sigma_0$  (i.e.,  $t_1 = t_2 = 0$ ,  $t_3 = \sigma_0$ ) as shown in Figure 10(b) and the uniform shear traction  $\tau_0$  along the  $x_1$ -axis (i.e.,  $t_1 = \tau_0$ ,  $t_2 = t_3 = 0$ ) as shown in Figure 10(c).

The first loading condition gives rise to a pure opening-mode problem with the mode-I stress intensity factor along the crack front being constant and independent of material properties, while the second loading condition yields nonzero mode-II and mode-III stress intensity factors that vary along the crack front. The analytical solutions for both cases can be found in the work of Fabrikant [4]. As a means to verify the coupling formulation and implementation, we choose the FEM-region to be a cube of dimensions  $2a \times 2a \times 2a$  centered at  $(0, 0, 2a)$  as illustrated in Figure 11(a). In the analysis, we generate three meshes for both the crack surface and the FEM-region as shown in Figure 11(b).

For the first loading condition, numerical solutions for the mode-I stress intensity factor normalized by the exact solution are reported in Table 2 for all three materials. Clearly

**Table 2:** Normalized mode-I stress intensity factor for isolated penny-shaped crack subjected to uniform normal traction.

Mesh	Isotropic material, $K_1/K_{1, \text{exact}}$		Transversely isotropic material, $K_1/K_{1, \text{exact}}$			
			Zinc		Graphite-reinforced composite	
	$\theta^\circ = 0$	$\theta^\circ = 90$	$\theta^\circ = 0$	$\theta^\circ = 90$	$\theta^\circ = 0$	$\theta^\circ = 90$
1	0.9919	0.9920	0.9890	0.9890	0.9841	0.9841
2	1.0008	1.0008	1.0001	1.0001	1.0053	1.0053
3	1.0002	1.0002	1.0004	1.0004	1.0006	1.0001

from these results, the current technique yields highly accurate stress intensity factors with error less than 1.6%, 0.6%, and 0.1% for mesh-1, mesh-2, and mesh-3, respectively. The weak dependence of numerical solutions on the level of mesh refinement is due mainly to the use of special crack-tip elements to model the near-tip field and directly capture the gradient of relative crack-face displacement along the crack front. Relatively coarse meshes can therefore be employed in the analysis to obtain sufficiently accurate stress intensity factors.

For the second loading condition, the normalized mode-II and mode-III stress intensity factors ( $K_2$  and  $K_3$ ) are shown in Figure 12 for isotropic material, zinc and graphite-reinforced composite. Based on this set of results, it can be concluded again that numerical solutions obtained from the three meshes are in excellent agreement with the exact solution; in particular, a coarse mesh also yields results of high accuracy. It should also be remarked that for this particular loading condition, the material anisotropy plays a significant role on values of the mixed-mode stress intensity factors.

#### 4.3. Infinite Medium Containing Both Penny-Shaped Crack and Spherical Void

As a final example, we choose to test the proposed technique by solving a more complex boundary value problem in order to demonstrate its capability. Let us consider an infinite medium containing a spherical void of radius  $a$  and a penny-shaped crack of the same radius as shown schematically in Figure 13. The medium is subjected to uniform pressure  $\sigma_0$  on the surface of the void, whereas the entire surface of the crack is traction-free. In the analysis, two constitutive models are investigated: one associated with an isotropic, linearly elastic material with Young's modulus  $E$  and Poisson ratio  $\nu = 0.3$  and the other corresponding to an isotropic hardening material with the bilinear uniaxial stress-strain relation similar to that employed in Section 4.1. The primary quantity to be sought is the mode-I stress intensity factor along the crack front induced by the application of the pressure to the void. In addition, influence of an inelastic zone induced in the high-load-intensity region on such fracture data is also of interest.

In the modeling, we first decompose the medium into the FEM-region and the BEM-region using a fictitious spherical surface of radius  $4a$  centered at the same location as that of the void as shown in Figure 14(a). Three meshes are adopted in numerical experiments as shown in Figure 14(b). In particular, the FEM-region, the interface, and the crack surface consist of  $\{24, 12, 8\}$ ,  $\{128, 32, 16\}$ , and  $\{1024, 128, 64\}$  elements for mesh-1, mesh-2, and mesh-3, respectively. It should be noted also that the mesh-1 is obviously very coarse; in particular, only eight elements are utilized to discretize the entire crack surface and only four relatively large crack-tip elements are used along the crack front.

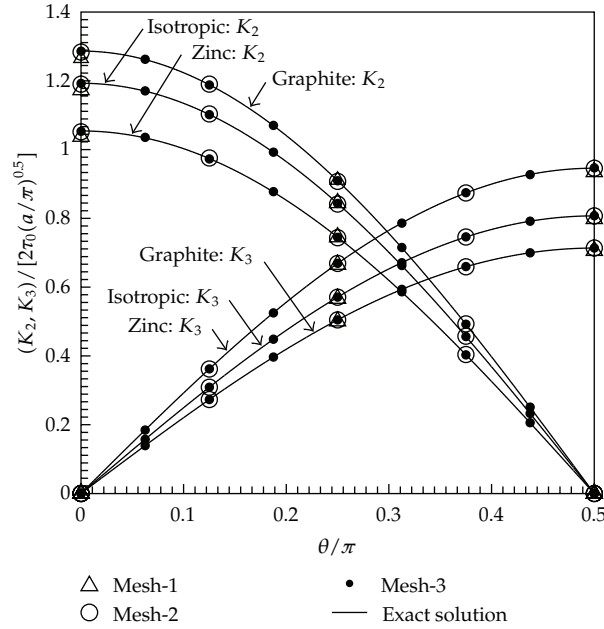


**Figure 12:** Normalized mode-II and mode-III stress intensity factors for isolated penny-shaped crack subjected to shear traction. Results are reported for isotropic material with  $\nu = 0.3$ , zinc and graphite-reinforced composite.

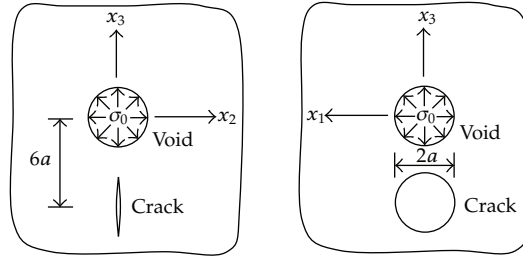


**Figure 13:** Schematic of infinite medium containing spherical void of radius  $a$  and penny-shaped crack of radius  $a$  and subjected to uniform pressure at surface of void.

First, the analysis is carried out for the elastic material with Poisson ratio  $\nu = 0.3$ , and the computed mode-I stress intensity factors are normalized and then reported as a function of angular position along the crack front for all three meshes in Figure 15. This set of results implies that the obtained numerical solutions exhibit good convergence; in particular, results obtained from the mesh-2 and mesh-3 are of comparable quality while results obtained from the mesh-1 still deviate from the converged solution. As confirmed by this convergence study, only the mesh-3 is used to generate other sets of useful results.

Next, we consider a medium made of an isotropic hardening material. In the analysis, we choose the modulus  $E_1 = E$  and Poisson ratio  $\nu = 0.3$  for the linear regime and choose either  $E_2 = E/3$  or  $E_2 = 0$  for the hardening regime. With this set of material parameters, the behavior in the linear regime (for a small level of applied pressure) is identical to that obtained in the previous case. To investigate the influence of the inelastic zone induced near

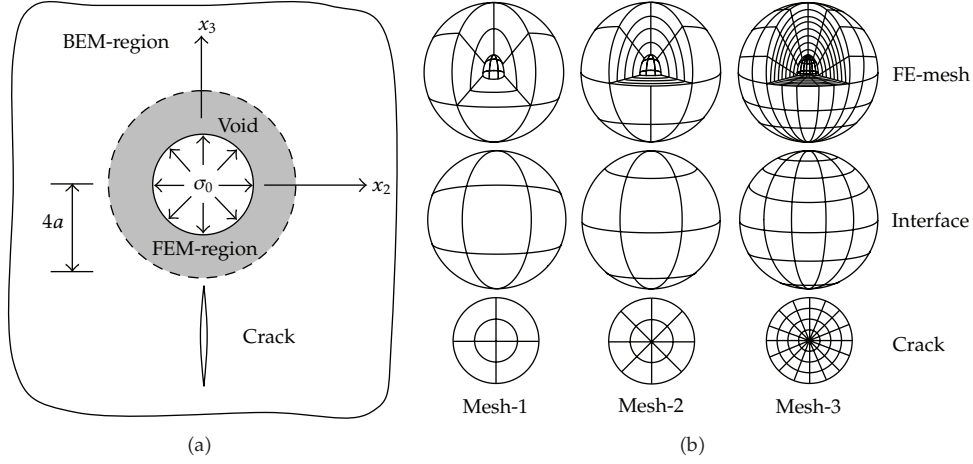


**Figure 14:** (a) Decomposition of domain into BEM-region and FEM-region by a fictitious spherical surface of radius  $4a$  and (b) three meshes adopted in analysis.

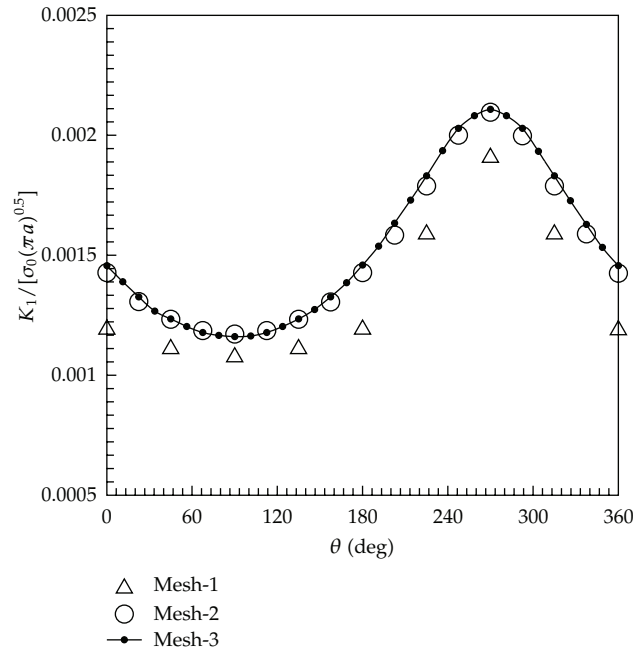


**Figure 15:** Normalized mode-I stress intensity factors of penny-shaped crack embedded within infinite medium containing spherical void under uniform pressure. Results are reported for isotropic linearly elastic material with  $\nu = 0.3$ .

the surface of the void on the stress intensity factor along the crack front, we carry out various experiments by varying the applied pressure  $\sigma_0$ . The distribution of the stress intensity factor along the crack front is reported in Figure 16 for a hardening material with  $E_1 = E$  and  $E_2 = E/3$  under five levels of the applied pressure  $\sigma_0 \in \{0.25\sigma_y, 1.00\sigma_y, 1.25\sigma_y, 1.50\sigma_y, 1.75\sigma_y\}$ . The body is entirely elastic at  $\sigma_0 = 0.25\sigma_y$ , slightly passes the initial yielding at  $\sigma_0 = 1.00\sigma_y$ , and possesses a larger inelastic zone as the pressure increases further. It is obvious from Figure 16

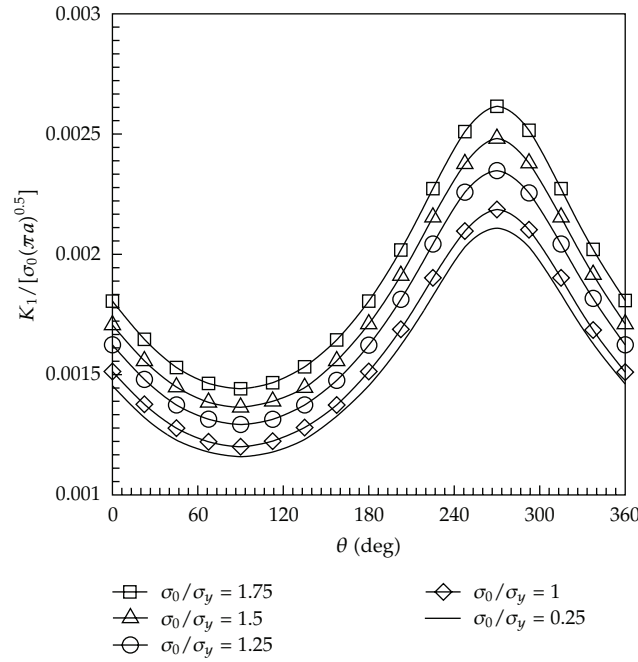


**Figure 16:** Normalized mode-I stress intensity factor of penny-shaped crack embedded within infinite medium containing spherical void under uniform pressure. Results are reported for isotropic hardening material with  $E_1 = E$  and  $E_2 = E/3$ .

that the presence of an elastic zone significantly alters the normalized values of the stress intensity factor from the linear elastic solution and such discrepancy becomes more apparent as the level of applied pressure increases. The localized inelastic zone acts as a stress riser, that is, it produces the stress field of higher intensity around the crack, and this therefore yields the higher normalized stress intensity factor when compared with the linear elastic case. Figure 17 shows an additional plot between the maximum normalized stress intensity factors versus the normalized applied pressure for both an isotropic linearly elastic material and two isotropic hardening materials (associated with  $E_2 = 0$  and  $E_2 = E/3$ ). Results for both materials are identical for a low level of the applied pressure (since the entire body is still elastic), and, for a higher level of the applied pressure, the maximum stress intensity factor for the case of the hardening material is significantly larger than that for the linear elastic material. In addition, such discrepancy tends to increase as the hardening modulus decreases.

## 5. Conclusions and Remarks

The coupling procedure between a standard finite element method (FEM) and a weakly singular, symmetric Galerkin boundary element method (SGBEM) has been successfully established for stress analysis of a three-dimensional infinite medium. The proposed technique has exploited the positive features of both the FEM and the SGBEM to enhance the modeling capability. The vast and very general features of the FEM have been employed as a basis to treat a localized region that may embed a zone exhibiting complex behavior, whereas the SGBEM has been used specifically to model the majority of the medium that is unbounded and possibly contains the surface of displacement discontinuities such as cracks

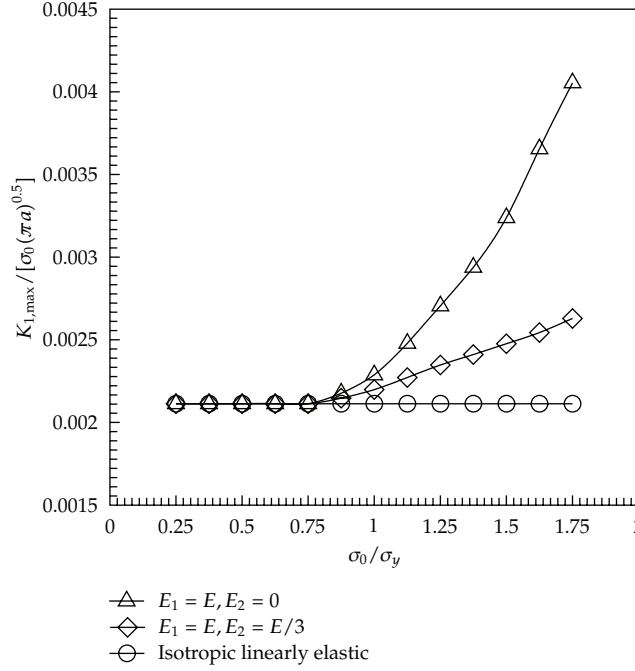


**Figure 17:** Maximum normalized mode-I stress intensity factor versus applied pressure at surface of void. Results are reported for isotropic linearly elastic material with  $\nu = 0.3$  and two isotropic hardening materials.

and dislocations. The coupling formulation has been based primarily on the domain decomposition technique along with the proper enforcement of continuity of the displacement and traction on the interface of the two regions (one modeled by the SGBEM and the other by the FEM) to form the coupling equations. For the FEM subdomain, the key formulation follows directly the well-known principle of virtual work, whereas, for the SGBEM subdomain, the governing equation is formulated based on a pair of weakly singular, weak-form boundary integral equations for the displacement and traction. The advantage of using the weakly singular integral equations is associated with the permission to apply a space of continuous interpolation functions in the discretization of primary unknowns on the SGBEM subdomain.

In the numerical implementation, various aspects have been considered in order to enhance the accuracy and computational efficiency of the coupling technique. For instance, special crack-tip elements have been employed to better approximate the near-tip field. Shape functions of these special elements have properly been enriched by a square root function such that the resulting interpolation functions can capture the relative crack-face displacement with sufficiently high level of accuracy. As a direct consequence, it allows relatively large crack-tip elements to be employed along the crack front while still yielding very accurate stress intensity factors. Another important consideration is the use of an interpolation strategy to approximate values of kernels for generally anisotropic materials; this substantially reduces the computational cost associated with the direct evaluation of the line integral. Finally, special numerical quadratures have been adopted to efficiently evaluate both the weakly singular and nearly singular double surface integrals. To demonstrate and gain an insight into the coupling strategy, the formulation has been implemented first in terms of an in-house computer code for linear elasticity boundary value problems. Subsequently,

the weakly singular SGBEM has successfully been coupled with a reliable commercial finite element package in order to exploit its rich features to model more complex localized region such as inelastic zones and inhomogeneities. As indicated by results from extensive numerical experiments, the current technique has been found promising and, in particular, numerical solutions exhibit good convergence and weak dependence on the level of mesh refinement.

As a final remark, while the developed technique is still restricted to an infinite domain and to conforming interfaces, it offers insight into the SGBEM-FEM coupling strategy in terms of the formulation, the implementation procedure, and its performance. This coupling strategy can directly be generalized to solve more practical boundary value problems involving a half space, for example, cracks and localized complex zone near the free surface. Another crucial extension is to enhance the feature of the current technique by using the weak enforcement of continuity across the interface. This will supply the flexibility of mesh generation.

## Acknowledgments

The first author gratefully acknowledges financial supports provided by “Chulalongkorn University for development of new faculty staff” and “Stimulus Package 2 (SP2) of Ministry of Education under the theme of Green Engineering for Green Society.”

## References

- [1] S. Timoshenko and N. Goodier, *The Theory of Elasticity*, McGraw-Hill, New York, NY, USA, 2nd edition, 1951.
- [2] I. N. Sneddon, *Fourier Transform*, McGraw-Hill, New York, NY, USA, 1951.
- [3] I. N. Sneddon, *Mixed Boundary Value Problems in Potential Theory*, John Wiley & Sons, New York, NY, USA, 1965.
- [4] V. I. Fabrikant, *Applications of Potential Theory in Mechanics: A Selection of New Results*, vol. 51 of *Mathematics and Its Applications*, Kluwer Academic Publishers, Dordrecht, The Netherlands, 1989.
- [5] V. I. Fabrikant, *Mixed Boundary Value Problems of Potential Theory and Their Applications in Engineering*, vol. 68 of *Mathematics and Its Applications*, Kluwer Academic Publishers, Dordrecht, The Netherlands, 1991.
- [6] J. T. Oden and G. F. Carey, *Finite Elements: Special Problems in Solid Mechanics*, vol. 5, Prentice-Hall, Englewood Cliffs, NJ, USA, 1984.
- [7] T. J. R. Hughes, *The Finite Element Method: Linear Static and Dynamic Finite Element Analysis*, Dover Publications, Mineola, NY, USA, 2000.
- [8] O. C. Zienkiewicz and R. L. Taylor, *The Finite Element Method: Solid Mechanics*, vol. 2, Butterworth-Heinemann, Oxford, UK, 5th edition, 2000.
- [9] D. V. Swenson and A. R. Ingraffea, “Modeling mixed-mode dynamic crack propagation using finite elements: theory and applications,” *Computational Mechanics*, vol. 3, no. 6, pp. 381–397, 1988.
- [10] L. F. Martha, P. A. Wawrzynek, and A. R. Ingraffea, “Arbitrary crack representation using solid modeling,” *Engineering with Computers*, vol. 9, no. 2, pp. 63–82, 1993.
- [11] A. O. Ayhan, A. C. Kaya, J. Laflen, R. D. McClain, and D. Slavik, “Fracture analysis of cracks in orthotropic materials using ANSYS,” Tech. Rep. GRC370, GEGlobal Research, General Electric Company, 2003.
- [12] T. A. Cruse, *Boundary Element Analysis in Computational Fracture Mechanics*, vol. 1 of *Mechanics: Computational Mechanics*, Kluwer Academic Publishers, Dordrecht, The Netherlands, 1988.
- [13] C. A. Brebbia and J. Dominguez, *Boundary Elements: An Introductory Course*, McGraw-Hill, New York, NY, USA, 1989.
- [14] G. Xu and M. Ortiz, “A variational boundary integral method for the analysis of 3-D cracks of arbitrary geometry modelled as continuous distributions of dislocation loops,” *International Journal for Numerical Methods in Engineering*, vol. 36, no. 21, pp. 3675–3701, 1993.



- [15] M. Bonnet, "Regularized direct and indirect symmetric variational BIE formulations for three-dimensional elasticity," *Engineering Analysis with Boundary Elements*, vol. 15, no. 1, pp. 93–102, 1995.
- [16] L. Xiao, *Symmetric weak-form integral equation method for three-dimensional fracture analysis*, Ph.D. Dissertation, University of Texas at Austin, Austin, Tex, USA, 1998.
- [17] S. Li and M. E. Mear, "Singularity-reduced integral equations for displacement discontinuities in three-dimensional linear elastic media," *International Journal of Fracture*, vol. 93, no. 1–4, pp. 87–114, 1998.
- [18] S. Li, M. E. Mear, and L. Xiao, "Symmetric weak-form integral equation method for three-dimensional fracture analysis," *Computer Methods in Applied Mechanics and Engineering*, vol. 151, no. 3–4, pp. 435–459, 1998.
- [19] G. Xu, "A variational boundary integral method for the analysis of three-dimensional cracks of arbitrary geometry in anisotropic elastic solids," *Journal of Applied Mechanics*, vol. 67, no. 2, pp. 403–408, 2000.
- [20] A. Frangi, G. Novati, R. Springhetti, and M. Rovizzi, "3D fracture analysis by the symmetric Galerkin BEM," *Computational Mechanics*, vol. 28, no. 3–4, pp. 220–232, 2002.
- [21] J. Rungamornrat, "Analysis of 3D cracks in anisotropic multi-material domain with weakly singular SGBEM," *Engineering Analysis with Boundary Elements*, vol. 30, no. 10, pp. 834–846, 2006.
- [22] J. Rungamornrat and M. E. Mear, "Weakly-singular, weak-form integral equations for cracks in three-dimensional anisotropic media," *International Journal of Solids and Structures*, vol. 45, no. 5, pp. 1283–1301, 2008.
- [23] J. Rungamornrat and M. E. Mear, "A weakly-singular SGBEM for analysis of cracks in 3D anisotropic media," *Computer Methods in Applied Mechanics and Engineering*, vol. 197, no. 49–50, pp. 4319–4332, 2008.
- [24] E. Schnack and K. Türke, "Domain decomposition with BEM and FEM," *International Journal for Numerical Methods in Engineering*, vol. 40, no. 14, pp. 2593–2610, 1997.
- [25] W. M. Elleithy, H. J. Al-Gahtani, and M. El-Gebeily, "Iterative coupling of BE and FE methods in elastostatics," *Engineering Analysis with Boundary Elements*, vol. 25, no. 8, pp. 685–695, 2001.
- [26] W. M. Elleithy and M. Tanaka, "Interface relaxation algorithms for BEM-BEM coupling and FEM-BEM coupling," *Computer Methods in Applied Mechanics and Engineering*, vol. 192, no. 26–27, pp. 2977–2992, 2003.
- [27] S. Ganguly, J. B. Layton, and C. Balakrishna, "Symmetric coupling of multi-zone curved Galerkin boundary elements with finite elements in elasticity," *International Journal for Numerical Methods in Engineering*, vol. 48, no. 5, pp. 633–654, 2000.
- [28] M. Haas and G. Kuhn, "Mixed-dimensional, symmetric coupling of FEM and BEM," *Engineering Analysis with Boundary Elements*, vol. 27, no. 6, pp. 575–582, 2003.
- [29] M. Haas, B. Helldörfer, and G. Kuhn, "Improved coupling of finite shell elements and 3D boundary elements," *Archive of Applied Mechanics*, vol. 75, no. 10–12, pp. 649–663, 2006.
- [30] B. Helldörfer, M. Haas, and G. Kuhn, "Automatic coupling of a boundary element code with a commercial finite element system," *Advances in Engineering Software*, vol. 39, no. 8, pp. 699–709, 2008.
- [31] L. J. Gray, L. F. Martha, and A. R. Inghraffa, "Hypersingular integrals in boundary element fracture analysis," *International Journal for Numerical Methods in Engineering*, vol. 29, no. 6, pp. 1135–1158, 1990.
- [32] P. A. Martin and F. I. Rizzo, "Hypersingular integrals: how smooth must the density be?" *International Journal for Numerical Methods in Engineering*, vol. 39, no. 4, pp. 687–704, 1996.
- [33] M. Bonnet, G. Maier, and C. Polizzotto, "Symmetric Galerkin boundary element methods," *Applied Mechanics Reviews*, vol. 51, no. 11, pp. 669–703, 1998.
- [34] A. Frangi and G. Novati, "BEM-FEM coupling for 3D fracture mechanics applications," *Computational Mechanics*, vol. 32, no. 4–6, pp. 415–422, 2003.
- [35] R. Springhetti, G. Novati, and M. Margonari, "Weak coupling of the symmetric galerkin BEM with FEM for potential and elastostatic problems," *Computer Modeling in Engineering and Sciences*, vol. 13, no. 1, pp. 67–80, 2006.
- [36] J. Rungamornrat and M. E. Mear, "SGBEM-FEM coupling for analysis of cracks in 3D anisotropic media," *International Journal for Numerical Methods in Engineering*, vol. 86, no. 2, pp. 224–248, 2011.
- [37] K. J. Bathe, *Finite Element Procedures*, Prentice-Hall, Upper Saddle River, NJ, USA, 1990.
- [38] T. Belytschko, W. K. Liu, and B. Moran, *Nonlinear Finite Elements for Continua and Structures*, John Wiley & Sons, New York, NY, USA, 2000.
- [39] H. B. Li, G. M. Han, and H. A. Mang, "A new method for evaluating singular integrals in stress analysis of solids by the direct boundary element method," *International Journal for Numerical Methods in Engineering*, vol. 21, no. 11, pp. 2071–2098, 1985.



- [40] K. Hayami and C. A. Brebbia, "Quadrature methods for singular and nearly singular integrals in 3-D boundary element method," in *Boundary Elements X*, pp. 237–264, Springer, Berlin, Germany, 1988.
- [41] K. Hayami, "A projection transformation method for nearly singular surface boundary element integrals," in *Lecture Notes in Engineering*, C. A. Brebbia and S. A. Orszag, Eds., vol. 73, pp. 1–2, Springer, Berlin, Germany, 1992.
- [42] K. Hayami and H. Matsumoto, "A numerical quadrature for nearly singular boundary element integrals," *Engineering Analysis with Boundary Elements*, vol. 13, no. 2, pp. 143–154, 1994.
- [43] J. Lubliner, *Plasticity Theory*, Macmillan, New York, NY, USA, 1990.
- [44] I. S. Sokolnikoff, *Mathematical Theory of Elasticity*, McGraw-Hill, New York, NY, USA, 1956.

## Research Article

# Finite Element Analysis of Dam-Reservoir Interaction Using High-Order Doubly Asymptotic Open Boundary

Yichao Gao,<sup>1</sup> Feng Jin,<sup>1</sup> Xiang Wang,<sup>2</sup> and Jinting Wang<sup>1</sup>

<sup>1</sup> State Key Laboratory of Hydrosience and Engineering, Tsinghua University, Beijing 100084, China

<sup>2</sup> Changjiang Institute of Survey, Planning, Design, and Research, Wuhan 430010, China

Correspondence should be addressed to Feng Jin, jinfeng@tsinghua.edu.cn

Received 30 May 2011; Accepted 23 August 2011

Academic Editor: Otto von Estorff

Copyright © 2011 Yichao Gao et al. This is an open access article distributed under the Creative Commons Attribution License, which permits unrestricted use, distribution, and reproduction in any medium, provided the original work is properly cited.

The dam-reservoir system is divided into the near field modeled by the finite element method, and the far field modeled by the excellent high-order doubly asymptotic open boundary (DAOB). Direct and partitioned coupled methods are developed for the analysis of dam-reservoir system. In the direct coupled method, a symmetric monolithic governing equation is formulated by incorporating the DAOB with the finite element equation and solved using the standard time-integration methods. In contrast, the near-field finite element equation and the far-field DAOB condition are separately solved in the partitioned coupled method, and coupling is achieved by applying the interaction force on the truncated boundary. To improve its numerical stability and accuracy, an iteration strategy is employed to obtain the solution of each step. Both coupled methods are implemented on the open-source finite element code OpenSees. Numerical examples are employed to demonstrate the performance of these two proposed methods.

## 1. Introduction

The coupled analysis of dam-reservoir interaction has great significance for the design and safety evaluation of concrete dams under earthquakes. The finite element method and substructure method are often applied for the analysis of dam-reservoir system (Figure 1). The dam structure as well as the near-field reservoir with irregular geometry is discretized with finite elements. The remaining part of the reservoir, called the far field, is simplified as a semi-infinite layer with constant depth. On the truncated boundary, which separates the near and far field, the equations of motion and continuity should be satisfied simultaneously. In the early studies, frequency-domain analysis methods [1, 2] are often used for linear problems. However, for a nonlinear analysis of the dam-reservoir system, it is necessary to develop a direct time domain analysis. Zienkiewicz and Bettess [3] as well as Küçükarslan et al. [4] studied fluid-structure interaction in the time domain by imposing the Sommerfeld

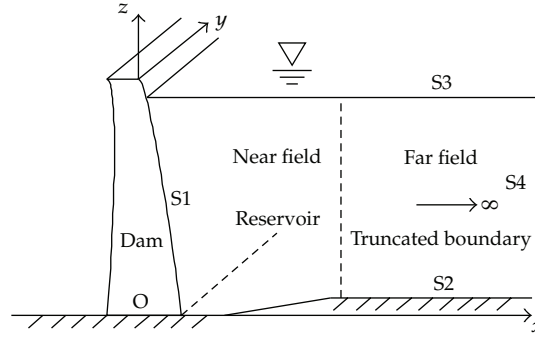


Figure 1: A typical dam-reservoir system.

radiation condition [5]. Tsai and his coworkers [6–8] established the time-domain models for the dynamic interaction analysis of dam-reservoir system by using the transmitting boundary. This approach is temporally global; that is, it requires the evaluation of convolution integrals. Boundary element method is undoubtedly a powerful numerical tool for analysis of problems involving unbounded domain. When the boundary element method [9–13] is applied to the direct time-domain analysis of dam-reservoir interaction, the formulation is temporally and spatially global. As a result, great numerical effort is required to solve the transient problems. This hinders its application to long-time analysis of large-scale engineering problems. The scaled boundary finite element method is a semianalytical method which is efficient for the analysis of dam-reservoir interaction. Details of this approach are given, for example, by Li et al. [14] and Lin et al. [15].

The high-order open boundaries are promising alternatives for the simulation of semi-infinite reservoir in the analysis of dam-reservoir system. The high-order open boundaries [16, 17] are of increasing accuracy as the order of approximation increases. Moreover, the formulations are temporally local so that they are computationally efficient. As demonstrated by Prempramote et al. [18], these high-order open boundaries are singly asymptotic at the high-frequency limit and are appropriate for the radiative fields, where virtually all of the field energy is propagating out to infinity [19]. However, in some classes of application, such as a semi-infinite reservoir with constant depth (also known as a wave guide), a cutoff frequency exists. When the excitation frequency is close to or below the cutoff frequency, the wave field is largely nonradiative. In such cases, the high-order transmitting boundaries break down at late times in a time domain analysis [18]. To model an unbounded domain with the presence of nonradiative wave fields, one advance is the introduction of the doubly asymptotic boundaries [19–22]. Thus, the dynamic stiffness is exact at both the high-frequency and the low-frequency limit (i.e., statics), with its formulation spatially global. However, the highest order denoting the accuracy reported in the literature is three [23].

Recently, a novel high-order doubly asymptotic open boundary for one-dimensional scalar wave equation is proposed by Prempramote et al. [18] by extending the work in [24]. This high-order doubly asymptotic open boundary is capable of accurately mimicking the unbounded domain over the entire frequency (i.e., from zero to infinity). This open boundary condition is constructed by using the continued fraction solution of dynamic stiffness matrix without explicitly evaluating its solution at discrete frequencies. When applied for a semi-infinite layer with a constant depth, the constants of the continued fraction solutions with any order are determined explicitly and recursively. Excellent accuracy and stability for long-time transient analysis are reported.

Wang et al. [25] extend the high-order doubly asymptotic open boundary condition by Prempramote et al. [18] to the analysis of the hydrodynamic pressure of a semi-infinite reservoir with constant depth. By applying the sequential staggered implicit-implicit partition algorithm, the high-order doubly asymptotic open boundary is coupled with the general purpose finite element software ABAQUS to analyze the gravity dam-reservoir interaction system. Numerical examples demonstrate the high accuracy and long-time stability of this proposed technique.

Givoli et al. [26] proposed a new finite element scheme for the solution of time-dependent semi-infinite wave-guide problems by incorporating with a high-order open boundary. Two versions of finite element formulation, namely, the augmented version and the split version, are proposed. Good performance of this scheme is demonstrated in numerical examples, but the global mass and stiffness matrices of the augmented formulation are nonsymmetric.

In this paper, two coupled numerical methods for dam-reservoir interaction analysis based on the excellent high-order doubly asymptotic open boundary [25] are proposed. In the direct coupled method, the high-order doubly asymptotic open boundary is directly incorporated with the near-field finite element equation. A monolithic governing equation for the whole dam-reservoir system is formulated with sparse and symmetric coefficients matrices, which can be solved using the standard time-integration methods. In the partitioned coupled method, the near-field finite element equation and the far-field high-order doubly asymptotic boundary condition are separately solved. The high-order doubly asymptotic open boundary is split into two parts. The first part is proved to be the Sommerfeld radiation boundary, which can be included in the damping matrix of the near-field finite element equation. The second part includes all the high-order terms and is governed by a system of first-order ordinary differential equations. These two sets of equations are solved by a sequential staggered implicit-implicit partition algorithm. To improve the stability and accuracy of this partitioned coupled method, an iteration strategy is employed to obtain the solution of each step. Both of these two coupled methods are numerically implemented on the open-source finite element code OpenSees to analyze the gravity dam-reservoir and arch dam-reservoir interaction.

This paper is organized as follows. In Section 2, the finite element formulation of dam-reservoir system is addressed. In Section 3, the scaled boundary finite element method is applied to 3-dimensional semi-infinite layer with constant depth. The governing equation on the truncated boundary is obtained. In Section 4, the scaled boundary finite element equation is decoupled by modal decomposition. Based on the continued fraction solutions of the dynamic stiffness, a high-order doubly asymptotic open boundary is constructed by introducing auxiliary variables. In Section 5, two coupled numerical methods are presented: the direct coupled method and the partitioned coupled method. Both numerical methods are implemented on the open source finite element code OpenSees. In Section 6, numerical examples of a gravity dam and an arch dam are presented. In the final section, conclusions are stated.

## 2. Modeling of Dam-Reservoir System

A typical dam-reservoir system is shown in Figure 1. The reservoir is divided into two parts: the near field with irregular geometry and the far field extending to the infinity with constant depth. The dam structure and near field reservoir are discretized with finite elements, and the far field reservoir is modeled with high-order doubly asymptotic boundary.

The hydrodynamic pressure is denoted as  $p = p(x, y, z, t)$ , and the acceleration of water particle is denoted as  $\{\ddot{u}\} = \{\ddot{u}(x, y, z, t)\}$ . Assuming the water in the reservoir to be compressible, inviscid, and irrotational with small amplitude movements, the hydrodynamic pressure  $p$  in the reservoir satisfies the scalar wave equation

$$\frac{1}{c^2} \frac{\partial^2 p}{\partial t^2} = \Delta p, \quad (2.1)$$

where  $\Delta$  is the Laplace operator and  $c$  is the compression wave velocity

$$c = \sqrt{\frac{K}{\rho}}, \quad (2.2)$$

where  $K$  is the bulk modulus of water and  $\rho$  is the mass density. On the dam-reservoir interface (S1),  $p$  satisfies the following boundary condition

$$\frac{\partial p}{\partial n} = -\rho \ddot{u}_n, \quad (2.3)$$

where  $n$  stands for the outward normal of the boundary. At the reservoir bottom (S2), the following boundary condition

$$\frac{\partial p}{\partial n} = 0 \quad \text{or} \quad \ddot{u}_n = 0 \quad (2.4)$$

applies. Neglecting the effect of surface waves, on the free surface (S3),

$$p = 0 \quad (2.5)$$

applies. At infinity (S4), A Sommerfeld-type radiation boundary condition should be satisfied; namely,

$$\frac{\partial p}{\partial n} = -\frac{\dot{p}}{c}. \quad (2.6)$$

Without considering the material damping, the finite element formulation for dam-reservoir system can be partitioned as

$$\begin{bmatrix} [M_s] & 0 & 0 \\ -[Q_{fs}] & [M_{ff}] & [M_{fb}] \\ 0 & [M_{bf}] & [M_{bb}] \end{bmatrix} \begin{Bmatrix} \{\ddot{u}_s\} \\ \{\ddot{p}_f\} \\ \{\ddot{p}_b\} \end{Bmatrix} + \begin{bmatrix} [K_s] & [Q_{sf}] & 0 \\ 0 & [K_{ff}] & [K_{fb}] \\ 0 & [K_{bf}] & [K_{bb}] \end{bmatrix} \begin{Bmatrix} \{u_s\} \\ \{p_f\} \\ \{p_b\} \end{Bmatrix} = \begin{Bmatrix} \{f_s\} \\ \{f_f\} \\ -\{r\} \end{Bmatrix}, \quad (2.7)$$

where  $[M]$ ,  $[K]$ , and  $[Q]$  are the mass matrix, static stiffness matrix, the coupling matrix between structure and acoustic fluid, respectively, and  $\{f\}$  is the external force vector.

Subscript  $s$  denotes the degrees of freedom of the dam structure; subscript  $b$  denotes the degrees of freedom on the truncated boundary; subscript  $f$  denotes the degrees of freedom of the near-field water except for those on the truncated boundary. The interaction load applied to the semi-infinite reservoir (far field) by the near-field reservoir is denoted as  $\{r\}$ , so the external load applied to the near-field reservoir on the truncated boundary is equal to  $-\{r\}$ . The mass and stiffness matrices of water treated as acoustic fluid are expressed as

$$\begin{aligned} [M_f] &= \int_{V_f} \frac{1}{K} [N]^T [N] dV, \\ [K_f] &= \int_{V_f} \frac{1}{\rho} \left( \frac{\partial [N]^T}{\partial x} \frac{\partial [N]}{\partial x} + \frac{\partial [N]^T}{\partial y} \frac{\partial [N]}{\partial y} + \frac{\partial [N]^T}{\partial z} \frac{\partial [N]}{\partial z} \right) dV, \\ [f_f] &= \int_{S_f} \frac{1}{\rho} [N] \frac{\partial [N]}{\partial n} dS, \end{aligned} \quad (2.8)$$

where  $[N]$  denotes the shape function of finite elements.

To solve (2.7) for the dam-reservoir system, the relationship between the interaction load  $\{r\}$  and the hydrodynamic pressure  $\{p\}$  of the semi-infinite reservoir is formulated in the following section.

### 3. Summary of the Scaled Boundary Finite Element Method for Semi-Infinite Reservoir with Constant Depth

The scaled boundary finite element method is a semianalytical method developed to model unbounded domains with arbitrary shape [27]. The scaled boundary finite element formulation for the two-dimensional semi-infinite reservoir with constant depth was described in detailed [25]. For the sake of completeness, a brief summary of the equations necessary for the interpretation of high-order doubly asymptotic open boundary for hydrodynamic pressure is presented in this section.

To facilitate the coupling with the finite elements of the near-field reservoir, the truncated boundary is discretized by elements that have the same nodes and shape function as the finite elements. The derivation is summarized for three-dimensional semi-infinite reservoir with a vertical boundary (Figure 2). Streamlined expressions are presented as follows.

For an acoustic fluid, the relationship between acceleration and hydrodynamic pressure is equivalent to that between stress and displacement in stress analysis and is expressed as

$$\{L\}p + \rho\{\ddot{u}\} = 0, \quad (3.1)$$

where  $\{L\} = \{\partial/\partial x \ \partial/\partial y \ \partial/\partial z\}$  is the differential operator. The equation of continuity without considering the volumetric stress-strain relationship of compressible water is written as

$$\{L\}^T \{\ddot{u}\} = -\frac{1}{K} \frac{\partial^2 p}{\partial t^2}. \quad (3.2)$$

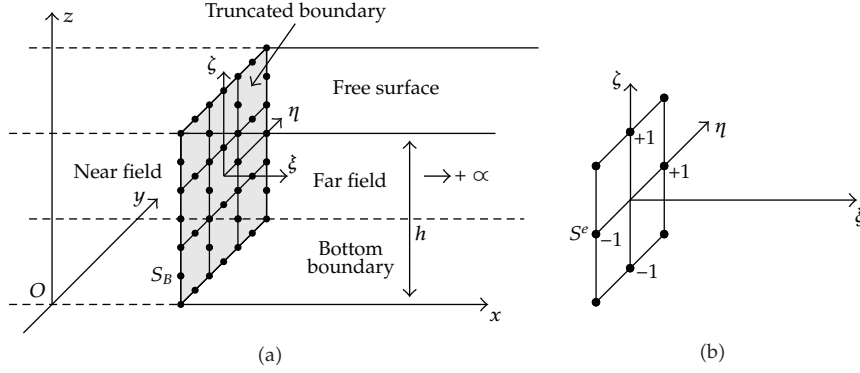


Figure 2: Semidiscretization of the truncated boundary.

The vertical truncated boundary of the semi-infinite reservoir is specified by a constant coordinate  $x_b$ . It is discretized by two-dimensional elements (Figure 2(a)). A typical element is shown in Figure 2(b). The geometry of an element is interpolated using the shape functions  $[N(\eta, \zeta)]$  formulated in the local coordinates  $\eta$  and  $\zeta$  as

$$y_b(\eta, \zeta) = [N(\eta, \zeta)] \{y_b\}, \quad z_b(\eta, \zeta) = [N(\eta, \zeta)] \{z_b\}. \quad (3.3)$$

The Cartesian coordinates of a point  $(x, y, z)$  and inside the semi-infinite reservoir are expressed as

$$\begin{aligned} x(\xi) &= x_b + \xi, \\ y(\xi, \eta, \zeta) &= y_b(\eta, \zeta) = [N(\eta, \zeta)] \{y_b\}, \\ z(\xi, \eta, \zeta) &= z_b(\eta, \zeta) = [N(\eta, \zeta)] \{z_b\}, \end{aligned} \quad (3.4)$$

where the coordinate  $\xi$  is equal to 0 on the vertical boundary. The Jacobian matrix for coordinate transformation from  $(x, y, z)$  to  $(\xi, \eta, \zeta)$  is expressed as

$$[J(\eta, \zeta)] = \begin{bmatrix} x_{,\xi} & y_{,\xi} & z_{,\xi} \\ x_{,\eta} & y_{,\eta} & z_{,\eta} \\ x_{,\zeta} & y_{,\zeta} & z_{,\zeta} \end{bmatrix} = \begin{bmatrix} 1 & 0 & 0 \\ 0 & y_{b,\eta} & z_{b,\eta} \\ 0 & y_{b,\zeta} & z_{b,\zeta} \end{bmatrix}. \quad (3.5)$$

For a three-dimensional problem,

$$dV = |J| d\xi d\eta d\zeta, \quad (3.6)$$

where  $|J|$  is the determinant of the Jacobian matrix. The partial differential operator defined in (3.1) is expressed as

$$\{L\} = [J(\eta, \zeta)]^{-1} \left[ \frac{\partial}{\partial \xi} \quad \frac{\partial}{\partial \eta} \quad \frac{\partial}{\partial \zeta} \right]^T = \{b^1\} \frac{\partial}{\partial \xi} + \{b^2\} \frac{\partial}{\partial \eta} + \{b^3\} \frac{\partial}{\partial \zeta}, \quad (3.7)$$

with

$$\{b^1\} = \begin{Bmatrix} 1 \\ 0 \\ 0 \end{Bmatrix}, \quad \{b^2\} = \frac{1}{|J|} \begin{Bmatrix} 0 \\ z_{b,\zeta} \\ -y_{b,\zeta} \end{Bmatrix}, \quad \{b^3\} = \frac{1}{|J|} \begin{Bmatrix} 0 \\ -z_{b,\eta} \\ y_{b,\eta} \end{Bmatrix}. \quad (3.8)$$

Along horizontal lines passing through a node on the boundary, the nodal hydrodynamic pressure functions  $\{p\} = \{p(\xi, t)\}$  are introduced. On the boundary, the nodal hydrodynamic pressure follows as  $\{p_b\} = \{p(\xi = 0, t)\}$ . One isoparametric element  $S^e$  is shown in Figure 2. The hydrodynamic pressure field  $p = p(\xi, \eta, \zeta, t)$  is obtained by interpolating the nodal hydrodynamic pressure functions

$$p = [N(\eta, \zeta)] \{p\}. \quad (3.9)$$

Substituting (3.9) and (3.7) into (3.1), the fluid particle acceleration  $\{\ddot{u}\} = \{\ddot{u}(\xi, \eta, \zeta)\}$  is expressed as

$$\{\ddot{u}\} = -\frac{1}{\rho} \left( [B^1] \{p\}_{,\xi} + [B^2] \{p\} \right), \quad (3.10)$$

with

$$[B^1] = \{b^1\} [N(\eta, \zeta)], \quad [B^2] = \{b^2\} [N(\eta, \zeta)]_{,\eta} + \{b^3\} [N(\eta, \zeta)]_{,\zeta}. \quad (3.11)$$

Applying Galerkin's weighted residual technique in the circumferential directions  $\eta, \zeta$  to (3.2), the scaled boundary finite element equation for the three-dimensional semi-infinite reservoir with constant depth is obtained as

$$[E^0] \{p\}_{,\xi\xi} - [E^2] \{p\} - \frac{1}{c^2} [E^0] \{\ddot{p}\} = 0, \quad (3.12)$$

where  $[E^0]$ ,  $[E^2]$ , and  $[M^0]$  are coefficient matrices

$$\begin{aligned} [E^0] &= \int_{S_i^e} [B^1]^T \frac{1}{\rho} [B^1] |J| d\eta d\zeta = \int_{S_i^e} [N(\eta, \zeta)]^T \frac{1}{\rho} [N(\eta, \zeta)] |J| d\eta d\zeta, \\ [E^2] &= \int_{S_i^e} [B^2]^T \frac{1}{\rho} [B^2] |J| d\eta d\zeta, \\ [M^0] &= \int_{S_i^e} [N(\eta, \zeta)]^T \frac{1}{K} [N(\eta, \zeta)] |J| d\eta d\zeta = \frac{1}{c^2} [E^0]. \end{aligned} \quad (3.13)$$

The coefficient matrices of (3.12) are evaluated by standard numerical integration techniques in the finite element method. Similar to the static stiffness and mass matrices in the finite element method, both of the coefficients  $[E^0]$  and  $[E^2]$  are sparse and positive definite. This formulation is the same as that of two-dimensional case [25]. It is applicable for



3-dimensional case with vertical truncated boundary of arbitrary geometry, such as the arch dam-reservoir system.

The acoustic nodal load vector  $r = \{r(\xi, t)\}$  on a vertical boundary with a constant  $\xi$  is obtained based on virtual work principle and is expressed as

$$\{r\} = [E^0] \{P\}_{,\xi}. \quad (3.14)$$

Assuming the time-harmonic behavior  $\{p(\xi, t)\} = \{P(\xi, \omega)\}e^{+i\omega t}$  and  $\{r(\xi, t)\} = \{R(\xi, \omega)\}e^{+i\omega t}$  ( $\omega$  is the excitation frequency) with the amplitudes of the hydrodynamic pressure  $\{P\} = \{P(\xi, \omega)\}$ , (3.12) is transformed into the frequency domain as

$$[E^0] \{P\}_{,\xi\xi} - [E^2] \{P\} + \frac{\omega^2}{c^2} [E^0] \{P\} = 0, \quad (3.15)$$

and the amplitudes of the acoustic nodal load  $\{R\} = \{R(\xi, \omega)\}$  are expressed as

$$\{R\} = -[E^0] \{P\}_{,\xi}. \quad (3.16)$$

#### 4. High-Order Doubly Asymptotic Open Boundary for Hydrodynamic Pressure

The derivation of high-order doubly asymptotic open boundary for hydrodynamic pressure is implemented based on the modal expression of (3.15). The streamlined expressions in [25] are summarized in this section.

##### 4.1. Modal Decomposition of Scaled Boundary Finite Element Equation

Following the procedure in detailed [25], the system of ordinary differential equations in (3.15) can be decoupled by a modal transformation. The modes are obtained from the following generalized eigenvalue problem ( $\langle \cdot \rangle$  stands for a diagonal matrix):

$$[E^2] [\Phi] = \frac{[E^0] [\Phi] \langle \lambda_j^2 \rangle}{h^2}, \quad (4.1)$$

where  $\langle \lambda_j^2 \rangle$  is the diagonal matrix of positive eigenvalues,  $h$  is a characteristic length (e.g., the depth of the semi-infinite layer) to nondimensionlize the eigenvalues, and  $[\Phi]$  are the matrix of eigenvectors representing the modes, which are normalized as

$$[\Phi]^T [E^0] [\Phi] = [I]. \quad (4.2)$$

As a result, the inverse of the eigenvector matrix can be obtained by the matrix multiplication

$$[\Phi]^{-1} = [\Phi]^T [E^0]. \quad (4.3)$$

Premultiplying (4.1) with  $[\Phi]^T$  results in

$$[\Phi]^T [E^2] [\Phi] = \frac{\langle \lambda_j^2 \rangle}{h^2}. \quad (4.4)$$

The relationship between amplitudes of the hydrodynamic pressure and amplitudes of the modal hydrodynamic pressure  $\{\tilde{P}\} = \{\tilde{P}(\xi, \omega)\}$  is defined as

$$\{P\} = [\Phi] \{\tilde{P}\}. \quad (4.5)$$

Substituting (4.5) into (3.15) premultiplied with  $[\Phi]^T$  and using (4.2) and (4.3) lead to a system of decoupled equations

$$\tilde{P}_{j,\xi\xi} + \frac{1}{h^2} (a_0^2 - \lambda_j^2) \tilde{P}_j = 0, \quad (4.6)$$

with the dimensionless frequency

$$a_0 = \frac{\omega h}{c}, \quad (4.7)$$

where index  $j$  indicates the modal number. Substituting (4.5) into (3.16), the acoustic nodal force vector is expressed as

$$\{R\} = -[E^0] [\Phi] \{\tilde{P}\}_{,\xi}. \quad (4.8)$$

The amplitude of the modal nodal force vector  $\{\tilde{R}\} = \{\tilde{R}(\xi, \omega)\}$  is defined as

$$\{\tilde{R}\} = -h \{\tilde{P}\}_{,\xi} \quad \text{or} \quad \tilde{R}_j = -h \tilde{P}_{j,\xi}. \quad (4.9)$$

Premultiplying (4.8) and using (4.2) and (4.9) yield

$$\{\tilde{R}\} = h [\Phi]^T \{R\}. \quad (4.10)$$

This equation transforms the amplitude of the acoustic nodal force vector to the amplitude of the modal force vector. The modal dynamic stiffness coefficient  $\tilde{S}_j(a_0)$  is defined as

$$\tilde{R}_j = \tilde{S}_j(a_0)\tilde{P}_j. \quad (4.11)$$

By eliminating  $\tilde{R}_j$  and  $\tilde{P}_j$  from (4.6), (4.9), and (4.11), an equation for the modal dynamic stiffness coefficient is derived as

$$\left(\tilde{S}_j(a_0)\right)^2 + a_0^2 - \lambda_j^2 = 0. \quad (4.12)$$

#### **4.2. Doubly Asymptotic Continued Fraction Solution for Modal Dynamic Stiffness**

Based on a doubly asymptotic solution of the modal dynamic stiffness coefficient  $\tilde{S}_j(a_0)$ , a temporally local open boundary [18] is constructed for a single mode of wave propagation. The solution of (4.12) is expressed as a doubly asymptotic continued fraction. An order  $M_H$  high-frequency continued fraction is constructed first as

$$\begin{aligned} \tilde{S}_j(a_0) &= (ia_0) - \lambda_j^2 \left( \tilde{Y}_j^{(1)}(a_0) \right)^{-1}, \\ \tilde{Y}_1^{(i)}(a_0) &= (-1)^i 2(ia_0) \tilde{Y}_{1,j}^{(i)} - \lambda_j^2 \left( \tilde{Y}_j^{(i+1)}(a_0) \right)^{-1} \quad (i = 1, 2, \dots, M_H). \end{aligned} \quad (4.13)$$

It is demonstrated by Prempramote et al. [18] that the high-frequency continued fraction solution does not converge when the excitation frequency is below the cutoff frequency. To determine a valid solution over the whole frequency range, an  $M_L$  order low-frequency continued fraction solution is constructed for the residual term  $\tilde{Y}_j^{(M_H+1)}(a_0)$ . Denoting the residual term for mode  $j$  as

$$\tilde{Y}_{L,j}(a_0) = \tilde{Y}_j^{(M_H+1)}(a_0). \quad (4.14)$$

The continued fraction solution for  $\tilde{Y}_{L,j}(a_0)$  at the low frequency limit is expressed as

$$\begin{aligned} \tilde{Y}_{L,j}(a_0) &= (-1)^{M_H+1} \lambda_j + (-1)^{M_H+1} (ia_0) - (ia_0)^2 \left( \tilde{Y}_{L,j}^{(1)}(a_0) \right)^{-1}, \\ \tilde{Y}_{L,j}^{(i)}(a_0) &= (-1)^{M_H+i+1} 2\lambda_j - (ia_0)^2 \left( \tilde{Y}_{L,j}^{(i+1)}(a_0) \right)^{-1} \quad (i = 1, 2, \dots, M_L). \end{aligned} \quad (4.15)$$

The doubly asymptotic continued fraction solution is constructed by combining the high-frequency continued fraction solution in (4.13) with the low-frequency solution in (4.15) using (4.14).

### 4.3. High-Order Doubly Asymptotic Open Boundary

Following the procedure developed for the modal space [18], the acoustic force-pressure relationship in the time domain is formulated by using the continued fraction solution of the dynamic stiffness coefficient and introducing auxiliary variables. A system of first-order ordinary differential equations with symmetric coefficient matrices is obtained, which represents a temporally local open boundary condition.

Substituting the continued fraction solution of the modal dynamic stiffness coefficient (4.13)–(4.15) into (4.11) and applying the inverse Fourier transform, the time-domain high-order doubly asymptotic open boundary in the modal space is expressed as

$$\frac{1}{h}\tilde{r}_j = \frac{1}{c}\dot{\tilde{p}}_j - \frac{1}{h}\lambda_j\tilde{p}_j^{(1)}, \quad (4.16)$$

$$0 = -\frac{1}{h}\lambda_j\tilde{p}_j - \frac{2}{c}\dot{\tilde{p}}_j^{(1)} - \frac{1}{h}\lambda_j\tilde{p}_j^{(2)}, \quad (4.17)$$

$$0 = -\frac{1}{h}\lambda_j\tilde{p}_j^{(i-1)} + (-1)^i \frac{2}{c}\dot{\tilde{p}}_j^{(i)} - \frac{1}{h}\lambda_j\tilde{p}_j^{(i+1)} \quad (i = 2, 3, \dots, M_H), \quad (4.18)$$

$$0 = -\frac{1}{h}\lambda_j\tilde{p}_j^{(M_H)} + (-1)^{M_H+1} \frac{1}{h}\lambda_j\tilde{p}_{L,j}^{(0)} + (-1)^{M_H+1} \frac{1}{c}\dot{\tilde{p}}_{L,j}^{(0)} - \frac{1}{c}\dot{\tilde{p}}_{L,j}^{(1)}, \quad (4.19)$$

$$0 = -\frac{1}{c}\dot{\tilde{p}}_{L,j}^{(i-1)} + (-1)^{M_H+i+1} \frac{2}{h}\lambda_j\tilde{p}_{L,j}^{(i)} - \frac{1}{c}\dot{\tilde{p}}_{L,j}^{(i+1)} \quad (i = 1, 2, \dots, M_L), \quad (4.20)$$

where  $\{\tilde{p}^{(i)}\}$  ( $i = 1, 2, \dots, M_H$ ) and  $\{\tilde{p}_L^{(i)}\}$  ( $i = 0, 1, 2, \dots, M_L$ ) are the auxiliary variables defined in modal space.

For an order  $M_H = M_L$  doubly asymptotic continued fraction solution, the residual term  $\tilde{p}_{L,j}^{(M_L+1)} = 0$  applies. Equations (4.16)–(4.20) constitute a system of first order ordinary differential equations relating the interaction load  $\{\tilde{r}_j\}$ , hydrodynamic pressure  $\{\tilde{p}_j\}$  and the modal auxiliary variables  $\tilde{p}_j^{(1)}, \dots, \tilde{p}_j^{(M_H)}, \tilde{p}_{L,j}^{(0)}, \tilde{p}_{L,j}^{(1)}, \dots, \tilde{p}_{L,j}^{(M_L)}$  in the modal space. This system of ordinary differential equations is a temporally local high-order doubly asymptotic open boundary condition for the semi-infinite reservoir with constant depth, which is directly established on the nodes of a vertical boundary. This boundary condition can be coupled seamlessly with finite element method.

## 5. Coupled Numerical Methods for Dam-Reservoir Interaction Analysis

Based on the high-order doubly asymptotic open boundary, two coupled numerical methods will be presented in this section: the direct coupled method and the partitioned coupled

method. Both coupled numerical methods are implemented on the open-source object-oriented finite element code OpenSees, that is, the open system for earthquake engineering simulation.

### 5.1. The Direct Coupled Method

In the direct coupled method, by incorporating the high-order doubly asymptotic open boundary with the near-field finite element equation, a monolithic governing equation for the near-field structure and auxiliary variables representing the far-field reservoir is formulated.

To derive a symmetric monolithic formulation, modal transform is applied to the auxiliary variables defined in modal space  $\{\tilde{p}^{(i)}\}$  and  $\{\tilde{p}_L^{(i)}\}$  as

$$\begin{aligned} \{p^{(i)}\} &= [\Phi] \{\tilde{p}^{(i)}\} \quad (i = 1, 2, \dots, M_H), \\ \{p_L^{(i)}\} &= [\Phi] \{\tilde{p}_L^{(i)}\} \quad (i = 0, 1, 2, \dots, M_L), \end{aligned} \quad (5.1)$$

where  $\{p^{(i)}\}$  and  $\{p_L^{(i)}\}$  are the auxiliary variables defined in real space.

Using (4.5), (4.10), (5.1), and left-multiplying (4.16)–(4.20) by  $[\Phi]^{-T}$  yield

$$\{r\} = \frac{1}{c} [E^0] \{\dot{p}\} - [A] \{p^{(1)}\}, \quad (5.2)$$

$$\{0\} = -[A] \{p\} - \frac{2}{c} [E^0] \{\dot{p}^{(1)}\} - [A] \{p^{(2)}\}, \quad (5.3)$$

$$\{0\} = -[A] \{p^{(i-1)}\} - (-1)^i \frac{2}{c} [E^0] \{\dot{p}^{(i)}\} - [A] \{p^{(i+1)}\} \quad (i = 2, 3, \dots, M_H), \quad (5.4)$$

$$\{0\} = -[A] \{p^{(M_H)}\} + (-1)^{M_H+1} [A] \{p_L^{(0)}\} + (-1)^{M_H+1} \frac{1}{c} [E^0] \{\dot{p}_L^{(0)}\} - \frac{1}{c} [E^0] \{\dot{p}_L^{(1)}\}, \quad (5.5)$$

$$\{0\} = -\frac{1}{c} [E^0] \{\dot{p}_L^{(i-1)}\} + (-1)^{M_H+i+1} 2[A] \{p_L^{(i)}\} - \frac{1}{c} [E^0] \{\dot{p}_L^{(i+1)}\} \quad (i = 1, 2, \dots, M_L) \quad (5.6)$$

with the symmetric and positive definite matrix

$$[A] = \frac{1}{h} [\Phi]^{-T} [\lambda_j] [\Phi]^{-1}. \quad (5.7)$$

The residual term  $[E^0] \{\dot{p}_L^{(M_L+1)}\}/c$  in (5.6) is setting to zero. Substituting (5.2)–(5.6) into (2.7) leads to a global linear system of ordinary differential equations in the time-domain

$$[M_g] \{\ddot{u}_g\} + [C_g] \{\dot{u}_g\} + [K_g] \{u_g\} = \{f_g\}. \quad (5.8)$$

Here, subscript  $g$  denotes global.  $[M_g]$ ,  $[C_g]$ , and  $[K_g]$  are the global mass matrix, global damping matrix, and global stiffness matrix, which are expressed as

$$\begin{aligned}
 [M_g] &= \begin{bmatrix} \mathbf{M}_s & 0 & 0 & & \\ -\mathbf{Q}_{fs} & \mathbf{M}_{ff} & \mathbf{M}_{fb} & & \\ 0 & \mathbf{M}_{bf} & \mathbf{M}_{bb} & 0 & \\ & & 0 & 0 & \ddots \\ & & & \ddots & \ddots & 0 \\ & & & & 0 & 0 \end{bmatrix}, \\
 [C_g] &= \frac{1}{c} \begin{bmatrix} 0 & 0 & 0 & & & \\ 0 & 0 & 0 & & & \\ 0 & 0 & \mathbf{C}_\infty & 0 & & \\ & 0 & \mathbf{Y}_1^{(1)} & \ddots & & \\ & & \ddots & \ddots & 0 & \\ & & & 0 & \mathbf{Y}_1^{(M_H)} & 0 \\ & & & 0 & \mathbf{Y}_{L1}^{(0)} & -\mathbf{C}_\infty \\ & & & & -\mathbf{C}_\infty & 0 & \ddots \\ & & & & & \ddots & \ddots & -\mathbf{C}_\infty \\ & & & & & & -\mathbf{C}_\infty & 0 \end{bmatrix}, \\
 [K_g] &= \begin{bmatrix} \mathbf{K}_s & \mathbf{Q}_{sf} & 0 & & & \\ 0 & \mathbf{K}_{ff} & \mathbf{K}_{fb} & & & \\ 0 & \mathbf{K}_{bf} & \mathbf{K}_{bb} & -\mathbf{A} & & \\ & & -\mathbf{A} & 0 & \ddots & \\ & & & \ddots & \ddots & -\mathbf{A} \\ & & & & -\mathbf{A} & 0 & -\mathbf{A} \\ & & & & & -\mathbf{A} & \mathbf{Y}_{L0}^{(0)} & 0 \\ & & & & & & 0 & \mathbf{Y}_{L0}^{(1)} & \ddots \\ & & & & & & & \ddots & \ddots & 0 \\ & & & & & & & & 0 & \mathbf{Y}_{L0}^{(M_L)} \end{bmatrix},
 \end{aligned} \tag{5.9}$$

with the block matrices

$$\begin{aligned}
 \mathbf{C}_\infty &= [E^0], \quad \mathbf{Y}_{L0}^{(0)} = (-1)^{M_H+1} [A], \quad \mathbf{Y}_{L1}^{(0)} = (-1)^{M_H+1} [E^0], \\
 \mathbf{Y}_1^{(i)} &= (-1)^i 2 [E^0] \quad (i = 1, 2, \dots, M_H), \\
 \mathbf{Y}_{L0}^{(i)} &= (-1)^{M_H+i+1} 2 [A] \quad (i = 1, 2, \dots, M_L).
 \end{aligned} \tag{5.10}$$

The global load vector  $[f_g]$  and unknowns  $[u_g]$  are expressed as (the semicolon “;” stands for the vertical concatenation of vectors)

$$\begin{aligned} \{u_g\} &= \left[ \{u_s\}^T; \{p_f\}^T; \{p_b\}^T; \{p^{(1)}\}^T; \cdots; \{p_L^{(M_L)}\}^T \right]^T, \\ \{f_g\} &= \left[ \{r_s\}^T; \{r_f\}^T; \{0\}^T; \{0\}^T; \cdots; \{0\}^T \right]^T. \end{aligned} \quad (5.11)$$

This system of linear equations describes the complete dam-reservoir system taking account of the influence of the semi-infinite reservoir. Similar to the near-field finite element formulation (2.7), the coefficient matrices of this formulation are sparse and symmetric. This dynamic system can be solved using a standard time-integration method, such as the Newmark family schemes.

Equation (5.8) is of order  $N_s + N_f + N_{fb} + (M_H + M_L + 2)N_{fb}$ , where  $N_s$  is the number of degrees of freedom of dam structure,  $N_f$  is the number of degrees of freedom of near-field reservoir except for those of the truncated boundary, and  $N_{fb}$  is the number of degrees of freedom of truncated boundary. Compared with the near-field finite element equation (2.7), additional auxiliary  $(M_H + M_L + 1)N_{fb}$  degrees of freedom are introduced in (5.8). From the point view of numerical implementation, (5.8) can be implemented on existing finite element code without any special treatment and solved by existing finite element solver. The block coefficient matrices  $[E^0]$  and  $[A]$  in (5.10) are evaluated only once in the analysis. However, the formulation of the direct coupled method involves additional auxiliary variables, which requires more computational effort and memory to solve this dynamic system.

## 5.2. The Partitioned Coupled Method

In the partitioned coupled method, the near-field finite element equation and the far-field high-order doubly asymptotic boundary condition are separately solved. They are coupled by the interaction force on the truncated boundary. The deviation of the partitioned coupled method is detailed in [25]. Streamlined expressions are presented as follows.

Using (4.3) and (4.10), (4.16) left-multiplied by  $[\Phi]^{-T}$  is rewritten as

$$\{r\} = \frac{1}{c} [E^0] \{\dot{p}\} - \frac{1}{h} [\Phi]^{-T} \langle \lambda_j \rangle \{\tilde{p}^{(1)}\}. \quad (5.12)$$

Substituting (5.12) into (2.7), the finite element formulation of the dam-reservoir system considering the interaction between the near-field and the semi-infinite reservoir is expressed as

$$\begin{aligned} & \begin{bmatrix} [M_s] & 0 & 0 \\ -[Q_{fs}] & [M_{ff}] & [M_{fb}] \\ 0 & [M_{bf}] & [M_{bb}] \end{bmatrix} \begin{Bmatrix} \{\ddot{u}_s\} \\ \{\ddot{p}_f\} \\ \{\ddot{p}_b\} \end{Bmatrix} + \frac{1}{c} \begin{bmatrix} 0 & 0 & 0 \\ 0 & 0 & 0 \\ 0 & 0 & [E^0] \end{bmatrix} \begin{Bmatrix} \{\dot{u}_s\} \\ \{\dot{p}_f\} \\ \{\dot{p}_b\} \end{Bmatrix} \\ & + \begin{bmatrix} [K_s] & [Q_{sf}] & 0 \\ 0 & [K_{ff}] & [K_{fb}] \\ 0 & [K_{bf}] & [K_{bb}] \end{bmatrix} \begin{Bmatrix} \{u_s\} \\ \{p_f\} \\ \{p_b\} \end{Bmatrix} = \begin{Bmatrix} \{f_s\} \\ \{f_f\} \\ \frac{[\Phi]^{-T} \langle \lambda_j \rangle \{\tilde{p}^{(1)}\}}{h} \end{Bmatrix}. \end{aligned} \quad (5.13)$$

The high-order doubly asymptotic open boundary is split into two parts. The first part is the additional damping term on left-hand side of (5.13), which is equivalent to the Sommerfeld radiation boundary as demonstrated in [25]. The second part is the coupling term  $[\Phi]^{-T} \langle \lambda_j \rangle \{\tilde{p}^{(1)}\} / h$  on the right-hand side of (5.13) representing the contribution of the high-order terms of the doubly asymptotic boundary. It can be regarded as an external load acted on the truncated boundary. For efficiency consideration in the numerical implementation, the coupling term  $[\Phi]^{-T} \langle \lambda_j \rangle \{\tilde{p}^{(1)}\} / h$  is evaluated in the modal space.

Assembling (4.17)–(4.20) multiplied by  $h/\lambda_j$ , a system of ordinary differential equation for the modal auxiliary variables is formulated as

$$[K_A] \{z_{A,j}(t)\} + \frac{h}{c\lambda_j} [C_A] \{\dot{z}_{A,j}(t)\} = \{f_{A,j}(t)\}, \quad (5.14)$$

where the coefficient matrices are expressed as

$$[K_A] = \begin{bmatrix} 0 & 1 & & & & \\ 1 & \ddots & \ddots & & & \\ & \ddots & 0 & 1 & & \\ & & 1 & (-1)^{M_H} & 0 & \\ & & & 0 & (-1)^{M_H+1} 2 & \ddots \\ & & & & \ddots & \ddots & 0 \\ & & & & & 0 & (-1)^{M_H+M_L} 2 \end{bmatrix}, \quad (5.15)$$

$$[C_A] = \begin{bmatrix} (-1)^0 2 & 0 & & & & \\ 0 & \ddots & \ddots & & & \\ & \ddots & (-1)^{M_H-1} 2 & 0 & & \\ & & 0 & (-1)^{M_H} & 1 & \\ & & & 1 & 0 & \ddots \\ & & & & \ddots & \ddots & 1 \\ & & & & & 1 & 0 \end{bmatrix}.$$

The unknown vector  $\{z_{A,j}(t)\}$  consists of the modal auxiliary variables of mode  $j$  (the semicolon “;” stands for the vertical concatenation of vectors)

$$\{z_{A,j}(t)\} = \{\tilde{p}_j^{(1)}; \dots; \tilde{p}_j^{(M_H)}; \tilde{p}_{L,j}^{(0)}; \tilde{p}_{L,j}^{(1)}; \dots; \tilde{p}_{L,j}^{(M_L)}\}. \quad (5.16)$$



The only nonzero entry on the right-hand side is the modal hydrodynamic pressure  $\tilde{p}_j$  obtained from (4.5)

$$\{f_{A,j}(t)\} = \{-\tilde{p}_j; 0; \dots; 0; 0; 0; \dots; 0\}. \quad (5.17)$$

It is demonstrated by Wang et al. [25] that (5.14) is stable up to the order  $M_H = M_L = 100$  at least.

Equations (5.13) for the near field and (5.14) for the far field are coupled by the auxiliary variables  $\{\tilde{p}^{(1)}\}$  defined in the modal space. Using the same time integration scheme, such as the trapezoidal rule, these two sets of equations are solved by a sequential staggered implicit-implicit partitioned procedure proposed in [28, 29]. The value of the modal auxiliary variables  $\{\tilde{p}^{(1)}\}$  at time station  $t_{n+1}$  is determined by the last-solution extrapolation predictor [28, 29]

$$\{\tilde{p}^{(1)}\}_{n+1}^p = \{\tilde{p}^{(1)}\}_n. \quad (5.18)$$

The auxiliary variables  $\{\tilde{p}^{(1)}\}$  are obtained by integrating (5.14) for prescribed hydrodynamic pressure  $\{p\}$ . The algorithm proposed in [25] to solve (5.13) and (5.14) proceeds as follows.

- Step 1.* Initialize variables  $\{u\}_0$  and  $\{p\}_0$  in (5.13) and  $\{z_{A,j}\}_0 = 0$  for each mode in (5.14).
- Step 2.* Extract  $\{\tilde{p}^{(1)}\}_n$  from  $\{z_{A,j}\}_n = 0$  of each mode and assigned to  $\{\tilde{p}^{(1)}\}_{n+1}^p$  in (5.18).
- Step 3.* Form the right-hand term of (5.13), compute  $\{u\}_{n+1}$  and  $\{p\}_{n+1}$  by using an implicit method.
- Step 4.* Calculate modal hydrodynamic pressure  $\{\tilde{p}\}_{n+1}$  and form the right-hand term of (5.14).
- Step 5.* Compute  $\{z_{A,j}\}_{n+1}$  for each mode by using an implicit method.
- Step 6.* Increment  $n$  to  $n + 1$  and go to Step 2.

Since the predicted vector  $\{\tilde{p}^{(1)}\}_{n+1}^p$  has been used rather than  $\{\tilde{p}^{(1)}\}_{n+1}$  in solving (5.13) and (5.14), this algorithm may lead to a numerical instability or poor accuracy. To avoid these, the solution algorithm for the partitioned coupled method in this paper is modified. The solution process within one step given by Step 2 to Step 5 is repeated a number of times in an iterative manner [26]. In each additional cycle,  $\{\tilde{p}^{(1)}\}_{n+1}^p$  in Step 2 is extracted by the last computed  $\{z_{A,j}\}_{n+1}$  in Step 5. Numerical experiments demonstrate that stability and accuracy are improved by performing a few additional iterations.

The order of (5.14) is only  $M_H + M_L + 1$ , and little computational effort is required to solve (5.14). Consequently, additional memory required for the solution of partitioned method is less than that of the direct coupled method.

This partitioned coupled method and the sequential staggered implicit-implicit partition algorithm [25] are both implemented in the open-source finite element code OpenSees rather than ABAQUS; as a result, the computational efficiency is greatly improved without any time costing restart analysis in ABAQUS.

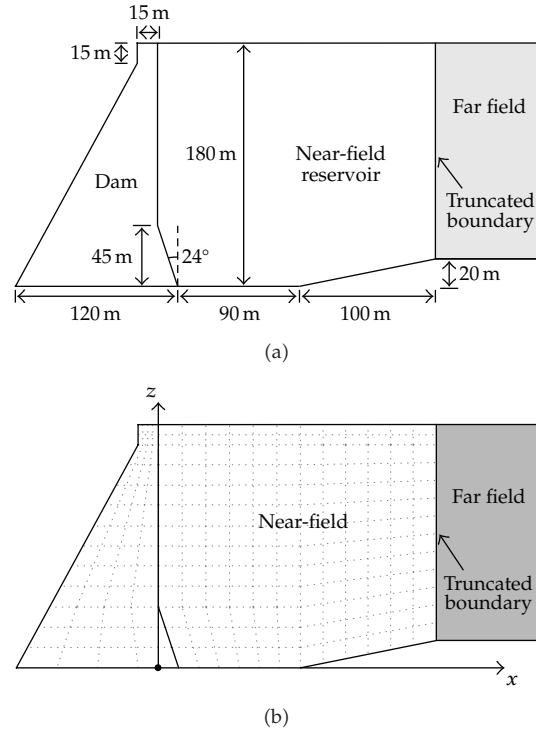


Figure 3: A gravity dam-reservoir system with irregular near field: (a) Geometry; (b) Mesh.

## 6. Numerical Examples

Two numerical examples are analyzed to evaluate the accuracy and efficiency of the two present coupled numerical methods. The first example is a gravity dam with an irregular near field reservoir. The open boundary is employed to represent the regular semi-infinite reservoir of a constant depth. The time integration for these two coupled numerical methods is performed by the trapezoidal integration.

It is demonstrated by Wang et al. [25] that an order  $M_H = M_L = 10$  high-order doubly asymptotic open boundary condition is of excellent accuracy. So, the order  $M_H = M_L = 10$  open boundary condition is chosen for these two numerical examples.

### 6.1. Gravity Dam

A typical gravity dam-reservoir system with an irregular near field is shown in Figure 3(a), which is the same as the flexible dam example in [25]. The dam body has a modulus of elasticity  $E = 35 \text{ GPa}$ , Poisson's ration  $\nu = 0.2$ , and mass density  $\rho = 2400 \text{ kg/m}^3$ . The water in the reservoir has a pressure wave velocity  $c = 1438.7 \text{ m/s}$  and mass density  $\rho = 1000 \text{ kg/m}^3$ .

The finite element mesh is shown in Figure 3(b). The system is divided into three parts: the dam body, the near-field reservoir, and the far-field semi-infinite reservoir with constant depth. The dam body is discretized with eight-node solid elements, the near-field reservoir with 156 eight-node acoustic fluid elements, and the dam-reservoir interface with 13 three-node interface elements. The far-field reservoir is modeled by 13 three-node quadratic line

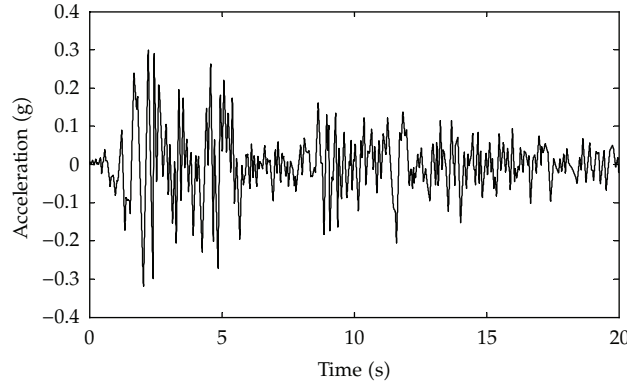


**Figure 4:** Time history of El Centro earthquake.

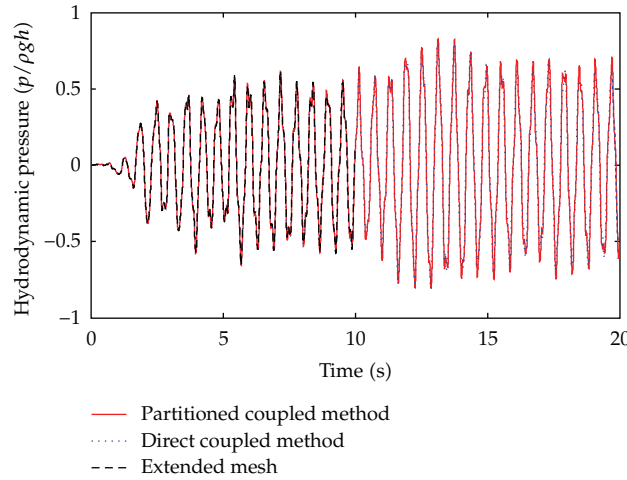


**Figure 5:** Hydrodynamic pressure at heel of the gravity dam under El Centro ground motion with a time step of 0.002 s.

elements on the truncated boundary, which share the same nodes and are compatible with those of the near-field acoustic fluid elements. The total number of nodes of the whole model is 653.

To verify the results, an extended mesh covering a far-field reservoir region of 7200 m is analyzed. The size of extended mesh is sufficiently large to avoid the pollution of the dam response by the waves reflected on the truncated boundary for a time duration of  $2 \times 7200/1438.7 \approx 10$  s.

The El Centro earthquake ground motion (see Figure 4) is imposed as the horizontal acceleration at the base of the dam. The time step is chosen as 0.002 s during which the pressure wave travels about one third of the distance between two adjacent nodes. The partitioned coupled method is performed without any additional iteration; that is, the solution process is the same as that in [25]. The responses of hydrodynamic pressure at heel of the gravity dam of the first 20 s are plotted in Figure 5. Excellent agreement between the solutions of both coupled numerical methods and the extended mesh solution is observed during the first 10 s.

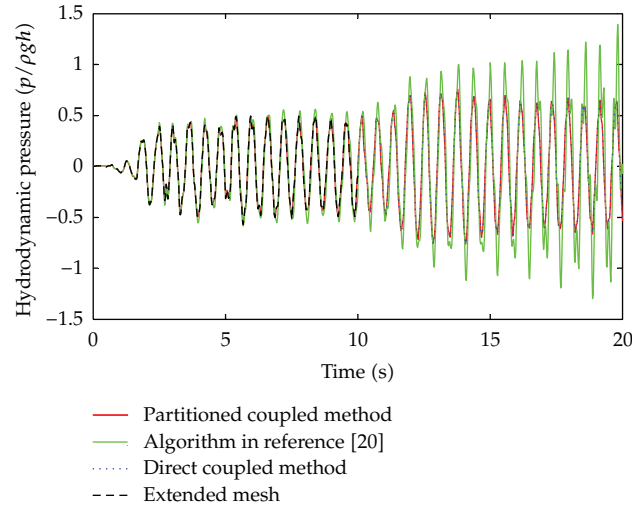


**Figure 6:** Hydrodynamic pressure at heel of the gravity dam under El Centro ground motion with a time step of 0.02 s.

**Table 1:** Computer time for the gravity dam example.

Time step (sec)	Extended mesh	Direct coupled method	Partitioned coupled method	Algorithm in [25]
0.002	2980 s	242 s	241 s	\
0.02	219 s	25 s	46 s	25 s

To demonstrate the improvement of the modified solution algorithm for partitioned coupled method, the time step is increased to 0.02 s. The responses of the first 20 s are plotted in Figure 6. As it is shown, the results of the solution algorithm proposed by Wang et al. [25] tend to be divergent and inaccurate. However, both the solutions of direct coupled method and partitioned coupled method agree with the solution of extended mesh very well. The number of additional iterations within each step for partitioned coupled method recorded is usually one and no more than four in this example.

The computer time for the gravity dam example list in Table 1 is recorded on a PC with a 2.93 GHz Intel Core i7 CPU. High computational efficiency of both coupled methods is observed. The computer time of the direct coupled method is about one tenth of that of the extended mesh. The computational effort of the partitioned coupled method is directly associated with the number of additional iterations. When there is no additional iteration, the computer time of the partitioned coupled method is nearly equal to that of the direct coupled method.

## 6.2. Arch Dam

An arch dam-reservoir system is shown in Figure 7. The physical properties of dam body and water are the same as that in the example of gravity dam. The arch dam is of a height of 22 m and the near-field reservoir covers a region of the dam height. The dam body is discretized with 272 twenty-node hexahedron solid elements, the near-field reservoir with 1088 twenty-

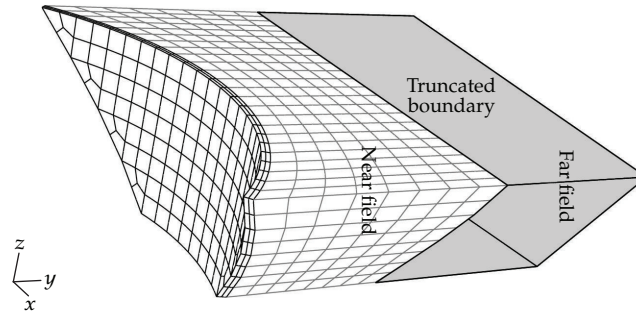


Figure 7: An arch dam-reservoir system.

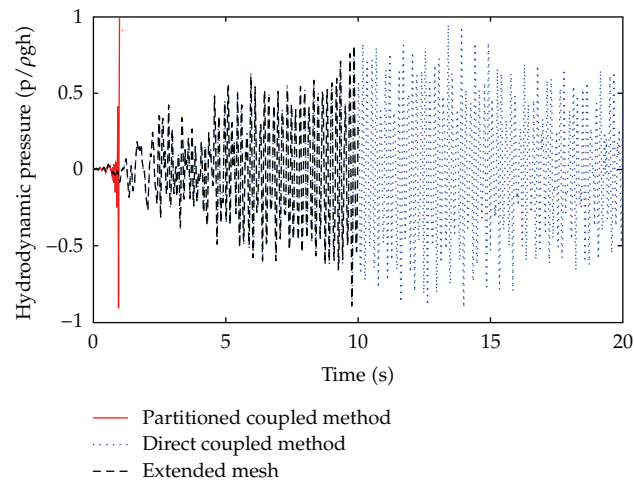


Figure 8: Hydrodynamic pressure at heel of the arch dam under El Centro ground motion with a time step of 0.02 s.

node hexahedron acoustic fluid elements, and the dam-reservoir interface with 136 eight-node interface elements. The far-field reservoir is modeled by 136 eight-node quadratic elements on the truncated boundary, which share the same nodes and are compatible with those of the near-field acoustic fluid elements. The total number of nodes of the whole model is 6652. To verify the results, a similar extended mesh covering the region of 7200 m is analyzed.

Similar to the gravity dam example, the El Centro earthquake ground motion is imposed as the horizontal ( $Y$  direction) acceleration at the base of the arch dam. The time step is chosen as 0.02 s. The responses of the hydrodynamic pressure at the heel of the arch dam are plotted in Figure 8. The solution of the direct coupled method agrees with solution of the extended mesh and is long time stable. However, as for the partitioned coupled method, numerical divergence is observed at the early time of the analysis. Numerical instability of such coupling strategy is also reported in [12]. It can be expected as the partitioned coupled method is conditional stable; that is, the integration time step is limited by stability limits. When the time step is greater than the stability limit, numerical instability may occur, for example, the results of the arch dam example. As the dam-reservoir system is quite complicated, it is difficult to determine the stability limits of different application cases. When the partitioned coupled method is applied, smaller time step should be used.

The computer time of the direct coupled method recorded is 1463 s, which is about one ninth of that of the extended mesh, that is, 12547 s. It also demonstrates the high computational efficiency of the direct coupled method.

## 7. Conclusions

Two coupled numerical methods were developed for the dam-reservoir interaction analysis by incorporating the finite element method with the excellent high-order doubly asymptotic open boundary. The dam-reservoir system is divided into the near-field with irregular geometry and the far-field by the truncated boundary. In the direct coupled method, a global monolithic equation for the whole dam-reservoir system is formulated with sparse and symmetric coefficient matrices, which can be solved by the standard finite element solver. In the partitioned coupled method, the near-field finite element equation and the high-order open boundary condition are separately solved. They are coupled by the interaction force applied on the truncated boundary. The partitioned coupled method is achieved by using a sequential staggered implicit-implicit procedure. To improve the numerical stability and accuracy of the algorithm, an iteration strategy was employed to obtain the solution of each step.

Both of the two coupled numerical methods are implemented on the open-source finite element code OpenSees. Numerical experiments demonstrated the high efficiency and accuracy of both coupled numerical methods. The memory required for the solution of the partitioned method is less than that of the direct coupled method. Although the numerical stability and accuracy of the partitioned coupled method can be improved by additional iterations within each step, the partitioned coupled method is conditionally stable yet. Its stability is also related to the predictor. Further research should be carried out to improve the stability of the partitioned coupled method. In contrast, the direct coupled method is unconditionally stable if only an unconditionally stable time integration algorithm such as trapezoidal integration is chosen. Consequently, larger time steps can be used in the direct coupled method than that in the partitioned coupled method.

## Acknowledgments

This research was supported by the State Key Laboratory of Hydrosience and Engineering of Tsinghua University under Grant no. 2008-TC-2, the National Science Foundation of China under Grants nos. 90510018, and 90715041, and by the National Key Technology R&D Program under Grant no. 2008BAB29B05. The authors are also grateful to Professor Chongmin Song's instructive suggestions on this research.

## References

- [1] A. K. Chopra and P. Chakrabarti, "Earthquake analysis of concrete gravity dams including dam water foundation rock interaction," *Earthquake Engineering and Structural Dynamics*, vol. 9, no. 4, pp. 363–383, 1981.
- [2] J. F. Hall and A. K. Chopra, "Two-dimensional dynamic analysis of concrete gravity and embankment dams including hydrodynamic effects," *Earthquake Engineering and Structural Dynamics*, vol. 10, no. 2, pp. 305–332, 1982.
- [3] O. C. Zienkiewicz and P. Bettess, "Fluid-structure dynamic interaction and wave forces. An introduction to numerical treatment," *International Journal for Numerical Methods in Engineering*, vol. 13, no. 1, pp. 1–16, 1978.

- [4] S. Küçükarıslan, S. B. Coşkun, and B. Taşkın, "Transient analysis of dam-reservoir interaction including the reservoir bottom effects," *Journal of Fluids and Structures*, vol. 20, no. 8, pp. 1073–1084, 2005.
- [5] A. Sommerfeld, *Partial Differential Equations in Physics*, Academic Press, New York, NY, USA, 1949.
- [6] C. S. Tsai, G. C. Lee, and R. L. Ketter, "Semi-analytical method for time-domain analyses of dam-reservoir interactions," *International Journal for Numerical Methods in Engineering*, vol. 29, no. 5, pp. 913–933, 1990.
- [7] C. S. Tsai and G. C. Lee, "Time-domain analyses of dam-reservoir system. II: substructure method," *Journal of Engineering Mechanics*, vol. 117, no. 9, pp. 2007–2026, 1991.
- [8] R. Yang, C. S. Tsai, and G. C. Lee, "Explicit time-domain transmitting boundary for dam-reservoir interaction analysis," *International Journal for Numerical Methods in Engineering*, vol. 36, no. 11, pp. 1789–1804, 1993.
- [9] T. Touhei and T. Ohmachi, "A FE-BE method for dynamic analysis of dam-foundation-reservoir systems in the time domain," *Earthquake Engineering and Structural Dynamics*, vol. 22, no. 3, pp. 195–209, 1993.
- [10] R. J. Câmara, "A method for coupled arch dam-foundation-reservoir seismic behaviour analysis," *Earthquake Engineering and Structural Dynamics*, vol. 29, no. 4, pp. 441–460, 2000.
- [11] O. Czygan and O. von Estorff, "Fluid-structure interaction by coupling BEM and nonlinear FEM," *Engineering Analysis with Boundary Elements*, vol. 26, no. 9, pp. 773–779, 2002.
- [12] D. Soares Jr., O. von Estorff, and W. J. Mansur, "Efficient non-linear solid-fluid interaction analysis by an iterative BEM/FEM coupling," *International Journal for Numerical Methods in Engineering*, vol. 64, no. 11, pp. 1416–1431, 2005.
- [13] A. Seghir, A. Tahakourt, and G. Bonnet, "Coupling FEM and symmetric BEM for dynamic interaction of dam-reservoir systems," *Engineering Analysis with Boundary Elements*, vol. 33, no. 10, pp. 1201–1210, 2009.
- [14] S. M. Li, H. Liang, and A. M. Li, "A semi-analytical solution for characteristics of a dam-reservoir system with absorptive reservoir bottom," *Journal of Hydrodynamics*, vol. 20, no. 6, pp. 727–734, 2008.
- [15] G. Lin, J. Du, and Z. Hu, "Dynamic dam-reservoir interaction analysis including effect of reservoir boundary absorption," *Science in China Series E: Technological Sciences*, vol. 50, no. 1, pp. 1–10, 2007.
- [16] S. V. Tsynkov, "Numerical solution of problems on unbounded domains. A review," *Applied Numerical Mathematics*, vol. 27, no. 4, pp. 465–532, 1998.
- [17] D. Givoli, "High-order local non-reflecting boundary conditions: a review," *Wave Motion*, vol. 39, no. 4, pp. 319–326, 2004, New computational methods for wave propagation.
- [18] S. Prempramote, C. Song, F. Tin-Loi, and G. Lin, "High-order doubly asymptotic open boundaries for scalar wave equation," *International Journal for Numerical Methods in Engineering*, vol. 79, no. 3, pp. 340–374, 2009.
- [19] T. Geers, "Singly and doubly asymptotic computational boundaries," in *Proceedings of the IUTAM Symposium on Computational Methods for Unbounded Domains*, pp. 135–141, Kluwer Academic Publishers, Dordrecht, The Netherlands, 1998.
- [20] T. L. Geers, "Doubly asymptotic approximations for transient motions of submerged structures," *Journal of the Acoustical Society of America*, vol. 64, no. 5, pp. 1500–1508, 1978.
- [21] P. Underwood and T. L. Geers, "Doubly asymptotic, boundary-element analysis of dynamic soil-structure interaction," *International Journal of Solids and Structures*, vol. 17, no. 7, pp. 687–697, 1981.
- [22] T. L. Geers and B. A. Lewis, "Doubly asymptotic approximations for transient elastodynamics," *International Journal of Solids and Structures*, vol. 34, no. 11, pp. 1293–1305, 1997.
- [23] T. L. Geers and B. J. Tothaker, "Third-order doubly asymptotic approximations for computational acoustics," *Journal of Computational Acoustics*, vol. 8, no. 1, pp. 101–120, 2000.
- [24] M. H. Bazzyar and C. Song, "A continued-fraction-based high-order transmitting boundary for wave propagation in unbounded domains of arbitrary geometry," *International Journal for Numerical Methods in Engineering*, vol. 74, no. 2, pp. 209–237, 2008.
- [25] X. Wang, F. Jin, S. Prempramote, and C. Song, "Time-domain analysis of gravity dam-reservoir interaction using high-order doubly asymptotic open boundary," *Computers and Structures*, vol. 89, no. 7–8, pp. 668–680, 2011.
- [26] D. Givoli, B. Neta, and I. Patlashenko, "Finite element analysis of time-dependent semi-infinite wave-guides with high-order boundary treatment," *International Journal for Numerical Methods in Engineering*, vol. 58, no. 13, pp. 1955–1983, 2003.



- [27] C. Song and J. P. Wolf, "The scaled boundary finite-element method—alias consistent infinitesimal finite-element cell method—for elastodynamics," *Computer Methods in Applied Mechanics and Engineering*, vol. 147, no. 3-4, pp. 329–355, 1997.
- [28] K.-C. Park, "Partitioned transient analysis procedures for coupled-field problems: stability analysis," *Journal of Applied Mechanics*, vol. 47, no. 2, pp. 370–376, 1980.
- [29] K. C. Park and C. A. Felippa, "Partitioned transient analysis procedures for coupled-field problems: accuracy analysis," *Journal of Applied Mechanics*, vol. 47, no. 4, pp. 919–926, 1980.



## Research Article

# Coupling the BEM/TBEM and the MFS for the Numerical Simulation of Wave Propagation in Heterogeneous Fluid-Solid Media

**António Tadeu and Igor Castro**

*CICC, Department of Civil Engineering, University of Coimbra, Rua Luís Reis Santos, Pólo II da Universidade, 3030-788 Coimbra, Portugal*

Correspondence should be addressed to António Tadeu, tadeu@itecons.uc.pt

Received 31 March 2011; Accepted 24 July 2011

Academic Editor: Luis Godinho

Copyright © 2011 A. Tadeu and I. Castro. This is an open access article distributed under the Creative Commons Attribution License, which permits unrestricted use, distribution, and reproduction in any medium, provided the original work is properly cited.

This paper simulates wave propagation in an elastic medium containing elastic, fluid, rigid, and empty heterogeneities, which may be thin. It uses a coupling formulation between the boundary element method (BEM)/the traction boundary element method (TBEM) and the method of fundamental solutions (MFS). The full domain is divided into subdomains, which are handled separately by the BEM/TBEM or the MFS, to overcome the specific limitations of each of these methods. The coupling is enforced by applying the prescribed boundary conditions at all medium interfaces. The accuracy, efficiency, and stability of the proposed algorithms are verified by comparing the results with reference solutions. The paper illustrates the computational efficiency of the proposed coupling formulation by computing the CPU time and the error. The transient analysis of wave propagation in the presence of a borehole driven in a cracked medium is used to illustrate the potential of the proposed coupling formulation.

## 1. Introduction

Various numerical methods have been proposed to simulate the propagation of waves in elastic and acoustic media, since analytical solutions are only known for simple and regular geometries (e.g., [1–6]). These techniques include the thin-layer method (TLM) [7], the boundary element method (BEM) [8], the finite element method (FEM) [9, 10], the finite difference method (FDM) [11], the ray tracing technique [12], and the method of fundamental solutions (MFS) [13].

Of these techniques, the FEM is the most widely used numerical method used by researchers and commercial software producers. It can be used to solve complex geometries, but it requires the full discretization of the media being modelled. This makes the FEM

computationally unfeasible for very large scale models, such as those involving unbounded domains, unless substantial shortcuts are implemented. These may entail the use of coarse elements, low frequency simulations, or the introduction of boundary artefacts.

The BEM is one of the most suitable techniques for modelling wave propagation in homogeneous unbounded systems containing irregular interfaces and inclusions, because only the boundaries of the heterogeneities and interfaces need to be discretized and the far-field conditions are automatically satisfied [14–16]. Despite this, the BEM still needs prior knowledge of fundamental solutions (Green's functions) and also requires the correct integration of the resulting singular and hypersingular integrals to guarantee its efficiency. In addition, the number of boundary elements depends on the excitation frequency, and many boundary elements are needed to model high-frequency responses, a situation which leads to an undesirably high computational cost.

Furthermore, the simulation of wave propagation in the presence of very thin heterogeneities such as cracks leads to singular boundary element matrix systems, thus leading to the mathematical degeneration of the numerical formulation [17]. The dual boundary element method (DBEM) is one of the main boundary element formulations adopted to overcome this problem. Derivatives of the original BEM displacement formulation to produce a traction formulation first became necessary when fracture mechanics problems began to be addressed [18]. But these hybrid BEM formulations do not necessarily have to be used for solving such problems. Good results have been obtained in 2D examples of both elastodynamic and coupled-field problems involving stationary cracks when conventional, displacement-based BEM formulations were used in a transformed domain, with special treatment of the cracks [19, 20].

Using the DBEM, after the discretization of the inclusion's surface, dipole loads are applied to the opposite surface, which is governed by the traction boundary integral equation [21], while monopole loads are applied to one part of the surface, which corresponds to applying the displacement boundary integral equation. In the case of a dimensionless empty crack, only a single line of boundary elements loaded with dipole loads is used to solve the problem, that is, by using only the traction boundary integral equation method [22–24]. The appearance of hypersingular integrals is one of the difficulties posed by these formulations. In the particular case of 2D and 2.5D wave propagation in elastic and acoustic media, the resulting hypersingular kernels can be computed analytically [25].

Meshless techniques that require neither domain nor boundary discretization have recently become popular [26, 27]. The origin of the MFS has two sources and lies in the indirect BEM [28] and the general definition of a Green's function [29]. The MFS copes with some of the mathematical complexity of the BEM and provides acceptable solutions for wave propagation problems at substantially lower computational cost [30, 31]. The MFS solution is based on a linear combination of fundamental solutions (Green's functions), generated by a set of fictitious sources to simulate the scattered and refracted field produced by the heterogeneities. To avoid singularities, these virtual sources are placed at some distance from the inclusion's boundary. The use of fundamental solutions allows the final solution to verify the unbounded boundary conditions automatically. Still the use of the MFS has its own limitations when thin inclusions such as cracks and inclusions with twisting (sinuous) boundaries are involved. The analysis would require the use of domain decompositions or/and the use of enriched functions, which increases computation costs [32]. The number of the virtual sources and their positions is another difficulty since the results are highly dependent on these parameters. Among the strategies that have been proposed to handle this problem is the verification of the solution's accuracy by computing the solution at points

other than the collocation ones, where the boundary and prescribed conditions are known a priori.

Researchers are currently trying to improve the results by coupling different methods so as to exploit the advantages of each technique and reduce their disadvantages, thereby speeding up analysis and ensuring efficiency, stability, accuracy, and flexibility.

BEM/FEM coupling has often been used, with each technique being applied to distinct subdomains [33–35]. The two approaches most often used are a direct coupling and iterative coupling [36–38]. Iterative coupling allows the subdomains to be analyzed separately, leading to smaller and better-conditioned systems of equations with independent discretizations being considered for each subdomain. Some authors have reported problems related to the convergence of ill-posed models, however. The coupling of meshless methods and the BEM is another approach. The coupling of the BEM/TBEM with the MFS to analyse acoustic wave propagation in the presence of multiple inclusions and thin heterogeneities is one example proposed by the authors. The full domain is first divided into subdomains which are modelled using the BEM/TBEM and the MFS. The subdomains are then coupled by imposing the required boundary conditions [39].

The paper extends that work with a formulation which couples the BEM/TBEM and the MFS to simulate the propagation of waves involving the fluid-solid interaction, as in the case of multielastic fluid layer systems, acoustic logging, and cross-hole surveying geophysical prospecting techniques [40, 41]. It is very often quite helpful to model the direct problem in order to better understand how waves propagate in the presence of such structures, particularly in cracked media and damaged zones, when it is not always easy to interpret the recorded results because of the unforeseen presence of those heterogeneities [42, 43].

The problem is formulated in the frequency domain. The waves generated by the virtual sources used by the MFS are seen as incident waves by the BEM/TBEM, while the BEM sees the collocation points used to impose the boundary conditions at the interfaces modelled by the MFS, as receivers. The approach is implemented for 2.5D problems in general. The accuracy of the proposed coupling algorithms, which use different combinations of BEM/TBEM and MFS formulations, is checked by means of a verification analysis using reference solutions.

The proposed coupling formulations for simulating wave propagation in the presence of fluid and elastic inclusions are described in the next section. The coupling formulations are first verified against solutions obtained using BEM/TBEM, taken as reference solutions. We then show the computational efficiency of the formulations by measuring the CPU time taken to compute the numerical responses provided by the different algorithms. Finally, the applicability of the proposed method is shown by means of a numerical example that simulates the propagation of waves generated by a line blast load in the vicinity of a fluid-filled borehole driven in a cracked elastic medium.

## 2. Boundary Integral Coupling Formulations

Consider two irregular two-dimensional cylindrical inclusions, 1 and 2, embedded in a homogeneous elastic medium (Medium 1) with density  $\rho_1$  (Figure 1) and allowing longitudinal (P-wave) and shear waves (S-wave) to travel at velocities  $\alpha_1$  and  $\beta_1$ , respectively. Medium 2, inside Inclusion 1, is fluid, has density  $\rho_2$ , and permits pressure waves (P-wave) to travel at velocity  $\alpha_2$ . Inclusion 2 is elastic (Medium 3), has density  $\rho_3$ , and allows longitudinal and shear waves to travel at velocities  $\alpha_3$  and  $\beta_3$ , respectively.

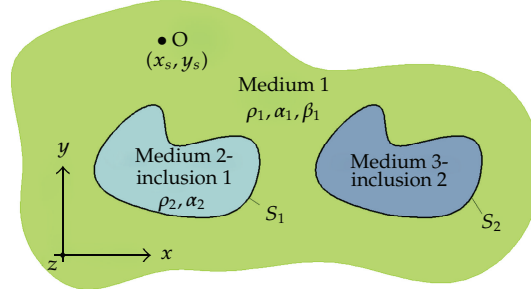


Figure 1: The geometry of the problem.

It is further assumed that this system is subjected to a dilatational line source placed at  $(x_s, y_s)$  whose amplitude varies sinusoidally in the third dimension ( $z$ ).

The incident wave field generated by this source can be expressed in the frequency domain by means of the classic dilatational potential:

$$\phi_{\text{inc}}(x, y, \omega, k_z) = \frac{-iA}{2} H_0(k_{\alpha_1} r), \quad (2.1)$$

in which  $H_n(\cdots)$  are second kind Hankel functions of the order  $n$ ,  $i = \sqrt{-1}$ ,  $k_{\alpha_1} = \sqrt{\omega^2/\alpha_1^2 - k_z^2}$  with  $\text{Im}(k_{\alpha_1}) < 0$ ,  $r = \sqrt{(x - x_s)^2 + (y - y_s)^2}$  and  $k_z$  is the wavenumber along  $z$ .

Then, the displacement field can be expressed as

$$\begin{aligned} u_x^{\text{inc}}(x, y, x_s, y_s, \omega) &= \frac{iA}{2} k_{\alpha_1} H_1(k_{\alpha_1} r) \frac{\partial r}{\partial x}, \\ u_y^{\text{inc}}(x, y, x_s, y_s, \omega) &= \frac{iA}{2} k_{\alpha_1} H_1(k_{\alpha_1} r) \frac{\partial r}{\partial y}, \\ u_z^{\text{inc}}(x, y, x_s, y_s, \omega) &= \frac{A}{2} k_z H_0(k_{\alpha_1} r). \end{aligned} \quad (2.2)$$

## 2.1. BEM/MFS Coupling Formulation

This section describes the coupling between the BEM and the MFS formulations used to obtain the wave field generated by the dilatational line source placed in the exterior medium, Medium 1. The first inclusion is modelled using the BEM while the other is solved with the MFS (see Figure 2).

Continuity of normal tractions and displacements and null tangential tractions are prescribed along the boundary of the fluid Inclusion 1. Three different boundary conditions may be ascribed to Inclusion 2's surface: continuity of displacements and tractions (simulating an elastic inclusion); null tractions (an empty inclusion); null displacements (a rigid inclusion).

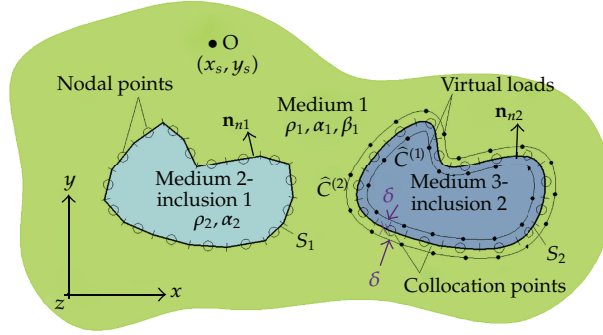


**Figure 2:** Discretization of the system: position of virtual loads, collocation points and boundary elements.

### 2.1.1. Fluid Inclusion 1 and Elastic Inclusion 2

Assuming Inclusion 1 to be bounded by a surface  $S_1$  and subjected to an incident field given by  $u^{\text{inc}}$ , the boundary integral equation can be constructed by applying the reciprocity theorem (e.g., Manolis and Beskos [44]) leading to the following.

(a) Along the Exterior Domain of Inclusion 1 (Medium 1),

$$c_{ij}u_i^{(1)}(x_0, y_0, \omega) = \int_{S_1} t_1^{(1)}(x, y, \mathbf{n}_{n1}, \omega) G_{i1}^{(1)}(x, y, x_0, y_0, \omega) ds - \sum_{j=1}^3 \int_{S_1} u_j^{(1)}(x, y, \omega) H_{ij}^{(1)}(x, y, \mathbf{n}_{n1}, x_0, y_0, \omega) ds + u_i^{\text{inc}}(x_0, y_0, x_s, y_s, \omega). \quad (2.3)$$

In this equation,  $i, j = 1, 2$  correspond to the normal and tangential directions relative to the inclusion surface, while  $i, j = 3$  correspond to the  $z$  direction. In these equations, the superscript 1 represents the exterior domain;  $\mathbf{n}_{n1}$  is the unit outward normal along boundary  $S_1$ , at  $(x, y)$ , defined by the vector  $\mathbf{n}_{n1} = (\cos \theta_{n1}, \sin \theta_{n1})$ .  $G_{ij}^{(1)}(x, y, x_0, y_0, \omega)$  and  $H_{ij}^{(1)}(x, y, \mathbf{n}_{n1}, x_0, y_0, \omega)$  define the fundamental solutions for displacements and tractions (Green's functions), in direction  $j$  on the boundary  $S_1$  at  $(x, y)$ , caused by a unit point force in direction  $i$  applied at the nodal point,  $(x_0, y_0)$  (see the appendix).  $u_j^{(1)}(x, y, \omega)$  corresponds to displacements in direction  $j$  at  $(x, y)$ ,  $t_j^{(1)}(x, y, \mathbf{n}_{n1}, \omega)$  specifies the nodal tractions in direction  $j$  on the boundary at  $(x, y)$  and  $u_i^{\text{inc}}(x_0, y_0, x_s, y_s, \omega)$  to the displacement incident field at  $(x_0, y_0)$  along direction  $i$ , when the source is located at  $(x_s, y_s)$ . The coefficient  $c_{ij}$  is equal to  $\delta_{ij}/2$ , with  $\delta_{ij}$  being the Kronecker delta, when the boundary is smooth.

Green's functions for displacements along the  $x$ ,  $y$ , and  $z$  directions in the solid medium are listed in the appendix, and their derivation can be found in [45].

Equation (2.3) does not yet take into account the presence of the neighbouring Inclusion 2, which is modelled using the MFS. The MFS assumes that the response of this neighbouring inclusion is found as a linear combination of fundamental solutions simulating the displacement field generated by two sets of  $NS$  virtual sources. These virtual loads

are distributed along the inclusion interface  $S_2$  at distances  $\delta$  from that boundary towards the interior and exterior of the inclusion (lines  $\widehat{C}^{(1)}$  and  $\widehat{C}^{(2)}$  in Figure 2) in order to avoid singularities. Sources inside the inclusion have unknown amplitudes  $a_{nj,n.\text{ext}}^{(2)}$ , while those placed outside the inclusion have unknown amplitudes  $a_{nj,n.\text{int}}^{(2)}$ . In the exterior, and interior elastic media the scattered displacement fields are given by

$$\begin{aligned} u_i^{(1)}(x, y, \omega) &= \sum_{n=1}^{NS} \sum_{j=1}^3 a_{nj,n.\text{ext}}^{(2)} G_{ji}^{(1)}(x, y, x_{n.\text{ext}}, y_{n.\text{ext}}, \omega), \\ u_i^{(3)}(x, y, \omega) &= \sum_{n=1}^{NS} \sum_{j=1}^3 a_{nj,n.\text{int}}^{(2)} G_{ji}^{(3)}(x, y, x_{n.\text{int}}, y_{n.\text{int}}, \omega), \end{aligned} \quad (2.4)$$

where  $G_{ji}^{(1)}(x, y, x_{n.\text{ext}}, y_{n.\text{ext}}, \omega)$  and  $G_{ji}^{(3)}(x, y, x_{n.\text{int}}, y_{n.\text{int}}, \omega)$  are the fundamental solutions which represent the displacements at points  $(x, y)$  in Mediums 1 and 3, in direction  $i$ , caused by a unit point force in direction  $j$  applied at the positions  $(x_{n.\text{ext}}, y_{n.\text{ext}})$  and  $(x_{n.\text{int}}, y_{n.\text{int}})$ .  $n_{\text{ext}}$  and  $n_{\text{int}}$  are the subscripts that denote the load order number placed along lines  $\widehat{C}^{(1)}$  and  $\widehat{C}^{(2)}$ .

The displacement field generated by this second inclusion can be viewed as an incident field that strikes the first inclusion. So (2.3) needs to be modified accordingly,

$$\begin{aligned} c_{ij} u_i^{(1)}(x_0, y_0, \omega) &= \int_{S_1} t_1^{(1)}(x, y, \mathbf{n}_{n1}, \omega) G_{i1}^{(1)}(x, y, x_0, y_0, \omega) ds \\ &\quad - \sum_{j=1}^3 \int_{S_1} u_j^{(1)}(x, y, \omega) H_{ij}^{(1)}(x, y, \mathbf{n}_{n1}, x_0, y_0, \omega) ds + u_i^{\text{inc}}(x_0, y_0, x_s, y_s, \omega) \\ &\quad + \sum_{n=1}^{NS} \sum_{j=1}^3 a_{nj,n.\text{ext}}^{(2)} G_{ji}^{(1)}(x_0, y_0, x_{n.\text{ext}}, y_{n.\text{ext}}, \omega). \end{aligned} \quad (2.5)$$

(b) In the Interior Domain of Inclusion 1 (Medium 2),

$$\begin{aligned} cp^{(2)}(x_0, y_0, \omega) &= \int_{S_1} q^{(2)}(x, y, -\mathbf{n}_{n1}, \omega) G_f^{(2)}(x, y, x_0, y_0, \omega) ds \\ &\quad - \int_{S_1} p^{(2)}(x, y, \omega) H_f^{(2)}(x, y, -\mathbf{n}_{n1}, x_0, y_0, \omega) ds. \end{aligned} \quad (2.6)$$

In (2.6), the superscript 2 corresponds to the domain inside Inclusion 1, Medium 2.  $G_f^{(2)}(x, y, x_0, y_0, \omega)$  and  $H_f^{(2)}(x, y, -\mathbf{n}_{n1}, x_0, y_0, \omega)$  are Green's functions for pressure and the gradient of pressure on the boundary  $S_1$  at  $(x, y)$ , caused by a unit point pressure at the nodal point,  $(x_0, y_0)$  (see the appendix).  $p^{(2)}(x, y, \omega)$  corresponds to the pressure at  $(x, y)$ ,  $q^{(2)}(x, y, \mathbf{n}_{n1}, \omega)$  specifies the nodal pressure gradients on the boundary at  $(x, y)$ . The coefficient  $c$  is equal to 1/2 when the boundary is smooth.

(c) *In the Interior and Exterior Domains of Inclusion 2 (Media 1 and 3),*

To determine the amplitudes of the unknown virtual point loads  $a_{nj,n.\text{ext}}^{(2)}$  and  $a_{nj,n.\text{int}}^{(2)}$ , it is also necessary to impose the continuity of displacements and tractions at interface  $S_2$ , which is the boundary of Inclusion 2, along  $NS$  collocation points  $(x_{\text{col}}, y_{\text{col}})$ . This must be done so as to take into account the scattered field generated at Inclusion 1. The following two equations are thus defined:

$$\begin{aligned}
 & \int_{S_1} t_1^{(1)}(x, y, \mathbf{n}_{n1}, \omega) G_{i1}^{(1)}(x, y, x_{\text{col}}, y_{\text{col}}, \omega) ds \\
 & - \sum_{j=1}^3 \int_{S_1} u_j^{(1)}(x, y, \omega) H_{ij}^{(1)}(x, y, \mathbf{n}_{n1}, x_{\text{col}}, y_{\text{col}}, \omega) ds \\
 & + u_i^{\text{inc}}(x_{\text{col}}, y_{\text{col}}, x_s, y_s, \omega) + \sum_{n=1}^{NS} \sum_{j=1}^3 a_{nj,n.\text{ext}}^{(2)} G_{ji}^{(1)}(x_{\text{col}}, y_{\text{col}}, x_{n.\text{ext}}, y_{n.\text{ext}}, \omega) \\
 & = \sum_{n=1}^{NS} \sum_{j=1}^3 a_{nj,n.\text{int}}^{(2)} G_{ji}^{(3)}(x_{\text{col}}, y_{\text{col}}, x_{n.\text{int}}, y_{n.\text{int}}, \omega), \\
 & \int_{S_1} t_1^{(1)}(x, y, \mathbf{n}_{n1}, \omega) \bar{G}_{i1}^{(1)}(x, y, \mathbf{n}_{n2}, x_{\text{col}}, y_{\text{col}}, \omega) ds \\
 & - \sum_{j=1}^3 \int_{S_1} u_j^{(1)}(x, y, \omega) \bar{H}_{ij}^{(1)}(x, y, \mathbf{n}_{n1}, \mathbf{n}_{n2}, x_{\text{col}}, y_{\text{col}}, \omega) ds \\
 & + \bar{u}_i^{\text{inc}}(x_{\text{col}}, y_{\text{col}}, \mathbf{n}_{n2}, x_s, y_s, \omega) + \sum_{n=1}^{NS} \sum_{j=1}^3 a_{nj,n.\text{ext}}^{(2)} \bar{G}_{ji}^{(1)}(x_{\text{col}}, y_{\text{col}}, \mathbf{n}_{n2}, x_{n.\text{ext}}, y_{n.\text{ext}}, \omega) \\
 & = \sum_{n=1}^{NS} \sum_{j=1}^3 a_{nj,n.\text{int}}^{(2)} \bar{G}_{ji}^{(3)}(x_{\text{col}}, y_{\text{col}}, \mathbf{n}_{n2}, x_{n.\text{int}}, y_{n.\text{int}}, \omega).
 \end{aligned} \tag{2.7}$$

$$\begin{aligned}
 & = \sum_{n=1}^{NS} \sum_{j=1}^3 a_{nj,n.\text{int}}^{(2)} \bar{G}_{ji}^{(3)}(x_{\text{col}}, y_{\text{col}}, \mathbf{n}_{n2}, x_{n.\text{int}}, y_{n.\text{int}}, \omega).
 \end{aligned} \tag{2.8}$$

Green's functions  $\bar{H}_{ij}^{(1)}(x, y, \mathbf{n}_{n1}, \mathbf{n}_{n2}, x_{\text{col}}, y_{\text{col}}, \omega)$  and  $\bar{G}_{ij}^{(1)}(x, y, \mathbf{n}_{n2}, x_{\text{col}}, y_{\text{col}}, \omega)$  are defined by applying the traction operator to  $H_{ij}^{(1)}(x, y, \mathbf{n}_{n1}, x_{\text{col}}, y_{\text{col}}, \omega)$  and  $G_{ij}^{(1)}(x, y, x_{\text{col}}, y_{\text{col}}, \omega)$ , which can be obtained by combining the derivatives of the former Green's functions, in order of  $x$ ,  $y$ , and  $z$ , so as to obtain the stresses (see the appendix). In these equations,  $\mathbf{n}_{n2}$  is the unit outward normal to the boundary  $S_2$  at the collocation points  $(x_{\text{col}}, y_{\text{col}})$ .

(d) *Final System of Equations.*

The global solution is obtained by solving (2.5)–(2.8). This requires the discretization of the interface  $S_1$ , which is the boundary of Inclusion 1. For the purposes of this work, this interface is discretized into  $N$  straight boundary elements, with one nodal point in the middle of each element (see Figure 2).



The required integrations in (2.5)–(2.8) are evaluated in closed form when the element to be integrated is the loaded element [45, 46], while a numerical integration that uses a Gaussian quadrature scheme applies when the element to be integrated is not the loaded one.

The final integral equations are manipulated and combined so as to impose the continuity of normal tractions and displacements, and null tangential tractions along the boundary of Inclusion 1, and the continuity of displacements and tractions along the boundary of Inclusion 2, to establish a system of  $[(6NS + 4N) \times (6NS + 4N)]$  equations. The relation  $u_1^{(1)} = -(1/\rho_2)(\partial p^{(2)}/\partial \mathbf{n}_1)$  is used to relate pressure gradients and displacements, while the normal pressure corresponds to normal tractions.

The solution of this system of equations gives the nodal tractions and displacements along the boundary  $S_1$  and the unknown virtual load amplitudes,  $a_{nj,n\_ext}^{(2)}$  and  $a_{nj,n\_int}^{(2)}$ , which allow the displacement field to be defined inside and outside the inclusions.

### 2.1.2. Empty Inclusion 2 (Null Tractions Along its Boundary)

In this case, null tractions are prescribed along the boundary  $S_2$ . Thus, (2.5) and (2.6) are kept as before and (2.8) is simplified to

$$\begin{aligned} & \int_{S_1} t_1^{(1)}(x, y, \mathbf{n}_1, \omega) \overline{G}_{i1}^{(1)}(x, y, \mathbf{n}_2, x_{col}, y_{col}, \omega) ds \\ & - \sum_{j=1}^3 \int_{S_1} u_j^{(1)}(x, y, \omega) \overline{H}_{ij}^{(1)}(x, y, \mathbf{n}_1, \mathbf{n}_2, x_{col}, y_{col}, \omega) ds \\ & + \overline{u}_i^{inc}(x_{col}, y_{col}, \mathbf{n}_2, x_s, y_s, \omega) + \sum_{n=1}^{NS} \sum_{j=1}^3 a_{nj,n\_ext}^{(2)} \overline{G}_{ji}^{(1)}(x_{col}, y_{col}, \mathbf{n}_2, x_{n\_ext}, y_{n\_ext}, \omega) = 0. \end{aligned} \quad (2.9)$$

The solution of the boundary integral along the surface ( $S_1$ ) again requires its discretization into  $N$  straight boundary elements, while the simulation of Inclusion 2 uses  $NS$  collocation points/virtual sources, following a procedure similar to the one described above. This leads to a system of  $[(3NS + 4N) \times (3NS + 4N)]$  equations.

### 2.1.3. Rigid Inclusion 2 (Null Displacements Along its Boundary)

Null displacements on the surface of Inclusion 2 are now prescribed, which leads to (2.5) and (2.6) and to the following equation:

$$\begin{aligned} & \int_{S_1} t_1^{(1)}(x, y, \mathbf{n}_1, \omega) G_{i1}^{(1)}(x, y, x_{col}, y_{col}, \omega) ds \\ & - \sum_{j=1}^3 \int_{S_1} u_j^{(1)}(x, y, \omega) H_{ij}^{(1)}(x, y, \mathbf{n}_1, x_{col}, y_{col}, \omega) ds \\ & + u_i^{inc}(x_{col}, y_{col}, x_s, y_s, \omega) + \sum_{n=1}^{NS} \sum_{j=1}^3 a_{nj,n\_ext}^{(2)} G_{ji}^{(1)}(x_{col}, y_{col}, x_{n\_ext}, y_{n\_ext}, \omega) = 0. \end{aligned} \quad (2.10)$$



The solution of these equations is once again obtained as described above, with a system of  $[(3NS + 4N) \times (3NS + 4N)]$  equations. Other coupling combinations can be solved in the same way.

## 2.2. TBEM/MFS Coupling Formulation

The traction boundary element method (TBEM) can be proposed to simulate the scattered wave field in the vicinity of thin inclusions, for which the BEM formulation described above fails [47, 48]. This technique can be formulated by applying dipoles (dynamic doublets) instead of monopole loads. Replace the former (2.5) and (2.6), to give the following (2.11), while modelling the first inclusion:

$$\begin{aligned}
 & a_{ij}u_i^{(1)}(x_0, y_0, \omega) + c_{i1}t_1^{(1)}(x_0, y_0, \mathbf{n}_{n1}, \omega) \\
 &= \int_{S_1} t_1^{(1)}(x, y, \mathbf{n}_{n1}, \omega) \overline{G}_{i1}^{(1)}(x, y, \mathbf{n}_{n2}, x_0, y_0, \omega) ds \\
 & - \sum_{j=1}^3 \int_{S_1} u_j^{(1)}(x, y, \omega) \overline{H}_{ij}^{(1)}(x, y, \mathbf{n}_{n1}, \mathbf{n}_{n2}, x_0, y_0, \omega) ds \\
 & + \overline{u}_i^{\text{inc}}(x_0, y_0, \mathbf{n}_{n2}, x_s, y_s, \omega) \\
 & + \sum_{n=1}^{NS} \sum_{j=1}^3 a_{n j n \text{ ext}}^{(2)} \overline{G}_{ji}^{(1)}(x_0, y_0, \mathbf{n}_{n2}, x_{n \text{ ext}}, y_{n \text{ ext}}, \omega), \\
 & ap^{(2)}(x_0, y_0, \omega) + cq^{(2)}(x_0, y_0, -\mathbf{n}_{n1}, \omega) \\
 &= \int_{S_1} q^{(2)}(x, y, -\mathbf{n}_{n1}, \omega) \overline{G}_f^{(2)}(x, y, \mathbf{n}_{n2}, x_0, y_0, \omega) ds \\
 & - \int_{S_1} \overline{H}_f^{(2)}(x, y, -\mathbf{n}_{n1}, \mathbf{n}_{n2}, x_0, y_0, \omega) p^{(1)}(x, y, \omega) ds.
 \end{aligned} \tag{2.11}$$

As noted by Guiggiani [49], the coefficients  $a_{ij}$  and  $a$  are zero for piecewise straight boundary elements. The factors  $c_{ij}$  and  $c$  are constants, defined as above.

Equations (2.7) and (2.8) can be kept the same for modelling the second inclusion.

The solutions of these equations are defined as before by discretizing the boundary surface ( $S_1$ ) into  $N$  straight boundary elements, with one nodal point in the middle of each element. The integrations in (2.11) are performed through a Gaussian quadrature scheme when the element being integrated is not the loaded one. When the element being integrated is the loaded one, the integrals become hypersingular. An indirect approach is used for the analytical solution of those hypersingular integrals. This consists of defining the dynamic equilibrium of an isolated semicylinder, above each boundary element (see [47, 48]).

Manipulating (2.7), (2.8) and (2.11) as described above, the cavity and the rigid inclusions and their combinations, can also be modelled.

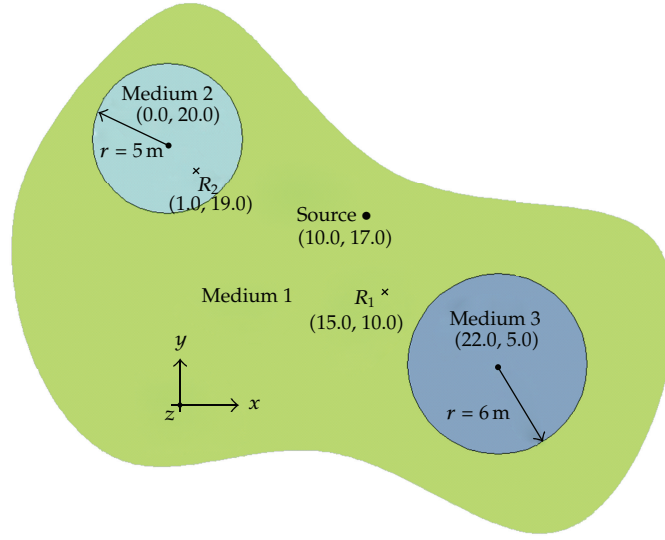


**Figure 3:** Two circular inclusions (fluid and elastic) embedded in an unbounded elastic medium.

### 2.3. Combined (TBEM + BEM)/MFS Coupling Formulation

The displacement and traction formulations can be combined so as to solve the problems described above. This has the advantage of allowing the solution to be defined when Inclusions 1 or/and 2 are thin. In these cases, part of the boundary surface of the inclusion is loaded with monopole loads (formulation in displacements), while the remaining part is loaded with dipoles (formulation in tractions).

## 3. Verification of the Coupling Algorithms

The proposed coupling algorithms (MFS/BEM and MFS/TBEM) described are verified against BEM and MFS solutions by solving the elastic field produced by two circular inclusions embedded in an unbounded elastic medium, centred at (0.0 m, 20.0 m) and (22.0 m, 5.0 m), with radii of 5.0 m and 6.0 m (see Figure 3). Three separate problems are solved by combining different types of Inclusion 2, namely, an elastic inclusion (Case 1), a cavity (Case 2), and a rigid inclusion (Case 3). Inclusion 1 is always filled with fluid.

The host elastic medium ( $\rho_1 = 2140 \text{ kg/m}^3$ ) is homogeneous, permitting a P-wave velocity of  $\alpha_1 = 4208 \text{ m/s}$  and an S-wave velocity of  $\beta_1 = 2656 \text{ m/s}$ . The fluid in Inclusion 1 exhibits a density equal to  $\rho_2 = 1000 \text{ kg/m}^3$  and allows P-wave velocity of  $\alpha_2 = 1500 \text{ m/s}$ , while the elastic Inclusion 2, of density  $\rho_3 = 2250 \text{ kg/m}^3$ , exhibits a dilatational and an S-wave of velocities  $\alpha_3 = 2630 \text{ m/s}$ ,  $\beta_3 = 1416 \text{ m/s}$ , respectively. The excitation source is assumed to be inside the host medium at point (10.0 m, 17.0 m). It is a harmonic dilatational line load whose amplitude varies sinusoidally in the third dimension according to  $k_z = 0.2 \text{ rad/m}$ .

The responses are computed at receiver  $R_1$  and  $R_2$ , placed at (15.0 m, 10.0 m) and (1.0 m, 19.0 m), respectively. The computations are performed in the frequency domain from 1 Hz to 200 Hz.

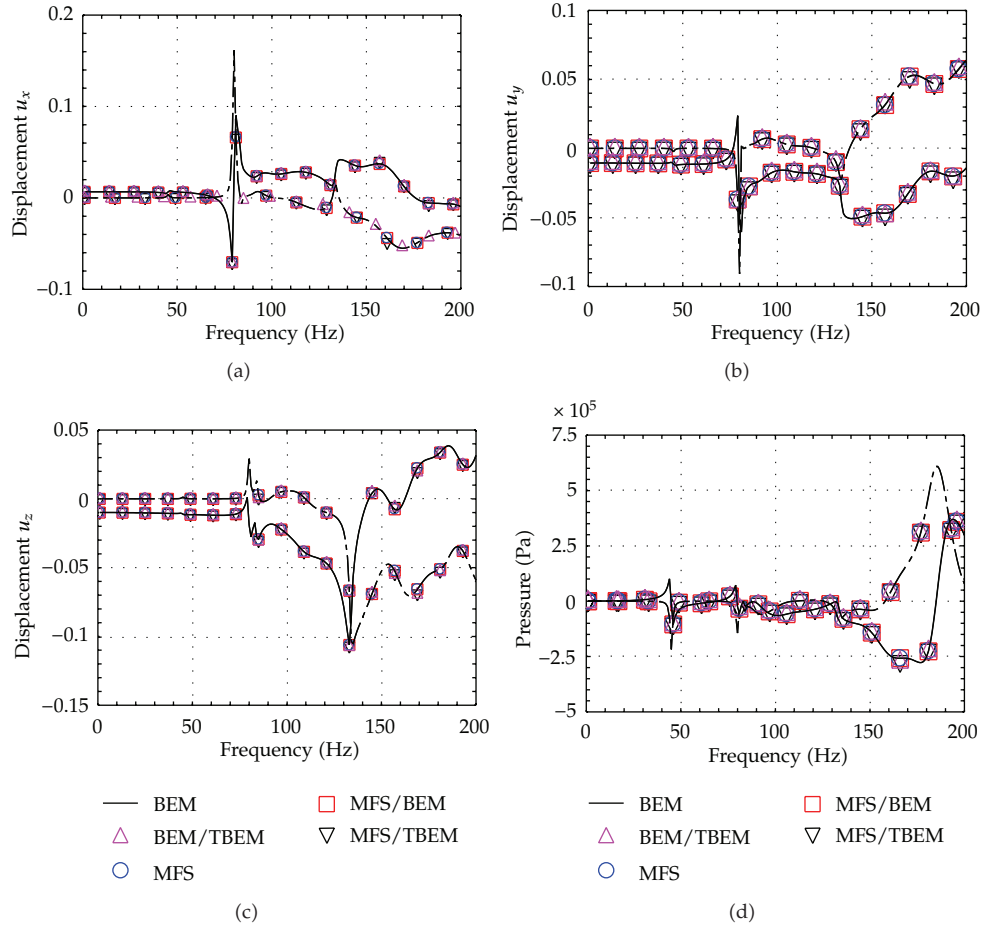


**Figure 4:** Case 1: BEM, TBEM, MFS, and coupling formulations' results: displacements at receiver ( $R_1$ ) and pressure at receiver ( $R_2$ ) when the system is excited by a blast load.

All the illustrated simulations used interior and exterior virtual sources respectively placed at distances  $0.9 \times r$  and  $1.1 \times r$  from the centre of the inclusion, with  $r$  being radii.

Figures 4, 5, and 6 present the real (solid line) and imaginary (dashed line) parts of the displacements  $u_x$ ,  $u_y$ , and  $u_z$  (receiver  $R_1$ ) and pressure response (receiver  $R_2$ ) for the three cases. The lines correspond to the BEM responses, that is, when the inclusions are each modelled with 200 boundary elements. Different BEM/TBEM, MFS, and coupling solutions are indicated by the marked points and labelled "BEM/TBEM", "MFS", "MFS/BEM", and "MFS/TBEM". 200 boundary elements and virtual sources are used in the MFS and coupling solutions for each inclusion. An analysis of the results shows very good agreement between the proposed coupling solutions and both the BEM and MFS models' solutions.

#### 4. Computational Efficiency of the Coupling Algorithms

The computational efficiency of the proposed coupling formulations is illustrated by calculating at a grid of receivers the displacements caused by an empty crack of null thickness, placed in the vicinity of a fluid-filled borehole (Figure 7(a)).

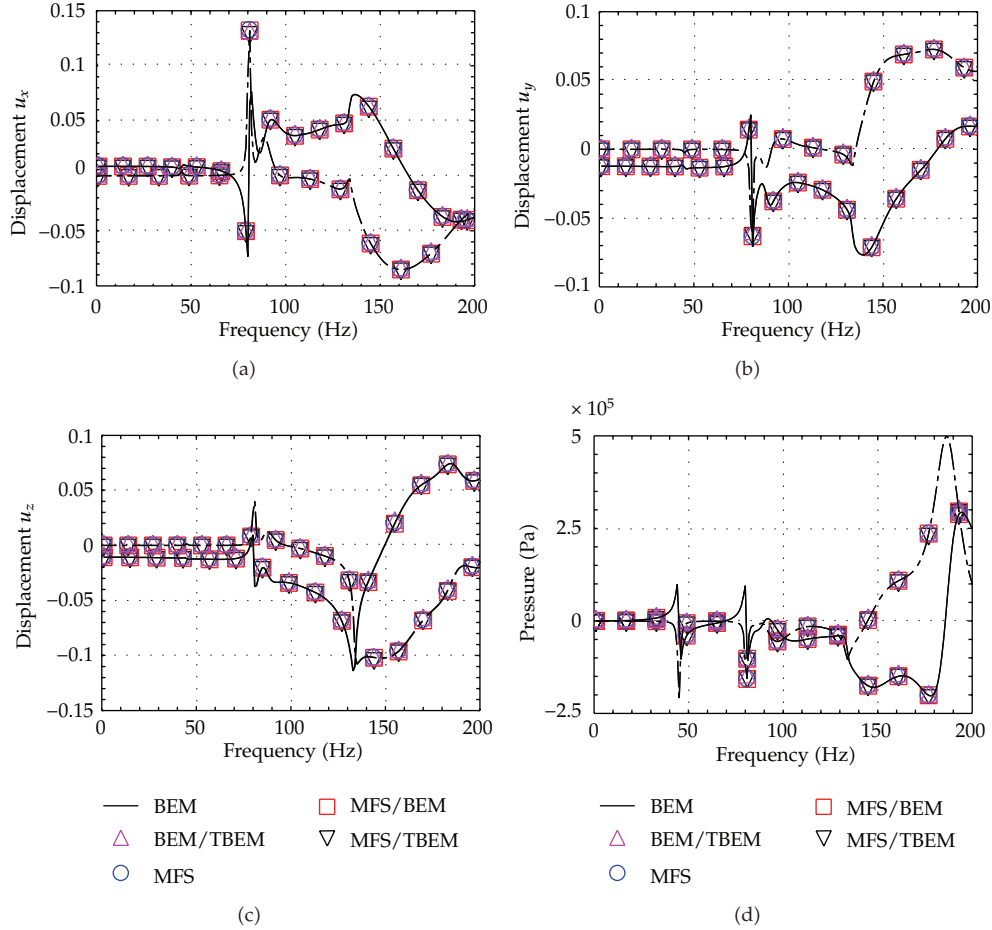


**Figure 5:** Case 2: BEM, TBEM, MFS, and coupling formulations' results: displacements at receiver ( $R_1$ ) and pressure at receiver ( $R_2$ ) when the system is excited by a blast load.

The host medium, with a density of  $2250 \text{ kg/m}^3$ , allows P-wave and S-wave velocities of  $2630 \text{ m/s}$  and  $1416 \text{ m/s}$ , respectively. The fluid-filled borehole is centred at  $(0.0 \text{ m}, 0.0 \text{ m})$  with a radius of  $0.05 \text{ m}$ . Its fluid has a mass density of  $1000 \text{ kg/m}^3$  and permits a P-wave speed of  $1500 \text{ m/s}$ . A null-thickness arc-shaped crack centred at  $(0.0 \text{ m}, 0.0 \text{ m})$  has a radius of  $0.10 \text{ m}$  and a length of  $(1.2\pi/32) \text{ m}$ .

This system is illuminated by a wave field generated by a dilatational line load placed  $0.05 \text{ m}$  ( $k_z = 0 \text{ rad/m}$ ) from the crack at  $(0.15 \text{ m}, 0.0 \text{ m})$ . The resulting displacement is obtained over a grid of 10140 receivers arranged along the  $x$  and  $y$  directions at equal intervals and placed from  $x = -0.10 \text{ m}$  to  $x = 0.25 \text{ m}$  and from  $y = -0.15 \text{ m}$  to  $y = 0.15 \text{ m}$ .

Computational efficiency was evaluated by determining the CPU time taken to compute the solution for the full grid of receivers by the BEM/TBEM, the MFS and the MFS/TBEM, at two specific frequencies:  $140 \text{ Hz}$  and  $9000 \text{ Hz}$ .

As there are no known analytical solutions, the BEM/TBEM solution for 770 boundary elements is used as reference solution. The crack is discretized as an open line and loaded with dipole loads (210 TBEM boundary elements), while the fluid-filled borehole boundary

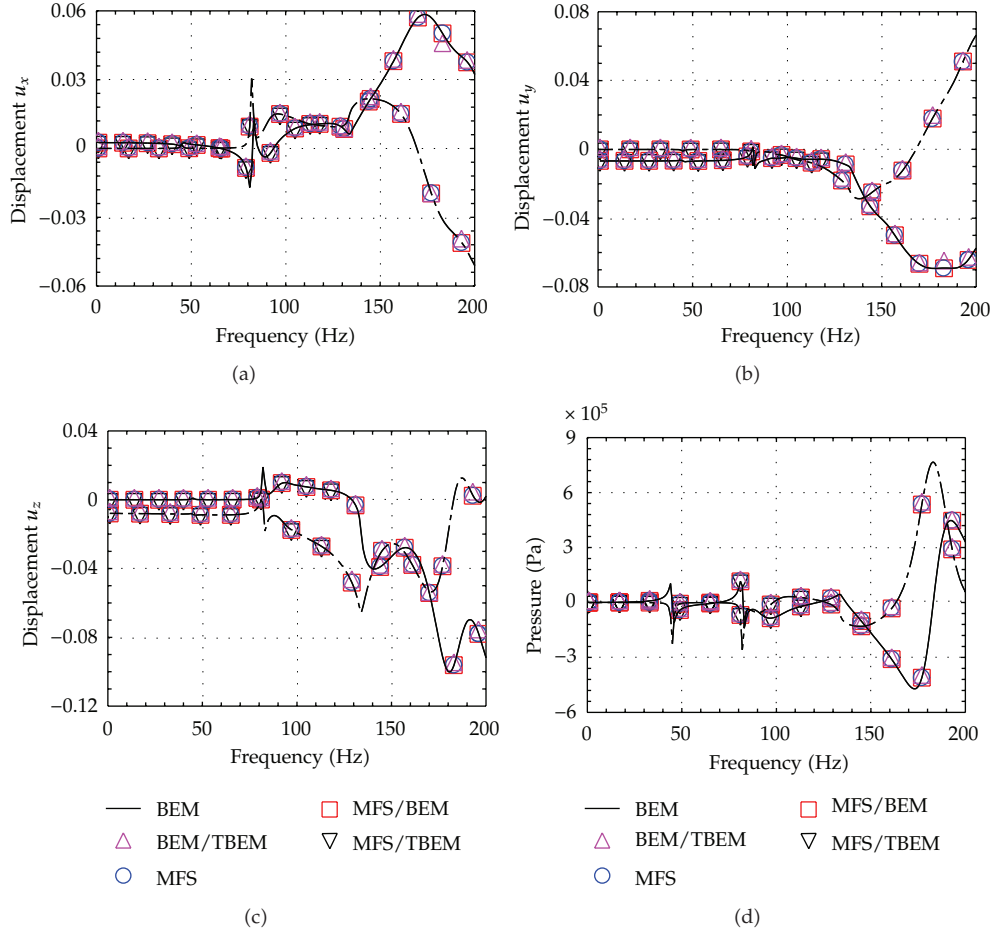


**Figure 6:** Case 3: BEM, TBEM, MFS, and coupling formulations' results: displacements at receiver ( $R_1$ ) and pressure at receiver ( $R_2$ ) when the system is excited by a blast load: BEM.

is discretized using a classical closed surface and loaded with monopole loads (560 BEM boundary elements) (see Figure 7(b)).

Figures 8 and 9 illustrate the real and imaginary part of the reference solutions for both excitation frequencies.

The MFS is less efficient at modelling thin inclusions such as cracks when good accuracy is required. The approach used here to model the displacement around the crack is based on the decomposition of the inner domain into two different subdomains, as illustrated in Figure 7(c). The interface between these two subdomains will be circular and contain the crack,  $T$ , and a fictitious interface,  $F$ . In order to correctly describe the behaviour of the null-thickness crack, null tractions are ascribed to both sides of interface  $T$  and continuity of displacements and tractions is imposed along the interface  $F$ . The distances between the virtual sources and the boundary have been defined by computing the errors along the boundary outside the collocation points, where prescribed conditions are known. The error along the boundary is computed as the integral of the error surface, which is defined by the difference between the responses and the prescribed conditions along the boundary. The final

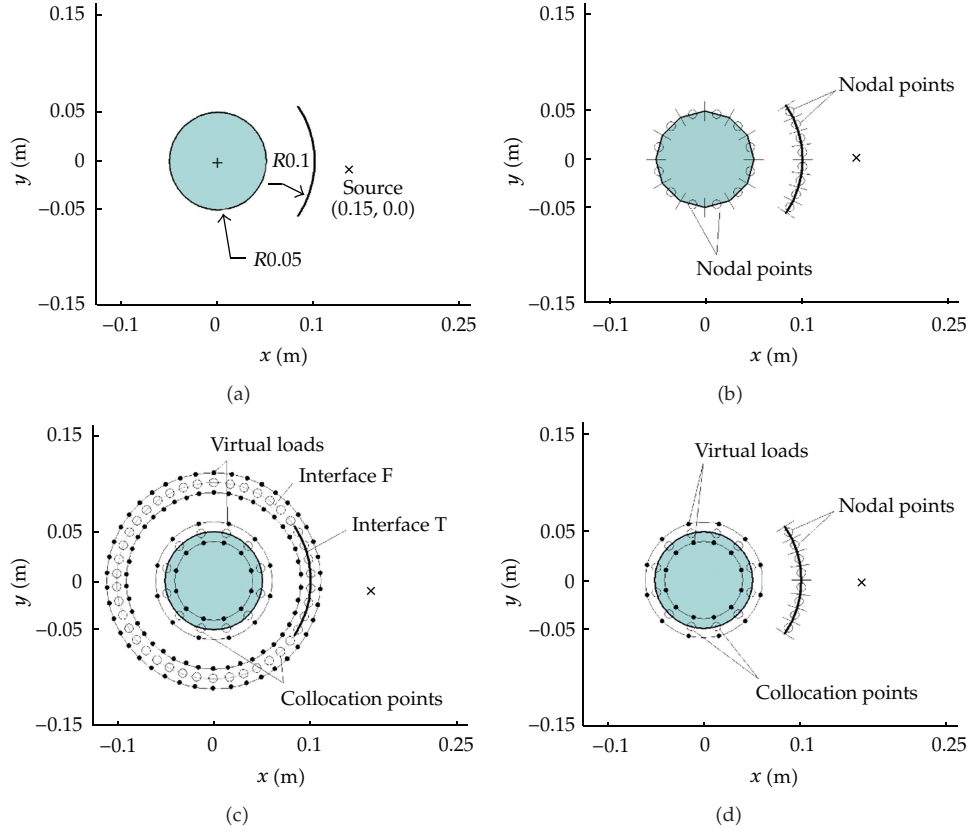


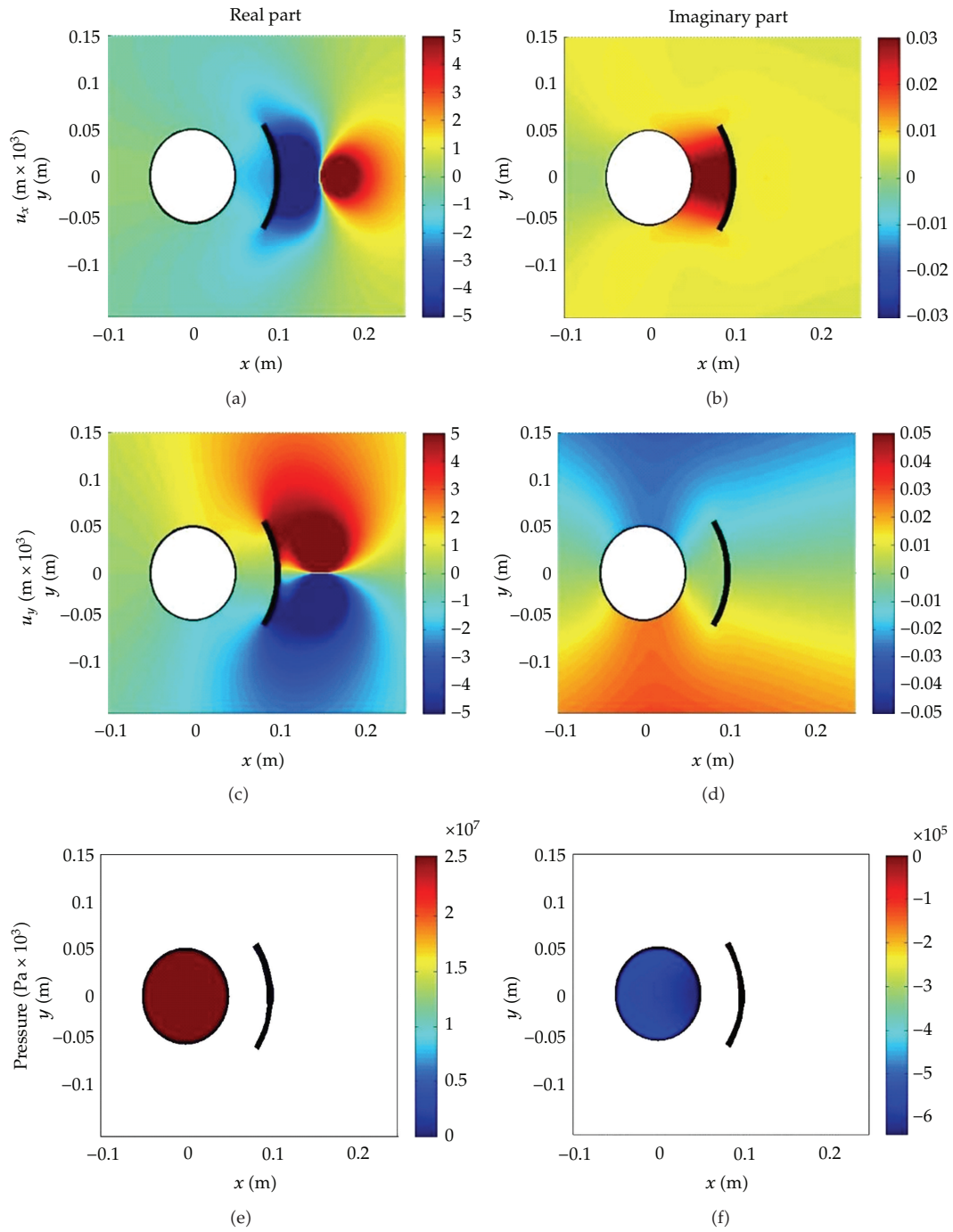
**Figure 7:** Numerical application used to illustrate the computational efficiency of the proposed algorithm: (a) geometry of a fluid-filled borehole with a null-thickness empty crack in its vicinity and position of the blast load; (b) boundary elements used by the BEM/TBEM model; (c) position of virtual loads and collocation points used by the MFS model; (d) position of virtual loads, collocation points (MFS), and boundary elements (TBEM) used by the proposed MFS/TBEM coupling formulation.

positions of the virtual sources were those that led to the slowest boundary errors. This is the same as the procedure proposed in [31], where a stability analysis is presented.

The MFS/TBEM coupling model discretizes the crack with boundary elements loaded with dipole loads (TBEM), while the fluid-filled borehole is modelled using a set of virtual point sources (MFS), whose positions are defined as explained above. The collocation points are evenly distributed along the wall surfaces.

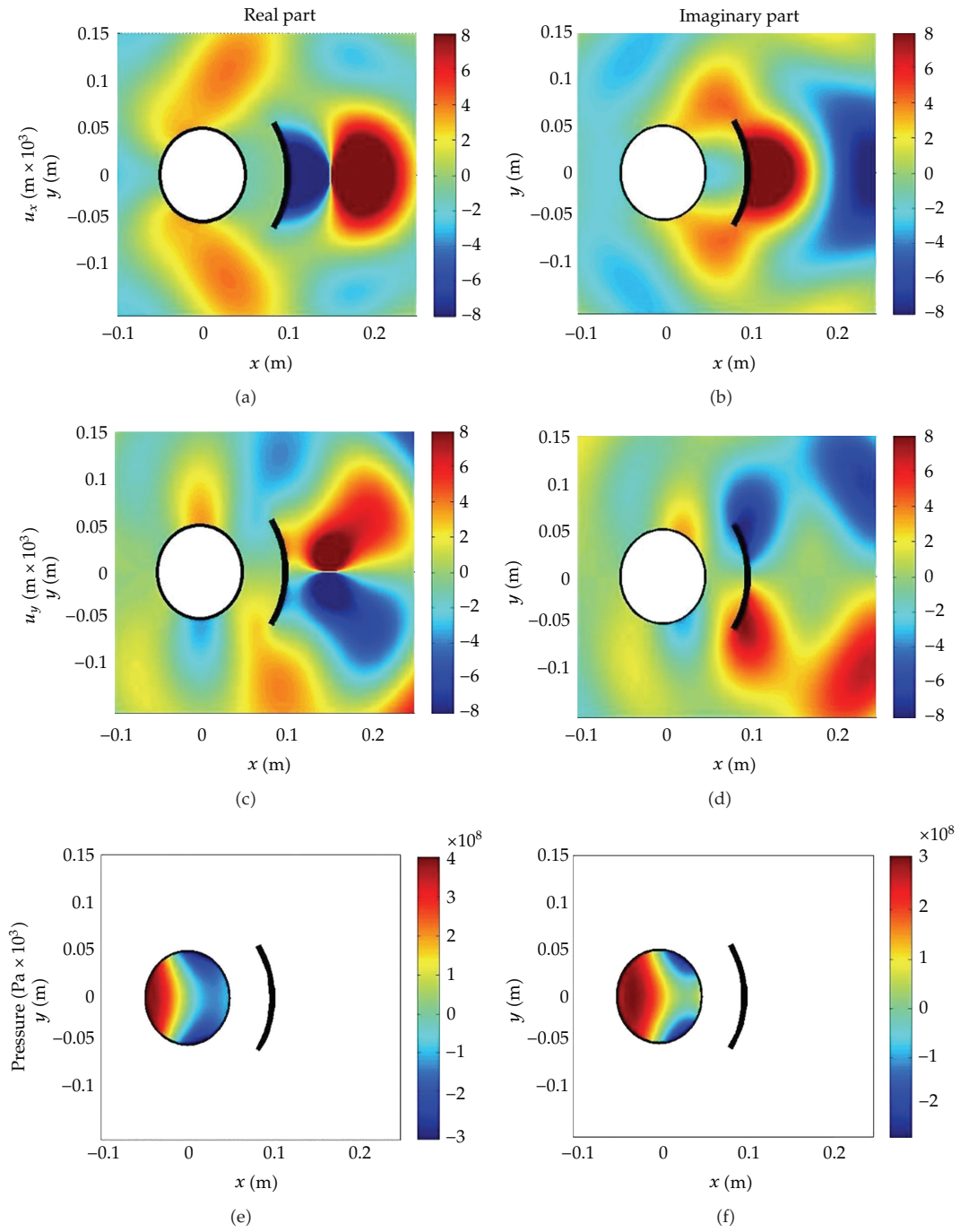
The errors yielded by the methods within the domain are assessed by comparing the responses obtained with those provided by the reference solution, the BEM/TBEM solution, found using 770 boundary elements. A global domain error is defined by computing the integration of the volume generated by the absolute value of the difference between the reference and the different model responses at the grid of receivers. To evaluate the computational efficiency, the CPU time taken by the three computational models to compute the solutions at the grid of receivers placed in the exterior medium (displacements) and at the grid of receivers placed within the borehole (pressures) is registered. All solutions were computed on a laptop computer with an Intel *Core Duo CPU E6750*.

Figure 10 illustrates the global domain error registered versus CPU time required by each formulation, for the two frequencies computed above and varying the number



**Figure 8:** Displacements and pressures solutions for the excitation frequency 140 Hz.





**Figure 9:** Displacements and pressures solutions for the excitation frequency 9000 Hz.



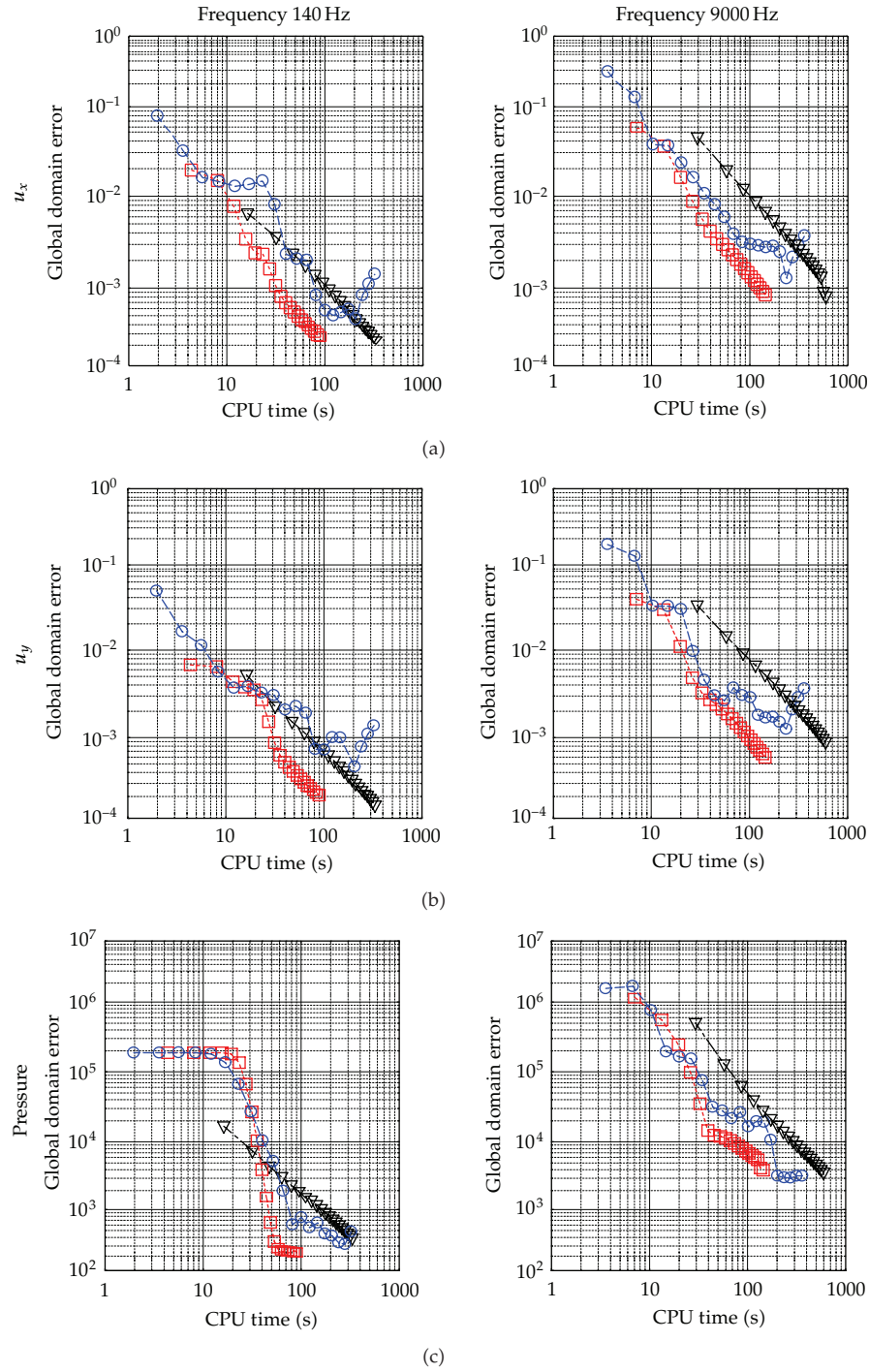


**Figure 10:** Global domain error versus CPU time for solving the system composed of a fluid-filled borehole placed in the vicinity of a crack.

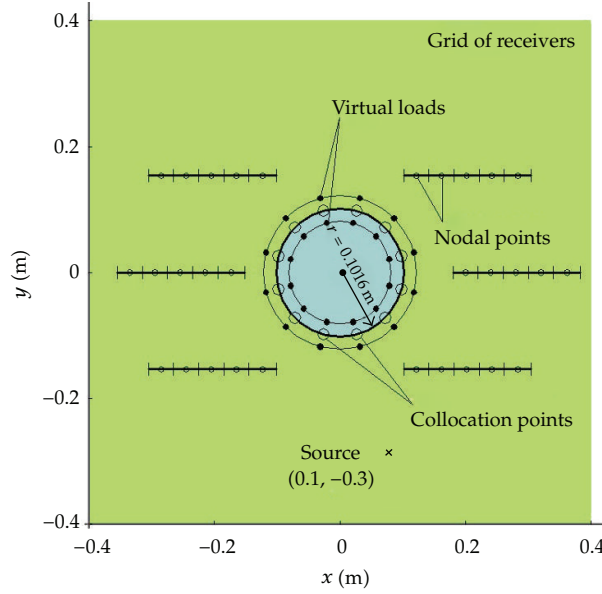


**Figure 11:** Geometry of a fluid-filled borehole driven in cracked medium: position of virtual loads, collocation points (MFS), and boundary elements (TBEM) used by the proposed MFS/TBEM coupling formulation.

of degrees of freedom, that is, changing the number of boundary elements and virtual sources/collocation points. For each formulation, the number of degrees of freedom varies according to the value of  $m = 1$  to 20, as follows: the BEM/TBEM solutions were computed by discretizing the borehole and the crack interfaces with  $10m$  and  $4m$  boundary elements, respectively; the MFS solutions were obtained by simulating the borehole and the crack interface with  $10m$  and  $20m$  virtual sources/collocation points, respectively; the coupling MFS/TBEM solutions were obtained using  $10m$  and  $4m$  virtual sources/collocation points.

The global domain errors shown in Figure 10 are displayed in a logarithmic scale to allow an easier interpretation of the results. An analysis of the responses shows that the BEM/TBEM and the MFS/TBEM register smaller errors as the number of degrees of freedom increases. The MFS does not exhibit a permanent trend and its behaviour fluctuates, particularly for larger numbers of virtual sources, since the global equation system may become ill-conditioned. The results show that the coupled MFS/TBEM formulation is the algorithm that requires the least CPU time for the same accuracy. In both cases, for the same CPU time, the coupled MFS/TBEM solution has the smallest global domain error, except when a very small number of degrees of freedom are used.

## 5. Numerical Application

The applicability of the proposed coupling formulations for solving more complex systems is illustrated by calculating the wave field in the vicinity of a fluid-filled circular borehole, with a radius of 0.1016 m, driven in a cracked medium, as illustrated in Figure 11. The system is subjected to a dilatational line source pulse, modelled as a Ricker wavelet placed at (0.1 m, -0.3 m), parallel to the borehole axis (two-dimensional application), with

a characteristic frequency of 30000 Hz and which starts acting at  $t = 0$  ms. A set of snapshots taken from computer animations is presented in Figure 12 to illustrate the resulting wave field at different time instants.

The responses in the time domain are computed by applying an inverse (fast) Fourier transform to the responses in the frequency domain  $\omega$ . The Ricker pulse modelled is expressed in the time domain by

$$u(\tau) = A(1 - 2\tau^2)e^{-\tau^2}, \quad (5.1)$$

where  $A$  represents the amplitude;  $\tau = (t - t_s)/t_0$ ,  $t$  corresponds to the time,  $t_s$  is the time when the wavelet takes its maximum value, and  $\pi t_0$  is the characteristic (dominant) period of the Ricker wavelet. In the frequency domain, this pulse is written as

$$U(\omega) = A[2t_0\sqrt{\pi}e^{-i\omega t_s}]\Omega^2e^{-\Omega^2}, \quad (5.2)$$

where  $\Omega = \omega t_0/2$ .

The Fourier transformation is computed by adding together a finite number of terms. The frequency increment,  $\Delta\omega$ , needs to be small enough to avoid the aliasing phenomena. These are almost completely eliminated by the introduction of complex frequencies with a small imaginary part of the form  $\omega_c = \omega - i\eta$  (with  $\eta = 0.7\Delta\omega$ ). This procedure is later taken into account by rescaling the responses in the time domain with an exponential factor  $e^{\eta t}$ .

The computations are performed in the frequency domain for frequencies ranging from 140 Hz to 71680 Hz, with a frequency increment of 140 Hz, which determines a total time window of 7.14 ms.

The results were computed using the MFS/TBEM coupling model. The empty crack is discretized using a number of boundary elements defined by the relation between the wavelength and the length of the boundary elements, which was set at 10. A minimum of 10 boundary elements were used. The inclusion is simulated by the MFS, using a minimum of 40 virtual loads/collocation points. The number of virtual sources/collocation points increases with the frequency, according to the relation, defined above, between the wavelength and the distance between collocation points. Figure 11 illustrates the position of the virtual sources, collocation points, and boundary elements.

The P-wave and S-wave velocities allowed in the host medium and its density remain constant at 4208 m/s, 2656 m/s, and 2140 kg/m<sup>3</sup>, respectively. The fluid-filled borehole is centered at (0.0 m, 0.0 m) with a radius 0.1016 m. Its medium has a mass density of 1000 kg/m<sup>3</sup>, a P-wave velocity of 1500 m/s. A null-thickness crack is embedded in the vicinity of this elastic inclusion.

The resulting displacement (in elastic medium) and pressure (into the fluid-filled borehole) are obtained over a two-dimensional grid of 10120 receivers arranged along the  $x$  and  $y$  directions at equal intervals and placed in the vicinity of the inclusion and crack from  $x = -0.4$  m to  $x = 0.4$  m and from  $y = -0.4$  m to  $y = 0.4$  m.

A set of snapshots taken from computer animations is presented in Figure 12 to illustrate the resulting wave field in both the fluid inside the borehole and in the vicinity of the crack, at different time instants. In this figure, the left and the centre columns present the horizontal displacements ( $u_x$ ) and the vertical displacements ( $u_y$ ) in the elastic medium,

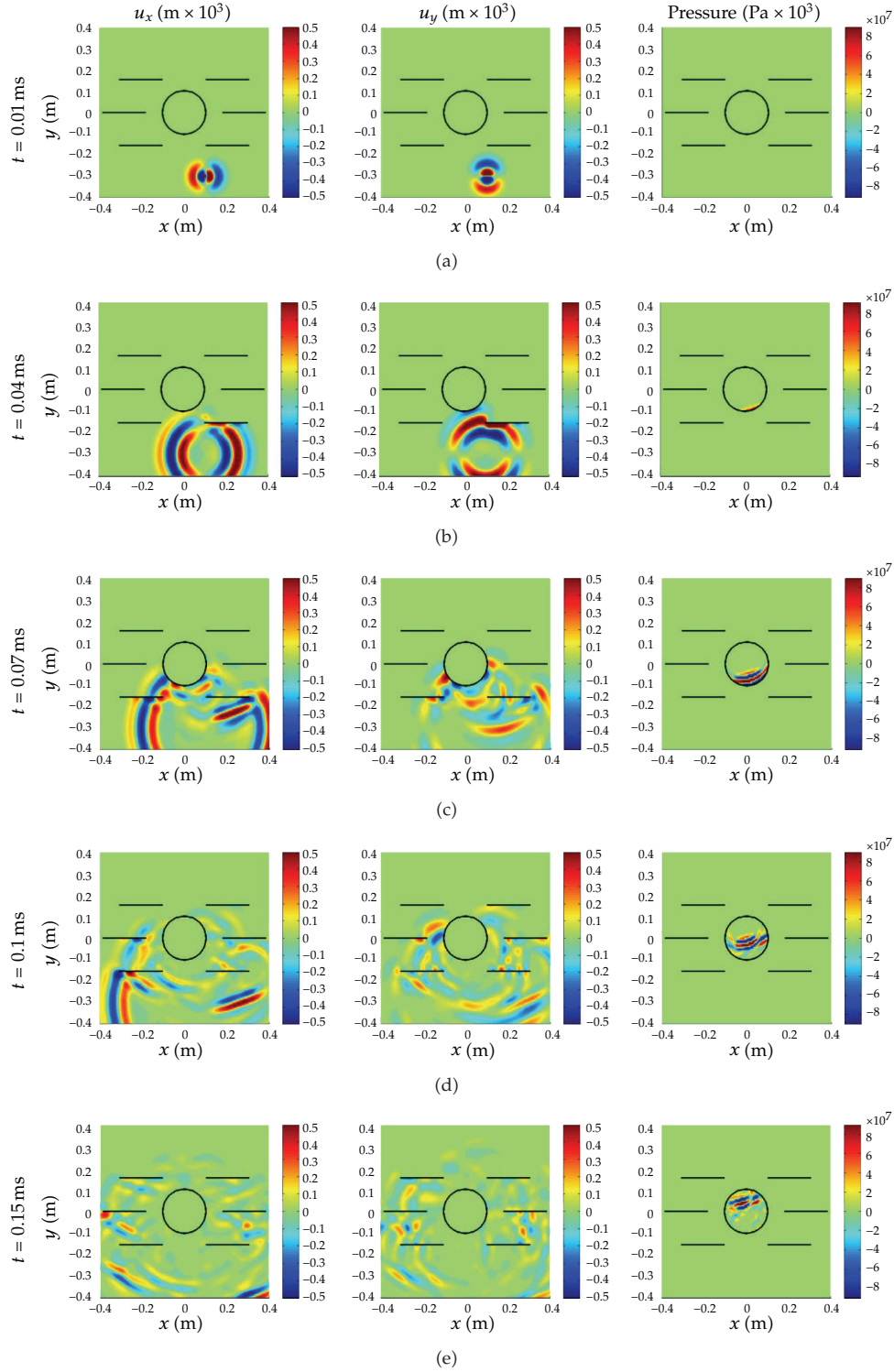


**Figure 12:** Snapshots illustrating the displacement,  $u_x$  and  $u_y$ , and the pressure generated by a line blast load, modelled as a Ricker pulse with a characteristic frequency of 30000 Hz.

while the right column exhibits the pressure inside the borehole. In these plots, a colour gradient between the red and the blue represents responses from positive to negative values.

In the first plots, at  $t = 0.01$  ms, the pulse excited by the dilatational source can be seen travelling in the elastic medium without perturbations as it has not yet reached the fluid-filled borehole. The fluid inside the borehole has not yet suffered any pressure variation. The differences of the component displacements in the horizontal and vertical direction can be seen clearly.

At  $t = 0.04$  ms, the incident pulses are partly reflected back as P-waves and S-waves after hitting the crack, propagating away from the crack on the right in the elastic medium and creating a shadow zone behind it. This is already perceptible at  $t = 0.07$  ms, but it is not easy to distinguish the two types of waves since they are almost coincident at this early stage. At  $t = 0.10$  ms, the reflected P- and S-waves are very well developed as they spread away from the crack. At  $t = 0.04$  ms, part of incident pulse that has just hit the borehole and been transmitted as P-waves into the fluid can also be seen in the pressure field generated within the borehole. Also note the diffracted wave field moving around the crack, once the incident pulses reach its ends. These waves generate refracted waves that travel along both sides of the crack as guided waves.

By  $t = 0.07$  ms, the waves have hit the first crack, which is on the left side of the borehole. The waves that pass through the borehole fluid (pressure) are in their initial development stages as P-waves and denote a delay in relation to the direct incident field, because of lower P-wave speed inside the fluid.

The last snapshots ( $t = 0.10$  ms and  $t = 0.15$  ms) show the first reflected waves continuing to propagate in the unbounded medium. Multiple reflections of waves are visible as they impinge upon the crack surfaces. The wave energy trapped between cracks and within the fluid borehole generates a complex wave field due to the multiple reflections and refractions. It can be seen that the pulses that have travelled around the exterior of the inclusion appear before those that have propagated through the fluid borehole, since waves may travel more slowly through this heterogeneity. The multiple reflected and diffracted pulses on the crack surfaces and within the fluid borehole will continue until the total energy had dissipated.

## 6. Conclusions

Coupled formulations between the boundary element method (BEM)/traction boundary element method (TBEM) and the method of fundamental solutions (MFS) have been developed and proposed for simulating wave propagation involving solid-fluid interaction in media containing multiple inclusions. The proposed coupling formulations overcome the limitations posed by each method individually and require less computational effort, while maintaining reasonable accuracy.

The formulations have been verified against referenced solutions. The wave field generated by fluid, rigid, free, and elastic heterogeneities embedded in an unbounded homogeneous elastic medium and subjected to waves originated by dilatational loads (blast loads) has been simulated. The results were found to closely match the behaviour of the conventional direct BEM or TBEM solutions.

The coupling formulation between the MFS and the TBEM was proposed to overcome the problems posed by thin inclusion, such as cracks. The simulation of the wave propagation in the vicinity of a fluid-filled borehole driven in a cracked medium has been presented to illustrate the stability and efficiency of the proposed coupling formulations.

## Appendix

### 2.5D Green's Functions for Unbounded Elastic and Fluid Media

#### Definitions

$\alpha$  : P-wave velocity,

$\beta$  : S-wave velocity,

$$k_\alpha = \sqrt{\omega^2 / \alpha^2 - k_z^2}, \text{ with } \text{Im}(k_\alpha) < 0,$$

$$k_\beta = \sqrt{(\omega^2 / \beta^2 - k_z^2)}, \text{ with } \text{Im}(k_\beta) < 0,$$

$$r = \sqrt{(x - x_0)^2 + (y - y_0)^2},$$

$$H_{n\alpha} = H_n(k_\alpha r),$$

$$H_{n\beta} = H_n(k_\beta r) \text{ Hankel functions,}$$

$$B_n = k_\beta^n H_{n\beta} - k_\alpha^n H_{n\alpha} B_n \text{ functions,}$$

$$\mathbf{n}_{n1} = (\cos \theta_{n1}, \sin \theta_{n1}) : \text{unit outward normal at } (x, y),$$

$$\mathbf{n}_{n2} = (\cos \theta_{n2}, \sin \theta_{n2}) : \text{unit outward normal at } (x_0, y_0), \text{ (the collocation point).}$$

#### Solid Media Green's Functions

One has

$$\begin{aligned} G_{xx} &= \frac{1}{4i\rho\omega^2} \left[ \frac{\omega^2}{\beta^2} H_{0\beta} - \frac{1}{r} B_1 + \left( \frac{x - x_0}{r} \right)^2 B_2 \right], \\ G_{yy} &= \frac{1}{4i\rho\omega^2} \left[ \frac{\omega^2}{\beta^2} H_{0\beta} - \frac{1}{r} B_1 + \left( \frac{y - y_0}{r} \right)^2 B_2 \right], \\ G_{zz} &= \frac{1}{4i\rho\omega^2} \left[ \frac{\omega^2}{\beta^2} H_{0\beta} - k_z^2 B_0 \right], \\ G_{xy} &= G_{yx} = \frac{1}{4i\rho\omega^2} \left( \frac{x - x_0}{r} \right) \left( \frac{y - y_0}{r} \right) B_2, \\ G_{xz} &= G_{zx} = ik_z \frac{1}{4i\rho\omega^2} \left( \frac{x - x_0}{r} \right) B_1, \\ G_{yz} &= G_{zy} = ik_z \frac{1}{4i\rho\omega^2} \left( \frac{y - y_0}{r} \right) B_1. \end{aligned} \tag{A.1}$$

The derivatives of the above Green's functions give the following tractions along the  $x$ ,  $y$ , and  $z$  directions, in the solid medium,

$$\begin{aligned} H_{rx} &= 2\mu \left[ \frac{\alpha^2}{2\beta^2} \frac{\partial G_{rx}}{\partial x} + \left( \frac{\alpha^2}{2\beta^2} - 1 \right) \left( \frac{\partial G_{ry}}{\partial y} + \frac{\partial G_{rz}}{\partial z} \right) \right] \cos \theta_{n1} + \mu \left[ \frac{\partial G_{ry}}{\partial x} + \frac{\partial G_{rx}}{\partial y} \right] \sin \theta_{n1}, \\ H_{ry} &= 2\mu \left[ \left( \frac{\alpha^2}{2\beta^2} - 1 \right) \left( \frac{\partial G_{rx}}{\partial x} + \frac{\partial G_{rz}}{\partial z} \right) + \frac{\alpha^2}{2\beta^2} \frac{\partial G_{ry}}{\partial y} \right] \sin \theta_{n1} + \mu \left[ \frac{\partial G_{ry}}{\partial x} + \frac{\partial G_{rx}}{\partial y} \right] \cos \theta_{n1}, \\ H_{rz} &= \mu \left[ \frac{\partial G_{rx}}{\partial z} + \frac{\partial G_{rz}}{\partial x} \right] \cos \theta_{n1} + \mu \left[ \frac{\partial G_{ry}}{\partial z} + \frac{\partial G_{rz}}{\partial y} \right] \sin \theta_{n1}, \end{aligned} \quad (\text{A.2})$$

with  $\mathbf{n}_{n1} = (\cos \theta_{n1}, \sin \theta_{n1})$ ,  $H_{rt} = H_{rt}(x, y, \mathbf{n}_{n1}, x_0, y_0, \omega)$ ,  $G_{rt} = G_{rt}(x, y, x_0, y_0, \omega)$ , and  $r, t = x, y, z$ . These expressions can be combined to obtain  $H_{ij}(x, y, \mathbf{n}_{n1}, x_0, y_0, \omega)$  in the normal and tangential directions. In these equations,  $\mu = \rho\beta^2$ .

#### *Solid Media Traction Green's Functions*

These Green's functions can be seen as the combination of the derivatives of the equations (A.1) and (A.2), in order along  $x$ ,  $y$ , and  $z$ , so as to obtain stresses  $\bar{G}_{ij}(x, y, \mathbf{n}_{n2}, x_{\text{col}}, y_{\text{col}}, \omega)$  and  $\bar{H}_{ij}(x, y, \mathbf{n}_{n1}, \mathbf{n}_{n2}, x_{\text{col}}, y_{\text{col}}, \omega)$ . Along the boundary element, at  $(x, y)$ , where the unit outward normal is defined by  $\mathbf{n}_{n1} = (\cos \theta_{n1}, \sin \theta_{n1})$ , and after the equilibrium of stresses, the following equations are expressed for  $x$ ,  $y$  and  $z$  generated by loads also applied along  $x$ ,  $y$  and  $z$  directions:

$$\begin{aligned} \bar{G}_{xr} &= 2\mu \left[ \frac{\alpha^2}{2\beta^2} \frac{\partial G_{xr}}{\partial x} + \left( \frac{\alpha^2}{2\beta^2} - 1 \right) \left( \frac{\partial G_{yr}}{\partial y} + \frac{\partial G_{zr}}{\partial z} \right) \right] \cos \theta_{n2} + \mu \left[ \frac{\partial G_{yr}}{\partial x} + \frac{\partial G_{xr}}{\partial y} \right] \sin \theta_{n2}, \\ \bar{G}_{yr} &= 2\mu \left[ \left( \frac{\alpha^2}{2\beta^2} - 1 \right) \left( \frac{\partial G_{xr}}{\partial x} + \frac{\partial G_{zr}}{\partial z} \right) + \frac{\alpha^2}{2\beta^2} \frac{\partial G_{yr}}{\partial y} \right] \sin \theta_{n2} + \mu \left[ \frac{\partial G_{yr}}{\partial x} + \frac{\partial G_{xr}}{\partial y} \right] \cos \theta_{n2}, \\ \bar{G}_{zr} &= \mu \left[ \frac{\partial G_{xr}}{\partial z} + \frac{\partial G_{zr}}{\partial x} \right] \cos \theta_{n2} + \mu \left[ \frac{\partial G_{yr}}{\partial z} + \frac{\partial G_{zr}}{\partial y} \right] \sin \theta_{n2}, \\ \bar{H}_{xr} &= 2\mu \left[ \frac{\alpha^2}{2\beta^2} \frac{\partial H_{xr}}{\partial x} + \left( \frac{\alpha^2}{2\beta^2} - 1 \right) \left( \frac{\partial H_{yr}}{\partial y} + \frac{\partial H_{zr}}{\partial z} \right) \right] \cos \theta_{n2} + \mu \left[ \frac{\partial H_{yr}}{\partial x} + \frac{\partial H_{xr}}{\partial y} \right] \sin \theta_{n2}, \\ \bar{H}_{yr} &= 2\mu \left[ \left( \frac{\alpha^2}{2\beta^2} - 1 \right) \left( \frac{\partial H_{xr}}{\partial x} + \frac{\partial H_{zr}}{\partial z} \right) + \frac{\alpha^2}{2\beta^2} \frac{\partial H_{yr}}{\partial y} \right] \sin \theta_{n2} + \mu \left[ \frac{\partial H_{yr}}{\partial x} + \frac{\partial H_{xr}}{\partial y} \right] \cos \theta_{n2}, \\ \bar{H}_{zr} &= \mu \left[ \frac{\partial H_{xr}}{\partial z} + \frac{\partial H_{zr}}{\partial x} \right] \cos \theta_{n2} + \mu \left[ \frac{\partial H_{yr}}{\partial z} + \frac{\partial H_{zr}}{\partial y} \right] \sin \theta_{n2} \end{aligned} \quad (\text{A.3})$$



with  $\mathbf{n}_{n2} = (\cos \theta_{n2}, \sin \theta_{n2})$  defining the unit outward normal at  $(x_0, y_0)$  (the collocation point),  $\bar{G}_{tr} = \bar{G}_{tr}(x, y, \mathbf{n}_{n2}, x_{col}, y_{col}, \omega)$ ,  $G_{tr} = G_{tr}(x, y, x_0, y_0, \omega)$ ,  $\bar{H}_{tr} = \bar{H}_{tr}(x, y, \mathbf{n}_{n1}, \mathbf{n}_{n2}, x_{col}, y_{col}, \omega)$ ,  $H_{tr} = H_{tr}(x, y, \mathbf{n}_{n1}, x_0, y_0, \omega)$  and  $r, t = x, y, z$ .

### Fluid Media Green's Functions

One has

$$\begin{aligned} G_f &= -\frac{i}{4} H_0(k_\alpha r), \\ H_f &= \frac{i}{4} k_\alpha H_0(k_\alpha r) \frac{\partial r}{\partial \mathbf{n}_{n1}}, \end{aligned} \quad (\text{A.4})$$

where  $G_f = G_f(x, y, x_0, y_0, \omega)$  and  $H_f = H_f(x, y, \mathbf{n}_{n1}, x_0, y_0, \omega)$ .

### Fluid Media Traction Green's Functions

One has

$$\begin{aligned} \bar{G}_f &= \frac{i}{4} k_\alpha H_1(k_\alpha r) \frac{\partial r}{\partial \mathbf{n}_{n2}}, \\ \bar{H}_f &= \frac{i}{4} k_\alpha \left\{ -k_\alpha H_2(k_\alpha r) \left[ \left( \frac{\partial r}{\partial x} \right)^2 \frac{\partial x}{\partial \mathbf{n}_{n1}} + \frac{\partial r}{\partial x} \frac{\partial r}{\partial y} \frac{\partial y}{\partial \mathbf{n}_{n1}} \right] + \frac{H_1(k_\alpha r)}{r} \left[ \frac{\partial x}{\partial \mathbf{n}_{n1}} \right] \right\} \frac{\partial x}{\partial \mathbf{n}_{n2}} \\ &\quad + \frac{i}{4} k_\alpha \left\{ -k_\alpha H_2(k_\alpha r) \left[ \frac{\partial r}{\partial x} \frac{\partial r}{\partial y} \frac{\partial x}{\partial \mathbf{n}_{n1}} + \left( \frac{\partial r}{\partial y} \right)^2 \frac{\partial y}{\partial \mathbf{n}_{n1}} \right] + \frac{H_1(k_\alpha r)}{r} \left[ \frac{\partial y}{\partial \mathbf{n}_{n1}} \right] \right\} \frac{\partial y}{\partial \mathbf{n}_{n2}}, \end{aligned} \quad (\text{A.5})$$

where  $\bar{G}_f = \bar{G}_f(x, y, \mathbf{n}_{n2}, x_0, y_0, \omega)$  and  $\bar{H}_f = \bar{H}_f(x, y, \mathbf{n}_{n1}, \mathbf{n}_{n2}, x_0, y_0, \omega)$ .

## Acknowledgment

The research work presented herein was supported by the Portuguese Foundation for Science and Technology (FCT), under Grant SFRH/BD/37425/2007.

## References

- [1] M. D. Trifunac, "Surface motion of a semi-cylindrical alluvial valley for incident plane SH waves," *Bulletin of the Seismological Society of America*, vol. 61, pp. 1755–1770, 1971.
- [2] Y. H. Pao and C. C. Mow, *Diffraction of Elastic Waves and Dynamic Stress Concentrations*, Crane and Russak, 1973.
- [3] H. L. Wong and M. D. Trifunac, "Surface motion of semi-elliptical alluvial valley for incident plane SH-waves," *Bulletin of the Seismological Society of America*, vol. 64, pp. 1389–1403, 1974.
- [4] V. W. Lee, "Three-dimensional diffraction of elastic waves by a spherical cavity in an elastic half-space, I: closed-form solutions," *Soil Dynamics and Earthquake Engineering*, vol. 7, no. 3, pp. 149–161, 1988.
- [5] V. W. Lee and J. Karl, "Diffraction of SV waves by underground, circular, cylindrical cavities," *Soil Dynamics and Earthquake Engineering*, vol. 11, no. 8, pp. 445–456, 1992.



- [6] F. J. Sánchez-Sesma and U. Iturrarán-Viveros, "Scattering and diffraction of SH waves by a finite crack: an analytical solution," *Geophysical Journal International*, vol. 145, no. 3, pp. 749–758, 2001.
- [7] G. Kausel, "Thin-layer method: formulation in the time domain," *International Journal for Numerical Methods in Engineering*, vol. 37, no. 6, pp. 927–941, 1994.
- [8] M. H. Aliabadi, Ed., *The Boundary Element Method: Appl. in Solids and Structures*, John Wiley & Sons, New York, NY, USA, 2002.
- [9] F. Ihlenburg, *Finite Element Analysis of Acoustic Scattering*, vol. 132 of *Applied Mathematical Sciences*, Springer-Verlag, New York, NY, USA, 1998.
- [10] L. L. Thompson, "A review of finite-element methods for time-harmonic acoustics," *Journal of the Acoustical Society of America*, vol. 119, no. 3, pp. 1315–1330, 2006.
- [11] L. Savioja, T. Rinne, and T. Takala, "Simulation of room acoustics with a 3-D finite difference mesh," in *Proceedings of the International Computer Music Conference (ICMC'94)*, pp. 463–466, Aarhus, Denmark, 1994.
- [12] A. Kulowski, "Algorithmic representation of the ray tracing technique," *Applied Acoustics*, vol. 18, no. 6, pp. 449–469, 1985.
- [13] C. S. Chen, A. Karageorghis, and Y. S. Smyrlis, Eds., *The Method of Fundamental Solutions: A Meshless Method*, Dynamic Publishers, 2008.
- [14] A. A. Stamos and D. E. Beskos, "3-D seismic response analysis of long lined tunnels in half-space," *Soil Dynamics and Earthquake Engineering*, vol. 15, no. 2, pp. 111–118, 1996.
- [15] A. J. B. Tadeu, J. M. P. António, and E. Kausel, "3D scattering of waves by a cylindrical irregular cavity of infinite length in a homogeneous elastic medium," *Computer Methods in Applied Mechanics and Engineering*, vol. 191, no. 27–28, pp. 3015–3033, 2002.
- [16] J. António and A. Tadeu, "3D seismic response of a limited valley via BEM using 2.5D analytical Green's functions for an infinite free-rigid layer," *Soil Dynamics and Earthquake Engineering*, vol. 22, no. 8, pp. 659–673, 2002.
- [17] D. N. Dell'erba, M. H. Aliabadi, and D. P. Rooke, "Dual boundary element method for three-dimensional thermoelastic crack problems," *International Journal of Fracture*, vol. 94, no. 1, pp. 89–101, 1998.
- [18] T. A. Cruse, "Fracture mechanics," in *Boundary Element Methods in Mechanics*, D. E. Beskos, Ed., pp. 333–365, North Holland, Amsterdam, The Netherlands, 1987.
- [19] P. S. Dineva and G. D. Manolis, "Scattering of seismic waves by cracks in multi-layered geological regions I. Mechanical model," *Soil Dynamics and Earthquake Engineering*, vol. 21, no. 7, pp. 615–625, 2001.
- [20] P. S. Dineva and G. D. Manolis, "Scattering of seismic waves by cracks in multi-layered geological regions II. Numerical results," *Soil Dynamics and Earthquake Engineering*, vol. 21, no. 7, pp. 627–641, 2001.
- [21] M. H. Aliabadi, "A new generation of boundary element methods in fracture mechanics," *International Journal of Fracture*, vol. 86, no. 1–2, pp. 91–125, 1997.
- [22] K. Takakuda, "Diffraction of plane harmonic waves by cracks," *Bulletin of the Japan Society of Mechanical Engineers*, vol. 26, no. 214, pp. 487–493, 1983.
- [23] T. A. Cruse, *Boundary Element Analysis in Computational Fracture Mechanics*, vol. 1 of *Mechanics: Computational Mechanics*, Kluwer Academic, Dordrecht, The Netherlands, 1988.
- [24] J. Sládek and V. Sládek, "A boundary integral equation method for dynamic crack problems," *Engineering Fracture Mechanics*, vol. 27, no. 3, pp. 269–277, 1987.
- [25] A. Tadeu, L. Godinho, J. António, and P. Amado Mendes, "Wave propagation in cracked elastic slabs and half-space domains-TBEM and MFS approaches," *Engineering Analysis with Boundary Elements*, vol. 31, no. 10, pp. 819–835, 2007.
- [26] G. Fairweather, A. Karageorghis, and P. A. Martin, "The method of fundamental solutions for scattering and radiation problems," *Engineering Analysis with Boundary Elements*, vol. 27, no. 7, pp. 759–769, 2003.
- [27] L. Godino, A. P. Mendes, A. Tadeu et al., "Numerical simulation of ground rotations along 2D topographical profiles under the incidence of elastic plane waves," *Bulletin of the Seismological Society of America*, vol. 99, no. 2, pp. 1147–1161, 2009.
- [28] M. A. Jawson and G. T. Symm, *Integral Equation Methods in Potential theory and Elastostatics*, Academic Press, London, UK, 1977.
- [29] M. D. Greenberg, *Application of Green's Functions in Science and Engineering*, Prentice Hall, Englewood Cliffs, NJ, USA, 1971.

- [30] L. Godinho, A. Tadeu, and N. A. Simões, "Accuracy of the MFS and BEM on the analysis of acoustic wave propagation and heat conduction problems," in *Advances in Meshless Methods*, S. Jan and S. Vladimir, Eds., Tech Science Press, 2006.
- [31] A. Tadeu, J. António, and L. Godinho, "Defining an accurate MFS solution for 2.5D acoustic and elastic wave propagation," *Engineering Analysis with Boundary Elements*, vol. 33, no. 12, pp. 1383–1395, 2009.
- [32] C. J. S. Alves and V. M. A. Leitão, "Crack analysis using an enriched MFS domain decomposition technique," *Engineering Analysis with Boundary Elements*, vol. 30, no. 3, pp. 160–166, 2006.
- [33] D. Soares Jr., W. J. Mansur, and O. Von Estorff, "An efficient time-domain FEM/BEM coupling approach based on FEM implicit Green's functions and truncation of BEM time convolution process," *Computer Methods in Applied Mechanics and Engineering*, vol. 196, no. 9–12, pp. 1816–1826, 2007.
- [34] A. Warszawski, D. Soares Jr., and W. J. Mansur, "A FEM-BEM coupling procedure to model the propagation of interacting acoustic-acoustic/acoustic-elastic waves through axisymmetric media," *Computer Methods in Applied Mechanics and Engineering*, vol. 197, no. 45–48, pp. 3828–3835, 2008.
- [35] Z. C. He, G. R. Liu, Z. H. Zhong, G. Y. Zhang, and A. G. Cheng, "A coupled ES-FEM/BEM method for fluid-structure interaction problems," *Engineering Analysis with Boundary Elements*, vol. 35, no. 1, pp. 140–147, 2011.
- [36] D. Soares Jr., O. Von Estorff, and W. J. Mansur, "Iterative coupling of BEM and FEM for nonlinear dynamic analyses," *Computational Mechanics*, vol. 34, no. 1, pp. 67–73, 2004.
- [37] D. Soares Jr., J. A. M. Carrer, and W. J. Mansur, "Non-linear elastodynamic analysis by the BEM: an approach based on the iterative coupling of the D-BEM and TD-BEM formulations," *Engineering Analysis with Boundary Elements*, vol. 29, no. 8, pp. 761–774, 2005.
- [38] D. Soares Jr., O. Von Estorff, and W. J. Mansur, "Efficient nonlinear solid-fluid interaction analysis by an iterative BEM/FEM coupling," *International Journal for Numerical Methods in Engineering*, vol. 64, pp. 1416–1431, 2005.
- [39] A. Tadeu, J. António, and I. Castro, "Coupling the BEM/TBEM and the MFS for the numerical simulation of acoustic wave propagation," *Engineering Analysis with Boundary Elements*, vol. 34, no. 4, pp. 405–416, 2010.
- [40] J. António, A. Tadeu, and P. A. Mendes, "Simulation of wave propagation in a fluid-filled borehole embedded in a cracked medium using a coupled BEM/TBEM formulation," *Bulletin of the Seismological Society of America*, vol. 99, no. 6, pp. 3326–3329, 2009.
- [41] A. Rodríguez-Castellanos, E. Flores, F. J. Sánchez-Sesma, C. Ortiz-Alemán, M. Nava-Flores, and R. Martin, "Indirect boundary element method applied to fluid—solid interfaces," *Engineering*, vol. 31, pp. 470–477, 2002.
- [42] G. Dresen, S. Stanchits, and E. Rybacki, "Borehole breakout evolution through acoustic emission location analysis," *International Journal of Rock Mechanics and Mining Sciences*, vol. 47, no. 3, pp. 426–435, 2010.
- [43] P. Qu, R. Shen, L. Fu, and Z. Wang, "Time delay effect due to pore pressure changes and existence of cleats on borehole stability in coal seam," *International Journal of Coal Geology*, vol. 85, no. 2, pp. 212–218, 2011.
- [44] G. D. Manolis and D. E. Beskos, *Boundary Element Methods in Elastodynamics*, Chapman & Hall, London, UK, 1988.
- [45] A. J. B. Tadeu and Kausel, "Green's functions for two-and-a-half-dimensional elastodynamic problems," *Journal of Engineering Mechanics*, vol. 126, no. 10, pp. 1093–1097, 2000.
- [46] A. J. B. Tadeu, P. F. A. Santos, and E. Kausel, "Closed-form integration of singular terms for constant, linear and quadratic boundary elements. Part 1. SH wave propagation," *Engineering Analysis with Boundary Elements*, vol. 23, no. 8, pp. 671–681, 1999.
- [47] A. Tadeu, P. A. Mendes, and J. António, "The simulation of 3D elastic scattering produced by thin rigid inclusions using the traction boundary element method," *Computers and Structures*, vol. 84, no. 31–32, pp. 2244–2253, 2006.
- [48] P. A. Mendes and A. Tadeu, "Wave propagation in the presence of empty cracks in an elastic medium," *Computational Mechanics*, vol. 38, no. 3, pp. 183–199, 2006.
- [49] M. Guiggiani, "Formulation and numerical treatment of boundary integral equations with hyper-singular kernels," in *Singular Integrals in Boundary Element Methods*, V. Sladek and J. Sladek, Eds., Computational Mechanics Publications, Boston, Mass, USA, 1998.

## *Research Article*

# **Dynamic Analysis of Partially Embedded Structures Considering Soil-Structure Interaction in Time Domain**

**Sanaz Mahmoudpour, Reza Attarnejad, and Cambyse Behnia**

*School of Civil Engineering, University of Tehran, Tehran, Iran*

Correspondence should be addressed to Reza Attarnejad, attarnjd@ut.ac.ir

Received 7 June 2011; Revised 8 August 2011; Accepted 12 August 2011

Academic Editor: Delfim Soares Jr.

Copyright © 2011 Sanaz Mahmoudpour et al. This is an open access article distributed under the Creative Commons Attribution License, which permits unrestricted use, distribution, and reproduction in any medium, provided the original work is properly cited.

Analysis and design of structures subjected to arbitrary dynamic loadings especially earthquakes have been studied during past decades. In practice, the effects of soil-structure interaction on the dynamic response of structures are usually neglected. In this study, the effect of soil-structure interaction on the dynamic response of structures has been examined. The substructure method using dynamic stiffness of soil is used to analyze soil-structure system. A coupled model based on finite element method and scaled boundary finite element method is applied. Finite element method is used to analyze the structure, and scaled boundary finite element method is applied in the analysis of unbounded soil region. Due to analytical solution in the radial direction, the radiation condition is satisfied exactly. The material behavior of soil and structure is assumed to be linear. The soil region is considered as a homogeneous half-space. The analysis is performed in time domain. A computer program is prepared to analyze the soil-structure system. Comparing the results with those in literature shows the exactness and competency of the proposed method.

## **1. Introduction**

In a dynamic soil-structure interaction problem, the structure is supported by an unbounded soil medium subjected to a dynamic load like an earthquake. The dynamic response of the structure is affected by the interaction between the structure, foundation, and soil.

In dynamic soil-structure interaction analysis, usually the higher modes of the structure are affected significantly by soil-structure interaction (SSI) effects. As the influence of higher modes on the seismic response of flexible high structures with small mass remains small, the SSI effects are negligible for these structures. On the other hand for stiff and massive structures on relatively soft ground, the effects of SSI are noticeable and lead to an increase in the natural period and a change in the damping ratio of the system [1–3]. Effects of

interaction can be expressed as inertial interaction and kinematic interaction. The interaction effect associated with the stiffness of the structure is termed kinematic interaction, and the corresponding mass-related effect is called inertial interaction [4]. Jennings and Bielak [5], Veletsos and Nair [6], and Bielak [7] studied effects of inertial interaction, and Todorovska and Trifunac [8], Aviles and Perez-Rocha [9], Betti et al. [10], and Aviles et al. [11] studied the effects of kinematic interaction.

In dynamic soil-structure interaction problems, analysis methods can be classified into three groups [12]: (1) time domain and frequency domain analysis methods, (2) substructure method and direct method, (3) rigorous methods and approximate simple physical models.

Time domain methods are capable of studying nonlinear behavior of soil medium, effects of pore water, and nonlinear conditions along the interface between soil and structure. In frequency domain, the solving procedure is easier than time domain but it can deal only with linear aspects.

In substructure, method the whole media is represented by an impedance matrix which could be attached to the dynamic stiffness of the structure. This hypothesis renders the soil-structure interaction problem simpler and reduces the analysis efforts. In direct method the soil region near the structure is modeled directly; hence, complex geometry, variations of soil properties, and nonlinear behavior of the medium could be considered. As mentioned in this method, the unbounded soil medium is replaced by a bounded region with artificial boundaries. It should be considered that in the numerical modeling of unbounded media, the boundaries should be expressed, so that the radiation condition is satisfied exactly, and the wave energy dissipates in the medium. Several studies have been performed, and methods to impose a wave-absorbing boundary condition have been proposed [13–17].

Simple physical models can be applied to help the analyst identify the key parameters of the dynamic system for preliminary design or investigate alternative designs. They are used to check the results of more rigorous procedures determined with sophisticated computer programs [12].

To solve the soil-structure interaction problems, several analytical and numerical methods have been developed. Applying analytical methods is limited to simple structures and uniform soil media, while numerical methods such as finite element method (FEM), infinite element method, and boundary element method (BEM) are widely used. The FEM method is well suited for nonhomogeneous, anisotropic materials of arbitrary-shaped structure with non-linear behavior [18]. BE methods require a fundamental solution satisfying the governing differential equations exactly [19–22]. This analytical solution is often complicated, exhibiting singularities. Certain shortage in modeling nonhomogeneous soil media is exhibited using BE methods. Cone models have been used to determine dynamic stiffness of foundations and the seismic effective foundation input motion as an alternative to rigorous boundary-element solutions [23–30]. The concept of infinite element method was introduced by Ungless [31] and Bettess [32, 33]. The concepts and formulation procedure in this method are similar to those of FEM methods. The scaled boundary finite element method (SBFEM) which is a semianalytical computational procedure can be used for modeling bounded and unbounded medium considering nonhomogeneous and incompressible material properties. This method has been applied to soil-structure interaction problems both in time and frequency domain by Wolf and Song [34, 35].

Combined models are used in soil-structure interaction analysis. The most widely used combined model is the coupled finite element and boundary element method in both time and frequency domain [36–38]. Qian et al. [39] Estorff and Prabucki [40], and Israil and Banerjee [41] used the coupled FEM-BEM model for analysis of homogeneous media.

Zhang et al. presented the analysis in time domain for layered soils [42]. Tanikulu et al. extended BEM formulation for infinite nonhomogeneous media [43]. They could model only three different layers. Coupled finite element-Infinite element models have been used in dynamic soil-structure interaction analysis [44–46]. Coupled finite element/boundary element/scaled boundary finite element model [47] has been used to solve soil-structure interaction problems.

Jeremić et al. [48] have studied the effects of nonuniformity of soils in large structures where they developed various models to simulate wave propagation through soils with elastoplastic behavior.

Ghannad and Mahsuli [49] studied the effect of foundation embedment using a simplified single degree of freedom model with idealized bilinear behavior for the structure and considered the soil as a homogeneous half-space as a discrete model based on cone model concepts. The foundation is modeled as a rigid cylinder embedded in the soil.

The scaled boundary finite element method is a boundary-element method based on finite elements. This method combines the advantages of the boundary and finite element methods. It also combines the advantages of the numerical and analytical procedures. This method can be applied in both frequency and time domains [35]. This method is a semianalytical procedure which transforms the partial differential equation to an ordinary differential equation using a virtual work statement as in finite elements. In this method, no fundamental solution is required, and no singular integrals occur. Only the boundary is discretized which results in a reduction of the spatial discretization by one. The analytical solution in the radial direction permits the boundary condition at infinity to be satisfied exactly [35]. A computer program named SIMILAR based on SBFEM is presented by Wolf and Song [50]. This program calculates the dynamic stiffness of the unbounded media in frequency and time domain.

In this study, the dynamic behavior of partially embedded structures is examined. The substructure method is used, and a coupled finite element, scaled boundary finite element model is applied. The scaled boundary finite element method is used to calculate the dynamic stiffness of the soil, and the finite element method is applied to analyze the dynamic behavior of the structure. In continuation, firstly, the equation of motion of the soil structure system in total and relative displacements is introduced. The dynamic stiffness matrix of the soil is obtained using SBFEM in the second section. In the third section, an iterative procedure is presented to calculate dynamic load using dynamic stiffness matrix of the soil. Applying Newmark method, the equation of motion of the system is solved, and the displacements of the structure are obtained. It is worth noting that although the formulation in the paper is not innovative, this is the first time a complete model of structure is studied and the dynamic response of the structure is examined. Previous studies have used simplified soil model or simplified structural model and/or both. Therefore, the present results seem to be the first ones obtained based on a complete soil-structure model. Moreover, from a practical point of view, the present results could lead to an interesting conclusion in the important topic of “choosing base shear level” which is not clearly defined in practice codes

Numerical examples are presented, and the final section is devoted to concluding remarks.

## 2. Equation of Motion

The dynamic behavior of the structure could be described by its static stiffness matrix  $[K]$  and the mass matrix  $[M]$ . The equation of motion of the structure in total displacements in time

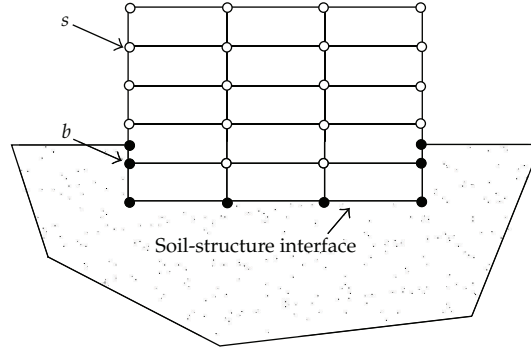


Figure 1: Soil-structure system.

domain is formulated as follows [35]:

$$\begin{bmatrix} [M_{ss}] & [M_{sb}] \\ [M_{bs}] & [M_{bb}] \end{bmatrix} \begin{Bmatrix} \{\ddot{u}_s^t(t)\} \\ \{\ddot{u}_b^t(t)\} \end{Bmatrix} + \begin{bmatrix} [K_{ss}] & [K_{sb}] \\ [K_{bs}] & [K_{bb}] \end{bmatrix} \begin{Bmatrix} \{u_s^t(t)\} \\ \{u_b^t(t)\} \end{Bmatrix} = \begin{Bmatrix} \{0\} \\ -\{R(t)\} \end{Bmatrix}. \quad (2.1)$$

Considering damping matrix of the structure,  $[C]$ , the above equation is written as follows:

$$\begin{bmatrix} [M_{ss}] & [M_{sb}] \\ [M_{bs}] & [M_{bb}] \end{bmatrix} \begin{Bmatrix} \{\ddot{u}_s^t(t)\} \\ \{\ddot{u}_b^t(t)\} \end{Bmatrix} + \begin{bmatrix} [C_{ss}] & [C_{sb}] \\ [C_{bs}] & [C_{bb}] \end{bmatrix} \begin{Bmatrix} \{\dot{u}_s^t(t)\} \\ \{\dot{u}_b^t(t)\} \end{Bmatrix} + \begin{bmatrix} [K_{ss}] & [K_{sb}] \\ [K_{bs}] & [K_{bb}] \end{bmatrix} \begin{Bmatrix} \{u_s^t(t)\} \\ \{u_b^t(t)\} \end{Bmatrix} = \begin{Bmatrix} \{0\} \\ -\{R(t)\} \end{Bmatrix}, \quad (2.2)$$

where  $\{\ddot{u}^t\}$ ,  $\{\dot{u}^t\}$ , and  $\{u^t\}$  are the acceleration, velocity, and displacement vectors of the structure. Subscripts are used to denote the nodes of the discretized system. As shown in Figure 1, nodes on the foundation structure interface are denoted by  $b$ , and the remaining nodes related to the structure are denoted by  $s$ .  $\{R(t)\}$  denotes the interaction forces of the unbounded soil acting on the interface nodes of soil-structure system. The interaction forces of the soil depend upon the motion relative to the effective foundation input motion  $\{u_b^g\}$ . The interaction force-displacement relationship in the time domain is formulated as:

$$\{R(t)\} = \int_0^t [S^\infty(t-\tau)] \{u(\tau)\} d\tau, \quad (2.3)$$

where  $[S^\infty(t)]$  is called the displacement unit impulse response matrix in time domain. The interaction force-displacement relationship can alternatively be written as

$$\{R(t)\} = \int_0^t [M^\infty(t-\tau)] \{\ddot{u}(\tau)\} d\tau, \quad (2.4)$$

in which  $[M^\infty(t)]$  is the acceleration unit-impulse response matrix in time domain.



Superscript  $\infty$  denotes the unbounded medium. For an unbounded medium initially at rest, we have

$$\begin{aligned}\{u(t=0)\} &= 0, \\ \{\dot{u}(t=0)\} &= 0.\end{aligned}\tag{2.5}$$

Substituting (2.6) in (2.1) results the equation of motion in total displacement [35]:

$$\begin{aligned}& \begin{bmatrix} [M_{ss}] & [M_{sb}] \\ [M_{bs}] & [M_{bb}] \end{bmatrix} \begin{Bmatrix} \{\ddot{u}_s(t)\} \\ \{\ddot{u}_b(t)\} \end{Bmatrix} + \begin{bmatrix} [C_{ss}] & [C_{sb}] \\ [C_{bs}] & [C_{bb}] \end{bmatrix} \begin{Bmatrix} \{\dot{u}_s(t)\} \\ \{\dot{u}_b(t)\} \end{Bmatrix} + \begin{bmatrix} [K_{ss}] & [K_{sb}] \\ [K_{bs}] & [K_{bb}] \end{bmatrix} \begin{Bmatrix} \{u_s(t)\} \\ \{u_b(t)\} \end{Bmatrix} \\ &= \begin{Bmatrix} \{0\} \\ -\int_0^t [M^\infty(t-\tau)](\{\ddot{u}_b^t\} - \{\ddot{u}_g\})d\tau \end{Bmatrix},\end{aligned}\tag{2.6}$$

in which  $\{\ddot{u}_g\}$  is the ground motion acceleration induced to the base of the structure during an earthquake.

In this paper, the equation of motion of soil-structure system in relative displacement is used

$$\begin{aligned}& \begin{bmatrix} [M_{ss}] & [M_{sb}] \\ [M_{bs}] & [M_{bb}] \end{bmatrix} \begin{Bmatrix} \{\ddot{u}_s(t)\} \\ \{\ddot{u}_b(t)\} \end{Bmatrix} + \begin{bmatrix} [C_{ss}] & [C_{sb}] \\ [C_{bs}] & [C_{bb}] \end{bmatrix} \begin{Bmatrix} \{\dot{u}_s(t)\} \\ \{\dot{u}_b(t)\} \end{Bmatrix} + \begin{bmatrix} [K_{ss}] & [K_{sb}] \\ [K_{bs}] & [K_{bb}] \end{bmatrix} \begin{Bmatrix} \{u_s(t)\} \\ \{u_b(t)\} \end{Bmatrix} \\ &= \begin{Bmatrix} -[M_{ss}]\{\ddot{u}_g\} \\ -[M_{sb}]\{\ddot{u}_g\} - \int_0^t [M^\infty(t-\tau)](\{\ddot{u}_b\})d\tau \end{Bmatrix}.\end{aligned}\tag{2.7}$$

As can be seen in (2.7), the unit impulse response matrix should be obtained a priori. The dynamic load on the right hand side of the equation is calculated a posteriori. In the next section, the unit impulse response matrix is obtained applying scaled boundary finite element method [35].

### 3. Obtaining Acceleration Unit-Impulse Response Matrix

The force displacement relationship in the frequency domain could be written as follows [35]:

$$\{R(\omega)\} = [M^\infty(\omega)](i\omega)^2\{u(\omega)\},\tag{3.1}$$

where  $\{R(\omega)\}$  and  $\{u(\omega)\}$  are force and displacement in frequency domain.  $[M^\infty(\omega)]$  is denoted as acceleration dynamic stiffness matrix in the frequency domain. The relationship between the acceleration and displacement dynamic stiffness matrices is

$$[M^\infty(\omega)] = \frac{[S^\infty(\omega)]}{(i\omega)^2}.\tag{3.2}$$

The scaled boundary finite element equation in dynamic stiffness for the unbounded medium is formulated as follows [35]:

$$\left([S^\infty(\omega)] + [E^1]\right)[E^0]^{-1} \left([S^\infty(\omega)] + [E^1]^T\right) - (s-2)[S^\infty(\omega)] - \omega[S^\infty(\omega)]_{,\omega} - [E^2] + \omega^2[M^0] = 0, \quad (3.3)$$

in which  $[E^0]$ ,  $[E^1]$ , and  $[E^2]$  are coefficient matrices in the Scaled Boundary Finite Element method introduced in [35].

Dividing (3.3) by  $(i\omega)^4$  and substituting (3.2) yields [35]

$$\begin{aligned} & [M^\infty(\omega)][E^0]^{-1}[M^\infty(\omega)] + [E^1][E^0]^{-1} \frac{[M^\infty(\omega)]}{(i\omega)^2} + \frac{[M^\infty(\omega)]}{(i\omega)^2} [E^0]^{-1}[E^1]^T - s \frac{[M^\infty(\omega)]}{(i\omega)^2} \\ & + \frac{1}{\omega} [M^\infty(\omega)]_{,\omega} - \frac{1}{(i\omega)^4} \left([E^2] - [E^1][E^0]^{-1}[E^1]^T\right) - \frac{1}{(i\omega)^2} [M^0] = 0. \end{aligned} \quad (3.4)$$

Applying the inverse Fourier transformation to (3.4) results in

$$\begin{aligned} & \int_0^t [M^\infty(t-\tau)][E^0]^{-1}[M^\infty(\tau)]d\tau + \left([E^1][E^0]^{-1} - \frac{s+1}{2}\right) \int_0^t \int_0^\tau [M^\infty(\tau')] d\tau' d\tau \\ & + \int_0^t \int_0^\tau [M^\infty(\tau')] d\tau' d\tau \left([E^0]^{-1}[E^1]^T - \frac{s+1}{2}\right) \\ & + t \int_0^t [M^\infty(\tau)]d\tau - \frac{t^3}{6} \left([E^2] - [E^1][E^0]^{-1}[E^1]^T\right) H(t) - t[M^0]H(t) = 0. \end{aligned} \quad (3.5)$$

The positive definite coefficient matrix  $[E^0]$  is decomposed by Cholesky's method as follows:

$$[E^0] = [U]^T[U], \quad (3.6)$$

where  $[U]$  is an upper-triangular matrix. Substituting (3.6) in (3.5) and premultiplying by  $([U]^{-1})^T$  and postmultiplying by  $[U]^{-1}$  yields

$$\begin{aligned} & \int_0^t [m^\infty(t-\tau)][m^\infty(\tau)]d\tau + [e^1] \int_0^t \int_0^\tau [m^\infty(\tau')] d\tau' d\tau + \int_0^t \int_0^\tau [m^\infty(\tau')] d\tau' d\tau [e^1]^T \\ & + t \int_0^t [m^\infty(\tau)]d\tau - \frac{t^3}{6} [e^2] H(t) - t[m^0]H(t) = 0, \end{aligned} \quad (3.7)$$

where

$$[m^\infty(t)] = ([U]^{-1})^T [M^\infty(t)][U]^{-1}. \quad (3.8)$$



And the coefficient matrices are

$$\begin{aligned} [e^1] &= ([U]^{-1})^T [E^1] [U]^{-1} - \frac{s+1}{2} [I], \\ [e^2] &= ([U]^{-1})^T \left( [E^2] - [E^1] [E^0]^{-1} [E^1]^T \right) [U]^{-1}, \\ [m^0] &= ([U]^{-1})^T [M^0] [U]^{-1}. \end{aligned} \quad (3.9)$$

Once obtained  $[m^\infty(t)]$  from (3.7), the acceleration unit-impulse response matrix is obtained as

$$[M^\infty(t)] = [U]^T [m^\infty(t)] [U]. \quad (3.10)$$

In this paper,  $[M^\infty(t)]$  is obtained using the program SIMILAR presented by Jeremić et al. [48].

#### 4. Calculating Dynamic Load

The dynamic load on the right hand side of (2.7) could be written as follows:

$$\begin{aligned} \{F_r(t)\} &= \{F_r^s(t)\} + \begin{Bmatrix} \{0\} \\ \{F_r^b(t)\} \end{Bmatrix}, \\ \{F_r^s(t)\} &= \begin{Bmatrix} \{F_r^{ss}(t)\} \\ \{F_r^{sb}(t)\} \end{Bmatrix}, \end{aligned} \quad (4.1)$$

where  $\{F_r^s(t)\}$  represents the dynamic load due to ground motion, respectively, and affects the total nodes of the system, while  $\{F_r^b(t)\}$  is the dynamic load related to interaction effects and affects the nodes on the foundation-structure interface denoted by  $b$  in Figure 2. The dynamic load vector on the right hand side of (2.7) could be written as follows:

$$\begin{Bmatrix} -[M_{ss}]\{\ddot{u}_g\} \\ -[M_{sb}]\{\ddot{u}_g\} - \int_0^t [M^\infty(t-\tau)](\{\ddot{u}_b\})d\tau \end{Bmatrix} = \begin{Bmatrix} -[M_{ss}]\{\ddot{u}_g\} \\ -[M_{sb}]\{\ddot{u}_g\} \end{Bmatrix} + \begin{Bmatrix} \{0\} \\ -\int_0^t [M^\infty(t-\tau)](\{\ddot{u}_b\})d\tau \end{Bmatrix}. \quad (4.2)$$

Comparing (4.1) and (4.2) results

$$\{F_r^s(t)\} = \begin{Bmatrix} -[M]\{\ddot{u}_g\} \end{Bmatrix}, \quad (4.3)$$

$$\{F_r^b(t)\} = \begin{Bmatrix} -\int_0^t [M^\infty(t-\tau)](\{\ddot{u}_b\})d\tau \end{Bmatrix}, \quad (4.4)$$

where  $[M]$  is the total mass matrix of structure, and  $[M^\infty(t)]$  is the acceleration unit-impulse response matrix.

The dynamic load  $F_r^b(t)$  could be written in discrete form as follows [51]:

$$F_r^b(t_n) = \sum_{j=1}^n M_{n-j}^\infty \int_{(j-1)\Delta t}^{j\Delta t} \ddot{u}_b(\tau) d\tau = \sum_{j=1}^n M_{n-j}^\infty (\dot{u}_{b(j)} - \dot{u}_{b(j-1)}), \quad (4.5)$$

where  $F_r(t_n)$  is the dynamic load at  $n$ th step.  $\ddot{u}$  and  $\dot{u}$  are the acceleration and velocity at the corresponding time step. In this paper, an iterative method is adopted to calculate  $F_r^b(t_n)$ . It is supposed that the acceleration is constant at each time step, so (4.5) could be written as follows:

$$F_r^b(t_n) = \sum_{j=1}^n M_{n-j}^\infty (\dot{u}_{b(j)} \Delta t). \quad (4.6)$$

For the first time step, the dynamic load is calculated assuming that  $\ddot{u}_b = 0$  (2.7) is solved applying Newmark scheme, and acceleration, velocity, and displacement vectors are obtained. The dynamic load is then calculated using calculated acceleration. Equation (2.7) is solved again and the magnitudes of acceleration, velocity, and displacements are obtained. This procedure is iterated until the convergence is achieved. In this study, the tolerance between two successive iterations is taken as 0.001.

The above procedure is outlined as in Table 1.

According to the above algorithm, an FORTRAN program is prepared to examine the dynamic behavior of the structure considering interaction effects. Numerical examples are presented in the next section.

## 5. Examples

2D frames on soft ground have been analyzed applying a coupled scaled boundary finite element-Finite element models. The analysis is performed in time domain and the material behavior of soil and structure is assumed to be linear. The soil-structure system is subjected to sine excitations, El Centro, and Tabas ground motions. The displacement and base shear are calculated. Base shear is assumed to be the algebraic summation of horizontal forces induced in the structure. Results are compared with those obtained by cone model.

*Example 5.1.* As the first example, the frames shown in Figures 2 and 3 are used in analysis. The damping ratio of the structure is considered as five percent of the mass matrix.

Structure properties are assumed as:

$$\begin{aligned} \text{Frame no. 1: } a &= b = 6 \text{ m, } h = 3 \text{ m,} \\ \text{Frame no. 2: } a &= 6 \text{ m, } h = 3 \text{ m.} \end{aligned} \quad (5.1)$$

The soil properties are

$$\rho = 1600 \text{ kg/m}^3, \quad V_s = 150 \text{ m/s, } \nu = 0.3. \quad (5.2)$$

**Table 1:** The Newmark algorithm and iteration procedure used in the analysis.

(A) Initial conditions	
(1) Form stiffness, mass, and damping matrices of the structure	$K, M, C$
(2) Initial values	$u^0, \dot{u}^0, \ddot{u}^0$
(3) Select time step and parameters $\alpha = 0.25, \delta = 0.5$ . Calculate integration constants	$a_0 = \frac{1}{\alpha \Delta t^2}, \quad a_1 = \frac{\delta}{\alpha \Delta t}, \quad a_2 = \frac{1}{\alpha \Delta t}, \quad a_3 = \frac{1}{2\alpha} - 1$ $a_4 = \frac{\delta}{\alpha} - 1, \quad a_5 = \frac{\Delta t}{2} \left( \frac{\delta}{\alpha} - 2 \right), \quad a_6 = \Delta t(1 - \delta), \quad a_7 = \delta \Delta t$
(4) Form effective stiffness matrix $\hat{K}$	$\hat{K} = K + a_0 M + a_1 C$
(B) For each time step	
(1) Use ${}^{t+\Delta t}\ddot{u}_g$ and calculate dynamic load due to ground motion (4.2)	${}^{t+\Delta t}F_r^s$
(2) Iterative procedure	
(2.1) Consider ${}^{t+\Delta t}\ddot{u}_b^k, k = 1, 2, 3, \dots$	${}^{t+\Delta t}\ddot{u}_b^1 = {}^t\ddot{u}_b$
(2.2) Calculate the interaction load induced on soil structure interface (4.6) using ${}^{t+\Delta t}\ddot{u}_b^k$	${}^{t+\Delta t}F_r^b$
(2.3) Calculate the dynamic load ${}^{t+\Delta t}R$	${}^{t+\Delta t}R = \left\{ \begin{array}{c} {}^{t+\Delta t}F_r^{ss} \\ {}^{t+\Delta t}F_r^{sb} + {}^{t+\Delta t}F_r^{bb} \end{array} \right\}$
(2.4) Calculate effective load $\hat{R}$ at time $t + \Delta t$	${}^{t+\Delta t}\hat{R} = {}^{t+\Delta t}R + M(a_0 {}^tU + a_2 {}^t\dot{U} + a_3 {}^t\ddot{U})$ $+ C(a_1 {}^tU + a_4 {}^t\dot{U} + a_5 {}^t\ddot{U})$
(2.5) Applying Gauss reduction scheme, displacements are calculated at time $t + \Delta t$	$\hat{K} {}^{t+\Delta t}U = {}^{t+\Delta t}\hat{R}$
(2.6) Calculate acceleration and velocities at time $t + \Delta t$	${}^{t+\Delta t}\ddot{U}^{k+1} = \left\{ \begin{array}{c} \ddot{u}_s^{k+1} \\ \ddot{u}_b^{k+1} \end{array} \right\} = a_0 ({}^{t+\Delta t}U - {}^tU) - a_2 {}^t\dot{U} - a_3 {}^t\ddot{U}$ ${}^{t+\Delta t}\dot{U} = {}^t\dot{U} + a_6 {}^t\ddot{U} + a_7 {}^{t+4\Delta t}\ddot{U}$
(2.7) Calculate the tolerance between two successive iterations	$\text{TLR} = \left\  {}^{t+\Delta t}\ddot{u}_b^{K+1} - {}^{t+\Delta t}\ddot{u}_b^K \right\ $
(2.8) Check TLR. If $\text{TLR} < 0.001$ , the iterative procedure finishes otherwise steps 2.2 to 2.8 are repeated using ${}^{t+\Delta t}\ddot{u}_b^{k+1}$	

**Table 2:** Properties of structural elements.

Element	$r$ (kgf/m <sup>3</sup> )	$A$ (m <sup>2</sup> )	$I$ (m <sup>4</sup> )	$E$ (kgf/m <sup>2</sup> )
Beam	2400	0.36	$1.08E - 2$	$2.531E9$
Column	2400	0.36	$1.08E - 2$	$2.531E9$

Firstly, a dynamic analysis is performed (ignoring SSI effects). The natural frequencies and periods of the structures are calculated and presented in Tables 3 and 4. Then the soil-structure system is subjected to sine excitations with unit amplitude. The loading frequency is con-

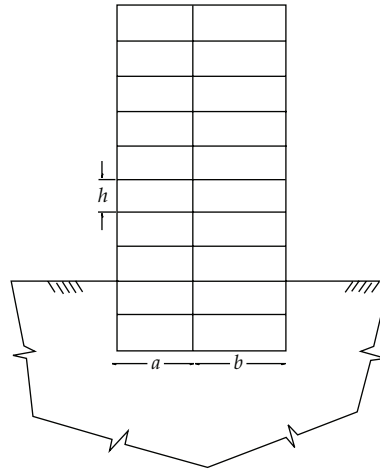


**Figure 2:** Frame no. 1 used in analysis.

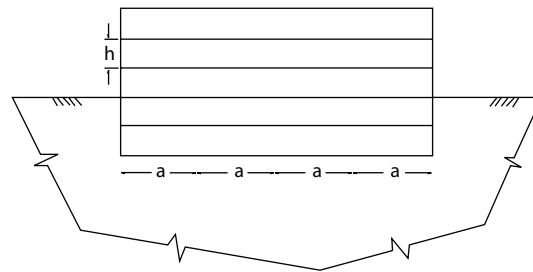


**Figure 3:** Frame no. 2 used in analysis.

**Table 3:** Natural frequencies and periods of first five modes of frame no. 1.

Modes	Natural frequency (Hz)	Period (s)
First mode	0.84	1.189
Second mode	2.579	0.388
Third mode	4.474	0.224
Fourth mode	6.594	0.152
Fifth mode	8.959	0.112

**Table 4:** Natural frequencies and periods of first five modes of frame no. 2.

Modes	Natural frequency (Hz)	Period (s)
First mode	1.66	0.603
Second mode	5.24	0.191
Third mode	9.41	0.106
Fourth mode	13.93	0.072
Fifth mode	17.64	0.057

**Table 5:** Relative reduction of displacement and base shear considering SSI effects for frame no. 1 subjected to sine excitation.

Maximum of	Relative reduction (%)	
	First mode	Second mode
Displacement	15.3	35.6
Base shear	12.7	60.65

**Table 6:** Relative reduction of displacement and base shear considering SSI effects for frame no. 2 subjected to sine excitation.

Maximum of	Relative reduction (%)	
	First mode	Second mode
Displacement	40.9	41.3
Base shear	63.8	82

**Table 7:** Relative reduction of displacement and base shear considering SSI effects for frame no. 1 subjected to El Centro ground motion.

Maximum of	Displacement (cm)	Base shear (Kgf)
Dynamic analysis ignoring SSI effect	10.9	214855
Dynamic analysis considering SSI effect	7.55	109885
Relative reduction (%)	30.73	48.75

**Table 8:** Relative reduction of displacement and base shear considering SSI effects for frame no. 2 subjected to El Centro ground motion.

Maximum of	Displacement (cm)	Base shear (Kgf)
Dynamic analysis ignoring SSI effect	6.61	357693
Dynamic analysis considering SSI effect	2.63	149835
Relative reduction (%)	60.2	58.1

sidered to be variable and selected so that it would be close to natural frequencies of the structure. The harmonic load used in the analysis could be expressed as follows:

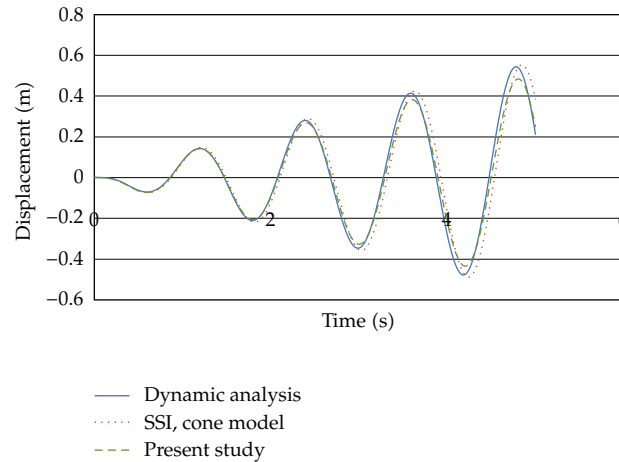
$$F = \sin\left(\frac{2\pi}{T}t\right), \quad (5.3)$$

where  $T$  is the period of sine function. The SSI effect on dynamic response of the structure is examined. Figures 4, 5, 6, 7, 8, 9, 10, 11, 12, 13, 14, 15, and 16 show the results obtained in analysis. Figures 17, 18, 19, and 20 show the variation of displacement and base shear versus period of dynamic load. The maximums (peaks) represent the obtained magnitudes with loading period close to the first and the second natural periods of the structure. As can be seen considering SSI effects, the maximum displacement and base shear are decreased. In Tables 5 and 6 the percentage of the relative reduction of displacement and base shear due to first and second modes is presented.

It is observed that considering SSI effect leads to reduction in displacement and base shear. The reduction in displacement and base shear is more significant when the loading frequency is close to natural frequencies of the structure. As shown in Tables 5 and 6, the

**Table 9:** Relative reduction of displacement and base shear considering SSI effects for frame no. 1 subjected to Tabas ground motion.

Maximum of	Displacement (cm)	Base shear (Kgf)
Dynamic analysis ignoring SSI effect	8.58	194230
Dynamic analysis considering SSI effect	4.03	41399
Relative reduction (%)	53	78.6

**Figure 4:** Comparison of displacement at the top of frame no. 1 subjected to sine excitation ( $T = 1.2$  s).**Table 10:** Relative reduction of displacement and base shear considering SSI effects for frame no. 2 subjected to Tabas ground motion.

Maximum of	Displacement (cm)	Base shear (Kgf)
Dynamic analysis ignoring SSI effect	5.86	367403
Dynamic analysis considering SSI effect	2.19	102447
Relative reduction (%)	62.6	72.1

percentage of relative reduction in displacement and base shear is more significant for the second mode than the first one. It could be concluded that SSI effect is more pronounced for higher modes of the structure. Comparing the results presented in Tables 5 and 6 shows that the relative reduction is more significant for frame no. 2. It could be concluded that SSI effects are more significant for stiff structures.

*Example 5.2.* In the second example, the frames are subjected to El Centro ground motion. It is worth noting that the predominant period of El Centro ground motion is 0.56 (sec) which is close to the first natural period of frame no. 2. The results are given in Figures 21, 22, 23, and 24. As can be observed in Tables 7 and 8, the relative reduction in displacement and shear base is more significant for frame no. 2. It can be concluded that when the predominant period of the earthquake is close to natural period of the structure, considering SSI effects leads to more significant reduction, and the dynamic response of the structure is more affected.

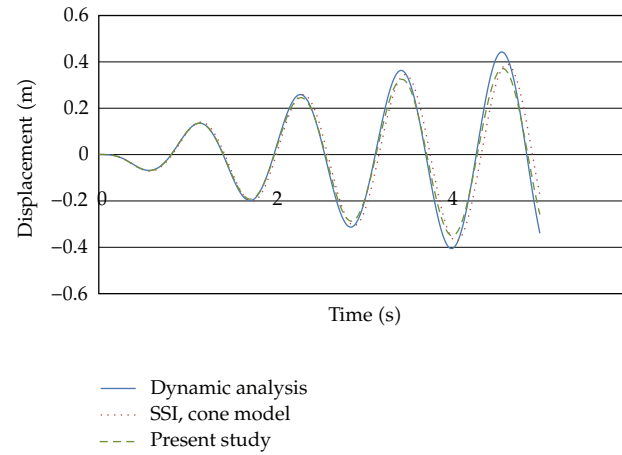


**Figure 5:** Comparison of displacement at the top of frame no. 1 subjected to sine excitation ( $T = 1.1$  s).

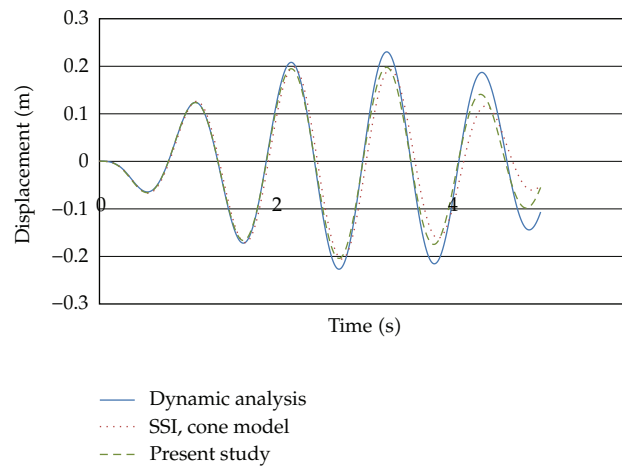


**Figure 6:** Comparison of displacement at the top of frame no. 1 subjected to sine excitation ( $T = 1$  s).

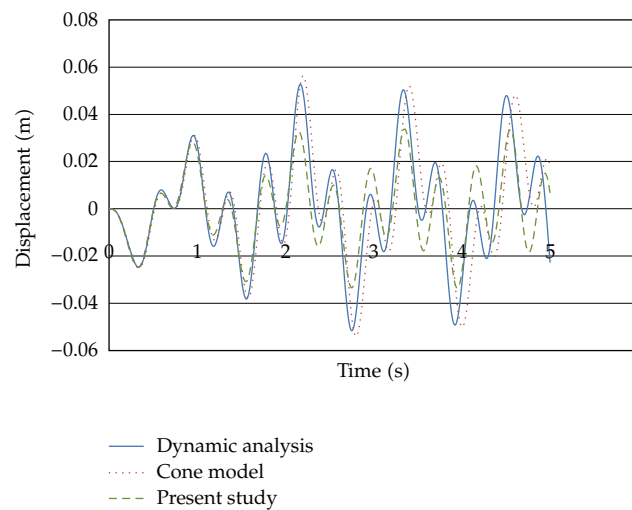


**Figure 7:** Comparison of displacement at the top of frame no. 1 subjected to sine excitation ( $T = 0.4$  s).

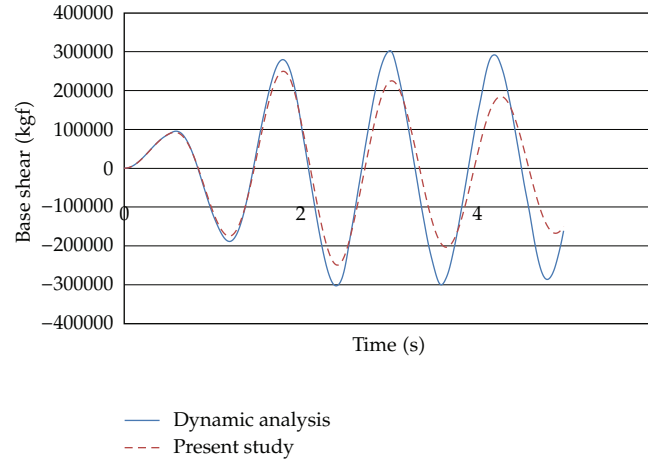


**Figure 8:** Comparison of base shear of frame on. 1 subjected to sine excitation ( $T = 1.2$  s).

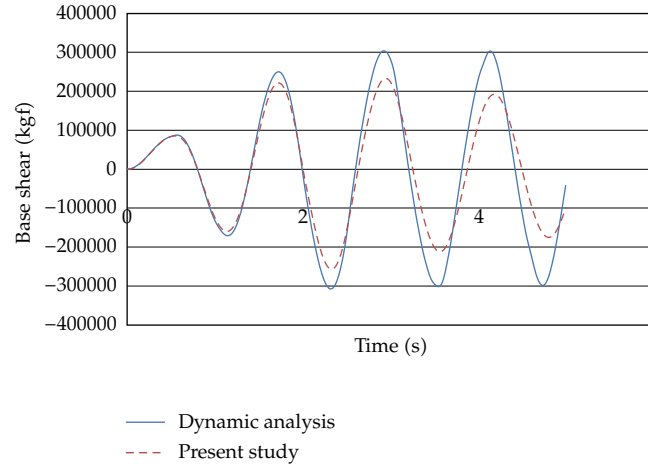


**Figure 9:** Comparison of base shear of frame no. 1 subjected to sine excitation ( $T = 1.1$  s).

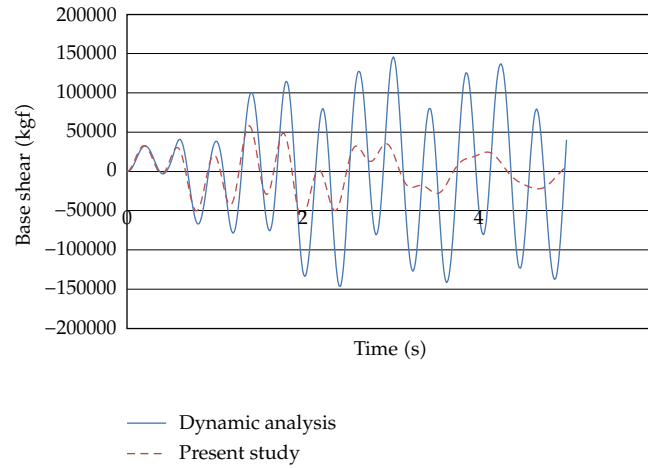


**Figure 10:** Comparison of base shear of frame no. 1 subjected to sine excitation ( $T = 0.4$  s).



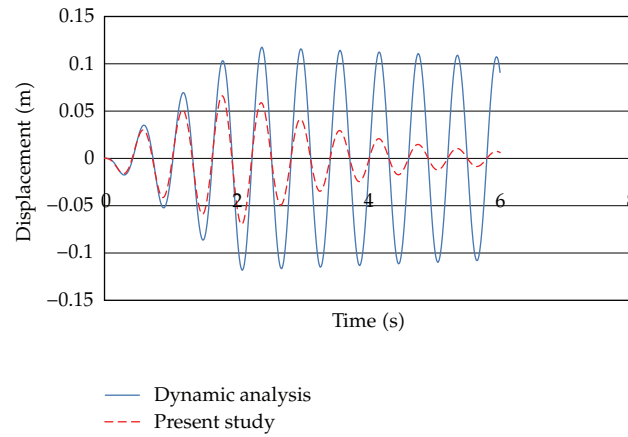


**Figure 11:** Comparison of displacement at top of frame no. 2 subjected to sine excitation ( $T = 0.6$  s).

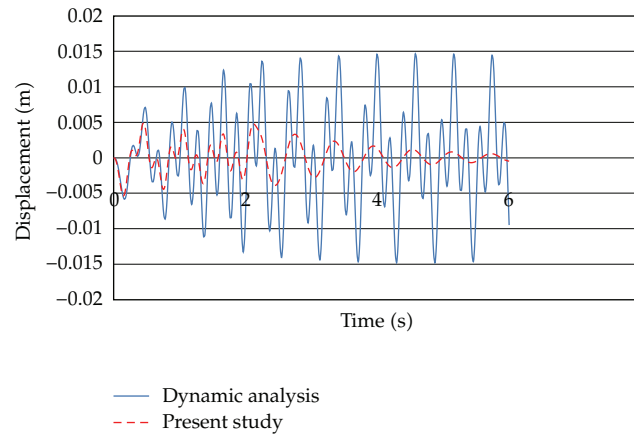


**Figure 12:** Comparison of displacement at top of frame no. 2 subjected to sine excitation ( $T = 0.2$  s).

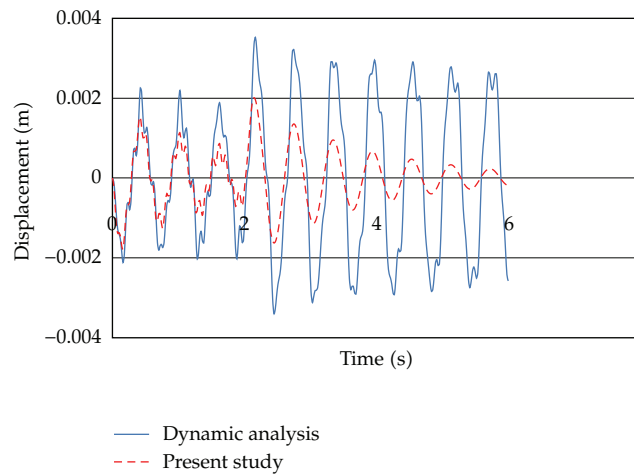


**Figure 13:** Comparison of displacement at top of frame no. 2 subjected to sine excitation ( $T = 0.1$  s).

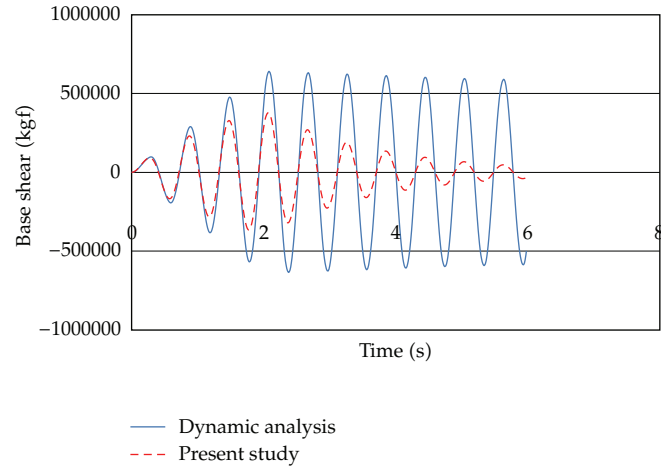


**Figure 14:** Comparison of base shear of frame no. 2 subjected to sine excitation ( $T = 0.6$  s).

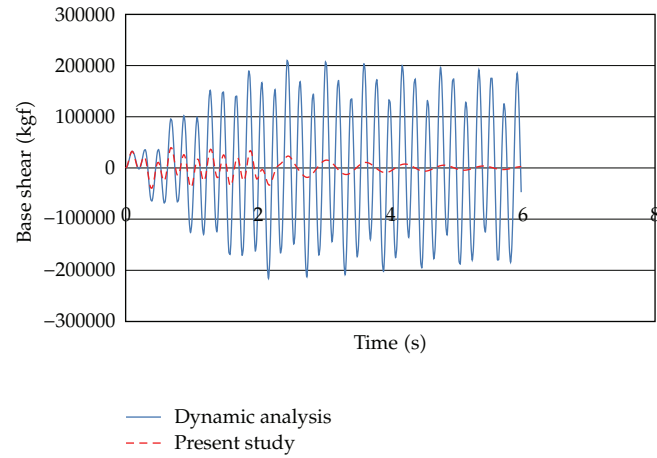


**Figure 15:** Comparison of base shear of frame no. 2 subjected to sine excitation ( $T = 0.2$  s).

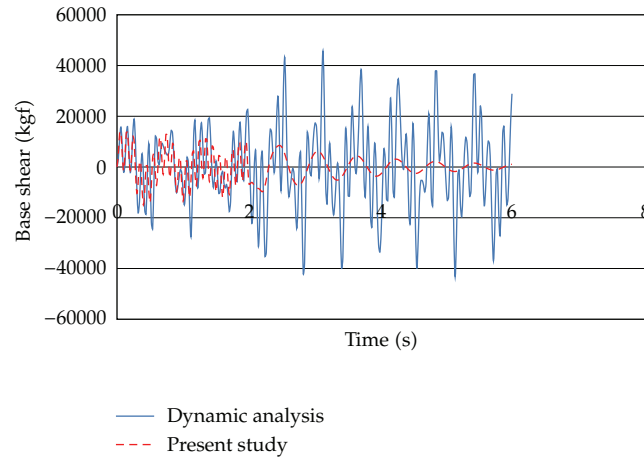


**Figure 16:** Comparison of base shear of frame no. 2 subjected to sine excitation ( $T = 0.1$  s).

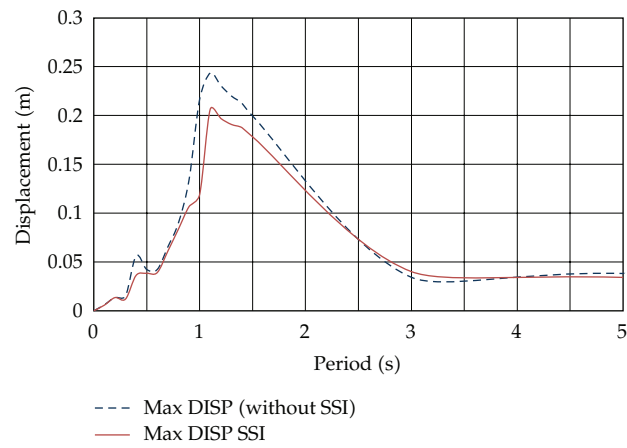


**Figure 17:** Comparison of displacement at top of frame no. 1.

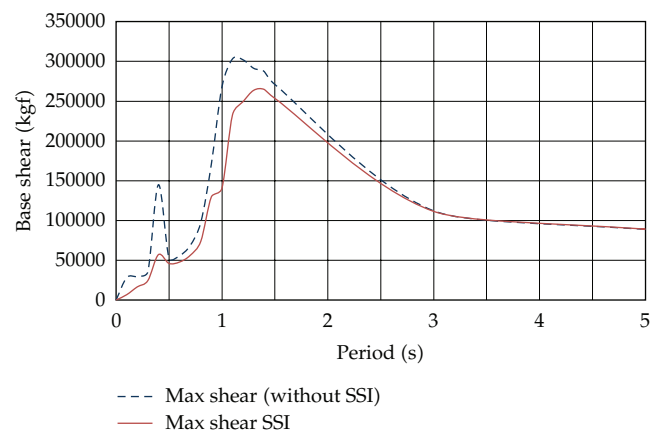


**Figure 18:** Comparison of base shear of frame no. 1.

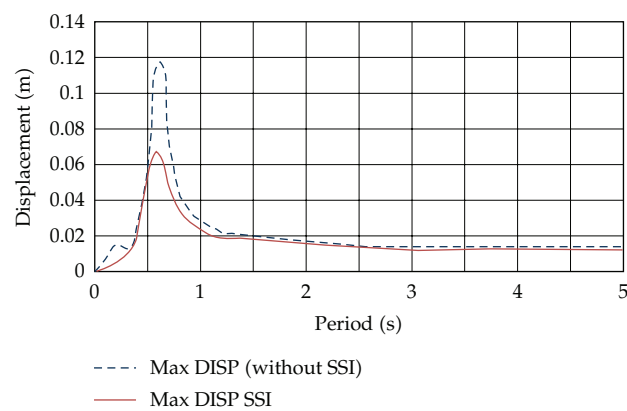


**Figure 19:** Comparison of displacement at top of frame no. 2.

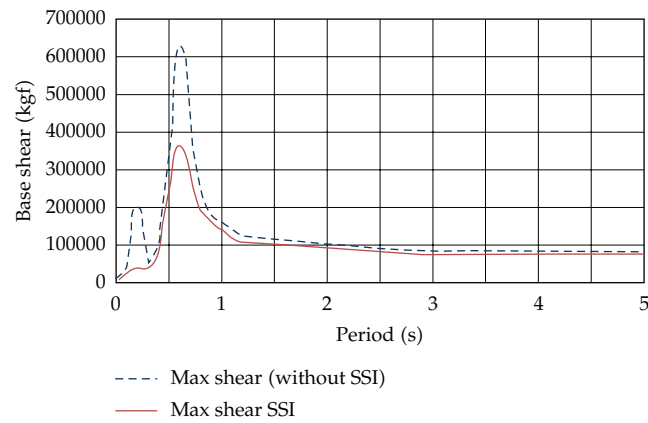


**Figure 20:** Comparison of base shear of frame no. 2.

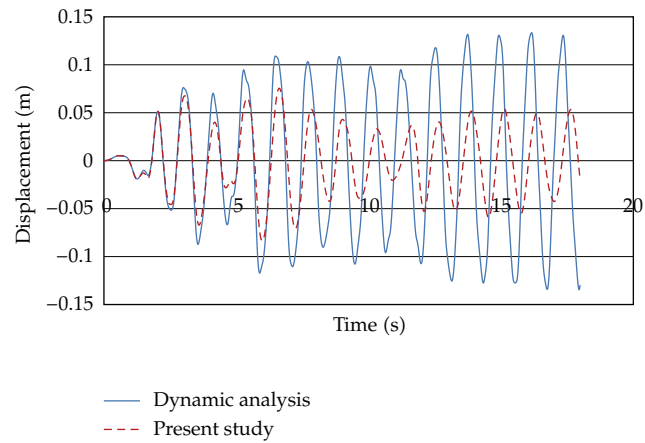


**Figure 21:** Comparison of displacement at the top of frame no. 1 subjected to El Centro ground motion.

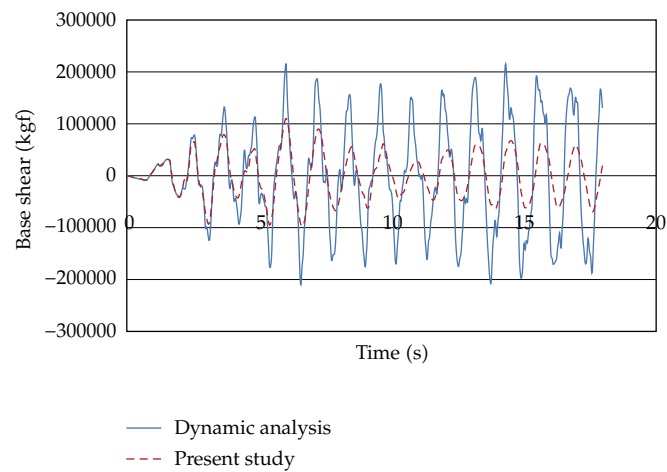


**Figure 22:** Comparison of base shear of frame no. 1 subjected to El Centro ground motion.

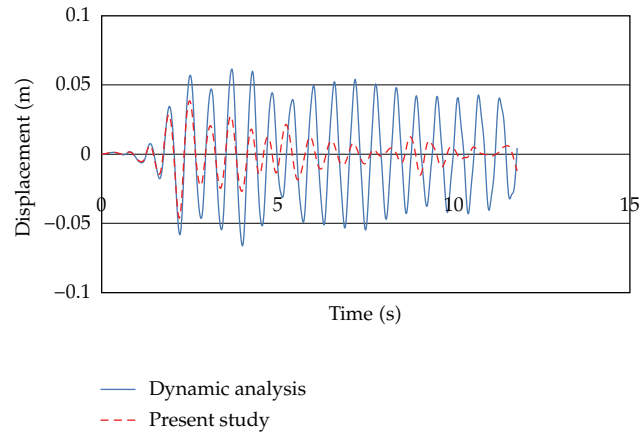


**Figure 23:** Comparison of displacement at the top of frame no. 2 subjected to El Centro ground motion.

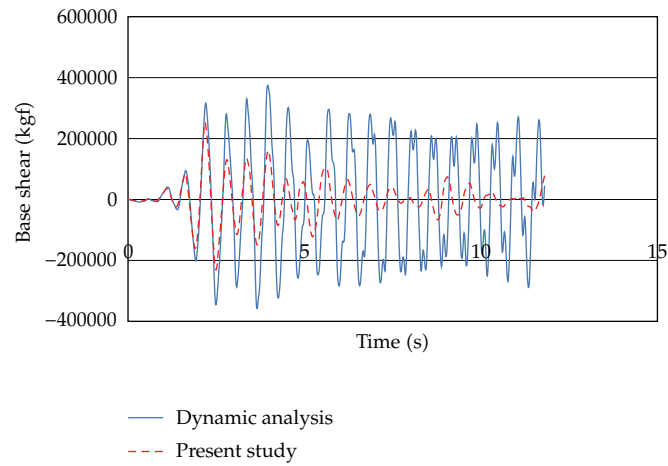


**Figure 24:** Comparison of base shear of frame no. 2 subjected to El Centro ground motion.

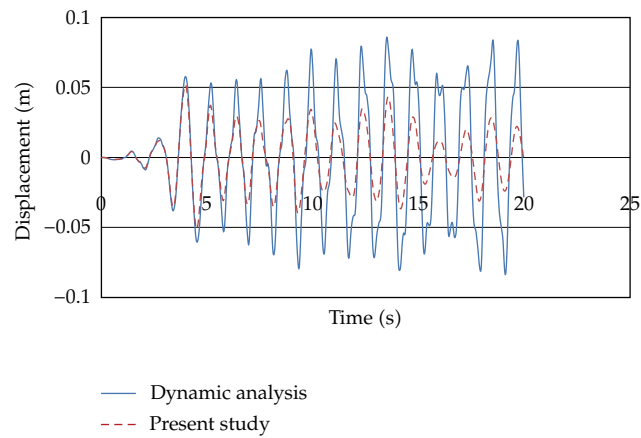


**Figure 25:** Comparison of displacement at top of frame no. 1 subjected to Tabas ground motion.

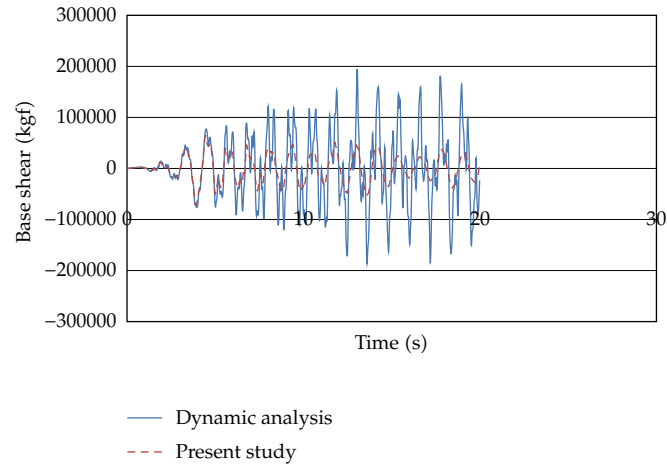


**Figure 26:** Comparison of base shear of frame no. 1 subjected to Tabas ground motion

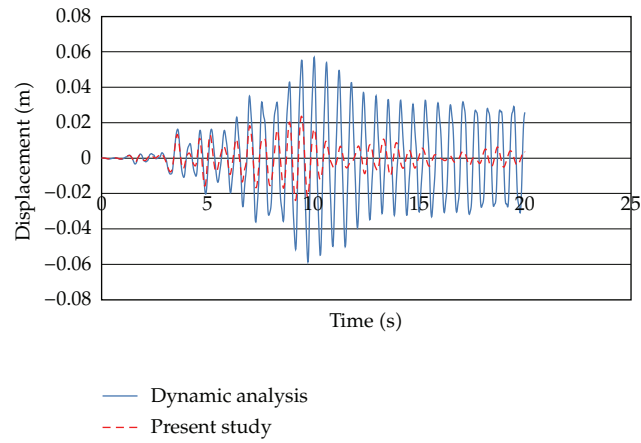


**Figure 27:** Comparison of displacement at the top of frame no. 2 subjected to Tabas ground motion.

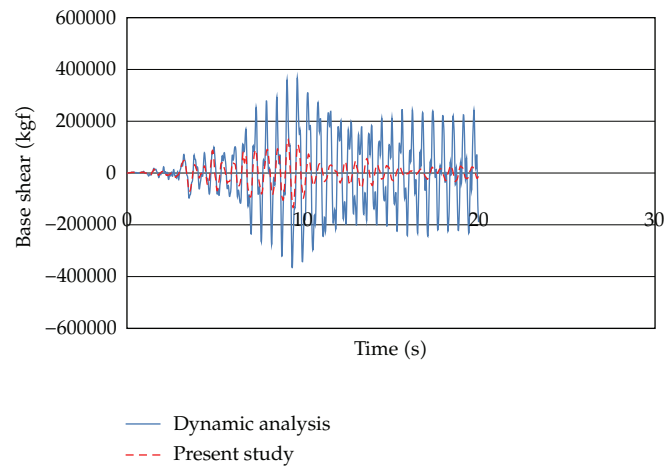


**Figure 28:** Comparison of base shear of frame no. 2 subjected to Tabas ground motion.

*Example 5.3.* In the third example, the frames are subjected to Tabas ground motion. The predominant period of Tabas ground motion is 0.2 (sec) which is close to the second natural period of frame no. 2. The results are given in Figures 25, 26, 27, and 28. As it is observed, considering SSI effect has a pronounced effect on results (Tables 9 and 10).

## 6. Conclusion

Analysis and design of structures subjected to arbitrary dynamic loadings especially earthquakes have been studied during past decades. In practice, the effects of soil-structure interaction on the dynamic response of structures are usually neglected. In this paper, a coupled scaled boundary finite element-finite element model is presented to examine the dynamic response of the structure considering soil-structure interaction. The substructure method is used to analyze the soil-structure interaction problem. The analysis is performed in time domain. The material behavior of soil and structure is assumed to be linear. The scaled boundary finite element method is used to calculate the dynamic stiffness of the soil, and the finite element method is applied to analyze the dynamic behavior of the structure. 2D frames have been analyzed using the proposed model. The results are compared with those obtained by cone model. Considering SSI effect leads to reduction in displacement and base shear. When the system is subjected to sine excitation, the reduction in displacement and base shear is more significant when the loading frequency is close to natural frequencies of the structure. The reduction in displacement and base shear is more significant for the second mode than the first one, thus considering SSI in dynamic analysis of the structure affects the higher modes more significantly. It is observed that when the soil-structure system is subjected to an earthquake whose predominant period is close to natural period of the structure, considering SSI effects leads to more significant reduction, and the dynamic response of the structure is more affected. It is obvious that considering SSI effects results in more effective design without decreasing safety margin.

## References

- [1] J. E. Luco, "Soil-structure interaction and identification of structural models," in *Proceedings of the ASCE Specialty Conference in Civil Engineering and Nuclear Power*, Tenn, USA, 1980.
- [2] J. P. Wolf, *Dynamic Soil-Structure Interaction*, Prentice Hall, Englewood Cliffs, NJ, USA, 1985.
- [3] J. Avilés and L. E. Pérez-Rocha, "Evaluation of interaction effects on the system period and the system damping due to foundation embedment and layer depth," *Soil Dynamics and Earthquake Engineering*, vol. 15, no. 1, pp. 11–27, 1996.
- [4] R. W. Clough and J. Penzien, *Dynamics of Structures*, McGraw-Hill, New York, NY, USA, 2003.
- [5] P. C. Jennings and J. Bielak, "Dynamics of building-soil interaction," *Bulletin of the Seismological Society of America*, vol. 63, pp. 9–48, 1973.
- [6] A. S. Veletsos and V. V. D. Nair, "Seismic interaction of structures on hysteretic foundations," *Journal of the Structural Division*, vol. 101, no. 1, pp. 109–129, 1975.
- [7] J. Bielak, "Dynamic behavior of structures with embedded foundations," *Earthquake Engineering and Structural Dynamics*, vol. 3, no. 3, pp. 259–274, 1975.
- [8] M. I. Todorovska and M. D. Trifunac, "The system damping, the system frequency and the system response peak amplitudes during in-plane building-soil interaction," *Earthquake Engineering and Structural Dynamics*, vol. 21, no. 2, pp. 127–144, 1992.
- [9] J. Aviles and L. E. Perez-Rocha, "Effects of foundation embedment during building-soil interaction," *Earthquake Engineering and Structural Dynamics*, vol. 27, no. 12, pp. 1523–1540, 1998.
- [10] R. Betti, A. M. Abdel-Ghaffar, and A. S. Niazy, "Kinematic soil-structure interaction for long-span cable-supported bridges," *Earthquake Engineering and Structural Dynamics*, vol. 22, no. 5, pp. 415–430, 1993.

- [11] J. Aviles, M. Suarez, and F. J. Sanchez-Sesma, "Effects of wave passage on the relevant dynamic properties of structures with flexible foundation," *Earthquake Engineering and Structural Dynamics*, vol. 31, pp. 139–159, 2002.
- [12] J. P. Wolf, *Foundation Vibration Analysis Using Simple Physical Models*, Prentice Hall, Englewood Cliffs, NJ, USA, 1994.
- [13] J. Lysmer and R. L. Kuhlemeyer, "Finite dynamic model for infinite media," *Journal of Engineering Mechanics Division*, vol. 95, no. 4, pp. 859–877, 1969.
- [14] W. D. Smith, "A nonreflecting plane boundary for wave propagation problems," *Journal of Computational Physics*, vol. 15, no. 4, pp. 492–503, 1974.
- [15] R. Clayton and B. Engquist, "Absorbing boundary conditions for acoustic and elastic wave equations," *Bulletin of the Seismological Society of America*, vol. 67, pp. 1529–1540, 1977.
- [16] W. White, S. Valliappan, and I. K. Lee, "Unified boundary for finite dynamic models," *Journal of Engineering Mechanics*, vol. 103, no. 5, pp. 949–964, 1977.
- [17] Z. P. Liao and H. L. Wong, "A transmitting boundary for the numerical simulation of elastic wave propagation," *International Journal of Soil Dynamics and Earthquake Engineering*, vol. 3, no. 4, pp. 174–183, 1984.
- [18] F. Medina and R. L. Taylor, "Finite element techniques for problems of unbounded domains," *International Journal for Numerical Methods in Engineering*, vol. 19, no. 8, pp. 1209–1226, 1983.
- [19] G. D. Manolis and D. E. Beskos, *Boundary Element Methods in Elastodynamics*, Unwin Hyman, London, UK, 1988.
- [20] J. Dominguez, *Boundary Elements in Dynamics*, Computational Mechanics Publications, Southampton, UK, 1993.
- [21] D. E. Beskos, "Boundary element methods in dynamic analysis: part II (1986–1996)," *Applied Mechanics Reviews*, vol. 50, no. 3, pp. 149–197, 1997.
- [22] W. S. Hall and G. Oliveto, *Boundary Element Methods for Soil-Structure Interaction*, Kluwer Academic, Dodrecht, The Netherlands, 2003.
- [23] J. W. Meek and J. P. Wolf, "Cone models for homogeneous soil. I," *Journal of the Geotechnical Engineering Division*, vol. 118, no. 5, pp. 667–685, 1992.
- [24] J. W. Meek and J. P. Wolf, "Cone models for soil layer on rigid rock. II," *Journal of the Geotechnical Engineering Division*, vol. 118, no. 5, pp. 686–703, 1992.
- [25] J. W. Meek and J. P. Wolf, "Cone models for nearly incompressible soil," *Earthquake Engineering and Structural Dynamics*, vol. 22, no. 8, pp. 649–663, 1993.
- [26] J. W. Meek and J. P. Wolf, "Cone models can present the elastic half-space," *Earthquake Engineering and Structural Dynamics*, vol. 22, no. 9, pp. 759–771, 1993.
- [27] J. W. Meek and J. P. Wolf, "Cone models for embedded foundation II," *Journal of the Geotechnical Engineering Division*, vol. 120, no. 1, pp. 60–80, 1994.
- [28] J. P. Wolf and J. W. Meek, "Cone models for a soil layer on a flexible rock half-space," *Earthquake Engineering and Structural Dynamics*, vol. 22, no. 3, pp. 185–193, 1993.
- [29] J. P. Wolf and J. W. Meek, "Rotational cone models for a soil layer on flexible rock half-space," *Earthquake Engineering and Structural Dynamics*, vol. 23, no. 8, pp. 909–925, 1994.
- [30] J. P. Wolf and J. W. Meek, "Dynamic stiffness of foundation on layered soil half-space using cone frustums," *Earthquake Engineering and Structural Dynamics*, vol. 23, no. 10, pp. 1079–1095, 1994.
- [31] R. F. Ungless, *An infinite element*, M.S. thesis, University of British Columbia, 1973.
- [32] P. Bettess, "Infinite elements," *International Journal for Numerical Methods in Engineering*, vol. 11, no. 1, pp. 53–64, 1977.
- [33] P. Bettess, *Infinite Elements*, Penshaw Press, Sunderland, UK, 1992.
- [34] J. P. Wolf and C. Song, *Finite Element Modeling of Unbounded Media*, Wiley, UK, 1996.
- [35] J. P. Wolf, *The Scaled Boundary Finite Element Method*, Wiley, UK, 2003.
- [36] D. L. Karabalis and D. E. Beskos, "Dynamic response of 3-D flexible foundations by time domain BEM and FEM," *International Journal of Soil Dynamics and Earthquake Engineering*, vol. 4, no. 2, pp. 91–101, 1985.
- [37] O. V. Estorff, "Dynamic response of elastic blocks by time domain BEM and FEM," *Computers and Structures*, vol. 38, no. 3, pp. 289–300, 1991.
- [38] F. Guan and M. Novak, "Transient response of an elastic homogeneous half-space to suddenly applied rectangular loading," *Transactions of the ASME*, vol. 61, no. 2, pp. 256–263, 1994.
- [39] J. Qian, L. G. Tham, and Y. K. Cheung, "Dynamic cross-interaction between flexible surface footings by combined BEM and FEM," *Earthquake Engineering and Structural Dynamics*, vol. 25, no. 5, pp. 509–526, 1996.



- [40] O. Von Estorff and M. J. Prabucki, "Dynamic response in the time domain by coupled boundary and finite elements," *Computational Mechanics*, vol. 6, no. 1, pp. 35–46, 1990.
- [41] A. S. M. Israil and P. K. Banerjee, "Effects of geometrical and material properties on the vertical vibration of three-dimensional foundations by BEM," *International Journal for Numerical and Analytical Methods in Geomechanics*, vol. 14, no. 1, pp. 49–70, 1990.
- [42] X. Zhang, J. L. Wegner, and J. B. Haddow, "Three-dimensional dynamic soil-structure interaction analysis in the time domain," *Earthquake Engineering and Structural Dynamics*, vol. 28, no. 12, pp. 1501–1524, 1999.
- [43] A. H. Tanrikulu, H. R. Yerli, and A. K. Tanrikulu, "Application of the multi-region boundary element method to dynamic soil-structure interaction analysis," *Computers and Geotechnics*, vol. 28, no. 4, pp. 289–307, 2001.
- [44] C. B. Yun, D. K. Kim, and J. M. Kim, "Analytical frequency-dependent infinite elements for soil-structure interaction analysis in two-dimensional medium," *Engineering Structures*, vol. 22, no. 3, pp. 258–271, 2000.
- [45] D. K. Kim and C. B. Yun, "Time domain soil-structure interaction analysis in two dimensional medium based on analytical frequency-dependent infinite elements," *International Journal for Numerical Methods in Engineering*, vol. 47, no. 7, pp. 1241–1261, 2000.
- [46] D. K. Kim and C. B. Yun, "Earthquake response analysis in the time domain for 2D soil-structure systems using analytical frequency-dependent infinite elements," *International Journal for Numerical Methods in Engineering*, vol. 58, no. 12, pp. 1837–1855, 2003.
- [47] M. C. Genes and S. Kocak, "Dynamic soil-structure interaction analysis of layered unbounded media via a coupled finite element/boundary element/scaled boundary finite element model," *International Journal for Numerical Methods in Engineering*, vol. 62, no. 6, pp. 798–823, 2005.
- [48] B. Jeremić, G. Jie, M. Preisig, and N. Tafazzoli, "Time domain simulation of soil-foundation-structure interaction in non-uniform soils," *Earthquake Engineering and Structural Dynamics*, vol. 38, no. 5, pp. 699–718, 2009.
- [49] M. Mahsuli and M. A. Ghannad, "The effect of foundation embedment on inelastic response of structures," *Earthquake Engineering and Structural Dynamics*, vol. 38, no. 4, pp. 423–437, 2009.
- [50] J. P. Wolf and Ch. Song, *Finite-Element Modelling of Unbounded Media*, John Wiley & Sons, Chichester, UK, 1996.
- [51] L. Lehmann, *Wave Propagation in Infinite Domains with Applications to Structure Interaction*, Springer, Berlin, Germany, 2007.

## Research Article

# A New Reduced Stabilized Mixed Finite-Element Method Based on Proper Orthogonal Decomposition for the Transient Navier-Stokes Equations

**Aiwen Wang,<sup>1</sup> Jian Li,<sup>2</sup> Zhenhua Di,<sup>3</sup> Xiangjun Tian,<sup>4</sup>  
and Dongxiu Xie<sup>1</sup>**

<sup>1</sup> School of Applied Science, Beijing Information Science and Technology University, Beijing 100192, China

<sup>2</sup> Department of Mathematics, Baoji University of Arts and Sciences, Baoji 721007, China

<sup>3</sup> College of Global Change and Earth System Science, Beijing Normal University, Beijing 100009, China

<sup>4</sup> Institute of Atmospheric Physics, Chinese Academy of Sciences, Beijing 100029, China

Correspondence should be addressed to Aiwen Wang, wawjianmo@126.com

Received 31 May 2011; Accepted 15 August 2011

Academic Editor: Jan Sladek

Copyright © 2011 Aiwen Wang et al. This is an open access article distributed under the Creative Commons Attribution License, which permits unrestricted use, distribution, and reproduction in any medium, provided the original work is properly cited.

A reduced stabilized mixed finite-element (RSMFE) formulation based on proper orthogonal decomposition (POD) for the transient Navier-Stokes equations is presented. An ensemble of snapshots is compiled from the transient solutions derived from a stabilized mixed finite-element (SMFE) method based on two local Gauss integrations for the two-dimensional transient Navier-Stokes equations by using the lowest equal-order pair of finite elements. Then, the optimal orthogonal bases are reconstructed by implementing POD techniques for the ensemble snapshots. Combining POD with the SMFE formulation, a new low-dimensional and highly accurate SMFE method for the transient Navier-Stokes equations is obtained. The RSMFE formulation could not only greatly reduce its degrees of freedom but also circumvent the constraint of inf-sup stability condition. Error estimates between the SMFE solutions and the RSMFE solutions are derived. Numerical tests confirm that the errors between the RSMFE solutions and the SMFE solutions are consistent with the theoretical results. Conclusion can be drawn that RSMFE method is feasible and efficient for solving the transient Navier-Stokes equations.

## 1. Introduction

Mixed finite-element (MFE) methods are one of the most important approaches for solving the nonstationary Navier-Stokes equations [1–3]. However, some fully discrete MFE formulations for the nonstationary Navier-Stokes equations involve generally many degrees of freedom. In addition, the importance of ensuring the compatibility of the approximations

for the velocity and pressure by satisfying the so-called inf-sup condition (LBB condition) is widely understood. Thus, an important problem is how to avoid the lack of the LBB stability and simplify the computational load by saving time-consuming calculations and resource demands in the actual computational process in a way that guarantees a sufficiently accurate numerical solution.

Proper orthogonal decomposition (POD) is an effective method for approximating a large amount of data. The method essentially finds a group of orthogonal bases from the given data to approximately represent them in a least squares optimal sense. In addition, as the POD is optimal in the least squares sense, it has the property that the model decomposition is completely dependent on the given data and does not require assuming any prior knowledge of the process. Combined with a Galerkin projection procedure, POD provides a powerful method for deriving lower dimensional models of dynamical systems from a high or even infinite dimensional space. A dynamic system is generally governed by related structures or the ensemble formed by a large number of different instantaneous solutions, and the POD method can capture the temporal and spatial structures of dynamic system by applying a statistical analysis to the ensemble of data. POD provides an adequate approximation for a large amount of data with a reduced number of degrees of freedom; it alleviates the computational load and provides substantial savings in memory requirements. POD has found widespread application in a variety of fields such as signal analysis and pattern recognition [4, 5], fluid dynamics and coherent structures [6–8], optimal flow control problems [9, 10], and land surface soil moisture data assimilation [11]. In fluid dynamics, Lumley first applied the POD method to capture the large eddy coherent structures in a turbulent boundary layer [12]. This method was further applied to study the relation between the turbulent structure and a chaotic dynamic system [13]. Sirovich introduced the method of snapshots and applied it to reduce the order of POD eigenvalue problem [14]. Kunisch and Volkwein presented Galerkin POD methods for parabolic problems and a general equation in fluid dynamics [15, 16]. More recently, a finite difference scheme (FDS) and a MFE formulation for the nonstationary Navier-Stokes equation based on POD were derived [17, 18], respectively. Finite-element formulation based on POD was also applied for parabolic equations and the Burgers equation [19, 20]. In other physical applications, an effective use of POD for a chemical vapor deposition reactor was demonstrated and some reduced-order FDS and MFE for the upper tropical Pacific Ocean model based on POD were presented [21–25]. An optimizing reduced FDS based on POD for the chemical vapor deposit (CVD) equations was also presented in [26]. Except for POD, the empirical orthogonal function (EOF) analysis is another effective method to extract information from large datasets in time and space [27, 28].

In order to avoid the lack of LBB stability, some kinds of stabilized techniques for the lowest-order finite elements appear in [29–44]. Luo et al. [45] has combined the POD method with a stabilize method [40] to deal with the non-stationary Navier-Stokes equations and obtained good results. But the stabilized mixed methods in [40, 45] are often developed using residuals of the momentum equation. These residual terms must be formulated using mesh-dependent parameters, whose optimal values are usually unknown. Particularly, for the lowest equal-order pairs of mixed elements such as  $P_1 - P_1$  and  $Q_1 - Q_1$ , pressure and velocity derivatives in the residual either vanish or are poorly approximated, causing difficulties in the application of consistent stabilization.

In this paper, we mainly consider the two-dimensional transient Navier-Stokes equations by combining a new stabilized finite-element method [29–31] based on two local Gauss' integrations with POD method. This new stabilized finite element method has some

prominent features: parameter-free, avoiding higher-order derivatives or edge-based data structures, and stabilization being completed locally at the element level. In this manner, we could not only ensure the stabilization of solutions of fully discrete stabilized mixed finite-element system but also greatly reduce degrees of freedom and save time-consuming calculations and resource demands in the actual computational process in a way that guarantees a sufficiently accurate numerical solution. We also derive the error estimates between the original SMFE solutions and the RSMFE solutions based on the POD technique. Numerical experiments show the errors between the original SMFE method and the RSMFE solutions are consistent with theoretical results.

The remainder of this paper is organized as follows. In Section 2, an abstract functional setting for the two-dimensional Navier-Stokes equations is given, together with some basic notations. Section 3 is to state the fully discrete stabilized finite-element method and to generate snapshots from transient solutions computed from the equation system derived by the classical SMFE formulation. In Section 4, the optimal orthogonal bases are reconstructed from the elements of the snapshots with POD method and a reduced SMFE formulation with lower-dimensional number based on POD method for the transient Navier-Stokes equations is developed. In Section 5, error estimates between the classical SMFE solutions and the RSMFE solutions based on the POD method are derived. In Section 6, a series of numerical experiments are given to illustrate the theoretical results. We conclude with a few remarks in the final section.

## 2. Functional Setting of the Navier-Stokes Equations

Let  $\Omega$  be a bounded domain in  $R^2$ , assumed to have a Lipschitz continuous boundary  $\Gamma$  and to satisfy further assumptions below. The transient Navier-Stokes equations are considered as follows:

$$u_t - \nu \Delta u + (u \cdot \nabla)u + \nabla p = f, \quad \operatorname{div} u = 0, \quad (x, t) \in \Omega \times (0, T], \quad (2.1)$$

$$u(x, 0) = u_0(x), \quad x \in \Omega, \quad u(x, t)|_{\Gamma} = 0, \quad t \in [0, T]. \quad (2.2)$$

Here  $u : \Omega \rightarrow R^2$  and  $p : \Omega \rightarrow R$  are the velocity and pressure,  $\nu > 0$  is the viscosity, and  $f$  represents the body forces,  $T > 0$  the final time, and  $u_t = \partial u / \partial t$ .

For the mathematical setting of problems (2.1)-(2.2), we introduce the following Sobolev spaces:

$$X = H_0^1(\Omega)^2, \quad M = L_0^2(\Omega) = \left\{ q \in L^2(\Omega); \int_{\Omega} q(x) dx = 0 \right\}, \quad (2.3)$$

$$D(A) = H^2(\Omega)^2 \cap X, \quad V = \{v \in V : \operatorname{div} v = 0\}. \quad (2.4)$$

Furthermore, we make a regularity assumption on the Stokes problem as follows.

*Assumption H1.* For a given  $g \in Y$  and the Stokes problem,

$$\begin{aligned} -\Delta v + \nabla q &= g, & \text{in } \Omega, \\ \operatorname{div} v &= 0, & \text{in } \Omega, \\ v|_{\Gamma} &= 0, & \text{on } \partial\Omega, \end{aligned} \quad (2.5)$$

satisfying the following regularity result:

$$\|v\|_2 + \|q\|_1 \leq \kappa \|g\|_0, \quad (2.6)$$

where  $\|\cdot\|_i$  is the norm of the Sobolev space  $H^i(\Omega)$  or  $H^i(\Omega)^2$ ,  $i = 0, 1, 2$ , as appropriate, and  $\kappa$  is a positive constant depending only on  $\Omega$ , which may stand for different value at its different occurrences. Subsequently, the positive constants  $\kappa$  and  $c$  (with or without a subscript) will depend only on the data  $(v, T, \Omega, u_0)$ . Because the norm and seminorm are equivalent on  $H_0^1(\Omega)^2$ , we use the same notation  $\|\cdot\|_1$  for them. It is well known that for each  $v \in X$  there hold the following inequalities:

$$\|v\|_{L^4} \leq 2^{1/4} \|v\|_0^{1/2} \|v\|_1^{1/2}. \quad (2.7)$$

*Assumption H2.* The initial velocity  $u_0 \in D(A)$  and the body force  $f(x, t) \in L^2(0, T; L^2(\Omega)^2)$  are assumed to satisfy

$$\|u_0\|_2 + \left( \int_0^T (\|f\|_0^2 + \|f_t\|_0^2) dt \right)^{1/2} \leq c. \quad (2.8)$$

Now, the bilinear forms  $a(\cdot, \cdot)$  and  $d(\cdot, \cdot)$ , on  $X \times X$  and  $X \times M$ , are defined, respectively, by

$$a(u, v) = \nu(\nabla u, \nabla v), \quad \forall u, v \in X, \quad d(v, q) = (q, \operatorname{div} v), \quad \forall (v, q) \in (X, M). \quad (2.9)$$

Also, a generalized bilinear form  $\mathcal{B}((\cdot, \cdot); (\cdot, \cdot))$  on  $(X, M) \times (X, M)$  is defined by

$$\mathcal{B}((u, p); (v, q)) = a(u, v) - d(v, p) + d(u, q). \quad (2.10)$$

Moreover, we define the trilinear form

$$\begin{aligned} b(u, v, w) &= ((u \cdot \nabla)v, w) + \frac{1}{2}((\operatorname{div} u)v, w) \\ &= \frac{1}{2}((u \cdot \nabla)v, w) - \frac{1}{2}((u \cdot \nabla)w, v), \quad \forall u, v, w \in X. \end{aligned} \quad (2.11)$$

By the above notations and the Hölder inequality, there hold the following estimates:

$$b(u, v, w) = -b(u, w, v), \quad \forall u \in X, v, w \in X,$$

$$|b(u, v, w)| \leq \frac{1}{2} c_0 \|u\|_0^{1/2} \|u\|_1^{1/2} \left( \|v\|_1 \|w\|_0^{1/2} \|w\|_1^{1/2} + \|v\|_0^{1/2} \|v\|_1^{1/2} \|w\|_1 \right), \quad \forall u, v, w \in X,$$

$$|b(u, v, w)| + |b(v, u, w)| + |b(w, u, v)| \leq c_1 \|u\|_1 \|v\|_2 \|w\|_0, \quad \forall u \in X, v \in D(A), w \in Y. \quad (2.12)$$

Also, the Poincare inequality holds:

$$\|v\|_0 \leq \gamma_0 \|v\|_1, \quad (2.13)$$

where  $c_0$ ,  $c_1$ , and  $\gamma_0$  are positive constants depending only on  $\Omega$ .

For a given  $f \in Y$ , the variational formulation of problem (2.1)-(2.2) reads as follows: find  $(u, p) \in (X, M)$ ,  $t > 0$  such that

$$\begin{aligned} (u_t, v) + \mathcal{B}((u, p); (v, q)) + b(u, u, v) &= (f, v), \quad \forall (v, q) \in (X, M), \\ u(0) &= u_0. \end{aligned} \quad (2.14)$$

For convenience, we recall the discrete Gronwall Lemma that will be frequently used.

**Lemma 2.1** (see [1, 45, 46]). *Let  $\{a_n\}$ ,  $\{b_n\}$ , and  $\{c_n\}$  be three positive sequences, and let  $\{c_n\}$  be monotone and satisfy*

$$a_n + b_n \leq c_n + \lambda \sum_{i=0}^{n-1} a_i, \quad \lambda > 0, \quad a_0 + b_0 \leq c_0, \quad (2.15)$$

then

$$a_n + b_n \leq c_n \exp(n\lambda), \quad n \geq 0. \quad (2.16)$$

The following existence and uniqueness result is classical (see [1, 46]).

**Theorem 2.2.** *Assume that (H1) and (H2) hold. Then, for any given  $T > 0$ , there exists a unique solution  $(u, p)$  satisfying the following regularities:*

$$\begin{aligned} \sup_{0 < t \leq T} \left( \|u(t)\|_2^2 + \|p(t)\|_1^2 + \|u_t(t)\|_0^2 \right) &\leq c, \\ \sup_{0 < t \leq T} \tau(t) \|u_t\|_1^2 + \int_0^T \tau(t) \left( \|u_t\|_2^2 + \|p_t\|_1^2 + \|u_{tt}\|_0^2 \right) dt &\leq c, \end{aligned} \quad (2.17)$$

where  $\tau(t) = \min\{1, t\}$ .

### 3. Fully Discrete SMFE Method and Generation of Snapshots

In this section, we focus on the stabilized method proposed by [29] for the Stokes equations. Let  $h > 0$  be a real positive parameter. Finite-element subspace  $(X_h, M_h)$  of  $(X, M)$  is characterized by  $\tau_h = \tau_h(\Omega)$ , a partitioning of  $\bar{\Omega}$  into triangles or quadrilaterals  $K$ , assumed to be regular in the usual sense; that is, for some  $\sigma$  and  $\omega$  with  $\sigma > 1$  and  $0 < \omega < 1$ ,

$$\begin{aligned} h_K &\leq \sigma \rho_K, \quad \forall K \in \tau_h, \\ |\cos \theta_{iK}| &\leq \omega, \quad i = 1, 2, 3, 4, \quad \forall K \in \tau_h, \end{aligned} \quad (3.1)$$

where  $h_K$  is the diameter of element  $K$ ,  $\rho_K$  is the diameter of the inscribed circle of element  $K$ , and  $\theta_{iK}$  are the angles of  $K$  in the case of a quadrilateral partitioning. The mesh parameter  $h$  is given by  $h = \max_{K \in \tau_h} h_K$ . The finite-element subspaces of this paper are defined by setting

$$R_1(K) = \begin{cases} P_1(K), & \text{if } K \text{ is triangular,} \\ Q_1(K), & \text{if } K \text{ is the quadrilateral.} \end{cases} \quad (3.2)$$

Then, the finite-element pairs are coupled as follows:

$$\begin{aligned} X_h &= \{v \in X; v|_K \in R_1(K), \quad i = 1, 2\}, \\ M_h &= \{q \in M : q|_K \in R_1(K), \quad \forall K \in \tau_h\}. \end{aligned} \quad (3.3)$$

It is well known that this lowest equal-order finite-element pair does not satisfy the inf-sup condition. We define the following local difference between a consistent and an under-integrated mass matrices the stabilized formulation [29–31]:

$$G(p_h, q_h) = p_i^T (M_k - M_1) q_j = p_i^T M_k q_j - p_i^T M_1 q_j. \quad (3.4)$$

Here, we set

$$\begin{aligned} p_i^T &= [p_0, p_1, \dots, p_{N-1}]^T, \quad q_j = [q_0, q_1, \dots, q_{N-1}], \\ M_{ij} &= (\phi_i, \phi_j), \quad p_h = \sum_{i=0}^{N-1} p_i \phi_i, \\ p_i &= p_h(x_i), \quad \forall p_h \in M_h, \quad i, j = 0, \dots, N-1, \end{aligned} \quad (3.5)$$

where  $\phi_i$  is the basis function of the pressure on the domain  $\Omega$  such that its value is one at node  $x_i$  and zero at other nodes; the symmetric and positive  $M_k, k \geq 2$  and  $M_1$  are pressure mass matrix computed by using the  $k$ -order and 1-order Gauss integrations in each direction; respectively, also,  $p_i$  and  $q_i, i = 0, 1, \dots, N$ , are the value of  $p_h$  and  $q_h$  at the node  $x_i$ .  $p_i^T$  is the transpose of the matrix  $p_i$ .

Let  $\Pi_h : M \rightarrow R_0$  be the standard  $L^2$ -projection with the following properties [29–32]:

$$\begin{aligned} (p, q_h) &= (\Pi_h p, q_h), \quad \forall p \in M, \quad q_h \in R_0, \\ \|\Pi_h p\|_0 &\leq c \|p\|_0, \quad \forall p \in M, \\ \|p - \Pi_h p\|_0 &\leq \|p\|_1, \quad \forall p \in H^1(\Omega) \cap M, \end{aligned} \quad (3.6)$$

where  $R_0 = \{q_h \in M : q_h|_K \text{ is a constant}, \forall K \in \mathcal{K}_h\}$ . Then we can rewrite the bilinear form  $G(\cdot, \cdot)$  by

$$G(p, q) = (p - \Pi_h p, q - \Pi_h q). \quad (3.7)$$

*Remark 3.1.* The bilinear form  $G(\cdot, \cdot)$  in (3.7) is a symmetric, semipositive definite form generated on each local set  $K$ . The term can alleviate and offset the inf-sup condition [29]. It differs from the stabilized term in [45]. It does not require a selection of mesh-dependent stabilization parameters or a calculation of higher-order derivatives. Its another valuable feature is that the action of stabilization operators can be performed locally at the element level with minimal additional cost.

With the above notation, we begin by choosing an integer  $N$  and defining the time step  $\tau = T/N$  and discrete times  $t_n = n\tau$ ,  $n = 0, 1, 2, \dots, N$ . We obtain the fully discrete scheme as follows: find functions  $\{u_h^n\}_{n \geq 0} \subset X_h$  and  $\{p_h^n\}_{n \geq 1} \subset M_h$  as solutions of the recursive linear algebraic equations,

$$\begin{aligned} (d_t u_h^n, v_h) + \mathcal{B}_h((u_h^n, p_h^n); (v_h, q_h)) + b(u_h^{n-1}, u_h, v_h) &= (f(t_n), v_h), \\ u_h^0 &= u_{0h}. \end{aligned} \quad (3.8)$$

for all  $(v_h, q_h) \in (X_h, M_h)$ , where

$$\begin{aligned} d_t u_h^n &= \frac{u_h^n - u_h^{n-1}}{\tau}, \\ \mathcal{B}_h((u_h, p_h); (v_h, q_h)) &= a(u_h, v_h) - d(v_h, p_h) + d(u_h, q_h) + G(p_h, q_h), \end{aligned} \quad (3.9)$$

and  $u_{0h}$  is the approximation of  $u_0$ . The solutions  $\{u_h^n\}_{n \geq 0}$  and  $\{\bar{p}_h^n\}_{n \geq 1}$  to (3.8)-(3.9) are expected to the approximations of  $\{u_h(t_n)\}_{n \geq 0}$  and  $\{\bar{p}_h(t_n)\}_{n \geq 1}$  with

$$\bar{p}_h(t_n) = \frac{1}{\tau} \int_{t_{n-1}}^{t_n} p_h(t) dt. \quad (3.10)$$

**Theorem 3.2** (see [29–32]). *Let  $(X_h, M_h)$  be defined as above, then there exists a positive constant  $\beta$ , independent of  $h$ , such that*

$$\begin{aligned} |\mathcal{B}((u, p); (v, q))| &\leq c(\|u\|_1 + \|p\|_0)(\|v\|_1 + \|q\|_0), \quad (u, p), (v, q) \in (X, M), \\ \beta(\|u_h\|_1 + \|p_h\|_0) &\leq \sup_{(v_h, q_h) \in (X_h, M_h)} \frac{|\mathcal{B}_h((u_h, p_h); (v_h, q_h))|}{\|v_h\|_1 + \|q_h\|_0}, \quad \forall (u_h, p_h) \in (X_h, M_h), \end{aligned} \quad (3.11)$$

$$|G(p, q)| \leq c\|p - \Pi_h p\|_0\|q - \Pi_h q\|_0, \quad \forall p, q \in M.$$

By using the same approaches as those in [45], we can prove the following result.

**Theorem 3.3.** *Under the assumptions of Theorems 2.2 and 3.2, if  $h$  and  $\tau$  are sufficiently small and  $h = O(\tau)$ , then problem (3.8)-(3.9) has a unique solution  $(u_h^n, p_h^n) \in X_h \times M_h$  such that*

$$\|u_h^n\|_0^2 + \sum_{j=1}^n \left( \tau v \|\nabla u_h^j\|_0^2 + \tau G(p_h^j, p_h^j) \right) \leq \|u_0\|_0^2 + c\tau v^{-1} \sum_{j=1}^n \|f^j\|_0^2. \quad (3.12)$$



**Theorem 3.4** (see [32]). *Under the assumptions of Theorem 3.3, the error  $(u(t_n) - u_h^n, p(t_n) - p_h^n)$  satisfies the following bound:*

$$\begin{aligned} \tau \sum_{n=1}^N \|u(t_n) - u_h^n\|_0^2 + \tau(t_m) \|u(t_m) - u_h^m\|_0^2 &\leq c(h^4 + \tau^2), \\ \tau \sum_{n=1}^N \|u(t_n) - u_h^n\|_1^2 + \tau(t_m) \|u(t_m) - u_h^m\|_1^2 &\leq c(h^2 + \tau^2), \\ \tau \sum_{n=1}^N \tau(t_n) \|p(t_n) - p_h^n\|_0^2 &\leq c(h^2 + \tau^2), \end{aligned} \quad (3.13)$$

for all  $t_m \in (0, T]$ .

If  $\nu$ , the time step increment  $\tau$ , and the right-hand side  $f$  are given, by solving problem (3.8)-(3.9), we can obtain solution ensemble  $\{u_{1h}^n, u_{2h}^n, p_h^n\}_{n=1}^L$ . Then we choose  $L$  (in general,  $L \leq N$ , e.g.,  $L = 20, N = 200$ ) instantaneous solutions  $U_i(x, y) = (u_{1h}^i, u_{2h}^i, p_h^i)$  ( $i = 1, 2, \dots, L$ ) from the  $L$  group of solutions  $(u_h^n, p_h^n)$  ( $1 \leq n \leq L$ ) for problems (3.8), which are known as snapshots.

**Remark 3.5.** When one computes actual problems, one may obtain the ensemble of snapshots from physical system trajectories by drawing samples from experiments and interpolation (or data assimilation). For example, when one finds numerical solutions to PDES representing weather forecast, one can use the previous weather prediction results to construct the ensemble of snapshots, then restructure the POD optimal basis for the ensemble of snapshots by the following POD method, next replace finite element space  $(X_h, M_h)$  with the subspace spanned by the optimal POD basis. Numerical weather forecast equation is reduced to a fully discrete algebra equation with fewer degrees of freedom. Thus, the forecast of future weather change can be quickly simulated, which is a result of major importance for real-life applications.

#### 4. Reduced SMFE Formulation Based on POD Method

The POD method has received much attention in recent years as a tool to analyze complex physical systems. In this section, we use POD technique to deal with the snapshots in Section 3 and then use the POD basis to develop an RSMFE formulation for the transient Navier-Stokes equations.

Let  $\hat{X} = X \times M$ , and let  $U_i(x, y) = (u_{1h}^i, u_{2h}^i, p_h^i)$  ( $i = 1, 2, \dots, L$ , see Section 3). Set

$$V = \text{span}\{U_1, U_2, \dots, U_L\}, \quad (4.1)$$

where  $V$  is the ensemble consisting of the snapshots  $\{U_i\}_{i=1}^L$ , at least one of which is supposed to nonzero. Let  $\{\Psi_j\}_{j=1}^l$  denote an orthogonal basis of  $V$  with  $l = \dim V$  ( $l \leq L$ ). Then each member of the ensemble is expressed as

$$U_i = \sum_{j=1}^l (U_i, \Psi_j)_{\hat{X}} \Psi_j, \quad \text{for } i = 1, 2, \dots, L, \quad (4.2)$$

where  $(U_i, \Psi_j)_{\hat{X}} = (u_{1h}^i, \Psi_{uj}) + (p_h^i, \Psi_{pj})$ ,  $\Psi_{uj}$  and  $\Psi_{pj}$  are the orthogonal basis corresponding to  $u$  and  $p$ , respectively.

The method of POD consists in finding the orthogonal basis such that, for every  $d$  ( $1 \leq d \leq L$ ), the mean square error between the elements  $U_i$  ( $1 \leq i \leq L$ ) and corresponding  $d$ th partial sum of (4.2) is minimized on average

$$\min_{\{\Psi_j\}_{j=1}^d} \frac{1}{L} \sum_{i=1}^L \left\| U_i - \sum_{j=1}^d (U_i, \Psi_j)_{\hat{X}} \Psi_j \right\|_{\hat{X}}^2, \quad (4.3)$$

subject to

$$(\Psi_i, \Psi_j)_{\hat{X}} = \delta_{ij}, \quad \text{for } 1 \leq i \leq d, \quad 1 \leq j \leq d, \quad (4.4)$$

where  $\|U_i\|_{\hat{X}} = (\|u_{1h}^i\|_1^2 + \|u_{2h}^i\|_1^2 + \|p_h^i\|_0^2)^{1/2}$ . A solution sequence  $\{\Psi_j\}_{j=1}^d$  of (4.3) and (4.4) is known as a POD basis of rank  $d$ .

We introduce the correlation matrix  $E = (E_{ij})_{L \times L} \in R^{L \times L}$  corresponding to the snapshots  $\{U_i\}_{i=1}^L$  by

$$E_{ij} = \frac{1}{L} (U_i, U_j)_{\hat{X}}. \quad (4.5)$$

The matrix  $E$  is positive semidefinite and has rank  $l$ . The solution of (4.3) and (4.4) can be found in [45].

**Proposition 4.1.** *Let  $\lambda_1 \geq \lambda_2 \geq \dots \geq \lambda_l > 0$  denote the positive eigenvalues of  $E$ , and let  $v_1, v_2, \dots, v_l$  be the associated eigenvectors. Then a POD basis of rank  $d \leq l$  is given by*

$$\Psi_i = \frac{1}{\sqrt{\lambda_i}} \sum_{j=1}^L (v_i)_j U_j, \quad i = 1, 2, \dots, d \leq l, \quad (4.6)$$

where  $(v_i)_j$  denotes the  $j$ th component of the eigenvector  $v_i$ . Furthermore, the following error formula holds:

$$\frac{1}{L} \sum_{i=1}^L \left\| U_i - \sum_{j=1}^d (U_i, \Psi_j)_{\hat{X}} \Psi_j \right\|_{\hat{X}}^2 = \sum_{j=d+1}^l \lambda_j. \quad (4.7)$$

Let  $V^d = \{\Psi_1, \Psi_2, \dots, \Psi_d\}$ , and let  $X^d \times M^d = V^d$  with  $X^d \subset X_h \subset X$ , and let  $M^d \subset M_h \subset M$ . Set the Ritz-projection  $P^h : X \rightarrow X_h$  (if  $P^h$  is restricted to the Ritz-projection from  $X_h$  to  $X^d$ , it is written as  $P^d$ ) such that  $P^h|_{X_h} = P^d : X_h \rightarrow X^d$  and  $P^h : X \setminus X_h \rightarrow X_h \setminus X^d$  and  $L^2$ -projection  $\rho^d : M \rightarrow M^d$  denoted by, respectively,

$$a(P^h u, v_h) = a(u, v_h), \quad \forall v_h \in X_h, \quad (4.8)$$

$$(\rho^d p, q_d)_0 = (p, q_d)_0, \quad q_d \in M^d, \quad (4.9)$$

where  $u \in X$  and  $p \in M$ . Owing to (4.8)-(4.9) the linear operators  $P^h$  and  $\rho^d$  are well defined and bounded:

$$\|P^d u\|_1 \leq \|u\|_1, \quad \|\rho^d p\|_0 \leq \|p\|_0, \quad \forall u \in X, \quad p \in M. \quad (4.10)$$

**Lemma 4.2** (see [45]). *For every  $d$  ( $1 \leq d \leq l$ ), the projection operators  $P^d$  and  $\rho^d$  satisfy, respectively,*

$$\frac{1}{L} \sum_{i=1}^L \|u_h^{n_i} - P^d u_h^{n_i}\|_1^2 \leq \sum_{j=d+1}^l \lambda_j, \quad (4.11)$$

$$\frac{1}{L} \sum_{i=1}^L \|u_h^{n_i} - P^d u_h^{n_i}\|_0^2 \leq Ch^2 \sum_{j=d+1}^l \lambda_j, \quad (4.12)$$

$$\frac{1}{L} \sum_{i=1}^L \|p_h^{n_i} - \rho^d p_h^{n_i}\|_0^2 \leq \sum_{j=d+1}^l \lambda_j, \quad (4.13)$$

where  $u_h^{n_i} = (u_{1h}^{n_i}, u_{2h}^{n_i})$  and  $(u_{1h}^{n_i}, u_{2h}^{n_i}, p_h^{n_i}) \in V$ .

Thus, using  $V^d = X^d \times M^d$ , we can obtain the reduced SMFE formulation for problems (3.8) as follows. Find  $\hat{u}_d^n = (u_d^n, p_d^n) \in V^d$  such that

$$(d_t u_d^n, v_d) + B_h((u_d^n, p_d^n); (v_d, q_d)) + b(u_d^{n-1}, u_d, v_d) = (f(t_n), v_d), \quad 1 \leq n \leq N, \quad (4.14)$$

$$u_d^0 = u_{0h}.$$

**Remark 4.3.** Problem (3.8) includes  $N_h$  ( $N_h$  is the number of triangles or quadrilaterals vertex in  $\tau_h$ ) freedom degrees, while problem (4.14) includes  $d$  ( $d \ll l \leq L \leq N$ ) freedom degrees. For actual science and engineering problems, the number of the vertex in  $\tau_h$  are tens of thousands, even hundreds of millions, but  $d$  is the number of the largest eigenvalues of  $l$  snapshots from  $L$  transient solutions; it is very small. For numerical example in Section 6,  $d = 7$ , but  $N_h = 32 \times 32 \times 3 = 3072$ . Thus, problem (4.14) is a simplified stabilized finite-element scheme. In addition, the future development of many natural phenomena is affected by previous information, such as biological evolution and weather change. Here, we use the existing data to construct the POD basis, which contains the information on past data. Thus, this method can not only save computational load, but also make better use of the existing information to capture the law of the future development of natural phenomena.

## 5. Existence and Error Analysis of Solution to the Optimizing RSMFE Formulation

This section is devoted to discussing the existence and error estimates of solutions to problem (4.14). We see from (4.6) that  $V^d = X^d \times M^d \subset V \subset X_h \times M_h \subset X \times M$ . Using the same approaches as proving Theorem 3.3, we could prove the following existence result for solutions of problem (4.14).

**Theorem 5.1.** *Under the assumptions of Theorems 2.2 and 3.3, Problem (4.14) has a unique solution sequence  $(u_d^n, p_d^n) \in X^d \times M^d$  and satisfies, for  $1 \leq n \leq N$ ,*

$$\|u_d^n\|_0^2 + \sum_{j=1}^n \left( \tau v \|u_d^j\|_1^2 + \tau G(p_d^j, p_d^j) \right) \leq \|u_0\|_0^2 + c \tau v^{-1} \sum_{j=1}^n \|f^j\|_0^2. \quad (5.1)$$

In the following theorem, the errors between the solution  $(u_d^n, p_d^n)$  to Problem (4.14)-(4.15) and the solution  $(u_h^n, p_h^n)$  to Problem (3.8) are derived.

**Theorem 5.2.** Under the assumptions of Theorem 5.1, if  $h$  and  $\tau$  are sufficiently small,  $h = O(\tau)$ , and  $\tau = O(L^{-2})$ , then the errors between the solutions  $(u_d^n, p_d^n)$  to Problem (4.14), and the solutions  $(u_h^n, p_h^n)$  to Problem (3.8) have the following error estimates, for  $1 \leq n \leq N$ :

$$\|u_h^n - u_d^n\|_0^2 + \tau \nu \sum_{j=n_1}^{n_i} \|u_h^j - u_d^j\|_1^2 + \tau \sum_{j=n_1}^{n_i} \|p_h^j - p_d^j\|_0^2 \leq C\tau^{1/2} \sum_{j=d+1}^l \lambda_j, \quad (5.2)$$

if  $n = n_i \in \{n_1, n_2, \dots, n_L\}$ ,

$$\begin{aligned} & \|u_h^n - u_d^n\|_0^2 + \tau \nu \left[ \|u_h^n - u_d^n\|_1^2 + \sum_{j=n_1}^{n_i} \|u_h^j - u_d^j\|_1^2 \right] \\ & + \tau \left[ \|p_h^n - p_d^n\|_0^2 + \sum_{j=n_1}^{n_i} \|p_h^j - p_d^j\|_0^2 \right] \leq C\tau^{1/2} \sum_{j=d+1}^l \lambda_j + C\tau^2, \end{aligned} \quad (5.3)$$

if  $n = n_i \notin \{n_1, n_2, \dots, n_L\}$ .

*Proof.* Let  $w_d^n = P^d u_h^n - u_d^n$ ,  $r_d^n = \rho^d p_h^n - p_d^n$ . Subtracting (3.8) from (4.14) yields that

$$\begin{aligned} & \frac{1}{\tau} (u_h^n - u_d^n, v_d) - \frac{1}{\tau} (u_h^{n-1} - u_d^{n-1}, v_d) + a(u_h^n - u_d^n, v_d) - b(p_h^n - p_d^n, v_d) \\ & + b(u_h^{n-1} - u_d^{n-1}, u_h^n, v_d) + b(u_d^{n-1}, u_h^n - u_d^n, v_d) + b(u_h^n - u_d^n, q_d) + G(p_h^n - p_d^n, q_d) = 0. \end{aligned} \quad (5.4)$$

Taking  $(v_d, q_d) = 2\tau(w_d^n, r_d^n)$  in (5.4), since  $a(u_h^n - P^d u_h^n, w_d^n) = 0$ ,  $b(u_h^n - u_d^n, r_d^n) + G(p_h^n - p_d^n, r_d^n) = 0$ , we deduce

$$\begin{aligned} & 2(w_d^n, w_d^n) - 2(w_d^{n-1}, w_d^n) + 2\tau a(w_d^n, w_d^n) = 2(u_h^{n-1} - P^d u_h^{n-1}, w_d^n) \\ & + 2(P^d u_h^n - u_h^n, w_d^n) + 2\tau b(p_h^n - \rho^d p_h^n, w_d^n) + 2\tau b(P^d u_h^{n-1} - u_h^{n-1}, u_h^n, w_d^n) \\ & - 2\tau b(w_d^{n-1}, u_h^n, w_d^n) + 2\tau b(u_d^{n-1}, P^d u_h^n - u_h^n, w_d^n). \end{aligned} \quad (5.5)$$

Using (2.12)-(2.13), the Hölder inequality and the Young inequality, we see that

$$\begin{aligned} & \left| (u_h^{n-1} - P^d u_h^{n-1}, w_d^n) + (P^d u_h^n - u_h^n, w_d^n) \right| \\ & \leq C_1 \left( \|u_h^{n-1} - P^d u_h^{n-1}\|_1^2 + \|u_h^n - P^d u_h^n\|_1^2 \right) + \frac{\nu}{10} \|w_d\|_1^2, \\ & \left| b(p_h^n - \rho^d p_h^n, w_d^n) \right| \leq C_4 \|p_h^n - \rho^d p_h^n\|_0^2 + \frac{\nu}{10} \|w_d^n\|_1^2, \\ & \left| b(P^d u_h^{n-1} - u_h^{n-1}, u_h^n, w_d^n) \right| \leq \frac{\nu}{10} \|w_d^n\|_1^2 + C_5 \left\| (u_h^{n-1} - P^d u_h^{n-1}) \right\|_1^2, \\ & \left| b(u_d^{n-1}, P^d u_h^n - u_h^n, w_d^n) \right| \leq \frac{\nu}{10} \|w_d^n\|_1^2 + C_6 \|u_h^n - P^d u_h^n\|_1^2, \\ & \left| -b(w_d^{n-1}, u_h^n, w_d^n) \right| \leq C_7 \|w_d^{n-1}\|_0^2 + \frac{\nu}{10} \|w_d^n\|_1^2. \end{aligned} \quad (5.6)$$

Noting that  $a(a-b) = [a^2 - b^2 + (a-b)^2]/2$  (for  $a \geq 0$  and  $b \geq 0$ ), owing to (5.6), we obtain that

$$\begin{aligned} \|w_d^n\|_0^2 - \|w_d^{n-1}\|_0^2 + \nu\tau\|w_d\|_1^2 &\leq C_7\tau\|w_d^{n-1}\|_0^2 \\ &+ C\tau\left(\|(u_h^n - P^d u_h^n)\|_1^2 + \|(u_h^{n-1} - P^d u_h^{n-1})\|_1^2 + \|p_h^n - \rho^d p_h^n\|_0^2\right). \end{aligned} \quad (5.7)$$

First, we consider the case of  $n \in \{n_1, n_2, \dots, n_L\}$ . Summing (5.7) from  $n_1$  to  $n_i$ ,  $i = 1, 2, \dots, L$ , and noting that  $u_h^0 - u_d^0 = 0$ , using Lemma 4.2, we can derive that

$$\|w_d^{n_i}\|_0^2 + \nu\tau \sum_{j=n_1}^{n_i} \|w_d^j\|_1^2 \leq C\tau L \sum_{j=d+1}^l \lambda_j + C_7\tau \sum_{j=n_0}^{n_{i-1}} \|w_d^j\|_0^2. \quad (5.8)$$

By using the discrete Gronwall inequality, we obtain that

$$\|w_d^{n_i}\|_0^2 + \nu\tau \sum_{j=n_1}^{n_i} \|w_d^j\|_1^2 \leq C\tau L \sum_{j=d+1}^l \lambda_j \exp(C_7\tau n_i). \quad (5.9)$$

If  $h$  and  $\tau$  are sufficiently small,  $\tau = O(L^{-2})$ , and noting that  $n_i\tau \leq n_i N \leq T$ , we find that

$$\|w_d^{n_i}\|_0^2 + \nu\tau \sum_{j=n_1}^{n_i} \|w_d^j\|_1^2 \leq C\tau^{1/2} \sum_{j=d+1}^l \lambda_j. \quad (5.10)$$

Thanks to  $b(u_h^n - u_d^n, r_d^n) + G(p_h^n - p_d^n, r_d^n) = 0$ , we obtain

$$\|p_h^n - p_d^n\|_0 \leq C\|u_h^n - u_d^n\|_1. \quad (5.11)$$

By combining (5.10)-(5.11) with Lemma 4.2, we obtain the error estimate result (5.2).  $\square$

Next, we consider the case of  $n \notin \{1, 2, \dots, L\}$ ; we assume that  $t_n \in (t_{n_i-1}, t_{n_i})$  and  $t_n$  is the nearest point to  $t_{n_i}$ .  $u_h^n$  and  $p_h^n$  are expanded into the Taylor series expansion at point  $t_{n_i}$ .

$$u_h^n = u_h^{n_i} - s\tau \frac{\partial u_h(\xi_1)}{\partial t}, \quad \xi_1 \in [t_{n_i}, t_n], \quad (5.12)$$

$$p_h^n = p_h^{n_i} - s\tau \frac{\partial p_h(\xi_2)}{\partial t}, \quad \xi_2 \in [t_{n_i}, t_n], \quad (5.13)$$

where  $s$  is the number of time steps from  $t_n$  to  $t_{n_i}$ . If the snapshots are equably taken, then  $s \leq N/L$ . Summing (5.7) from  $n_1$  to  $n_i$ , and using (5.12), if  $|\partial u_h(\xi_1)/\partial t|$  and  $|\partial p_h(\xi_2)/\partial t|$  are bounded, by discrete Gronwall inequality and Lemma 4.2 and (3.12), we obtain that

$$\|w_d^n\|_0^2 + \nu\tau \left[ \|w_d^n\|_1^2 + \sum_{j=n_1}^{n_i} \|w_d^j\|_1^2 \right] \leq C\tau L \sum_{j=d+1}^l \lambda_j + C\tau^2. \quad (5.14)$$

If  $\tau = O(L^{-2})$ , by (5.14) we obtain that

$$\|w_d^n\|_0^2 + \nu\tau \left[ \|w_d^n\|_1^2 + \sum_{j=n_1}^{n_i} \|w_d^j\|_1^2 \right] \leq C\tau^{1/2} \sum_{j=d+1}^l \lambda_j + C\tau^2. \quad (5.15)$$

Hence, combining (5.11), (5.13), and (5.15) with Lemma 4.2 yields (5.3).

**Theorem 5.3.** *Under hypotheses of Theorems 3.4 and 5.2, the error estimates between the solution  $(u(t), p(t))$  to Problem (2.1)-(2.2) and the solutions  $(u_d^n, p_d^n)$  to Problem (4.14) are as follows:*

$$\begin{aligned} & \|u(t_n) - u_d^n\|_0^2 + \tau\nu \sum_{j=1}^n \|u^j - u_d^j\|_1^2 + \tau \sum_{j=1}^n \|p^j - p_d^j\|_0^2 \\ & \leq c(h^2 + \tau^2) + C\tau^{1/2} \sum_{j=d+1}^l \lambda_j, \quad n = 1, 2, \dots, N. \end{aligned} \quad (5.16)$$

## 6. Numerical Examples

In order to illustrate and verify the theoretical results of Theorem 5.3, we present the results obtained in a simple test case. We set  $\Omega$  is the unit square  $[0, 1] \times [0, 1]$  and viscosity  $\nu = 0.05$ . The velocity and pressure are designed on the same uniform triangulation of  $\Omega$ . The exact solution is given by

$$\begin{aligned} u &= (u_1(x, y), u_2(x, y)), \quad p(x, y) = 10(2x - 1)(2y - 1) \cos(t), \\ u_1(x, y) &= 10x^2(1 - x)^2 y(1 - y)(1 - 2y) \cos(t), \\ u_2(x, y) &= -10x(1 - x)(1 - 2x)y^2(1 - y)^2 \cos(t), \end{aligned} \quad (6.1)$$

and  $f$  is determined by (2.1).

All the numerical experiments have been performed using the conforming  $Q_1$  finite element for both velocity and pressure. The implicit (backward) Euler's scheme is used for the time discretization. For simplicity, the unit square is divided into  $n \times n$  small squares with side length  $h = 1/n$ . In order to make  $\tau = O(h)$ , we take time step increment as  $\tau = 1/n$ .

We obtain 20 values (i.e., snapshots) outputting at time  $t = 10\tau, 20\tau, 30\tau, \dots, 200\tau$  by solving the SMFE formulation. We use 7 optimal POD bases to obtain the solutions of the reduced formulation problem (4.14) as  $t = 200\tau$ . In Table 1, we present the velocity and

**Table 1:** Numerical results for the SMFE method.

$h^{-1}$	$\frac{\ u - u_h\ _1}{\ u\ _1}$	$u_{H^1}$ rate	$\frac{\ p - p_h\ _0}{\ p\ _0}$	$p_{L^2}$ rate	CPU time (seconds)
24	0.1443070	—	0.0175033	—	1081
32	0.0973051	1.3699	0.0104506	1.7927	2906
40	0.0752875	1.1497	0.0072136	1.6612	11403
48	0.0619347	1.0708	0.0054000	1.5882	25375
56	0.0510066	1.2593	0.0042171	1.6040	42132
64	0.0437541	1.1486	0.0034805	1.4375	61320

**Table 2:** Numerical results for the RSMFE method.

$h^{-1}$	$\frac{\ u - u_d\ _1}{\ u\ _1}$	$u_{H^1}$ rate	$\frac{\ p - p_d\ _0}{\ p\ _0}$	$p_{L^2}$ rate	CPU time (seconds)
24	0.1486190	—	0.0174335	—	3
32	0.1069230	1.1446	0.0107643	1.6760	14
40	0.079740	1.3146	0.0071930	1.8066	36
48	0.0637586	1.2268	0.0053759	1.5971	83
56	0.0525842	1.2500	0.0041878	1.6202	152
64	0.0445977	1.2337	0.0034562	1.4379	216

pressure relative error estimates, convergence rates, and CPU times using the SMFE method, and, in Table 2, we give the corresponding results obtained using the RSMFE method. In particular, as  $n = 32$ , the SMFE solutions ( $u_{hi}^{200}, i = 1, 2$ )(c), the exact solutions ( $u_i^{200}, i = 1, 2$ )(b), and the RSMFE solutions ( $u_{di}^{200}, i = 1, 2$ )(a) are depicted, respectively, in Figures 1 and 3. Moreover, the difference ( $u_i^{200} - u_{di}^{200}, i = 1, 2$ )(a) between the exact solutions and the RSMFE solutions and the difference ( $u_{hi}^{200} - u_{di}^{200}, i = 1, 2$ )(b) between the SMFE solutions and RSMFE solutions are depicted in Figures 2 and 4, respectively. From Tables 1, 2, and Figures 1–4, we can find that the RSMFE solutions has the same accuracy as the reduced SMFE solutions and the exact solutions. As  $n = 32$ , for the SMFE Problem (3.8)-(3.9), there are  $3 \times 32 \times 32 = 3072$  freedom degrees; the performing time required is 2906 seconds, while the reduced SMFE Problem (4.14) with 7 POD bases only has 7 freedom degrees and the corresponding time is only 14 seconds, that is, the required implementing time to solve the usual SMFE Problem (3.8) is as 207 times as that to do the reduced SMFE problem (4.14) with 7 POD bases, while the errors between their respective solutions do not exceed  $3 \times 10^{-3}$ . As  $n = 56$ , Figure 5 shows the velocity  $H^1$  relative errors between solutions with different number of optimal POD bases and solutions obtained with full bases at  $t = 100\tau$  and  $t = 200\tau$ . It is shown that the reduced SMFE problem (4.14) is very effective and feasible. In addition, the results obtained for the numerical examples are consistent with the theoretical ones.

## 7. Conclusions

In this paper, we have combined the POD techniques with a SMFE formulation based on two local Gauss' integrations to derive a reduced SMFE method for the transient Navier-Stokes equations. The discretization uses a pair of spaces of finite elements  $P_1 - P_1$  over triangles or  $Q_1 - Q_1$  over quadrilateral elements. This SMFE method differs from that in [45]. It has some prominent features: parameter-free, avoiding higher-order derivatives or

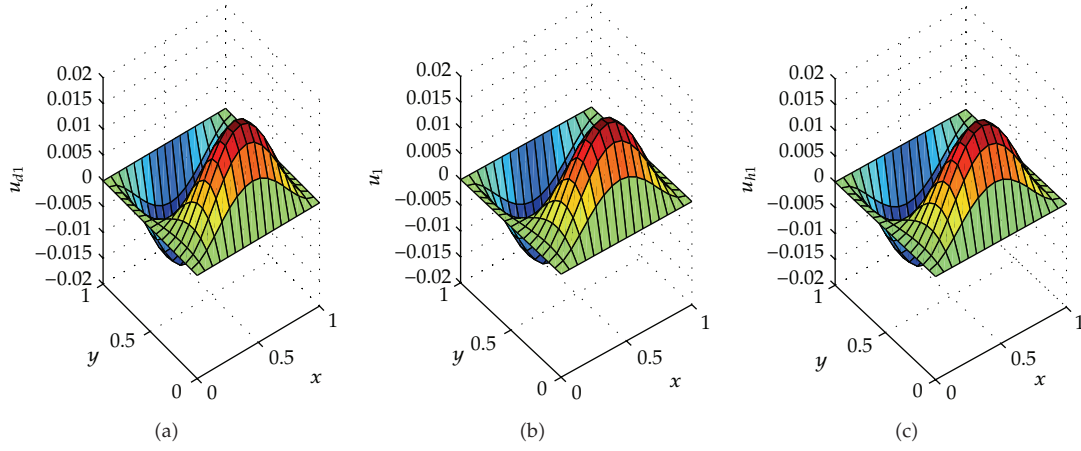


**Figure 1:** RSMFE solutions (a), the exact solutions (b), and SMFE solutions (c).

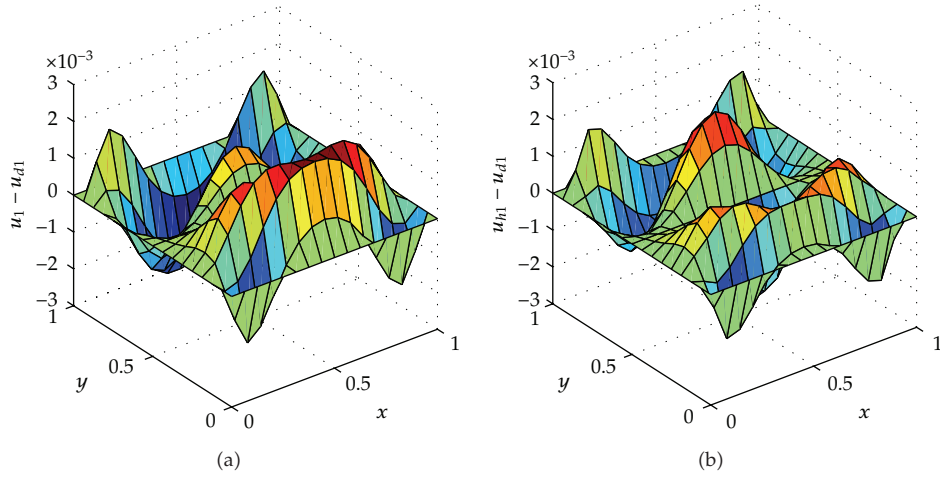


**Figure 2:** Difference between the RSMFE solutions and the exact solutions (a) and difference between the SMFE solutions and the RSMFE solutions (b).

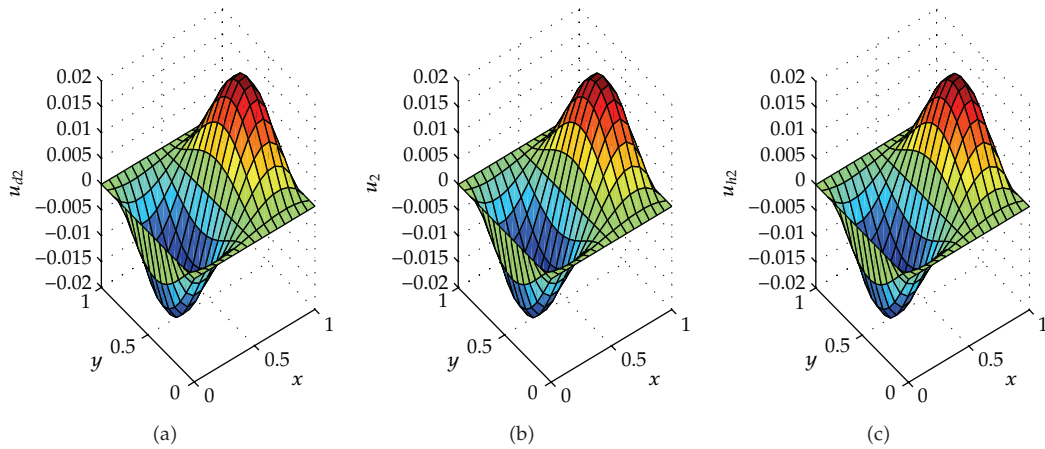


**Figure 3:** RSMFE solutions (a), the exact solutions (b), and SMFE solutions (c).



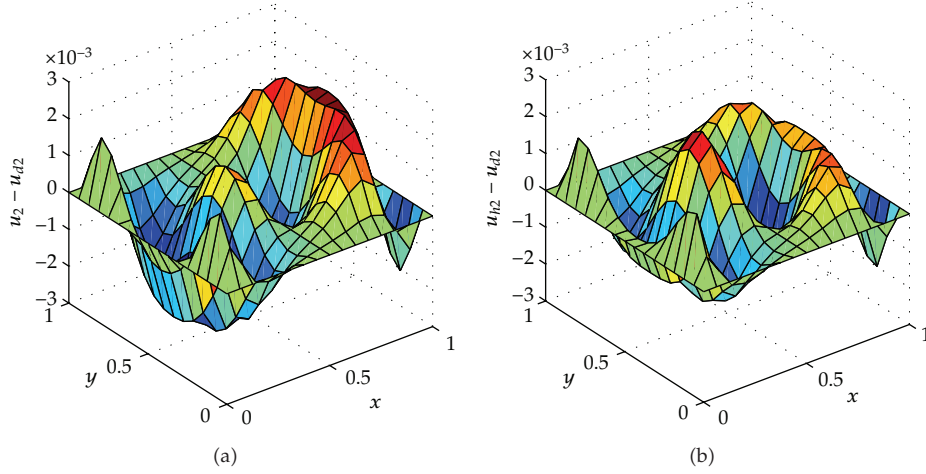


**Figure 4:** Difference between the RSMFE solutions and the exact solutions (a) and difference between the SMFE solutions and the RSMFE solutions (b).

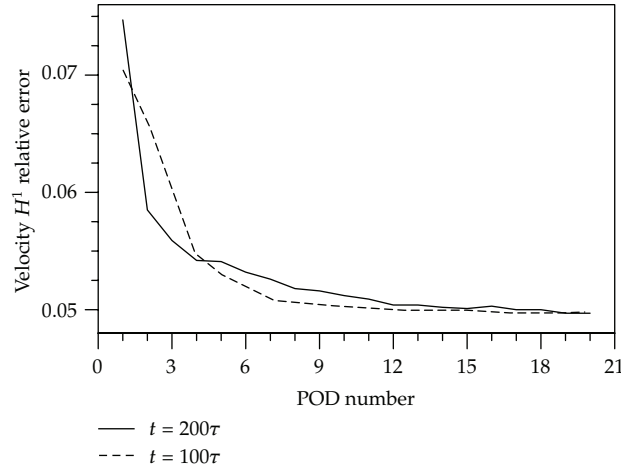


**Figure 5:** The velocity  $H^1$ -error changing with the number of POD basis as  $n = 56$ .

edge-based data structures, and stabilization being completed locally at the element level. We have also analyzed the errors between the solutions of their usual SMFE formulation and the solutions of the reduced SMFE based on POD basis and discussed theoretically the relation of the number of snapshots and the number of solutions at all time instances, which have shown that our present method has improved and innovated the existing methods. We have validated the correctness of our theoretical results with numerical examples. Though snapshots and the POD basis of our numerical examples are constructed with the solutions of the usual SMFE formulation, when one computes actual problems, one may structure the snapshots and the POD basis with interpolation or data assimilation by drawing samples from experiments, then solve Problem (4.14), while it is unnecessary to solve Problem (3.8). Thus, the time-consuming calculations and resource demands in the computational process are greatly saved, and the computational efficiency is vastly improved. Therefore, the method in this paper holds a good prospect of extensive applications.

Future research work in this area aims at addressing some practical engineering problems arising in the fluid dynamics and more complicated PDES, extending the optimizing reduced SMFE formulation, applying it to a realistic atmosphere quality forecast system, and to a set of more complicated nonlinear PDES, for instance, 3D realistic model equations coupling strongly nonlinear properties, nonhomogeneous variable flux, and boundary.

## Acknowledgments

This work is supported by the Scientific Research Common Program of the Beijing Municipal Commission of Education (Grant no. KM201110772019), the Knowledge Innovation Program of the Chinese Academy of Sciences (Grant no. KZCX2-EW-QN207), the National Natural Science Foundation of China (Grant no. 11071193 and 41075076), the Academic Human Resources Development in the Institutions of Higher Learning under the Jurisdiction of Beijing Municipality (Grant no. PHR201006116), the Natural Science New Star of Science and Technologies Research Plan in Shaanxi Province of China (Grant no. 2011kjxx12), Research Program of the Education Department of the Shaanxi Province (Grant no. 11JK0490). The author would like to thank the referees for their valuable comments and suggestions.

## References

- [1] V. Girault and P.-A. Raviart, *Finite Element Methods for Navier-Stokes Equations: Theory and Algorithms*, vol. 5 of *Springer Series in Computational Mathematics*, Springer, New York, NY, USA, 1986.
- [2] J. G. Heywood and R. Rannacher, "Finite element approximation of the nonstationary Navier-Stokes problem: I. Regularity of solutions and second-order error estimates for spatial discretization," *SIAM Journal on Numerical Analysis*, vol. 19, no. 2, pp. 275–311, 1982.
- [3] Z. H. Luo, "The third order estimate of mixed finite element for the Navier-Stokes problems," *Chinese Quarterly Journal of Mathematics*, vol. 10, pp. 9–12, 1995.
- [4] K. Fukunaga, *Introduction to Statistical Pattern Recognition*, Computer Science and Scientific Computing, Academic Press, New York, NY, USA, 2nd edition, 1990.
- [5] I. T. Jolliffe, *Principal Component Analysis*, Springer Series in Statistics, Springer, New York, NY, USA, 2nd edition, 2002.
- [6] P. Holmes, J. L. Lumley, and G. Berkooz, *Turbulence, Coherent Structures, Dynamical Systems and Symmetry*, Cambridge Monographs on Mechanics, Cambridge University Press, Cambridge, UK, 1996.
- [7] P. Moin and R. D. Moser, "Characteristic-eddy decomposition of turbulence in a channel," *Journal of Fluid Mechanics*, vol. 200, pp. 471–509, 1989.
- [8] M. Rajaei, S. K. F. Karlsson, and L. Sirovich, "Low-dimensional description of free-shear-flow coherent structures and their dynamical behaviour," *Journal of Fluid Mechanics*, vol. 258, pp. 1–29, 1994.
- [9] R. D. Joslin, M. D. Gunzburger, R. A. Nicolaides, G. Erlebacher, and M. Y. Hussaini, "A self-contained automated methodology for optimal flow control validated for transition delay," *AIAA Journal*, vol. 35, no. 5, pp. 816–824, 1997.
- [10] H. V. Ly and H. T. Tran, "Proper orthogonal decomposition for flow calculations and optimal control in a horizontal CVD reactor," *Quarterly of Applied Mathematics*, vol. 60, no. 4, pp. 631–656, 2002.
- [11] X. J. Tian and Z. H. Xie, "An explicit four-dimensional variational data assimilation method based on the proper orthogonal decomposition: theoretics and evaluation," *Science in China D*, vol. 52, no. 2, pp. 279–286, 2009.
- [12] J. Lumley, "Coherent structures in turbulence," in *Transition and Turbulence*, R. E. Meyer, Ed., Academic Press, New York, NY, USA, 1981.
- [13] N. Aubry, P. Holmes, J. L. Lumley, and E. Stone, "The dynamics of coherent structures in the wall region of a turbulent boundary layer," *Journal of Fluid Mechanics*, vol. 192, pp. 115–173, 1988.
- [14] L. Sirovich, "Turbulence and the dynamics of coherent structures: part I–III," *Quarterly of Applied Mathematics*, vol. 45, no. 3, pp. 561–590, 1987.
- [15] K. Kunisch and S. Volkwein, "Galerkin proper orthogonal decomposition methods for parabolic problems," *Numerische Mathematik*, vol. 90, no. 1, pp. 117–148, 2001.

- [16] K. Kunisch and S. Volkwein, "Galerkin proper orthogonal decomposition methods for a general equation in fluid dynamics," *SIAM Journal on Numerical Analysis*, vol. 40, no. 2, p. 492–515 (electronic), 2002.
- [17] Z. D. Luo, R. W. Wang, and J. Zhu, "Finite difference scheme based on proper orthogonal decomposition for the nonstationary Navier-Stokes equations," *Science in China A*, vol. 50, no. 8, pp. 1186–1196, 2007.
- [18] Z. D. Luo, J. Chen, I. M. Navon, and X. Z. Yang, "Mixed finite element formulation and error estimates based on proper orthogonal decomposition for the nonstationary Navier-Stokes equations," *SIAM Journal on Numerical Analysis*, vol. 47, no. 1, pp. 1–19, 2008.
- [19] Z. D. Luo, J. Chen, P. Sun, and X. Z. Yang, "Finite element formulation based on proper orthogonal decomposition for parabolic equations," *Science in China A*, vol. 52, no. 3, pp. 585–596, 2009.
- [20] Z. D. Luo, X. Z. Yang, and Y. J. Zhou, "A reduced finite element formulation based on proper orthogonal decomposition for Burgers equation," *Applied Numerical Mathematics*, vol. 59, no. 8, pp. 1933–1946, 2009.
- [21] Y. H. Cao, J. Zhu, Z. D. Luo, and I. M. Navon, "Reduced-order modeling of the upper tropical Pacific Ocean model using proper orthogonal decomposition," *Computers & Mathematics with Applications*, vol. 52, no. 8-9, pp. 1373–1386, 2006.
- [22] Y. H. Cao, J. Zhu, I. M. Navon, and Z. D. Luo, "A reduced-order approach to four-dimensional variational data assimilation using proper orthogonal decomposition," *International Journal for Numerical Methods in Fluids*, vol. 53, no. 10, pp. 1571–1583, 2007.
- [23] Z. D. Luo, J. Zhu, R. W. Wang, and I. M. Navon, "Proper orthogonal decomposition approach and error estimation of mixed finite element methods for the tropical Pacific Ocean reduced gravity model," *Computer Methods in Applied Mechanics and Engineering*, vol. 196, no. 41–44, pp. 4184–4195, 2007.
- [24] Z. D. Luo, J. Chen, J. Zhu, R. W. Wang, and I. M. Navon, "An optimizing reduced order FDS for the tropical Pacific Ocean reduced gravity model," *International Journal for Numerical Methods in Fluids*, vol. 55, no. 2, pp. 143–161, 2007.
- [25] R. W. Wang, J. Zhu, Z. D. Luo, and I. M. Navon, "An equation-free reduced order modeling approach to tropic Pacific simulation," *Advances in Geosciences*, vol. 12, pp. 1–16, 2007.
- [26] J. Du, J. Zhu, Z. D. Luo, and I. M. Navon, "An optimizing finite difference scheme based on proper orthogonal decomposition for CVD equations," *International Journal for Numerical Methods in Biomedical Engineering*, vol. 27, no. 1, pp. 78–94, 2011.
- [27] H. L. Yu and H. J. Chu, "Understanding space-time patterns of groundwater system by empirical orthogonal functions: a case study in the Choshui River alluvial fan, Taiwan," *Journal of Hydrology*, vol. 381, no. 3-4, pp. 239–247, 2010.
- [28] T. Bernard, O. Krol, H. Linke, and T. Rauschenbach, "Optimal management of regional water supply systems using a reduced finite-element groundwater model," *Automatisierungstechnik*, vol. 57, no. 12, pp. 593–600, 2009.
- [29] J. Li and Y. N. He, "A stabilized finite element method based on two local Gauss integrations for the Stokes equations," *Journal of Computational and Applied Mathematics*, vol. 214, no. 1, pp. 58–65, 2008.
- [30] J. Li, Y. N. He, and Z. X. Chen, "A new stabilized finite element method for the transient Navier-Stokes equations," *Computer Methods in Applied Mechanics and Engineering*, vol. 197, no. 1–4, pp. 22–35, 2007.
- [31] J. Li, *Finite element methods for the two-dimensional incompressible Navier-Stokes equations*, Ph.D. thesis, Xi'an Jiaotong University, 2007.
- [32] S. Li and Y. R. Hou, "A fully discrete stabilized finite element method for the time-dependent Navier-Stokes equations," *Applied Mathematics and Computation*, vol. 215, no. 1, pp. 85–99, 2009.
- [33] P. B. Bochev, C. R. Dohrmann, and M. D. Gunzburger, "stabilization of low-order mixed finite elements," *SIAM Journal on Numerical Analysis*, vol. 42, pp. 1189–1208, 2006.
- [34] A. W. Wang and J. Li, "Stabilization of the lowest-order mixed finite elements for the steady Navier-Stokes equations," *Chinese Journal of Engineering Mathematics*, vol. 17, pp. 249–257, 2010.
- [35] Y. N. He, A. W. Wang, and L. Q. Mei, "Stabilized finite-element method for the stationary Navier-Stokes equations," *Journal of Engineering Mathematics*, vol. 51, no. 4, pp. 367–380, 2005.
- [36] T. J. R. Hughes, L. P. Franca, and M. Balestra, "A new finite element formulation for computational fluid dynamics: V. Circumventing the Babuska-Brezzi condition: a stable Petrov-Galerkin formulation of the Stokes problem accommodating equal-order interpolations," *Computer Methods in Applied Mechanics and Engineering*, vol. 59, no. 1, pp. 85–99, 1986.

- [37] T. J. R. Hughes and L. P. Franca, "A new finite element formulation for computational fluid dynamics: VII. The Stokes problem with various well-posed boundary conditions: symmetric formulations that converge for all velocity/pressure spaces," *Computer Methods in Applied Mechanics and Engineering*, vol. 65, no. 1, pp. 85–96, 1987.
- [38] J. Douglas and J. P. Wang, "An absolutely stabilized finite element method for the Stokes problem," *Mathematics of Computation*, vol. 52, no. 186, pp. 495–508, 1989.
- [39] C. Johnson and J. Saranen, "Streamline diffusion methods for the incompressible Euler and Navier-Stokes equations," *Mathematics of Computation*, vol. 47, no. 175, pp. 1–18, 1986.
- [40] B. Kragel, *Streamline diffusion POD models in optimization*, Ph.D. thesis, Universitat Trier, 2005.
- [41] P. Hansbo and A. Szepessy, "A velocity-pressure streamline diffusion finite element method for the incompressible Navier-Stokes equations," *Computer Methods in Applied Mechanics and Engineering*, vol. 84, no. 2, pp. 175–192, 1990.
- [42] M. A. Behr, L. P. Franca, and T. E. Tezduyar, "Stabilized finite element methods for the velocity-pressure-stress formulation of incompressible flows," *Computer Methods in Applied Mechanics and Engineering*, vol. 104, no. 1, pp. 31–48, 1993.
- [43] J. Blasco and R. Codina, "Space and time error estimates for a first order, pressure stabilized finite element method for the incompressible Navier-Stokes equations," *Applied Numerical Mathematics*, vol. 38, no. 4, pp. 475–497, 2001.
- [44] R. Codina and J. Blasco, "Analysis of a pressure-stabilized finite element approximation of the stationary Navier-Stokes equations," *Numerische Mathematik*, vol. 87, no. 1, pp. 59–81, 2000.
- [45] Z. D. Luo, J. Du, Z. Xie, and Y. Guo, "A reduced stabilized mixed finite element formulation based on proper orthogonal decomposition for the non-stationary Navier-Stokes equations," *International Journal for Numerical Methods in Engineering*, vol. 88, no. 1, pp. 31–46, 2011.
- [46] R. Temam, *Navier-Stokes Equations: Theory and Numerical Analysis*, vol. 2 of *Studies in Mathematics and its Applications*, North-Holland, Amsterdam, The Netherlands, 3rd edition, 1984.

## *Research Article*

# **A Hybrid Analytical-Numerical Model Based on the Method of Fundamental Solutions for the Analysis of Sound Scattering by Buried Shell Structures**

**L. Godinho, P. Amado-Mendes, and A. Pereira**

*CICC, Department of Civil Engineering, University of Coimbra, Pinhal de Marrocos,  
3030-788 Coimbra, Portugal*

Correspondence should be addressed to L. Godinho, lgodinho@dec.uc.pt

Received 30 May 2011; Accepted 31 July 2011

Academic Editor: Delfim Soares Jr.

Copyright © 2011 L. Godinho et al. This is an open access article distributed under the Creative Commons Attribution License, which permits unrestricted use, distribution, and reproduction in any medium, provided the original work is properly cited.

Several numerical and analytical models have been used to study underwater acoustics problems. The most accurate and realistic models are usually based on the solution of the wave equation using a variety of methods. Here, a hybrid numerical-analytical model is proposed to address the problem of underwater sound scattering by an elastic shell structure, which is assumed to be circular and that is buried in a fluid seabed below a water waveguide. The interior of the shell is filled with a fluid that may have different properties from the host medium. The analysis is performed by coupling analytical solutions developed both for sound propagation in the waveguide and in the vicinity of the circular hollow pipeline. The coupling between solutions is performed using the method of fundamental solutions. This strategy allows a compact description of the propagation medium while being very accurate and highly efficient from the computational point of view.

## **1. Introduction**

The detection of buried objects in solid and fluid media has been an active research topic, making use of different approaches. Techniques based on wave propagation have received particular interest from researchers, leading to the development of a broad variety of analytical and numerical models to simulate this propagation and to an intense research on the interpretation of field results. In fact, the measurement of spatial and temporal variations, recorded at hydrophones or geophones, resulting from the generation of waves produced by dynamic sources, placed inside elastic or acoustic media, is frequently used to infer the presence of buried structures or the geological configuration of a specific site. Some early reference works on this topic are due to Claerbout [1] or Griffiths and King [2], addressing the specific

application of such methods to geophysics; in the case of underwater acoustics, reference works include the now classic book by Jensen et al. [3], which describes a number of formulations that can be used in both shallow water and deep water scattering problems.

In this paper, the authors focus on the scattering of waves in underwater configurations, for which different methods have been used in the past, ranging from the analytical methods presented by Pao and Mow [4] for studying wave diffraction near cylindrical circular inclusions to purely numerical methods, such as finite difference (e.g., Stephens [5] or Wang [6]) and finite elements techniques (e.g., Marfurt [7] or Zampolli et al. [8]), combined with transmitting boundaries.

Methods relying on the description of the relevant boundaries of the problem have also been developed and form a very interesting class for this type of applications. An important early work on acoustic scattering in the open ocean using the boundary element method is due to Dawson and Fawcett [9], which analyses a waveguide with flat surfaces, except for a compact area of deformation, where the acoustic scattering takes place. A hybrid model which combines the standard boundary element method (BEM) in an inner region with varying bathymetry and an eigenfunction expansion in the outer region of constant depth was later proposed by Grilli et al. [10]. Works by Santiago and Wrobel [11] described the implementation of the subregion technique in boundary element formulation for the analysis of two-dimensional acoustic wave propagation in a shallow water region with irregular seabed topography, allowing for the analysis of more general underwater systems. In their approach, the bottom and surface boundaries of the regions are modeled using Neumann and Dirichlet conditions, allowing for the use of Green's functions that satisfy either the free surface boundary condition or both the boundary conditions on the free surface and rigid bottom.

The use of specific Green's functions that account for part of the boundaries of the analysis domain has been an important strategy when dealing with boundary element methods, since they may allow for smaller discretization schemes, leading to lower computational effort, and therefore many researchers have focused their attention in their development. A relevant example are the works of Tadeu and Kausel [12] and of Tadeu and António [13], who proposed 2.5D Greens's functions for acoustic and elastic wave propagation in layered media, built as a superposition of the effects of plane waves with different inclinations; these functions have, in fact, been extensively used in subsequent works. António et al. [14] developed a boundary element formulation incorporating Green's functions to describe 2.5 D wave propagation for the case of a waveguide with an elastic bottom and used them to study the scattering of waves by a buried or submerged object. A recent work by Pereira et al. [15] described a formulation based on the BEM which allows simulating the scattering of sound in an underwater configuration including a fluid seabed with multiple layers and a bottom discontinuity.

Recently, meshless methods have also been used for the study of underwater sound scattering in different types of environments. Different meshless methods are described in the literature, including Meshless-Local-Petrov-Galerkin (MLPG) methods (see, e.g., Atluri [16]), RBF collocation methods (see, e.g., Kansa [17, 18]), or the method of fundamental solutions (MFS) (e.g., Golberg and Chen [19]). Examples of the application of these strategies to underwater acoustics can be found in recent works by Godinho et al. [20], using RBF base local interpolation methods formulated in the time domain, or by Costa et al. [21], making use of the MFS together with the fundamental solutions for a flat waveguide and for a perfect wedge.



The scattering by a submerged object located within a fluid medium has also been investigated by researchers, and works describing the scattering features of submerged circular cylindrical elastic shell structures have also been published. The wave scattering by submerged elastic circular cylindrical shells, filled with air, struck by plane harmonic acoustic waves was analyzed by Veksler et al. [22]. In that work, the standard resonance scattering theory was used to study the modal resonances, focusing on the generation of bending waves. More recently, Godinho et al. [23] described an analytical solution for the scattering of such structures buried in a homogeneous fluid medium. Later, the same authors [24] used a BEM formulation to analyze the effect of a construction defect in the vibration of such structures. However, it is important to note that this BEM formulation degenerates whenever the thickness of the structure is very small, and therefore, alternative methods should be used.

In the present work, the authors address the case in which a regular circular shell structure is buried within a fluid seabed under a water-filled flat waveguide. The approach proposed here is based on a hybrid approach which incorporates the analytical solutions described in [23] for the submerged circular shell structures, together with the analytical solution known for a waveguide with a fluid bottom (using the methodology proposed in [13]). The coupling of these solutions is performed in the fluid medium that describes the bottom by using the MFS and defining a virtual coupling boundary around the shell structure, along which the continuity of pressures and normal displacements is imposed. This formulation can easily incorporate multiple scattering objects, with different properties, although they are restricted to have a circular shape. More importantly, the method allows accounting for the full solid-fluid and fluid-fluid interaction that occurs at the physical interfaces of the system in an accurate manner, leading to precise results, since it is based on analytical solutions of each individual problem. Additionally, since it uses the analytical solution for a submerged circular shell, it allows modeling thin structures, overcoming the difficulties identified above for the BEM.

The paper is structured as follows: first, the governing equations of the problem are described in the frequency domain; then, the frequency domain multiregion MFS strategy for the coupling of the waveguide with the solid shells is formulated; there follows a description of the analytical solutions to be used for the submerged shell structures and for the waveguide with a fluid bottom; then, the proposed model is verified against BEM models; a procedure for obtaining time responses from the computed frequency-domain results is then described; finally, a numerical simulation is presented, illustrating the applicability of the model to a realistic configuration.

## 2. Governing PDEs

Within the scope of this work, the 2D scattering of waves by cylindrical shell structures embedded within a fluid medium is analyzed. Thus, the governing equations of the problem correspond to the vectorial and scalar wave equations, respectively, for the solid and for the fluid regions of the analysis domain.

Considering a homogeneous, linear isotropic elastic domain with mass density  $\rho_s$ , shear wave velocity  $\beta_s$ , and compressional wave velocity  $\alpha_s$ , the propagation of elastic waves can be described by vectorial wave equation

$$\alpha_s^2 (\nabla \nabla \cdot \underline{\mathbf{u}}) - \beta_s^2 \nabla \times \nabla \times \underline{\mathbf{u}} = -\omega^2 \underline{\mathbf{u}}, \quad (2.1)$$

where the vector  $\mathbf{u}$  represents the displacement,  $\omega$  is the circular frequency, and, for a two-dimensional problem,  $\nabla = (\partial/\partial x)\hat{\mathbf{i}} + (\partial/\partial y)\hat{\mathbf{j}}$ ;  $\hat{\mathbf{i}}$  and  $\hat{\mathbf{j}}$  are the unit vectors along the  $x$  and  $y$  directions.

If the propagation medium is a fluid, with mass density  $\rho_f$ , the propagation is governed by the Helmholtz equation, which can be written as

$$\nabla^2 p + k_f^2 p = 0, \quad (2.2)$$

where  $p$  is the pressure and  $k_f = \omega/\alpha_f$  is the wave number, with  $\alpha_f$  being the speed of sound in the fluid medium; for this scalar equation,  $\nabla^2 = (\partial^2/\partial x^2) + (\partial^2/\partial y^2)$ . Within this fluid medium, the displacements can be defined as a function of the first spatial derivative of  $p$ , and are given by

$$\begin{aligned} u_x &= -\frac{1}{\rho_f \omega^2} \frac{\partial p}{\partial x}, \\ u_y &= -\frac{1}{\rho_f \omega^2} \frac{\partial p}{\partial y}. \end{aligned} \quad (2.3)$$

### 3. Formulation of the Hybrid Numerical-Analytical Model

Consider a fluid waveguide, with a fluid bottom simulating a sedimentary seabed. Within this seabed, consider the presence of an arbitrary number of circular, shell structures, made of elastic materials, and filled with a fluid material. This configuration is depicted in Figure 1(a).

A hybrid analytical-numerical model based on the method of fundamental solutions (MFS) is proposed in this paper to calculate the pressure field within the waveguide generated by an acoustic source in the presence of such configurations. For this purpose, consider that in the presence of NR shell structures, the problem is divided in NR+1 subregions, one of them being the outer region, incorporating both the waveguide and the fluid bottom, and each of the NR subregions is defined around the shell structure, as represented in Figure 1(b).

If the fundamental solutions are known for each of the defined subregions, it becomes possible to establish a coupled model, which accounts for the full interaction between the involved fluids and the solids that compose the shell structures, by just establishing the continuity of pressures and displacements along the boundaries connecting the subregions. Using the MFS, the acoustic field in the outer subregion, containing the waveguide, can be defined by considering a number of virtual sources,  $\sum_{j=1}^{\text{NR}} \text{NVS}_j$  placed within the remaining subregions, and combining their effects in a linear manner as

$$p(\mathbf{x}) = \sum_{j=1}^{\text{NR}} \sum_{l=1}^{\text{NVS}_j} a_{j,l} G^{\text{waveguide}}(\mathbf{x}, \mathbf{x}_{j,l}^{vs}) + G^{\text{waveguide}}(\mathbf{x}, \mathbf{x}_0), \quad (3.1a)$$



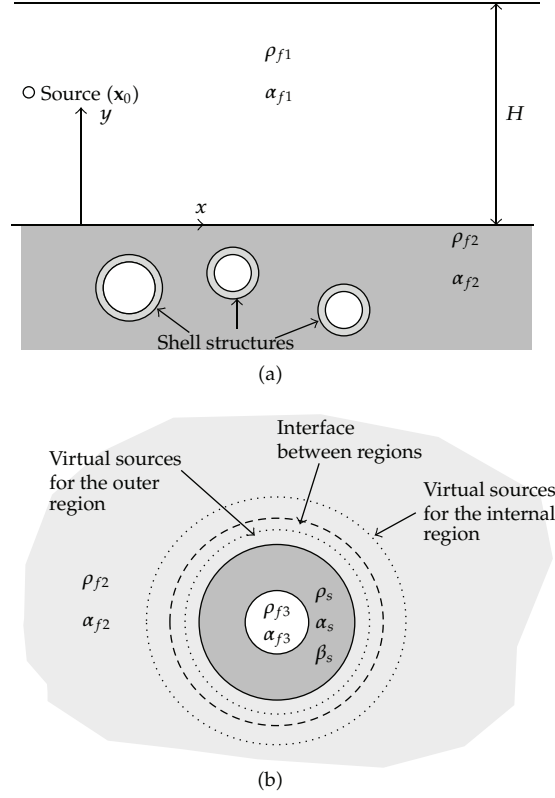


**Figure 1:** (a) Schematic representation of the problem to be solved; (b) Detail of the interface around one of the shell structures, indicating the distribution of virtual sources and the coupling boundary interface.

while for a receiver placed within fluid of the  $j$ th inner subregion, we have

$$p(\mathbf{x}) = \sum_{l=1}^{NVS_j} a_{j,l} G^{\text{shell}}(\mathbf{x}, \mathbf{x}_{j,l}^{vs}), \quad (3.1b)$$

where  $\mathbf{x}$  represents a point of coordinates  $(x, y)$ ,  $\mathbf{x}_0$  is the position of the real source illuminating the system,  $\mathbf{x}_{j,l}^{vs}$  is the position of each of the  $NVS_j$  virtual sources placed within subregion  $j$ ,  $G^{\text{waveguide}}(\mathbf{x}, \mathbf{x}_0)$  is the fundamental solution for the waveguide with fluid bottom at a point  $\mathbf{x}$  originated by a source positioned at  $\mathbf{x}_0$ ;  $G^{\text{shell}}(\mathbf{x}, \mathbf{x}_0)$  is the fundamental solution for each interior subregion, incorporating the full interaction between the shell structures and the outer and inner fluids; the coefficients  $a_{j,l}$  are, “a-priori”, unknown and must be determined by establishing a system of equations, enforcing the continuity of pressures and displacements along each of the NR boundaries separating the outer subregion from each internal subregion. Assuming that the boundary conditions are enforced at  $NVS_j$  collocation points along the  $k$ th boundary (as illustrated in Figure 1(b)),

the continuity equations along the  $m$ th collocation point  $\mathbf{x}_m^{c,k}$  of that boundary can be written as

$$\begin{aligned} \sum_{j=1}^{NR} \sum_{l=1}^{NVS_j} a_{j,l} G^{\text{waveguide}}(\mathbf{x}_m^{c,k}, \mathbf{x}_{j,l}^{vs}) + G^{\text{waveguide}}(\mathbf{x}_m^{c,k}, \mathbf{x}_0) &= \sum_{l=1}^{NVS_k} b_{k,l} G^{\text{shell}}(\mathbf{x}_m^{c,k}, \mathbf{x}_{k,l}^{vs,\text{shell}}), \\ \sum_{j=1}^{NR} \sum_{l=1}^{NVS_j} a_{j,l} \frac{\partial}{\partial \vec{n}} G^{\text{waveguide}}(\mathbf{x}_m^{c,k}, \mathbf{x}_{j,l}^{vs}) + \frac{\partial}{\partial \vec{n}} G^{\text{waveguide}}(\mathbf{x}_m^{c,k}, \mathbf{x}_0) & \\ = \sum_{l=1}^{NVS_k} b_{k,l} \frac{\partial}{\partial \vec{n}} G^{\text{shell}}(\mathbf{x}_m^{c,k}, \mathbf{x}_{k,l}^{vs,\text{shell}}), & \end{aligned} \quad (3.2)$$

where the coefficients  $b_{k,l}$  are, “a-priori”, unknown amplitudes of the fundamental solution for the region containing the shell structure.

A  $N \times N$  linear system of equations, with  $N = 2 \times \sum_{j=1}^{NR} NVS_j$ , can then be built. Once this system of equations is solved, one may obtain the pressure at any internal point by applying equations (3.1a) and (3.1b).

An important point that should be highlighted concerning this formulation is that the coupling between subregions is enforced in fluid-fluid interfaces at some distance from the interfaces with the solid media that constitutes the shell structures. This strategy allows the coupling to be performed in a region with smooth variations of the pressure, which greatly improves the performance of the MFS. Additionally, since the interface between subregions is virtual, it can assume a smooth shape, such as that of a circle, which has been demonstrated in previous works that leads to very accurate results [25]. Finally, if the fundamental solutions are computed analytically within each subregion, a further step can be given towards obtaining high accuracy. In what follows, these fundamental solutions are described.

### 3.1. Analytical Solution for a Fluid Waveguide with a Fluid Bottom

Green’s function for a flat fluid waveguide bounded below by a fluid halfspace (simulating a seabed) and above by a free surface can be obtained using the definition of displacement potentials, using the decomposition of the wavefield in terms of plane waves. These solutions are known for layered systems and can be derived following the methodology presented by Tadeu et al. [12, 13]. In this technique, the solutions can be expressed as the sum of the source terms equal to those in full space and of surface terms generated at the free surface and at the interface between the waveguide and the fluid halfspace. The calculation of the surface terms requires knowledge of the potentials’ amplitudes. For the definition of these functions, consider the geometry depicted in Figure 2.

For an infinite fluid space the wavefield produced by a linear pressure load is here defined by a pressure potential as a superposition of plane waves by means of a discrete wavenumber representation, obtained by applying a Fourier transform along the  $x$  direction. The integrals of the expressions are transformed into a summation, by assuming an infinite number of virtual plane sources distributed along the  $x$  direction, at equal intervals,  $L_x$ . To avoid the influence of neighboring fictitious sources in the response, complex frequencies of

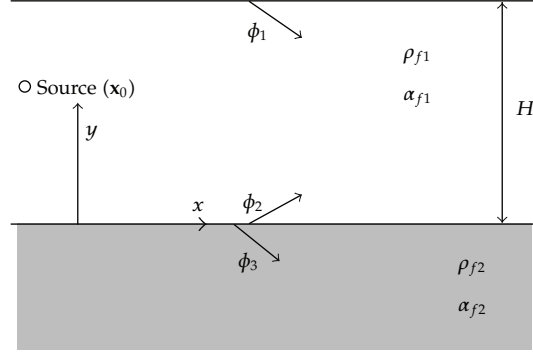


Figure 2: System with a fluid waveguide over a fluid seabed.

the form  $\omega_c = \omega - i \times \xi$  are used here following the methodology described, for example, in [13]. This procedure allows to obtain the following pressure potential:

$$\phi_{\text{full}} = -\frac{i}{2L_x} \left( -\frac{1}{\rho_{f1}\omega^2} \right) \sum_{n=-N}^{n=+N} \left[ \frac{E_{f1}}{\nu_n^{f1}} \right] E_d, \quad (3.3)$$

where  $E_{f1} = e^{-i\nu_n^{f1}|y-y_0|}$ ,  $E_d = e^{-ik_n(x-x_0)}$ , and  $\nu_n^{f1} = \sqrt{k_{\alpha1}^2 - k_n^2}$  with  $\text{Im}(\nu_n^{f1}) \leq 0$ ,  $k_{\alpha1} = \omega/\alpha_{f1}$ . By adequate derivation of this potential, one obtains Green's function at point  $\mathbf{x}$  for a infinite homogeneous fluid medium, when a pressure load is applied at  $\mathbf{x}_0$ , with coordinates  $(x_0, y_0)$ , as follows:

$$G^{\text{full}}(\mathbf{x}, \mathbf{x}_0) = -\frac{i}{2L_x} \sum_{n=-N}^{n=+N} \left( \frac{E_{f1}}{\nu_n^{f1}} \right) E_d = -\frac{i}{4} H_0(k_{\alpha1}r), \quad (3.4)$$

where  $r = \sqrt{(x-x_0)^2 + (y-y_0)^2}$  and  $H_n(\dots)$  represent Hankel functions of the second kind and order  $n$ .

The scattered wavefield in the waveguide can be defined in a similar way, by means of two displacement potentials, one representing the contribution of the top free surface ( $\phi_1$ ) and the other related to the interface with the bottom halfspace ( $\phi_2$ ). These potentials are written as

$$\begin{aligned} \phi_1 &= -\frac{i}{2L_x} \left( -\frac{1}{\rho_{f1}\omega^2} \right) \sum_{n=-N}^{n=+N} \left[ \frac{E_{f1}^1}{\nu_n^{f1}} B_n^1 \right] E_d, \\ \phi_2 &= -\frac{i}{2L_x} \left( -\frac{1}{\rho_{f1}\omega^2} \right) \sum_{n=-N}^{n=+N} \left[ \frac{E_{f1}^2}{\nu_n^{f1}} B_n^2 \right] E_d, \end{aligned} \quad (3.5)$$

with  $E_f^1 = e^{-i\nu_n^{f1}|y-H|}$  and  $E_f^2 = e^{-i\nu_n^{f1}|y|}$ .

To define the wavefield in the bottom halfspace, an additional potential must be defined in a similar manner, and is given by

$$\phi_3 = -\frac{i}{2L_x} \left( -\frac{1}{\rho_{f2}\omega^2} \right) \sum_{n=-N}^{n=+N} \left[ \frac{E_{f2}^2}{v_n^{f2}} B_n^3 \right] E_d, \quad (3.6)$$

with  $E_f^3 = e^{-iv_n^{f2}|y|}$ ,  $v_n^{f2} = \sqrt{k_{a2}^2 - k_n^2}$  with  $\text{Im}(v_n^{f2}) \leq 0$ ,  $k_{a2} = \omega/\alpha_{f2}$ .

In these expressions  $B_n^1$ ,  $B_n^2$ , and  $B_n^3$  are unknown coefficients to be determined after solving a system of equations, built so that the field, produced simultaneously by the source and the surface terms, should give the appropriate boundary conditions at the interfaces. The imposition of null pressure at the free surface, and of continuity of pressure and normal displacements at the fluid-fluid interface for each value of  $n$ , yields a system of three equations in the three unknowns (see the appendix). Once the unknown coefficients have been calculated, the scattered pressure associated with the surface terms can be obtained. Green's functions for the fluid layer are then given by the sum of the source terms and the surface terms originated in both interfaces.

If a source acts in the top fluid (waveguide), this leads to the following expressions for the pressure field in the system:

$$\begin{aligned} G^{\text{waveguide}}(\mathbf{x}, \mathbf{x}_0) &= G^{\text{full}}(\mathbf{x}, \mathbf{x}_0) - \frac{i}{2L_x} \sum_{n=-N}^{n=+N} \left( \frac{E_f^1}{v_n^{f1}} B_n^1 + \frac{E_f^2}{v_n^{f1}} B_n^2 \right) E_d, \quad \text{if } y > 0, \\ G^{\text{waveguide}}(\mathbf{x}, \mathbf{x}_0) &= -\frac{i}{2L_x} \sum_{n=-N}^{n=+N} \left( \frac{E_f^3}{v_n^{f2}} B_n^3 \right) E_d, \quad \text{if } y \leq 0. \end{aligned} \quad (3.7)$$

If the source is positioned in the seabed, a similar procedure can be used, including the source term in the pressure field of the bottom halfspace. From these equations, it becomes straightforward to apply (2.3) in order to obtain the displacements at any field point.

### 3.2. Analytical Solution for a Circular Cylindrical Shell Embedded in a Fluid Medium

Consider a circular shell solid structure, defined by the internal and external radii  $r_A$  and  $r_B$ , respectively, and submerged in a homogenous fluid medium, as illustrated in Figure 3. A harmonic dilatational source, placed in the exterior fluid medium, is assumed to illuminate the system, generating waves that hit the surface of the submerged structure. Part of the incident energy is then reflected back to the exterior fluid medium, with the rest being transmitted into the solid material, where they propagate as body and guided waves. These waves continue to propagate and may eventually hit the inner surface of the structure, where similar phenomena occur.

The wavefield generated in the exterior fluid medium (Fluid 2) depends both on the incident pressure waves and on those coming from the external surface of the shell. The latter propagate away from the cylindrical shell and can be defined using the following

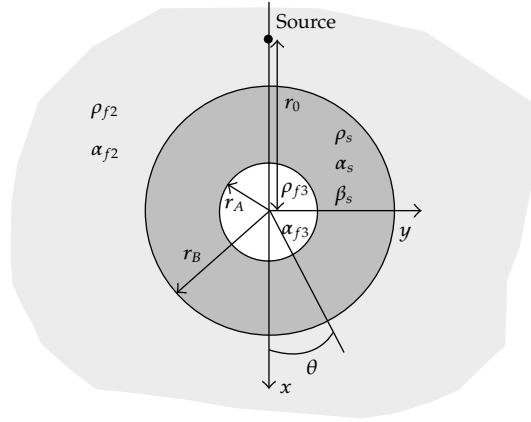


**Figure 3:** Circular cylindrical shell structure submerged in a fluid medium.

displacement potential when a cylindrical coordinate system is centered on the axis of the circular cylindrical shell,

$$\hat{\varphi}_1 = -\frac{1}{\rho_{f2}\omega^2} \sum_{n=0}^{\infty} A_n^1 H_n(k_{\alpha 2} r) \cos(n\theta), \quad (3.8)$$

Inside the solid material of the shell, two distinct groups of waves exist, corresponding to inward travelling waves, generated at the external surface, and to outward travelling waves, generated at the internal surface of the shell. Each of these groups of waves can be represented using one dilatational and one shear potential

$$\begin{aligned} \hat{\varphi}_2 &= \sum_{n=0}^{\infty} A_n^2 J_n(k_{\alpha s} r) \cos(n\theta); & \hat{\varphi}_2 &= \sum_{n=0}^{\infty} A_n^3 J_n(k_{\beta s} r) \sin(n\theta), \\ \hat{\varphi}_3 &= \sum_{n=0}^{\infty} A_n^4 H_n(k_{\alpha s} r) \cos(n\theta); & \hat{\varphi}_3 &= \sum_{n=0}^{\infty} A_n^5 H_n(k_{\beta s} r) \sin(n\theta), \end{aligned} \quad (3.9)$$

where  $k_{\alpha s} = \omega/\alpha_s$ ,  $k_{\beta s} = \omega/\beta_s$ , and  $\alpha_s$  and  $\beta_s$  are, respectively, the dilatational and shear wave velocities permitted in the solid material  $J_n(\dots)$  correspond to Bessel functions of the first kind and order  $n$ .

In the fluid that fills the shell structure (Fluid 3), only inward propagating waves are generated. For this case, the relevant dilatational potential is given by

$$\hat{\varphi}_4 = -\frac{1}{\rho_{f3}\omega^2} \sum_{n=0}^{\infty} A_n^6 J_n(k_{\alpha 3} r) \cos(n\theta), \quad (3.10)$$

where  $k_{\alpha 3} = \omega/\alpha_{f3}$  and  $\alpha_{f3}$  is the pressure wave velocity in the inner fluid. The terms  $A_n^j$  ( $j = 1, 6$ ) for each potential of (3.8), (3.9), and (3.10) are unknown coefficients to be determined by imposing the required boundary conditions. For this case, the necessary boundary conditions

are the continuity of normal displacements and stresses, and null tangential stresses on the two solid-fluid interfaces.

Consider, now, that the incident field, in terms of displacement potential, generated by the acoustic source located at  $(x_0, y_0)$  can be defined at a point  $(x, y)$  as

$$\hat{\varphi}_{\text{inc}} = -\frac{i}{4} \left( -\frac{1}{\rho_{f2}\omega^2} \right) H_0 \left( k_{a2} \sqrt{(x-x_0)^2 + (y-y_0)^2} \right). \quad (3.11)$$

In order to establish the appropriate equation system, this incident field must also be expressed in terms of waves centered on the axis of the circular cylindrical shell structure. This can be achieved with the aid of Graf's addition theorem, leading to the expression (in cylindrical coordinates)

$$\hat{\varphi}_{\text{inc}} = -\frac{i}{4} \left( -\frac{1}{\rho_{f2}\omega^2} \right) \sum_{n=0}^{\infty} (-1)^n \varepsilon_n H_n(k_{a2}r_0) J_n(k_{a2}r) \cos(n\theta), \quad (3.12)$$

where  $r_0$  is the distance from the source to the axis of the circular cylindrical shell and  $\varepsilon_n$  is 1 if  $n = 0$  and 2 in the remaining cases.

The solution of the equation system can then be used to compute the stresses in the solid medium as a summation of solutions obtained for pairs of values of  $n$  and  $k_z$ . The final equation system can be found in published works, namely, [23, 24].

After the solution of the corresponding equation system is computed, the unknown values  $A_n^j$  ( $j = 1, 6$ ) can be used to determine the final wavefields. For the outer fluid, the pressure field at a point  $(x, y)$  can be written as

$$G^{\text{shell}}(\mathbf{x}, \mathbf{x}_0) = -\frac{i}{4} H_0 \left( k_{a2} \sqrt{(x-x_0)^2 + (y-y_0)^2} \right) + \sum_{n=0}^N A_n^1 H_n(k_{a2}r) \cos(n\theta). \quad (3.13)$$

The corresponding displacement field can then be easily determined by applying (2.3).

#### 4. Calculation of Responses in the Time Domain

The pressure field in the spatial-temporal domain is obtained by modeling a Ricker wavelet, whose Fourier transform is

$$U(\omega) = A \left[ 2\pi^{1/2} t_o e^{-i\omega t_s} \right] \Omega^2 e^{-\Omega^2}, \quad (4.1)$$

in which  $\Omega = \omega t_o/2$ ,  $A$  is the amplitude,  $t_s$  is the time when the maximum occurs, and  $\pi t_o$  is the characteristic (dominant) period of the wavelet.

This wavelet form has been chosen, because it decays rapidly, both in time and frequency, reducing computational effort and allowing easier interpretation of the computed time series and synthetic waveforms.

The analysis uses complex frequencies, where  $\omega_c = \omega - i\zeta$ , with  $\zeta = 0.7\Delta\omega$ , which further reduces the influence of the neighboring fictitious sources and avoids the aliasing

phenomena. In the time domain, this shift is later taken into account by applying an exponential window  $e^{\delta t}$  to the response [26].

## 5. Model Verification

To verify the proposed coupling strategy, its results were compared with those obtained using alternative methodologies for a number of situations. Since no analytical solution is known for the complete problem to be solved here, this verification was performed against other numerical methods, namely, the boundary element method (BEM). In what follows, two verification examples are described for specific cases, and a brief note on the stability of the procedure is presented.

### 5.1. Verification Example 1: A Circular Shell in an Halfspace Fluid Medium

In a first verification example, consider the case of an acoustic water halfspace, allowing a propagation velocity of 1500 m/s, and exhibiting a density of 1000 kg/m<sup>3</sup>, hosting a circular shell structure, made of an elastic material with a density of 1400 kg/m<sup>3</sup>, and allowing propagation velocities for the P and S waves of 2182.2 m/s and of 1336.6 m/s, respectively. This structure has an external radius of 1.5 m and an internal radius of 0.75 m, is filled with water, and is positioned with its centre at coordinates  $x = 3.0$  m and  $y = -4.0$  m. An acoustic source, located at  $x = 0.0$  m and  $y = 5.0$  m, illuminates this system, as illustrated in Figure 4(a).

The described configuration has been modeled using two different approaches. In the first, the proposed coupling strategy, making use of the fundamental solutions described above, is used. To allow the use of the fundamental solution for a waveguide over a fluid seabed, a virtual interface is considered at  $y = 0.0$  m, and the same properties are ascribed to the waveguide and to the fluid bottom. A virtual circular interface is also considered around the shell structure, with a radius of 1.6 m, in order to allow coupling the two fundamental solutions. 80 collocation points are placed along this boundary, and two sets of 80 virtual sources are positioned as described in Section 3, at a distance of 0.5 m from the interface. The second model makes use of the boundary element method, as described in [24], and a total of 240 elements is used to discretize the structure (160 for the outer boundary and 80 for the inner boundary). To account for the free surface of the halfspace, proper Green's functions are used for the outer medium. These functions are defined making use of the image source technique, where a single source is placed symmetrically to the real source with respect to the free surface, and with inverted polarity.

In both cases, the response is computed at a receiver positioned at  $x = 6.0$  m and  $y = -3.0$  m, for frequencies ranging from 20 Hz to 2500 Hz, with an increment of 20 Hz. Complex frequencies defined as,  $\omega_c = \omega - i \times 0.7 \times \Delta\omega$  are used in the calculation.

The results computed making use of both methods are depicted in Figure 4(b). As can be seen in this figure, the two sets of results match perfectly along the full set of frequencies analyzed.

### 5.2. Verification Example 2: Two Rigid Circular Inclusions Buried in a Fluid Seabed under a Fluid Waveguide

A second verification example has been analysed in order to assess the correctness of the results in the presence of more than two buried inclusions, positioned within a seabed with

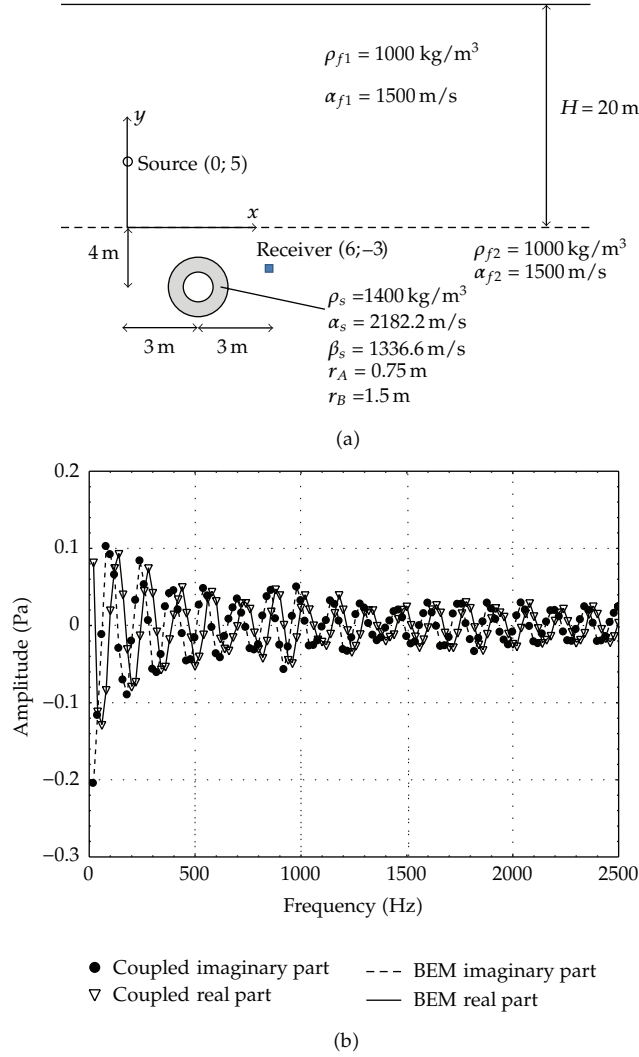


**Figure 4:** (a) Schematic representation of the first verification example. (b) Responses provided by the BEM and by the proposed coupled numerical-analytical model.

different properties from the waveguide. For this test, consider the case of an acoustic water waveguide (medium properties are given in the previous section), with a depth of 20.0 m; bellow this waveguide, a fluid seabed is considered, allowing sound to travel at 2100 m/s, and exhibiting a density of 1800 kg/m<sup>3</sup>. Within the seabed, two circular rigid inclusions, with a radius of 0.5 m, are modeled. These inclusions are positioned at  $x = 3.0 \text{ m}$  and  $y = -4.0 \text{ m}$  and at  $x = 6.0 \text{ m}$  and  $y = -4.0 \text{ m}$ . An acoustic source, located at  $x = 0.0 \text{ m}$  and  $y = 5.0 \text{ m}$ , illuminates this system, as illustrated in Figure 5(a).

The described configuration has been modeled using two different approaches. Once again, the first corresponds to the proposed coupling strategy. Two virtual circular interfaces are considered around the circular inclusions, with a radius of 0.75 m, in order to allow coupling the fundamental solutions for the inner and outer domains. One should note that in this case, the fundamental solution for the case of a rigid inclusion can easily be obtained from



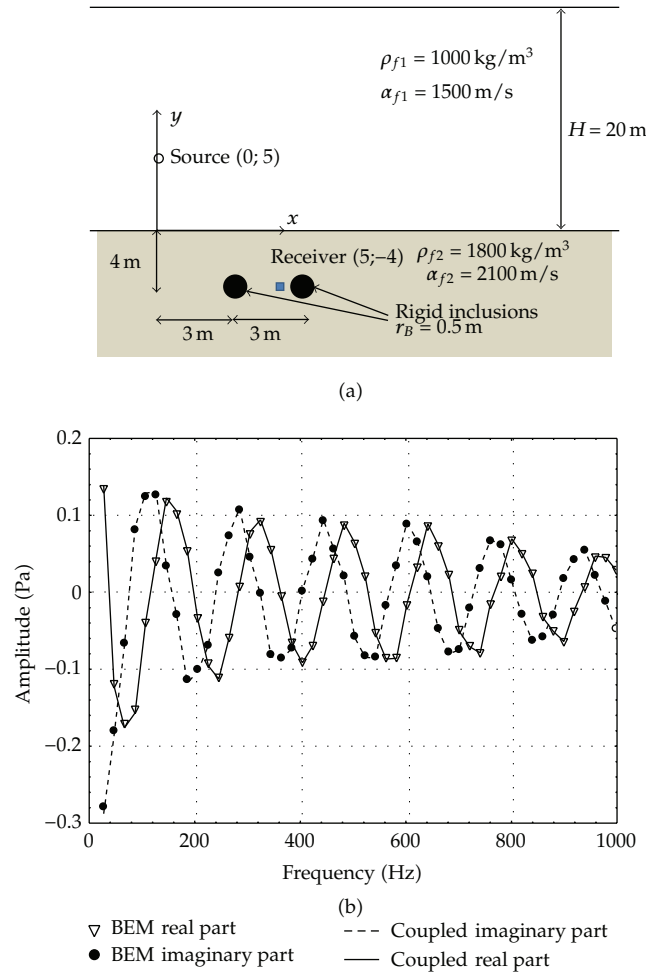


**Figure 5:** (a) Schematic representation of the second verification example. (b) Results provided by the BEM and by the proposed coupled numerical-analytical model.

Section 3.2, just considering the potential corresponding to the outer fluid and imposing the necessary null normal displacements at the outer interface. 30 collocation points are placed along this virtual interface, and two sets of 30 virtual sources are positioned as described in Section 3, at a distance of 0.5 m from the interface. In a second model, the boundary element method is used, discretizing each of the two inclusions using 30 elements and the interface between the waveguide and the seabed using 950 elements. In order to limit the number of boundary elements used to discretize this interface, complex frequencies with an imaginary part are used ( $\zeta = 0.7(2\pi/T)$ ). This considerably attenuates the contribution of the responses from the boundary elements placed at  $L = 2\alpha_f T$ , reducing the length of the interface to be discretized (see, e.g., [15]). In our calculations a value of  $T = 0.05 \text{ s}$  and  $L = 210 \text{ m}$  were used to define this discretization. The free surface of the halfspace is accounted using Green's functions defined by the image source technique.

In both cases, the response is computed at a receiver positioned at  $x = 6.0 \text{ m}$  and  $y = -3.0 \text{ m}$ , for frequencies ranging from 20 Hz to 1000 Hz, with an increment of 20 Hz. As

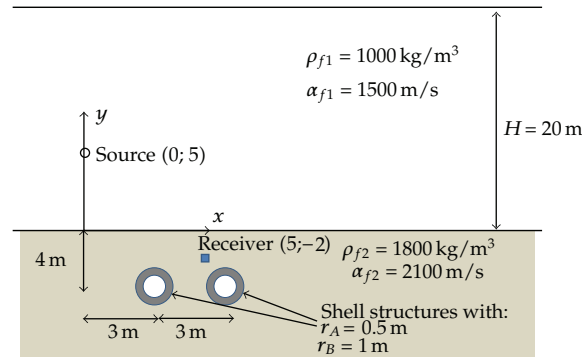


**Figure 6:** Schematic representation of the system with two buried shell structures.

**Table 1:** Response at the field point ( $x = 5$  m;  $y = -2$  m) when 30 collocation points are used and for different positions of the virtual sources.

D/R	Real part	Imaginary part
0.05	-0.0264173	0.0279363
0.10	-0.0391006	0.0249389
0.20	-0.0393479	0.0235543
0.30	-0.0392936	0.0235595
0.40	-0.0392874	0.0235757
0.50	-0.0392888	0.0235806
0.60	-0.0392900	0.0235815

in the previous case, the results calculated making use of the two strategies are displayed in Figure 5(b). Again, the results match perfectly along the full set of frequencies analyzed here.

### 5.3. Behavior of the Coupled Model in the Presence of Two Circular Shell Structures Buried in a Fluid Seabed

An additional study was performed to better understand the behavior of the proposed model concerning the variability of its results with the number of collocation points and with the position of the virtual sources. For this purpose, consider the example illustrated in Figure 6, in which two buried elastic shell structures are embedded within a seabed with different properties from the waveguide. The properties of the acoustic water waveguide, 20.0 m deep, and of the fluid seabed are similar to those used in verification example described in the Section 5.2. The two circular structures have an external radius of 1.0 m and an internal radius of 0.5 m and are positioned at  $x = 3.0$  m and  $y = -4.0$  m and at  $x = 6.0$  m and  $y = -4.0$  m. The elastic properties of the shell structure are defined in Section 5.1. To couple the waveguide with the two structures, two virtual interfaces with a radius of 1.2 m are defined.

The response has been calculated for a frequency of 2000 Hz, at a receiver placed at  $x = 5.0$  m and  $y = -2.0$  m, using different numbers of collocation points and positioning the virtual sources at different distances from the virtual interfaces between the shell regions and the waveguide region.

Table 1 presents the results at that receiver calculated for 30 collocation points when the distance between the virtual sources and the interface (D) assumes different values. In

**Table 2:** Response at the field point ( $x = 5$  m;  $y = -2$  m) when different numbers of collocation points are used and the distance from the virtual sources to the interface is 0.4 times the radius of the fictitious interface.

$N$	Real part	Imaginary part
10	-0.0124778	0.0189048
20	-0.0389532	0.0231320
30	-0.0392874	0.0235757
40	-0.0392905	0.0235811
50	-0.0392906	0.0235813
60	-0.0392906	0.0235813
70	-0.0392906	0.0235813

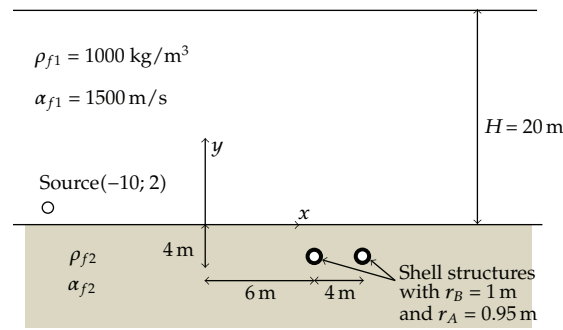


**Figure 7:** Geometry defined for the numerical applications.

that table, the relation  $D/R$  is used to define the distance as a function of the radius of the coupling interface ( $R$ ). As can be observed in that table, the response is stable as long as the virtual sources are not very close to the interface. In fact, for that case, a singularity of the fundamental solution occurs very close to the boundary, degrading the quality of the result. When  $D/R$  is 0.3 or larger, the variation of the response is very small and indicates a good behavior of the coupling strategy.

Table 2 presents the results computed when  $D/R = 0.4$ , and for varying numbers of collocation points. Here, the response can be seen to stabilize above 30 collocation points, corresponding to a relation between the wavelength and the distance between collocation points of just 5. This relation is relatively small when compared with those required for BEM discretizations (around 7 to 8).

## 6. Numerical Application

In order to illustrate the applicability of the proposed numerical approach, consider now a fluid waveguide, 20.0 m deep, with a sedimentary seabed, as displayed in Figure 7. Assume that the fluid inside the waveguide is water, with a density  $\rho_{f1} = 1000.0$  kg/m<sup>3</sup> and allowing a dilatational wave velocity  $\alpha_{f1} = 1500.0$  m/s. The sedimentary seabed is first modeled with a density  $\rho_{f2} = 1800.0$  kg/m<sup>3</sup> and permits the propagation of dilatational waves with a velocity  $\alpha_{f2} = 2100.0$  m/s. A second scenario is also considered, in which the seabed assumes a density  $\rho_{f2} = 1500.0$  kg/m<sup>3</sup> and allows a sound velocity of  $\alpha_{f2} = 1600.0$  m/s, which corresponds to approaching the properties of the seabed to those of the fluid medium.

Within the seabed, consider the presence of two similar circular shell structures with external and internal radii  $r_B = 1.0$  m and  $r_A = 0.95$  m, respectively, made of an elastic material with density  $\rho_s = 7850.0$  kg/m<sup>3</sup>, and allowing a dilatational wave velocity  $\alpha_s = 6009.0$  m/s and a shear wave velocity  $\beta_s = 3212.0$  m/s; these structures are filled with a fluid material with the same properties as water. The described scenario is excited by a cylindrical pressure source placed near the bottom of the waveguide at  $x = -10.0$  m and  $y = 2.0$  m.

To simulate this problem, two virtual circular interfaces with a radius of 1.2 m are defined to account for the two subdomains containing the buried structures. Each of those interfaces is defined using 35 collocation points, and two sets of virtual sources are positioned at a distance of 0.4 times the radius of the virtual interface.

Calculations are then performed over a frequency range between 20.0 Hz and 2560.0 Hz, assuming a frequency step of 20.0 Hz; for the purpose of calculating time responses, the defined increment allows a total analysis time of  $T = 50.0$  ms. Time domain signals are computed by means of an inverse Fourier transform, using the methodology described earlier.

The pressure field in the waveguide was computed over a grid of receivers, equally spaced at  $\Delta x = 0.5$  m,  $\Delta y = 0.5$  m, placed between  $x = 0.0$  m and  $x = 25.0$  m and  $y = 0.0$  m and  $y = 20.0$  m. A sequence of snapshots displaying the pressure wave field over the grid of receivers, at different instants, is presented to illustrate the results. Figure 8 displays snapshots of the pressure response, for different time instants, over the grid of receivers placed in the waveguide, generated by a source emitting a Ricker pulse with a characteristic frequency  $f_k = 400$  Hz. A grayscale is used to represent the amplitudes of the waves arriving at the receivers, with lighter colors corresponding to higher values and darker colors representing lower values. These responses were computed assuming the waveguide with a sedimentary seabed which allows the propagation of dilatational waves with a velocity  $\alpha_{f2} = 2100.0$  m/s without shell structures buried.

At time  $t = 0.0$  ms, the load creates a cylindrical pressure wave that propagates away from it. In the snapshot of Figure 8(a), corresponding to  $t = 14.6$  ms, this incident pulse is visible (identified as P1), followed by a first reflection from the bottom of the waveguide (identified as P2). At receivers placed near the ground, a third reflection may also be identified, which is related to the head wave generated in the surface of the seabed (identified as P3). This wave is originated at the interface between the two media and travels along this interface with the velocity of the faster medium, which is the seabed, with  $\alpha_{f2} = 2100.0$  m/s; therefore, it appears in the plot at receivers placed farther from the source. As time increases, it is possible to identify the reflections generated at the free surface (identified as P4), with inverted polarity (see Figure 8(b)). For subsequent instants, a sequence of pulses originated by multiple reflections in the surface and bottom of the waveguide can be identified (see Figures 8(c) and 8(d)). These reflections tend to lose energy as time increases, with part of the energy being transmitted to the seabed, and a stationary field is generated inside the waveguide by these waves, which travel up and down between the surfaces of the channel and tend to become flat as time increases.

When the two shell structures are buried in the seabed a different wave pattern inside the waveguide may be created. In order to assess the presence of these structures under different conditions, snapshots of the sound propagation within the waveguide were captured for two different sets of properties of the seabed:  $\alpha_{f2} = 2100.0$  m/s (see first column of Figure 9) and  $\alpha_{f2} = 1600.0$  m/s (see second column of Figure 9), respectively. When the seabed allows a velocity  $\alpha_{f2} = 2100.0$  m/s (see first column of Figure 9), a set of additional pulses appear in the response (labeled as Pshell), which refer to reflections originated by

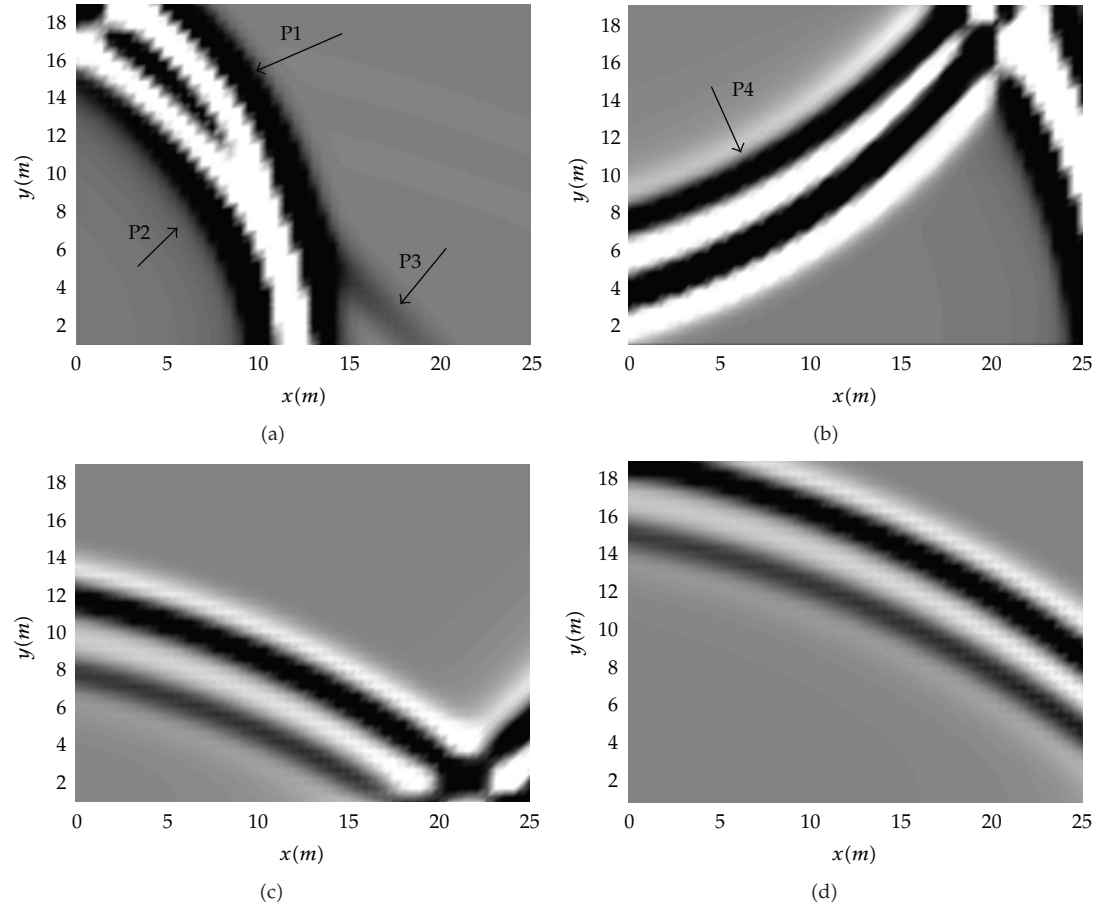


**Figure 8:** Snapshots displaying the pressure wave field over the grid of receivers at different instants, in the waveguide assuming the seabed with  $\alpha_{f2} = 2100.0$  m/s, without the shell structures: (a)  $t = 14.6$  ms; (b)  $t = 24.4$  ms; (c)  $t = 34.2$  ms; (d)  $t = 39.1$  ms.

the presence of the shell structures. These reflections can further be identified in the snapshots corresponding to subsequent instants (see Figures 9(b1)–9(d1)) although displaying smaller amplitudes, due to the contrast between media, which tends to hinder energy exchanges. As expected, when the seabed assumes a dilatational wave velocity which approaches that of the fluid in the waveguide (see plots provided in the second column of Figure 9), the amplitudes of the scattered pulses provided by the shell structures are increased, providing a clear perception of their presence. For later instants, the responses display multiple pulses, related not only to reflections of waves generated in the waveguide, but also to several reflections originated at the shell structures, at the top and at the bottom of the waveguide. It is also interesting to note that for both cases, the reflection pattern originated at the buried structures is quite complex, revealing multiple reverberation effects that occur not only between the structures and the sea bottom, but also within the structures themselves and within the fluid that fills their interior.

With the aim of understanding how the properties of the fluid inside the shell structures may influence the responses, the time domain response, originated by a source emitting a Ricker pulse with a characteristic frequency  $f_k = 800$  Hz, has been calculated along a line

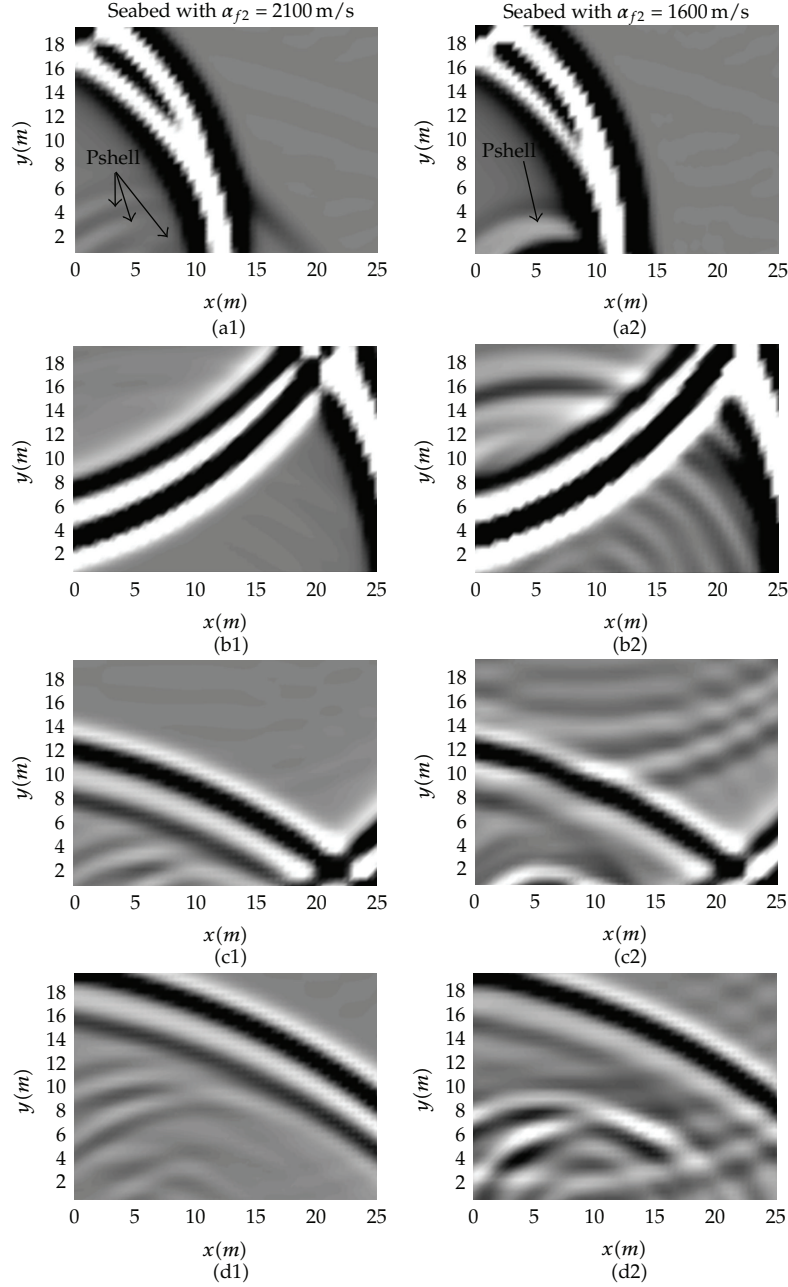


**Figure 9:** Snapshots displaying the pressure wave field over the grid of receivers placed in the waveguide with a seabed, where shell structures are buried: (a)  $t = 14.6$  ms; (b)  $t = 24.4$  ms; (c)  $t = 34.2$  ms; (d)  $t = 39.1$  ms.

of receivers placed at  $y = 0.5$  m and between  $x = 0.0$  m and  $x = 25.0$  m (see Figure 10). Three different cases were analyzed with this purpose: in the first case, the structure is filled with a fluid with the properties of the water; in a second case, the filling fluid is air ( $\rho_{f3} = 1.22 \text{ kg/m}^3$  and  $\alpha_{f3} = 340.0 \text{ m/s}$ ), simulating empty structures; in a third case, rigid inclusions are modeled. A first set of simulations was performed for a seabed allowing an acoustic wave



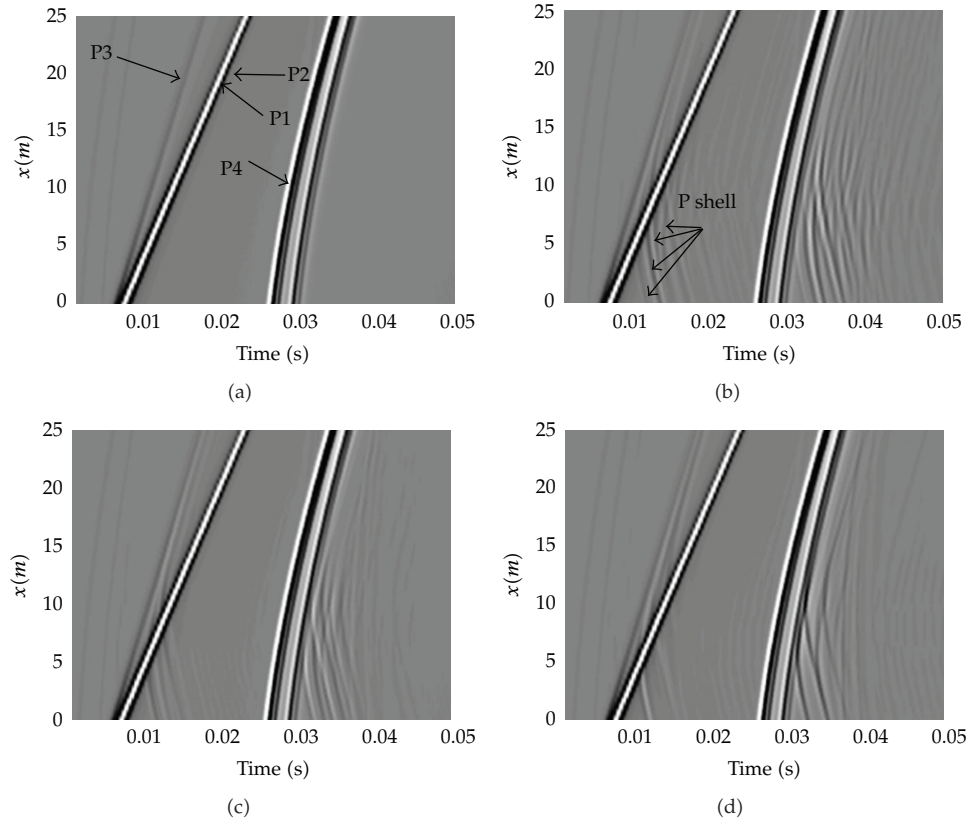


**Figure 10:** Time domain responses captured along a line of receivers placed at  $y = 0.50$  m, assuming the waveguide with a seabed allowing a dilatational wave velocity of  $\alpha_{f2} = 2100.0$  m/s: (a) without any shell structures; (b) with the two buried shell structures, filled with water; (c) with the two buried shell structures, filled with air; (d) with two buried rigid inclusions.

velocity of  $\alpha_{f2} = 2100.0$  m/s. Responses computed for the waveguide without the buried structures are displayed in Figure 10(a) as a reference. In that first plot, the initial reflections occurring between the free surface and the fluid-fluid interface can clearly be identified, with a  $180^\circ$  phase change occurring when the incident pulse is reflected at the free surface (P2 and P4). The so-called “head wave” can also be identified in this plot (P3), travelling at 2100 m/s along the interface. When water-filled shell structures are introduced (Figure 10(b)) a clear identification of a sequence of scattered pulses originated by these structures is also possible. Interestingly, this sequence allows identifying a reverberation effect in which multiple reflections are occurring within the structure, both on the solid shell and on the filling fluid. This effect is even clearer in the second series of pulses, originated when the pulses coming from the free surface hit the buried structure. In fact, as the incident pulse hits the interface at an almost tangent angle, it is mainly reflected back to the waveguide, and very little energy penetrates the seabed; this no longer occurs for the second set of pulses, which reach this surface at larger angles, and thus allow more energy to be transmitted to the bottom. Some differences are visible when the shell structure is filled with air, for which case the scattered pulses are captured at these receivers with smaller amplitudes; in fact, the high contrast between the solid and the interior fluid (air), makes the energy exchanges among

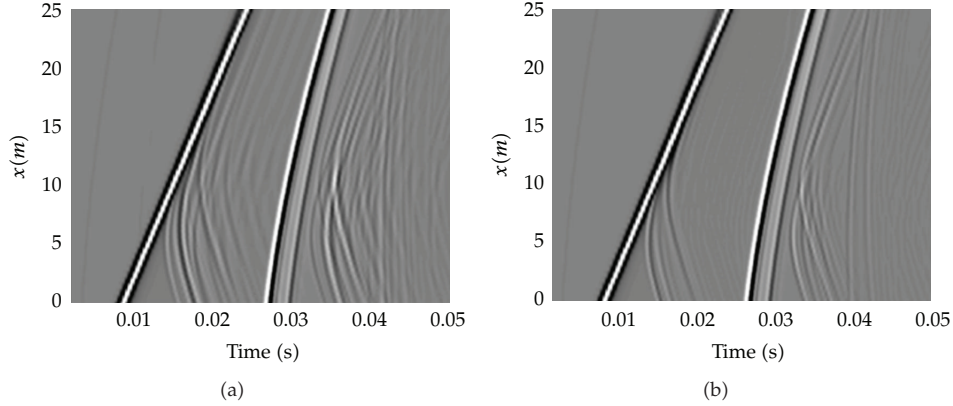


**Figure 11:** Time domain responses, captured along a line of receivers placed at  $y = 0.5$  m, assuming the waveguide with a seabed, allowing a dilatational wave velocity of  $\alpha_{f2} = 1600.0$  m/s and with (a) the shell structures filled with water and (b) the shell structures filled with air.

materials more difficult to happen. As a consequence, energy tends to dissipate faster, as time increases, and thus reduces significantly the reverberation effect. In the reference result of Figure 10(d), considering the external boundary of the inclusions to be rigid, no energy propagates to the interior of the shell, and, as a result, the response reveals fewer pulses coming from the buried structures. These results clearly show the importance of accurately modeling both the solid of the shell and the fluid in its interior and show that the commonly used approximation of assuming a rigid behavior of the structures neglects important parts of the propagation phenomena.

To emphasize these findings, two further plots are presented in Figure 11, considering the water-filled and air-filled structures buried in a seabed which allows a propagation velocity of 1600 m/s. In Figures 11(a) and 11(b), plots are presented illustrating the time responses for water-filled shells and air-filled shells. For these cases, the difference between the scattering patterns is significantly increased, due to the smaller contrast between the waveguide and the seabed. The reverberation effect is now very clear in the case of water-filled shells, with rings of pulses being generated due to multiple reflections within the structure and filling fluid. This effect is much less pronounced when the structure is filled with air. One additional feature of this response corresponds to the presence of two distinct sets of pulses, originated at each of the two inclusions; the first arrival of each set occurs approximately at the receivers placed immediately above the buried structure and allows an identification of the presence of the two separate shells.

## 7. Conclusions

In this paper, the coupling between different analytical solutions using the MFS is proposed to address the problem of scattering of acoustic waves in a waveguide in the presence of buried structures. The scattering structure is assumed to be buried in the fluid seabed below a water waveguide and is a circular elastic shell filled with a fluid that may have different properties from the host medium. The proposed strategy was formulated and implemented and was shown to provide good results when compared with alternative numerical modeling techniques. Since it performs the coupling between closed-form solutions, the method provides accurate results, while allowing a compact and simple model description. One major



advantage of the proposed model is that it allows the simulation of very thin solid structures, without the problems usually associated with thin bodies when using alternative methods. A number of applications were presented, revealing that taking into account both the elastic properties of the buried shell and the properties of a fluid which fills that structure can be important, leading to marked differences when results are compared with usual simplifications, such as considering the buried structure to be rigid.

## Appendix

This appendix presents the system of equations required to obtain Green's function for a flat fluid waveguide bounded below by a fluid halfspace and above by a free surface as defined in Figure 2.

This system can be defined as

$$\begin{bmatrix} 1 & e^{-iv_n^{f1}H} & 0 \\ e^{-iv_n^{f1}H} & 1 & -\frac{v_n^{f1}}{v_n^{f2}} \\ -\frac{e^{-iv_n^{f1}H}}{\rho_{f1}} & \frac{1}{\rho_{f1}} & \frac{1}{\rho_{f2}} \end{bmatrix} \begin{bmatrix} B_n^1 \\ B_n^2 \\ B_n^3 \end{bmatrix} = C, \quad (\text{A.1})$$

with

$$C = \begin{bmatrix} -e^{-iv_n^{f1}|H-y_0|} & -e^{-iv_n^{f1}|-y_0|} & \frac{e^{-iv_n^{f1}|-y_0|}}{\rho_{f1}} \end{bmatrix}^T \quad \text{if } y_0 > 0, \quad (\text{A.2})$$

$$C = \begin{bmatrix} 0 & -e^{-iv_n^{f2}|-y_0|} & \frac{e^{-iv_n^{f2}|-y_0|}}{\rho_{f2}} \end{bmatrix}^T \quad \text{if } y_0 \leq 0.$$

## References

- [1] J. F. Claerbout, *Fundamentals of Geophysical Data Processing*, McGraw-Hill, 1976.
- [2] D. H. Griffiths and R. F. King, *Applied Geophysics for Geologists and Engineers*, Pergamon Press, 1981.
- [3] F. B. Jensen, W. A. Kuperman, M. B. Porter, and H. Schmidt, *Computational Ocean Acoustics*, AIP Series in Modern Acoustics and Signal Processing, American Institute of Physics, New York, NY, USA, 1994.
- [4] Y. H. Pao and C. C. Mow, *Diffraction of Elastic Waves and Dynamic Stress Concentrations*, Crane and Russak, 1973.
- [5] R. A. Stephens, "A review of finite difference methods for seismo-acoustic problems at the seafloor," *Reviews of Geophysics*, vol. 26, pp. 445–458, 1988.
- [6] S. Wang, "Finite-difference time-domain approach to underwater acoustic scattering problems," *Journal of the Acoustical Society of America*, vol. 99, no. 4, pp. 1924–1931, 1996.
- [7] K. J. Marfurt, "Accuracy of finite-difference and finite-element modeling of the scalar and elastic wave equations," *Geophysics*, vol. 49, no. 5, pp. 533–549, 1984.
- [8] M. Zampolli, A. Tesei, F. B. Jensen, N. Malm, and J. B. Blottman, "A computationally efficient finite element model with perfectly matched layers applied to scattering from axially symmetric objects," *Journal of the Acoustical Society of America*, vol. 122, no. 3, pp. 1472–1485, 2007.
- [9] T. W. Dawson and J. A. Fawcett, "A boundary integral equation method for acoustic scattering in a waveguide with nonplanar surfaces," *Journal of the Acoustical Society of America*, vol. 87, no. 3, pp. 1110–1125, 1990.

- [10] S. Grilli, T. Pedersen, and P. Stepanishen, "A hybrid boundary element method for shallow water acoustic propagation over an irregular bottom," *Engineering Analysis with Boundary Elements*, vol. 21, no. 2, pp. 131–145, 1998.
- [11] J. A. F. Santiago and L. C. Wrobel, "A boundary element model for underwater acoustics in shallow water," *Computer Modeling in Engineering and Sciences*, vol. 1, no. 3, pp. 73–80, 2000.
- [12] A. J. B. Tadeu and E. Kausel, "Green's functions for two-and-a-half-dimensional elastodynamic problems," *Journal of Engineering Mechanics*, vol. 126, no. 10, pp. 1093–1097, 2000.
- [13] A. Tadeu and J. António, "2.5D Green's functions for elastodynamic problems in layered acoustic and elastic formations," *Computer Modeling in Engineering and Sciences*, vol. 2, no. 4, pp. 477–495, 2001.
- [14] J. António, A. Tadeu, and L. Godinho, "2.5D scattering of waves by rigid inclusions buried under a fluid channel via BEM," *European Journal of Mechanics. A*, vol. 24, no. 6, pp. 957–973, 2005.
- [15] A. Pereira, A. Tadeu, L. Godinho, and J. A. F. Santiago, "2.5D BEM modeling of underwater sound scattering in the presence of a slippage interface separating two flat layered regions," *Wave Motion*, vol. 47, no. 8, pp. 676–692, 2010.
- [16] S. N. Atluri, *The Meshless Method (MLPG) for Domain & BIE Discretizations*, Tech Science Press, 2004.
- [17] E. J. Kansa, "Multiquadrics—a scattered data approximation scheme with applications to computational fluid-dynamics. I. Surface approximations and partial derivative estimates," *Computers & Mathematics with Applications*, vol. 19, no. 8-9, pp. 127–145, 1990.
- [18] E. J. Kansa, "Multiquadrics—a scattered data approximation scheme with applications to computational fluid-dynamics. II. Solutions to parabolic, hyperbolic and elliptic partial differential equations," *Computers & Mathematics with Applications*, vol. 19, no. 8-9, pp. 147–161, 1990.
- [19] M. A. Golberg and C. S. Chen, "The method of fundamental solutions for potential, Helmholtz and diffusion problems," in *Boundary Integral Methods: Numerical and Mathematical Aspects*, M. A. Golberg, Ed., vol. 1 of *Comput. Eng.*, pp. 103–176, WIT Press/Comput. Mech. Publ., Boston, Mass, USA, 1999.
- [20] L. Godinho, C. Dors, D. Soares, and P. Amado-Mendes, "Solution of time-domain acoustic wave propagation problems using a RBF interpolation model with "a priori" estimation of the free parameter," *Wave Motion*, vol. 48, no. 5, pp. 423–440, 2011.
- [21] E. G. A. Costa, L. Godinho, J. A. F. Santiago, A. Pereira, and C. Dors, "Efficient numerical models for the prediction of acoustic wave propagation in the vicinity of a wedge coastal region," *Engineering Analysis with Boundary Elements*, vol. 35, no. 6, pp. 855–867, 2011.
- [22] N. D. Veksler, J. L. Izbicki, and J. M. Conoir, "Bending A wave in the scattering by a circular cylindrical shell: Its relation with the bending free modes," *Journal of the Acoustical Society of America*, vol. 96, no. 1, pp. 287–293, 1994.
- [23] L. Godinho, A. Tadeu, and F. J. G. Branco, "Dynamic analysis of submerged fluid-filled pipelines subjected to a point pressure load," *Journal of Sound and Vibration*, vol. 271, no. 1-2, pp. 257–277, 2004.
- [24] L. Godinho, A. Tadeu, and F. J. Branco, "Wave scattering by infinite cylindrical shell structures submerged in a fluid medium," *Wave Motion*, vol. 38, no. 2, pp. 131–149, 2003.
- [25] L. Godinho, A. Tadeu, and P. A. Mendes, "Wave propagation around thin structures using the MFS," *Computers, Materials and Continua*, vol. 5, no. 2, pp. 117–127, 2007.
- [26] E. Kausel and J. M. Roësset, "Frequency domain analysis of undamped systems," *Journal of Engineering Mechanics*, vol. 118, no. 4, pp. 724–734, 1992.

## *Review Article*

# **Modeling and Simulation of Fiber Orientation in Injection Molding of Polymer Composites**

**Jang Min Park<sup>1</sup> and Seong Jin Park<sup>1,2</sup>**

<sup>1</sup> *Department of Mechanical Engineering, Pohang University of Science and Technology,  
San 31, Hyoja-dong, Nam-gu, Gyeongbuk, Pohang 790-784, Republic of Korea*

<sup>2</sup> *Division of Advanced Nuclear Engineering, Pohang University of Science and Technology,  
San 31, Hyoja-dong, Nam-gu, Gyeongbuk, Pohang 790-784, Republic of Korea*

Correspondence should be addressed to Seong Jin Park, [sjpark87@postech.ac.kr](mailto:sjpark87@postech.ac.kr)

Received 1 June 2011; Accepted 15 August 2011

Academic Editor: Jan Sladek

Copyright © 2011 J. M. Park and S. J. Park. This is an open access article distributed under the Creative Commons Attribution License, which permits unrestricted use, distribution, and reproduction in any medium, provided the original work is properly cited.

We review the fundamental modeling and numerical simulation for a prediction of fiber orientation during injection molding process of polymer composite. In general, the simulation of fiber orientation involves coupled analysis of flow, temperature, moving free surface, and fiber kinematics. For the governing equation of the flow, Hele-Shaw flow model along with the generalized Newtonian constitutive model has been widely used. The kinematics of a group of fibers is described in terms of the second-order fiber orientation tensor. Folgar-Tucker model and recent fiber kinematics models such as a slow orientation model are discussed. Also various closure approximations are reviewed. Therefore, the coupled numerical methods are needed due to the above complex problems. We review several well-established methods such as a finite-element/finite-difference hybrid scheme for Hele-Shaw flow model and a finite element method for a general three-dimensional flow model.

## **1. Introduction**

Short fiber reinforced polymer composites are widely used in manufacturing industries due to their light weight and enhanced mechanical properties. The short fiber composite products are commonly manufactured by injection molding, compression molding, and extrusion processes. During those processes, the fibers orient themselves due to the flow and interactions between neighboring fibers and/or cavity wall. This orientation is anisotropic in general, which results in an anisotropic property of final products. Thus, the prediction of the fiber orientation during the process has been the subject of considerable amount of research during past decades.

The injection molding process is a well-established mass-production method for polymeric materials. In this process, the molten polymer or polymer composite is injected

into a mold cavity, which is namely a filling stage. After cooling the polymer material inside the mold, the final product is ejected from the mold. The overall processing time is usually less than one minute, and a complex three-dimensional shape can be produced quite easily. In the injection molding of short fiber polymer composites, the fiber orientation develops during the filling stage of the process. In this paper, we review the modeling and simulation of fiber orientation during injection molding filling stage. The prediction of fiber orientation in injection molding involves two subjects of fiber orientation simulation and injection molding simulation. In this paper, we give more attentions in the first subject of the fiber orientation while the later one is rather briefly discussed.

## 2. Fiber Orientation

### 2.1. Fiber Orientation Kinematics

The orientation state of a group of fibers can be represented by a probability distribution function  $\psi(\mathbf{p})$  where  $\mathbf{p}$  represents the fiber orientation vector. When the fibers are assumed to move with the bulk flow of the fluid, the conservation equation of the distribution function is written as follows [1]:

$$\frac{D}{Dt}\psi = -\frac{\partial}{\partial \mathbf{p}} \cdot (\psi \dot{\mathbf{p}}), \quad (2.1)$$

where  $\dot{\mathbf{p}}$  is the angular velocity vector of the fiber and  $D/Dt$  is the material time derivative. For a concentrated fiber suspension where hydrodynamic interactions and direct contacts take place between neighboring fibers, Folgar and Tucker [2] gave the following model for the angular velocity:

$$\dot{\mathbf{p}} = -\frac{1}{2}\boldsymbol{\omega} \cdot \mathbf{p} + \frac{1}{2}\lambda(\dot{\boldsymbol{\gamma}} \cdot \mathbf{p} - \dot{\boldsymbol{\gamma}} : \mathbf{p} \otimes \mathbf{p} \otimes \mathbf{p}) - \frac{D_r}{\psi} \frac{\partial \psi}{\partial \mathbf{p}}, \quad (2.2)$$

where  $\boldsymbol{\omega}$  is the vorticity tensor,  $\dot{\boldsymbol{\gamma}}$  is the rate-of-strain tensor, and  $\lambda$  is a geometrical parameter of the particle. The last term in the right-hand side of (2.2) with  $D_r$  is a rotary diffusivity term which is an additional term to the original work of Jeffery [3] to take the effect of the interactions between fibers. For an accurate calculation of the fiber orientation state, one needs to solve (2.1) and (2.2), which requires huge computational resources for a practical implementation in injection molding simulation. For the efficiency of the computation, orientation tensors by Advani and Tucker [1] have been widely accepted, which enables a compact representation of the orientation state. The second- and the fourth-order orientation tensors are defined as follows:

$$\begin{aligned} \mathbf{a} &= \oint \mathbf{p} \mathbf{p} \psi \, d\mathbf{p}, \\ \mathbf{A} &= \oint \mathbf{p} \mathbf{p} \mathbf{p} \mathbf{p} \psi \, d\mathbf{p}. \end{aligned} \quad (2.3)$$

The orientation tensors satisfy the full symmetric property and the normalization property as follows:

$$\begin{aligned} a_{ij} &= a_{ji}, & A_{ijkl} &= A_{jikl} = A_{ijlk} = A_{klij}, \\ a_{ii} &= 1, & A_{ijkk} &= a_{ij}. \end{aligned} \quad (2.4)$$

From (2.1) and (2.2), the evolution equation of the second-order orientation tensor can be derived as follows:

$$\frac{D}{Dt}\mathbf{a} = -\frac{1}{2}(\boldsymbol{\omega} \cdot \mathbf{a} - \mathbf{a} \cdot \boldsymbol{\omega}) + \frac{\lambda}{2}(\dot{\boldsymbol{\gamma}} \cdot \mathbf{a} + \mathbf{a} \cdot \dot{\boldsymbol{\gamma}} - 2\mathbf{A} : \dot{\boldsymbol{\gamma}}) + 2D_r(\mathbf{I} - 3\mathbf{a}). \quad (2.5)$$

It should be noted that the fourth-order orientation tensor  $\mathbf{A}$  appears in (2.5). In a similar manner, the evolution equation of any orientation tensor contains next higher even-order tensor. Thus, one needs a closure approximation to close the set of the evolution equations of the orientation tensors. Several closure approximations are discussed in the following.

## 2.2. Closure Approximations

The closure approximation represents the fourth-order orientation tensor as a function of the second-order orientation. A hybrid closure approximation is a simple and stable model thus has been widely used in many numerical simulations [1]. It combines linear and quadratic closure approximations. The hybrid closure tends to overpredict the fiber orientation tensor components in comparison with the distribution function results. Also the full symmetric property of  $\mathbf{A}$  is not satisfied due to the quadratic closure term ( $A_{ijkl}^{\text{qua}}$ ).

The orthotropic closure approximations had been developed by Cintra and Tucker [4] and improved further by Chung and Kwon [5]. In the orthotropic closure, three independent components of  $\mathbf{A}$  in the eigenspace system, namely  $A_1$ ,  $A_2$ , and  $A_3$ , are assumed to depend on the eigenvalues of  $\mathbf{a}$  as follows:

$$A_K = C_K^1 + C_K^2 a_1 + C_K^3 (a_1)^2 + C_K^4 a_2 + C_K^5 (a_2)^2 + C_K^6 a_1 a_2, \quad K = 1, 2, 3, \quad (2.6)$$

where  $a_1$  and  $a_2$  are two largest eigenvalues of  $\mathbf{a}$  and  $C_K^i$  ( $i = 1, 2, \dots, 6$ ) are eighteen fitting parameters. The orthotropic closure satisfies the full symmetry condition. There are several different versions of the orthotropic closure approximation which were developed to improve the accuracy and to overcome some nonphysical behaviors of the original model. The performance of the orthotropic closure approximation is quite successful. However, it requires additional computation for tensor transformations between the global coordinate and the principal coordinate, which is its drawback in terms of the computational efficiency.

The invariant-based closure approximation uses the general expression of the fourth-order tensor in terms of the second-order tensors of  $\mathbf{a}$  and  $\boldsymbol{\delta}$  as follows [6]:

$$\begin{aligned} A_{ijkl} = & \beta_1 S(\delta_{ij}\delta_{kl}) + \beta_2 S(\delta_{ij}a_{kl}) + \beta_3 S(a_{ij}a_{kl}) + \beta_4 S(\delta_{ij}a_{km}a_{ml}) \\ & + \beta_5 S(a_{ij}a_{km}a_{ml}) + \beta_6 S(a_{im}a_{mj}a_{kn}a_{nl}), \end{aligned} \quad (2.7)$$

where  $S$  is the symmetric operator. The six coefficients of  $\beta_i$  are assumed to be the function of the second and third invariants of  $\mathbf{a}$ . The invariant-based closure is as accurate as the eigenvalue-based closures, while its computational time is much less (about 30%) than that of the eigenvalue-based closures since it does not require any coordinate transformations.

The neural-network-based closure approximation was developed recently, which assumes two-layer neural network between the fourth- and second-order orientation tensors as follows [7]:

$$\mathbf{A} = f_2(\mathbf{W}_2 f_1(\mathbf{W}_1 \mathbf{a} + \mathbf{b}_1) + \mathbf{b}_2), \quad (2.8)$$

where  $\mathbf{W}_i$  are weighting coefficients,  $\mathbf{b}_i$  are biases coefficients, and  $f_i$  are transfer functions. A linear function and tangent hyperbolic function were used for the transfer function. The neural network closure is accurate for a wide range of the flow fields, and also its computational time is much lower than the orthotropic closures. However, it requires huge numbers of coefficients for  $\mathbf{W}_i$  and  $\mathbf{b}_i$ , which can be quite troublesome for a practical application. The quantitative comparison of the computational cost and the accuracy between different closure approximations could be found in [6–8].

There were attempts to solve the evolution equation for the fourth-order orientation where one needs the closure approximation for the sixth-order orientation tensor [9]. The invariant-based approach was employed, and more accurate prediction of the fiber orientation could be achieved. However, there still remains a trade-off between the accuracy of solution and the additional computational cost to solve more equations.

### 2.3. Slow Orientation Model

The kinematic equation of (2.5) has been widely accepted in the numerical simulations in the past decades. However, there are some experimental observations that the actual fiber orientation kinematics might be two- to ten-times slower than the model predicts [10, 11]. One simple way to describe the slow orientation kinematics was to scale the velocity gradient with a constant factor [10, 11]. This idea is based on an assumption that the effective velocity gradient experienced by the group of fibers is less than the bulk velocity gradient due to the cluster structure of the fibers. A modified model is written as follows:

$$\frac{1}{\kappa} \frac{D}{Dt} \mathbf{a} = -\frac{1}{2} (\boldsymbol{\omega} \cdot \mathbf{a} - \mathbf{a} \cdot \boldsymbol{\omega}) + \frac{\lambda}{2} (\dot{\boldsymbol{\gamma}} \cdot \mathbf{a} + \mathbf{a} \cdot \dot{\boldsymbol{\gamma}} - 2\mathbf{A} : \dot{\boldsymbol{\gamma}}) + 2D_r(\mathbf{I} - 3\mathbf{a}), \quad (2.9)$$

where  $1/\kappa$  is, namely, the strain reduction factor. However, this model is not objective, which means that it is coordinate dependent, thus cannot be used for a general flow field.

Recently, an objective model for the slow orientation was developed [12]. In this model, the growth rates of the eigenvalues of  $\mathbf{a}$  are multiplied by  $\kappa$  and the resulting evolution equation is as follows:

$$\begin{aligned} \frac{D}{Dt} \mathbf{a} &= -\frac{1}{2} (\boldsymbol{\omega} \cdot \mathbf{a} - \mathbf{a} \cdot \boldsymbol{\omega}) + \frac{\lambda}{2} (\dot{\boldsymbol{\gamma}} \cdot \mathbf{a} + \mathbf{a} \cdot \dot{\boldsymbol{\gamma}} - 2\mathbf{A}^{\text{RSC}} : \dot{\boldsymbol{\gamma}}) + 2\kappa D_r(\mathbf{I} - 3\mathbf{a}), \\ \mathbf{A}^{\text{RSC}} &= \mathbf{A} + (1 - \kappa)(\mathbf{L} - \mathbf{M} : \mathbf{A}), \end{aligned} \quad (2.10)$$

where  $\mathbf{L}$  and  $\mathbf{M}$  are defined in terms of eigenvalues and eigenvectors of  $\mathbf{a}$ . The only difference with the standard model of (2.5) appears in the fourth-order orientation tensor term and the fiber interaction term. This model could fit the experimental data of transient shear viscosity, especially the shear strain where the viscosity has a peak, better than the standard model. Also the fiber orientation prediction results using the slow orientation model were in a better agreement with the experimental result [13]. Figure 1 shows the effect of slow orientation on the fiber orientation result in a center-gated disk geometry [14].

### 2.4. Fiber Interaction Model

In most of the previous works, the rotary diffusivity ( $D_r$ ) of the following form has been widely used [2]:

$$D_r = C_I \dot{\boldsymbol{\gamma}}, \quad (2.11)$$

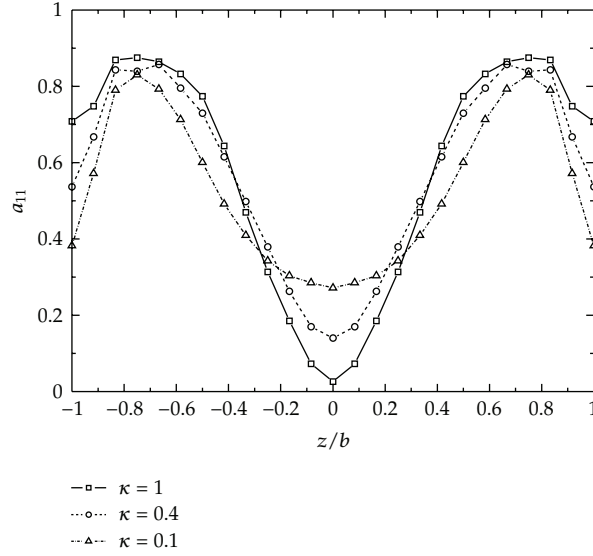


**Figure 1:** Effect of slow orientation ( $\kappa$ ) on fiber orientation prediction in a center-gated disk at radial position of  $r/b = 12.4$  where  $b$  is the half-gap thickness of the disk.

where  $C_I$  is the fiber interaction coefficient and  $\dot{\gamma}$  is the generalized shear rate. There are several models regarding  $C_I$  depending on the fiber concentration. Bay [15] had carried out extensive experimental works and suggested a fitting curve for  $C_I$  as a function of  $\phi_f L/D$  as follows:

$$C_I = 0.0184 \exp\left(-0.7148 \frac{\phi_f L}{D}\right). \quad (2.12)$$

This result shows the screening effect of the fiber interaction in the concentrated suspensions. Ranganathan and Advani [16] proposed a theoretical model using Doi-Edwards theory as follows:

$$C_I = \frac{K}{a_c/L}, \quad (2.13)$$

where  $K$  is a proportionality constant and  $a_c$  is the average interfiber spacing. In this model, the fiber interaction depends on the orientation states via  $a_c$ . Particularly, for fiber suspension in a viscoelastic media, Ramazani et al. [17] modified (2.13) as follows:

$$C_I = \frac{K}{a_c/L} \frac{1}{(\mathbf{a} : \mathbf{c})^n}, \quad (2.14)$$

where  $\mathbf{c}$  is the polymer conformation tensor and  $n$  is a constant. According to this model, the fiber interaction decreases as the polymers are stretched in the direction of the fiber orientation. Park and Kwon [18] also used (2.14) in developing a rheological model for a



fiber suspension in a viscoelastic media, and the coupling effect between fiber and polymer in  $C_I$  was found to be dominant only at the high shear rate regime.

Also there had been several anisotropic diffusivity models developed in the literature [19–21]. The anisotropic diffusivity model could fit the experimental data better than the isotropic model particularly for a long fiber composite [21].

### 3. Governing Equation

The fiber orientation develops during the filling stage of the injection molding process where the flow can be assumed to be incompressible. In addition, the inertia is negligible because of the high viscosity of the polymer melt. As a result, the mass and momentum conservation equations can be written as follows:

$$\begin{aligned}\nabla \cdot \mathbf{u} &= 0, \\ -\nabla p + \nabla \cdot \boldsymbol{\tau} &= 0,\end{aligned}\tag{3.1}$$

where  $\mathbf{u}$  is velocity vector,  $p$  is the pressure, and  $\boldsymbol{\tau}$  is the stress tensor. The energy conservation equation is as follows:

$$\rho c_p \frac{D}{Dt} T = \nabla \cdot (k \nabla T) + \eta \dot{\gamma}^2,\tag{3.2}$$

where  $\rho$  is the density,  $c_p$  is the heat capacity,  $\eta$  is the viscosity, and  $k$  is the heat conductivity. The last term in the right-hand side comes from the viscous dissipation.

For a thin cavity geometry which is a usual situation in injection molding process, one can simplify the mass and momentum conservation equations using Hele-Shaw approximation [22]. Then, one obtains the so-called pressure equation as follows:

$$\begin{aligned}\frac{\partial}{\partial x} \left( S \frac{\partial p}{\partial x} \right) + \frac{\partial}{\partial y} \left( S \frac{\partial p}{\partial y} \right) &= 0, \\ S &= \int_0^b \frac{z^2}{\eta} dz,\end{aligned}\tag{3.3}$$

where  $S$  is the fluidity and  $b$  is the half-gap thickness of the cavity. It might be mentioned that a generalized Newtonian constitutive relation has been used to derive (3.3) which will be discussed in Section 4. Also the energy conservation equation is rewritten as

$$\rho c_p \left( \frac{\partial T}{\partial t} + u \frac{\partial T}{\partial x} + v \frac{\partial T}{\partial y} \right) = \frac{\partial}{\partial z} \left( k \frac{\partial T}{\partial z} \right) + \eta \dot{\gamma}^2.\tag{3.4}$$

The in-plane velocities of  $u$  and  $v$  can be written in terms of the pressure gradient as

$$u = -\frac{\partial p}{\partial x} \int_z^b \frac{\bar{z}}{\eta} d\bar{z}, \quad v = -\frac{\partial p}{\partial y} \int_z^b \frac{\bar{z}}{\eta} d\bar{z}.\tag{3.5}$$



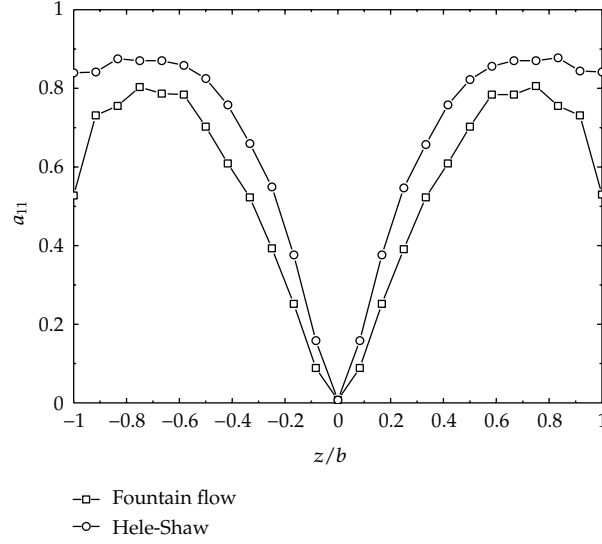


**Figure 2:** Effect of fountain flow on fiber orientation prediction in a center-gated disk at radial position of  $r/b = 22.8$  where  $b$  is the half-gap thickness of the disk.

The Hele-Shaw flow model have been successfully employed in the injection molding simulation and the fiber orientation prediction in the past decades [23–28].

However, it should be noted that the three-dimensional flow at the melt front region, namely, the fountain-flow, could not be described by Hele-Shaw approximation, which can result in an inaccurate prediction of fiber orientation at the melt front region and skin layer. Figure 2 shows the effect of fountain flow in fiber orientation prediction [8]. Only a limited number of studies could be found which includes the fountain-flow effect since one should solve the three-dimensional governing equation to describe the fountain flow, which requires huge computational costs. Instead of solving the three-dimensional equations, Bay and Tucker [29] and Han and Im [30] introduced a special treatment particularly at the melt front region to describe the fountain flow. Ko and Youn [31] studied the details of gap-wise distributions of the fiber orientation for simple geometries without Hele-Shaw approximation. Han [32] and Chung and Kwon [33] studied the fountain flow effect using finite element method in an axisymmetric geometry of center-gated disk. VerWeyst et al. [34] used a hybrid approach where three-dimensional flow simulation is carried out locally with the help of Hele-Shaw flow simulation providing the boundary conditions.

#### 4. Constitutive Model

A generalized Newtonian model for polymer melts has been widely accepted for injection molding simulation, which can be written as follows:

$$\boldsymbol{\tau} = \eta \dot{\boldsymbol{\gamma}}, \quad \eta = \eta(\dot{\boldsymbol{\gamma}}, T). \quad (4.1)$$

This model is simple and accurate for injection molding process where the shear deformation dominates the flow [22]. There are several models for shear thinning viscosity of the polymer

melt such as the power law model, the Cross-model, and so on. The temperature dependency of the shear viscosity can be described by means of an Arrhenius model or WLF model.

The generalized Newtonian model has been well adopted for fiber orientation prediction during injection molding in many literatures. Rigorously speaking, however, the fiber orientation is coupled with the momentum balance equation via constitutive relation. This coupling effect can be important depending on the flow regime [27, 28, 33, 35]. The stress tensor where the fiber anisotropic contribution is taken into account can be written as follows:

$$\boldsymbol{\tau} = \eta \dot{\boldsymbol{\gamma}} + \eta N_p \dot{\boldsymbol{\gamma}} : \mathbf{A}, \quad (4.2)$$

where  $N_p$  is a particle number. It should be noted that this model is for slender fibers where fiber thickness can be ignored and  $\eta$  is the viscosity of the neat polymer matrix. There are several models for  $N_p$  depending on the fiber concentration [34–37]. In practical applications in injection molding simulation, the Dinh and Armstrong model [35] could be readily employed because of simplicity in spite of its inaccuracy. The effects of coupling on the fiber orientation and flow have been studied in [26, 27, 31, 33, 38]. In the injection molding simulation, it was observed that the coupling effect is important particularly at the core and transition layers near the gate region [27, 33].

There are some models in which both the polymer viscoelasticity and fiber anisotropy are taken into account in the stress tensor [17, 18, 39, 40]. In this case, the stress tensor is written as follows:

$$\boldsymbol{\tau} = \eta_s \dot{\boldsymbol{\gamma}} + \eta_m N_p \dot{\boldsymbol{\gamma}} : \mathbf{A} + \frac{\eta_p}{\theta} \mathbf{c}, \quad (4.3)$$

where  $\eta_s$  is the solvent viscosity (which is Newtonian),  $\eta_m$  is the viscosity of matrix (which is non-Newtonian),  $\eta_p$  is the polymer viscosity,  $\theta$  is the polymer relaxation time, and  $\mathbf{c}$  is the polymer conformation tensor. Generally, the evolution equation of the polymer conformation tensor has the following form:

$$\frac{D}{Dt} \mathbf{c} - \nabla \mathbf{u}^T \cdot \mathbf{c} - \mathbf{c} \cdot \nabla \mathbf{u} = \mathbf{f}(\mathbf{c}), \quad (4.4)$$

where the left-hand side is the upper-convective time derivative of  $\mathbf{c}$  and the right-hand side represents the dissipation process of the polymer. As noted in [13], this viscoelastic model would not be useful practically in predicting the fiber orientation since already simple models of the generalized Newtonian model (4.1) or fiber suspension model (4.2) can give accurate predictions of the flow and fiber orientation results. Instead, this model would be useful to study the viscoelastic deformation or residual stress of the polymer.

## 5. Numerical Methods

The prediction of fiber orientation during injection molding involves a coupled analysis of flow, temperature, moving free surface, and fiber orientation evolution. This coupling between the equations can be treated in an explicit manner at each step of time integration or melt front advancement. Commonly, the flow field is solved first, then the temperature and fiber orientation are solved using the flow field solution. Finally, the melt front is advanced and then the next time step begins. Particularly in the momentum and energy conservation

equations, there is nonlinearity due to the viscosity which depends on the shear rate ( $\dot{\gamma}$ ) and the temperature ( $T$ ). The nonlinearity has been solved by the iteration method at each time step. For the moving free surface problem, there are several different methods in the literature. When one uses Hele-Shaw flow model, the melt front advancement is simply carried out based on the nodal value of the pressure. For each node, a scalar quantity, namely, fill factor, is defined, which is updated for each time step according to the pressure solution. For three-dimensional flow model, the free surface capturing is carried out by solving additional problem of convection equation. In this method, an artificial scalar quantity, namely, pseudo-concentration, is defined for each node so that the fluid region and the air region can be distinguished depending on the value of pseudo-concentration.

### 5.1. Hele-Shaw Flow

For the flow and temperature fields simulation, a finite-element/finite-difference coupled scheme has been successfully employed for injection molding simulations when the Hele-Shaw flow is assumed with a generalized Newtonian constitutive model [22]. In this method, the in-plane discretization is achieved by the finite element method while the thickness discretization is achieved by the finite difference method. For instance, the pressure and temperature fields can be approximated as follows:

$$\begin{aligned} p(x, y, t) &= N_i(x, y)p_i(t), \\ T(x, y, z_l, t) &= N_i(x, y)T_i^l(t), \end{aligned} \quad (5.1)$$

where  $N_i$  is the finite element interpolation function of  $i$ th node,  $p_i$  is the pressure at the  $i$ th node, and  $T_i^l$  is the temperature at the  $i$ th node of  $l$ th finite difference layer. Commonly, a triangular linear interpolation is used for  $N_i$ . Since the thickness directional discretization is independent of the in-plane discretization in this method, one can have a fine discretization for the thickness directional distribution of physical quantities such as temperature, viscosity, and fiber orientation tensor components, which is quite important in the injection molding simulation. The finite difference method appears where the physical quantity depends on the in the thickness direction ( $z$ ) of the cavity. For instance, the conduction term in the energy conservation equation (when the conductivity is assumed to be constant) can be approximated by the finite-element/finite-difference scheme as follows:

$$k \frac{\partial^2}{\partial z^2} T(x, y, z_l, t) = N_i k \frac{1}{\Delta z^2} (T_i^{l+1}(t) - 2T_i^l(t) + T_i^{l-1}(t)). \quad (5.2)$$

In most previous studies, the orientation tensor is defined only at the centroid of the element of each finite difference layer. To solve the evolution of the orientation tensor ((2.5) or (2.10)), the velocity gradient should be calculated at the centroid of each element from the flow field solution. For the Hele-Shaw flow, the velocity gradient tensor is as follows:

$$\nabla \mathbf{u} = \begin{bmatrix} \frac{\partial u}{\partial x} & \frac{\partial u}{\partial y} & \frac{\partial u}{\partial z} \\ \frac{\partial v}{\partial x} & \frac{\partial v}{\partial y} & \frac{\partial v}{\partial z} \\ 0 & 0 & 0 \end{bmatrix}, \quad (5.3)$$

where the velocity can be calculated from (3.5). The velocity gradients in thickness direction, that is,  $\partial u/\partial z$  and  $\partial v/\partial z$ , can be easily defined by the finite difference method. However, one needs a special treatment to obtain the other components. It should be noted that the velocity interpolation becomes one order lower than the pressure interpolation by (3.5). For a triangular linear interpolation of the pressure, which is the most case in practice, the velocity is constant within an element. Thus, one needs to introduce a special method to calculate the velocity gradient components, which is usually done using the velocities of the neighboring elements. Another way to tackle this problem would be to use higher-order interpolation of the pressure, which has not been reported in the literature yet.

As for the time integration of the energy conservation equation, commonly the first-order implicit method has been widely employed, while higher integration scheme such as fourth-order Runge-Kutta method has been used to solved the fiber orientation evolution [26–28]. For the convective terms in the energy equation and fiber orientation evolution equation, one should introduce, namely, upwinding scheme to avoid numerical oscillation or wiggling of the solution. The basic concept of the upwinding scheme is to introduce different weightings for each node depending on the sign of dot product of the velocity and the outward normal vector at each node.

The finite-element/finite-difference hybrid method has been quite successful because very fine refinement is possible in the gap-wise finite difference method independently of the finite element method. This is the most important advantage of the hybrid method in the injection molding simulation because of the high shear nature of the flow inside the cavity.

## 5.2. Three-Dimensional Flow

The significance of the three-dimensional flow in the fiber orientation prediction has been discussed in many studies [29–33]. For the three-dimensional flow and temperature fields model, the finite element method is most widely used in the polymer processing simulation because of its flexibility for complex geometry problems [41–45]. A mixed velocity and pressure formulation has been widely used where the incompressibility is treated by a Lagrange multiplier method. One should be careful about the interpolation functions of the pressure and the velocity due to the Babuška-Brezzi condition which states that the pressure interpolation should be one order lower than the velocity interpolation. One can also find a stabilized formulation which enables equal-order interpolation of the velocity and the pressure for a convenience of finite element formulations [46]. For the three-dimensional finite element case, the numerical formulation is rather simple than for that of the finite-element/finite-difference hybrid scheme. However, one major issue arising with the three-dimensional flow model is the huge computational cost particularly for a fine discretization in the thickness direction of the cavity, which limits the practicality of the three-dimensional model [45].

As mentioned above for convective problems such as energy conservation equation and fiber orientation evolution equation, one should use a stabilizing method, namely upwinding scheme, to get a stable and accurate solution without wiggling. In the finite element formulation, a streamline-upwind/Petrov-Galerkin (SUPG) method has been adopted widely in the literature [13, 33, 42]. For a convective problem of

$$R = \frac{\partial X}{\partial t} + \mathbf{u} \cdot \nabla X - F(X) = 0, \quad (5.4)$$

where  $R$  is the residual and  $X$  can be either temperature or orientation tensor, the SUPG formulation can be written as follows:

$$(R, Y) + \sum_e R \zeta_e (\mathbf{u} \cdot \nabla Y)_e = 0, \quad (5.5)$$

where  $Y$  is the weighting function and  $\zeta_e$  is a stabilizing parameter which can depend on the element size and characteristic velocity at the element.

## 6. Conclusions

This study reviews modeling and simulation of fiber orientation during injection molding of polymer composites. The prediction of fiber orientation requires coupled analysis between the flow, temperature, free surface, and fiber orientation. The coupling can be treated in an explicit manner for each step of time integration or melt front advancement. The nonlinearity in the equations has been solved using iteration schemes.

For the flow field during injection molding filling stage, it is commonly assumed that the inertia is negligible and the flow is incompressible. Hele-Shaw approximation is adopted to simplify the flow equation, which is accurate for most part of the flow in a thin cavity geometry. For Hele-Shaw flow model, a finite-element/finite-difference hybrid scheme is widely accepted to solve the pressure equation and the energy conservation equation. Since the discretization in the thickness direction is independent of the in-plane discretization, one can achieve a fine solution in the thickness direction which is quite important in the injection molding simulation. In the Hele-Shaw flow model, however, the fountain flow at the melt front could not be described, which could result in a poor prediction of the fiber orientation near the melt front region particularly in the shell and skin layers. Also Hele-Shaw model is not suitable for a general three-dimensional geometry with a varying thickness. Several finite element methods have been developed to solve three-dimensional flow field in injection molding filling simulation. Because of the computational cost, however, three-dimensional flow simulation remains as one of the major problems for the accurate prediction of the fiber orientation.

The orientation state of fibers is commonly described by the orientation tensors for the efficiency of computation. Using the orientation tensor results in a need for a closure approximation to close the set of evolution equations of orientation tensors. Various closures from different bases have been developed to achieve both the accuracy and the computational efficiency. Invariant-based closure is as accurate as orthotropic closures while its computational cost is much less than orthotropic closures. Neural network closure might be as good as invariant-based closure, but it requires a lot of fitting coefficients. As for the kinematics of the fiber orientation, a modified Jeffery model by Folgar and Tucker has been a basis to understand the fiber orientation behavior. There are recent progresses in the fiber kinematic equation such as slow orientation model and anisotropic rotary diffusivity model. The slow orientation model enables more accurate prediction of the orientation state especially near the gate region. The anisotropic rotary diffusivity model would be useful particularly for the long fiber composites. The initial condition of the orientation state also can affect the final results of the simulation depending on the cavity geometry. Thus, the simulation including the sprue region could improve the accuracy of the fiber orientation prediction.

The fiber orientation can be solved either in a coupled manner or in a decoupled manner with the flow field depending on the type of constitutive model. The coupling effect is significant particularly near the core and transition layers. Most of the commercial simulation

software use the decoupled analysis because of the convenience in developing each problem solver independently like a module. The coupled analysis would be more accurate than the decoupled analysis, but the constitutive model and the numerical scheme become more complicated.

## Acknowledgment

The authors would like to thank financial and technical supports from the WCU (World Class University) program through the National Research Foundation of Korea funded by the Ministry of Education, Science and Technology (R31-30005).

## References

- [1] S. G. Advani and C. L. Tucker, "The use of tensors to describe and predict fiber orientation in short fiber composites," *Journal of Rheology*, vol. 31, no. 8, pp. 751–784, 1987.
- [2] F. Folgar and C. L. Tucker, "Orientation behavior of fibers in concentrated suspensions," *Journal of Reinforced Plastics and Composites*, vol. 3, no. 2, pp. 98–119, 1984.
- [3] G. B. Jeffery, "The motion of ellipsoidal particles immersed in a viscous fluid," *Proceedings of the Royal Society A*, vol. 102, no. 715, pp. 161–179, 1922.
- [4] J. S. Cintra and C. L. Tucker, "Orthotropic closure approximations for flow-induced fiber orientation," *Journal of Rheology*, vol. 39, no. 6, pp. 207–227, 1984.
- [5] D. H. Chung and T. H. Kwon, "Improved model of orthotropic closure approximation for flow induced fiber orientation," *Polymer Composites*, vol. 22, no. 5, pp. 636–649, 2001.
- [6] D. H. Chung and T. H. Kwon, "Invariant-based optimal fitting closure approximation for the numerical prediction of flow-induced fiber orientation," *Journal of Rheology*, vol. 46, no. 1, pp. 169–194, 2002.
- [7] D. A. Jack, B. Schache, and D. E. Smith, "Neural network-based closure for modeling short-fiber suspensions," *Polymer Composites*, vol. 31, no. 7, pp. 1125–1141, 2010.
- [8] D. H. Chung, *Modeling and simulation of fiber orientation distribution during molding processes of short fiber reinforced polymer-based composites*, Ph.D. thesis, Pohang University of Science and Technology, Pohang, Republic of Korea, 2002.
- [9] D. A. Jack, *Advanced analysis of short-fiber polymer composite material behavior*, Ph.D. thesis, University of Missouri, Columbia, Mo, USA, 2006.
- [10] H. M. Hyun, *Improved fiber orientation predictions for injection-molded composites*, M.S. thesis, University of Illinois, Champaign, Ill, USA, 2001.
- [11] M. Sepehr, G. Ausias, and P. J. Carreau, "Rheological properties of short fiber filled polypropylene in transient shear flow," *Journal of Non-Newtonian Fluid Mechanics*, vol. 123, no. 1, pp. 19–32, 2004.
- [12] J. Wang, C. L. Tucker, and J. F. O'Gara, "An objective model for slow orientation kinetics in concentrated fiber suspensions: theory and rheological evidence," *Journal of Rheology*, vol. 52, no. 5, pp. 1179–1200, 2008.
- [13] J. M. Park and T. H. Kwon, "Nonisothermal transient filling simulation of fiber suspended viscoelastic liquid in a center-gated disk," *Polymer Composites*, vol. 32, no. 3, pp. 427–437, 2011.
- [14] J. M. Park, *Rheological modeling and injection molding simulation of short fiber reinforced polymer composite*, Ph.D. thesis, Pohang University of Science and Technology, Pohang, Republic of Korea, 2011.
- [15] R. S. Bay, *Fiber orientation in injection molded composites: a comparison of theory and experiment*, Ph.D. thesis, University of Illinois, Champaign, Ill, USA, 1991.
- [16] S. Raganathan and S. G. Advani, "Fiber-fiber interactions in homogeneous flows of nondilute suspensions," *Journal of Rheology*, vol. 35, pp. 1499–1522, 1991.
- [17] A. A. Ramazani, A. Ait-Kadi, and M. Grmela, "Rheology of fiber suspensions in viscoelastic media: experiments and model predictions," *Journal of Rheology*, vol. 45, no. 4, pp. 945–962, 2001.
- [18] J. M. Park and T. H. Kwon, "Irreversible thermodynamics based constitutive theory for fiber suspended polymeric liquids," *Journal of Rheology*, vol. 55, no. 3, pp. 517–543, 2011.
- [19] D. L. Koch, "A model for orientational diffusion in fiber suspensions," *Physics of Fluids*, vol. 7, no. 8, pp. 2086–2088, 1995.
- [20] N. Phan-Thien, X. J. Fan, and R. Zheng, "A numerical simulation of suspension flow using a constitutive model based on anisotropic interparticle interactions," *Rheologica Acta*, vol. 39, no. 2, pp. 122–130, 2000.



- [21] J. H. Phelps and C. L. Tucker, "An anisotropic rotary diffusion model for fiber orientation in short- and long-fiber thermoplastics," *Journal of Non-Newtonian Fluid Mechanics*, vol. 156, no. 3, pp. 165–176, 2009.
- [22] C. A. Hieber and S. F. Shen, "A finite-element/finite-difference simulation of the injection-molding filling process," *Journal of Non-Newtonian Fluid Mechanics*, vol. 7, no. 1, pp. 1–32, 1980.
- [23] M. C. Altan, S. Subbiah, S. I. Güçeri, and R. B. Pipes, "Numerical prediction of three-dimensional fiber orientation in Hele-Shaw flows," *Polymer Engineering and Science*, vol. 30, no. 14, pp. 848–859, 1990.
- [24] T. Matsuoka, J.-I. Takabatake, Y. Inoue, and H. Takahashi, "Prediction of fiber orientation in injection molded parts of short-fiber-reinforced thermoplastics," *Polymer Engineering and Science*, vol. 30, no. 16, pp. 957–966, 1990.
- [25] H. H. De Frahan, V. Verleye, F. Dupret, and M. J. Crochet, "Numerical prediction of fiber orientation in injection molding," *Polymer Engineering and Science*, vol. 32, no. 4, pp. 254–266, 1992.
- [26] M. Gupta and K. K. Wang, "Fiber orientation and mechanical properties of shot-fiber-reinforced injection-molding composites: simulated and experimental results," *Polymer Composites*, vol. 14, no. 5, pp. 367–382, 1993.
- [27] S. T. Chung and T. H. Kwon, "Numerical simulation of fiber orientation in injection molding of short-fiber-reinforced thermoplastics," *Polymer Engineering and Science*, vol. 35, no. 7, pp. 604–618, 1995.
- [28] S. T. Chung and T. H. Kwon, "Coupled analysis of injection molding filling and fiber orientation, including in-plane velocity gradient effect," *Polymer Composites*, vol. 17, no. 6, pp. 859–872, 1996.
- [29] R. S. Bay and C. L. Tucker, "Fiber orientation in simple injection moldings. Part I: theory and numerical methods," *Polymer Composites*, vol. 13, no. 4, pp. 317–331, 1992.
- [30] K.-H. Han and Y.-T. Im, "Numerical simulation of three-dimensional fiber orientation in injection molding including fountain flow effect," *Polymer Composites*, vol. 23, no. 2, pp. 222–238, 2002.
- [31] J. Ko and J. R. Youn, "Prediction of fiber orientation in the thickness plane during flow molding of short fiber composites," *Polymer Composites*, vol. 16, no. 2, pp. 114–124, 1995.
- [32] K.-H. Han, *Enhancement of accuracy in calculating fiber orientation distribution in short fiber reinforced injection molding*, Ph.D. thesis, Korea Advanced Institute of Science and Technology, Daejeon, Republic of Korea, 2000.
- [33] D. H. Chung and T. H. Kwon, "Numerical studies of fiber suspensions in an axisymmetric radial diverging flow: the effects of modeling and numerical assumptions," *Journal of Non-Newtonian Fluid Mechanics*, vol. 107, no. 1–3, pp. 67–96, 2002.
- [34] B. E. VerWeyst, C. L. Tucker, P. H. Foss, and J. F. O'Gara, "Fiber orientation in 3-D injection molded features: prediction and experiment," *International Polymer Processing*, vol. 14, no. 4, pp. 409–420, 1999.
- [35] B. E. VerWeyst and C. L. Tucker, "Fiber suspensions in complex geometries: flow/orientation coupling," *Canadian Journal of Chemical Engineering*, vol. 80, no. 6, pp. 1093–1106, 2002.
- [36] G.K. Batchelor, "The stress generated in a non-dilute suspension of elongated particles by pure straining motion," *The Journal of Fluid Mechanics*, vol. 46, no. 4, pp. 813–829, 1971.
- [37] S. M. Dinh and R. C. Armstrong, "A rheological equation of state for semiconcentrated fiber suspensions," *Journal of Rheology*, vol. 28, no. 3, pp. 207–227, 1984.
- [38] E. S. G. Shaqfeh and G. H. Fredrickson, "The hydrodynamic stress in a suspension of rods," *Physics of Fluids A*, vol. 2, no. 1, pp. 7–24, 1990.
- [39] J. Azaiez, "Constitutive equations for fiber suspensions in viscoelastic media," *Journal of Non-Newtonian Fluid Mechanics*, vol. 66, no. 1, pp. 35–54, 1996.
- [40] M. Rajabian, C. Dubois, and M. Grmela, "Suspensions of semiflexible fibers in polymeric fluids: rheology and thermodynamics," *Rheologica Acta*, vol. 44, no. 5, pp. 521–535, 2005.
- [41] J.-F. Héty, D. M. Gao, A. Garcia-Rejon, and G. Salloum, "3D finite element method for the simulation of the filling stage in injection molding," *Polymer Engineering and Science*, vol. 38, no. 2, pp. 223–236, 1998.
- [42] G. A. Haagh and F. N. Van De Vosse, "Simulation of three-dimensional polymer mould filling processes using a pseudo-concentration method," *International Journal for Numerical Methods in Fluids*, vol. 28, no. 9, pp. 1355–1369, 1998.
- [43] S.-W. Kim and L.-S. Turng, "Three-dimensional numerical simulation of injection molding filling of optical lens and multiscale geometry using finite element method," *Polymer Engineering and Science*, vol. 46, no. 9, pp. 1263–1274, 2006.
- [44] F. Ilincă and J.-F. Héty, "Three-dimensional simulation of multi-material injection molding: application to gas-assisted and co-injection molding," *Polymer Engineering and Science*, vol. 43, no. 7, pp. 1415–1427, 2003.

- [45] S.-W. Kim and L.-S. Turng, "Developments of three-dimensional computer-aided engineering simulation for injection moulding," *Modelling and Simulation in Materials Science and Engineering*, vol. 12, no. 3, pp. S151–S173, 2004.
- [46] L. P. Franca and S. L. Frey, "Stabilized finite element methods. II. The incompressible Navier-Stokes equations," *Computer Methods in Applied Mechanics and Engineering*, vol. 99, no. 2-3, pp. 209–233, 1992.



## Research Article

# A Fully Discrete Galerkin Method for a Nonlinear Space-Fractional Diffusion Equation

Yunying Zheng<sup>1</sup> and Zhengang Zhao<sup>2,3</sup>

<sup>1</sup> Department of Mathematics, Huaibei Normal University, Huaibei 235000, China

<sup>2</sup> Department of Fundamental Courses, Shanghai Customs College, Shanghai 201204, China

<sup>3</sup> Department of Mathematics, Shanghai University, Shanghai 200444, China

Correspondence should be addressed to Zhengang Zhao, zgzhao999@yahoo.com.cn

Received 13 May 2011; Revised 27 July 2011; Accepted 27 July 2011

Academic Editor: Delfim Soares Jr.

Copyright © 2011 Y. Zheng and Z. Zhao. This is an open access article distributed under the Creative Commons Attribution License, which permits unrestricted use, distribution, and reproduction in any medium, provided the original work is properly cited.

The spatial transport process in fractal media is generally anomalous. The space-fractional advection-diffusion equation can be used to characterize such a process. In this paper, a fully discrete scheme is given for a type of nonlinear space-fractional anomalous advection-diffusion equation. In the spatial direction, we use the finite element method, and in the temporal direction, we use the modified Crank-Nicolson approximation. Here the fractional derivative indicates the Caputo derivative. The error estimate for the fully discrete scheme is derived. And the numerical examples are also included which are in line with the theoretical analysis.

## 1. Introduction

The normal diffusive motion is modeled to describe the standard Brownian motion. The relation between the flow and the divergence of the particle displacement represents

$$J(x, t) = -a \frac{\partial c}{\partial x} + bc, \quad (1.1)$$

where  $J$  is the diffusive flow. Inserting the above equation into the equation of mass conservation

$$\frac{\partial J}{\partial x} = -\frac{\partial c}{\partial t}, \quad (1.2)$$

we obtain the standard convection-diffusion equation. From the viewpoint of physics, it means that during the method of time random walkers, the overall particle displacement up to time  $t$  can be represented as a sum of independent random steps, in the case that both the mean-squared displacement per step and the mean time needed to perform a step are finite. The measured variance growth in the direction of flow of tracer plumes is typically at a Fickian rate,  $\langle (c - \bar{c})^2 \rangle \sim t$ .

The transport process in fractal media cannot be described with the normal diffusion. The process is nonlocal and it does not follow the classical Fickian law. It depicts a particle in spreading tracer cloud which has a standard deviation, and which grows like  $t^{2\alpha}$  for some  $0 < \alpha < 1$ , excluding the Fickian case  $\alpha = 1/2$ . The description of anomalous diffusion means that the measure variance growth in the direction of flow has a deviation from the Fickian case, it follows the super-Fickian rate  $\langle (c - \bar{c})^2 \rangle \sim t^{2\alpha}$  when  $\alpha > 1/2$ , or does the subdiffusion rate  $\langle (c - \bar{c})^2 \rangle \sim t^{2\alpha}$  if  $0 < \alpha < 1/2$ . With the help of the continuous time random walk and the Fourier transform, the governing equation with space fractional derivative can be derived as follows

$$\frac{\partial u}{\partial t} = D \left( a(u) {}_a D_x^\beta u \right) + b(u) Du + f(x, t, u), \quad 0 < \beta < 1, \quad (1.3)$$

where  $D$  denotes integer derivative respect to  $x$ , and  $D^\beta$  is fractional derivative. There are some authors studying the spacial anomalous diffusion equation in theoretical analysis and numerical simulations [1–10]. Now the fractional anomalous diffusion becomes a hot topic because of its widely applications in the evolution of various dynamical systems under the influence of stochastic forces. For example, it is a well-suited tool for the description of anomalous transport processes in both absence and presence of external velocities or force fields. Since the groundwater velocities span many orders of magnitude and give rise to diffusion-like dispersion (a term that combines molecular diffusion and hydrodynamic dispersion), the fractional diffusion is an important process in hydrogeology. It can be used to describe the systems with reactions and diffusions across a wide range of applications including nerve cell signaling, animal coat patterns, population dispersal, and chemical waves. In general, fractional anomalous diffusions have numerous applications in statistical physics, biophysics, chemistry, hydrogeology, and biology [4, 11–20].

In this paper, we mainly study one kind of typical nonlinear space-fractional partial differential equations by using the finite element method, which reads in the following form:

$$\begin{aligned} \frac{\partial u}{\partial t} &= D \left( a(u) {}_a D_x^\beta u \right) + b(u) Du + f(x, t, u), \quad x \in \Omega, \quad t \in (0, T], \\ u|_{t=0} &= \varphi(x), \quad x \in \Omega, \\ u|_{\partial\Omega} &= g, \quad t \in (0, T], \end{aligned} \quad (1.4)$$

where  $\Omega$  is a spacial domain with boundary  $\partial\Omega$ ,  $D^\beta$  is the  $\beta$ th ( $0 < \beta < 1$ ) order fractional derivative with respect to the space variable  $x$  in the Caputo sense (which will be introduced later on),  $a$ ,  $b$ ,  $f$  are functions of  $x$ ,  $t$ ,  $u$ ,  $\varphi$  and  $g$  are known functions which satisfy the conditions requested by the theorem of error estimations.

The rest of this paper is constructed as follows. In Section 2 the fractional integral, fractional derivative, and the fractional derivative spaces are introduced. The error estimates

of the finite element approximation for (1.4) are studied in Section 3, and in Section 4, numerical examples are taken to verify the theoretical results derived in Section 3.

## 2. Fractional Derivative Space

In this section, we firstly introduce the fractional integral (or Riemann-Liouville integral), the Caputo fractional derivative, and their corresponding fractional derivative space.

*Definition 2.1.* The  $\alpha$ th order left and right Riemann-Liouville integrals of function  $u(x)$  are defined as follows

$$\begin{aligned} {}_a I_x^\alpha u(x) &= \frac{1}{\Gamma(\alpha)} \int_a^x (x-s)^{\alpha-1} u(s) ds, \\ {}_x I_b^\alpha u(x) &= \frac{1}{\Gamma(\alpha)} \int_x^b (s-x)^{\alpha-1} u(s) ds, \end{aligned} \quad (2.1)$$

where  $\alpha > 0$ , and  $\Gamma(\cdot)$  is the Gamma function.

*Definition 2.2.* The  $\alpha$ th order Caputo derivative of function  $u(x)$  is defined as,

$$\begin{aligned} {}_a D_x^\alpha u(x) &= {}_a I_x^{n-\alpha} \frac{d^n u(x)}{dx^n}, \quad n-1 < \alpha < n \in \mathbb{Z}^+, \\ {}_x D_b^\alpha u(x) &= (-1)^n {}_x I_b^{n-\alpha} \frac{d^n u(x)}{dx^n}, \quad n-1 < \alpha < n \in \mathbb{Z}^+. \end{aligned} \quad (2.2)$$

The  $\alpha$ th order Riemann-Liouville derivative of function  $u(x)$  is defined by changing the order of integration and differentiation.

**Lemma 2.3** (see [8]). *If  $u(0) = u'(0) = \dots = u^{(n-1)}(0) = 0$ , then the Caputo fractional derivative is equal to the Riemann-Liouville derivative.*

*Definition 2.4.* The fractional derivative space  $J^\alpha(\Omega)$  is defined as follows:

$$J^\alpha(\Omega) = \left\{ u \in L^2(\Omega) : {}_a D_x^\alpha u \in L^2(\Omega), \quad n-1 \leq \alpha < n \right\}, \quad (2.3)$$

endowed with the seminorm

$$|u|_{J^\alpha} = \| {}_a D_x^\alpha u \|_{L^2(\Omega)}, \quad (2.4)$$

and the norm

$$\|u\|_{J^\alpha} = \left( |u|_{J^\alpha}^2 + \sum_{k \leq [\alpha]} \|D^k u\|^2 \right)^{1/2}. \quad (2.5)$$

Let  $J_0^\alpha(\Omega)$  denote the closure of  $C_0^\infty(\Omega)$  with respect to the above norm and seminorm.

*Definition 2.5.* Define the seminorm

$$|u|_{H^\alpha} = \| |i\omega|^\alpha F(u) \|_{L^2(\Omega)}, \quad (2.6)$$

and the norm

$$\|u\|_{H^\alpha} = \left( |u|_{H^\alpha}^2 + \sum_{k \leq [\alpha]} \|D^k u\|^2 \right)^{1/2}, \quad (2.7)$$

where  $i$  is the imaginary unit, and  $F$  is the Fourier transform, and which can define another fractional derivative space  $H^\alpha(\Omega)$ .

Let  $H_0^\alpha(\Omega)$  denote the closure of  $C_0^\infty(\Omega)$  with respect to the norm and seminorm.

*Definition 2.6.* The fractional space  $J_s^\alpha(\Omega)$  is defined below

$$J_s^\alpha(\Omega) = \left\{ u \in L^2(\Omega) : {}_a D_x^\alpha u \in L^2(\Omega), {}_x D_b^\alpha u \in L^2(\Omega), n-1 \leq \alpha < n \right\}, \quad (2.8)$$

endowed with the seminorm

$$|u|_{J_s^\alpha} = \left( ({}_a D_x^\alpha u, {}_x D_b^\alpha u)^{1/2} \right)_{L^2(\Omega)}, \quad (2.9)$$

and the norm

$$\|u\|_{J_s^\alpha} = \left( \sum_{k \leq [\alpha]} \|D^k u\|^2 + |u|_{J_s^\alpha}^2 \right)^{1/2}. \quad (2.10)$$

**Theorem 2.7** (see [3, 6]).  $J_s^\alpha$ ,  $J^\alpha$ , and  $H^\alpha$  are equal with equivalent seminorm and norm.

The following are some useful results.

**Lemma 2.8** (see [3]). For  $u \in J_0^\alpha(\Omega)$ ,  $0 < \beta < \alpha$ , then

$${}_a D_x^\alpha u(x) = {}_a D_x^{\alpha-\beta} {}_a D_x^\beta u. \quad (2.11)$$

**Lemma 2.9** (see [2]). For  $u \in H_0^\alpha(\Omega)$ , one has

$$\|u\|_{L^2(\Omega)} \leq c |u|_{H_0^\alpha}. \quad (2.12)$$

For  $0 < \beta < \alpha$ ,

$$|u|_{H_0^\beta(\Omega)} \leq c |u|_{H_0^\alpha}. \quad (2.13)$$

Since  $J_s^\alpha$ ,  $J^\alpha$ , and  $H^\alpha$  are equal with equivalent seminorm and norm, the norms with each space which will be used following are without distinction, and the notations are used seminorm  $|\cdot|_\alpha$  and norm  $\|\cdot\|_\alpha$ .

### 3. Finite Element Approximation

Let  $\Omega = [a, b]$ , and  $0 \leq \beta < 1$ . Define  $\alpha = (1 + \beta)/2$ . In this section, we will formulate a fully discrete Galerkin finite element method for a type of nonlinear anomalous diffusion equation as follows.

*Problem 1* (Nonlinear spacial anomalous diffusion equation). We consider equations of the form

$$\begin{aligned} \frac{\partial u}{\partial t} &= D\left(a(u)_a D_x^\beta u\right) + b(u)Du + f(x, t, u), \quad (x, t) \in \Omega \times (0, T], \\ u(x, t) &= \phi(x, t), \quad x \in \partial\Omega \times (0, T], \\ u(x, 0) &= g(x), \quad x \in \overline{\Omega}. \end{aligned} \quad (3.1)$$

We always assume that

$$0 < m < a(u) < M, \quad 0 < m < b(u) < M, \quad 0 < m < f(u) < M. \quad (3.2)$$

The algorithm and analysis in this paper are applicable for a large class of linear and nonlinear functions (including polynomials and exponentials) in the unknown variables. Throughout the paper, we assume the following mild Lipschitz continuity conditions on  $a$ ,  $b$ , and  $f$ : there exist positive constants  $L$  and  $c$  such that for  $x \in \Omega, t \in (0, T]$ , and  $s, r \in R$ ,

$$|a(x, t, s) - a(x, t, r)| \leq L|s - r|, \quad (3.3)$$

$$|b(x, t, s) - b(x, t, r)| \leq L|s - r|, \quad (3.4)$$

$$|f(x, t, s) - f(x, t, r)| \leq L|s - r|. \quad (3.5)$$

In order to derive a variational form of Problem 1, we suppose that  $u$  is a sufficiently smooth solution of Problem 1. Multiplying an arbitrary  $v \in H_0^\alpha(\Omega)$  in both sides yields

$$\int_\Omega \frac{\partial u}{\partial t} v \, dx = \int_\Omega D\left(a(u)_a D_x^\beta u\right) v \, dx + \int_\Omega b(u) Duv \, dx + \int_\Omega f(x, t, u) v \, dx. \quad (3.6)$$

Rewriting the above expression yields

$$\int_\Omega \frac{\partial u}{\partial t} v \, dx + \int_\Omega a(u)_a D_x^\beta u Dv \, dx - \int_\Omega b(u) Duv \, dx = \int_\Omega f(x, t, u) v \, dx. \quad (3.7)$$

We define the associated bilinear form  $A : J_0^\alpha(\Omega) \times J_0^\alpha(\Omega) \rightarrow R$  as

$$A(u, v) = \left( a(u)_a D_x^\beta u, Dv \right) - (b(u) Du, v), \quad (3.8)$$

where  $(\cdot, \cdot)$  denotes the inner product on  $L^2(\Omega)$  and  $J_0^\alpha(\Omega)$ .

For given  $f \in J^{-\alpha}(\Omega)$ , we define the associated function  $F : J_0^\alpha(\Omega) \rightarrow R$  as

$$F(v) = \langle f, v \rangle. \quad (3.9)$$

*Definition 3.1.* A function  $u \in J_0^\alpha(\Omega)$  is a variational solution of Problem 1 provided that

$$\left( \frac{\partial u}{\partial t}, v \right) + A(u, v) = F(v), \quad \forall v \in J_0^\alpha(\Omega). \quad (3.10)$$

Now we are ready to describe a fully discrete Galerkin finite element method to solve nonlinear Problem 1. In our new scheme, the finite element trial and test spaces for Problem 1 are chosen to be same.

For a positive integer  $N$ , let  $\prod^t = \{t_n\}_{n=0}^N$  be a uniform partition of the time interval  $(0, T]$  such that  $t_n = n\tau$ , where  $\tau = T/N$ , and let  $t_{n-1/2} = t_n - \tau/2$ . Throughout the paper, we use the following notation for a function  $\phi$ :

$$\phi^n = \phi(t_n), \quad \bar{\partial}_t \phi^n = \frac{\phi^n - \phi^{n-1}}{\tau}, \quad \bar{\phi}^n = \frac{\phi^n + \phi^{n-1}}{2}, \quad \tilde{\phi}^n = \frac{3\phi^{n-1} - \phi^{n-2}}{2}. \quad (3.11)$$

Let  $\mathcal{K}_h = \{K\}$  be a partition of spatial domain  $\Omega$ . Define  $h_k$  as the diameter of the element  $K$  and  $h = \max_{K \in \mathcal{K}_h} h_K$ . And let  $S_h$  be a finite element space

$$S_h = \{v \in H_0^\alpha(\Omega) : v|_K \in P_{r-1}(K), K \in \mathcal{K}_h\}, \quad (3.12)$$

where  $P_{r-1}(K)$  is the set of polynomials of degree  $r-1$  on a given domain  $K$ . And the functions in  $S_h$  are continuous on  $\Omega$ . Our fully discrete quadrature scheme to solve Problem 1 is to find  $u_h$ : for  $v \in S_h$  such that

$$\left( \bar{\partial}_t u_h^n, v \right) + \left( a(\tilde{u}_h^n)_a D_x^\beta \bar{u}_h^n, Dv \right) - (b(\tilde{u}_h^n) D\bar{u}_h^n, v) = \langle f(\tilde{u}_h^n), v \rangle. \quad (3.13)$$

The linear systems in the above equation requires selecting the value of  $u_h^0$  and  $u_h^1$ . Given  $u_h^0$  depending on the initial data  $g(x)$ , we select  $u_h^1$  by solving the following predictor-corrector linear systems:

$$\begin{aligned} & \left( \frac{u_h^{1,0} - u_h^0}{\tau}, v \right) + \left( a(u_h^0) {}_a D_x^\beta \frac{u_h^{1,0} + u_h^0}{2}, Dv \right) - \left( b(u_h^0) D \frac{u_h^{1,0} + u_h^0}{2}, v \right) = \langle f(u_h^0), v \rangle, \\ & \left( \frac{u_h^1 - u_h^0}{\tau}, v \right) + \left( a \left( \frac{u_h^{1,0} + u_h^0}{2} \right) {}_a D_x^\beta \frac{u_h^1 + u_h^0}{2}, Dv \right) - \left( b \left( \frac{u_h^{1,0} + u_h^0}{2} \right) D \frac{u_h^1 + u_h^0}{2}, v \right) \\ & = \left\langle f \left( \frac{u_h^{1,0} + u_h^0}{2} \right), v \right\rangle. \end{aligned} \quad (3.14)$$

**Lemma 3.2.** For  $u, v, w \in J_{s,0}^\alpha(\Omega)$ ,  $0 < m \leq a(u) \leq M$ ,  $\alpha = (1 + \beta)/2$ , there exist constants  $\gamma_1, \gamma_2$  such that

$$\left( a(u) {}_a D_x^\beta u, Dv \right) \leq \gamma_1 \|u\|_\alpha \cdot \|v\|_\alpha, \quad \left( a(w) {}_a D_x^\beta v, Dv \right) \geq \gamma_2 \|v\|_\alpha^2. \quad (3.15)$$

*Proof.* With the assumption of  $a(u)$  in (3.3) and the property of dual space

$$\begin{aligned} \left( a(w) {}_a D_x^\beta u, Dv \right) & \leq \left\| a(w) {}_a D_x^\beta u \right\|_{1-\alpha} \cdot \|Dv\|_{-(1-\alpha)} \\ & \leq Mc \|u\|_{1-\alpha+\beta} \cdot \|v\|_{-(1-\alpha)+1} \leq \gamma_1 \|u\|_\alpha \cdot \|v\|_\alpha, \\ \left( a(w) {}_a D_x^\beta v, Dv \right) & = - \left( Da(w) {}_a D_x^\beta v, v \right) \\ & = - \left( {}_a D_x^{(1-\beta)/2} a(w) {}_a D_x^\beta v, {}_x D_b^{(1+\beta)/2} v \right) \geq m |v|_{J_s^\alpha}^2 \geq \gamma_2 \|v\|_\alpha^2. \end{aligned} \quad (3.16)$$

□

**Lemma 3.3** (see [2]). For  $\Omega \subset R^n$ ,  $\alpha > n/4$ ,  $v, w \in H_0^\alpha(\Omega)$ ,  $\varepsilon > 0$ , one has

$$(vb(w), \nabla v) \leq c_0 \frac{(q\varepsilon)^{-p/q}}{p} \|\nabla b(w)\|^p \cdot \|v\|^2 + \varepsilon \|v\|_\alpha^2, \quad (3.17)$$

where  $p = 4\alpha/(4\alpha - n)$ ,  $q = 4\alpha/n$ .

**Theorem 3.4.** Let  $u_h^n$  be bounded, then for a sufficiently small step  $\tau$ , there exists a unique solution  $u_h^n \in S_h$  satisfying scheme (3.13).

*Proof.* As scheme represents a finite system of problem, the continuity and coercivity of  $(\bar{u}_h^n, \bar{w}_h^n)/\tau + A(\bar{u}_h^n, \bar{w}_h^n)$  is the sufficient and essential condition for the existence and uniqueness of  $u_h^n$ . Let  $v = \bar{u}_h^n$ ,  $w = \bar{w}_h^n$ , then

$$\begin{aligned} \frac{(v, v)}{\tau} + A(v, v) &= \frac{(v, v)}{\tau} + \left( a(w)_a D_x^\beta v, Dv \right) - (b(w)Dv, v) \\ &\geq \frac{\|v\|^2}{\tau} + \gamma_2 \|v\|_\alpha - c_0 \|Db(w)\|^2 \|v\|^2 - \varepsilon \|v\|_\alpha^2 \\ &= (\gamma_2 - \varepsilon) \|v\|_\alpha^2 + \left( \tau^{-1} - c_0 \|Db(w)\|^2 \right) \|v\|^2 \\ &\geq c \|v\|_\alpha^2. \end{aligned} \quad (3.18)$$

For the chosen sufficiently small  $\tau$ , the above inequality holds.

$$\begin{aligned} \frac{(v, w)}{\tau} + A(v, w) &= \frac{(v, w)}{\tau} + \left( a(u)_a D_x^\beta v, Dw \right) + (Db(u)v, Dw) \\ &\leq \frac{\|u\| \cdot \|w\|}{\tau} + \gamma_1 \|v\|_\alpha \|w\|_\alpha + \|v\| \cdot \|D(b(u)w)\| \\ &\leq \frac{\|u\| \cdot \|w\|}{\tau} + \gamma_1 \|v\|_\alpha \|w\|_\alpha + M \frac{\|v\| \cdot \|w\|}{h} \\ &\leq c \|v\|_\alpha \|w\|_\alpha. \end{aligned} \quad (3.19)$$

Hence, the scheme (3.13) is uniquely solvable for  $u_h^n$ .

Let  $\rho^n = P_h u^n - u^n$ , and  $\theta^n = u_h^n - P_h u^n$ , then

$$u_h^n - u^n = u_h^n - P_h u^n + P_h u^n - u^n = \theta^n + \rho^n, \quad (3.20)$$

where  $P_h u^n$  is a Rits-Galerkin projection operator defined as follows:

$$\begin{aligned} \left( a(w)_a D_x^\beta (u^n - P_h u^n), Dv \right) &= 0, \\ \left( a(u_0)_a D_x^\beta (u^n - P_h u^n), Dv \right) &= 0. \end{aligned} \quad (3.21)$$

□

**Lemma 3.5.** Let  $a(u)$ ,  $b(u)$  be smooth functions on  $\Omega$ ,  $0 < m \leq a(u)$ ,  $b(u) \leq M$ , and  $P_h u^n$  is defined as above, then

$$\begin{aligned} \|_a D_x^\alpha (u^n - P_h u^n)\| &\leq ch^{k+1-\alpha} \|u\|_{k+1}, \\ \|(P_h u^n - u^n)\| &\leq ch^{k+1} \|u\|_{k+1}. \end{aligned} \quad (3.22)$$



*Proof.* Using the definition of  $P_h u^n$ , one gets

$$\begin{aligned} \|{}_a D_x^\alpha (P_h u^n - u^n)\|^2 &= |({}_a D_x^\alpha (P_h u^n - u^n), {}_a D_x^\alpha (P_h u^n - u^n))| \\ &\leq c \|{}_a D_x^\alpha (P_h u^n - u^n)\| \cdot \|{}_a D_x^\alpha (\chi - u^n)\|, \end{aligned} \quad (3.23)$$

where  $\chi \in S_h$ . Utilizing the interpolation of  $I_h u^n$  leads to

$$\|{}_a D_x^\alpha (P_h u^n - u^n)\| \leq \inf_{\chi \in S_h} c \|\chi - u\|_\alpha \leq c \|I_h u^n - u^n\|_\alpha \leq c h^{k+1-\alpha} \|u\|_{k+1}. \quad (3.24)$$

Next we estimate  $\|P_h u^n - u^n\|$ . For all  $\phi \in L^2(\Omega)$ ,  $w$  is the solution of the following equation:

$$\begin{aligned} -{}_a D_x^{2\alpha} w &= \phi, \quad w \in \Omega, \\ w &= 0, \quad w \in \partial\Omega. \end{aligned} \quad (3.25)$$

So we have

$$\|w\|_{2\alpha} \leq \gamma_3 \|\phi\|. \quad (3.26)$$

For all  $\chi \in S_h$ , with the help of approximation properties of  $S_h$  and the weak form, we can obtain

$$\begin{aligned} (P_h u^n - u^n, \phi) &= -({}_a D_x^{2\alpha} w, \phi) = -({}_a D_x^\alpha (P_h u^n - u^n), {}_a D_x^\alpha w) \\ &= -({}_a D_x^\alpha (P_h u^n - u^n), {}_a D_x^\alpha (w - \chi)) \leq \|P_h u^n - u^n\|_\alpha \|w - \chi\|_\alpha \\ &\leq \|P_h u^n - u^n\|_\alpha \inf_{\chi \in S_h} \|w - \chi\|_\alpha \\ &\leq c h^{r-\alpha} \|u\|_r h^\alpha \|w\|_{2\alpha} = c h^r \|u\|_r \|\phi\|, \end{aligned} \quad (3.27)$$

$$\|P_h u^n - u^n\| = \sup_{0 \neq \phi \in L^2(\Omega)} \frac{(P_h u^n - u^n, \phi)}{\|\phi\|} \leq c h^r \|u\|_r.$$

□

**Lemma 3.6** (see [21]). Let  $T_h$ ,  $0 < h \leq 1$ , denote a quasiuniform family of subdivisions of a polyhedral domain  $\Omega \subset \mathbb{R}^d$ . Let  $(K', P, N)$  be a reference finite element such that  $P \subset W^{l,p}(K') \cap W^{m,q}(K')$  is a finite-dimensional space of functions on  $K'$ ,  $N$  is a basis for  $P'$ , where  $1 \leq p \leq \infty, 1 \leq p \leq \infty$ , and  $0 \leq m \leq l$ . For  $K \in T_h$ , let  $(K, P_K, N_K)$  be the affine equivalent element, and  $V_h = v : v$  is measurable and  $v|_K \in P_K$ , for all  $K \in T_h$ . Then there exists a constant  $C = C(l, p, q)$  such that

$$\left[ \sum_{K \in T_h} \|v\|_{W^{l,p}(K)}^2 \right]^{1/p} \leq C h^{m-l+\min(0, d/p-d/q)} \cdot \left[ \sum_{K \in T_h} \|v\|_{W^{m,q}(K)}^q \right]^{1/q}. \quad (3.28)$$

The following Gronwall's lemma is useful for the error analysis later on.

**Lemma 3.7** (see [2]). Let  $\Delta t, H$  and  $a_n, b_n, c_n, \gamma_n$  (for integer  $n \geq 0$ ) be nonnegative numbers such that

$$a_N + \Delta t \sum_{n=0}^N b_n \leq \Delta t \sum_{n=0}^N \gamma_n a_n + \Delta t \sum_{n=0}^N c_n + H, \quad (3.29)$$

for  $N \geq 0$ . Suppose that  $\Delta t \gamma_n < 1$ , for all  $n$ , and set  $\sigma_n = (1 - \Delta t \gamma_n)^{-1}$ . Then

$$a_N + \Delta t \sum_{n=0}^N b_n \leq \exp \left( \Delta t \sum_{n=0}^N \sigma_n \gamma_n \right) \left\{ \Delta t \sum_{n=0}^N c_n + H \right\}, \quad (3.30)$$

for  $N \geq 0$ .

The following norms are also used in the analysis:

$$\begin{aligned} \|v\|_{\infty, k} &= \max_{0 \leq n \leq N} \|v^n\|_k, \\ \|v\|_{0, k} &= \left[ \sum_{n=0}^N \tau \|v^n\|_k^2 \right]^{1/2}. \end{aligned} \quad (3.31)$$

**Theorem 3.8.** Assume that Problem 1 has a solution  $u$  satisfying  $u_{tt}, u_{ttt} \in L^2(0, T, L^2(\Omega))$  with  $u, u_t \in L^2(0, T, H^{k+1})$ . If  $\Delta t \leq ch$ , then the finite element approximation is convergent to the solution of Problem 1 on the interval  $(0, T]$ , as  $\Delta t, h \rightarrow 0$ . The approximation  $u_h$  also satisfies the following error estimates

$$\begin{aligned} \|u - u_h\|_{0, \alpha} &\leq C \left( h^{k+1} \|u_t\|_{0, k+1} + h^{k+1-\alpha} \|u\|_{0, k+1} + \tau^2 \|u_{tt}\|_{0, 0} \right. \\ &\quad \left. + \tau h^{k+1-\alpha} \|u_{tt}\|_{0, k+1} + \tau^2 \|u_{ttt}\|_{0, 0} \right), \end{aligned} \quad (3.32)$$

$$\begin{aligned} \|u - u_h\|_{\infty, 0} &\leq C \left( h^{k+1} \|u_t\|_{0, k+1} + h^{k+1-\alpha} \|u\|_{0, k+1} + \tau^2 \|u_{tt}\|_{0, 0} \right. \\ &\quad \left. + \tau h^{k+1-\alpha} \|u_{tt}\|_{0, k+1} + \tau^2 \|u_{tt}\|_{0, 0} + h^{k+1} \|u\|_{\infty, k+1}^2 \right). \end{aligned} \quad (3.33)$$

*Proof.* For  $t = t_n - \tau/2 = t_{n-1/2}$ ,  $n = 0, 1, \dots, N$ , find  $u^{n-1/2}$  such that

$$\left( \partial_t u^{n-1/2}, v \right) + \left( a \left( u^{n-1/2} \right) {}_a D_x u^{n-1/2}, Dv \right) - \left( b \left( u^{n-1/2} \right) D u^{n-1/2}, v \right) = \left\langle f \left( u^{n-1/2} \right), v \right\rangle. \quad (3.34)$$

Subtracting the above equation from the fully discrete scheme (3.13), and substituting  $u_h^n - u^n = (u_h^n - P_h u^n) + (P_h u^n - u^n) = \theta^n + \rho^n$  into it, we obtain the following error formulation relating to  $\theta^n$  and  $\rho^n$ :

$$\begin{aligned}
& (\bar{\partial}_t \theta^n, v) + (a(\tilde{u}_h^n) {}_a D_x^\beta \bar{\theta}^n, Dv) - (b(\tilde{u}_h^n) D\bar{\theta}^n, v) \\
&= (a(\tilde{u}_h^n) {}_a D_x^\beta \bar{I}_h u^n, Dv) + (b(\tilde{u}_h^n) {}_a D_x^\beta \bar{I}_h u^n, v) + (\partial_t u^{n-1/2}, v) - (\bar{\partial}_t I_h u^n, v) \\
&+ (a(u^{n-1/2}) {}_a D_x^\beta u^{n-1/2}, Dv) - (b(u^{n-1/2}) D u^{n-1/2}, v) + (f(\tilde{u}_h^n), v) - (f(u^{n-1/2}), v) \\
&= -(a(\tilde{u}_h^n) {}_a D_x^\beta \bar{\rho}^n, Dv) + \left\{ (a(u^{n-1/2}) {}_a D_x^\beta u^{n-1/2} - a(\tilde{u}_h^n) {}_a D_x^\beta \bar{u}^n, Dv) \right\} \\
&+ (b(\tilde{u}_h^n) D\bar{\rho}^n, v) + \left\{ (b(\tilde{u}_h^n) D\bar{u}^n - (b(u^{n-1/2}) D u^{n-1/2}, Dv) \right\} \\
&+ \left\{ (f(\tilde{u}_h^n) - f(u^{n-1/2}), v) \right\} + \left\{ (\partial_t u^{n-1/2} - \bar{\partial}_t I_h u^n, v) \right\} \\
&= R_1(v) + R_2(v) + R_3(v) + R_4(v) + R_5(v) + R_6(v).
\end{aligned} \tag{3.35}$$

Setting  $v = \bar{\theta}^n$ , we obtain

$$\begin{aligned}
& (\bar{\partial}_t \theta^n, \bar{\theta}^n) + (a(\tilde{u}_h^n) {}_a D_x^\beta \bar{\theta}^n, D\bar{\theta}^n) - (b(\tilde{u}_h^n) D\bar{\theta}^n, \bar{\theta}^n) \\
&= R_1(\bar{\theta}^n) + R_2(\bar{\theta}^n) + R_3(\bar{\theta}^n) + R_4(\bar{\theta}^n) + R_5(\bar{\theta}^n) + R_6(\bar{\theta}^n).
\end{aligned} \tag{3.36}$$

Note that

$$(\bar{\partial}_t \theta^n, \bar{\theta}^n) = \left( \frac{\theta^n - \theta^{n-1}}{\tau}, \frac{\theta^n + \theta^{n-1}}{2} \right) = \frac{1}{2\tau} (\|\theta^n\|^2 - \|\theta^{n-1}\|^2). \tag{3.37}$$

According to (3.2) and Lemma 3.2, we have

$$(a(\tilde{u}_h^n) {}_a D_x^\beta \bar{\theta}^n, D\bar{\theta}^n) \geq m \|\bar{\theta}^n\|_\alpha^2 \geq c \left( \|\theta^n\|_\alpha^2 + \|\theta^{n-1}\|_\alpha^2 \right). \tag{3.38}$$

From Lemma 3.3, the following inequality can be derived:

$$\begin{aligned}
& (b(\tilde{u}_h^n) \bar{\theta}^n, D\bar{\theta}^n) \leq c_0 \varepsilon_2^{-c_1} \|Db(\tilde{u}_h^n)\|^{c^2} \|\bar{\theta}^n\|^2 + \varepsilon_3 \|\bar{\theta}^n\|_\alpha^2 \\
&= c_0 \varepsilon_2^{-c_1} \|Db(\tilde{u}_h^n)\|^{c^2} \left\| \frac{\theta^n + \theta^{n-1}}{2} \right\|^2 + \varepsilon_3 \left\| \frac{\theta^n + \theta^{n-1}}{2} \right\|_\alpha^2 \\
&\leq c_3 \varepsilon_2^{-c_1} \|Db(\tilde{u}_h^n)\|^{c^2} \left( \|\theta^n\|^2 + \|\theta^{n-1}\|^2 \right) + c_4 \varepsilon_3 \left( \|\theta^n\|_\alpha^2 + \|\theta^{n-1}\|_\alpha^2 \right).
\end{aligned} \tag{3.39}$$

Substituting (3.37)–(3.39) into (3.36) then multiplying (3.36) by  $2\tau$ , summing from  $n = 1$  to  $N$ , we have

$$\begin{aligned}
& \|\theta^n\|^2 - \|\theta^2\|^2 + \tau \sum_{n=1}^N (2mc - 2c_4\epsilon_3) \left( \|\theta^n\|_\alpha^2 + \|\theta^{n-1}\|_\alpha^2 \right) \\
& \leq 2\tau \sum_{n=1}^N c_3\epsilon_2^{-c_1} \|Db(\tilde{u}_h^n)\|^{c_2} \left( \|\theta^n\|^2 + \|\theta^{n-1}\|^2 \right) \\
& \quad + 2\tau \sum_{n=3}^N \left[ R_1(\bar{\theta}^n) + R_2(\bar{\theta}^n) + R_3(\bar{\theta}^n) + R_4(\bar{\theta}^n) + R_5(\bar{\theta}^n) + R_6(\bar{\theta}^n) \right].
\end{aligned} \tag{3.40}$$

We now estimate  $R_1$  to  $R_6$  in the right hand of (3.40),

$$\begin{aligned}
R_1(\bar{\theta}^n) &= \left( {}_aD_x^{1-\alpha} \left( a(\tilde{u}_h^n) {}_aD_x^\beta \bar{\rho}^n \right), {}_aD_x^\alpha \bar{\theta}^n \right) \\
&\leq M \left( {}_aD_x^\alpha \bar{\rho}^n, {}_aD_x^\alpha \bar{\theta}^n \right) \leq M \|{}_aD_x^\alpha \bar{\rho}^n\| \|{}_aD_x^\alpha \bar{\theta}^n\| \\
&\leq \epsilon_4 \|\bar{\theta}^n\|_\alpha^2 + \frac{c_5^2}{4\epsilon_4} \|\bar{\rho}^n\|_\alpha^2 \\
&= \frac{\epsilon_4}{2} \|\rho^n + \rho^{n-1}\|_\alpha^2 + \frac{c_5^2}{16\epsilon_4} \|\theta^n + \theta^{n-1}\|_\alpha^2 \\
&\leq \epsilon_4 c_6 \left( \|\theta^n\|_\alpha^2 + \|\theta^{n-1}\|_\alpha^2 \right) + \frac{c_7}{\epsilon_4} \left( \|\rho^n\|_\alpha^2 + \|\rho^{n-1}\|_\alpha^2 \right).
\end{aligned} \tag{3.41}$$

Secondly, we deduce the estimation of  $R_2$ ,

$$\begin{aligned}
R_2(\bar{\theta}^n) &= \left( -a(\tilde{u}_h^n) {}_aD_x^\beta \bar{u}^n, D\bar{\theta}^n \right) + \left( a(u^{n-1/2}) {}_aD_x^\beta u^{n-1/2}, D\bar{\theta}^n \right) \\
&= \left( \left( a(u^{n-1/2}) - a(\tilde{u}_h^n) \right) {}_aD_x^\beta \bar{u}^n, D\bar{\theta}^n \right) + \left( a(u^{n-1/2}) \left( {}_aD_x^\beta u^{n-1/2} - {}_aD_x^\beta \bar{u}^n \right), D\bar{\theta}^n \right) \\
&= R_{21} + R_{22},
\end{aligned} \tag{3.42}$$

where

$$\begin{aligned}
R_{21} &= \left( \left[ a(u^{n-1/2}) - a(\tilde{u}_h^n) \right] {}_aD_x^\beta \bar{u}^n, D\bar{\theta}^n \right) \\
&\leq \frac{c_8}{4\epsilon_5} \left\| \left[ a(u^{n-1/2}) - a(\tilde{u}_h^n) \right] {}_aD_x^\beta \bar{u}^n \right\|_{1-\alpha}^2 + \epsilon_5 \|D\bar{\theta}^n\|_{\alpha-1}^2 \\
&\leq c_9 \left\| a(u^{n-1/2}) - a(\tilde{u}_h^n) \right\| \left\| {}_aD_x^\beta \bar{u}^n \right\|_{1-\alpha}^2 + \epsilon_5 \|\bar{\theta}^n\|_\alpha^2 \\
&\leq c_9 L \|u^{n-1/2} - \tilde{u}_h^n\| + \epsilon_5 \|\bar{\theta}^n\|_\alpha^2,
\end{aligned}$$

$$\begin{aligned}
R_{22} &= \left( a(u^{n-1/2}) \left( {}_a D_x^\beta u^{n-1/2} - {}_a D_x^\beta \bar{u}^n \right), D\bar{\theta}^n \right) \\
&\leq \frac{c_{10}}{4\varepsilon_6} \left\| a(u^{n-1/2}) \left[ {}_a D_x^\beta u^{n-1/2} - {}_a D_x^\beta \bar{u}^n \right] \right\|_{1-\alpha}^2 + \varepsilon_6 \left\| D\bar{\theta}^n \right\|_{-1+\alpha}^2 \\
&\leq c_{10} \left\| a(u^{n-1/2}) \right\|^2 \left\| {}_a D_x^\beta u^{n-1/2} - {}_a D_x^\beta \bar{u}^n \right\|_{1-\alpha}^2 + \varepsilon_6 \left\| \bar{\theta}^n \right\|_\alpha^2 \\
&\leq c_{10} M^2 \left\| u^{n-1/2} - \bar{u}^n \right\|_\alpha^2 + \varepsilon_6 c \left( \left\| \theta^n \right\|_\alpha^2 + \left\| \theta^{n-1} \right\|_\alpha^2 \right).
\end{aligned} \tag{3.43}$$

The estimations of  $\|\tilde{u}^n - u^{n-1/2}\|$  and  $\|\bar{u}^n - u^{n-1/2}\|_\alpha$  can be derived as follows:

$$\begin{aligned}
\left\| \tilde{u}^n - u^{n-1/2} \right\| &= \left\| \frac{3}{2} \left[ u^{n-1/2} - \frac{\tau}{2} u_t^{n-1/2} + \frac{u_{tt}^{n-1/2}}{2!} \left( \frac{\tau}{2} \right)^2 + O(\tau^3) \right] \right. \\
&\quad \left. - \frac{1}{2} \left[ u^{n-1/2} - \frac{3\tau}{2} u_t^{n-1/2} + \frac{u_{tt}^{n-1/2}}{2!} \left( \frac{3\tau}{2} \right)^2 + O(\tau^3) \right] - u^{n-1/2} \right\| \\
&\leq c_{11} \tau^2 \|u_{tt}(t_{n-1/2})\| \leq c_{11} \tau^2 \int_{t_{n-1}}^{t_n} \|u_{tt}(\cdot, s)\| ds, \\
\left\| \bar{u}^n - u^{n-1/2} \right\|_\alpha &= \left\| \tau^{-1} \left\{ \int_{t_{n-1/2}}^{t_n} (s - t_n)^2 u_{tt}(s) ds + \int_{t_{n-1}}^{t_{n-1/2}} (s - t_{n-1})^2 u_{tt}(s) ds \right\} \right\|_\alpha \\
&\leq c_{12} \tau \left\| \int_{t_{n-1}}^{t_n} u_{tt}(s) ds \right\|_\alpha \\
&\leq c_{12} \tau \int_{t_{n-1}}^{t_n} \|u_{tt}(s)\|_\alpha ds \\
&\leq c_{12} \tau h^{k+1-\alpha} \int_{t_{n-1}}^{t_n} \|u_{tt}(s)\|_{k+1} ds.
\end{aligned} \tag{3.44}$$

Thirdly, it is turn to consider  $R_3$ ,

$$\begin{aligned}
R_3(\bar{\theta}^n) &= \left( b(\tilde{u}_h^n) D\bar{\rho}^n, \bar{\theta}^n \right) \leq \|b(\tilde{u}_h^n) D\bar{\rho}^n\|_{-\alpha} \left\| \bar{\theta}^n \right\|_\alpha \\
&\leq \frac{c_{13}}{4\varepsilon_7} \|b(\tilde{u}_h^n)\|^2 \left\| \bar{\rho}^n \right\|_{1-\alpha}^2 + \varepsilon_7 \left\| \bar{\theta}^n \right\|_\alpha^2 \\
&\leq \frac{c_{14}}{4\varepsilon_7} \left( \left\| \rho^n \right\|_{1-\alpha}^2 + \left\| \rho^{n-1} \right\|_{1-\alpha}^2 \right) + \varepsilon_7 c_{15} \left( \left\| \theta^n \right\|_\alpha^2 + \left\| \theta^{n-1} \right\|_\alpha^2 \right).
\end{aligned} \tag{3.45}$$

Next,

$$\begin{aligned}
 R_4(\bar{\theta}^n) &= \left( b(\tilde{u}_h^n) D\bar{u}^n, \bar{\theta}^n \right) - \left( b(u^{n-1/2}) D u^{n-1/2}, \bar{\theta}^n \right) \\
 &= \left( \left( b(\tilde{u}_h^n) D\bar{u}^n - b(u^{n-1/2}) D\bar{u}^n \right), \bar{\theta}^n \right) + \left( b(u^{n-1/2}) (D\bar{u}^n - D u^{n-1/2}), \bar{\theta}^n \right) \\
 &= R_{41} + R_{42},
 \end{aligned} \tag{3.46}$$

where

$$\begin{aligned}
 R_{41} &\leq \frac{c_{16}}{4\varepsilon_8} \left\| \left\{ b(\tilde{u}_h^n) - b(u^{n-1/2}) \right\} D\bar{u}^n \right\|_{1-\alpha}^2 + \varepsilon_8 \left\| \bar{\theta}^n \right\|_\alpha^2 \\
 &\leq \frac{c_{16}L}{4\varepsilon_8} \left\| \tilde{u}_h^n - u^{n-1/2} \right\|^2 \left\| D\bar{u}^n \right\|_{1-\alpha}^2 + \varepsilon_8 \left\| \bar{\theta}^n \right\|_\alpha^2 \\
 &= \frac{c_{16}L}{4\varepsilon_8} \left\| \tilde{u}_h^n - \tilde{u}^n + \tilde{u}^n - u^{n-1/2} \right\|^2 \left\| D\bar{u}^n \right\|_{1-\alpha}^2 + \varepsilon_8 \left\| \bar{\theta}^n \right\|_\alpha^2 \\
 &\leq c_{17} \left\| \tilde{u}_h^n - \tilde{u}^n \right\|^2 + c_{17} \left\| \tilde{u}^n - u^{n-1/2} \right\|^2 + \varepsilon_8 \left\| \bar{\theta}^n \right\|_\alpha^2 \\
 &\leq c_{17} \left\| \tilde{\theta}^n + \tilde{\rho}^n \right\|^2 + c_{17} \left\| \tilde{u}^n - u^{n-1/2} \right\|^2 + \varepsilon_8 \left\| \bar{\theta}^n \right\|_\alpha^2 \\
 &\leq c_{18} \left( \left\| \tilde{\theta}^n \right\|^2 + \left\| \tilde{\rho}^n \right\|^2 \right) + c_{17} \left\| \tilde{u}^n - u^{n-1/2} \right\|^2 + \varepsilon_8 \left\| \bar{\theta}^n \right\|_\alpha^2.
 \end{aligned} \tag{3.47}$$

Rewriting  $R_{42}$  by the aid of (3.20), we have

$$R_{42} \leq \frac{c_{19}}{4\varepsilon_9} \left\| \bar{u}^n - u^{n-1/2} \right\|^2 + \varepsilon_9 \left\| \bar{\theta}^n \right\|_\alpha^2. \tag{3.48}$$

The estimation of  $R_5$  is deduced as follows:

$$\begin{aligned}
 R_5(\bar{\theta}^n) &\leq \left\| f(\tilde{u}_h^n) - f(u^{n-1/2}) \right\| \left\| \bar{\theta}^n \right\| \\
 &\leq L \left\| \tilde{u}_h^n - u^{n-1/2} \right\| \left\| \bar{\theta}^n \right\| \\
 &\leq \frac{Lc_{20}}{4\varepsilon_{10}} \left\| \tilde{u}_h^n - u^{n-1/2} \right\|^2 + \varepsilon_{10} \left\| \bar{\theta}^n \right\|^2 \\
 &\leq Lc_{21} \left( \left\| \tilde{\theta}^n + \tilde{\rho}^n \right\|^2 + \left\| \tilde{u}^n - u^{n-1/2} \right\|^2 \right) + \varepsilon_{10} \left\| \bar{\theta}^n \right\|^2 \\
 &\leq c_{22} \left( \left\| \tilde{\theta}^n \right\|^2 + \left\| \tilde{\rho}^n \right\|^2 \right) + Lc_{21} \left\| \tilde{u}^n - u^{n-1/2} \right\|^2 + \varepsilon_{10} \left\| \bar{\theta}^n \right\|^2.
 \end{aligned} \tag{3.49}$$

Last, we estimate  $R_6$ ,

$$\begin{aligned}
R_6(\bar{\theta}^n) &= (\partial_t u^{n-1/2}, \bar{\theta}^n) - (\bar{\partial}_t P_h u^n, \bar{\theta}^n) \\
&= (\partial_t u^{n-1/2} - \bar{\partial}_t u^n, \bar{\theta}^n) + (\bar{\partial}_t u^n - \bar{\partial}_t P_h u^n, \bar{\theta}^n) \\
&= (\partial_t u^{n-1/2} - \bar{\partial}_t u^n, \bar{\theta}^n) + (\bar{\partial}_t \rho^n, \bar{\theta}^n) \\
&\leq \|\partial_t u^{n-1/2} - \bar{\partial}_t u^n\| \|\theta^n\| + \|\bar{\partial}_t \rho^n\| \|\theta^n\|,
\end{aligned} \tag{3.50}$$

where

$$\begin{aligned}
\|\partial_t u^{n-1/2} - \bar{\partial}_t u^n\| &= (2\tau)^{-1} c_{23} \left\| \int_{t_{n-1/2}}^{t_n} (s - t_n)^2 u_{ttt}(s) ds + \int_{t_{n-1}}^{t_{n-1/2}} (s - t_{n-1})^2 u_{ttt}(s) ds \right\| \\
&\leq c_{23} \tau \left\| \int_{t_{n-1}}^{t_n} u_{ttt}(s) ds \right\| \\
&\leq c_{23} \tau \int_{t_{n-1}}^{t_n} \|u_{ttt}(s)\| ds, \\
\|\bar{\partial}_t \rho^n\| &= \left\| \frac{\rho^n - \rho^{n-1}}{\tau} \right\| \leq \tau^{-1} \left\| \int_{t_{n-1}}^{t_n} \rho_t^n(s) ds \right\| \\
&\leq \tau^{-1} \int_{t_{n-1}}^{t_n} \|u_t(s)\| ds \leq \tau^{-1} \int_{t_{n-1}}^{t_n} 1 ds \int_{t_{n-1}}^{t_n} \|u_t(s)\| ds \\
&= \int_{t_{n-1}}^{t_n} \|u_t(s)\| \leq h^{k+1} \int_{t_{n-1}}^{t_n} \|u_t(s)\|_{k+1} ds.
\end{aligned} \tag{3.51}$$

The  $\|\theta^2\|$  should be estimated with (3.14). Let  $n = 1$  then subtracting (3.34) from the two equations of (3.14), respectively, one gets

$$\begin{aligned}
&(\bar{\partial}_t \theta^{1,0}, v) + \left( a(u_h^0) {}_a D_x^\beta \bar{\theta}^{1,0}, Dv \right) - b\left( (u_h^0) D\bar{\theta}^{1,0}, v \right) \\
&= -\left( a(u_h^0) {}_a D_x^\beta \bar{\rho}^{1,0}, Dv \right) - \left\{ \left( a(u^{1/2}) {}_a D_x^\beta u^{1/2} - a(u_h^0) {}_a D_x^\beta \bar{u}^{1,0}, Dv \right) \right\} \\
&\quad + \left( b(u_h^0) D\bar{\rho}^{1,0}, v \right) + \left\{ \left( b(u_h^0) D\bar{u}^{1,0} - b(u^{1/2}) Du^{1/2}, Dv \right) \right\} \\
&\quad + \left\{ \left( f(u_h^0) - f(u^{1/2}), v \right) \right\} + \left\{ \left( \partial_t u^{1/2} - \bar{\partial}_t I_h u^{1,0}, v \right) \right\} \\
&= R_1(v) + R_2(v) + R_3(v) + R_4(v) + R_5(v) + R_6(v),
\end{aligned}$$

$$\begin{aligned}
& (\bar{\partial}_t \theta^1, v) + \left( a \left( u_h^0 \right)_a D_x^\beta \bar{\theta}^1, Dv \right) - b \left( \left( u_h^0 \right) D \bar{\theta}^1, v \right) \\
&= - \left( a \left( \frac{u_h^0 + u_h^{1,0}}{2} \right) {}_a D_x^\beta \bar{\rho}^1, Dv \right) - \left\{ \left( a \left( u^{1/2} \right) {}_a D_x^\beta u^{1/2} - a \left( \frac{u_h^0 + u_h^{1,0}}{2} \right) {}_a D_x^\beta \bar{u}^1, Dv \right) \right\} \\
&+ \left( b \left( \frac{u_h^0 + u_h^{1,0}}{2} \right) D \bar{\rho}^1, v \right) + \left\{ \left( b \left( \frac{u_h^0 + u_h^{1,0}}{2} \right) D \bar{u}^1 - \left( b \left( u^{1/2} \right) D u^{1/2}, Dv \right) \right\} \\
&+ \left\{ \left( f \left( \frac{u_h^0 + u_h^{1,0}}{2} \right) - f \left( u^{1/2} \right), v \right) \right\} + \left\{ \left( \partial_t u^{1/2} - \bar{\partial}_t I_h u^1, v \right) \right\} \\
&= R_1(v) + R_2(v) + R_3(v) + R_4(v) + R_5(v) + R_6(v).
\end{aligned} \tag{3.52}$$

Setting  $v = \bar{\theta}^{1,0}$ , and using the similar estimation (see (3.40)), one has

$$\begin{aligned}
\left\| \theta^{1,0} \right\|^2 &\leq c \left\{ \tau^2 \int_{t_0}^{t_1} \|u_{tt}(s)\|_\alpha^2 ds + h^{2(k+1-\alpha)} \|u\|_{k+1}^2 + \tau^2 \int_{t_0}^{t_1} \|u_{ttt}(s)\|^2 ds \right. \\
&\quad \left. + ch^{2(k+1)} \int_{t_0}^{t_1} \|u_t(s)\|_{k+1}^2 ds \right\}.
\end{aligned} \tag{3.53}$$

Letting  $v = \bar{\theta}^1$ , applying the above result of  $\theta^{1,0}$ , and using the similar estimation (see (3.53)), we get

$$\begin{aligned}
\left\| \theta^1 \right\|^2 &\leq c \left\{ \tau^2 \int_{t_0}^{t_1} \|u_{tt}(s)\|_\alpha^2 ds + h^{2(k+1-\alpha)} \|u\|_{k+1}^2 + \tau^2 \int_{t_0}^{t_1} \|u_{ttt}(s)\|^2 ds \right. \\
&\quad \left. + ch^{2(k+1)} \int_{t_0}^{t_1} \|u_t(s)\|_{k+1}^2 ds \right\}.
\end{aligned} \tag{3.54}$$

Using  $T = N\tau$  and Gronwall's lemma, we get

$$\|\theta\|_{0,\alpha}^2 = \sum_{n=0}^N \tau \|\theta\|_\alpha^2. \tag{3.55}$$

Hence, using the interpolation property and

$$\|u - u_h\|_{0,\alpha} \leq \|\theta\|_{0,\alpha} + \|\rho\|_{0,\alpha'}, \tag{3.56}$$

the estimate (3.32) holds.



Also using the interpolation property, Gronwall's lemma, and the approximation properties, we get

$$\begin{aligned} \|u - u_h\|_{\infty,0} &\leq \| \theta \|_{\infty,0} + \| \rho \|_{\infty,0} \\ &\leq \max_{0 \leq n \leq N} \| \theta^n \|_{\infty,0}^2 + h^{2k+1} \| u \|_{\infty,k+1}^2, \end{aligned} \quad (3.57)$$

which is just the estimate (3.33).  $\square$

#### 4. Numerical Examples

In this section, we present the numerical results which confirm the theoretical analysis in Section 3.

Let  $K$  denote a uniform partition on  $[0, a]$ , and  $S_h$  the space of continuous piecewise linear functions on  $K$ , that is,  $k = 1$ . In order to implement the Galerkin finite element approximation, we adapt finite element discrete along the space axis, and finite difference scheme along the time axis. We associate shape function of space  $X_h$  with the standard basis of hat functions on the uniform grid of size  $h = 1/n$ . We have the predicted rates of convergence if the condition  $\Delta t = ch$  of

$$\begin{aligned} \|u - u_h\|_{0,\alpha} &\sim O(h^{2-\alpha}), \\ \|u - u_h\|_{\infty,0} &\sim O(h^{2-\alpha}), \end{aligned} \quad (4.1)$$

provided that the initial value  $\varphi(x)$  is smooth enough.

*Example 4.1.* The following equation

$$\begin{aligned} \frac{\partial u}{\partial t} &= D(u^2 {}_0D_x^{0.5} u(x, t)) - 2x(x-1) \left( \frac{2x^{1.5}}{\Gamma(2.5)} - \frac{x^{0.5}}{\Gamma(1.5)} \right) e^{-2t} Du - u(x, t) \\ &\quad - u^2 e^{-t} \left( \frac{2x^{0.5}}{\Gamma(1.5)} - \frac{x^{-0.5}}{\Gamma(0.5)} \right), \quad 0 \leq x \leq 1, \quad 0 \leq t \leq 1, \\ u(x, 0) &= x(x-1), \quad 0 \leq x \leq 1, \\ u(0, t) &= u(1, t) = 0, \quad 0 \leq t \leq 1, \end{aligned} \quad (4.2)$$

has a unique solution  $u(x, t) = e^{-t} x(x-1)$ .

If we select  $\Delta t = ch$  and note that the initial value  $u^0$  is smooth enough, then we have

$$\begin{aligned} \|u - u_h\|_{0,0.75} &\sim O(h^{1.25}), \\ \|u - u_h\|_{\infty,0} &\sim O(h^{1.25}). \end{aligned} \quad (4.3)$$

**Table 1:** Numerical error result for Example 4.1.

$h$	$\ u - u_h\ _{\infty,0}$	cvge. rate	$\ u - u_h\ _{0,0.75}$	cvge. rate
1/5	2.2216E-003	—	1.0213E-003	—
1/10	1.3551E-003	0.7132	6.0779E-004	0.74875
1/20	5.5865E-004	1.2784	2.3188E-004	1.3901
1/40	3.0515E-004	0.8724	1.0545E-004	1.1367
1/80	1.2423E-004	1.2964	3.9883E-005	1.4027
1/160	5.1033E-005	1.2835	2.1310E-005	0.9042

Table 1 includes numerical calculations over a regular partition of  $[0, 1]$ . We can observe the experimental rates of convergence agree with the theoretical rates for the numerical solution.

*Example 4.2.* The function  $u(x, t) = \cos(t)x^2(2-x)^2$  solves the equation in the following form:

$$\begin{aligned} \frac{\partial u}{\partial t} &= {}_0D_x^{1.7} u(x, t) + b(u)Du - u[4(1-x) + \tan t] + f(x, t), \quad x \in (0, 2), t \in [0, 1), \\ u(x, 0) &= x^2(2-x)^2, \quad 0 \leq x \leq 2, \\ u(0, t) &= 0, \quad u(2, t) = 0, \quad 0 \leq t \leq 1, \end{aligned} \quad (4.4)$$

where

$$\begin{aligned} b(u) &= \frac{\sqrt{u}}{\sqrt{\cos t}}, \\ f(x, t) &= \frac{\cos t}{\cos(0.85\pi)} \left[ \frac{24(x^{2.3} + (2-x)^{2.3})}{\Gamma(3.3)} - \frac{24(x^{1.3} + (2-x)^{1.3})}{\Gamma(2.3)} - \frac{8(x^{0.3} + (2-x)^{0.3})}{\Gamma(1.3)} \right]. \end{aligned} \quad (4.5)$$

If we select  $\Delta t = ch$ , then

$$\begin{aligned} \|u - u_h\|_{0,0.85} &\sim O(h^{1.15}), \\ \|u - u_h\|_{\infty,0} &\sim O(h^{1.15}). \end{aligned} \quad (4.6)$$

Table 2 shows the error results at different size of space grid. We can observe that the experimental rates of convergence still support the theoretical rates.

**Table 2:** Numerical error result for Example 4.2.

$h$	$\ u - u_h\ _{\infty,0}$	cvge. rate	$\ u - u_h\ _{0,0.85}$	cvge. rate
1/5	1.3010E-001	—	3.2223E-002	—
1/10	4.6402E-002	1.4878	1.4133E-002	1.1890
1/20	1.6843E-002	1.4620	6.2946E-003	1.1669
1/40	6.6019E-003	1.6843	2.8571E-003	1.1395
1/80	2.7979E-003	1.2386	1.3137E-003	1.1209
1/160	1.2665E-003	1.1434	6.0848E-004	1.1103

**Table 3:** Numerical error result for Example 4.3.

$h$	$\ u - u_h\ _{\infty,0}$	cvge. rate	$\ u - u_h\ _{0,0.85}$	cvge. rate
1/5	8.3052E-002	—	2.8009E-002	—
1/10	3.6038E-002	1.2045	1.0086E-002	1.4735
1/20	1.3839E-002	1.3807	3.2327E-003	1.6414
1/40	5.0631E-003	1.4507	1.1789E-003	1.4554
1/80	1.8920E-003	1.4201	5.9555E-004	0.9851
1/160	9.9899E-004	0.9214	3.0034E-004	0.9876

*Example 4.3.* Consider the following space-fractional differential equation with the nonhomogeneous boundary conditions,

$$\begin{aligned}
 \frac{\partial u}{\partial t} &= {}_0D_x^{1.7} u(x, t) - \frac{3}{x} \int_0^x u \, dx - \frac{2x^{0.3}e^{-t}}{\Gamma(1.3)}, \quad 0 \leq x \leq 1, \quad 0 \leq t \leq 1, \\
 u(x, 0) &= x^2, \quad 0 \leq x \leq 1, \\
 u(0, t) &= 0, \quad u(1, t) = e^{-t}, \quad 0 \leq t \leq 1,
 \end{aligned} \tag{4.7}$$

whose exact solution is  $u(x, t) = e^{-t}x^2$ .

We still choose  $\Delta t = ch$ , then get the convergence rates

$$\begin{aligned}
 \|u - u_h\|_{0,0.85} &\sim O(h^{1.15}), \\
 \|u - u_h\|_{\infty,0} &\sim O(h^{1.15}).
 \end{aligned} \tag{4.8}$$

The numerical results are presented in Table 3 which are in line with the theoretical analysis.

## 5. Conclusion

In this paper, we propose a fully discrete Galerkin finite element method to solve a type of fractional advection-diffusion equation numerically. In the temporal direction we use the modified Crank-Nicolson method, and in the spatial direction we use the finite element method. The error analysis is derived on the basis of fractional derivative space. The numerical results agree with the theoretical error estimates, demonstrating that our algorithm is feasible.

## Acknowledgments

This work was partially supported by the National Natural Science Foundation of China under grant no. 10872119, the Key Disciplines of Shanghai Municipality under grant no. S30104, the Key Program of Shanghai Municipal Education Commission under grant no. 12ZZ084, and the Natural Science Foundation of Anhui province KJ2010B442.

## References

- [1] S. Chen and F. Liu, "ADI-Euler and extrapolation methods for the two-dimensional fractional advection-dispersion equation," *Journal of Applied Mathematics and Computing*, vol. 26, no. 1, pp. 295–311, 2008.
- [2] V. J. Ervin, N. Heuer, and J. P. Roop, "Numerical approximation of a time dependent, nonlinear, space-fractional diffusion equation," *SIAM Journal on Numerical Analysis*, vol. 45, no. 2, pp. 572–591, 2008.
- [3] V. J. Ervin and J. P. Roop, "Variational formulation for the stationary fractional advection dispersion equation," *Numerical Methods for Partial Differential Equations*, vol. 22, no. 3, pp. 558–576, 2006.
- [4] B. I. Henry, T. A. M. Langlands, and S. L. Wearne, "Anomalous diffusion with linear reaction dynamics: from continuous time random walks to fractional reaction-diffusion equations," *Physical Review E*, vol. 74, no. 3, article 031116, 2006.
- [5] C. P. Li, A. Chen, and J. J. Ye, "Numerical approaches to fractional calculus and fractional ordinary differential equation," *Journal of Computational Physics*, vol. 230, no. 9, pp. 3352–3368, 2011.
- [6] C. P. Li, Z. G. Zhao, and Y. Q. Chen, "Numerical approximation of nonlinear fractional differential equations with subdiffusion and superdiffusion," *Computers & Mathematics with Applications*, vol. 62, pp. 855–875, 2011.
- [7] F. Liu, V. Anh, and I. Turner, "Numerical solution of the space fractional Fokker-Planck equation," *Journal of Computational and Applied Mathematics*, vol. 166, no. 1, pp. 209–219, 2004.
- [8] I. Podlubny, *Fractional Differential Equations*, vol. 198, Academic Press, San Diego, Calif, USA, 1999.
- [9] R. K. Saxena, A. M. Mathai, and H. J. Haubold, "Fractional reaction-diffusion equations," *Astrophysics and Space Science*, vol. 305, no. 3, pp. 289–296, 2006.
- [10] Y. Y. Zheng, C. P. Li, and Z. G. Zhao, "A note on the finite element method for the space-fractional advection diffusion equation," *Computers & Mathematics with Applications*, vol. 59, no. 5, pp. 1718–1726, 2010.
- [11] B. Baeumer, M. Kovács, and M. M. Meerschaert, "Fractional reproduction-dispersal equations and heavy tail dispersal kernels," *Bulletin of Mathematical Biology*, vol. 69, no. 7, pp. 2281–2297, 2007.
- [12] S. Bhalekar, V. Daftardar-Gejji, D. Baleanu, and R. Magin, "Fractional Bloch equation with delay," *Computers & Mathematics with Applications*, vol. 61, no. 5, pp. 1355–1365, 2011.
- [13] A. V. Chechkin, V. Y. Gonchar, R. Gorenflo, N. Korabel, and I. M. Sokolov, "Generalized fractional diffusion equations for accelerating subdiffusion and truncated Levy flights," *Physical Review E*, vol. 78, no. 2, article 021111, 2008.
- [14] P. D. Demontis and G. B. Suffritti, "Fractional diffusion interpretation of simulated single-file systems in microporous materials," *Physical Review E*, vol. 74, no. 5, article 051112, 2006.
- [15] S. A. Elwakil, M. A. Zahran, and E. M. Abulwafa, "Fractional (space-time) diffusion equation on comb-like model," *Chaos, Solitons & Fractals*, vol. 20, no. 5, pp. 1113–1120, 2004.
- [16] A. Kadem, Y. Luchko, and D. Baleanu, "Spectral method for solution of the fractional transport equation," *Reports on Mathematical Physics*, vol. 66, no. 1, pp. 103–115, 2010.
- [17] R. L. Magin, O. Abdullah, D. Baleanu, and X. J. Zhou, "Anomalous diffusion expressed through fractional order differential operators in the Bloch-Torrey equation," *Journal of Magnetic Resonance*, vol. 190, no. 2, pp. 255–270, 2008.
- [18] M. M. Meerschaert, D. A. Benson, and B. Baeumer, "Operator Levy motion and multiscaling anomalous diffusion," *Physical Review E*, vol. 63, no. 2 I, article 021112, 2001.
- [19] W. L. Vargas, J. C. Murcia, L. E. Palacio, and D. M. Dominguez, "Fractional diffusion model for force distribution in static granular media," *Physical Review E*, vol. 68, no. 2, article 021302, 2003.
- [20] V. V. Yanovsky, A. V. Chechkin, D. Schertzer, and A. V. Tur, "Levy anomalous diffusion and fractional Fokker-Planck equation," *Physica A: Statistical Mechanics and its Applications*, vol. 282, no. 1-2, pp. 13–34, 2000.
- [21] S. C. Brenner and L. R. Scott, *The Mathematical Theory of Finite Element Methods*, vol. 15, Springer, Berlin, Germany, 1994.

## *Review Article*

# **Coupled Numerical Methods to Analyze Interacting Acoustic-Dynamic Models by Multidomain Decomposition Techniques**

**Delfim Soares Jr.**

*Structural Engineering Department, Federal University of Juiz de Fora, Cidade Universitária, 36036-330 Juiz de Fora, MG, Brazil*

Correspondence should be addressed to Delfim Soares Jr., [delfim.soares@ufjf.edu.br](mailto:delfim.soares@ufjf.edu.br)

Received 11 May 2011; Accepted 12 July 2011

Academic Editor: Luis Godinho

Copyright © 2011 Delfim Soares Jr. This is an open access article distributed under the Creative Commons Attribution License, which permits unrestricted use, distribution, and reproduction in any medium, provided the original work is properly cited.

In this work, coupled numerical analysis of interacting acoustic and dynamic models is focused. In this context, several numerical methods, such as the finite difference method, the finite element method, the boundary element method, meshless methods, and so forth, are considered to model each subdomain of the coupled model, and multidomain decomposition techniques are applied to deal with the coupling relations. Two basic coupling algorithms are discussed here, namely the explicit direct coupling approach and the implicit iterative coupling approach, which are formulated based on explicit/implicit time-marching techniques. Completely independent spatial and temporal discretizations among the interacting subdomains are permitted, allowing optimal discretization for each sub-domain of the model to be considered. At the end of the paper, numerical results are presented, illustrating the performance and potentialities of the discussed methodologies.

## **1. Introduction**

Usually, an engineer is faced with the analysis of a problem where two or more different physical systems interact with each other, so that the independent solution of any one system is impossible without simultaneous solution of the others. Such systems are known as coupled, and the intensity of such coupling is dependent on the degree of interaction [1]. Numerical algorithms consider that coupled systems may interact by means of common interfaces and/or overlapped subdomains. The former, usually referred to as interface-coupling, considers that coupling occurs on domain interfaces via the boundary conditions imposed there. Generally, distinct domains describe different physical situations, but it is possible to consider coupling between domains that are physically similar in which different discretization processes have been used. In the second case (problems in which the various

domains totally or partially overlap), coupling occurs through the differential governing equations, describing different physical phenomena. In this work, only interface coupling problems are considered, and the interactions between acoustic fluids and elastodynamic solids are focused. In this context, one can mention a number of different applications: interaction between fluids such as air, water, or lubricants and structural elements such as buildings, dams, offshore structures, mechanical components, pressure vessels, and so forth, systems composed of the same medium, with subdomains discretized by different numerical methods (finite difference, finite elements, boundary elements, etc.) and/or different refinement levels, and so forth.

In the present work, several numerical methods are considered to discretize the different subdomains of the global model, taking into account interface coupled analyses. Although nowadays there are several powerful numerical techniques available, none of them can be considered most appropriate for all kinds of analysis, and, usually, the coupling of different numerical methodologies is necessary to analyze complex problems more effectively. In this context, the coupling of different numerical methods is recommended, in order to profit from their respective advantages and to evade their disadvantages. Two basic coupling algorithms are discussed here, considering multidomain decomposition techniques. In the first algorithm, explicit time-marching procedures are employed for wave propagation analysis at some subdomains of the model. Since explicit algorithms allow the computation of the current time-step response as function of only previous time-steps information; those subdomains can be independently analyzed directly, at each time step, allowing the development of an explicit direct coupling approach (ExDCA). On the other hand, when implicit time-marching procedures are considered, the computation of the current time-step response depends on the current time-step information, and interacting subdomains modeled by these techniques cannot be independently analyzed directly, being an iterative procedure necessary to analyze these coupled subdomains, once multidomain decomposition techniques are regarded. For this case, a second coupling algorithm is discussed here, referred to as implicit iterative coupling approach (ImICA).

Taking into account an explicit direct or an implicit iterative multidomain decomposition technique, the coupling of several numerical procedures is carried out here. In this work, the coupling of the finite difference method (FDM), finite element method (FEM), boundary element method (BEM), and meshless local Petrov-Galerkin method (MLPG) is focused. In the last decades, these methodologies have been intensively applied to model acoustic-dynamic coupled models, taking into account different coupling strategies and time- and frequency-domain analyses. Considering the FDM, Vireaux [2] employed staggered grids to analyze acoustic-dynamic models in the 80s; nowadays, several advanced techniques are available based on the FDM, including those based on coupled methods [3–5]. In fact, it did not take long to couple numerical methods to analyze interacting acoustic-dynamic models, and most of these procedures are based on FEM-BEM coupling techniques [6–17] although there are several other procedures based on different numerical methodologies [18–30].

When time-domain acoustic-dynamic coupled analyses are focused, the coupling of media with different properties (high properties contrast) and/or the coupling of numerical procedures with different spatial/temporal behavior may lead to inaccurate results or, even worse, instabilities. Thus, it is important to develop robust discretization techniques that not only are able to provide accurate and stable analyses, but also are computationally efficient. In this work, a multilevel time-step procedure is presented, as well as nonmatching interface nodes techniques are referred, allowing each subdomain of the model to be independently and optimally discretized, efficiently improving the accuracy and the stability of the analyses.

The paper is organized as follows: first, basic equations concerning acoustic and dynamic models are presented, as well as interface interacting relations; in the sequence, numerical modeling of the acoustic/dynamic subdomains is briefly addressed taking into account domain- and boundary-discretization techniques. In Section 4, coupling algorithms are discussed, focusing on explicit direct and implicit iterative procedures. At the end of the paper, three numerical applications (taking into account several different configurations) are presented, illustrating the performance and potentialities of the discussed methodologies.

## 2. Governing Equations

In this section, acoustic and elastic wave equations are briefly presented. Each one of these wave propagation models is used to mathematically describe different subdomains of the global problem. At the end of the section, basic equations concerning the coupling of acoustic and dynamic subdomains are described.

### 2.1. Acoustic Subdomains

The scalar wave equation is given by

$$(\kappa p_{,i})_{,i} - \rho \ddot{p} - \xi \dot{p} + S = 0, \quad (2.1)$$

where  $p(X, t)$  stands for hydrodynamic pressure distribution and  $S(X, t)$  for body source terms. Inferior commas (indicial notation is adopted) and over dots indicate partial space ( $p_{,i} = \partial p / \partial x_i$ ) and time ( $\dot{p} = \partial p / \partial t$ ) derivatives, respectively.  $\xi(X)$  stands for the viscous damping coefficient;  $\rho(X)$  is the mass density, and  $\kappa(X)$  is the bulk modulus of the medium. In homogeneous media,  $\rho$  and  $\kappa$  are constant, and the classical wave equation (disregarding damping) can be written as

$$p_{,ii} - \frac{\ddot{p}}{c^2} + s = 0, \quad (2.2)$$

where  $c = \sqrt{\kappa/\rho}$  is the wave propagation velocity. The boundary and initial conditions of the problem are given by

(i) boundary conditions ( $t > 0$ ,  $X \in \Gamma$  where  $\Gamma = \Gamma_1 \cup \Gamma_2$ ):

$$p(X, t) = \bar{p}(X, t) \quad \text{for } X \in \Gamma_1, \quad (2.3a)$$

$$q(X, t) = p_{,j}(X, t)n_j(X) = \bar{q}(X, t) \quad \text{for } X \in \Gamma_2, \quad (2.3b)$$

(ii) initial conditions ( $t = 0$ ,  $X \in \Gamma \cup \Omega$ ):

$$p(X, 0) = \bar{p}_0(X), \quad (2.4a)$$

$$\dot{p}(X, 0) = \dot{\bar{p}}_0(X), \quad (2.4b)$$

where the prescribed values are indicated by over bars, and  $q$  represents the flux along the boundary whose unit outward normal vector components are represented by  $n_j$ . The boundary of the model is denoted by  $\Gamma$  ( $\Gamma_1 \cup \Gamma_2 = \Gamma$  and  $\Gamma_1 \cap \Gamma_2 = \emptyset$ ) and the domain by  $\Omega$ .

## 2.2. Dynamic Subdomains

The elastic wave equation for homogenous media is given by

$$\left(c_d^2 - c_s^2\right)u_{j,ji} + c_s^2 u_{i,jj} - \dot{u}_i - \zeta \dot{u}_i + b_i = 0, \quad (2.5)$$

where  $u_i$  and  $b_i$  stand for the displacement and the body force distribution components, respectively. The notation for time and space derivatives employed in (2.1) is once again adopted. In (2.5),  $c_d$  is the dilatational wave velocity and  $c_s$  is the shear wave velocity; they are given by  $c_d^2 = (\lambda + 2\mu)/\rho$  and  $c_s^2 = \mu/\rho$ , where  $\rho$  is the mass density, and  $\lambda$  and  $\mu$  are the Lamé's constants.  $\zeta$  stands for viscous damping-related parameters. Equation (2.5) can be obtained from the combination of the following basic mechanical equations (proper to model heterogeneous media):

$$\sigma_{ij,j} - \rho \ddot{u}_i - \rho \zeta \dot{u}_i + \rho b_i = 0, \quad (2.6a)$$

$$\sigma_{ij} = \lambda \delta_{ij} \varepsilon_{kk} + 2\mu \varepsilon_{ij}, \quad (2.6b)$$

$$\varepsilon_{ij} = \frac{u_{i,j} + u_{j,i}}{2}, \quad (2.6c)$$

where  $\sigma_{ij}$  and  $\varepsilon_{ij}$  are, respectively, stress and strain tensor components, and  $\delta_{ij}$  is the Kronecker delta ( $\delta_{ij} = 1$ , for  $i = j$ , and  $\delta_{ij} = 0$ , for  $i \neq j$ ). Equation (2.6a) is the momentum equilibrium equation; (2.6b) represents the constitutive law of the linear elastic model, and (2.6c) stands for kinematical relations. The boundary and initial conditions of the elastodynamic problem are given by

(i) boundary conditions ( $t > 0$ ,  $X \in \Gamma$  where  $\Gamma = \Gamma_1 \cup \Gamma_2$ ):

$$u_i(X, t) = \bar{u}_i(X, t) \quad \text{for } X \in \Gamma_1, \quad (2.7a)$$

$$\tau_i(X, t) = \sigma_{ij}(X, t)n_j(X) = \bar{\tau}_i(X, t) \quad \text{for } X \in \Gamma_2, \quad (2.7b)$$

(ii) initial conditions ( $t = 0$ ,  $X \in \Gamma \cup \Omega$ ):

$$u_i(X, 0) = \bar{u}_{i0}(X), \quad (2.8a)$$

$$\dot{u}_i(X, 0) = \dot{\bar{u}}_{i0}(X), \quad (2.8b)$$



where the prescribed values are indicated by over bars, and  $\tau_i$  denotes the traction vector along the boundary ( $n_j$ , as indicated previously, stands for the components of the unit outward normal vector).

### 2.3. Acoustic-Dynamic Interacting Interfaces

On the acoustic-dynamic interface boundaries, the dynamic subdomain normal (normal to the interface) accelerations ( $\ddot{u}_n$ ) are related to the acoustic subdomain fluxes ( $q$ ), and the acoustic subdomain hydrodynamic pressures ( $p$ ) are related to the dynamic subdomain normal tractions ( $\tau_n$ ). These relations are expressed by the following equations:

$$\ddot{u}_n - \left(\frac{1}{\rho}\right)q = 0, \quad (2.9a)$$

$$\tau_n + p = 0, \quad (2.9b)$$

where in (2.9a) and (2.9b) the sign of the different subdomain outward normal directions is taken into account (outward normal vectors on the same interface point are opposite for each subdomain). In (2.9a),  $\rho$  is the mass density of the interacting acoustic subdomain medium.

## 3. Numerical Modelling

Several numerical methods can be applied to discretize each subdomain of the coupled acoustic-dynamic model, according to their properties and advantages/disadvantages. In the following sub-sections, some numerical methods are briefly discussed, addressing their basic characteristics.

### 3.1. Domain-Discretization Methods

In the numerical methods based on domain discretization, the whole domain of the model is discretized into basic structures (elements, cells, points, etc.), and the spatial treatment of the governing equations is carried out considering these basic structures. In this case, matrix system of equations, as indicated in (3.1), is usually obtained, where the mass ( $\mathbf{M}$ ), damping ( $\mathbf{C}$ ), and stiffness ( $\mathbf{K}$ ) matrices, as well as the load vector ( $\mathbf{F}$ ), are computed according to the spatial discretization techniques being employed

$$\mathbf{M}\ddot{\mathbf{X}}(t) + \mathbf{C}\dot{\mathbf{X}}(t) + \mathbf{K}\mathbf{X}(t) = \mathbf{F}(t). \quad (3.1)$$

In (3.1),  $\mathbf{X}(t)$  stands for the pressure/displacement vector ( $\mathbf{X} \equiv \mathbf{P}$  or  $\mathbf{X} \equiv \mathbf{U}$  for acoustic or dynamic formulations, respectively) at time  $t$  (spatial and temporal discretizations are considered separately). In the present work, the finite difference method (FDM), the finite element method (FEM), and the meshless local Petrov-Galerkin method (MLPG) are focused, taking into account domain-discretization techniques.

The FDM was one of the first methods developed to analyze complex problems governed by differential equations [31, 32]. It is easy to implement and considerably efficient; however, it may become extremely restricted when complex geometries are considered,

because it is usually based on a regular distribution of points. The FEM, on the other hand, is well suited to analyze complex geometries, requiring in counterpart a considerably amount of input data [1, 33–36]. It is also quite an efficient technique, being the most popular method available nowadays to analyze intricate engineering problems. It is easy to implement and can be generalized to analyze complex models quite easily. Its main disadvantages are related to modelling unbounded domains and high gradient variations, as well as difficulties related to mesh generation. In the past few years, meshless methods have emerged essentially stimulated by these difficulties related to mesh generation [37, 38]. Mesh generation is delicate in many situations, for instance, when the domain has complicated geometry; when the mesh changes with time, as in crack propagation, and remeshing is required at each time step; when a Lagrangian formulation is employed, especially with nonlinear PDEs, and so forth. In addition, the need for flexibility in the selection of approximating functions (e.g., the flexibility to use nonpolynomial approximating functions) has played a significant role in the development of meshless methods (many meshless approximations give continuous variation of the first- or higher-order derivatives of a primitive function in counterpart to classical polynomial approximation where secondary fields have a jump on the interface of elements. Therefore, meshless approximations are leading to more accurate results in many cases). The main disadvantages of meshless methods are still their high computational costs and, in some cases, their lack of stability.

Once the spatial treatment of the governing equations is carried out by a domain-discretization technique and (3.1) is obtained, its time domain analysis must also be considered. In this case, finite difference techniques are usually applied, rendering an algebraic system of equations, as described in (3.2), which must be solved at each time step  $n$

$$\mathbf{A}\mathbf{X}^n = \mathbf{B}^m. \quad (3.2)$$

In (3.2),  $\mathbf{A}$  and  $\mathbf{B}$  stand for the effective matrix and vector of the model, respectively, and the entries of  $\mathbf{X}$  stand for the unknown variables. One should observe that vector  $\mathbf{B}$  accounts for boundary prescribed conditions and domain sources, as well as some other previous step contributions (previous to  $m$ ). Taking into account explicit time-marching techniques,  $m = n - 1$ , whereas, for implicit time-marching techniques,  $m = n$ . In this work, several explicit and implicit techniques are considered. The central difference method and the Green-Newmark method [39–41], for instance, are explicit techniques that are here considered associated with the FDM and the FEM. Similarly, the Houbolt method [42] and the Newmark method [43] are implicit techniques that are here considered associated with the MLPG and the FEM.

### 3.2. Boundary-Discretization Methods

In boundary-discretization methods, just the boundary of the model is discretized, taking into account once again some basic structure, such as elements and point distributions. In this case, transient fundamental solutions are employed, and mixed approaches are focused, rendering numerical procedures based on more than one field incognita. The matrix system of equations that arises considering this kind of discretization can be written as

$$\mathbf{A}\mathbf{X}^n = \mathbf{B}\mathbf{Y}^n + \mathbf{Z}^n, \quad (3.3)$$

where the entries of  $\mathbf{X}$  and  $\mathbf{Y}$  stand for the unknown and known (i.e., prescribed conditions) variables at the boundary of the model, respectively.  $\mathbf{A}$  and  $\mathbf{B}$  are effective matrices related to these variables at the current time step, and  $\mathbf{Z}$  accounts for eventual domain-discretized terms (body sources, initial conditions etc.) and time convolution contributions.

In the present work, the boundary element method (BEM) is focused as a boundary-discretization technique [44–47]. As it is well known, the BEM is well suited to analyze unbounded domains and to model high gradient variations, once it is based on fundamental solutions that satisfy the Sommerfeld radiation condition and that can properly deal with singularities in the model. The BEM is also flexible and efficient, allowing the discretization of complex geometries, as long as homogeneous media are considered. For heterogeneous media (or other more complex models, such as those considering anisotropy and nonlinear behavior), the BEM may be considered an inappropriate numerical tool, since, in these cases, its formulation may become very complex and prohibitive.

There are also some “hybrid” formulations that are difficult to classify as a domain- or a boundary-discretization technique. This is the case, for instance, for some meshless techniques that are based on local boundary discretization (see, e.g., the LBIE—local boundary integral equation method [37]). In these meshless techniques, only boundary discretization is considered; however, the boundaries in focus are those of fictitious domains inside the real domain and, as a consequence, the whole real domain is in fact being discretized. Another hybrid formulation that is focused here is the domain boundary element method (DBEM) [40, 48, 49]. In this approach, nontransient fundamental solutions are considered, and the matrix system of equations that arises is a mix of (3.1) and (3.3), with some matrices being computed based on boundary discretizations and others being computed based on domain discretizations. Analogously as described in the previous subsection, the DBEM also requires time-marching techniques to treat the time domain ordinary differential matrix equation that arises. Here, the Houbolt method is considered as such numerical technique.

## 4. Coupling Procedures

In this work, the global model is divided in different subdomains, and each subdomain is analysed independently (as an uncoupled model), taking into account the numerical discretization techniques discussed in Section 3. The interactions between the different subdomains of the global model are considered taking into account the accelerations/tractions and fluxes/pressures at the common interfaces, as well as the continuity equations (2.9a) and (2.9b). Two coupling procedures are discussed here, namely, (i) an explicit direct coupling approach (ExDCA); (ii) an implicit iterative coupling approach (ImICA).

In the first procedure (i.e., the ExDCA), explicit time-marching schemes (e.g., the central difference method, the Green-Newmark method, etc.) are employed in some of the subdomains that are analyzed by domain-discretization methods. In the second procedure (ImICA), implicit time-marching schemes are considered within the subdomains. Since the ImICA is based on implicit algorithms ( $m = n$  in (3.2)), successive renewals of variables at common interfaces are considered in the coupling analysis (iterative coupling process), until convergence is achieved. On the other hand, the ExDCA is based on explicit algorithms ( $m = n - 1$  in (3.2)), and, as consequence, a direct coupling procedure can be developed, as it is described in the subsections that follow.

For both explicit direct and implicit iterative coupling procedures, it is appropriate to consider different temporal discretizations within each subdomain. This is the case since

optimal time steps are usually quite different taking into account dynamic and acoustic models, as well as different discretization techniques (especially taking into account some time-marching schemes that are conditionally stable). For instance, as it has been extensively reported in the literature, for small time steps, the time-domain BEM may become unstable, whereas, for large time-steps, excessive numerical damping may occur [44, 45]. Thus, in order to ensure stability and/or accuracy, usually a much smaller FEM time-step is required when coupled BEM-FEM analyses are considered (especially if the central difference method is employed associated to the FEM, which requires a low critical time-step). This situation may be amplified if subdomains with considerably different wave propagation velocities are interacting. In the next subsection, the adoption of different temporal discretizations within each subdomain of the global model is briefly discussed. In the sequence, the ExDCA and the ImICA are described.

#### ***4.1. Multilevel Time-Step Discretization***

In order to consider different time steps in each subdomain, interpolation/extrapolation procedures along time are performed. Here, several schemes are considered for this temporal data manipulation, according to the discretization techniques involved. For instance, when the BEM is considered discretizing an interacting subdomain, temporal interpolation and extrapolation procedures are carried out based on the BEM time interpolation functions. In this case, time extrapolation procedures can be applied with confidence since they are consistent with the time-domain BEM formulation. Once time interpolation and extrapolation techniques are being employed, coupled implicit subdomains can be easily independently analysed (ImICA) taking into account different time steps. If explicit subdomains are considered (ExDCA), a subdomain solution can be computed independently of the current time step. As a consequence, just time interpolation procedures, associated with subcycling techniques, may be necessary if different time steps are required. Using these temporal data manipulations, optimal modelling in each subdomain may be achieved, which is very important regarding flexibility, efficiency, accuracy, and stability.

#### ***4.2. Explicit Direct Coupling***

In the explicit direct coupling (as well as in the implicit iterative coupling), natural boundary conditions are prescribed at the acoustic and at the dynamic subdomains common interfaces. Two explicit direct coupling approaches are discussed here, the first one considering acoustic explicit subdomains and the second one considering dynamic explicit subdomains. For both approaches, the acoustic subdomain time steps are considered larger than the dynamic subdomain time steps (when different time-steps are regarded), since the wave propagation velocities in solids are usually higher than in acoustic fluids.

In the first explicit direct coupling algorithm discussed here, the pressures related to the acoustic subdomains are computed directly, since their evaluation only takes into account results corresponding to previous time steps ( $m = n - 1$  in (3.2)). Once the acoustic pressures are evaluated, they are employed to compute tractions which are employed as prescribed interface boundary conditions (natural boundary condition) for the dynamic subdomains, and the displacements/velocities/accelerations of the model are computed by analysing these subdomains. The accelerations are then employed to evaluate the acoustic fluxes which are applied as prescribed interface boundary conditions (natural boundary condition) for

**Table 1:** ExDCA-1 algorithm.

---

Time-step loop (based on $t_p$ )
(1) Acoustic subdomains analyses: evaluation of $\mathbf{P}^{t_p}$ .
(2) Subcycling (until $t_u = t_p$ ):
(2.1) pressure temporal interpolation: $\mathbf{P}^{t_u} = \sum_{j=0}^{J_u} \beta_j \mathbf{P}^{(t-j\Delta t)_p}$ ,
(2.2) force-pressure compatibility (spatial interpolation): $\mathbf{F}^{t_u} = N_u(\mathbf{P}^{t_u})$ ,
(2.3) dynamic subdomains analyses: evaluation of $\mathbf{U}^{t_u}$ ,
(2.4) evaluation of time derivatives of $\mathbf{U}^{t_u}$ : $\dot{\mathbf{U}}^{t_u}$ (if necessary), $\ddot{\mathbf{U}}^{t_u}$ .
(3) Flux-acceleration compatibility (spatial interpolation): $\mathbf{Q}^{t_p} = N_p(\ddot{\mathbf{U}}^{t_p})$ .
(4) Evaluation of time derivatives of $\mathbf{P}^{t_p}$ : $\dot{\mathbf{P}}^{t_p}$ , $\ddot{\mathbf{P}}^{t_p}$ (if necessary).

---

the acoustic subdomains. If necessary, the time derivatives of the acoustic pressures can be computed. The next time-step computations are then initiated, repeating the above-described procedures.

The detailed algorithm for this first ExDCA is presented in Table 1, taking into account different temporal discretizations for the acoustic and for the dynamic subdomains ( $t_p$  and  $t_u$ , respectively— $\beta_j$  and  $\zeta_j$  stand for time interpolation/extrapolation coefficients in the tables that follow). Space interpolation procedures may also be adopted in order to consider independent subdomain spatial discretizations (i.e., disconnected interface nodes); this can be accomplished by considering proper interface interpolating functions  $N_u(\cdot)$  and  $N_p(\cdot)$ , which are based on relations (2.9a) and (2.9b).

In this work, this first algorithm is employed associated to FEM-FEM coupled procedures in which the acoustic subdomains are modelled considering the Green-Newmark method (explicit technique), and the dynamic subdomains are modelled considering the Newmark method (implicit technique), as well as to FEM-FEM, and FEM-FDM coupled procedures in which all subdomains are modelled considering the central difference method (explicit technique).

In the second explicit direct coupling algorithm focused here, the displacements related to the dynamic subdomains are computed directly, since their evaluation only takes into account results corresponding to previous time steps ( $m = n - 1$  in (3.2)). Once the displacements are evaluated, they are employed to compute the accelerations and, as a consequence, the acoustic fluxes, which are employed as prescribed interface boundary conditions (natural boundary condition) for the acoustic subdomains. The acoustic subdomains are then analyzed, and the acoustic pressures are computed. The pressures are then employed to evaluate the normal tractions which are applied as prescribed interface boundary conditions (natural boundary condition) for the dynamic subdomains. If necessary, the velocities of the model are computed. The next time-step computations are then initiated, repeating the above-described procedures.

The detailed algorithm for this second ExDCA is presented in Table 2, taking into account different temporal and spatial discretizations for the acoustic and for the dynamic subdomains. In this work, this methodology is considered applied to FEM-BEM coupled procedures in which acoustic subdomains are modelled by the BEM, and dynamic subdomains are modelled by the FEM associated to the Green-Newmark method (explicit technique).

**Table 2:** ExDCA-2 algorithm.

---

Time-step loop (based on $t_u$ )
(1) Dynamic subdomains analyses: evaluation of $\mathbf{U}^{t_u}$ .
(2) Evaluation of time derivatives of $\mathbf{U}^{t_u}$ : $\dot{\mathbf{U}}^{t_u}$ .
(3) Acceleration temporal extrapolation: $\ddot{\mathbf{U}}^{t_p} = \sum_{j=0}^{J_p} \zeta_j \ddot{\mathbf{U}}^{(t-j\Delta t)_u}$ .
(4) Flux-acceleration compatibility (spatial interpolation): $\mathbf{Q}^{t_p} = N_p(\ddot{\mathbf{U}}^{t_p})$ .
(5) Acoustic subdomains analyses: evaluation of $\mathbf{P}^{t_p}$ .
(6) Pressure temporal interpolation: $\mathbf{P}^{t_u} = \sum_{j=0}^{J_u} \beta_j \mathbf{P}^{(t-j\Delta t)_p}$ .
(7) Force-pressure compatibility (spatial interpolation): $\mathbf{F}^{t_u} = N_u(\mathbf{P}^{t_u})$ .
(8) Evaluation of time derivatives of $\mathbf{U}^{t_u}$ : $\dot{\mathbf{U}}^{t_u}$ (if necessary).
(9) Evaluation of time derivatives of $\mathbf{P}^{t_p}$ : $\dot{\mathbf{P}}^{t_p}, \ddot{\mathbf{P}}^{t_p}$ (if necessary, when $t_u = t_p$ ).

---

### 4.3. Implicit Iterative Coupling

In the implicit iterative approach, each subdomain of the model is analysed independently (as in the ExDCA), and a successive renewal of the variables at the common interfaces is performed, until convergence is achieved. In order to maximize the efficiency and robustness of the iterative coupling algorithm, the evaluation of an optimised relaxation parameter is introduced, taking into account the minimisation of a square error functional.

Initially, in the ImICA, the dynamic subdomains are analysed and the displacements at the common interfaces are evaluated, as well as its time derivatives. A relaxation parameter  $\alpha$  is introduced in order to ensure and/or to speed up convergence, such that (superscript  $k$  stands for the iterative step)

$$^{(k+1)}\mathbf{X}^t = (\alpha) ^{(k+\alpha)}\mathbf{X}^t + (1 - \alpha) ^{(k)}\mathbf{X}^t, \quad (4.1)$$

where the relaxation parameter can be introduced associated to the displacement variable ( $\mathbf{X} \equiv \mathbf{U}$ ) or to the acceleration variable ( $\mathbf{X} \equiv \ddot{\mathbf{U}}$ ). Once the accelerations are computed, they are employed to calculate the acoustic fluxes, which are prescribed as interface boundary conditions (natural boundary condition) for the acoustic subdomains. The acoustic subdomains are then analyzed, and the pressures of the model are computed, which are employed to evaluate dynamic forces at the common interfaces (natural boundary condition). The dynamic subdomains are then once again analyzed, repeating the whole process until convergence is achieved. Once convergence is achieved, the next time-step computations are initiated, repeating the above-described procedures.

The algorithm representing the ImICA is presented in Table 3, taking into account different temporal and spatial discretizations within each subdomain of the model. In this work, this algorithm is employed associated to FEM-BEM, BEM-BEM (as well as DBEM-BEM), and MLPG-MLPG coupling procedures (for MLPG-MLPG coupled analyses, different time-steps techniques are not considered here).

The effectiveness of the iterative coupling methodology is intimately related to the relaxation parameter selection; an inappropriate selection for  $\alpha$  can drastically increase the number of iterations in the analysis or, even worse, make convergence unfeasible. Once appropriate  $\alpha$  values are considered, convergence is usually achieved in quite few iterative



**Table 3:** ImICA algorithm.

---

Time-step loop (based on  $t_u$ )

(1) Iterative analysis (until convergence):

(1.1) dynamic subdomains analyses: evaluation of  $^{(k+\alpha)}\mathbf{U}^{t_u}$ ,(1.2 or 1.3) evaluation of time derivatives of  $^{(k+\lambda)}\mathbf{U}^{t_u} : ^{(k+\lambda)}\dot{\mathbf{U}}^{t_u}$ ,(1.3 or 1.2) adoption of a relaxation parameter:  $^{(k+1)}\mathbf{X}^{t_u} = \alpha ^{(k+\alpha)}\mathbf{X}^{t_u} + (1 - \alpha) ^{(k)}\mathbf{X}^{t_u}$ ,(1.4) acceleration temporal extrapolation:  $^{(k+1)}\dot{\mathbf{U}}^{t_p} = \zeta_0 ^{(k+1)}\dot{\mathbf{U}}^{t_u} + \sum_{j=1}^{J_p} \zeta_j \dot{\mathbf{U}}^{(t-j\Delta t)_u}$ ,(1.5) flux-acceleration compatibility (spatial interpolation):  $^{(k+1)}\mathbf{Q}^{t_p} = N_p(^{(k+1)}\dot{\mathbf{U}}^{t_p})$ ,(1.6) acoustic subdomains analyses: evaluation of  $^{(k+1)}\mathbf{P}^{t_p}$ ,(1.7) pressure temporal interpolation:  $^{(k+1)}\mathbf{P}^{t_u} = \beta_0 ^{(k+1)}\mathbf{P}^{t_p} + \sum_{j=1}^{J_u} \beta_j \mathbf{P}^{(t-j\Delta t)_p}$ ,(1.8) force-pressure compatibility (spatial interpolation):  $^{(k+1)}\mathbf{F}^{t_u} = N_u(^{(k+1)}\mathbf{P}^{t_u})$ ,(2) Evaluation of time derivatives of  $\mathbf{U}^{t_u}$ :  $\dot{\mathbf{U}}^{t_u}$  (if necessary).(3) Evaluation of time derivatives of  $\mathbf{P}^{t_p}$ :  $\dot{\mathbf{P}}^{t_p}$ ,  $\ddot{\mathbf{P}}^{t_p}$  (if necessary, when  $t_u = t_p$ ).  


---

steps, providing an efficient and robust iterative coupling technique. In order to evaluate an optimal relaxation parameter, the following square error functional is here minimized:

$$f(\alpha) = \left\| ^{(k+1)}\mathbf{X}^t(\alpha) - ^{(k)}\mathbf{X}^t(\alpha) \right\|^2. \quad (4.2)$$

Substituting (4.1) into (4.2) yields

$$\begin{aligned} f(\alpha) &= \left\| \alpha ^{(k+\alpha)}\mathbf{W}^t + (1 - \alpha) ^{(k)}\mathbf{W}^t \right\|^2 \\ &= \left( \alpha^2 \left\| ^{(k+\alpha)}\mathbf{W}^t \right\|^2 + 2\alpha(1 - \alpha) \left( ^{(k+\alpha)}\mathbf{W}^t, ^{(k)}\mathbf{W}^t \right) + (1 - \alpha)^2 \left\| ^{(k)}\mathbf{W}^t \right\|^2 \right), \end{aligned} \quad (4.3)$$

where the inner product definition is employed (e.g.,  $(\mathbf{W}, \mathbf{W}) = \|\mathbf{W}\|^2$ ) and new variables, as defined in (4.4), are considered

$$^{(k+\lambda)}\mathbf{W}^t = ^{(k+\lambda)}\mathbf{X}^t - ^{(k+\lambda-1)}\mathbf{X}^t. \quad (4.4)$$

To find the optimal  $\alpha$  that minimizes the functional  $f(\alpha)$ , (4.3) is differentiated with respect to  $\alpha$ , and the result is set to zero, yielding

$$\alpha = \frac{\left( ^{(k)}\mathbf{W}^t, ^{(k)}\mathbf{W}^t - ^{(k+\alpha)}\mathbf{W}^t \right)}{\left\| ^{(k)}\mathbf{W}^t - ^{(k+\alpha)}\mathbf{W}^t \right\|^2}, \quad (4.5)$$

which is an efficient and easy to implement expression that provides an optimal value for the relaxation parameter  $\alpha$ , at each iterative step. It is important to note that the relation  $0 < \alpha \leq 1$  must hold. In the present work, the optimal relaxation parameter is evaluated according to (4.5) and if  $\alpha \notin (0.01; 1.00)$ , the previous iterative-step relaxation parameter is adopted. For the first iterative step,  $\alpha = 0.5$  is selected.

## 5. Numerical Aspects and Applications

In the following sub-sections, some numerical applications are presented, illustrating the performance and potentialities of the discussed coupling methodologies. In the first application, a multidomain column is analyzed, considering several geometrical and physical configurations, as well as coupling procedures. In this case, acoustic-acoustic, acoustic-dynamic, and dynamic-dynamic coupled models are discussed, taking into account axisymmetric, two-dimensional, and three-dimensional configurations. In the second application, a dam-reservoir system is analyzed, considering once more several coupling techniques. In this case, a two-dimensional model is focused, and some advanced analyses are carried out, such as the modeling of nonlinear behavior and infinite media. In the last application, a tube of steel, submerged in water, is analyzed. In this case, axisymmetric models are focused, and, once again, several geometric and numeric configurations are considered. Along the applications discussed here, a large scope of coupling procedures is presented, namely: (i) for the ExDCA—FEM-FEM, FEM-BEM and FEM-FDM coupling procedures; (ii) for the ImICA—FEM-BEM, DBEM-BEM (which is referred to here as BEM-BEM 1), BEM-BEM (which is referred to here as BEM-BEM 2) and MLPG-MLPG coupling procedures. In this way, the reader can compare and better visualize some benefits and drawbacks of each methodology, considering an ample range of configurations.

### 5.1. Multidomain Column

The first example is that of a prismatic body behaving like a one-dimensional column. Initially, the column is analysed as an acoustic model [50]. It is fixed at one end ( $\bar{p}(t) = 0$ ) and subjected to a unitary Heaviside type forcing function acting at the opposite end ( $\bar{q}(t) = H(t)$ ). A sketch of the model is shown in Figure 1(a). The material properties of the column are  $c = 1.0 \text{ m/s}$  and  $\rho = 1.0 \text{ kg/m}^3$ . The geometry of the model is defined by  $L = 1.0 \text{ m}$ . As depicted in Figure 1(a), 28 boundary elements of equal length and 40 quadrilateral finite elements are employed in the coupled mesh. Regarding time discretization, three different cases of analysis are considered here, namely, (i)  $\Delta t_F = 1.0 \Delta t_B$ , (ii)  $\Delta t_F = 0.2 \Delta t_B$ , and (iii)  $\Delta t_F = 0.1 \Delta t_B$ ; where  $\Delta t_B = 0.06 \text{ s}$ , and the subscripts  $F$  and  $B$  are related to the FEM and to the BEM, respectively.

In Figure 2, time history results are depicted, at points A and B (see Figure 1(a)), taking into account the ExDCA and the ImICA. Potential (pressure) and flux results are presented considering the three different cases of analysis, and they are compared to the analytical solution [51], plotted as a solid line. As can be seen, a higher level of accuracy is observed when different time steps are considered within each subdomain, regarding their optimal temporal discretization. The robustness of the multilevel time-step algorithm must be highlighted: as illustrated in the present application, the algorithm deals properly with highly different subdomain temporal discretizations.

In a second approach for the column model, the acoustic-dynamic coupled problem is focused (fluid-solid column [27, 28]). A sketch of the problem is depicted in Figure 1(b). The geometry of the model is defined once again by  $L = 1.0 \text{ m}$ , and the column is submitted to a time Heaviside force acting at one of its ends. The physical properties of the media are (i) fluid subdomain:  $\kappa = 100 \text{ N/m}^2$  (bulk modulus) and  $\rho = 1 \text{ kg/m}^3$  (density); (ii) solid subdomain:  $E = 100 \text{ N/m}^2$  (Young modulus),  $\nu = 0$  (Poisson rate), and  $\rho = 1 \text{ kg/m}^3$  (density).



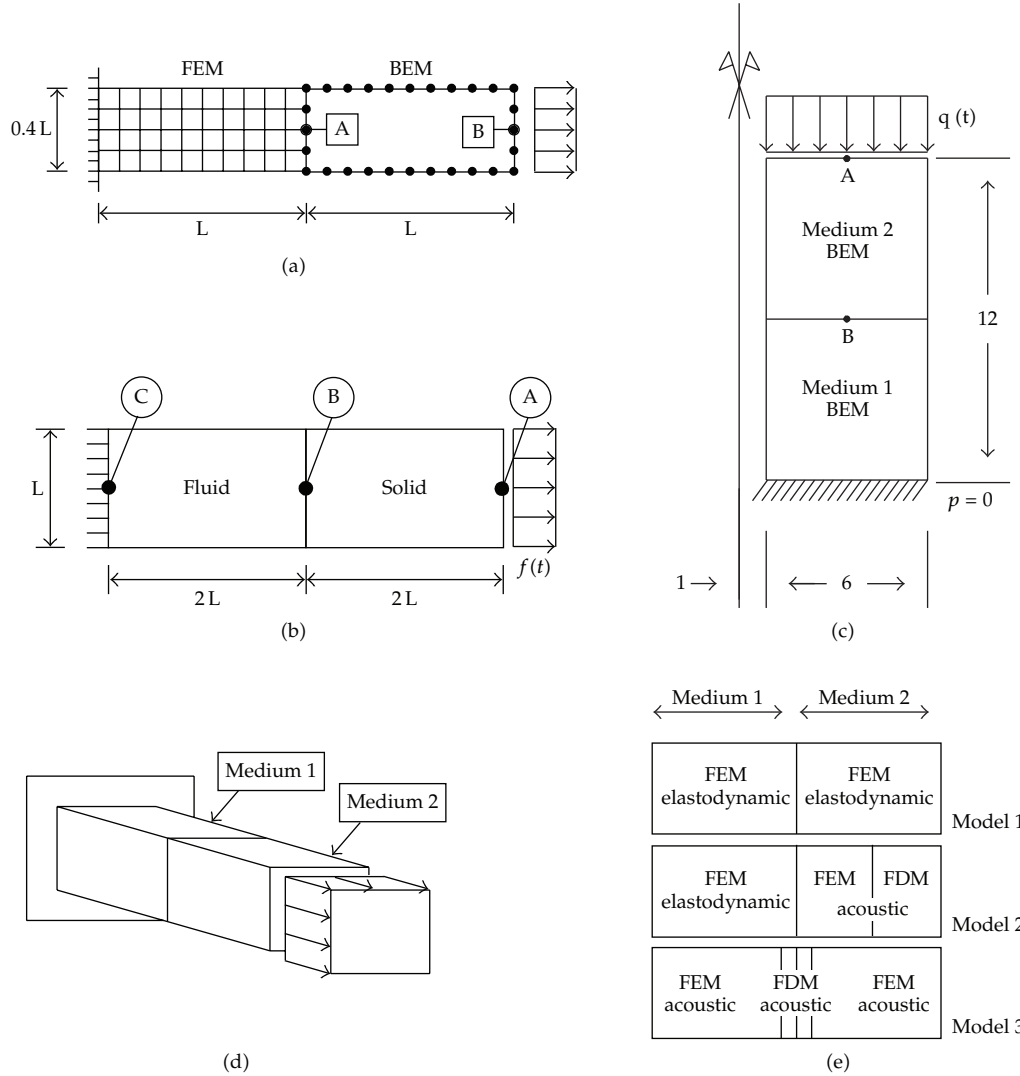


**Figure 1:** Column model: (a) FEM-BEM acoustic-acoustic two-dimensional model; (b) MLPG-MLPG and FEM-FEM acoustic-dynamic two-dimensional model; (c) FEM-BEM acoustic-acoustic axisymmetric model; (d) FEM-FEM and FEM-FDM acoustic-acoustic/acoustic-dynamic/dynamic-dynamic three-dimensional model; (e) sketch of the three-dimensional model spatial discretization.

Two spatial-temporal MLPG discretizations are considered to analyse the model, namely: (i) discretization 1—153 nodes are employed to spatially discretize each subdomain, and the time step adopted is  $\Delta t = 0.0025$  s; (ii) discretization 2—561 nodes are employed to spatially discretize each subdomain, and the time-step adopted is  $\Delta t = 0.00125$  s. In Figure 3, displacement time-history results at points A and B of the solid subdomain and hydrodynamic pressure time-history results at points B and C of the fluid subdomain are plotted, considering discretizations 1 and 2 and the MLPG-MLPG ImICA. Analytical time histories are also depicted in Figure 3, highlighting the good accuracy of the numerical results.

The same fluid-solid column is analysed considering FEM-FEM coupled procedures based on the Green-Newmark method and on the Newmark method (ExDCA). In this case,

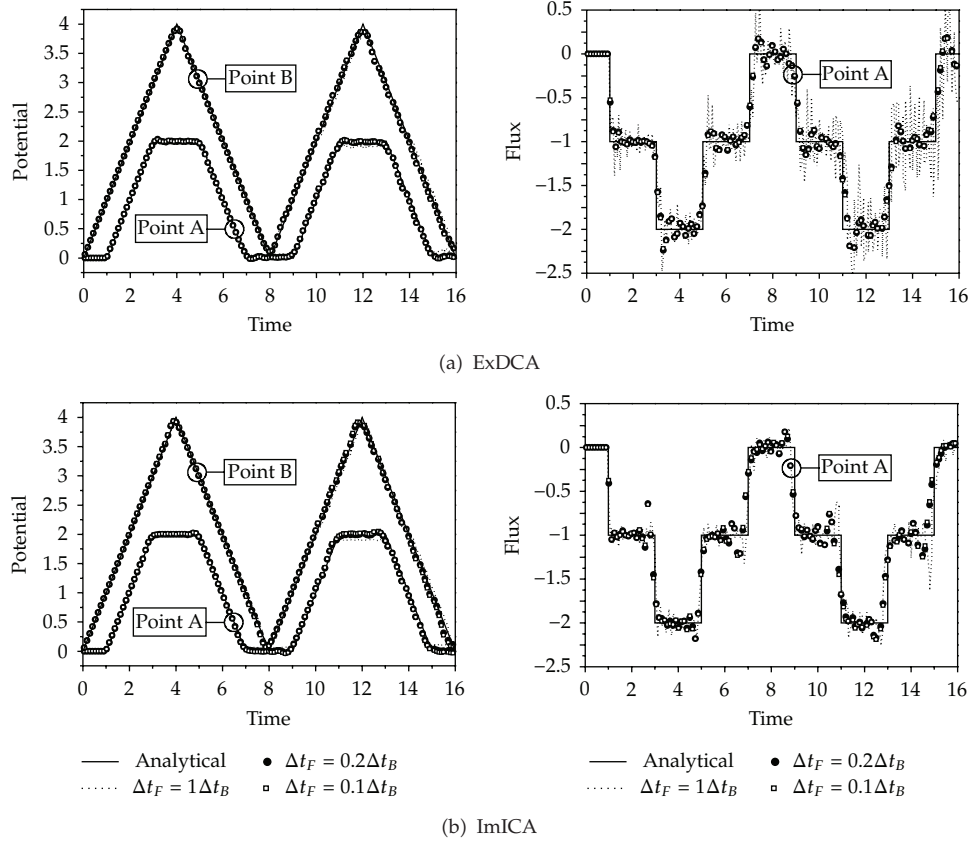


**Figure 2:** Time-history results at points A and B taking into account FEM-BEM coupling procedures and different temporal discretizations for each subdomain: (a) explicit direct coupling analysis; (b) implicit iterative coupling analysis.

200 square finite elements are employed to discretize each subdomain of the model, and the time discretization is specified by  $\Delta t = 0.002$  s. The obtained results are depicted in Figure 4(a). In this analysis, the same wave propagation velocities are considered within the solid and fluid subdomains, that is,  $c_d = c = 10$  m/s. Taking into account a steel-water column, the physical properties of the media are (i) fluid subdomain:  $\kappa = 2.3175 \cdot 10^9$  N/m<sup>2</sup>,  $\rho = 1030$  kg/m<sup>3</sup>; (ii) solid subdomain:  $E = 2.1 \cdot 10^{11}$  N/m<sup>2</sup>,  $\nu = 0.3$ , and  $\rho = 7700$  kg/m<sup>3</sup>; in this case,  $c_d = 6059$  m/s and  $c = 1500$  m/s. In Figure 4(b), the displacement and hydrodynamic pressure time-history results at point B are depicted, considering  $\Delta t_f = \Delta t_s$  and  $\Delta t_f = 4\Delta t_s$ , where  $\Delta t_s = 3.33 \cdot 10^{-6}$  s, and the subscripts  $s$  and  $f$  are related to the solid and fluid subdomains, respectively. As one can observe, good agreement between the results is observed, in spite of the different time discretizations adopted within each subdomain.

In a third approach for the column model, the propagation of acoustic waves through a prismatic circular column is analysed (axisymmetric model [16]). A sketch of the problem is depicted in Figure 1(c). The downside half of the column is modelled by the BEM, and the upside half is modelled by the FEM. The properties of the media are (i) *Medium 1* (BEM)— $\rho = 1.0$  kg/m<sup>3</sup> and  $c = 1.0$  m/s; (ii) *Medium 2* (FEM)— $\rho = 1.0$  kg/m<sup>3</sup> and  $c = 2.0$  m/s. The spatial discretization is considered as follows: 32 linear boundary elements discretize *Medium 1*,

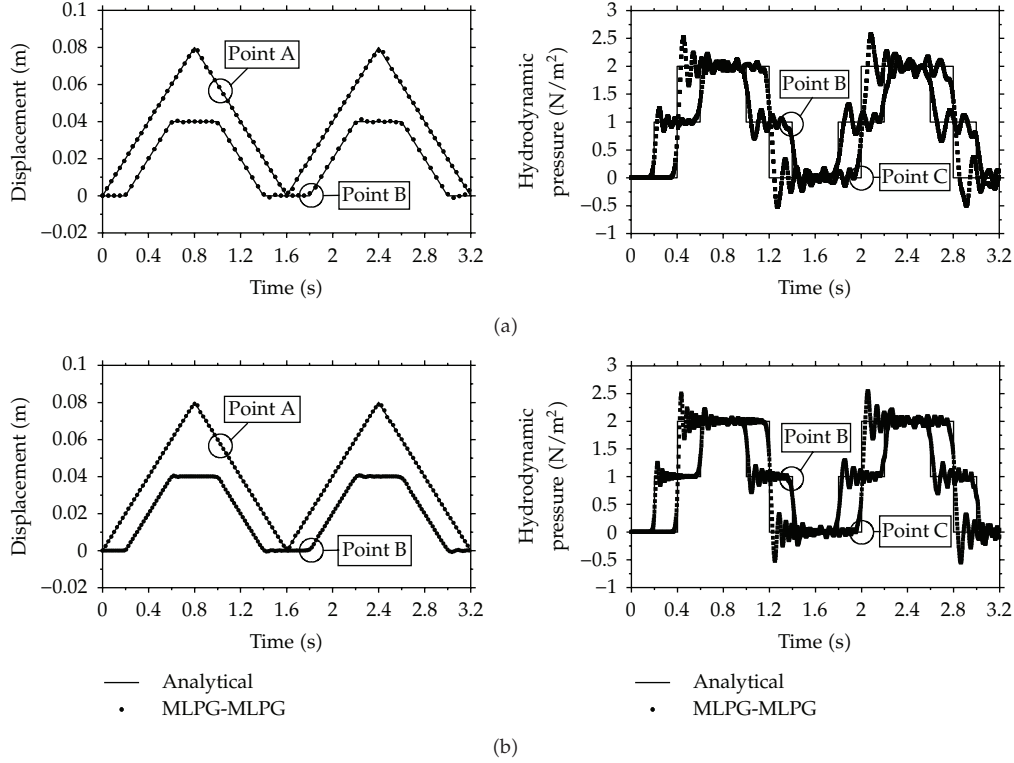


**Figure 3:** Time-history results at points A, B, and C taking into account MLPG-MLPG coupling procedures (ImICA) and different refinement levels: (a) discretization 1; (b) discretization 2.

and 64 linear-square finite elements discretize *Medium 2*. The time steps selected are  $\Delta t_B = 0.60$  s and  $\Delta t_F = 0.15$  s. Time history acoustic pressures at points A and B (see Figure 1(c)) are depicted in Figure 5. The numerical results are compared with those of a finite difference solution (based on the work presented by Cohen and Joly [52]) and, as one may observe, the time responses are quite similar considering these two different methodologies.

In a fourth approach for the column model, three-dimensional analyses are considered, taking into account FEM-FEM and FEM-FDM explicit coupling approaches (ExDCA) based on the central difference time-marching method [24]. A sketch for the three-dimensional column is depicted in Figure 1(d). The geometrical dimensions of the column are:  $10 \text{ m} \times 10 \text{ m} \times 50 \text{ m}$ . Two media (of equal length and cross-section) compose the column; the physical properties of each medium are (null Poisson rate is adopted for elastodynamic subdomains) (i) *Medium 1*— $\rho = 1.0 \text{ kg/m}^3$  and  $c_{(d)} = 10 \text{ m/s}$ ; (ii) *Medium 2*— $\rho = 1.0 \text{ kg/m}^3$  and  $c_{(d)} = 5 \text{ m/s}$ .

Three different numerical models are considered to simulate this problem, taking into account different coupling procedure combinations. A sketch of the three models adopted is presented in Figure 1(e). Details about each numerical model are given by (i) Model 1: elastodynamic FEM formulations are employed. Two independent FEM meshes are adopted, the first one with 2600 linear hexahedral elements and the other one with 2500 linear hexahedral elements (100 elements, i.e., one “element layer”, are used for mesh superposition, as described in [24]); (ii) Model 2: elastodynamic and acoustic FEM

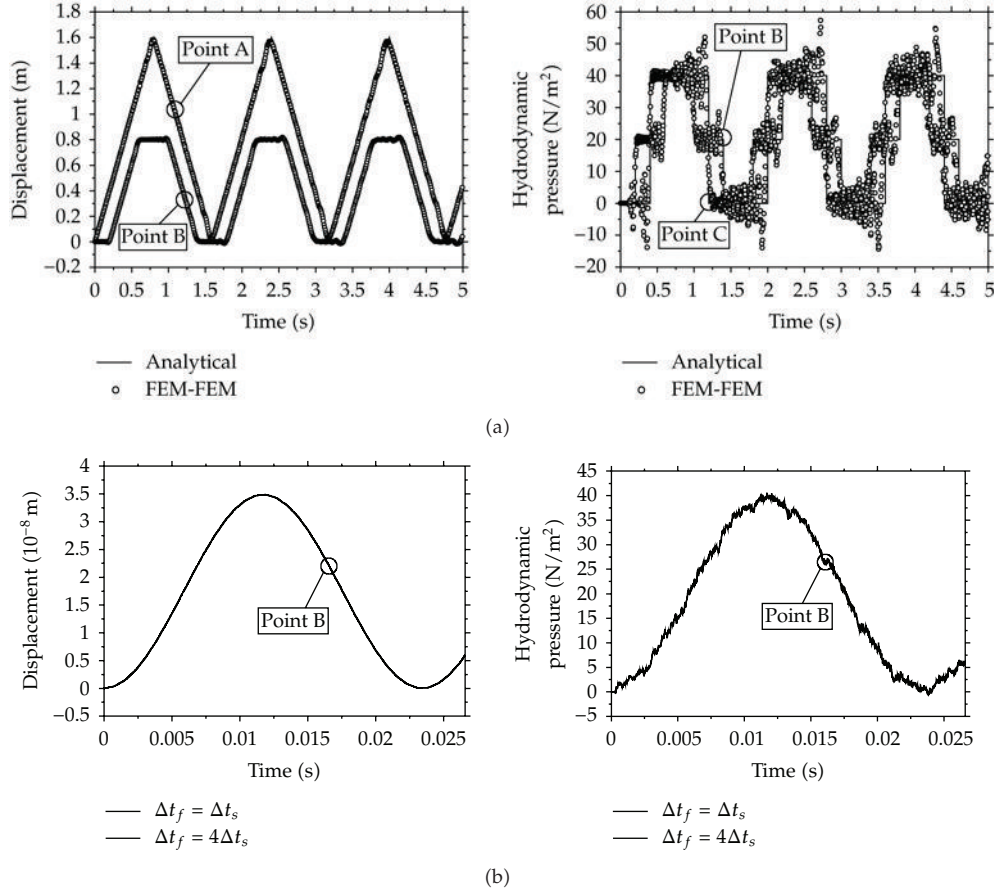


**Figure 4:** Time-history results for the solid-fluid column at points A, B, and C taking into account FEM-FEM coupling procedures (ExDCA) and different physical models: (a) homogeneous wave propagation velocities; (b) heterogeneous wave propagation velocities.

formulations are employed, as well as acoustic FDM formulation. 2500 linear hexahedral elements are adopted for the FEM elastodynamic mesh, and 1000 linear hexahedral elements are adopted for the FEM acoustic mesh. 2178 grid points are employed by the space fourth-order FDM discretization (grid points for mesh superposition included); (iii) Model 3: acoustic FEM and FDM formulations are employed. Two independent FEM meshes are adopted, each one with 2000 linear hexahedral elements. 1815 grid points are employed by the space fourth-order FDM discretization (grid points for mesh superposition included).

Two numerical analyses are considered, namely: (i) homogeneous analysis, where the entire column is considered composed by *Medium 1*; (ii) heterogeneous analysis, where half of the column is considered composed by *Medium 1*, and the other half by *Medium 2*. The results achieved for the three different numerical models described above are depicted in Figure 6. The heterogeneous analysis considers two different time steps, namely,  $\Delta t_1 = 0.05$  s (*Medium 1*) and  $\Delta t_2 = 0.10$  s (*Medium 2*). For the homogeneous analysis,  $\Delta t = 0.05$  s is adopted for the entire domain. In Figure 6, reference results are also depicted; these results correspond to a standard FEM simulation with 5000 linear hexahedral elements and  $\Delta t = 0.05$  s.

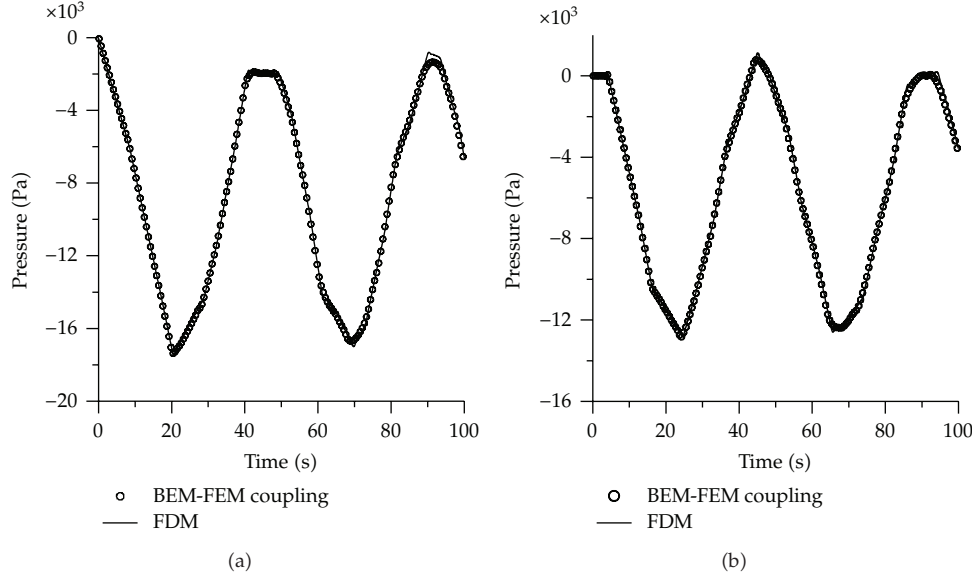


**Figure 5:** Time-history results for acoustic pressures taking into account FEM-BEM coupling procedures (ImICA) applied to a heterogeneous axisymmetric model: (a) results at point A; (b) results at point B.

(homogeneous and heterogeneous analyses). As one can see, results for all simulations are in good agreement.

Considering this first example, the advantages of the discussed multidomain decomposition procedures may be highlighted under several aspects: different time steps are easily adopted for each subdomain and, as a consequence, the algorithm becomes quite robust even when considering media with high properties contrast; moreover, less systems of equations need to be solved along the time-marching process; not all subdomains need to be considered at initial time steps, the activation/initialisation of different subdomains may be controlled based on the properties of the model (wave propagation velocities, etc.), saving most of the computational effort of the first time steps, and so forth.

## 5.2. Dam-Reservoir System

In this second example, a dam-reservoir system, as depicted in Figure 7, is analyzed. The structure is subjected to a sinusoidal distributed vertical load, acting on its crest with an angular frequency of  $\omega = 18$  rad/s. The material properties of the dam are  $\nu = 0.25$ ;  $E = 3.437 \cdot 10^9$  N/m<sup>2</sup>;  $\rho = 2000$  kg/m<sup>3</sup>. The adjacent water is characterized by a mass density  $\rho = 1000$  kg/m<sup>3</sup> and a wave velocity  $c = 1436$  m/s. The model is analyzed considering water levels defined by  $H = 50$  m and  $H = 35$  m.

Several ImICA and ExDCA are employed to analyze the dam-reservoir system. Taking into account the ImICA, the following discretizations are considered: (i) FEM-BEM—in this case, 93 quadrilateral finite elements are employed to discretize the dam, and the fluid is discretized by constant-length boundary elements ( $\ell = 5$  m). The time-steps adopted are  $\Delta t_f = 0.00350$  s and  $\Delta t_s = 0.00175$  s [14]; (ii) MLPG-MLPG—113 nodes are employed to discretize the dam, and the fluid is discretized by a regular equally spaced (horizontally sufficiently

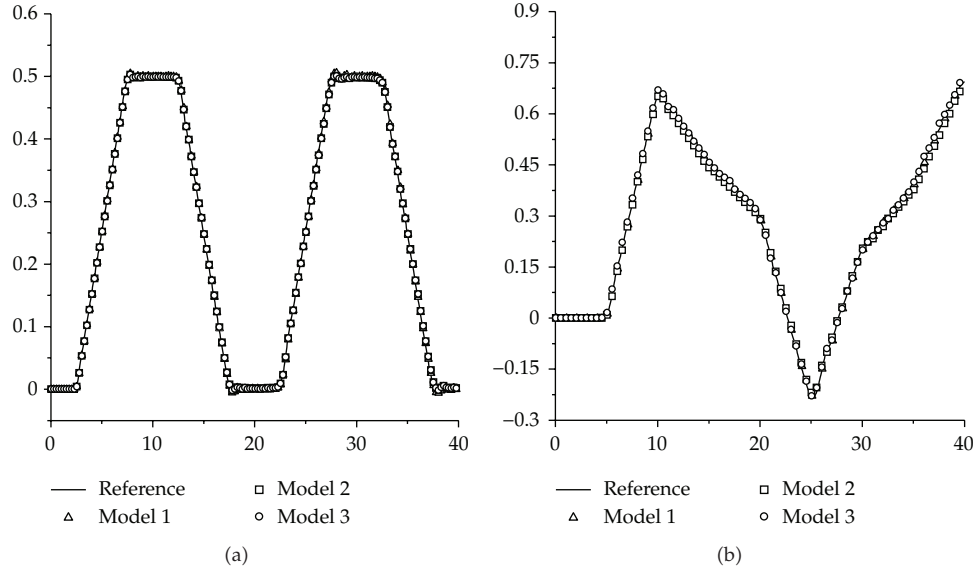


**Figure 6:** Time-history results (displacement/pressure  $\times$  time) at the interface of the three-dimensional column taking into account FEM-FEM and FEM-FDM coupling procedures (ExDCA): (a) homogeneous analysis; (b) heterogeneous analysis.

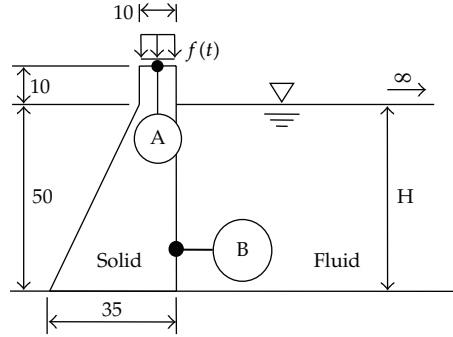


**Figure 7:** Sketch of the dam-reservoir system.

extended) distribution of nodes. The time-step adopted for the analyses is  $\Delta t = 0.002$  s [27]; (iii) BEM-BEM 1—34 linear boundary elements of equal length and 102 linear triangular cells are employed to model the dam, and the fluid is discretized by constant-length boundary elements ( $\ell = 5$  m). The time-steps adopted are  $\Delta t_f = 0.003$  s and  $\Delta t_s = 0.001$  s [23]; (iv) BEM-BEM 2—same as before, without the domain triangular cell mesh. The time-step adopted for the analyses is  $\Delta t = 0.003$  s [25]. Results for these ImICA are depicted in Figure 8, taking into account  $H = 50$  m and  $H = 35$  m.

Taking into account the ExDCA, the following discretizations are considered: (i) FEM-BEM—same as in the ImICA. The time-steps adopted are  $\Delta t_f = 0.00350$  s and  $\Delta t_s = 0.000875$  s [15]; (ii) FEM-FEM—77 quadrilateral elements are employed to discretize the dam, and the fluid is discretized by a regular (horizontally sufficiently extended) distribution of square elements. The time-steps adopted for the analyses are  $\Delta t_f = 0.0014$  s and

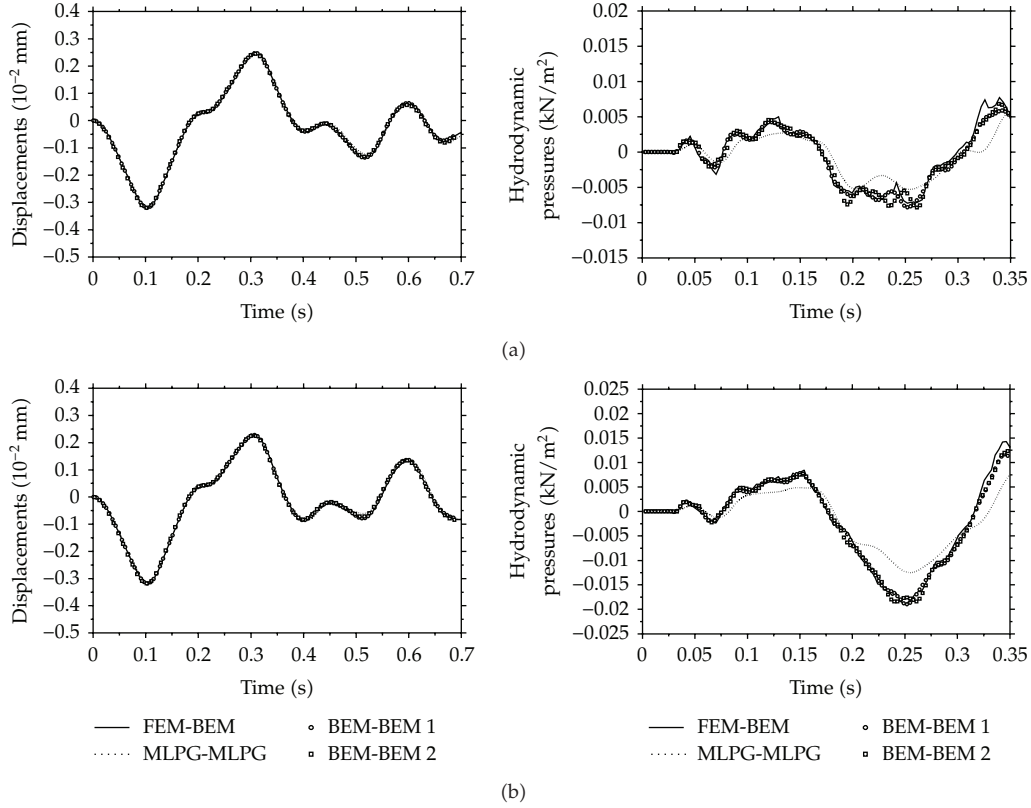


**Figure 8:** Time-history results for the dam-reservoir system considering the ImICA: (a)  $H = 35$  m; (b)  $H = 50$  m.

$\Delta t_s = 0.0007$  s [28]. Results for these ExDCA are depicted in Figure 9, taking into account  $H = 50$  m and  $H = 35$  m.

In this example, the advantages of employing different discretization procedures to analyze different subdomains of the global model can be explored. For instance, for the semi-infinite fluid domain, the BEM can be regarded as an appropriate discretization technique (infinite domain analysis), whereas domain-discretization methods can be applied to model the dam and consider some eventual more complicate behavior. In Figure 10, results are depicted ( $H = 50$  m) considering linear and nonlinear behavior (elastoplastic analysis, von Mises yield criterion) for the dam and an FEM-BEM discretization [17] for the model (ImICA).

The results presented so far are obtained taking into account a closed-domain dam, (null displacements are prescribed at the base of the dam and null fluxes are prescribed at the base of the storage lake). As is well known, boundary element formulations are an extremely elegant tool to model infinite media. As a consequence, in the present BEM-BEM 2 coupling context, analyses considering an opened-domain dam (acoustic-dynamic coupling also being carried out at the base of the storage lake) can be provided very easily. For the opened-domain dam case, time-history results are depicted in Figure 11 ( $H = 50$  m), considering the BEM-BEM 2 [25]. In Figure 12, some time snap shots are depicted, describing the displacement evolution of the closed/opened-domain dam.



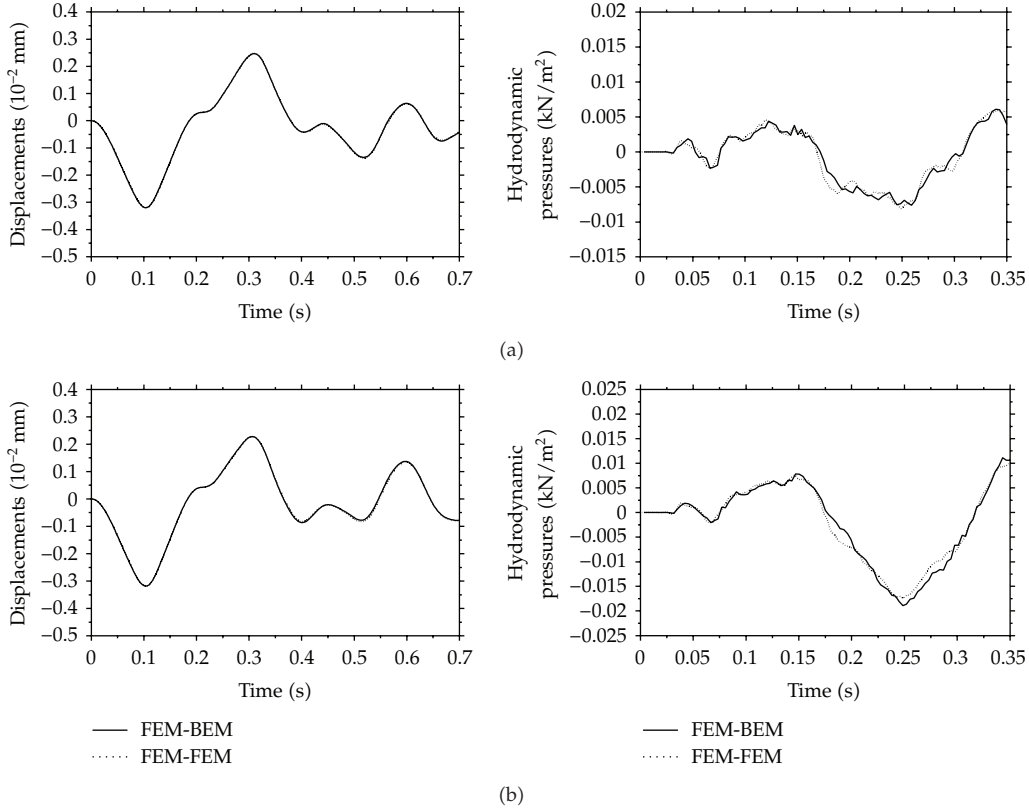


**Figure 9:** Time-history results for the dam-reservoir system considering the ExDCA: (a)  $H = 35$  m; (b)  $H = 50$  m.

### 5.3. Tube of Steel Submerged in Water

In this application, two analyses of a tube of steel submerged in water (axisymmetric models) are carried out. A sketch of the first model is depicted in Figure 13(a) [16]. A punctual source is located at the centre of the tube (axisymmetric axis), and it emits a signal characterized by three time-sinusoidal cycles ( $s(t) = \sin(\omega t)$ , where  $\omega = 10$  kHz). The properties of the media are (i) water:  $\rho = 1000 \text{ kg/m}^3$  and  $c = 1500 \text{ m/s}$ ; (ii) steel:  $\rho = 7700 \text{ kg/m}^3$ ,  $E = 2.1 \cdot 10^{11} \text{ N/m}^2$ , and  $\nu = 0.3$ . In an FEM-BEM ImICA, the boundary of the tube (water cavity) is discretized by acoustic linear boundary elements with length  $\ell = 0.02 \text{ m}$ . The tube itself is discretized by elastodynamic linear-square finite elements. The time steps selected are  $\Delta t_f = 8.0 \cdot 10^{-6} \text{ s}$  and  $\Delta t_s = 2.0 \cdot 10^{-6} \text{ s}$ . In an FEM-FDM ExDCA, analogous discretization is adopted for the tube, and part of the fluid is discretized by a sufficiently extended FDM mesh. Time-history hydrodynamic pressures at points A and B and displacements at point C (see Figure 13(a)) are depicted in Figure 14, for the FEM-BEM ImICA and for the FEM-FDM ExDCA. As one may observe, the time responses of these two different methodologies are quite similar.

A sketch of the second model is depicted in Figure 13(b) [24]. In this case, most of the domain is modelled by the FDM acoustic formulation (water). The metallic tube (marine riser) is modelled by the FEM elastodynamic formulation. A thin water layer surrounding the tube is also modelled by the FEM (acoustic formulation). Two different modelling procedures



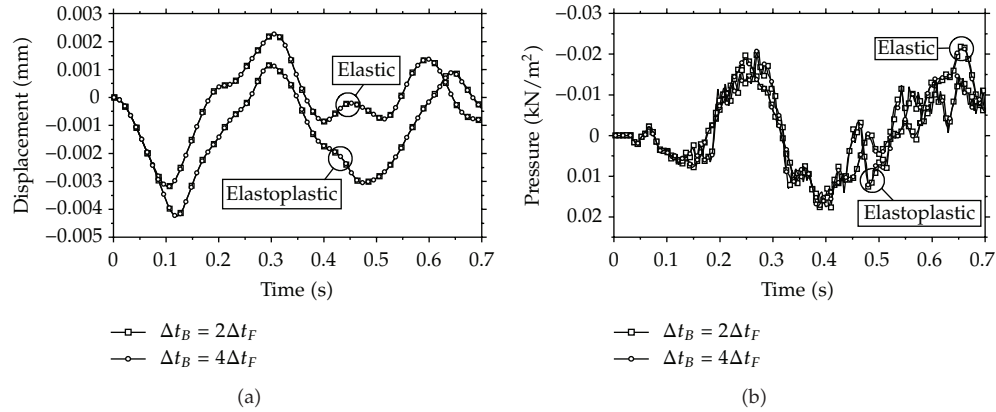


**Figure 10:** Time-history results considering linear and nonlinear material behavior and FEM-BEM implicit iterative coupling analyses.

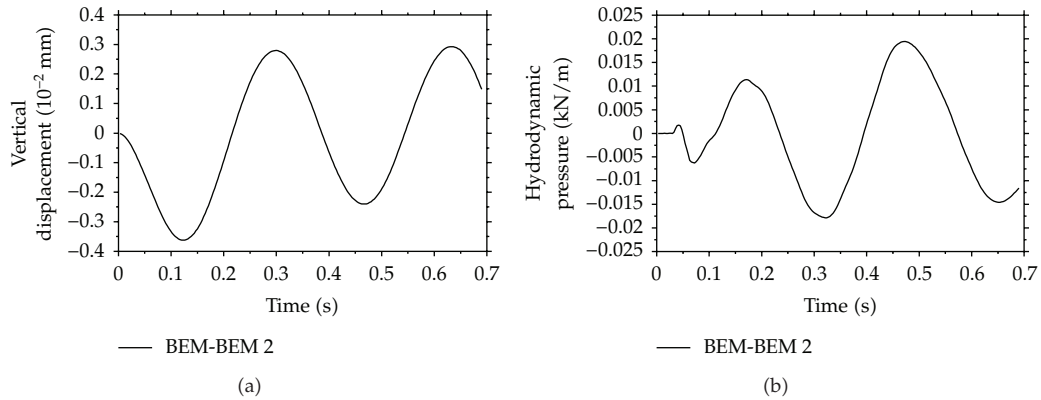


**Figure 11:** Time-history results for the opened-domain dam-reservoir system considering a BEM-BEM implicit iterative coupling analysis.

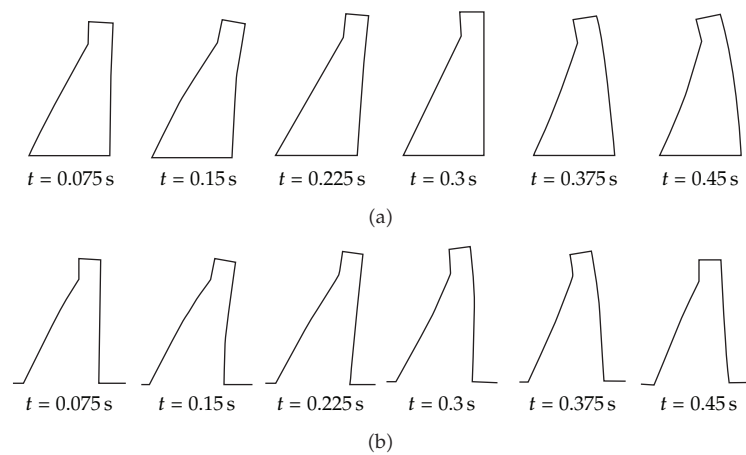


**Figure 12:** Scaled displacement results for the dam ( $H = 50$  m) along time: (a) closed-domain dam; (b) opened-domain dam.

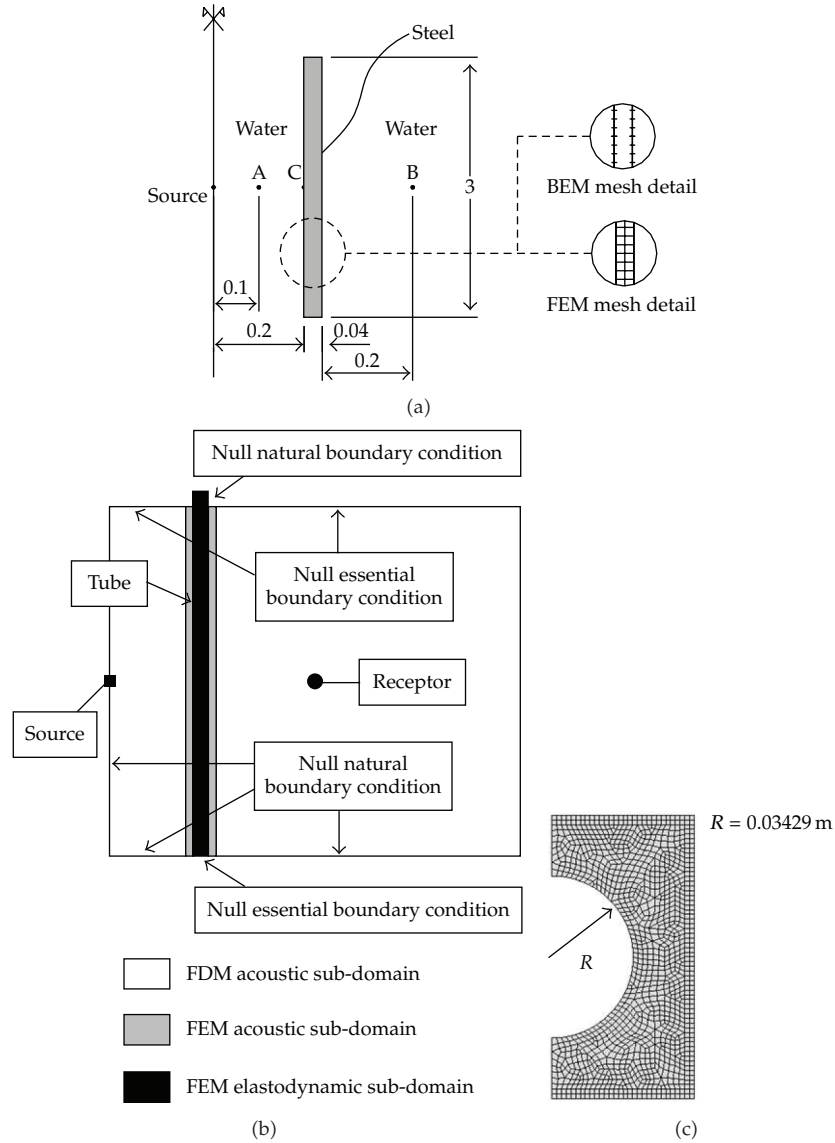


**Figure 13:** Sketch of the tube submerged in water: (a) first case of analysis; (b) second case of analysis; (c) detail of the FEM mesh adopted to model the neighbourhood of the spherical source.

are adopted to simulate the source: (i) the source is considered punctual, and an excitation term is introduced in the correspondent grid point of the FDM mesh; (ii) the source is considered spherical (radius  $0.03429$  m), and an FEM mesh is introduced to properly model its neighbourhood (this mesh is depicted in Figure 13(c)). Results obtained from a laboratory experiment [53], as illustrated in Figure 16, are used to validate the numerical response. The marine riser is characterized by  $\phi = 410$  mm (external diameter),  $t = 12$  mm (thickness), and  $h = 4.7$  m (height). The source produces a sinusoidal excitation with frequency of  $20$  kHz and duration of  $3.0 \cdot 10^{-4}$  s. The time steps adopted for each subdomain of the numerical model

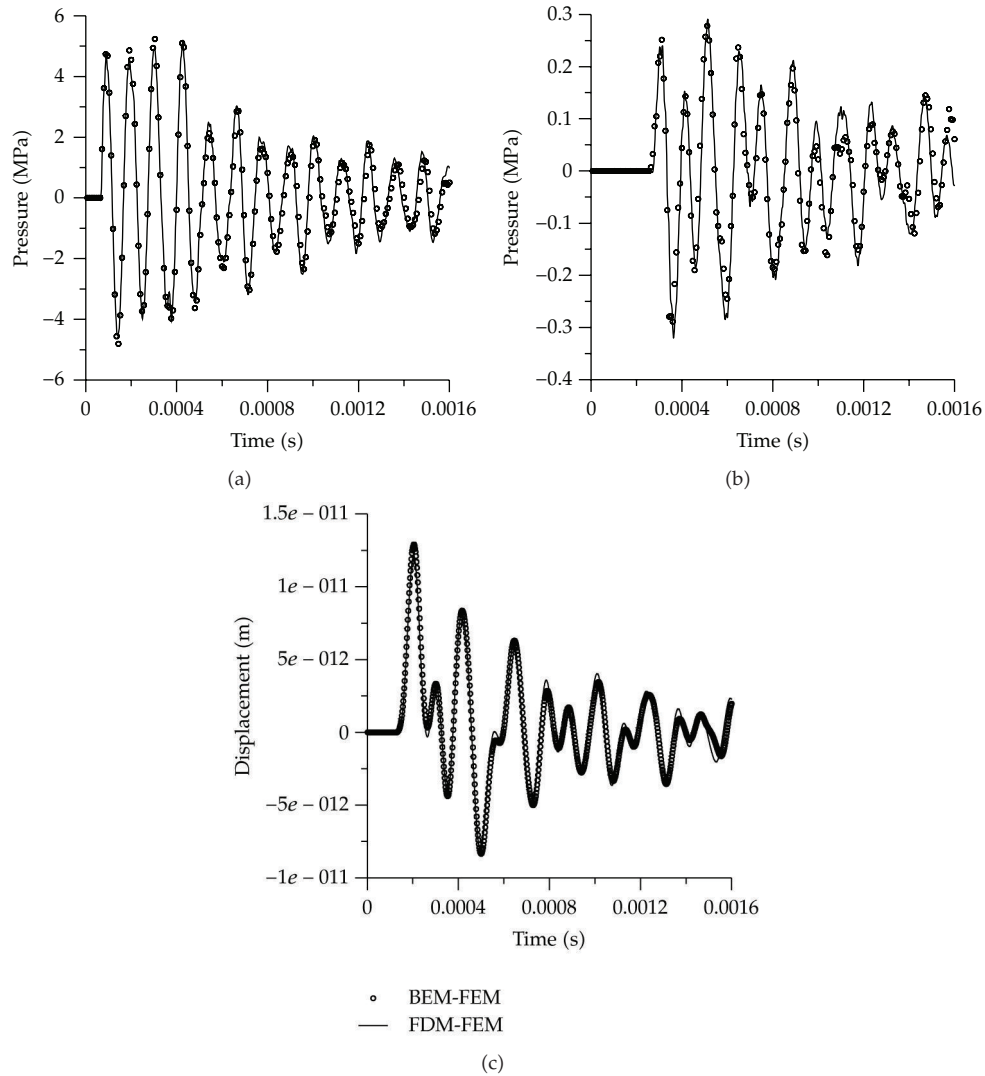


**Figure 14:** Time-history results for the tube of steel submerged in water (first case of analysis): (a) pressures at point A; (b) pressures at point B; (c) horizontal displacements at point C.

are  $\Delta t_1 = 2.0 \cdot 10^{-7}$  s (FDM mesh and FEM spherical source mesh);  $\Delta t_2 = 1.0 \cdot 10^{-7}$  s (FEM mesh surrounding the tube);  $\Delta t_3 = 0.5 \cdot 10^{-7}$  s (FEM tube mesh).

The results achieved for the hydrodynamic pressure at the receiver (hydrophone) are depicted in Figures 15(a) and 15(b), for the punctual and spherical source cases, respectively. The results obtained by the experimental analysis are depicted in Figure 15(c). As one may observe, good agreement between experimental and numerical (spherical source case) simulations is obtained (the scale of the graphics should be ignored, since the source intensities adopted in each analysis are different). Comparing the results depicted in Figures 15(a) and 15(b), one can clearly observe the energy dissipation in the source-receptor direction, due to the scattering induced by the spherical source. Figure 17 depicts three snap shots (FDM mesh) of the numerical analysis (punctual source case) and shows some

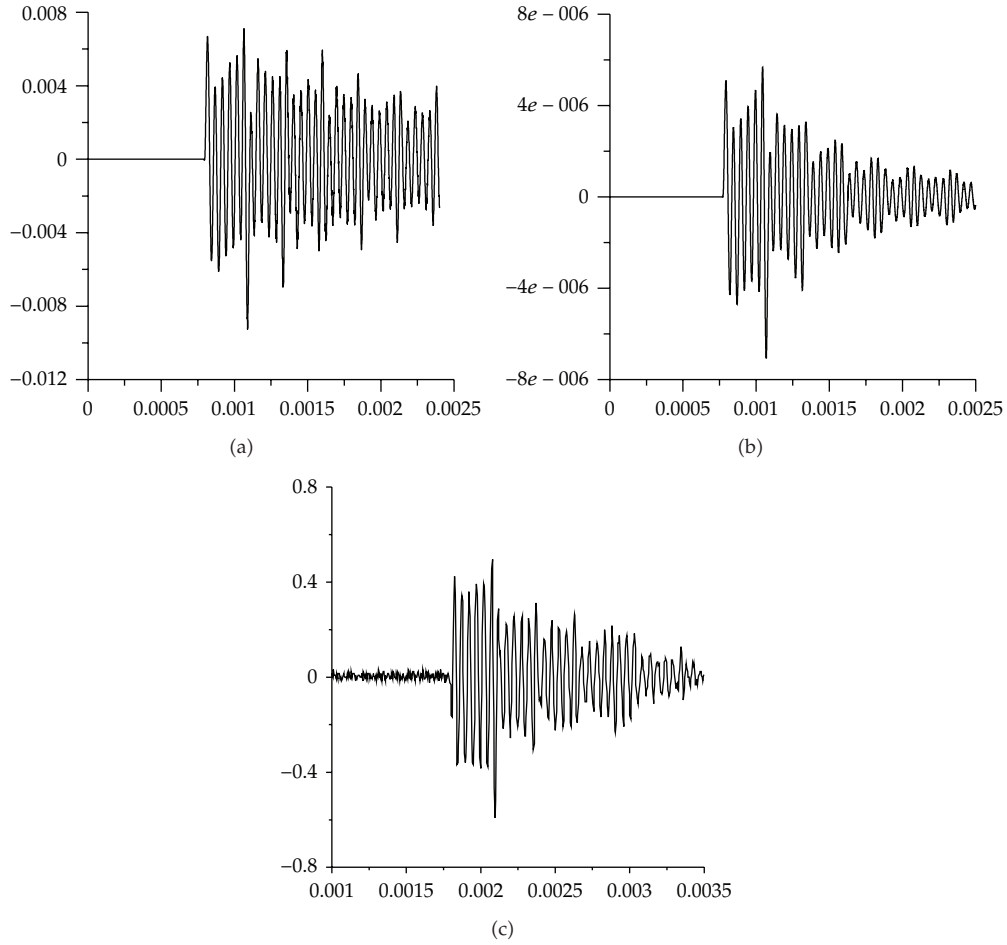


**Figure 15:** Numerical results (pressure  $\times$  time) at the receiver (second case of analysis) considering FEM-FDM explicit direct coupling procedures and (a) punctual and (b) spherical sources. (c) Experimental results at the receiver.

interesting and important features related to the present wave propagation configuration as, for instance, wave fronts (head waves) arising from the faster propagation through the tube (Figure 17(b)) generate a reinforcement of amplitude at the wave front region close to the tube (Figure 17(c)). If one interprets the phenomenon thinking on rays (ray tracing theory), one may be led to erroneously interpret this reinforcement of the amplitude at oblique incidence.

## 6. Conclusions

The present paper discusses multidomain decomposition techniques to model the propagation of interacting acoustic-elastic waves considering several coupling procedures. Two basic algorithms are presented here, namely, the ExDCA (explicit direct coupling approach) and the ImICA (implicit iterative coupling approach), which are based on explicit and implicit time-marching schemes, respectively, and multidomain decomposition coupling procedures. Within the context of these two basic algorithms, several coupled

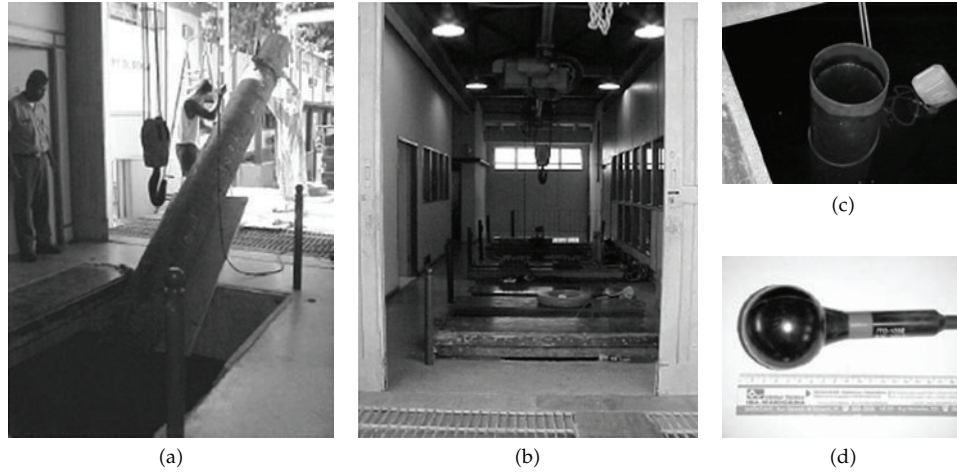


**Figure 16:** Photos of the experiment: (a) tube installation through the water tank input gate; (b) tank facilities; (c) tube inside the tank (view through the gate); (d) acoustic transducer ITC 1032 (source/receptor).

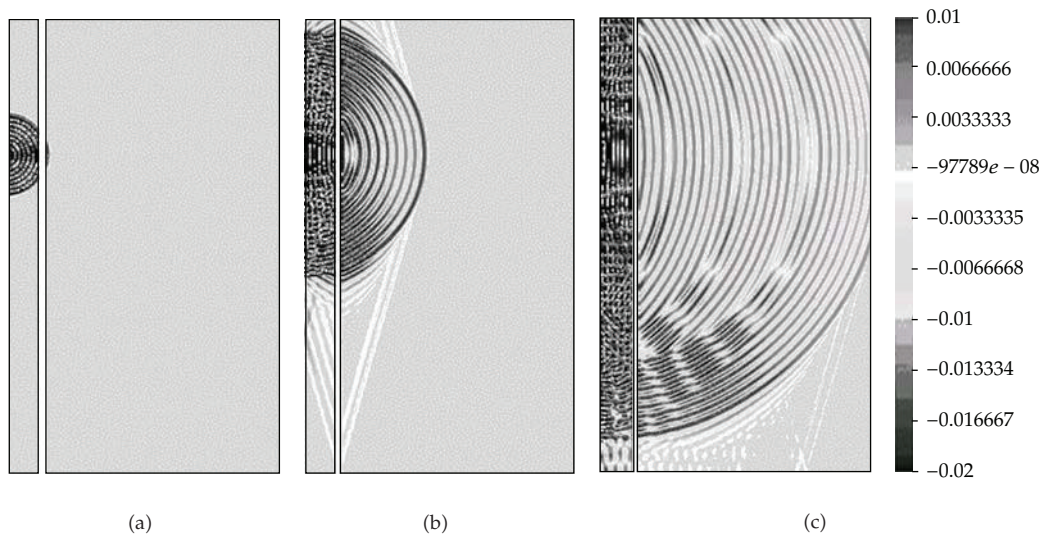


**Figure 17:** Pressure distribution for the punctual source case (FDM mesh) at three different moments: (a) begin of propagation; (b) wave fronts due to the faster propagation through the tube wall (head waves); (c) reinforcement of amplitude.

numerical methods are presented along the paper, such as FEM-FEM, FEM-FDM, FEM-BEM, BEM-BEM, DBEM-BEM, and MLPG-MLPG. Independent temporal and spatial (i.e., no matching nodes in common interfaces) discretizations within interacting subdomains are also discussed in the paper, being several applications of the discussed multilevel time-step algorithm presented along Section 5, illustrating its good performance and potentialities. As a matter of fact, in Section 5, several numerical applications are considered (e.g., acoustic-acoustic/acoustic-dynamic/dynamic-dynamic wave propagation problems, two-dimensional/three-dimensional/axisymmetric models, different coupled numerical

procedures, etc.), illustrating as a whole the good flexibility, accuracy, stability, and robustness of the discussed methodologies.

## Acknowledgments

The financial support by CNPq (Conselho Nacional de Desenvolvimento Científico e Tecnológico), FAPEMIG (Fundação de Amparo à Pesquisa do Estado de Minas Gerais), and PETROBRAS (Project no. 0050.0011058.05.3) is greatly acknowledged.

## References

- [1] O. C. Zienkiewicz and R. L. Taylor, *The Finite Element Method*, vol. 1, Butterworth-Heinemann, Oxford, UK, 5th edition, 2002.
- [2] J. Virieux, "P- SV wave propagation in heterogeneous media: velocity- stress finite-difference method," *Geophysics*, vol. 51, no. 4, pp. 889–901, 1986.
- [3] B. Lombard and J. Piraux, "Numerical treatment of two-dimensional interfaces for acoustic and elastic waves," *Journal of Computational Physics*, vol. 195, no. 1, pp. 90–116, 2004.
- [4] H. Y. Lee, S. C. Lim, D. J. Min, B. D. Kwon, and M. Park, "2D time-domain acoustic-elastic coupled modeling: a cell-based finite-difference method," *Geosciences Journal*, vol. 13, no. 4, pp. 407–414, 2009.
- [5] K. M. Lim and H. Li, "A coupled boundary element/finite difference method for fluid-structure interaction with application to dynamic analysis of outer hair cells," *Computers and Structures*, vol. 85, no. 11-14, pp. 911–922, 2007.
- [6] O. Von Estorff and H. Antes, "On FEM-BEM coupling for fluid-structure interaction analyses in the time domain," *International Journal for Numerical Methods in Engineering*, vol. 31, no. 6, pp. 1151–1168, 1991.
- [7] S. Amini, P. J. Harris, and D. T. Wilton, *Coupled Boundary and Finite Element Methods for the Solution of the Dynamic Fluid-Structure Interaction Problem*, Springer, Berlin, Germany, 1992.
- [8] X. G. Zeng and F. Zhao, "A coupled FE and boundary integral equation method based on exterior domain decomposition for fluid-structure interface problems," *International Journal of Solids and Structures*, vol. 31, no. 8, pp. 1047–1061, 1994.
- [9] H. M. Koh, J. K. Kim, and J. H. Park, "Fluid-structure interaction analysis of 3-D rectangular tanks by a variationally coupled BEM-FEM and comparison with test results," *Earthquake Engineering and Structural Dynamics*, vol. 27, no. 2, pp. 109–124, 1998.
- [10] S. T. Lie, G. Yu, and Z. Zhao, "Coupling of BEM/FEM for time domain structural-acoustic interaction problems," *Computer Modeling in Engineering and Sciences*, vol. 2, no. 2, pp. 171–181, 2001.
- [11] O. Czygan and O. Von Estorff, "Fluid-structure interaction by coupling BEM and nonlinear FEM," *Engineering Analysis with Boundary Elements*, vol. 26, no. 9, pp. 773–779, 2002.
- [12] L. Gaul and W. Wenzel, "A coupled symmetric BE-FE method for acoustic fluid-structure interaction," *Engineering Analysis with Boundary Elements*, vol. 26, no. 7, pp. 629–636, 2002.
- [13] A. Márquez, S. Meddahi, and V. Selgas, "A new BEM-FEM coupling strategy for two-dimensional fluid-solid interaction problems," *Journal of Computational Physics*, vol. 199, no. 1, pp. 205–220, 2004.
- [14] D. Soares, O. von Estorff, and W. J. Mansur, "Efficient non-linear solid-fluid interaction analysis by an iterative BEM/FEM coupling," *International Journal for Numerical Methods in Engineering*, vol. 64, no. 11, pp. 1416–1431, 2005.
- [15] D. Soares and W. J. Mansur, "An efficient time-domain BEM/FEM coupling for acoustic-elastodynamic interaction problems," *Computer Modeling in Engineering and Sciences*, vol. 8, no. 2, pp. 153–164, 2005.
- [16] A. Warszawski, D. Soares, and W. J. Mansur, "A FEM-BEM coupling procedure to model the propagation of interacting acoustic-acoustic/acoustic-elastic waves through axisymmetric media," *Computer Methods in Applied Mechanics and Engineering*, vol. 197, no. 45–48, pp. 3828–3835, 2008.
- [17] D. Soares, "Fluid-structure interaction analysis by optimised boundary element-finite element coupling procedures," *Journal of Sound and Vibration*, vol. 322, no. 1-2, pp. 184–195, 2009.
- [18] O. C. Zienkiewicz and P. Bettess, "Fluid-structure dynamic interaction and wave forces. An introduction to numerical treatment," *International Journal for Numerical Methods in Engineering*, vol. 13, no. 1, pp. 1–16, 1978.



- [19] D. Komatitsch, C. Barnes, and J. Tromp, "Wave propagation near a fluid-solid interface: a spectral-element approach," *Geophysics*, vol. 65, no. 2, pp. 623–631, 2000.
- [20] K. C. Park, C. A. Felippa, and R. Ohayon, "Partitioned formulation of internal fluid-structure interaction problems by localized lagrange multipliers," *Computer Methods in Applied Mechanics and Engineering*, vol. 190, no. 24-25, pp. 2989–3007, 2001.
- [21] L. Godinho, A. Tadeu, and F. J. Branco, "Wave scattering by infinite cylindrical shell structures submerged in a fluid medium," *Wave Motion*, vol. 38, no. 2, pp. 131–149, 2003.
- [22] X. Feng and Z. Xie, "A priori error estimates for a coupled finite element method and mixed finite element method for a fluid-solid interaction problem," *IMA Journal of Numerical Analysis*, vol. 24, no. 4, pp. 671–698, 2004.
- [23] D. Soares and W. J. Mansur, "Dynamic analysis of fluid-soil-structure interaction problems by the boundary element method," *Journal of Computational Physics*, vol. 219, no. 2, pp. 498–512, 2006.
- [24] D. Soares, W. J. Mansur, and D. L. Lima, "An explicit multi-level time-step algorithm to model the propagation of interacting acoustic-elastic waves using finite element/finite difference coupled procedures," *Computer Modeling in Engineering and Sciences*, vol. 17, no. 1, pp. 19–34, 2007.
- [25] D. Soares, "Numerical modelling of acoustic-elastodynamic coupled problems by stabilized boundary element techniques," *Computational Mechanics*, vol. 42, no. 6, pp. 787–802, 2008.
- [26] M. R. Ross, C. A. Felippa, K. C. Park, and M. A. Sprague, "Treatment of acoustic fluid-structure interaction by localized Lagrange multipliers: formulation," *Computer Methods in Applied Mechanics and Engineering*, vol. 197, no. 33-40, pp. 3057–3079, 2008.
- [27] D. Soares, "An iterative time-domain algorithm for acoustic-elastodynamic coupled analysis considering meshless local Petrov-Galerkin formulations," *Computer Modeling in Engineering and Sciences*, vol. 54, no. 2, pp. 201–221, 2009.
- [28] D. Soares, G. G. Rodrigues, and K. A. Gonçalves, "An efficient multi-time-step implicit-explicit method to analyze solid-fluid coupled systems discretized by unconditionally stable time-domain finite element procedures," *Computers & Structures*, vol. 88, no. 5-6, pp. 387–394, 2010.
- [29] Z. C. He, G. R. Liu, Z. H. Zhong, G. Y. Zhang, and A. G. Cheng, "Coupled analysis of 3D structuralacoustic problems using the edge-based smoothed finite element method/finite element method," *Finite Elements in Analysis and Design*, vol. 46, no. 12, pp. 1114–1121, 2010.
- [30] Z. C. He, G. R. Liu, Z. H. Zhong, G. Y. Zhang, and A. G. Cheng, "A coupled ES-FEM/BEM method for fluidstructure interaction problems," *Engineering Analysis with Boundary Elements*, vol. 35, no. 1, pp. 140–147, 2011.
- [31] R. J. LeVeque, *Finite Difference Methods for Ordinary and Partial Differential Equations: Steady-State and Time-Dependent Problems*, Society for Industrial and Applied Mathematics (SIAM), Philadelphia, Pa, USA, 2007.
- [32] G. C. Cohen, *Higher-Order Numerical Methods for Transient Wave Equations*, Springer, Berlin, Germany, 2002.
- [33] T. J. R. Hughes, *The Finite Element Method*, Dover, New York, NY, USA, 1987.
- [34] K. J. Bathe, *Finite Element Procedures*, Prentice-Hall, Englewood Cliffs, NJ, USA, 1996.
- [35] M. A. Crisfield, *Non-linear Finite Element Analysis of Solid Structures*, vol. 1-2, John Wiley & Sons, Chichester, UK, 1991.
- [36] T. Belytschko, W. K. Liu, and B. Moran, *Nonlinear Finite Elements for Continua and Structures*, John Wiley & Sons, Chichester, UK, 2000.
- [37] S. Atluri, *The Meshless Method (MLPG) for Domain & BIE Discretizations*, Tech Science Press, Encino, Calif, USA, 2004.
- [38] G. R. Liu, *Meshfree Methods, Moving beyond the Finite Element Method*, CRC Press, Boca Raton, Fla, USA, 2nd edition, 2010.
- [39] D. Soares and W. J. Mansur, "A time domain FEM approach based on implicit Green's functions for non-linear dynamic analysis," *International Journal for Numerical Methods in Engineering*, vol. 62, no. 5, pp. 664–681, 2005.
- [40] D. Soares, "A time-marching scheme based on implicit Green's functions for elastodynamic analysis with the domain boundary element method," *Computational Mechanics*, vol. 40, no. 5, pp. 827–835, 2007.
- [41] D. Soares, "A new family of time marching procedures based on Green's function matrices," *Computers & Structures*, vol. 89, no. 1-2, pp. 266–276, 2011.
- [42] J. C. Houbolt, "A recurrence matrix solution for the dynamic response of elastic aircraft," *Journal of the Aeronautical Sciences*, vol. 17, pp. 540–550, 1950.
- [43] N. M. Newmark, "A method of computation for structural dynamics," *ASCE Journal of Engineering Mechanics Division*, vol. 85, pp. 67–94, 1959.

- [44] W. J. Mansur, *A time-stepping technique to solve wave propagation problems using the boundary element method*, Ph.D. thesis, University of Southampton, England, UK, 1983.
- [45] J. Dominguez, *Boundary Elements in Dynamics*, International Series on Computational Engineering, Computational Mechanics Publications, Southampton, UK, 1993.
- [46] *Boundary Elements in Acoustics*, vol. 9 of *Advances in Boundary Elements*, WIT Press, Southampton, UK, 2000.
- [47] D. Beskos and G. Maier, *Boundary Element Advances in Solid Mecha*, Springer, New York, NY, USA, 2003.
- [48] J. A. M. Carrer and J. C. F. Telles, "A boundary element formulation to solve transient dynamic elastoplastic problems," *Computers & Structures*, vol. 45, no. 4, pp. 707–713, 1992.
- [49] J. A. M. Carrer and W. J. Mansur, "Alternative time-marching schemes for elastodynamic analysis with the domain boundary element method formulation," *Computational Mechanics*, vol. 34, no. 5, pp. 387–399, 2004.
- [50] D. Soares, "Acoustic modelling by BEM-FEM coupling procedures taking into account explicit and implicit multi-domain decomposition techniques," *International Journal for Numerical Methods in Engineering*, vol. 78, no. 9, pp. 1076–1093, 2009.
- [51] J. W. Milles, "Integral transforms," in *Modern Mathematics for the Engineer*, E. F. Beckenbach, Ed., pp. 82–84, McGraw-Hill, London, UK, 1961.
- [52] G. Cohen and P. Joly, "Fourth order schemes for the heterogeneous acoustics equation," *Computer Methods in Applied Mechanics and Engineering*, vol. 80, pp. 397–407, 1990.
- [53] D. L. Lima, *Through-riser acoustic communication system for ultra-deep water completion*, M.S. thesis, Federal University of Rio de Janeiro, Brazil, 2004.



## Research Article

# Interior Noise Prediction of the Automobile Based on Hybrid FE-SEA Method

**S. M. Chen,<sup>1,2</sup> D. F. Wang,<sup>1,2</sup> and J. M. Zan<sup>3</sup>**

<sup>1</sup> State Key Laboratory of Automotive Simulation and Control, Jilin University, Changchun 130022, China

<sup>2</sup> College of Automobile Engineering, Jilin University, No. 5988 Renmin Street, Changchun 130022, China

<sup>3</sup> State Key Laboratory of Vehicle NVH and Safety Technology, Chongqing 401120, China

Correspondence should be addressed to D. F. Wang, caewdf@jlu.edu.cn

Received 6 May 2011; Accepted 11 July 2011

Academic Editor: Delfim Jr. Soares

Copyright © 2011 S. M. Chen et al. This is an open access article distributed under the Creative Commons Attribution License, which permits unrestricted use, distribution, and reproduction in any medium, provided the original work is properly cited.

In order to predict the interior noise of the automobile in the low and middle frequency band in the design and development stage, the hybrid FE-SEA model of an automobile was created using hybrid FE-SEA method. The modal density was calculated using analytical method and finite element method; the damping loss factors of the structural and acoustic cavity subsystems were also calculated with analytical method; the coupling loss factors between structure and structure, structure and acoustic cavity were both calculated. Four different kinds of excitations including road excitations, engine mount excitations, sound radiation excitations of the engine, and wind excitations are exerted on the body of automobile when the automobile is running on the road. All the excitations were calculated using virtual prototype technology, computational fluid dynamics (CFD), and experiments realized in the design and development stage. The interior noise of the automobile was predicted and verified at speed of 120 km/h. The predicted and tested overall SPLs of the interior noise were 73.79 and 74.44 dB(A) respectively. The comparison results also show that the prediction precision is satisfied, and the effectiveness and reliability of the hybrid FE-SEA model of the automobile is verified.

## 1. Introduction

Statistical Energy Analysis (SEA) method is widely used by many automobile industries and institutes to model automotive vibroacoustic system at high frequencies [1–4]. The subsystems with many modes show a short wavelength behavior and suit the application of the SEA method. At low frequencies, the assumptions of random resonance frequencies and mode shapes become less useful. The subsystems with few modes display a long wavelength behavior, and they are usually modeled using Finite Element Method (FEM). In order to deal with low and middle frequencies, a hybrid modeling method including finite element and statistical energy analysis (Hybrid FE-SEA) is used to develop the vibroacoustic model of the automobile system [5–9]. Meanwhile, the finite element method is a deterministic method,

and the SEA is a statistical method, the hybrid FE-SEA method combines two different methods to produce noniterative hybrid method which includes equations of dynamic equilibrium and power balance.

Langley [10–13] has an important contribution to the development of the hybrid FE-SEA method. And with the development of the hybrid FE-SEA method; it is widely used in automobile industry gradually. Charpentier et al. [14] predicted the structure-borne noise transmission in a trimmed automotive vehicle. And then, he also improved the design for interior noise using a hybrid FE-SEA model of a trimmed vehicle. And the sample prediction results illustrating the impact of design changes on interior noise level were shown along with the experimental validation result [15]. Musser and Rodrigues [16] improved the mid-frequency prediction accuracy for fully trimmed vehicle using hybrid FE-SEA technique. Shorter et al. [17] predicted and diagnosed component transmission loss using the hybrid FE-SEA method. Cotoni et al. [18] built a model of aircraft to predict the interior noise using the hybrid FE-SEA method, and it was demonstrated that the hybrid FE-SEA method can be successfully used to improve SEA models by including some details to the model that affect the vibroacoustic performance of the system. Manning [19] explored the hybrid method to expand SEA to the mid- and low frequency range where the assumption of high modal density is not valid. Cordioli et al. [20] investigated the acoustic performance of various slits using fast 3D numerical models based on the hybrid FE-SEA method, and the numerical investigation of the transmission loss of the seals and slits was performed for airborne SEA predictions.

In this research, a simplified hybrid FE-SEA model was built to predict the automobile interior noise. It is not the normal prediction with some experiments, but the interior noise was predicted at the development and design stage of the automobile. It is based on the prediction of the parameters and excitations. The parameters include modal density, damping loss factor, and coupling loss factor, and the excitations incorporate sound excitation of engine cabin, excitation of engine mounts, excitation of road roughness, and wind excitations.

## 2. Principle of Hybrid FE-SEA Method

The degrees of freedom  $q$  for one of the subsystems describe the displacement on the boundary. The relationship between  $q$  and a corresponding set of external forces  $f$  acting at the boundary can be written as:

$$f = Dq, \quad (2.1)$$

where  $D$  is the frequency-dependent dynamic stiffness matrix.

Formula (2.1) can be derived as

$$f_{\text{rev}} = D_{\text{dir}}q - Dq, \quad (2.2)$$

where  $D_{\text{dir}}$  is the “direct field” dynamic stiffness matrix and  $f_{\text{rev}}$  is “reverberant” force.

Formula (2.2) is substituted into Formula (2.1), and the new equation can be written as:

$$f_{\text{rev}} + f = D_{\text{dir}}q \quad (2.3)$$

The correlation between the response at node  $j$  of structure and node  $k$  of acoustic cavity can be written as

$$S_{qq} = -\left(\frac{4E}{\pi\omega n}\right) \text{Im}\{H_{\text{dir}}\} \Rightarrow E[q_j q_k^*] = -\left(\frac{4E}{\pi\omega n}\right) \text{Im}\{G(r_{jk})\}, \quad (2.4)$$

where  $H_{\text{dir}}$  is receptance matrix, and it is also the inverse of  $D_{\text{dir}}$ ,  $E$  is the vibrational energy of the structural subsystem,  $G$  is the Green function, and  $r_{ij}$  is the distance between the grid points  $i$  and  $j$ .  $\omega$  is the angular frequency, and  $n$  is the modal density of subsystem.

The hybrid FE-SEA equation can be written as

$$\begin{aligned} \sum_k \omega \eta_{jk} n_j \left( \frac{E_j}{n_j} - \frac{E_k}{n_k} \right) + \omega E_j (\eta_j + \eta_{dj}) &= P_j + P_{\text{in},j}^{\text{ext}}, \quad j = 1, 2, 3, \dots, \\ \omega \eta_{dj} &= \left( \frac{2}{\pi n_j} \right) \sum_{r,s} \text{Im} \{D_{d,rs}\} \left( D_{\text{tot}}^{-1} \text{Im} \{D_{\text{dir}}^{(j)}\} D_t^{-1*T} \right)_{rs} \\ \omega \eta_{jk} n_j &= \left( \frac{2}{\pi} \right) \sum_{r,s} \text{Im} \{D_{\text{dir},rs}^{(j)}\} \left( D_t^{-1} \text{Im} \{D_{\text{dir}}^{(j)}\} D_t^{-1*T} \right)_{rs} \\ P_{\text{in},j}^{\text{ext}} &= \left( \frac{\omega}{2} \right) \sum_{r,s} \text{Im} \{D_{\text{dir},rs}^{(j)}\} \left( D_t^{-1} S_{ff} D_t^{-1*T} \right)_{rs}, \end{aligned} \quad (2.5)$$

where  $\eta_j$  is the damping loss factor of the subsystem  $j$ ,  $P_j$  is the input power of subsystem  $j$ ,  $P_{\text{in},j}^{\text{ext}}$  is the power that arises from forces applied to the deterministic system,  $\eta_{jk}$  is the coupling loss factor between subsystem  $j$  and  $k$ ,  $n_j$  is the modal density of subsystem  $j$ , and  $S_{ff}$  is the cross-spectrum of the forces applied to the deterministic system.

### 3. Hybrid FE-SEA Model of the Automobile

The finite element model of the body in white (BIW) of the passenger automobile was created. The model is shown in Figure 1, and it includes 249481 nodes and 249963 elements. The mesh was mainly generated using quadrilateral elements, and some triangular elements are also included in the finite element model.

According to the finite element model of the body in white of the passenger automobile, a hybrid FE-SEA model was built. The subsystems of the hybrid FE-SEA model must be divided into FE subsystems or SEA subsystems. The large plate subsystems can be divided into SEA subsystems due to the high density such as roof, front and rear windshields, window glasses, and floor, and the beam-type subsystems can be divided into FE subsystems, such as A-pillar, B-pillar, C-pillar, and subframe. The division and properties of the subsystems of the hybrid FE-SEA model are shown in Table 1. Then, according to the nodes and elements of the FE model, the FE subsystems were created in the hybrid FE-SEA model, such as shock tower and longitudinal beams. Also, the SE subsystems were built based on the nodes from FE subsystems, such as roof and engine hood. The subsystems must be connected between FE and SE subsystems, FE and FE subsystems, and SE and SE subsystems in order to ensure that energy can transfer between connected subsystems. The last step of the modeling is to apply external excitations to the hybrid FE-SEA model.

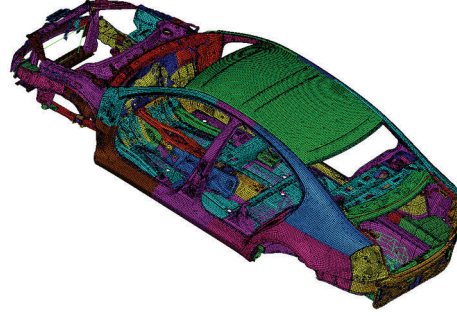


**Figure 1:** Finite element model of the body in white.

**Table 1:** Subsystem division and properties of the hybrid FE-SEA model.

Subsystem	Property	Subsystem	Property
Left-front door	SE curved plate	Right-front door	SE curved plate
Left-rear door	SE curved plate	Right-rear door	SE curved plate
Left-front window glass	SE plate	Right-front window glass	SE plate
Left-rear window glass	SE plate	Right-rear window glass	SE plate
Front windshield	SE plate	Rear windshield	SE plate
Front floor	SE plate	Rear floor	SE plate
Left-rear side wall	SE curved plate	Right-rear side wall	SE curved plate
Left A-pillar	FE	Right A-pillar	FE
Left B-pillar	FE	Right B-pillar	FE
Left C-pillar	FE	Right C-pillar	FE
Left-front fender	SE curved plate	Right-front fender	SE curved plate
Left-rear fender	SE curved plate	Right-rear fender	SE curved plate
Left-front mudguard	SE curved plate	Right-front mudguard	SE curved plate
Left-rear mudguard	SE curved plate	Right-rear mudguard	SE curved plate
Left-front shock tower	FE	Right-front shock tower	FE
Front bumper	SE curved plate	Rear bumper	SE curved plate
Left longitudinal beam	FE	Right longitudinal beam	FE
Subframe	FE	Firewall	FE
Trunk	SE curved plate	Engine hood	SE plate
Roof	SE curved plate	Trunk floor	SE plate
Passenger compartment cavity	SE cavity	Trunk cavity	SE cavity

The hybrid FE-SEA model is shown in Figure 2. It contains 89605 nodes. The hybrid FE-SEA is 159876 nodes less than the body in white of the automobile. Meanwhile, the whole body of the automobile including windshields, and doors contains 336305 nodes, and the hybrid FE-SEA model is 246700 nodes less than the whole body of the automobile. The acoustic cavities in the hybrid FE-SEA model are shown in Figure 3.

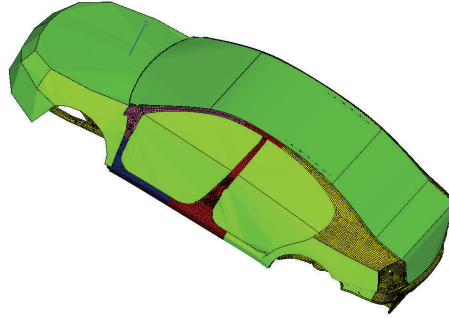


**Figure 2:** Hybrid FE-SEA model of the automobile.

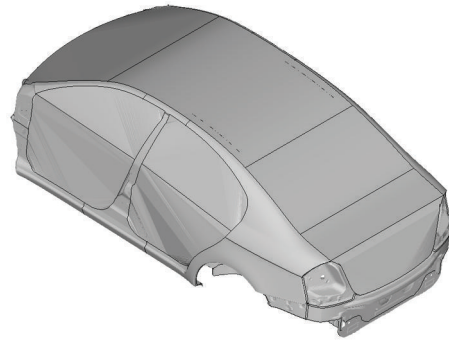


**Figure 3:** Acoustic cavities in the hybrid FE-SEA model.

## 4. Parameters of the Hybrid FE-SEA Model

### 4.1. Modal Density

In the hybrid FE-SEA model of automobile, FE subsystems and SE subsystems are included in the model. The SE subsystems can be simplified into regularly shaped plate. The modal densities of the SE subsystems such as roof, engine hood, trunk, and windows can be calculated with following equation:

$$n(f) = \frac{A_p}{2RC_l}, \quad (4.1)$$

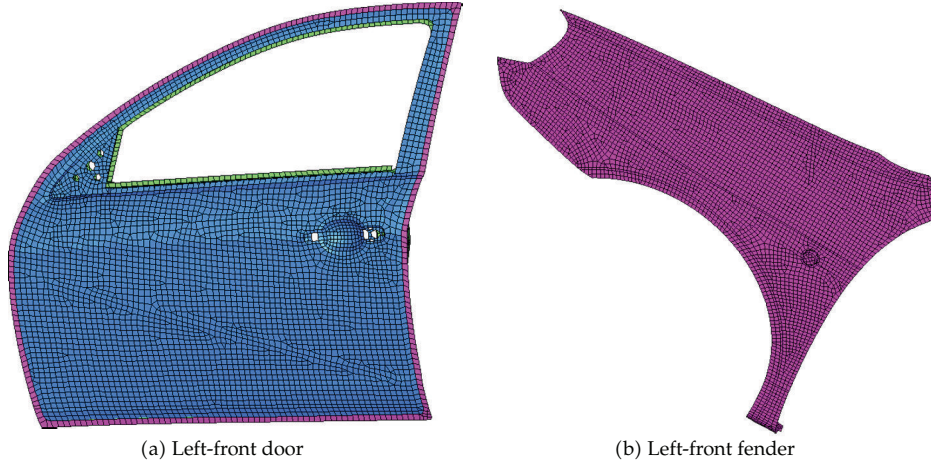
where  $A_p$  is the area of the two-dimensional flat plate,  $R$  is radius of gyration, and  $C_l$  is longitudinal wave velocity. Some flat plates and curved plates were simplified to flat plates, and the modal densities of the SE subsystems are shown in Table 2.

The modal density is defined as

$$n(f) = \frac{N}{f_u - f_d}, \quad (4.2)$$

**Table 2:** Modal densities of the subsystems simplified to flat plates.

No.	SE subsystem	Property	Simplified	Modal density (Hz <sup>-1</sup> )
1	Front windshield	SE plate	Flat plate	0.0747
2	Rear windshield	SE plate	Flat plate	0.0781
3	Roof	SE curved plate	Flat plate	0.8422
4	Left-front window	SE plate	Flat plate	0.0305
5	Left-rear window	SE plate	Flat plate	0.0299
6	Right-front window	SE plate	Flat plate	0.0306
7	Right-rear window	SE plate	Flat plate	0.0300
8	Trunk	SE curved plate	Flat plate	0.3699
9	Engine hood	SE plate	Flat plate	0.4995

**Figure 4:** Finite element models of the subsystems.

where  $N$  is the mode numbers between  $f_u$  and  $f_d$ ,  $f_u$  is the upper limit frequency of 1/3 octave band,  $f_d$  is the lower limit frequency of 1/3 octave band, and  $f$  is the center frequency of 1/3 octave band.

The modal densities of the FE subsystems and complicated SE subsystems can be calculated by formula (4.2). The modal densities of the FE subsystems can be calculated through finite element analysis. In order to obtain the modal information of the subsystems, finite element models of the subsystems in the hybrid FE-SEA model were created, and the left-front door and left-front fender are shown in Figure 4. Meanwhile, the modal analysis was performed for the finite element subsystem models. The modal density of the A-pillar is shown in Figure 5. The maximal modal density of the A-pillar is 0.1370 Hz<sup>-1</sup> at 31.5 Hz. Three zero points of the modal density are at 20, 25, and 50 Hz, respectively. The modal density of the A-pillar increases from 63 to 1000 Hz in the view of the overall curve.

Taking spatial acoustic field of a cuboid with rigid walls ( $r_1, r_2, r_3, 0 \leq x_i \leq r_i, i = 1, 2, 3$ ) into consideration, it is assumed that the energy will not be loss, and the sound pressure can be written as

$$p = P\varphi(x_1, x_2, x_3)e^{i\omega t}, \quad (4.3)$$

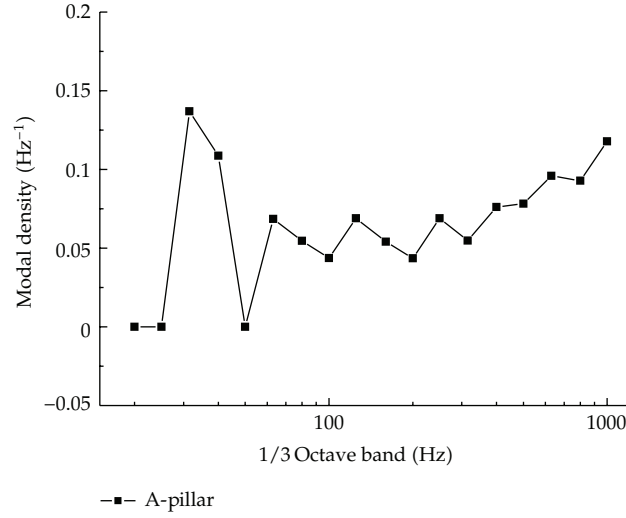


**Figure 5:** Modal density of the A-pillar.

where  $P$  is the amplitude of the sound pressure and  $\varphi(x_1, x_2, x_3)$  is the acoustic mode function. The sound pressure is satisfied with wave equation and the condition of rigid walls:

$$\left( \frac{\partial^2}{\partial x_1^2} + \frac{\partial^2}{\partial x_2^2} + \frac{\partial^2}{\partial x_3^2} \right) \varphi + k^2 \varphi = 0, \quad (4.4)$$

$$\frac{\partial \varphi}{\partial x_i} = 0,$$

where  $k$  is wave number, and  $k = \omega/c$ ,  $\omega$  is the circular frequency, and  $c$  is the sound speed. The mode number can be given by

$$N(k) = \frac{k^3 V_0}{6\pi^2}, \quad (4.5)$$

where  $V_0$  is the volume of the acoustic field.

The modal density of the acoustic cavity can be expressed as

$$n(k) = \frac{k^2 V_0}{2\pi^2}, \quad (4.6)$$

$$n(\omega) = \frac{\omega^2 V_0}{2\pi^2 c^3}.$$

Taking the influence of the surface area and total length of edges of the acoustic field on the modal density into account, the modal density of the acoustic cavity can be expressed as

$$n(\omega) = \frac{\omega^2 V_0}{2\pi^2 c^3} + \frac{\omega^2 A_s}{16\pi c^2} + \frac{\omega l_r}{16\pi c}, \quad (4.7)$$

where  $A_s$  is the surface area of the acoustic cavity and  $l_r$  is the total length of the edges.



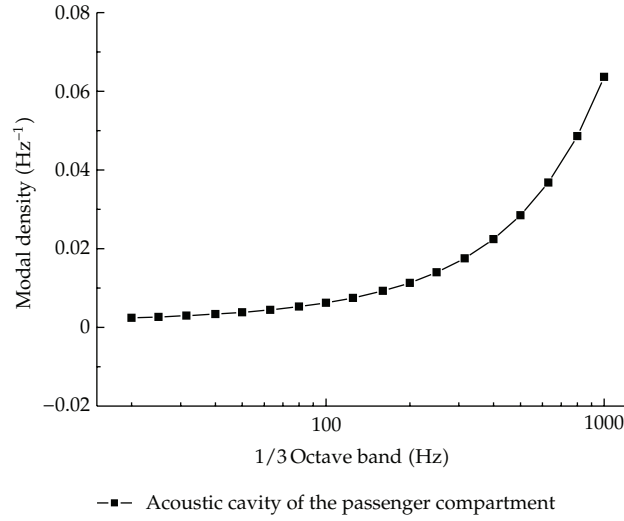


**Figure 6:** Modal density of the acoustic cavity of the passenger compartment.

The modal density of the acoustic cavity of the passenger compartment is shown in Figure 6. It increases as the frequency increases. The maximal modal density is  $0.0636 \text{ Hz}^{-1}$  at 1000 Hz.

#### 4.2. Damping Loss Factor

Damping loss factor (DLF) is the rate of dissipative losses of subsystem energy. It is composed of three independent damping mechanisms, and it can be written as

$$\eta = \eta_s + \eta_r + \eta_b, \quad (4.8)$$

where  $\eta_s$  is the structural loss factor consisted of material inner friction of subsystem, and  $\eta_r$  is the loss factor formed by acoustic radiation of subsystem,  $\eta_b$  is the loss factor formed by border connection damping among subsystems.

Structural loss factor is relative to material performance. The different subsystems of vehicle body are mainly composed of steel, glass, and engineering plastics. The structural loss factors of some common materials are shown in Table 3.

Damping loss factor of acoustic radiation  $\eta_r$  can be expressed as

$$\eta_r = \frac{\rho_0 c \sigma}{\omega \rho_s}, \quad (4.9)$$

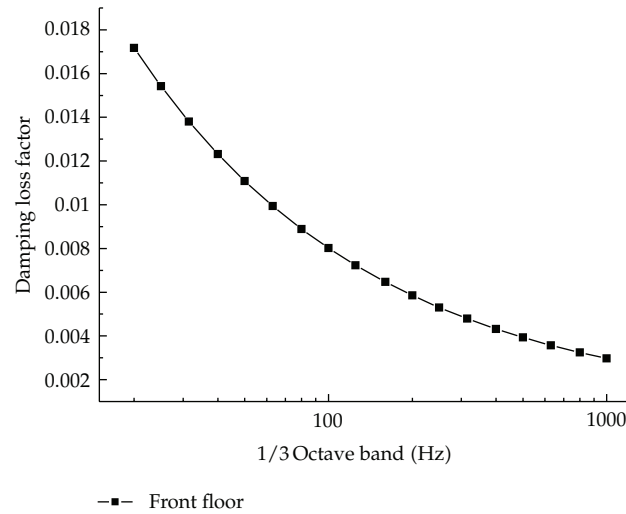
where  $\rho_0$  is air density,  $c$  is sound speed,  $\rho_s$  is area density of structure, and  $\sigma$  is the radiation ratio of the structure.

Additionally,  $\eta_b$  is extremely small. Thus, it can be ignored. The damping loss factor of the front floor is shown in Figure 7. The DLF of the front floor decreases as the frequency increases. The maximum and minimum values of the damping loss factors of the front floor are 0.0172 and 0.0030, respectively.



**Table 3:** Structural loss factors of some common used materials.

Material	Structural loss factor $\eta_s$
Steel	$3 \times 10^{-4}$
Glass	$1 \times 10^{-3}$
Engineering plastics	0.3
Aluminum	$1 \times 10^{-4}$
Brass	$2 \times 10^{-3}$
Cast iron	$1 \times 10^{-3}$
Plywood	$1.5 \times 10^{-2}$
PVC	0.3

**Figure 7:** Damping loss factor of the front floor.

The interior acoustic cavity can be regarded as semifree sound field. Meanwhile, the sound absorption coefficient of the interior acoustic cavity of the automobile can be obtained in acoustics handbooks. The relationship between the damping loss factor and sound absorption coefficient of the interior acoustic cavity of the automobile can be expressed as

$$\eta_{ac} = \frac{\alpha c S}{8\pi f V}, \quad (4.10)$$

where  $\eta_{ac}$  is damping loss factor,  $\alpha$  is sound absorption coefficient,  $S$  is the surface area of sound cavity,  $c$  is the velocity of sound,  $f$  is the center frequency of 1/3 octave band, and  $V$  is the volume of sound cavity.

The damping loss factor of the acoustic cavity of the passenger compartment is shown in Figure 8. It fluctuates between 0.0001 and 0.0005. The minimum and maximum damping loss factors of the acoustic cavity of the passenger compartment are 0.00012 and 0.00042 at 1000 and 80 Hz, respectively.

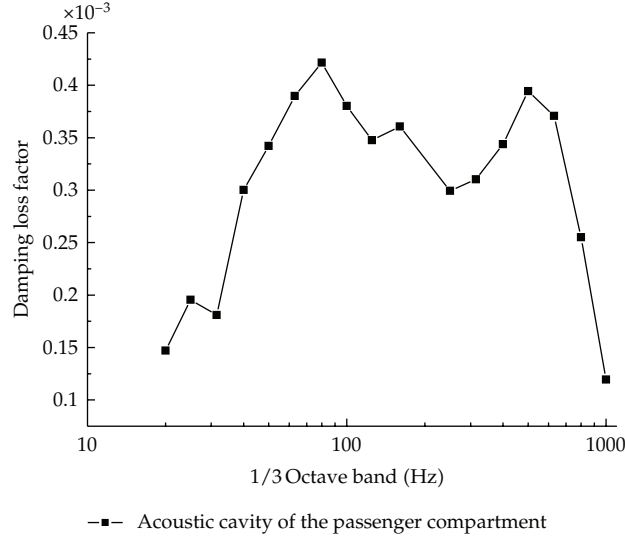


Figure 8: Damping loss factor of the acoustic cavity of the passenger compartment.

### 4.3. Coupling Loss Factor

It is assumed that subsystem  $i$  and subsystem  $j$  are connected with a line. Meanwhile, the length of the coupling line is far more than the wave length of the free wave in the subsystems. Linear connection among the structural subsystems is the most common junction form in structure-structure coupling of the automobile body, and the coupling loss factor (CLF) of linear connection between subsystems  $i$  and  $j$  can be described as:

$$\eta_{ij} = \frac{lc_g}{\pi\omega A_i} \langle \tau_{ij} \rangle, \quad (4.11)$$

where  $l$  is the length of coupling line,  $c_g$  is bending wave velocity of subsystem,  $A_i$  is surface area of subsystem  $i$ , and  $\tau_{ij}$  is the wave transmission coefficient from subsystem  $i$  to  $j$ . The CLFs between firewall and front floor are shown in Figure 9.

Structure-cavity coupling is also a kind of common connection form between structural subsystem and acoustic cavity. The coupling loss factors from structural subsystem to acoustic cavity can be depicted as:

$$\eta_{sc} = \frac{\rho_0 c \sigma}{\omega \rho_s}, \quad (4.12)$$

where  $\rho_0$  is the density of air,  $\sigma$  is the sound radiation coefficient,  $c$  is the sound speed,  $\rho_s$  is the area density of structure, and  $\omega$  is the circular frequency.

According to the reciprocity theorem, CFL from cavity to structural subsystem can be written as

$$\eta_{cs} = \frac{\sigma \rho_0 c n_s}{\omega \rho_s n_c}, \quad (4.13)$$

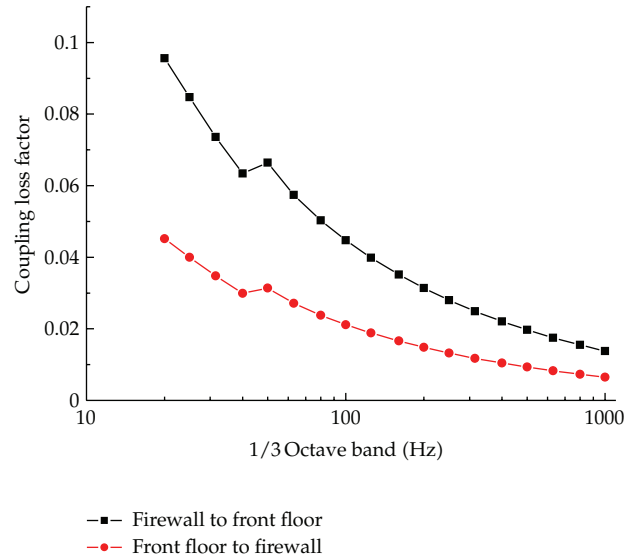


Figure 9: CLFs between firewall and front floor.

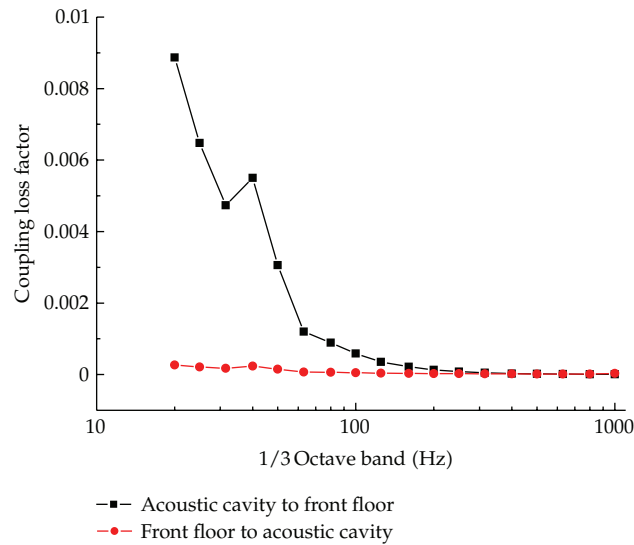


Figure 10: CLFs between acoustic cavity and front floor.

where  $n_s$  is the modal density of structural subsystem and  $n_c$  is the modal density of acoustic cavity.

The CLFs between acoustic cavity and front floor are shown in Figure 10. The CLFs from acoustic cavity to front floor are basically larger than the corresponding values from front floor to acoustic cavity. The CLFs from front floor to acoustic cavity are extremely small, and their values are smaller than 0.0003. The maximum CLF from acoustic cavity to front floor is 0.0089.

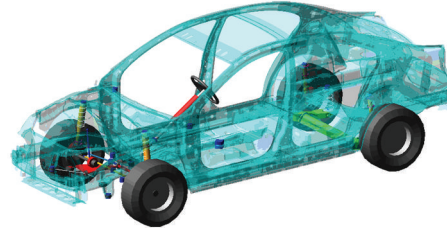


Figure 11: Rigid-elastic coupling multibody dynamics model.

## 5. Excitations of Hybrid FE-SEA Model

Vehicle body is excited when it is running on the road. There are four basic excitations including road excitation, engine mount excitation, sound radiation excitation of engine, and wind excitation. The excitations can be obtained through different method during the development and design stage of the automobile.

### 5.1. Road Excitations

The body of the automobile is excited by road when the automobile is running, and the road excitation acts through tyre, front and rear suspensions. Physical prototype of an automobile is not available to measure road excitation during the design and development stage of automobile. As the development of the virtual prototype technology, the virtual prototype model of an automobile can be created during the design and development stage. In order to obtain the road excitation, a multibody system model of the automobile was built according to the basic parameters of the chassis and body systems. Taking the effect of elastic body on the precision of the road excitation into consideration, a rigid-elastic coupling multibody dynamics model was built using mode synthesis method. The rigid-elastic coupling model is shown in Figure 11.

The rigid-elastic coupling model was driven on B-level road at 120 km/h. The excitations were measured at front shock towers and rear shock towers of spring and damping shock absorbers, respectively. A total of six excitation points were included in the model, and they were left-front shock tower, right-front shock tower, left-rear shock towers of spring and damping shock absorber, and right-rear shock towers of spring and damping shock absorber. The road excitations are shown in Figure 12. They fluctuate from 20 to 1000 Hz. The minimum and maximum road excitations are 0.0353 and 0.2006  $\text{m/s}^2$  at 400 and 50 Hz, respectively, for right-front shock tower. The first three maximum values are 0.4305, 0.2553, and 0.2006  $\text{m/s}^2$  for left-front shock tower, left-rear damping, and right-front shock tower, respectively.

### 5.2. Engine Mount Excitations

The excitation of engine mounts to body also cannot be measured during the design and development stage before prototype manufactured. The layout of automobile must be confirmed at the beginning of the design and develop stage. Then, the engine and its mounts of the designed automobile also can be determined. The excitations of engine mounts to body can be obtained through engine rig test.

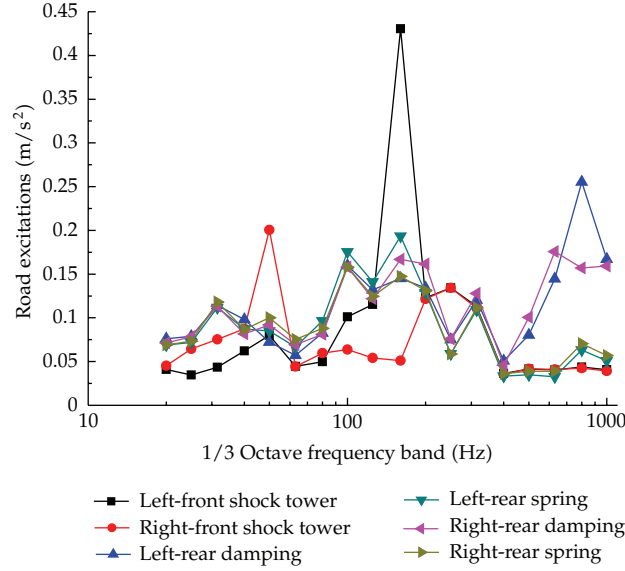


Figure 12: Road excitations.

The running speed of the vehicle was 120 km/h, and it was equal to 3200 r/min of the engine speed. In order to acquire the excitations at the passive sides of the engine mounts, an experiment was presented on the test rig in a semianechoic room. The engine was installed on a dynamometer. Because the engine mount system was comprised of four engine mounts including front mount, left mount, right mount, and rear mount, four accelerometers were installed in on the initiative sides of the engine mounts. Finally, the vibration accelerations at four different mounts were measured at speed of 3200 r/min. The relationship between the accelerations at initiative and passive sides of the engine mount can be written as

$$T = 20 \log \frac{|a_u|}{|a_d|}, \quad (5.1)$$

where  $T$  is the transmissibility of the engine mount,  $a_u$  is the vibration acceleration of the engine mount at initiative side, and  $a_d$  is the acceleration of the engine mount at passive side.

The acceleration at initiative side  $a_u$  was measured, and the transmissibility of the mount  $T$  was known. The acceleration at passive side  $a_d$  can be calculated as follows:

$$|a_d| = \frac{|a_u|}{10^{T/20}}. \quad (5.2)$$

The excitations of the engine mounts were calculated according to formula (5.2). The excitations of the engine mounts are shown in Figure 13. For the front engine mount, it is nearly horizontal from 20 to 100 Hz; it fluctuates up and down from 125 to 1000 Hz; the maximum acceleration of the front engine mount is 1.9640 m/s<sup>2</sup> at 400 Hz. The values of the excitation of the left engine mount are extremely small. It is strongly fluctuated from 80 Hz to 800 Hz for right engine mount, the maximum value of which is 10.0879 m/s<sup>2</sup> at 400 Hz. Meanwhile, the maximum value of the excitation of the rear engine mount is 1.3984 m/s<sup>2</sup> at 500 Hz.

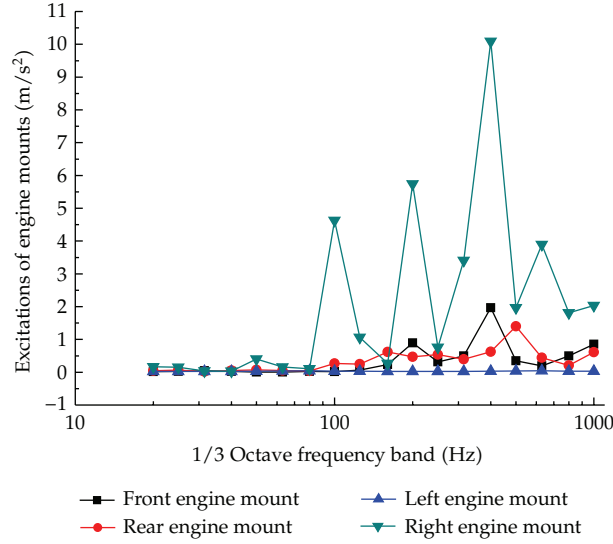


Figure 13: Excitations of engine mounts.

### 5.3. Sound Radiation Excitations of the Engine

Sound radiation excitation of engine cabin received by engine cabin panels is one of the most major excitations to the body of automobile. The measurement of the sound radiation excitation is not available during the design and development stage of automobile. However, it can be acquired throughout indoor testing according to ISO 6798: 1995 "Reciprocating internal combustion engines—Measurement of emitted airborne noise—Engineering method and survey method." Emitting sound power of the engine could be measured with engineering method. Meanwhile, on the basis of point sound source theory, sound radiation excitation of engine received by engine cabin panels can be calculated by the following equation:

$$L_{se} = L_e - 20 \log \frac{r_2}{r_1}, \quad (5.3)$$

where  $L_{se}$  is sound pressure level (SPL) of engine cabin inner surface;  $L_e$  is the measuring point SPL of engine sound power experiment;  $r_1$  is the distance between measuring point and engine, generally,  $r_1 = 1$ ;  $r_2$  is the distance between prediction point and engine.

From formula (5.3), if  $L_e$  and  $r_2$  are known, the sound excitation at every surface of engine cabin could be calculated.

The layout of the sound power test of the engine was the same as illustrated in Section 5.2. Nine microphones were placed at different positions according to ISO 6798: 1995 "Reciprocating internal combustion engines—Measurement of emitted airborne noise—Engineering method and survey method." The SPLs of the engine were measured at speed of 3200 r/min. The sound radiation excitation of the engine was calculated by formula (5.3). The sound excitations of the engine cabin are shown in Figure 14. For the left-front fender, it goes up gradually and fluctuates up and down from 20 to 1000 Hz; the minimum and maximum SPLs of the sound excitation of the left-front fender are 38.42 and 91.40 dB(A) at 20 and 500 Hz, respectively. The other four sound excitations were also applied on the right-front fender, engine hood, front bumper, and firewall, respectively. Meanwhile, these four

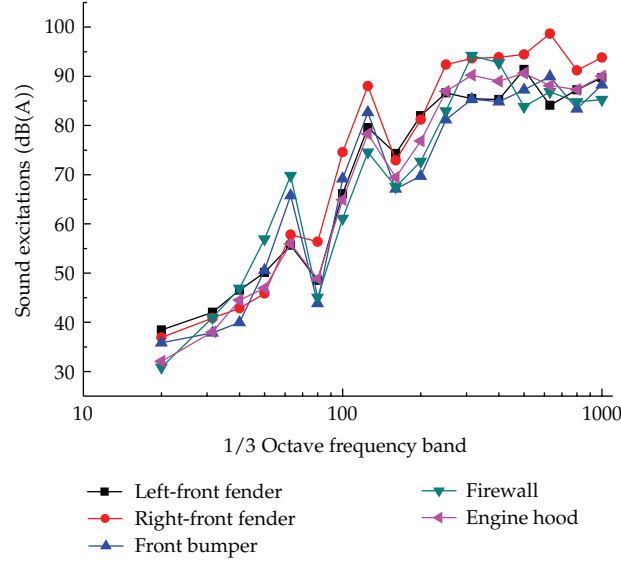


Figure 14: Sound excitations of the engine cabin.

sound excitations have the same trend, and the amplitudes of these four sound excitations are fluctuating near the sound excitation values of the left-front fender.

#### 5.4. Wind Excitations

The body of automobile is excited by wind when the automobile is running on the road. Also, the wind excitation becomes a major noise source at high speeds. Wind excitations can be measured through wind tunnel test. However, the wind tunnel test is extremely expensive, and the wind excitations are not available without physical prototype of automobile during the design and development stage of automobile. For the purpose of acquiring the wind excitation, the Ffowcs Williams and Hawkings (FW-H) model was used with computational fluid dynamics (CFD) software of Fluent.

The Ffowcs Williams and Hawkings (FW-H) equation can be written as [21, 22]

$$\begin{aligned} \frac{1}{a_0^2} \frac{\partial^2 p'}{\partial t^2} - \nabla^2 p' &= \frac{\partial^2}{\partial x_i \partial x_j} [T_{ij} H(f)] - \frac{\partial}{\partial x_i} \{ [P_{ij} n_j + \rho u_i (u_n - v_n)] \delta(f) \} \\ &+ \frac{\partial}{\partial t} \{ [\rho_0 v_n + \rho (u_n - v_n)] \delta(f) \}, \end{aligned} \quad (5.4)$$

where  $u_i$  is the fluid velocity component in the  $x_i$  direction,  $v_i$  is the surface velocity components in the  $x_i$  direction,  $u_n$  is the fluid velocity component normal to the surface  $f = 0$ , and  $f = 0$  means a mathematical surface introduced to "embed" the exterior flow problem ( $f > 0$ ) in an unbounded space, which facilitates the use of generalized function theory and the free-space Green function to obtain the solution.  $v_n$  is the surface velocity component normal to the surface,  $H(f)$  is the Heaviside function,  $\delta(f)$  is the Dirac delta function,  $p'$  is the sound pressure at the far field ( $p' = p - p_0$ ),  $n_i$  is the unit normal vector pointing toward

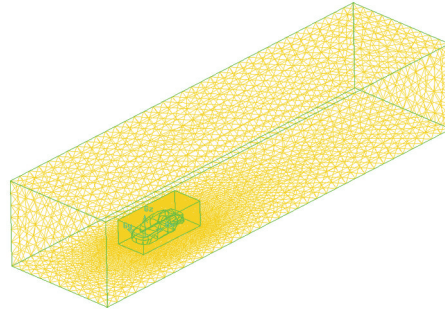


Figure 15: CFD model of the automobile.

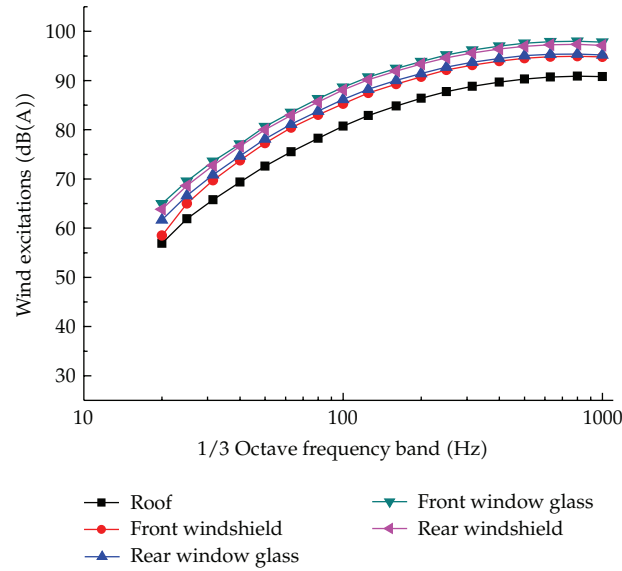


Figure 16: Wind excitations of the subsystems.

the exterior region,  $a_0$  is the far-field sound speed,  $\rho$  is the density of air,  $T_{ij}$  is the Lighthill stress tensor, and  $P_{ij}$  is the compressive stress tensor.

The CFD model of the automobile was created according to the CFD method. The size of simulation wind tunnel in CFD model was 8 times length, 5 times width, and 5 times height of the automobile. The corresponding length, width, and height were 36400 mm, 9500 mm, and 7000 mm, respectively. TGrid-type grid was used in the CFD model which was divided into 233280 grids. The CFD model of the automobile is shown in Figure 15. The sound excitations were calculated at different body panels using large eddy simulation (LES). Three monitoring points were placed at every different body panel on the left half of body because of the symmetry of the automobile. The inlet velocity was set as 120 km/h, and the walls of the wind tunnel and the surfaces of the automobile were both set to walls. After the simulation, the wind excitations at three monitoring points of every body panel were averaged, and the averaged SPLs were the wind excitations of the automobile. The simulation results are validated by Yang's wind tunnel test [23]. The wind excitations of the



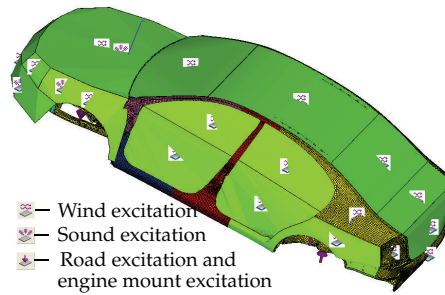


Figure 17: Hybrid FE-SEA model with parameters and excitations.



Figure 18: Microphone at driver's right ear position.

subsystems are shown in Figure 16. They go up until 800 Hz. The maximum wind excitation is front window glass, and the minimum and maximum values are 64.94 and 97.98 dB(A) at 20 and 800 Hz, respectively.

## 6. Interior Noise Prediction

All the input parameters including modal density, damping loss factors, and coupling loss factors were added in the hybrid FE-SEA model. Meanwhile, the excitations including road excitations, engine mount excitations, sound radiation excitations of the engine, and wind excitations were also excited on the hybrid FE-SEA model. Simultaneously, the sound absorption and insulation effects of the trimmed body were taken into consideration. The hybrid FE-SEA model with parameters and excitations is shown in Figure 17.

The interior SPL of the automobile was predicted at driver's right ear with the hybrid FE-SEA model. Meanwhile, in order to verify the correctness of the prediction results, the interior noise of the automobile was measured with a physical prototype vehicle on an asphalt road at speed of 120 km/h. A microphone shown in Figure 18 was placed at the side of driver's right ear. The interior noise signal was recorded using LMS SCADAS data acquisition front end. After data acquisition, the noise signal was processed by Fast Fourier Transform (FFT) and A-weighted network.

The comparison between the predicted and measured sound pressure levels of the automobile is shown in Figure 19. The SPL of the prediction fluctuates up and down around the corresponding value of the test, and it also shows a good agreement of experimentation

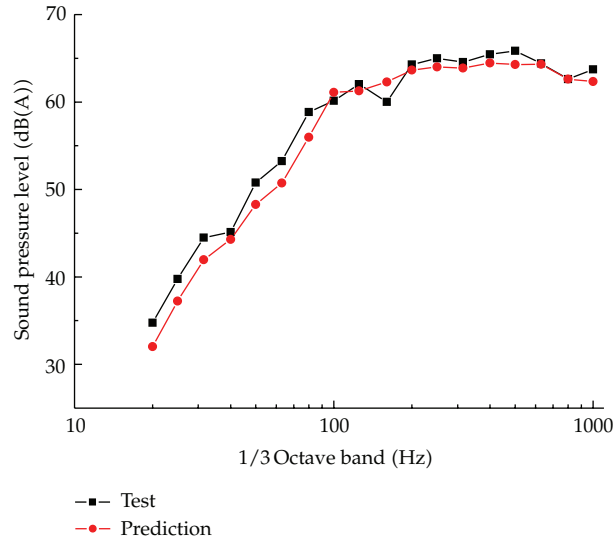


**Figure 19:** Comparison between sound pressure levels of prediction and test.

and prediction from 20 to 1000 Hz. The errors from 20 to 100 Hz are basically larger than the values from 200 to 1000 Hz. The minimum and maximum errors are 0.01 and 2.87 dB(A) at 800 and 160 Hz, respectively. The maximum absolute error is less than 3 dB(A). The overall A-weighted sound pressure levels of prediction and test are 73.79 and 74.44 dB(A), respectively. The absolute error is 0.65 dB(A), and the relative error is 0.87%. The overall relative error is less than 1%, and the absolute error is less than 1.0 dB(A). The comparison results also show that the prediction precision is satisfied, and the effectiveness and reliability of the hybrid FE-SEA model of the automobile are verified.

## 7. Conclusions

The hybrid FE-SEA method was used to predict interior noise of the automobile at the design and development stage in this paper. The hybrid FE-SEA model of the automobile was created using hybrid FE-SEA method. The parameters of the hybrid FE-SEA model including modal density, damping loss factor, and coupling loss factor were calculated using analytical and finite element methods. The excitations including road excitations, engine mount excitations, sound radiation excitations of the engine, and wind excitations were calculated using virtual technology and engine tests. All the parameters and excitations can be available at the design and development stage. Furthermore, the interior noise of the automobile was predicted and verified.

It is shown that the predicted SPLs of the interior noise have a good agreement with the corresponding values of the test. The predicted and tested overall SPLs of the interior noise were 73.79 and 74.44 dB(A), respectively. The absolute error is 0.65 dB(A), and the relative error is 0.87%. The overall relative error is less than 1%, and the absolute error is less than 1.0 dB(A). The comparison results also show that the prediction precision is satisfied, and the effectiveness and reliability of the hybrid FE-SEA model of the automobile is verified. The prediction of the interior noise of the automobile can be realized through various calculation methods, presented in this paper in the design and development stage.

## Acknowledgments

This paper is supported by National Natural Science Foundation Project (no. 50975119) and National Key Technology R&D Program of China (no. 2011BAG03B01). The authors would like to express their appreciations for the above fund support.

## References

- [1] W. Jeong and K. Park, "Application of virtual SEA for the prediction of acoustic performance of cockpit," SAE Paper 2009-01-0767, 2009.
- [2] R. Gujarathi, D. Copley, R. Romick et al., "Modeling interior noise in off-highway trucks using statistical energy analysis," SAE Paper 2009-01-2239, 2009.
- [3] H. Uehara, T. Koizumi, N. Tsujiuchi et al., "Application of statistical energy analysis to noise prediction of co-generation system," in *Proceedings of the Small Engine Technology Conference*, SAE International Warrendale Pennsylvania, Milwaukee, Wis, USA, 2008.
- [4] C. T. Musser and T. Bharj, "Component-level vehicle target setting using statistical energy analysis," in *Proceedings of the JSAE Spring Conference*, SAE International Warrendale Pennsylvania, Tokyo, Japan, 2008.
- [5] P. J. Shorter and R. S. Langley, "Modeling structure-borne noise with the Hybrid FE-SEA method," in *Structural Dynamics—EURODYN 2005*, vol. 1–3, pp. 1205–1210, IOS Press, 2005.
- [6] P. J. Shorter and R. S. Langley, "Vibro-acoustic analysis of complex systems," *Journal of Sound and Vibration*, vol. 288, no. 3, pp. 669–699, 2005.
- [7] R. Rashid and R. S. Langley, "A hybrid method for modelling in-vehicle boom noise," in *Proceedings of the 2004 International Conference on Noise and Vibration Engineering, ISMA*, pp. 3487–3499, bel, September 2004.
- [8] I. Vaz and J. Pan, "Vibro-acoustic modeling of the APAMAT II test system," SAE Paper 2009-01-2210, 2009.
- [9] S. G. Mattson, D. Labyak, J. Pruetz, and T. Connelly, "Prediction of muffler insertion loss by a hybrid FE acoustic-SEA model," *SAE International Journal of Passenger Cars - Mechanical Systems*, vol. 2, no. 1, pp. 1323–1329, 2009.
- [10] R. S. Langley and P. Bremner, "A hybrid method for the vibration analysis of complex structural-acoustic systems," *Journal of the Acoustical Society of America*, vol. 105, no. 3, pp. 1657–1671, 1999.
- [11] R. S. Langley and J. A. Cordioli, "Hybrid deterministic-statistical analysis of vibro-acoustic systems with domain couplings on statistical components," *Journal of Sound and Vibration*, vol. 321, no. 3–5, pp. 893–912, 2009.
- [12] R. S. Langley and V. Cotoni, "Response variance prediction for uncertain vibro-acoustic systems using a hybrid deterministic-statistical method," *Journal of the Acoustical Society of America*, vol. 122, no. 6, pp. 3445–3463, 2007.
- [13] P. J. Shorter and R. S. Langley, "On the reciprocity relationship between direct field radiation and diffuse reverberant loading," *Journal of the Acoustical Society of America*, vol. 117, no. 1, pp. 85–95, 2005.
- [14] A. Charpentier, P. Streedhar, and K. Fukui, "Using the hybrid FE-SEA method to predict structure-borne noise transmission in a trimmed automotive vehicle," SAE Paper 2007-01-2181, 2007.
- [15] A. Charpentier, P. Streedhar, G. Gardner et al., "Use of a hybrid FE-SEA model of a trimmed vehicle to improve the design for interior noise," SAE Paper 2009-01-2199, 2009.
- [16] C. T. Musser and A. B. Rodrigues, "Mid-frequency prediction accuracy improvement for fully trimmed vehicle using hybrid SEA-FEA technique," SAE Paper 2008-36-0564, 2008.
- [17] P. Shorter, Q. Zhang, and A. Parrett, "Using the hybrid FE-SEA method to predict and diagnose component transmission loss," SAE Paper 2007-01-2172, 2007.
- [18] V. Cotoni, B. Gardner, J. A. Cordioli et al., "Advanced modelling of aircraft interior noise using the hybrid FE-SEA method," SAE Paper 2008-36-0575, 2008.
- [19] J. E. Manning, "Hybrid SEA for mid-frequencies," SAE Paper 2007-01-2305, 2007.
- [20] J. Cordioli, V. Cotoni, and P. Shorter, "Numerical investigation of the transmission loss of seals and slits for airborne SEA predictions," SAE Paper 2009-01-2205, 2009.
- [21] J. E. Ffowcs Williams and D. L. Hawkings, "Sound generation by turbulence and surfaces in arbitrary motion," *Philosophical Transactions of the Royal Society of London. Series A*, vol. 264, no. 1151, pp. 321–342, 1969.

- [22] K. S. Brentner and F. Farassat, "Analytical comparison of the acoustic analogy and Kirchhoff formulation for moving surfaces," *AIAA Journal*, vol. 36, no. 8, pp. 1379–1386, 1998.
- [23] B. Yang, X. Hu, and Y. Zhang, "Study on unsteady flow field and aerodynamic noise of the automobile rear view mirror region," *Journal of Mechanical Engineering*, vol. 46, no. 22, pp. 151–155, 2010.

## Research Article

# A Numerical Treatment of Nondimensional Form of Water Quality Model in a Nonuniform Flow Stream Using Saul'yev Scheme

Nopparat Pochai<sup>1,2</sup>

<sup>1</sup> Department of Mathematics, Faculty of Science, King Mongkut's Institute of Technology Ladkrabang, Bangkok 10520, Thailand

<sup>2</sup> Centre of Excellence in Mathematics, Commission on Higher Education (CHE), Si Ayutthaya Road, Bangkok 10400, Thailand

Correspondence should be addressed to Nopparat Pochai, nop\_math@yahoo.com

Received 11 April 2011; Revised 21 June 2011; Accepted 6 July 2011

Academic Editor: Delfim Soares Jr.

Copyright © 2011 Nopparat Pochai. This is an open access article distributed under the Creative Commons Attribution License, which permits unrestricted use, distribution, and reproduction in any medium, provided the original work is properly cited.

The stream water quality model of water quality assessment problems often involves numerical methods to solve the equations. The governing equation of the uniform flow model is one-dimensional advection-dispersion-reaction equations (ADREs). In this paper, a better finite difference scheme for solving ADRE is focused, and the effect of nonuniform water flows in a stream is considered. Two mathematical models are used to simulate pollution due to sewage effluent. The first is a hydrodynamic model that provides the velocity field and elevation of the water flow. The second is an advection-dispersion-reaction model that gives the pollutant concentration fields after input of the velocity data from the hydrodynamic model. For numerical techniques, we used the Crank-Nicolson method for system of a hydrodynamic model and the explicit schemes for the dispersion model. The revised explicit schemes are modified from two computation techniques of uniform flow stream problems: forward time central space (FTCS) and Saul'yev schemes for dispersion model. A comparison of both schemes regarding stability aspect is provided so as to illustrate their applicability to the real-world problem.

## 1. Introduction

Field measurement and mathematical simulation are methods to detect the amount of pollutant in water area. For the shallow water mass transport problems that presented in [1], the method of characteristics has been reported as being applied with success, but it presents in real cases some difficulties. In [2], the finite element method for solving a steady water pollution control to achieve a minimum cost is presented. The numerical techniques for solving the uniform flow of stream water quality model, especially the one-dimensional

advection-diffusion-reaction equation, are presented in [3–7]. A two-dimensional model for natural convection in shallow water that reduces to a degenerated elliptic equation for the pressure, an explicit formula for horizontal components of the velocity and a vertical diffusion for the vertical component, is derived [8]. In [9], a rigorous nonlinear mathematical model is used to explain the seasonal variability of plankton in previous shallow coastal lagoons. The particle trajectories in a constant vorticity shallow water term flow over a flat bed as periodic waves propagate on the water's free surface are investigated in [10].

The most of nonuniform flow model requires data concerned with velocity of the current at any point and any time in the domain. The hydrodynamics model provides the velocity field and tidal elevation of the water. In [11–13], they used the hydrodynamics model and convection-diffusion equation to approximate the velocity of the water current in a bay, a uniform reservoir, and a channel, respectively.

The numerical techniques to solve the nonuniform flow of stream water quality model, one-dimensional advection-diffusion-reaction equation, is presented in [14] by using the fully implicit schemes: Crank-Nicolson method system of hydrodynamic model and backward time central space (BTCS) for dispersion model.

The finite difference methods, including both explicit and implicit schemes, are mostly used for one-dimensional problems such as in longitudinal river systems [15]. Researches on finite difference schemes have considered on numerical accuracy and stability. There are several high quality numerical schemes, such as QUICK/QUICKest schemes, Lax-Wendroff scheme, Crandall scheme, and Dufort-Frankel scheme have been developed to enhance model performances. These schemes have outstanding stability and high-order accuracy. They are requirements for advection-dominated systems. Although these schemes need boundary and initial conditions that make them difficult to use. They need more computing effort since iterations for more grids are involved in each computation step. For example, the QUICKest scheme uses a three-point upstream-weighted quadratic interpolation and needs the stop criteria controlled iterations for each grid in order to enhance accuracy. The scheme carries out a heavy computing load. Since it involves two upstream points, the upper boundary conditions need to be defined carefully before starting computation [4].

The simple finite difference schemes become more inviting for general model use. The simple explicit schemes include Forward-Time/Centered-Space (FTCS) scheme and the Saul'yev scheme. These schemes are either first-order or second-order accurate [4] and have the advantages of simplicity in coding and time effectiveness in computing without losing too much accuracy and thus are preceding for several model applications.

In this paper, we will use more economical computation techniques than the method in [14]. For numerical techniques, we used the Crank-Nicolson method to the system of hydrodynamic model and the explicit schemes to the dispersion model. The revised explicit schemes are modified from two computation techniques of uniform flow stream problems: forward in time/central in space (FTCS) and Saul'yev schemes.

The results from hydrodynamic model are data of the water flow velocity for advection-diffusion-reaction equation which provides the pollutant concentration field. The term of friction forces due to the drag of sides of the stream is considered. The theoretical solution of the model at the end point of the domain that guaranteed the accurate of the approximate solution is presented in [13, 14].

The stream has a simple one-space dimension as shown in Figure 1. Averaging the equation over the depth, discarding the term due to Coriolis force, it follows that the one-dimensional shallow water and advection-diffusion-reaction equations are applicable. We use the Crank-Nicolson method and the forward in time/central in space (FTCS) and Saul'yev

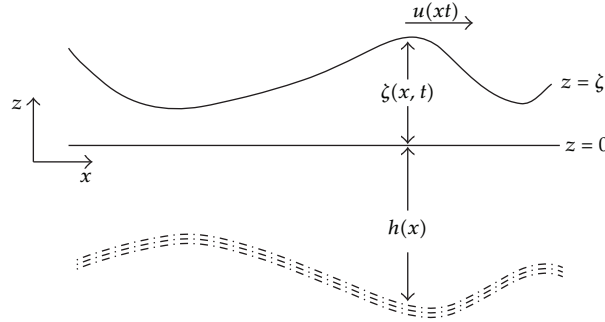


Figure 1: The shallow water system.

schemes to approximate the velocity and the tidal elevation and the concentration from the foresaid models, respectively.

## 2. Mathematical Model

### 2.1. The Hydrodynamic Model

The continuity and momentum equations are governed by the hydrodynamic behavior of the stream. If we average the equations over the depth, discarding the term due to Coriolis parameter, shearing stresses, and surface wind [11, 13, 14, 16], we obtain the one-dimensional shallow water equations:

$$\begin{aligned}\frac{\partial \zeta}{\partial t} + \frac{\partial}{\partial x} [(h + \zeta)u] &= 0, \\ \frac{\partial u}{\partial t} + g \frac{\partial \zeta}{\partial x} &= 0,\end{aligned}\tag{2.1}$$

where  $x$  is longitudinal distance along the stream (m),  $t$  is time (s),  $h(x)$  is the depth measured from the mean water level to the stream bed (m),  $\zeta(x, t)$  is the elevation from the mean water level to the temporary water surface or the tidal elevation (m/s), and  $u(x, t)$  is the velocity components (m/s), for all  $x \in [0, l]$ .

Assume that  $h$  is a constant and  $\zeta \ll h$ . Then (2.1) leads to

$$\begin{aligned}\frac{\partial \zeta}{\partial t} + h \frac{\partial u}{\partial x} &\doteq 0, \\ \frac{\partial u}{\partial t} + g \frac{\partial \zeta}{\partial x} &= 0.\end{aligned}\tag{2.2}$$

We will consider the equation in dimensionless problem by letting  $U = u/\sqrt{gh}$ ,  $X = x/l$ ,  $Z = \zeta/h$ , and  $T = t\sqrt{gh}/l$ . Substituting them into (2.2) leads to

$$\begin{aligned}\frac{\partial Z}{\partial T} + \frac{\partial U}{\partial X} &= 0, \\ \frac{\partial U}{\partial T} + \frac{\partial Z}{\partial X} &= 0.\end{aligned}\tag{2.3}$$

We now introduce a damping term into (2.3) to represent frictional forces due to the drag of sides of the stream, thus

$$\begin{aligned}\frac{\partial Z}{\partial T} + \frac{\partial U}{\partial X} &= 0, \\ \frac{\partial U}{\partial T} + \frac{\partial Z}{\partial X} &= -U,\end{aligned}\tag{2.4}$$

with the initial conditions at  $t = 0$  and  $0 \leq X \leq 1$  being specified:  $Z = 0$  and  $U = 0$ . The boundary conditions for  $t > 0$  are specified:  $Z = e^{it}$  at  $X = 0$  and  $\partial Z / \partial X = 0$  at  $X = 1$ . The system of (2.4) is called the damped equation. We solve the damped equation by using the finite difference method. In order to solve (2.4) in  $[0, 1] \times [0, T]$ , for convenient using  $u, d$  for  $U$  and  $Z$ , respectively,

$$\begin{aligned}\frac{\partial u}{\partial t} + \frac{\partial d}{\partial x} &= -u, \\ \frac{\partial d}{\partial t} + \frac{\partial u}{\partial x} &= 0,\end{aligned}\tag{2.5}$$

with the initial conditions  $u = 0, d = 0$  at  $t = 0$  and the boundary conditions  $d(0, t) = f(t)$  and  $\partial d / \partial x = 0$  at  $x = 1$ .

## 2.2. Dispersion Model

In a stream water quality model, the governing equations are the dynamic one-dimensional advection-dispersion-reaction equations (ADREs). A simplified representation by averaging the equation over the depth is shown in [3–5, 7, 14] as

$$\frac{\partial C}{\partial t} + u \frac{\partial C}{\partial x} = D \frac{\partial^2 C}{\partial x^2} - KC,\tag{2.6}$$

where  $C(x, t)$  is the concentration averaged in depth at the point  $x$  and at time  $t$ ,  $D$  is the diffusion coefficient,  $K$  is the mass decay rate, and  $u(x, t)$  is the velocity component, for all  $x \in [0, 1]$ . We will consider the model with following conditions. The initial condition  $C(x, 0) = 0$  at  $t = 0$  for all  $x > 0$ . The boundary conditions  $C(0, t) = C_0$  at  $x = 0$  and  $\partial C / \partial x = 0$  at  $x = 1$ , where  $C_0$  is a constant.

## 3. Numerical Experiment

The hydrodynamic model provides the velocity field and elevation of the water. Then the calculated results of the model will be input into the dispersion model which provides the pollutant concentration field.



### 3.1. Crank-Nicolson Method for the Hydrodynamic Model

We will follow the numerical techniques of [13]. To find the water velocity and water elevation from (2.5), we make the following change of variable,  $v = e^t u$ , and substituting them into (2.5), we have

$$\begin{aligned}\frac{\partial v}{\partial t} + e^{-t} \frac{\partial d}{\partial x} &= 0, \\ \frac{\partial d}{\partial t} + e^{-t} \frac{\partial v}{\partial x} &= 0.\end{aligned}\tag{3.1}$$

Equation (3.1) can be written in the matrix form

$$\begin{pmatrix} v \\ d \end{pmatrix}_t + \begin{bmatrix} 0 & e^t \\ e^{-t} & 0 \end{bmatrix} \begin{pmatrix} v \\ d \end{pmatrix}_x = \begin{pmatrix} 0 \\ 0 \end{pmatrix}.\tag{3.2}$$

That is,

$$U_t + AU_x = \bar{0},\tag{3.3}$$

where

$$\begin{aligned}A &= \begin{bmatrix} 0 & e^t \\ e^{-t} & 0 \end{bmatrix}, \\ U &= \begin{pmatrix} v \\ d \end{pmatrix}, \quad \begin{pmatrix} v \\ d \end{pmatrix}_t = \begin{pmatrix} \frac{\partial v}{\partial t} \\ \frac{\partial d}{\partial t} \end{pmatrix},\end{aligned}\tag{3.4}$$

with the initial condition  $d = v = 0$  at  $t = 0$ . The left boundary conditions for  $x = 0, t > 0$  are specified:  $d(0, t) = \sin t$  and  $\partial v / \partial x = -e^t \cos t$ , and the right boundary conditions for  $x = 1, t > 0$  are specified:  $\partial d / \partial x = 0$  and  $v(0, t) = 0$ .

We now discretize (3.3) by dividing the interval  $[0, 1]$  into  $M$  subintervals such that  $M\Delta x = 1$  and the interval  $[0, T]$  into  $N$  subintervals such that  $N\Delta t = T$ . We can then approximate  $d(x_i, t_n)$  by  $d_i^n$ , value of the difference approximation of  $d(x, t)$  at point  $x = i\Delta x$  and  $t = n\Delta t$ , where  $0 \leq i \leq M$  and  $0 \leq n \leq N$ , and similarly defined for  $v_i^n$  and  $U_i^n$ . The grid points  $(x_n, t_n)$  are defined by  $x_i = i\Delta x$  for all  $i = 0, 1, 2, \dots, M$  and  $t_n = n\Delta t$  for all  $n = 0, 1, 2, \dots, N$  in which  $M$  and  $N$  are positive integers. Using the Crank-Nicolson method [17] to (3.3), the following finite difference equation can be obtained:

$$\left[ I - \frac{1}{4} \lambda A (\Delta_x + \nabla_x) \right] U_i^{n+1} = \left[ I + \frac{1}{4} \lambda A (\Delta_x + \nabla_x) \right] U_i^n,\tag{3.5}$$

where

$$U_i^n = \begin{pmatrix} v_i^n \\ d_i^n \end{pmatrix}, \quad \Delta_x U_i^n = U_{i+1}^n - U_i^n, \quad \nabla_x U_i^n = U_i^n - U_{i-1}^n,\tag{3.6}$$

$I$  is the unit matrix of order 2 and  $\lambda = \Delta t / \Delta x$ . Applying the initial and boundary conditions given for (3.1), the general form can be obtained

$$G^{n+1} \bar{U}^{n+1} = E^n \bar{U}^n + F^n, \quad (3.7)$$

where

$$G^{n+1} = \begin{bmatrix} 1 & 0 & 0 & -\frac{\lambda}{4} a_1^{n+1} & 0 & 0 \\ \frac{\lambda}{4} a_2^{n+1} & 1 & -\frac{\lambda}{4} a_2^{n+1} & 0 & 0 & 0 \\ 0 & \frac{\lambda}{4} a_1^{n+1} & 1 & 0 & 0 & -\frac{\lambda}{4} a_1^{n+1} \\ \frac{\lambda}{4} a_2^{n+1} & 0 & 0 & 1 & -\frac{\lambda}{4} a_2^{n+1} & 0 \\ \ddots & \ddots & \ddots & \ddots & \ddots & \ddots \\ 0 & 0 & 0 & \frac{\lambda}{4} a_1^{n+1} & 1 & -\frac{\lambda}{4} a_1^{n+1} \\ 0 & 0 & \frac{\lambda}{4} a_2^{n+1} & 0 & 0 & 1 \end{bmatrix},$$

$$E^n = \begin{bmatrix} 1 & 0 & 0 & -\frac{\lambda}{4} a_1^n & 0 & 0 \\ -\frac{\lambda}{4} a_2^n & 1 & \frac{\lambda}{4} a_2^n & 0 & 0 & 0 \\ 0 & -\frac{\lambda}{4} a_1^n & 1 & 0 & 0 & \frac{\lambda}{4} a_1^n \\ -\frac{\lambda}{4} a_2^n & 0 & 0 & 1 & \frac{\lambda}{4} a_2^n & 0 \\ \ddots & \ddots & \ddots & \ddots & \ddots & \ddots \\ 0 & 0 & 0 & -\frac{\lambda}{4} a_1^n & 1 & \frac{\lambda}{4} a_1^n \\ 0 & 0 & -\frac{\lambda}{4} a_2^n & 0 & 0 & 1 \end{bmatrix}, \quad \bar{U}^n = \begin{pmatrix} U_1^{n+1} \\ U_2^{n+1} \\ \vdots \\ U_{M-1}^{n+1} \end{pmatrix}, \quad (3.8)$$

$$F^n = \begin{pmatrix} -\frac{\lambda}{4} a_1^{n+1} \sin(t_{n+1}) - \frac{\lambda}{4} a_1^n \sin(t_n) \\ -\frac{\lambda}{4} a_2^{n+1} \Delta x e^{-t_{n+1}} \cos(t_{n+1}) - \frac{\lambda}{4} a_2^n \Delta x e^{-t_n} \cos(t_n) \\ 0 \\ 0 \\ \vdots \\ 0 \\ 0 \end{pmatrix},$$

where  $a_1^n = e^{t_n}$ ,  $a_2^n = e^{-t_n}$ , and  $t_n = n\Delta t$  for all  $n = 0, 1, 2, \dots, N$ . The Crank-Nicolson scheme is unconditionally stable [15, 17].

### 3.2. The Explicit Schemes for the Advection-Diffusion-Reaction Equation

We can then approximate  $C(x_i, t_n)$  by  $C_i^n$ , the value of the difference approximation of  $C(x, t)$  at point  $x = i\Delta x$  and  $t = n\Delta t$ , where  $0 \leq i \leq M$  and  $0 \leq n \leq N$ . The grid points  $(x_n, t_n)$  are defined by  $x_i = i\Delta x$  for all  $i = 0, 1, 2, \dots, M$  and  $t_n = n\Delta t$  for all  $n = 0, 1, 2, \dots, N$  in which  $M$  and  $N$  are positive integers.

#### 3.2.1. Forward Time Central Space Explicit Finite Difference Scheme

Taking the forward time central space technique [17] into (2.6), we get the following discretization:

$$\begin{aligned} C &\cong C_i^n, \\ \frac{\partial C}{\partial t} &\cong \frac{C_i^{n+1} - C_i^n}{\Delta t}, \\ \frac{\partial C}{\partial x} &\cong \frac{C_{i+1}^n - C_{i-1}^n}{2\Delta x}, \\ \frac{\partial^2 C}{\partial x^2} &\cong \frac{C_{i+1}^n - 2C_i^n + C_{i-1}^n}{(\Delta x)^2}, \\ u &\cong \hat{U}_i^n. \end{aligned} \quad (3.9)$$

Substituting (3.9) into (2.6), we get

$$\frac{C_i^{n+1} - C_i^n}{\Delta t} + \hat{U}_i^n \left( \frac{C_{i+1}^n - C_{i-1}^n}{2\Delta x} \right) = D \left( \frac{C_{i+1}^n - 2C_i^n + C_{i-1}^n}{(\Delta x)^2} \right) - KC_i^n, \quad (3.10)$$

for  $1 \leq i \leq M$  and  $0 \leq n \leq N - 1$ . Letting  $\lambda = D\Delta t/(\Delta x)^2$  and  $\gamma_i^{n+1} = (\Delta t/\Delta x)\hat{U}_i^{n+1}$ , (3.10) becomes

$$C_i^{n+1} = \left( \frac{1}{2}\gamma_i^n + \lambda \right) C_{i-1}^n + (1 - 2\lambda - K\Delta t)C_i^n + \left( \lambda - \frac{1}{2}\gamma_i^n \right) C_{i+1}^n. \quad (3.11)$$

For  $i = 1$ , plugging the known value of the left boundary  $C_0^n = C_0$  to (3.11) in the right-hand side, we obtain

$$C_1^{n+1} = \left( \frac{1}{2}\gamma_1^n + \lambda \right) C_0 + (1 - 2\lambda - K\Delta t)C_1^n + \left( \lambda - \frac{1}{2}\gamma_1^n \right) C_2^n. \quad (3.12)$$

For  $i = M$ , substituting the approximate unknown value of the right boundary by [4], we can let  $C_{M+1}^n = 2C_M^n - C_{M-1}^n$  and by rearranging, we obtain

$$C_M^{n+1} = (2\lambda)C_{M-1}^n + (1 - 4\lambda - K\Delta t - \gamma_m^n)C_M^n. \quad (3.13)$$

The forward time central space scheme is conditionally stable subject to constraints in (3.10). The stability requirements for the scheme are [4, 18]

$$\begin{aligned}\lambda &= \frac{D\Delta t}{(\Delta x)^2} < \frac{1}{2}, \\ \gamma_i^n &= \frac{U_i^n \Delta t}{\Delta x} < 1,\end{aligned}\tag{3.14}$$

where  $\lambda$  is the diffusion number (dimensionless) and  $\gamma_i^n$  is the advection number or Courant number (dimensionless). It can be obtained that the strictly stability requirements are the main disadvantage of this scheme.

The finite difference formula (3.11) has been derived in [19] that the truncation error for this method is  $O\{(\Delta x^2), \Delta t\}$ .

### 3.2.2. Saul'yev Explicit Finite Difference Scheme

The Saul'yev scheme is unconditionally stable [6]. It is clear that the nonstrictly stability requirement of Saul'yev scheme is the main of advantage and economical to use. Taking Saul'yev technique [6] into (2.6), it can be obtained the following discretization:

$$\begin{aligned}C &\cong C_i^n, \\ \frac{\partial C}{\partial t} &\cong \frac{C_i^{n+1} - C_i^n}{\Delta t}, \\ \frac{\partial C}{\partial x} &\cong \frac{C_{i+1}^n - C_{i-1}^{n+1}}{2\Delta x}, \\ \frac{\partial^2 C}{\partial x^2} &\cong \frac{C_{i+1}^n - C_i^n - C_i^{n+1} + C_{i-1}^{n+1}}{(\Delta x)^2}, \\ u &\cong \hat{U}_i^n.\end{aligned}\tag{3.15}$$

Substituting (3.15) into (2.6), we get

$$\frac{C_i^{n+1} - C_i^n}{\Delta t} + \hat{U}_i^n \left( \frac{C_{i+1}^n - C_{i-1}^{n+1}}{2\Delta x} \right) = D \left( \frac{C_{i+1}^n - C_i^n - C_i^{n+1} + C_{i-1}^{n+1}}{(\Delta x)^2} \right) - kC_i^n,\tag{3.16}$$

for  $1 \leq i \leq M$  and  $0 \leq n \leq N - 1$ . Leting  $\lambda = D\Delta t/(\Delta x)^2$  and  $\gamma_i^{n+1} = (\Delta t/\Delta x)\hat{U}_i^{n+1}$ , (3.16) becomes

$$C_i^{n+1} = \left( \frac{1}{1+\lambda} \right) \left( \left( \frac{1}{2}\gamma_i^n + \lambda \right) C_{i-1}^{n+1} + (1-\lambda-K\Delta t)C_i^n + \left( \lambda - \frac{1}{2}\gamma_i^n \right) C_{i+1}^n \right).\tag{3.17}$$

For  $i = 1$ , plugging the known value of the left boundary  $C_0^{n+1} = C_0$  to (3.17) in the right-hand side, we obtain

$$C_1^{n+1} = \left( \frac{1}{1 + \lambda} \right) \left( \left( \frac{1}{2} \gamma_1^n + \lambda \right) C_0 + (1 - \lambda - K \Delta t) C_1^n + \left( \lambda - \frac{1}{2} \gamma_1^n \right) C_2^n \right). \quad (3.18)$$

For  $i = M$ , substituting the approximate unknown value of the right boundary by [20], we can let  $C_{M+1}^n = C_M^n + C_M^{n+1} - C_{M-1}^{n+1}$  and by rearranging, we obtain

$$C_M^{n+1} = \left( \frac{1}{1 + (1/2) \gamma_M^n} \right) \left( \gamma_M^n C_{M-1}^{n+1} + \left( 1 - K \Delta t - \frac{1}{2} \gamma_M^n \right) C_M^n \right). \quad (3.19)$$

Using Taylor series expansions on the approximation, [21] has shown that the truncation error is  $O\{(\Delta x)^2 + (\Delta t)^2 + (\Delta t / \Delta x)^2\}$  or  $O\{2, 2, (1/1)^2\}$ .

From (3.16) to (3.19), it can be obtained that the technique does not generate the system of linear equations. It follows that the application of the technique is economical computer implementation.

#### 4. The Accuracy of the Hydrodynamic Approximation

It is not hard to find the analytical solution  $d(x, t)$  in (2.5) with  $f(t) = \sin t$ . By changing of variables,  $d(x, t) = e^{it} \mathfrak{D}(x)$  and  $u(x, t) = e^{it} \mathcal{U}(x)$  for some  $\mathfrak{D}(x), \mathcal{U}(x) \in C_0^2[0, 1]$  and substitute into (2.5). Using a separable variables technique, we can obtain  $d(1, t)$  a solution [14]

$$d(1, t) = \frac{\sin t \cos \beta \cosh \alpha - \cos t \sin \beta \sinh \alpha}{\cos^2 \beta \cosh^2 \alpha + \sin^2 \beta \sinh^2 \alpha}, \quad (4.1)$$

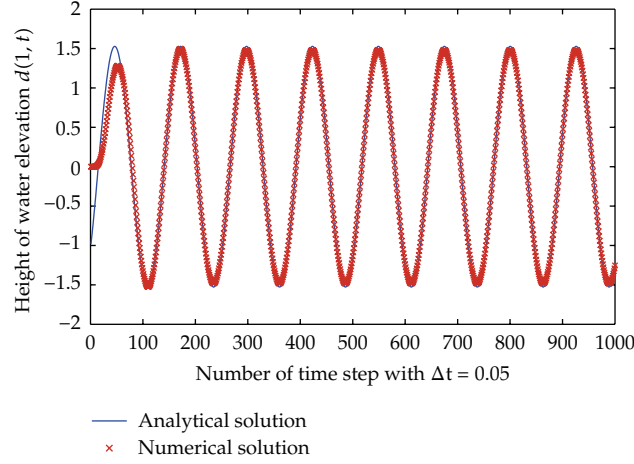
where  $\alpha = 2^{1/4} \cos(3\pi/8)$  and  $\beta = 2^{1/4} \sin(3\pi/8)$ . Anyhow, it is not easy to find the analytical solution  $u(x, t)$  of (2.5). We use the solution  $d(1, t)$  obtained in (4.1) to verify to our approximate solution obtained by the Crank-Nicolson method (3.7). Actually when using the Crank-Nicolson method, we get the approximate solution both  $d(x, t)$  and  $u(x, t)$ . We assume that when we get a good approximation for  $d(x, t)$  this implied that the method gives a good approximation for  $u(x, t)$ . The verification of the approximate solution  $\bar{d}(1, t)$  is shown in Table 1 and Figure 2.

Figure 2 shows the comparison between the analytical solutions  $d(1, t)$  and the approximate solutions  $\bar{d}(1, t)$  only at the end of the domain. Table 1 shows that an estimate of the maximum error is less than 7.0%.

Unfortunately, the analytical solutions of hydrodynamic model could not found over entire domain. This implies that the analytical solutions of dispersion model could not carry out at any points on the domain as well.

#### 5. Application to the Stream Water Quality Assessment Problem

Suppose that the measurement of pollutant concentration  $C$  ( $\text{Kg}/\text{m}^3$ ) in a uniform stream at time  $t$  (sec) is considered. A stream is aligned with longitudinal distance, 1.0 km total



**Figure 2:** Comparison of analytical solution for height of water elevation with results obtained by numerical technique at the end point of the domain.

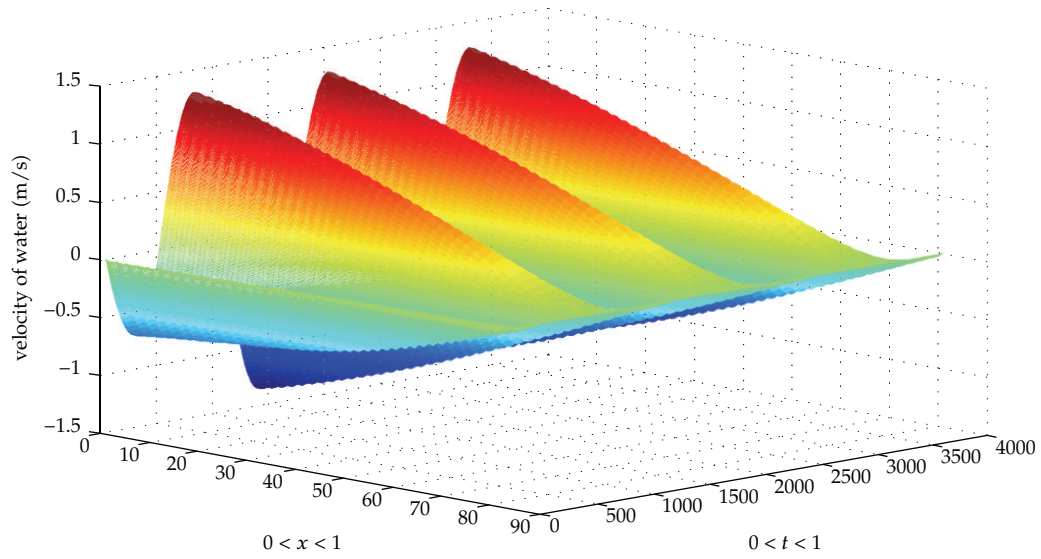
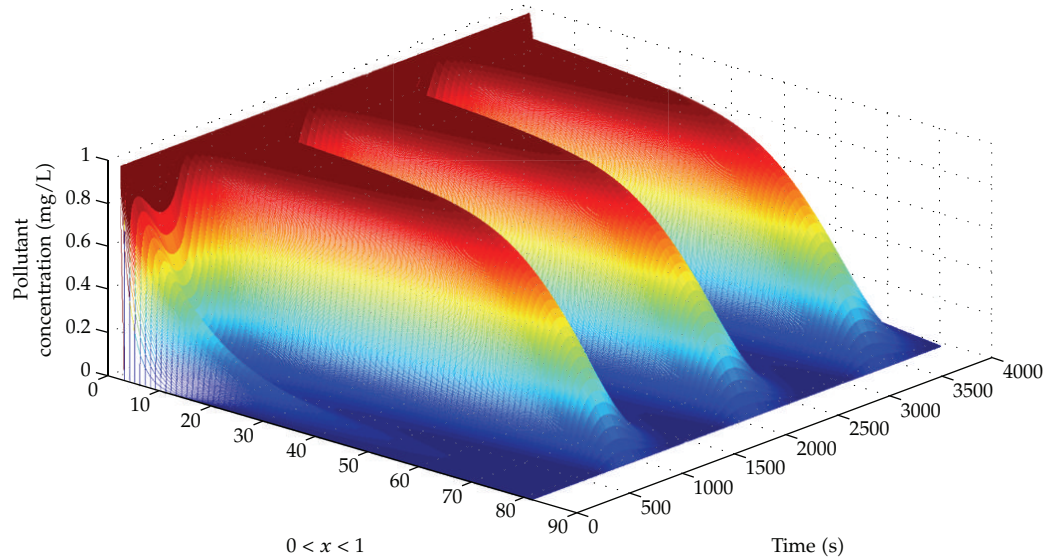
**Table 1:** The error defined by  $\text{error}(T) = \max |d(1, t) - \bar{d}(1, t)|$  for all  $T - \pi \leq t \leq T + \pi$  at fixed  $\Delta t / \Delta x = 0.25$ .

$T$	$\Delta x$	$\Delta t$	$d(1, t)$	$\bar{d}(1, t)$	error( $T$ )
20	0.200	0.05000	1.50158	1.45659	0.04499
	0.100	0.02500	0.09392	0.38856	0.29465
	0.050	0.01250	-0.25831	-0.40244	0.14413
	0.025	0.00625	-0.33323	-0.40433	0.07110
30	0.200	0.05000	1.49666	1.45165	0.04501
	0.100	0.02500	-0.09358	-0.38821	0.29463
	0.050	0.01250	0.25798	0.40198	0.14401
	0.025	0.00625	0.33290	0.40389	0.07099
40	0.200	0.05000	1.50146	1.45644	0.04502
	0.100	0.02500	0.09324	0.38787	0.29463
	0.050	0.01250	-0.25765	-0.40165	0.14401
	0.025	0.00625	-0.33257	-0.40356	0.07099

length, and 1.0 m depth. There is a plant which discharges waste water into the stream, and the pollutant concentration at discharge point is  $C(0, t) = C_0 = 1 \text{ Kg/m}^3$  at  $x = 0$  for all  $t > 0$  and  $C(x, 0) = 0 \text{ Kg/m}^3$  at  $t = 0$ . The elevation of water at the discharge point can be described as a function  $d(0, t) = f(t) = \sin t \text{ m}$  for all  $t > 0$ , and the elevation is not changed at  $x = 1.0 \text{ km}$ . The physical parameters of the stream system are diffusion coefficient  $D = 0.05 \text{ m}^2/\text{s}$ , and a first-order reaction rate  $10^{-5} \text{ s}^{-1}$ . In the analysis conducted in this study, meshes the stream into 20, 40, 80, and 160 elements with  $\Delta x = 0.05, 0.025, 0.0125, 0.00625$ , respectively, and time increment are 3.2, 1.6, 0.8, 0.4, 0.2, 0.1 s with  $\Delta t = 0.01, 0.005, 0.0025, 0.00125, 0.000625, 0.0003125$ , respectively. Using (3.7), it can be obtained the water velocity  $u(x, t)$  on Table 2 and Figure 3. Next, the approximate water velocity can be plugged into the finite difference equations of FTCS and Saul'yev schemes on (3.11)–(3.13) and (3.17)–(3.19), respectively. The comparison of concentration of the FTCS method and Saul'yev method is presented in Figure 5 for two different instants. We then have the stabilities of both schemes for each  $\Delta x$  and  $\Delta t$  in Table 5 that are consistence

**Table 2:** The velocity of water flow  $u(x, t)$ .

$t$	$x = 0$	$x = 0.1$	$x = 0.2$	$x = 0.3$	$x = 0.4$	$x = 0.5$	$x = 0.6$	$x = 0.7$	$x = 0.8$	$x = 0.9$	$x = 1.0$
10	-0.5478	-0.5695	-0.5666	-0.5199	-0.4711	-0.4061	-0.3352	-0.2571	-0.1747	-0.0878	0.0000
20	1.3101	1.2213	1.1232	1.0160	0.8931	0.7504	0.6097	0.4595	0.3099	0.1554	0.0000
30	-0.4468	-0.3731	-0.3085	-0.2527	-0.2057	-0.1651	-0.1252	-0.0875	-0.0573	-0.0276	0.0000
40	-1.0361	-0.9898	-0.9258	-0.8459	-0.7513	-0.6439	-0.5258	-0.4004	-0.2711	-0.1367	0.0000
50	1.0939	0.9918	0.8867	0.7791	0.6700	0.5594	0.4479	0.3356	0.2233	0.1114	0.0000

**Figure 3:** The water velocity  $u(x, t)$ .**Figure 4:** The pollutant concentration  $C(x, t)$ .

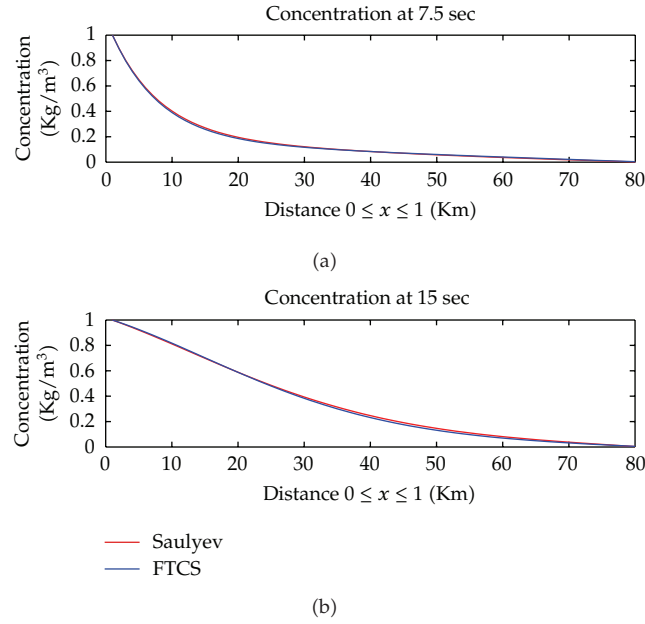


**Figure 5:** The comparison of concentration at two different time instants of the FTCS and Saulyeu methods.

**Table 3:** The pollutant concentration  $C(x, t)$  of FTCS scheme,  $\Delta x = 0.0125$  (40 m),  $\Delta t = 0.0003125$  (0.1 s).

$t$	$x = 0$	$x = 0.1$	$x = 0.2$	$x = 0.3$	$x = 0.4$	$x = 0.5$	$x = 0.6$	$x = 0.7$	$x = 0.8$	$x = 0.9$	$x = 1.0$
10	1.0000	0.3231	0.1154	0.0517	0.0292	0.0194	0.0141	0.0109	0.0090	0.0079	0.0075
20	1.0000	0.9996	0.9971	0.9873	0.9575	0.8873	0.7588	0.5774	0.3828	0.2324	0.1720
30	1.0000	0.9981	0.9956	0.9910	0.9830	0.9706	0.9533	0.9327	0.9122	0.8966	0.8903
40	1.0000	0.9260	0.9166	0.9150	0.9145	0.9141	0.9138	0.9136	0.9135	0.9134	0.9133
50	1.0000	0.9993	0.9966	0.9902	0.9788	0.9633	0.9468	0.9327	0.9231	0.9179	0.9162

**Table 4:** The pollutant concentration  $C(x, t)$  of Saulyeu scheme,  $\Delta x = 0.0125$  (40 m),  $\Delta t = 0.005$  (1.6 s).

$t$	$x = 0$	$x = 0.1$	$x = 0.2$	$x = 0.3$	$x = 0.4$	$x = 0.5$	$x = 0.6$	$x = 0.7$	$x = 0.8$	$x = 0.9$	$x = 1.0$
10	1.0000	0.3297	0.1225	0.0570	0.0327	0.0212	0.0144	0.0096	0.0059	0.0028	0.0000
20	1.0000	0.9995	0.9970	0.9878	0.9619	0.9020	0.7908	0.6251	0.4238	0.2136	0.0000
30	1.0000	0.9972	0.9919	0.9798	0.9536	0.9026	0.8136	0.6760	0.4859	0.2530	0.0000
40	1.0000	0.3128	0.2031	0.1624	0.1321	0.1052	0.0807	0.0581	0.0372	0.0179	0.0000
50	1.0000	0.9913	0.9631	0.8991	0.7879	0.6342	0.4610	0.2988	0.1694	0.0753	0.0000

with (3.14). The approximation of pollutant concentration  $C$  of both schemes are shown in Tables 3 and 4 and Figure 4. The concentration along a stream at only 24 min with varied diffusion coefficients is shown in Figure 6. These imply that the Peclet number was  $Pe = (U_i^n \Delta x / D) < 10$ , which indicated the stream system was advection not dominated [15].



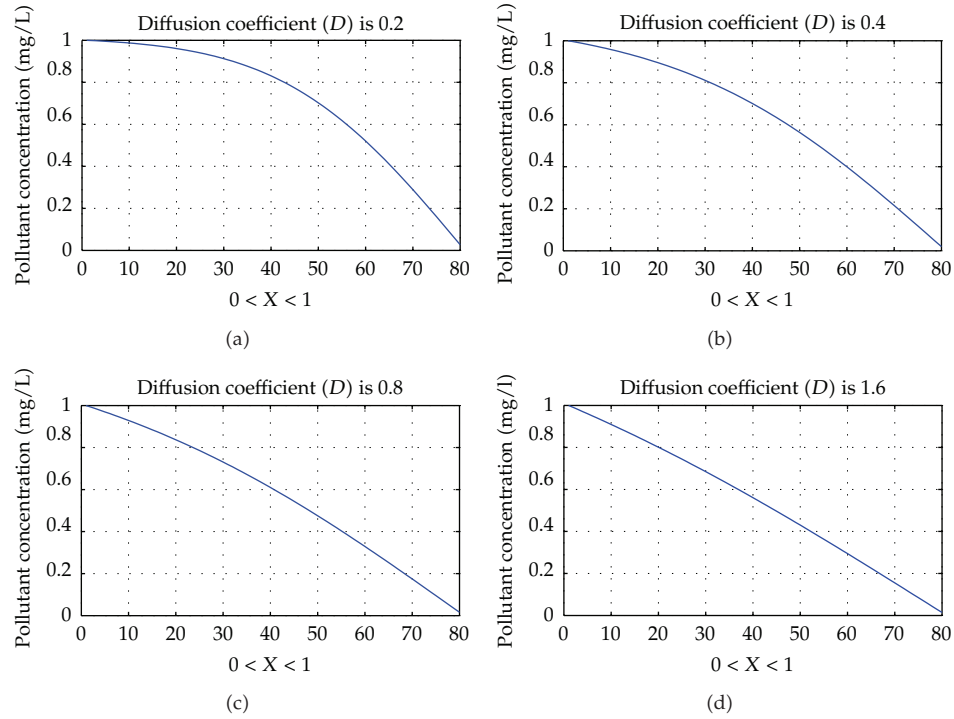


Figure 6: The pollutant concentration  $C(x, t)$  for each diffusion coefficients at  $t = 24$  min.

## 6. Discussion and Conclusions

The approximation of the pollutant concentrations from the FTCS technique is shown in Tables 3 and 5; it can be concluded that stability requirements is one of the disadvantages of the technique. The real-world problems require a small amount of time interval in obtaining accurate solutions. We can see that the FTCS scheme is not good agreement for real application. In Table 4, it can be obtained that the Saul'yev technique has an advantage over compared to FTCS. It is unconditionally stable, easy, and economical to implement.

By Figure 6, we can see that the diffusion coefficients of pollutant matter can reduce the concentration in a nonuniform stream. If sewage effluent with a low diffusion coefficient has discharged into a nonuniform flow stream, then the water quality will be lower than a discharging of high diffusion coefficients of other pollutant matters.

In this paper, it can be combined the hydrodynamic model and the convection-diffusion-reaction equation to approximate the pollutant concentration in a stream when the current which reflects water in the stream is not uniform. The technique developed in this paper the response of the stream to the two different external inputs: the elevation of water and the pollutant concentration at the discharged point. The Saul'yev technique can be used in the dispersion model since the scheme is very simple to implement. By the Saul'yev finite difference formulation, we obtain that the proposed technique is applicable and economical to be used in the real-world problem as a result of the simplicity of programming and the straight forwardness of the implementation. It is also possible to find tentative better locations and the periods of time of the different discharged points to a stream.

**Table 5:** The stability of FTCS and Saul'yev schemes,  $\gamma = \max\{\gamma_i^n : 1 \leq i \leq M, 0 \leq n \leq N - 1\}$ .

$\Delta x$	$\Delta t$	$\lambda$	$\gamma$	FTCS scheme	Saul'yev scheme
0.0125	0.010000	3.2	1.0665	Unstable	Stable
	0.005000	1.6	0.5332	Unstable	Stable
	0.002500	0.8	0.2667	Unstable	Stable
	0.001250	0.4	0.1333	Stable	Stable
	0.000625	0.2	0.0080	Stable	Stable
0.0125	0.010000	3.2	1.0665	Unstable	Stable
	0.005000	1.6	0.5332	Unstable	Stable
	0.002500	0.8	0.2667	Unstable	Stable
	0.001250	0.4	0.1333	Stable	Stable
	0.000625	0.2	0.0080	Stable	Stable
0.0125	0.010000	3.2	1.0665	Unstable	Stable
	0.005000	1.6	0.5332	Unstable	Stable
	0.002500	0.8	0.2667	Unstable	Stable
	0.001250	0.4	0.1333	Stable	Stable
	0.000625	0.2	0.0080	Stable	Stable

## Acknowledgments

This paper is supported by the Centre of Excellence in Mathematics, the Commission on Higher Education, Thailand. The author greatly appreciates valuable comments received from the referees.

## References

- [1] A. Garzon and L. D'Alpaos, "A modified method of the characteristic technique combined with Gelerkin finite element method to solve shallow water mass transport problems," in *Proceedings 23rd International Conference in Coastal Engineering*, vol. 3, pp. 3068–3080, 1992.
- [2] N. Pochai, S. Tangmanee, L. J. Crane, and J. J. H. Miller, "A mathematical model of water pollution control using the finite element method," *Proceedings in Applied Mathematics and Mechanics*, vol. 6, no. 1, pp. 755–756, 2006.
- [3] J. Y. Chen, C. H. Ko, S. Bhattacharjee, and M. Elimelech, "Role of spatial distribution of porous medium surface charge heterogeneity in colloid transport," *Colloids and Surfaces A*, vol. 191, no. 1–2, pp. 3–15, 2001.
- [4] G. Li and C. R. Jackson, "Simple, accurate, and efficient revisions to MacCormack and Saul'yev schemes: high Peclet numbers," *Applied Mathematics and Computation*, vol. 186, no. 1, pp. 610–622, 2007.
- [5] E. M. O'Loughlin and K. H. Bowmer, "Dilution and decay of aquatic herbicides in flowing channels," *Journal of Hydrology*, vol. 26, no. 3–4, pp. 217–235, 1975.
- [6] M. Dehghan, "Numerical schemes for one-dimensional parabolic equations with nonstandard initial condition," *Applied Mathematics and Computation*, vol. 147, no. 2, pp. 321–331, 2004.
- [7] A. I. Stamou, "Improving the numerical modeling of river water quality by using high order difference schemes," *Water Research*, vol. 26, no. 12, pp. 1563–1570, 1992.
- [8] S. Marušić, "Natural convection in shallow water," *Nonlinear Analysis: Real World Applications*, vol. 8, no. 5, pp. 1379–1389, 2007.
- [9] A. Dube and G. Jayaraman, "Mathematical modelling of the seasonal variability of plankton in a shallow lagoon," *Nonlinear Analysis: Theory, Methods & Applications*, vol. 69, no. 3, pp. 850–865, 2008.

- [10] D. Ionescu-Kruse, "Particle trajectories beneath small amplitude shallow water waves in constant vorticity flows," *Nonlinear Analysis: Theory, Methods & Applications*, vol. 71, no. 9, pp. 3779–3793, 2009.
- [11] P. Tabuenca, J. Vila, and J. Cardona, "Finite element simulation of dispersion in the Bay of Santander," *Advances in Engineering Software*, vol. 28, no. 5, pp. 313–332, 1997.
- [12] N. Pochai, "A numerical computation of the non-dimensional form of a non-linear hydrodynamic model in a uniform reservoir," *Nonlinear Analysis: Hybrid Systems*, vol. 3, no. 4, pp. 463–466, 2009.
- [13] N. Pochai, S. Tangmanee, L. J. Crane, and J. J. H. Miller, "A water quality computation in the uniform channel," *Journal of Interdisciplinary Mathematics*, vol. 11, no. 6, pp. 803–814, 2008.
- [14] N. Pochai, "A numerical computation of a non-dimensional form of stream water quality model with hydrodynamic advection-dispersion-reaction equations," *Nonlinear Analysis: Hybrid Systems*, vol. 3, no. 4, pp. 666–673, 2009.
- [15] S. C. Chapra, *Surface Water-Quality Modeling*, McGraw-Hill, New York, NY, USA, 1997.
- [16] H. Ninomiya and K. Onishi, *Flow Analysis Using a PC*, CRC Press, Boca Raton, Fla, USA, 1991.
- [17] A. R. Mitchell, *Computational Methods in Partial Differential Equations*, John Wiley & Sons, London, UK, 1969.
- [18] W. F. Ames, *Numerical Methods for Partial Differential Equations*, Computer Science and Scientific Computing, Academic Press, Boston, Mass, USA, 2nd edition, 1977.
- [19] M. Dehghan, "Weighted finite difference techniques for the one-dimensional advection-diffusion equation," *Applied Mathematics and Computation*, vol. 147, no. 2, pp. 307–319, 2004.
- [20] W. Zeng, *A model for understanding and managing the impacts of sediment behavior on river water quality*, Ph.D. thesis, University of Georgia, Athens, Ga, USA, 2000.
- [21] L. Lapidus and G. F. Pinder, *Numerical Solution of Partial Differential Equations in Science and Engineering*, John Wiley & Sons, New York, NY, USA, 1982.

## *Research Article*

# **A Corotational Finite Element Method Combined with Floating Frame Method for Large Steady-State Deformation and Free Vibration Analysis of a Rotating-Inclined Beam**

**Ming Hsu Tsai,<sup>1</sup> Wen Yi Lin,<sup>2</sup> Yu Chun Zhou,<sup>1</sup> and Kuo Mo Hsiao<sup>1</sup>**

<sup>1</sup> Department of Mechanical Engineering, National Chiao Tung University, Hsinchu 300, Taiwan

<sup>2</sup> Department of Mechanical Engineering, De Lin Institute of Technology, Tucheng 236, Taiwan

Correspondence should be addressed to Kuo Mo Hsiao, kmhsiao@mail.nctu.edu.tw

Received 30 March 2011; Accepted 19 May 2011

Academic Editor: Delfim Soares Jr.

Copyright © 2011 Ming Hsu Tsai et al. This is an open access article distributed under the Creative Commons Attribution License, which permits unrestricted use, distribution, and reproduction in any medium, provided the original work is properly cited.

A corotational finite element method combined with floating frame method and a numerical procedure is proposed to investigate large steady-state deformation and infinitesimal-free vibration around the steady-state deformation of a rotating-inclined Euler beam at constant angular velocity. The element nodal forces are derived using the consistent second-order linearization of the nonlinear beam theory, the d'Alembert principle, and the virtual work principle in a current inertia element coordinates, which is coincident with a rotating element coordinate system constructed at the current configuration of the beam element. The governing equations for linear vibration are obtained by the first-order Taylor series expansion of the equation of motion at the position of steady-state deformation. Numerical examples are studied to demonstrate the accuracy and efficiency of the proposed method and to investigate the steady-state deformation and natural frequency of the rotating beam with different inclined angle, angular velocities, radius of the hub, and slenderness ratios.

## **1. Introduction**

Rotating beams are often used as a simple model for propellers, turbine blades, and satellite booms. Rotating beam differs from a nonrotating beam in having additional centrifugal force and Coriolis effects on its dynamics. The vibration analysis of rotating beams has been extensively studied [1–25]. However, the vibration analysis of rotating beam with inclination angle, which is considered in the recent computer cooling fan design on the natural frequencies of rotating beams [21], is rather rare in the literature [10, 19, 21, 22].

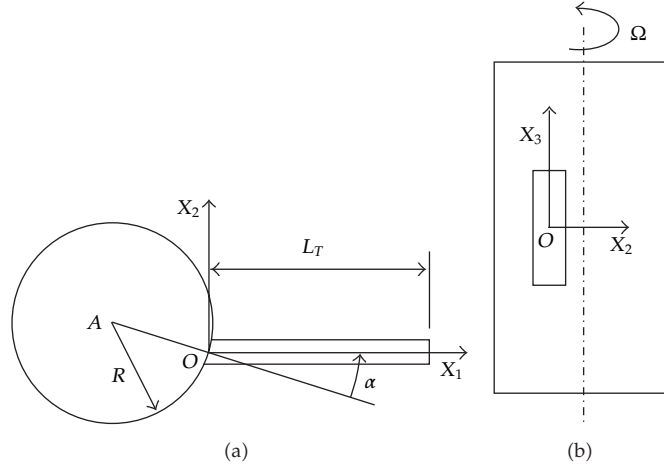


**Figure 1:** A rotating inclined beam, (a) top view, (b) side view.

In [21, 22], the effect of the steady-state axial deformation and the inclination angle on the natural frequencies of the rotating beam was investigated. However, the lateral steady-state deformation and its effects on the natural frequencies of the rotating beam were not considered in [21, 22]. To the authors' knowledge, the lateral steady-state deformation and its effects on the lagwise bending and axial vibration of rotating inclined beams are not reported in the literature.

It is well known that the spinning elastic bodies sustain a steady-state deformation (time-independent deformation) induced by constant rotation [26]. For rotating beams with an inclination angle as shown in Figure 1, the steady-state deformations include axial deformation and lateral deformation. The linear solution of the steady-state deformation of rotating-inclined beam induced by constant rotation can be easily obtained using mechanics of materials. However, the centrifugal stiffening effect on the steady lateral deformation is significant for slender rotating-inclined beam, and the centrifugal force is configuration dependent load; thus the linear solution of the steady-state deformation of rotating inclined beam may be not accurate enough. The lagwise bending and axial vibration of rotating inclined beams are coupled due to the Coriolis effects [15, 24] and the lateral steady-state deformation. The accuracy of the frequencies obtained from linearizing about the steady-state deformation is dependent on the accuracy of the steady-state deformation and the accuracy of the linearized perturbation [6, 12]. Thus, the geometrical nonlinearities that arise due to steady-state deformation should be considered. In [6], the rotating beam with pretwist, precone, and setting angle is studied. The undeformed state of the rotating beam is chosen to be the reference state to define the deformation parameters of the rotating beam. The geometric nonlinearities up to the second degree are considered. The Galerkin method, with vibration modes of nonrotating beam, is employed for the solution of both steady-state nonlinear equations and linear perturbation equations. In [8], it is reported that for a cantilever beam with a tip mass, even up to the third degree geometric nonlinearities are considered, in some cases, very inaccurate eigenvalues for the perturbed linearized equation of motion are obtained. The formulation used in [6, 8, 12] may be regarded as a total Lagrangian (TL) formulation combined with the floating frame method. In order to capture correctly all inertia effects and coupling among bending, twisting, and stretching

deformations of the rotating beam, the governing equations of the rotating beam might be derived by the fully geometrically nonlinear beam theory [12, 27, 28]. The exact expressions for the inertia, deformation forces, and the governing equations of the rotating beam, which are required in a TL formulation for large displacement/small strain problems, are highly nonlinear functions of deformation parameters. However, the dominant factors in the geometrical nonlinearities of beam structures are attributable to finite rotations, with the strains remaining small. For a beam structures discretized by finite elements, this implies that the motion of the individual elements to a large extent will consist of rigid body motion. If the rigid body motion part is eliminated from the total displacements and the element size is properly chosen, the deformational part of the motion is always small relative to the local element axes; thus in conjunction with the corotational formulation, the higher-order terms of nodal deformation parameters in the element deformation and inertia nodal forces may be neglected by consistent linearization [28, 29]. In [29], Hsiao et al. presented a corotational finite element formulation and numerical procedure for the dynamic analysis of planar beam structures. Both the element deformation and inertia forces are systematically derived by consistent linearization of the fully geometrically nonlinear beam theory using the d'Alembert principle and the virtual work principle. This formulation and numerical procedure were proven to be very effective by numerical examples studied in [29]. However, because the nodal displacements and rotations, velocities, accelerations, and the equations of motion of the system are defined in terms of a fixed global coordinate system, the formulation proposed in [29] cannot be used for steady-state deformation and free vibration analysis of a rotating-inclined beam. The absolute nodal coordinate formulation [30, 31] is used to large rotation and large deformation problems. Numerical results show that the absolute nodal coordinate formulation can be effectively used in the large deformation problems. However, the mass matrix of the finite elements in [30, 31] is a constant matrix, and therefore, the centrifugal and Coriolis forces are equal to zero. Thus, the absolute nodal coordinate formulation cannot be used for steady-state deformation and free vibration analysis of a rotating inclined beam.

The objective of this study is to present a corotational finite element method combined with floating frame method and a numerical procedure for large steady-state deformation and free vibration analysis of a rotating-inclined beam at constant angular velocity. The nodal coordinates, displacements and rotations, absolute velocities, absolute accelerations, and the equations of motion of the system are defined in terms of an inertia global coordinate system which is coincident with a rotating global coordinate system rigidly tied to the rotating hub, while the total deformations in the beam element are measured in an inertia element coordinate system which is coincident with a rotating element coordinate system constructed at the current configuration of the beam element. The rotating element coordinates rotate about the hub axis at the angular speed of the hub. The inertia nodal forces and deformation nodal forces of the beam element are systematically derived by the virtual work principle, the d'Alembert principle, and consistent second-order linearization of the fully geometrically nonlinear beam theory [27–29] in the element coordinates. Due to the consideration of the exact kinematics of Euler beam, some coupling terms of axial and flexural deformations are retained in the element internal nodal forces. The element equations are constructed first in the inertia element coordinate system and then transformed to the inertia global coordinate system using standard procedure.

The infinitesimal-free vibrations of rotating beam are measured from the position of the corresponding steady-state deformation. The governing equations for linear vibration of

rotating beam are obtained by the first-order Taylor series expansion of the equation of motion at the position of steady-state deformation.

Dimensionless numerical examples are studied to demonstrate the accuracy and efficiency of the proposed method and to investigate the effect of inclination angle and slenderness ratio on the steady-state deformation and the natural frequency for rotating inclined Euler beams at different angular speeds.

## 2. Formulation

### 2.1. Description of Problem

Consider an inclined uniform Euler beam of length  $L_T$  rigidly mounted with an inclination angle  $\alpha$  on the periphery of rigid hub with radius  $R$  rotating about its axis fixed in space at a constant angular speed  $\Omega$  as shown in Figure 1. The axis of the rotating hub is perpendicular to one of the principal directions of the cross section of the beam. The deformation displacements of the beam are defined in an inertia rectangular Cartesian coordinate system which is coincident with a rotating rectangular Cartesian coordinate system rigidly tied to the hub.

Here only axial and lagwise bending vibrations are considered. It is well known that the beam sustains a steady-state deformations (time-independent deformation displacements) induced by constant rotation [26]. In this study, large displacement and rotation with small strain are considered in the steady-state deformation. The vibration (time-dependent deformation displacements) of the beam is measured from the position of the steady-state deformation, and only infinitesimal-free vibration is considered. Note that the axial and lagwise vibrations, which are coupled due to the Coriolis effects and the lateral steady-state deformation, cannot be analyzed independently. Here the engineering strain and stress are used for the measure of the strain and stress.

### 2.2. Basic Assumptions

The following assumptions are made in derivation of the beam element behavior.

- (1) The beam is prismatic and slender, and the Euler-Bernoulli hypothesis is valid.
- (2) The unit extension of the centroid axis of the beam element is uniform.
- (3) The deformation displacements and rotations of the beam element are small.
- (4) The strains of the beam element are small.

In conjunction with the corotational formulation and rotating frame method, the third assumption can always be satisfied if the element size is properly chosen. Thus, only the terms up to the second order of deformation parameters and their spatial derivatives are retained in element position vector, strain, and deformation nodal forces by consistent second-order linearization in this study.

### 2.3. Coordinate Systems

In order to describe the system, we define three sets of right-handed rectangular Cartesian coordinate systems.



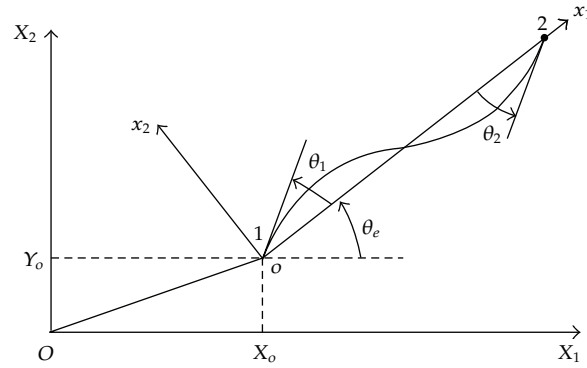


Figure 2: Coordinate systems.

- (1) A rotating global set of coordinates,  $X_i$  ( $i = 1, 2, 3$ ) (see Figures 1 and 2); the coordinates rotate about the hub axis at a constant angular speed  $\Omega$  as shown in Figure 1. The origin of this coordinate system is chosen to be the intersection of the centroid axes of the hub and the undeformed beam. The  $X_1$  axis is chosen to coincide with the centroid axis of the undeformed beam, and the  $X_2$  and  $X_3$  axes are chosen to be the principal directions of the cross section of the beam at the undeformed state. The direction of the axis of the rotating hub is parallel to the  $X_3$  axis. The nodal coordinates, nodal deformation displacements, absolute nodal velocity, absolute nodal acceleration, and equations of motion of the system are defined in terms of an inertia global coordinate system which is coincident with the rotating global coordinate system.
- (2) Element coordinates;  $x_i$  ( $i = 1, 2, 3$ ) (see Figure 2), a set of element coordinates is associated with each element, which is constructed at the current configuration of the beam element. The coordinates rotate about the hub axis at a constant angular speed  $\Omega$ . The origin of this coordinate system is located at the element node 1, the centroid of the end section. The  $x_1$  axis is chosen to pass through two end nodes of the element; the directions of the  $x_2$  and  $x_3$  axes are chosen to coincide with the principal direction of the cross section in the undeformed state. Because only the displacements in  $X_1X_2$  plane are considered, the directions of  $x_3$  axis and  $X_3$  axis are coincident. The position vector, deformations, absolute velocity, absolute acceleration, internal nodal forces, stiffness matrices, and inertia matrices of the elements are defined in terms of an inertia element coordinate system which is coincident with the rotating element coordinate system.

In this study, the direction of the axis of the rotating hub is parallel to the  $X_3$  axis and only the displacements in  $X_1X_2$  plane are considered. Thus, the angular velocity of the hub referred to the global coordinates may be given by

$$\Omega_G = \{0 \ 0 \ \Omega\}, \quad (2.1)$$

where the symbol  $\{ \}$  denotes a column matrix, which is used through the paper.



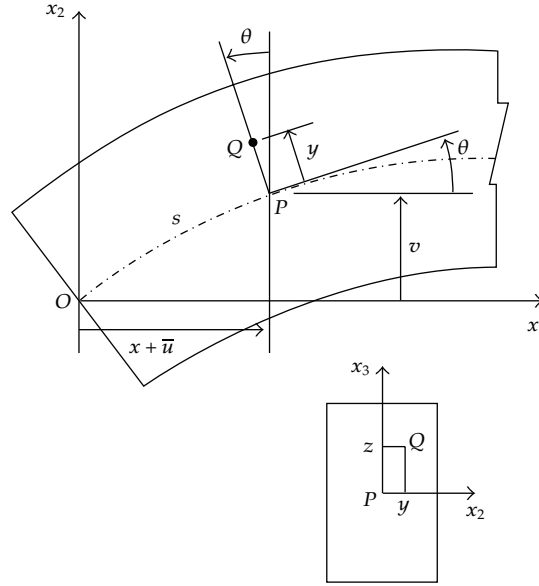


Figure 3: Kinematics of Euler beam.

#### 2.4. Kinematics of Beam Element

Let  $Q$  (Figure 3) be an arbitrary point in the beam element and  $P$  the point corresponding to  $Q$  on the centroid axis. The position vector of point  $Q$  in the undeformed configurations referred to the current element coordinate system may be expressed as

$$\mathbf{r}_0 = \{x, y, z\}. \quad (2.2)$$

Using the approximation  $\cos \theta \approx 1 - (1/2)\theta^2$ ,  $\sin \theta \approx \theta$ , and  $(1 + \varepsilon_c) \approx 1$ , retaining all terms up to the second order, the position vector of point  $Q$  in the deformed configurations referred to the current element coordinate system may be expressed as

$$\mathbf{r} = \{r_1, r_2, r_3\} = \left\{ x_p - y\theta, y \left( 1 - \frac{1}{2}\theta^2 \right) + v, z \right\}, \quad (2.3)$$

$$\theta \approx \sin \theta = \frac{\partial v(x, t)}{\partial s} = \frac{\partial v(x, t)}{\partial x} \frac{\partial x}{\partial s} = \frac{v'}{1 + \varepsilon_c} \approx v', \quad (2.4)$$

$$\varepsilon_c = \frac{\partial s}{\partial x} - 1, \quad (2.5)$$

where  $x_p(x, t)$  and  $v(x, t)$  are the  $x_1$  and  $x_2$  coordinates of point  $P$ , respectively, in the deformed configuration,  $t$  is time,  $\theta = \theta(x, t)$  is the angle counterclockwise measured from  $x_1$  axis to the tangent of the centroid axis of the deformed beam,  $\varepsilon_c$  is the unit extension of the centroid axis, and  $s$  is the arc length of the deformed centroid axis measured from node 1 to point  $P$ . In this paper,  $( )'$  denotes  $( )_{,x} = \partial( ) / \partial x$ .

Here, the lateral deflection of the centroid axis,  $v(x, t)$ , is assumed to be the Hermitian polynomials of  $x$  and may be expressed by

$$v(x, t) = \{N_1, N_2, N_3, N_4\}^t \{v_1, v'_1, v_2, v'_2\} = \mathbf{N}_b^t \mathbf{u}_b, \quad (2.6)$$

where  $v_j = v_j(t)$  and  $v'_j = v'_j(t)$  ( $j = 1, 2$ ) are nodal values of  $v$  and  $v_{,x}$ , respectively, at nodes  $j$ . Note that, due to the definition of the element coordinates, the values of  $v_j$  ( $j = 1, 2$ ) are zero. However, their variations and time derivatives are not zero.  $N_i$  ( $i = 1-4$ ) are shape functions and are given by

$$N_1 = \frac{1}{4}(1 - \xi)^2(2 + \xi), \quad N_2 = \frac{L}{8}(1 - \xi^2)(1 - \xi), \quad (2.7)$$

$$N_3 = \frac{1}{4}(1 + \xi)^2(2 - \xi), \quad N_4 = \frac{L}{8}(-1 + \xi^2)(1 + \xi),$$

$$\xi = -1 + \frac{2x}{L}, \quad (2.8)$$

where  $L$  is the length of the undeformed beam element.

Making use of assumptions  $v_{,x} \ll 1$  and  $\varepsilon_c \ll 1$ , the relationship between  $x_p(x, t)$ ,  $v(x, t)$ , and  $x$  in (2.3) may be approximated by

$$x_p(x, t) = u_1 + \int_0^x \left(1 + \varepsilon_c - \frac{1}{2}v_{,x}^2\right) dx, \quad (2.9)$$

where  $u_1$  is the displacement of node 1 in the  $x_1$  direction. Note that due to the definition of the element coordinate system, the value of  $u_1$  is equal to zero. However, the variation and time derivatives of  $u_1$  are not zero.

The axial displacements of the centroid axis may be determined from the lateral deflections and the unit extension of the centroid axis using (2.9).

From (2.9), one may obtain

$$\ell = L + u_2 - u_1 = x_c(L, t) - x_c(0, t) = \int_0^L \left(1 + \varepsilon_c - \frac{1}{2}v_{,x}^2\right) dx \quad (2.10)$$

in which  $\ell$  is the current chord length of the centroid axis of the beam element and  $u_2$  is the displacement of node 2 in the  $x_1$  direction. Using the assumption of uniform extension of the centroid axis and (2.10),  $\varepsilon_c$  in (2.10) maybe expressed by

$$\varepsilon_c = \frac{1}{L} \left( \mathbf{G}_a^t \mathbf{u}_a + \frac{1}{2} \mathbf{G}_b^t \mathbf{u}_b \right),$$

$$\mathbf{G}_a = \{-1, 1\},$$

$$\mathbf{u}_a = \{u_1, u_2\}, \quad (2.11)$$

$$\mathbf{G}_b = \int_0^L \mathbf{N}_b' v_{,x} dx.$$

Substituting (2.11) into (2.9), one may obtain

$$x_p(x, t) = \mathbf{N}_a^t \mathbf{u}_a + x + \frac{x}{2L} \mathbf{G}_b^t \mathbf{u}_b - \frac{1}{2} \int_0^x v_{,x}^2 dx, \quad (2.12)$$

$$\mathbf{N}_a = \left\{ \frac{1-\xi}{2}, \frac{1+\xi}{2} \right\}.$$

From (2.3) and the definition of engineering strain [32, 33], making use of the assumption of small strain, and retaining the terms up to the second order of deformation parameters, the engineering strain in the Euler beam may be approximated by

$$\varepsilon_{11} = \varepsilon_c - yv''. \quad (2.13)$$

The absolute velocity and acceleration vectors of point  $Q$  in the beam element may be expressed as

$$\mathbf{v} = \{v_1, v_2, v_3\} = \mathbf{v}_o + \boldsymbol{\Omega} \times \mathbf{r} + \dot{\mathbf{r}}, \quad (2.14)$$

$$\mathbf{a} = \{a_1, a_2, a_3\} = \mathbf{a}_o + \dot{\boldsymbol{\Omega}} \times \mathbf{r} + \boldsymbol{\Omega} \times (\boldsymbol{\Omega} \times \mathbf{r}) + 2\boldsymbol{\Omega} \times \dot{\mathbf{r}} + \ddot{\mathbf{r}}, \quad (2.15)$$

$$\mathbf{v}_o = \boldsymbol{\Omega} \times \mathbf{r}_{Ao}, \quad (2.16)$$

$$\mathbf{a}_o = \{a_{o1}, a_{o2}, a_{o3}\} = \boldsymbol{\Omega} \times (\boldsymbol{\Omega} \times \mathbf{r}_{Ao}), \quad (2.17)$$

$$\boldsymbol{\Omega} = \mathbf{A}_{GE}^t \boldsymbol{\Omega}_G, \quad (2.18)$$

$$\mathbf{r}_{Ao} = \mathbf{A}_{GE}^t \mathbf{r}_{AoG}, \quad (2.19)$$

$$\mathbf{r}_{AoG} = \mathbf{r}_{AO} + \mathbf{r}_{OoG} = \{R \cos \alpha + X_o, -R \sin \alpha + Y_o, 0\}, \quad (2.20)$$

where  $\mathbf{r}$  is the position vector of point  $Q$  given in (2.3) referred to the current moving element coordinate system, the symbol  $(\dot{\phantom{x}})$  denotes time derivative,  $\boldsymbol{\Omega}$  is the vector of angular velocity referred to the current inertia element coordinates,  $\boldsymbol{\Omega}_G$  is the angular velocity of the hub referred to the global coordinates given in (2.1),  $\mathbf{A}_{GE}$  is the transformation matrix between the current global coordinates and the current element coordinates,  $\mathbf{v}_o$  and  $\mathbf{a}_o$  are the absolute velocity and absolute acceleration of point  $o$ , the origin of the current element coordinates,  $X_o$  and  $Y_o$  are coordinates of point  $o$  referred to the current global coordinates,  $R$  is the radius of the hub, and  $\alpha$  is inclination angle of the rotating beam.  $\boldsymbol{\Omega} \times (\boldsymbol{\Omega} \times \mathbf{r})$  and  $2\boldsymbol{\Omega} \times \dot{\mathbf{r}}$  are centripetal acceleration and Coriolis acceleration, respectively.  $\dot{\mathbf{r}}$  and  $\ddot{\mathbf{r}}$  are the velocity and acceleration of point  $Q$  relative to the current moving element coordinates. From (2.3), (2.11) and (2.12),  $\dot{\mathbf{r}}$  and  $\ddot{\mathbf{r}}$  may be expressed as

$$\dot{\mathbf{r}} = \{\dot{r}_1, \dot{r}_2, \dot{r}_3\} = \{\dot{x}_p - y\dot{v}_{,x}, \dot{v} - y\dot{v}_{,x}v_{,x}, 0\},$$

$$\ddot{\mathbf{r}} = \{\ddot{r}_1, \ddot{r}_2, \ddot{r}_3\} = \{\ddot{x}_p - y\ddot{v}_{,x}, \ddot{v} - y\ddot{v}_{,x}^2 - y\ddot{v}_{,x}v_{,x}, 0\},$$

$$\dot{x}_p = \mathbf{N}_a^t \dot{\mathbf{u}}_a + \frac{x}{L} \mathbf{G}_b^t \dot{\mathbf{u}}_b - \int_0^x v_{,x} \dot{v}_{,x} dx,$$

$$\begin{aligned}
\dot{\varepsilon}_c &= \frac{1}{L} (\mathbf{G}_a^t \dot{\mathbf{u}}_a + \mathbf{G}_b^t \dot{\mathbf{u}}_b), \\
\ddot{x}_p &= \mathbf{N}_a^t \ddot{\mathbf{u}}_a + \frac{x}{L} (\mathbf{G}_b^t \ddot{\mathbf{u}}_b + \dot{\mathbf{G}}_b^t \dot{\mathbf{u}}_b) - \int_0^x (v_{,x} \ddot{v}_{,x} + \dot{v}_{,x} \dot{v}_{,x}) dx, \\
\ddot{\varepsilon}_c &= \frac{1}{L} (\mathbf{G}_a^t \ddot{\mathbf{u}}_a + \dot{\mathbf{G}}_b^t \dot{\mathbf{u}}_b + \mathbf{G}_b^t \ddot{\mathbf{u}}_b).
\end{aligned} \tag{2.21}$$

Note that the current element coordinates constructed at the current configuration of the beam element rotate about the hub axis at the angular velocity of the hub. Thus, the centripetal acceleration and Coriolis acceleration corresponding to the inertia forces of the rotating beam are unique. For nonrotating beam,  $\boldsymbol{\Omega} = \mathbf{0}$  and  $\dot{\mathbf{r}}$  and  $\ddot{\mathbf{r}}$  are the absolute velocity and acceleration referred to the current element coordinate.

### 2.5. Element Nodal Force Vector

Let  $u_j, \delta v_j$ , and  $\delta v'_j$  ( $j = 1, 2$ ) denote the virtual displacements in the  $x_1$  and  $x_2$  directions of the current inertia element coordinates, and virtual rotations applied at the element nodes  $j$ . The element nodal force corresponding to virtual nodal displacements  $\delta u_j$ ,  $\delta v_j$ , and  $\delta v'_j$  ( $j = 1, 2$ ) are  $f_{ij}$ , the forces in the  $x_i$  ( $i = 1, 2$ ) directions, and  $m_j$  moments about the  $x_3$  axis, at element local nodes  $j$ .

The element nodal force vector is obtained from the d'Alembert principle and the virtual work principle in the current inertia element coordinates. The virtual work principle requires that

$$\delta \mathbf{u}_a^t \mathbf{f}_a + \delta \mathbf{u}_b^t \mathbf{f}_b = \int_V (\delta \varepsilon_{11} \sigma_{11} + \rho \delta \mathbf{r}^t \mathbf{a}) dV, \tag{2.22}$$

$$\delta \mathbf{u}_a = \{\delta u_1, \delta u_2\}, \tag{2.23}$$

$$\delta \mathbf{u}_b = \{\delta v_1, \delta v'_1, \delta v_2, \delta v'_2\}, \tag{2.24}$$

$$\mathbf{f}_a = \mathbf{f}_a^D + \mathbf{f}_a^I = \{f_{11}, f_{12}\}, \tag{2.25}$$

$$\mathbf{f}_b = \mathbf{f}_b^D + \mathbf{f}_b^I = \{f_{21}, m_1, f_{22}, m_2\}, \tag{2.26}$$

$$\mathbf{f}_a^D = \{f_{11}^D, f_{12}^D\}, \tag{2.27}$$

$$\mathbf{f}_b^D = \{f_{21}^D, m_1^D, f_{22}^D, m_2^D\}, \tag{2.28}$$

$$\mathbf{f}_a^I = \{f_{11}^I, f_{12}^I\}, \tag{2.29}$$

$$\mathbf{f}_b^I = \{f_{21}^I, m_1^I, f_{22}^I, m_2^I\}, \tag{2.30}$$

where  $\mathbf{f}_i$  ( $i = a, b$ ) are the generalized force vectors corresponding to  $\delta \mathbf{u}_a$  and  $\delta \mathbf{u}_b$ , respectively,  $\mathbf{f}_i^D$  and  $\mathbf{f}_i^I$  ( $i = a, b$ ) are element deformation nodal force vector and inertia

nodal force vector corresponding to  $\mathbf{f}_i$ , respectively,  $V$  is the volume of the undeformed beam element, and  $\delta\epsilon_{11}$  is the variation of  $\epsilon_{11}$  in (2.13) corresponding to  $\delta\mathbf{u}_a$  and  $\delta\mathbf{u}_b$ .  $\sigma_{11}$  is the engineering stress. For linear elastic material,  $\sigma_{11} = E\epsilon_{11}$ , where  $E$  is Young's modulus.  $\rho$  is the density,  $\delta\mathbf{r}$  is the variation of  $\mathbf{r}$  in (2.3) (referred to the current inertia element coordinate system) corresponding to  $\delta\mathbf{u}_a$  and  $\delta\mathbf{u}_b$ , and  $\mathbf{a}$  is the absolute acceleration in (2.15).

If the element size is chosen to be sufficiently small, the values of the deformation parameters of the deformed element defined in the current element coordinate system may always be much smaller than unity. Thus the higher-order terms of deformation parameters in the element internal nodal forces may be neglected. However, in order to include the nonlinear coupling among the bending and stretching deformations, the terms up to the second order of deformation parameters and their spatial derivatives are retained in element deformation nodal forces by consistent second-order linearization of  $\delta\epsilon_{11}\sigma_{11}$  in (2.22). Here, only infinitesimal-free vibration is considered, thus only the terms up to the first order of time derivatives of deformation parameters and their spatial derivatives are retained in element inertia nodal forces by consistent first-order linearization of  $\delta\mathbf{r}^t\mathbf{a}$  in (2.22).

From (2.6) and (2.11), the variation of  $\epsilon_{11}$  in (2.13) may be expressed as

$$\begin{aligned}\delta\epsilon_{11} &= \delta\epsilon_c - y\delta v_{,xx}, \\ \delta\epsilon_c &= \frac{1}{L}(\delta\mathbf{u}_a^t\mathbf{G}_a + \delta\mathbf{u}_b^t\mathbf{G}_b), \\ \delta v_{,xx} &= \delta\mathbf{u}_b^t\mathbf{N}_b''.\end{aligned}\tag{2.31}$$

From (2.3), (2.6), and (2.12),  $\delta\mathbf{r}$  the variation of  $\mathbf{r}$  in (2.3) may be expressed as

$$\begin{aligned}\delta\mathbf{r} &= \{\delta r_1, \delta r_2, \delta r_3\} = \{\delta x_p - y\delta v_{,x}, \delta v - yv_{,x}\delta v_{,x}, 0\}, \\ \delta x_p &= \delta\mathbf{u}_a^t\mathbf{N}_a + \frac{x}{L}\delta\mathbf{u}_b^t\mathbf{G}_b - \int_0^x v_{,x}\delta v_{,x}dx, \\ \delta v_{,x} &= \delta\mathbf{u}_b^t\mathbf{N}_b'.\end{aligned}\tag{2.32}$$

Substituting (2.15)–(2.21) and (2.31)–(2.32) into (2.22), using  $\int ydA = 0$ , neglecting the higher order terms, we may obtain

$$\mathbf{f}_a^D = EA\epsilon_c\mathbf{G}_a,\tag{2.33}$$

$$\mathbf{f}_b^D = EI \int \mathbf{N}_b''v_{,xx}dx + f_{12}^D \int \mathbf{N}_b'v_{,x}dx,\tag{2.34}$$

$$\mathbf{f}_a^I = \rho A \int \mathbf{N}_a\mathbf{N}_a^tdx\ddot{\mathbf{u}}_a + \underbrace{\Omega^2\rho Aa_{o1} \int \mathbf{N}_adx}_{\text{}} - \underbrace{\Omega^2\rho A \int \mathbf{N}_a(\mathbf{N}_a^t\mathbf{u}_a + x)dx}_{\text{}} - 2\Omega\rho A \int \mathbf{N}_a\dot{v}dx,\tag{2.35}$$

$$\begin{aligned}\mathbf{f}_b^I &= \rho A \int \mathbf{N}_b\ddot{v}dx + \rho I \int \mathbf{N}_b'\ddot{v}_{,x}dx \\ &\quad + \underbrace{\Omega^2\rho Aa_{o2} \int \mathbf{N}_bdx}_{\text{}} - \underbrace{\Omega^2\rho A \int \mathbf{N}_bvdx}_{\text{}} - \underbrace{\Omega^2\rho I \int \mathbf{N}_b'v'dx}_{\text{}} + 2\Omega\rho A \int \mathbf{N}_b\mathbf{N}_a^tdx\dot{\mathbf{u}}_a.\end{aligned}\tag{2.36}$$

where the range of integration for the integral  $\int(\cdot)dx$  in (2.34)–(2.36) is from 0 to  $L$ ,  $A$  is the cross section area,  $I$  is moment of inertia of the cross section,  $a_{oi}$  ( $i = 1, 2$ ) are the  $x_i$  components of  $\mathbf{a}_o$  in (2.17). The underlined terms in (2.35) and (2.36) are the inertia nodal force corresponding to the steady-state deformation induced by the constant rotation.

## 2.6. Element Matrices

The element matrices considered are element tangent stiffness matrix, mass matrix, centripetal stiffness matrix, and gyroscopic matrix. The element matrices may be obtained by differentiating the element nodal force vectors in (2.33)–(2.36) with respect to nodal parameters and time derivatives of nodal parameters.

Using the direct stiffness method, the element tangent stiffness matrix may be assembled by the following submatrices:

$$\begin{aligned} \mathbf{k}_{aa} &= \frac{\partial \mathbf{f}_a^D}{\partial \mathbf{u}_a} = \frac{EA}{L} \mathbf{G}_a \mathbf{G}_a^t, \\ \mathbf{k}_{ab} &= \mathbf{k}_{ba}^t = \frac{\partial \mathbf{f}_a^D}{\partial \mathbf{u}_b} = \mathbf{0}, \\ \mathbf{k}_{bb} &= \frac{\partial \mathbf{f}_b^D}{\partial \mathbf{u}_b} = EI \int \mathbf{N}_b'' \mathbf{N}_b'''^t dx + f_{12}^D \int \mathbf{N}_b' \mathbf{N}_b'^t dx. \end{aligned} \quad (2.37)$$

The element mass matrix may be assembled by the following submatrices:

$$\begin{aligned} \mathbf{m}_{aa} &= \frac{\partial \mathbf{f}_a^I}{\partial \ddot{\mathbf{u}}_a} = \rho A \int \mathbf{N}_a \mathbf{N}_a^t dx, \\ \mathbf{m}_{ab} &= \mathbf{m}_{ba}^t = \frac{\partial \mathbf{f}_a^I}{\partial \ddot{\mathbf{u}}_b} = \mathbf{0}, \\ \mathbf{m}_{bb} &= \frac{\partial \mathbf{f}_b^I}{\partial \ddot{\mathbf{u}}_b} = \rho A \int \mathbf{N}_b \mathbf{N}_b^t dx + \rho I (1 - \varepsilon_c)^2 \int \mathbf{N}_b' \mathbf{N}_b'^t dx. \end{aligned} \quad (2.38)$$

The element centripetal stiffness matrix may be assembled by the following submatrices:

$$\begin{aligned} \mathbf{k}_{\Omega aa} &= \frac{\partial \mathbf{f}_a^I}{\Omega^2 \partial \mathbf{u}_a} = -\rho A \int \mathbf{N}_a \mathbf{N}_a^t dx, \\ \mathbf{k}_{\Omega ab} &= \mathbf{k}_{\Omega ab}^t = \frac{\partial \mathbf{f}_a^I}{\Omega^2 \partial \mathbf{u}_b} = \mathbf{0}, \\ \mathbf{k}_{\Omega bb} &= \frac{\partial \mathbf{f}_b^I}{\Omega^2 \partial \mathbf{u}_b} = -\rho A \int \mathbf{N}_b \mathbf{N}_b^t dx. \end{aligned} \quad (2.39)$$

**Table 1:** Dimensionless variables.

	Variables	Dimensionless variables
Coordinates	$x, X_o, Y_o$	$\bar{x} = \frac{x}{L_T}, \bar{X}_o = \frac{X_o}{L_T}, \bar{Y}_o = Y_o/L_T,$
Time	$t$	$\tau = \frac{t}{L_T} \sqrt{\frac{E}{\rho}}$
Length of beam element	$L$	$\bar{L} = L/L_T$
Area moment of inertia	$I$	$\bar{I} = \frac{I}{AL_T^2}$
Radius of hub	$R$	$\bar{R} = R/L_T$
Displacements	$u, v$	$\bar{u} = u/L_T, \bar{v} = v/L_T$
spatial derivatives of displacement	$u', u'', v', v''$	$\bar{u}' = \frac{\partial \bar{u}}{\partial \bar{x}} = u', \bar{u}'' = \frac{\partial^2 \bar{u}}{\partial \bar{x}^2} = L_T u'', \bar{v}' = \frac{\partial \bar{v}}{\partial \bar{x}} = v', \bar{v}'' = \frac{\partial^2 \bar{v}}{\partial \bar{x}^2} = L_T v''$
Time derivatives of displacement	$\dot{u}, \ddot{u}, \dot{v}, \ddot{v}$	$\bar{\dot{u}} = \frac{\partial \bar{u}}{\partial \tau} = \dot{u} \sqrt{\frac{\rho}{E}}, \bar{\ddot{u}} = \frac{\partial^2 \bar{u}}{\partial \tau^2} = L_T \frac{\rho}{E} \ddot{u}, \bar{\dot{v}} = \frac{\partial \bar{v}}{\partial \tau} = \dot{v} \sqrt{\frac{\rho}{E}}, \bar{\ddot{v}} = \frac{\partial^2 \bar{v}}{\partial \tau^2} = L_T \frac{\rho}{E} \ddot{v}$
Force and moment	$f_{ij}, m_j$	$\bar{f}_{ij} = \frac{f_{ij}}{EA}, (i = 1, 2; j = 1, 2)$
Angular velocity	$\Omega$	$k = \Omega L_T \sqrt{\rho/E}$
Natural frequency	$\omega$	$K = \omega L_T \sqrt{\rho/E}$

The element gyroscopic matrix may be assembled by the following submatrices:

$$\begin{aligned}
\mathbf{c}_{aa} &= \frac{\partial \mathbf{f}_a^I}{\Omega \partial \dot{\mathbf{u}}_a} = \mathbf{0}, \\
\mathbf{c}_{ab} &= -\mathbf{c}_{ba}^t = \frac{\partial \mathbf{f}_a^I}{\Omega \partial \dot{\mathbf{u}}_b} = -2\rho A \int \mathbf{N}_a \mathbf{N}_b^t dx, \\
\mathbf{c}_{bb} &= \frac{\partial \mathbf{f}_b^I}{\Omega \partial \dot{\mathbf{u}}_b} = \mathbf{0}.
\end{aligned} \tag{2.40}$$

## 2.7. Equations of Motion

For convenience, the dimensionless variables defined in Table 1 are used here.

The dimensionless nonlinear equations of motion for a rotating beam with constant angular velocity may be expressed by

$$\boldsymbol{\varphi} = \mathbf{F}^D(\hat{\mathbf{Q}}) + \mathbf{F}^I(k^2, \hat{\mathbf{Q}}, \dot{\hat{\mathbf{Q}}}, \ddot{\hat{\mathbf{Q}}}) = \mathbf{0}, \tag{2.41}$$

$$\hat{\mathbf{Q}} = \mathbf{Q}_s + \mathbf{Q}(\tau), \tag{2.42}$$

where  $k$  and  $\tau$  are dimensionless time and dimensionless angular speed of rotating beam, respectively, defined in Table 1.  $\boldsymbol{\varphi}$ ,  $\mathbf{F}^D$ , and  $\mathbf{F}^I$  are the dimensionless unbalanced force

vector, the dimensionless deformation nodal force vector, and the dimensionless inertia nodal force vector of the structural system, respectively.  $\mathbf{F}^I$  and  $\mathbf{F}^D$  are assembled from the dimensionless element nodal force vectors, which are calculated using (2.33)–(2.36) and the dimensionless variables defined in Table 1 first in the current element coordinates and then transformed from element coordinate system to global coordinate system before assemblage using standard procedure.  $\hat{\mathbf{Q}}$  is the dimensionless nodal displacement vector of the rotating beam,  $\dot{\hat{\mathbf{Q}}} = \partial \hat{\mathbf{Q}} / \partial \tau$  and  $\ddot{\hat{\mathbf{Q}}} = \partial^2 \hat{\mathbf{Q}} / \partial \tau^2$  are the dimensionless nodal velocity vector and the dimensionless nodal acceleration vector of the rotating beam, respectively,  $\mathbf{Q}_s$  is the dimensionless steady-state nodal displacement vector induced by constant dimensionless rotation speed  $k$ , and  $\mathbf{Q}(\tau)$  is the time-dependent dimensionless nodal displacements vector caused by the free vibration of the rotating beam. Here only infinitesimal vibration is considered.

## 2.8. Governing Equations for Steady-state Deformation

For the steady-state deformations,  $\mathbf{Q}(\tau) = \mathbf{0}$ . Thus (2.41) can be reduced to nonlinear dimensionless steady-state equilibrium equations and expressed by

$$\boldsymbol{\varphi} = \mathbf{F}_s^D(\mathbf{Q}_s) + k^2 \mathbf{F}_s^I(\mathbf{Q}_s) = \mathbf{0}, \quad (2.43)$$

where  $\mathbf{F}_s^D(\mathbf{Q}_s)$  and  $k^2 \mathbf{F}_s^I(\mathbf{Q}_s)$  are the dimensionless deformation nodal force vector and the dimensionless inertia nodal force (the centrifugal force) vector of the structural system corresponding to the dimensionless steady-state nodal displacement vector  $\mathbf{Q}_s$ , respectively.  $k^2 \mathbf{F}_s^I(\mathbf{Q}_s)$  is corresponding to the underlined terms of (2.35) and (2.36). Note that  $k^2 \mathbf{F}_s^I(\mathbf{Q}_s)$  is deformation dependent. Thus  $k^2 \mathbf{F}_s^I(\mathbf{Q}_s)$  should be updated at each new configuration.

Here, an incremental-iterative method based on the Newton-Raphson method is employed for the solution of nonlinear dimensionless steady-state equilibrium equations at different dimensionless rotation speed  $k$ . In this paper, a weighted Euclidean norm of the unbalanced force is employed for the equilibrium iterations and is given by

$$\frac{\|\boldsymbol{\varphi}\|}{k^2 \sqrt{N} \|\mathbf{F}_s^I\|} \leq e_{\text{tol}}, \quad (2.44)$$

where  $N$  is number of the equations of the system and  $e_{\text{tol}}$  is a prescribed value of error tolerance. Unless otherwise stated, the error tolerance  $e_{\text{tol}}$  is set to  $10^{-5}$  in this study.

## 2.9. Governing Equations for Free Vibration Measured from the Position of Steady-State Deformation

Substituting (2.42) into (2.41) and setting the first-order Taylor series expansion of the unbalanced force vector  $\boldsymbol{\varphi}$  around  $\mathbf{Q}_s$  to zero, one may obtain the dimensionless governing equations for linear free vibration of the rotating beam measured from the position of the steady-state deformation as follows.

$$\mathbf{M}\ddot{\mathbf{Q}} + \mathbf{C}\dot{\mathbf{Q}} + (\mathbf{K} + k^2 \mathbf{K}_\Omega) \mathbf{Q} = \mathbf{0}, \quad (2.45)$$



where  $\mathbf{M}$ ,  $\mathbf{C}$ ,  $\mathbf{K}$ , and  $\mathbf{K}_\Omega$  are dimensionless mass matrix, gyroscopic matrix, tangent stiffness matrix, and centripetal stiffness matrix of the rotating beam, respectively.  $\mathbf{M}$ ,  $\mathbf{C}$ ,  $\mathbf{K}$ , and  $\mathbf{K}_\Omega$  are assembled from the dimensionless element mass matrix, gyroscopic matrix, tangent stiffness matrix, and centripetal stiffness matrix, which are calculated using (2.37)–(2.40) and the dimensionless variables defined in Table 1 first in the current element coordinates and then transformed from element coordinate system to global coordinate system before assemblage using standard procedure.

We will seek a solution of (2.45) in the form

$$\mathbf{Q} = (\mathbf{Q}_R + i\mathbf{Q}_I)e^{iK\tau}, \quad (2.46)$$

where  $i = \sqrt{-1}$ ,  $K$  and  $\tau$  are dimensionless natural frequency of rotating beam and dimensionless time defined in Table 1, and  $\mathbf{Q}_R$  and  $\mathbf{Q}_I$  are real part and imaginary part of the vibration mode.

Substituting (2.46) into (2.45), one may obtain a set of homogeneous equations expressed by

$$\mathbf{H}\mathbf{Z} = \mathbf{0}, \quad (2.47)$$

$$\mathbf{H} = \mathbf{H}(K, k) = \begin{bmatrix} \mathbf{K} + k^2\mathbf{K}_\Omega - K^2\mathbf{M} & k\mathbf{K}\mathbf{C}^t \\ k\mathbf{K}\mathbf{C} & \mathbf{K} + k^2\mathbf{K}_\Omega - K^2\mathbf{M} \end{bmatrix}, \quad (2.48)$$

$$\mathbf{Z} = \{\mathbf{Q}_R, \mathbf{Q}_I\}, \quad (2.49)$$

where  $\mathbf{H}(K, k)$  denotes  $\mathbf{H}$  being a function of  $K$  and  $k$ . Note that  $\mathbf{H}$  is a symmetric matrix.

Equation (2.47) is a quadratic eigenvalue problem. For a nontrivial  $\mathbf{Z}$ , the determinant of matrix  $\mathbf{H}$  in (2.47) must be equal to zero. The values of  $K$  which make the determinant vanishes are called eigenvalues of matrix  $\mathbf{H}$ . The bisection method is used here to find the eigenvalues. Note that when  $k = 0$ , (2.47) will degenerate to a generalized eigenvalue problem.

### 3. Numerical Examples

To verify the accuracy of the present method and to investigate the steady deformation and the natural frequencies of rotating-inclined beams with different inclination angle  $\alpha$ , dimensionless radius of the hub  $\bar{R}$ , and slenderness ratios  $\eta = L_T\sqrt{A/I}$  at different dimensionless angular velocities  $k$ , several dimensionless numerical examples are studied here.

For simplicity, only the uniform beam with rectangular cross section is considered here. The maximum steady-state axial strain  $\varepsilon_{\max}$  of rotating beam is the sum of the maximum steady-state membrane strain  $\varepsilon_c^{\max}$  and bending strain  $\varepsilon_b^{\max}$ , which occur at the root of the rotating beam. In practice, rotating structures are designed to operate in the elastic range of the materials. Thus, it is considered that  $\varepsilon_{\max} \leq \varepsilon_y$  (say 0.01) in this study. At the same dimensionless angular speed  $k$ ,  $\varepsilon_{\max}$  are different for rotating beams with different  $\eta$ ,  $\alpha$ , and  $\bar{R}$ . Thus, the allowable  $k$  are different for rotating beams with different  $\eta$ ,  $\alpha$ , and  $\bar{R}$  in this study.

**Table 2:** Comparison of results for different cases ( $\eta = 20$ ,  $\bar{R} = 1.5$ ).

$\alpha$	$k$		$\varepsilon_c^{\max}$ ( $10^{-3}$ )	$\varepsilon_b^{\max}$ ( $10^{-3}$ )	$v_{\text{tip}}/L_T$ ( $10^{-3}$ )	$K_1$	$K_2$	$K_3(a)$	$K_4$	$K_5(a)$	$K_6$	$K_7(a)$
$0^\circ$	0	EA10	0	0	0	.174788	1.05957	1.57241	2.82495	4.75610	5.19546	8.00214
		EA50	0	0	0	.174787	1.05953	1.57086	2.82431	4.71413	5.19120	7.86206
		EA100	0	0	0	.174787	1.05953	1.57081	2.82431	4.71283	5.19119	7.85600
		[24]	0	0	0	.17479	1.05953	1.57080	2.82431	4.71239	5.19119	—
		[34]	0	0	0	.17580	1.10172	1.57080	3.08486	4.71239	6.04510	—
	0.06	EA10	6.93309	0	0	.198616	1.08756	1.57615	2.85333	4.75729	5.22384	8.02928
		EA50	7.15492	0	0	.198514	1.08726	1.57616	2.85243	4.71534	5.21931	7.86274
		EA100	7.18210	0	0	.198511	1.08726	1.57457	2.85242	4.71403	5.21930	7.85669
		[24]	7.20000	0	0	.19862	1.08760	1.57455	2.85276	4.71360	5.21962	—
		LAS	7.20000	0	0	—	—	—	—	—	—	—
$5^\circ$	0.03	EA10	1.72680	1.93098	5.47630	.181049	1.06661	1.57335	2.83206	4.75639	5.20256	8.00889
		EA50	1.78195	1.93546	5.47699	.181021	1.06651	1.57180	2.83136	4.71443	5.19823	7.86221
		EA100	1.78870	1.93560	5.47701	.181020	1.06651	1.57175	2.83136	4.71312	5.19822	7.85616
		LAS	1.79486	2.03794	5.88301	—	—	—	—	—	—	—
$30^\circ$	0.01	EA10	.173298	1.29008	3.72294	.175410	1.06028	1.57252	2.82567	4.75613	5.19619	8.00281
		EA50	.178615	1.29224	3.72299	.175407	1.06024	1.57097	2.82503	4.71416	5.19191	7.86207
		EA100	.179264	1.29231	3.72300	.175407	1.06024	1.57092	2.82503	4.71285	5.19190	7.85601
		LAS	.179904	1.29904	3.75000	—	—	—	—	—	—	—
$90^\circ$	0.01	EA10	.0500345	2.59364	7.49504	.174836	1.05978	1.57253	2.82520	4.75612	5.19573	8.00229
		EA50	.0500384	2.59784	7.49506	.174835	1.05974	1.57098	2.82456	4.71415	5.19145	7.86205
		EA100	.0500216	2.59797	7.49507	.174835	1.05974	1.57093	2.82456	4.71284	5.19144	7.85599
		LAS	.0500000	2.59807	7.50000	—	—	—	—	—	—	—

To investigate the effect of the lateral deflection on the steady-state deformation and the natural frequency of rotating Euler beams, here cases with and without considering the lateral deflection are considered. The corresponding elements are referred to as EA element and EB element, respectively. For EA element, all terms in (2.33)–(2.40) are considered; for EB element, all terms in (2.33)–(2.40) are considered except the underlined terms in (2.36), which are the lateral inertia nodal force corresponding to the steady-state deformation induced by the constant rotation. In this section,  $v_{\text{tip}}/L_T$  denotes the dimensionless lateral tip deflection of the steady-state deformation;  $K_i$  denotes the  $i$ th dimensionless natural frequency of the rotating beam and denote that the corresponding vibration mode is lateral vibration at  $k = 0$ ; in all tables, the entries with “(a)” denotes that the corresponding vibration mode is axial vibration at  $k = 0$ .

The example first considered is the rotating-inclined beams with dimensionless radius of the hub  $\bar{R} = 1.5$ , inclination angle  $\alpha = 0^\circ, 5^\circ, 30^\circ, 90^\circ$ , and slenderness ratios  $\eta = 20, 1000$ . The present results are shown in Tables 2 and 3 together with some results available in the literature. In Tables 2 and 3, EAn,  $n = 10, 50, 100$ , denote that  $n$  equal EA elements are used for discretization, and LAS denotes the linear analytical solution of the steady-state deformation. It can be seen that for higher natural frequencies of lateral vibration, the discrepancy between the present results and the analytical solutions given in [34], in which the rotary inertia is not considered, increases with decrease of the slenderness ratio. It seems that the effect of

**Table 3:** Comparison of results for different cases ( $\eta = 1000$ ,  $\bar{R} = 1.5$ ).

$\alpha$	$k$	$\varepsilon_c^{\max}$ ( $10^{-3}$ )	$\varepsilon_b^{\max}$ ( $10^{-3}$ )	$v_{\text{tip}}/L_T$	$K_1$ ( $10^{-2}$ )	$K_2$ ( $10^{-1}$ )	$K_3$ ( $10^{-1}$ )	$K_4$	$K_5$	$K_6$	$K_7$	
0°	0	EA10	0	0	0	.351601	.220349	.617105	.121008	.200340	.300117	.421052
		EA50	0	0	0	.351601	.220341	.616949	.120893	.199838	.298509	.416903
		EA100	0	0	0	.351601	.220341	.616948	.120893	.199837	.298506	.416896
		[24]	0	0	0	.352	.2203	.6169	.12089	.19984	.29851	—
		[34]	0	0	0	.3516	.22034	.616972	.120902	—	—	—
	0.06	EA10	6.93309	0	0	9.00457	2.50186	4.13423	.591446	.784725	.992927	1.21760
		EA50	7.15492	0	0	8.96239	2.47424	4.06068	.580524	.771309	.976120	1.19365
		EA100	7.18210	0	0	8.96152	2.47312	4.05756	.580088	.770833	.975634	1.19316
		[24]	7.20000	0	0	8.952	2.4708	4.0536	.57955	.77017	.97486	—
		LAS	7.20000	0	0	—	—	—	—	—	—	—
5°	0.03	EA10	1.73113	3.88303	.0835171	4.54714	1.27448	2.17658	.323098	.443024	.577262	.726698
		EA50	1.78396	6.00526	.0838194	4.53348	1.26220	2.15028	.319777	.439167	.572464	.719965
		EA100	1.78936	6.20203	.0838218	4.53320	1.26179	2.14942	.319678	.439068	.572368	.719873
		LAS	1.79486	101.897	14.70753	—	—	—	—	—	—	—
30°	0.008	EA10	.117174	8.73588	.429688	1.29068	.405580	.836390	.143462	.221484	.319586	.439110
		EA50	.114341	9.36150	.429979	1.28848	.404156	.836065	.143631	.221433	.318254	.434653
		EA100	.113410	9.38784	.429986	1.28840	.404108	.836056	.143643	.221458	.318289	.434691
		LAS	.115138	41.5692	6.00000	—	—	—	—	—	—	—
90°	0.003	EA10	00632587	8.11012	.747138	.561367	.232168	.566051	.113317	.190889	.289637	.409722
		EA50	00388224	8.15298	.747250	.560585	.232182	.566299	.113204	.190326	.287895	.405359
		EA100	.00351740	8.15396	.747254	.560558	.232181	.566306	.113202	.190322	.287886	.405342
		LAS	.00450000	11.6913	1.68750	—	—	—	—	—	—	—

the rotary inertia on the higher natural frequencies of the Euler beam is not negligible when the slenderness ratio is small. It can be seen from Tables 2 and 3 that the differences between the results of EA50 and EA 100 are negligible for all cases studied. Thus, in the rest of the section, all numerical results are obtained using 50 equal elements. For  $\alpha = 0$ , and  $k \neq 0$ , the steady-state deformation is axial deformation only as expected. The analytical solution of the maximum steady-state membrane strain  $\varepsilon_c^{\max} = k^2(\bar{R} \cos \alpha + 1/2)$  given in [15] and the linear solution are identical. It can be seen that at the same dimensionless angular speed  $k$ ,  $\varepsilon_c^{\max}$  is independent of the slenderness ratio  $\eta$ . Thus, for  $\alpha = 0$ , the allowable  $k$  is limited by  $\varepsilon_c^{\max}$  and is the same for the rotating beam with different slenderness ratio  $\eta$ . Very good agreement is observed between the natural frequencies obtained by the present study and those given in [24], which are obtained using the power series method. It can be seen from Table 3 that for slenderness ratio  $\eta = 1000$ , with increase of the inclination angle  $\alpha$ , the values of  $\varepsilon_b^{\max}$  and  $v_{\text{tip}}/L_T$  increase significantly and the value of the allowable dimensionless angular speed  $k$  decreases significantly. Comparing  $\varepsilon_b^{\max}$  and  $v_{\text{tip}}/L_T$  of EA with the results of linear analytical solution, respectively, it is found that the difference between the results of EA and LAS is insignificant for  $\eta = 20$  but is remarked for  $\eta = 1000$ . These may be explained as follows. The centrifugal stiffening effect is significant for slender beam, and the lateral component of the centrifugal force in the rotating inclined beam decreases with the increase of the steady-state lateral deflection.

**Table 4:** Dimensionless frequencies for rotating beam with different inclination angle ( $\eta = 70$ ,  $\bar{R} = 1$ ,  $k = 5/70$ ).

$\alpha$	$\varepsilon_c^{\max}(10^{-3})$		$\varepsilon_b^{\max}$	$v_{\text{tip}}/L_T$		$K_1$		$K_2$		
	EA	EB		EA	EA	EB	[21]	EA	EB	[21]
0°	7.61582	7.61579	0	0	.105565	.105427	.105	.411754	.410792	.418
10°	7.53275	7.53893	.021843	.119537	.105513	.104869	.105	.411356	.410001	.417
20°	7.28556	7.31066	.043509	.236923	.105359	.103195	.103	.410160	.407642	.414
30°	6.88032	6.93792	.064820	.350059	.105101	.100399	.100	.408162	.403758	.410
40°	6.32700	6.43205	.085602	.456935	.104737	.0964721	.096	.405357	.398421	.405
50°	5.63927	5.80840	.105681	.555686	.104264	.0913941	.091	.401742	.391733	.398
60°	4.83425	5.08596	.124890	.644628	.103679	.0851262	.085	.397314	.383830	.390
70°	3.93214	4.28663	.143064	.722301	.102976	.0775919	.077	.392079	.374876	.381
80°	2.95575	3.43472	.160043	.787503	.102151	.0686418	.068	.386048	.365073	.371
90°	1.93010	2.55611	.175673	.839324	.101193	.0579597	.057	.379245	.354659	.361

**Table 5:** Dimensionless frequencies for rotating beam with different inclination angle ( $\eta = 39$ ,  $\bar{R} = 1$ ).

$\alpha$	$k$	$\varepsilon_c^{\max}(10^{-4})$	$\varepsilon_b^{\max}(10^{-3})$	$v_{\text{tip}}/L_T(10^{-3})$	$K_1(10^{-1})$	$K_2$	$K_3$	$K_4$	$K_5$	$K_6(a)$
0°	0	0	0	0	.900168	.559057	1.54325	1.57086 (a)	2.96396	4.71413
	.010	1.48999	0	0	.909817	.560283	1.54452	1.57097 (a)	2.96528	4.71415
	.020	5.96060	0	0	.938126	.563945	1.54830	1.57130 (a)	2.96926	4.71421
	.030	13.4138	0	0	.983359	.569996	1.55455	1.57190 (a)	2.97586	4.71432
	.040	23.8528	0	0	1.04313	.578359	1.56302	1.57296 (a)	2.98509	4.71449
	.050	37.2822	0	0	1.11488	.588935	1.57113	1.57704 (a)	2.99691	4.71472
	.060	53.7078	0	0	1.19620	.601604	1.57358 (a)	1.58936	3.01129	4.71502
5°	.005	.371545	.073310	.412011	.902582	.559363	1.54357	1.57089 (a)	2.96429	4.71414
	.010	1.48623	.289977	1.62160	.909786	.560280	1.54449	1.57100 (a)	2.96528	4.71415
	.015	3.34417	.640707	3.55360	.921661	.561805	1.54595	1.57126 (a)	2.96693	4.71416
	.020	5.94559	1.11150	6.09535	.938019	.563932	1.54784	1.57177 (a)	2.96925	4.71416
	.025	9.29075	1.68547	9.11211	.958617	.566654	1.55003	1.57268 (a)	2.97222	4.71415
	.030	13.3800	2.34473	12.4630	.983170	.569962	1.55233	1.57416 (a)	2.97585	4.71413
	.002	.054292	.067510	.379956	.900509	.559102	1.54330	1.57087 (a)	2.96401	4.71413
30°	.004	.217174	.269614	1.51631	.901534	.559237	1.54341	1.57090 (a)	2.96415	4.71413
	.006	.488657	.605041	3.39858	.903243	.559461	1.54355	1.57103 (a)	2.96440	4.71412
	.008	.868763	1.07170	6.00953	.905635	.559775	1.54362	1.57132 (a)	2.96474	4.71409
	.010	1.35752	1.66673	9.32547	.908710	.560177	1.54351	1.57191 (a)	2.96518	4.71403
	.002	.019999	.135091	.760426	.900208	.559076	1.54327	1.57087 (a)	2.96398	4.71413
	.004	.080009	.540362	3.04080	.900333	.559132	1.54324	1.57098 (a)	2.96404	4.71412
	.006	.180072	1.21579	6.83830	.900554	.559224	1.54295	1.57140 (a)	2.96415	4.71407
90°	.008	.320253	2.16132	12.1478	.900889	.559349	1.54211	1.57246 (a)	2.96431	4.71394
	.010	.500631	3.37678	18.9613	.901363	.559506	1.54041	1.57447 (a)	2.96451	4.71365

To investigate the effect of the lateral deflection on the steady-state deformation and the natural frequency of rotating-inclined beams, the cases with and without considering the lateral deflection are studied for  $\eta = 70$ ,  $\bar{R} = 1$ , and  $k = 5/70$ . The present results are shown in Table 4. The results transcribed from the figure given in [21], in which the steady-state lateral deflection and the rotary inertia are not considered, are also shown in Table 4 for

**Table 6:** Dimensionless frequencies for rotating beam with different inclination angle ( $\eta = 50$ ,  $\bar{R} = 1$ ).

$\alpha$	$k$	$\varepsilon_c^{\max} (10^{-4})$	$\varepsilon_b^{\max} (10^{-3})$	$v_{\text{tip}}/L_T (10^{-3})$	$K_1 (10^{-1})$	$K_2$	$K_3$	$K_4 (a)$	$K_5$	$K_6$
$0^\circ$	0	0	0	0	.702550	.437859	1.21530	1.57086	2.35176	3.82646
	.010	1.48998	0	0	.714917	.439441	1.21696	1.57096	2.35349	3.82822
	.020	5.96058	0	0	.750712	.444154	1.22192	1.57125	2.35868	3.83349
	.030	13.4137	0	0	.806600	.451898	1.23014	1.57173	2.36731	3.84227
	.040	23.8527	0	0	.878442	.462516	1.24155	1.57241	2.37932	3.85452
	.050	37.2820	0	0	.962316	.475813	1.25605	1.57328	2.39467	3.87021
	.060	53.7076	0	0	1.05500	.491563	1.27352	1.57435	2.41329	3.88930
$5^\circ$	.005	.371544	.093761	.674835	.705653	.438254	1.21571	1.57089	2.35219	3.82689
	.010	1.48623	.368279	2.62905	.714878	.439437	1.21695	1.57096	2.35349	3.82821
	.015	3.34418	.804892	5.66932	.729982	.441402	1.21900	1.57111	2.35565	3.83040
	.020	5.94560	1.37717	9.52433	.750592	.444136	1.22184	1.57134	2.35869	3.83347
	.025	9.29074	2.05594	13.8991	.776240	.447626	1.22547	1.57166	2.36258	3.83740
	.030	13.3799	2.81357	18.5209	.806412	.451854	1.22987	1.57208	2.36734	3.84221
$30^\circ$	.002	.054292	.086522	.624206	.702990	.437917	1.21536	1.57087	2.35182	3.82652
	.004	.217177	.345191	2.48734	.704308	.438091	1.21554	1.57088	2.35202	3.82671
	.006	.488671	.773349	5.56121	.706507	.438381	1.21583	1.57093	2.35234	3.82704
	.008	.868803	1.36665	9.79986	.709585	.438785	1.21621	1.57103	2.35280	3.82749
	.010	1.35760	2.11921	15.1409	.713543	.439301	1.21666	1.57120	2.35340	3.82806
$90^\circ$	.002	.019999	.173193	1.24980	.702604	.437883	1.21532	1.57087	2.35179	3.82648
	.004	.080020	.692767	4.99671	.702772	.437956	1.21539	1.57090	2.35188	3.82657
	.006	.180129	1.55866	11.2327	.703078	.438073	1.21545	1.57103	2.35204	3.82670
	.008	.320419	2.77065	19.9428	.703561	.438232	1.21544	1.57135	2.35228	3.82688
	.010	.500997	4.32814	31.1020	.704273	.438426	1.21527	1.57200	2.35265	3.82709

comparison. It can be seen from Table 4 that except  $\alpha = 0$ , the values of  $\varepsilon_b^{\max}$  are much larger than the yield strain for most engineering materials at  $k = 5/70$ . Thus the results in Table 4 are only displayed for the purpose of comparisons between the results of EB and those given in [21]. There is a very good agreement between the natural frequencies obtained using the EB element and those given in [21]. Although the comparisons are beyond the yield point of most engineering materials, results of EA and EB show that the differences between the cases with and without considering the lateral deflection become apparent for the rotating-inclined beam with large inclination angle  $\alpha$  at high-dimensionless angular speed. It can be seen from Table 4 that the difference between the natural frequencies of EA and EB is not significant for small  $\alpha$ , but the first natural frequency of EB is much smaller than that of EA for large  $\alpha$ . The natural frequencies of EA slightly decrease with increase of  $\alpha$ , but those of EB significantly decrease with increase of  $\alpha$  for  $\alpha \geq 50^\circ$ . These may be partially attributed to the fact that the decrease of the centrifugal stiffening effect of the rotating-inclined beam caused by the increase of the inclination angle is alleviated by the increase of lateral deflection induced by the lateral centrifugal force.

To investigate the effect of angular speed on the steady-state deformation and natural frequency of rotating beams with different slenderness ratios and inclination angles, the following cases are considered: slenderness ratio  $\eta = 39, 50, 100, 1000$ , inclination angle  $\alpha = 0^\circ, 5^\circ, 30^\circ, 90^\circ$ , and dimensionless radius of the rotating hub  $\bar{R} = 1$ . Tables 5, 6, 7, and 8

**Table 7:** Dimensionless frequencies for rotating beam with different inclination angle ( $\eta = 100$ ,  $\bar{R} = 1$ ).

$\alpha$	$k$	$\varepsilon_c^{\max} (10^{-4})$	$\varepsilon_b^{\max} (10^{-3})$	$v_{\text{tip}}/L_T (10^{-3})$	$K_1 (10^{-1})$	$K_2$	$K_3$	$K_4 (a)$	$K_5$	$K_6$
$0^\circ$	0	.000000	0	0	.351520	.219989	.614602	1.20047	1.57086	1.97619
	.010	1.48998	0	0	.375696	.223163	.617963	1.20402	1.57096	1.97983
	.020	5.96058	0	0	.439855	.232418	.627926	1.21458	1.57124	1.99072
	.030	13.4137	0	0	.528670	.247050	.644140	1.23194	1.57172	2.00872
	.040	23.8527	0	0	.630838	.266138	.666082	1.25578	1.57240	2.03361
	.050	37.2820	0	0	.740095	.288755	.693127	1.28568	1.57327	2.06512
	.060	53.7076	0	0	.853195	.314093	.724614	1.32116	1.57433	2.10288
$5^\circ$	.005	.371547	.184139	2.62891	.357708	.220785	.615441	1.20136	1.57089	1.97710
	.010	1.48624	.688585	9.52242	.375636	.223154	.617940	1.20397	1.57105	1.97985
	.015	3.34416	1.40679	18.5127	.403666	.227045	.622062	1.20826	1.57140	1.98446
	.020	5.94540	2.23838	27.6550	.439745	.232381	.627773	1.21419	1.57195	1.99093
	.025	9.29010	3.11970	35.8627	.481914	.239066	.635040	1.22176	1.57261	1.99922
	.030	13.3786	4.01960	42.7784	.528564	.246988	.643816	1.23096	1.57329	2.00929
	.002	.054294	.172596	2.48732	.352403	.220106	.614725	1.20060	1.57087	1.97632
$30^\circ$	.004	.217197	.683326	9.79956	.355052	.220456	.615081	1.20096	1.57097	1.97675
	.006	.488756	1.51188	21.5060	.359467	.221033	.615636	1.20145	1.57136	1.97753
	.008	.869003	2.62713	36.9471	.365637	.221832	.616344	1.20197	1.57227	1.97873
	.010	1.35790	3.99065	55.3127	.373528	.222846	.617163	1.20241	1.57395	1.98043
	.002	.020005	.346383	4.99669	.351634	.220038	.614651	1.20052	1.57089	1.97625
$90^\circ$	.004	.080103	1.38532	19.9425	.352038	.220178	.614748	1.20053	1.57127	1.97654
	.006	.180478	3.11497	44.6708	.352915	.220392	.614736	1.20014	1.57288	1.97728
	.008	.321226	5.52831	78.7975	.354553	.220651	.614373	1.19878	1.57704	1.97891
	.010	.502064	8.60794	121.586	.357326	.220924	.613368	1.19581	1.58523	1.98201

tabulate the maximum steady-state membrane strain and bending strain, dimensionless lateral tip deflection, and first six dimensionless natural frequencies for different  $\eta$ . It can be seen from Tables 5–8 that the values of  $v_{\text{tip}}/L_T$  increase significantly with the increase of the dimensionless angular velocities  $k$  and slenderness ratio  $\eta$ . However, the values of  $v_{\text{tip}}/L_T$  are very small for  $\eta = 39$  and 50. Because the stiffening effect of the centrifugal force is significant for slender beam, as expected, it can be seen from Table 8 that the lower natural frequencies of lateral vibration increase remarked with increase of the dimensionless angular speed for  $\eta = 1000$ .

Figures 4–6 show the deformed configurations, axial displacements, and lateral displacements for the steady-state deformation of rotating beams with  $\eta = 100$ ,  $\alpha = 90^\circ$ , and  $\eta = 1000$ ,  $\alpha = 5^\circ, 90^\circ$  at different dimensionless angular speeds. In Figures 4–6, the  $X_1$  and  $X_2$  coordinates of the deformed configurations of rotating beam are present at the same scale, and  $X_1^0$  denotes the global Lagrangian coordinate of the beam axis. Very large displacement and rotation are observed in Figure 6.

Figures 7–10 show the first six vibration modes for rotating beams with  $\eta = 39$ ,  $\alpha = 0^\circ, 5^\circ$ , and  $\eta = 1000$ ,  $\alpha = 5^\circ, 90^\circ$  at different dimensionless angular speeds. In Figures 7–10,  $U$  and  $V$  denote the  $X_1$  and  $X_2$  components of the vibration mode, respectively. The definitions of  $U$

**Table 8:** Dimensionless frequencies for rotating beam with different inclination angle ( $\eta = 1000$ ,  $\bar{R} = 1$ ).

$\alpha$	$k$	$\varepsilon_c^{\max} (10^{-5})$	$\varepsilon_b^{\max} (10^{-3})$	$v_{\text{tip}}/L_T (10^{-2})$	$K_1 (10^{-2})$	$K_2 (10^{-1})$	$K_3 (10^{-1})$	$K_4$	$K_5$	$K_6$
$0^\circ$	0	.000000	0	0	.351601	.220341	.616949	.120893	.199838	.298509
	.010	14.8998	0	0	1.32581	.432338	.886010	.151855	.233376	.333736
	.020	59.6058	0	0	2.52842	.766172	1.38410	.216189	.309541	.419056
	.030	134.137	0	0	3.73648	1.11402	1.92511	.289167	.400408	.525942
	.040	238.527	0	0	4.94495	1.46597	2.47903	.364653	.496007	.640880
	.050	372.820	0	0	6.15267	1.81983	3.03912	.441165	.593428	.759068
	.060	537.076	0	0	7.35907	2.17482	3.60301	.518237	.691707	.878747
$5^\circ$	.005	3.71469	.765147	5.97092	.741097	.289190	.695401	.129392	.208701	.307598
	.010	14.8600	1.67568	7.33938	1.32573	.432307	.885745	.151766	.233190	.333432
	.015	33.4431	2.57966	7.79173	1.92549	.595911	1.12500	.182037	.268266	.371976
	.020	59.4713	3.46977	8.02050	2.52834	.766160	1.38402	.216153	.309441	.418839
	.025	92.9513	4.34189	8.15957	3.13220	.939307	1.65211	.252155	.353965	.470793
	.030	133.889	5.19316	8.25360	3.73641	1.11401	1.92507	.289150	.400356	.525817
	.002	.542410	1.31449	16.2578	.436039	.231506	.625674	.121676	.200527	.299138
$30^\circ$	.004	2.15709	3.45499	31.0603	.628044	.264068	.655502	.124160	.202509	.300711
	.006	4.84203	5.61881	37.4726	.851755	.312455	.712896	.129772	.207598	.305211
	.008	8.61268	7.78502	40.6536	1.08530	.369468	.788930	.138176	.215896	.313013
	.0005	.012524	.216407	3.11010	.352489	.220632	.617142	.120911	.199852	.298522
$90^\circ$	.0010	.050204	.860794	12.1582	.357434	.221288	.616084	.120749	.199640	.298279
	.0015	.112068	1.89528	25.7173	.371925	.221920	.610342	.119952	.198654	.297181
	.0020	.194123	3.21653	40.7205	.400095	.222722	.599365	.118425	.196788	.295121
	.0025	.290775	4.68879	54.0272	.440751	.224723	.587411	.116669	.194633	.292734
	.0030	.398355	6.21301	64.2905	.489485	.228876	.578807	.115177	.192740	.290595
	.0035	.516056	7.74385	71.7152	.542488	.235452	.575106	.114128	.191302	.288900

and  $V$  are given by

$$\begin{aligned}
 U &= \left( U_R^2 + U_I^2 \right)^{1/2} \text{sign}(\sin \phi_u), & \sin \phi_u &= \frac{U_I}{(U_R^2 + U_I^2)^{1/2}}, & -\pi \leq \phi_u \leq \pi, \\
 V &= \left( V_R^2 + V_I^2 \right)^{1/2} \text{sign}(\sin \phi_v), & \sin \phi_v &= \frac{V_I}{(V_R^2 + V_I^2)^{1/2}}, & -\pi \leq \phi_v \leq \pi, \\
 \text{sign}(x) &= \begin{cases} 1 & \text{for } x > 0, \\ -1 & \text{for } x < 0, \end{cases}
 \end{aligned} \tag{3.1}$$

where  $U_R$  and  $V_R$ , and  $U_I$  and  $V_I$  are the  $X_1$  and  $X_2$  components of  $\mathbf{Q}_R$  and  $\mathbf{Q}_I$ , real part and imaginary part of the vibration mode given in (2.47), respectively.  $\phi_u$  and  $\phi_v$  are phase angles. Mode  $j$  ( $j = 1-6$ ) denotes the vibration mode dominated by the vibration mode corresponding to the  $j$ th natural frequency of the nonrotating beam. It can be seen from Figures 7–10, and Tables 5 and 8 that all vibration modes shown in Figures 7–10 are lateral



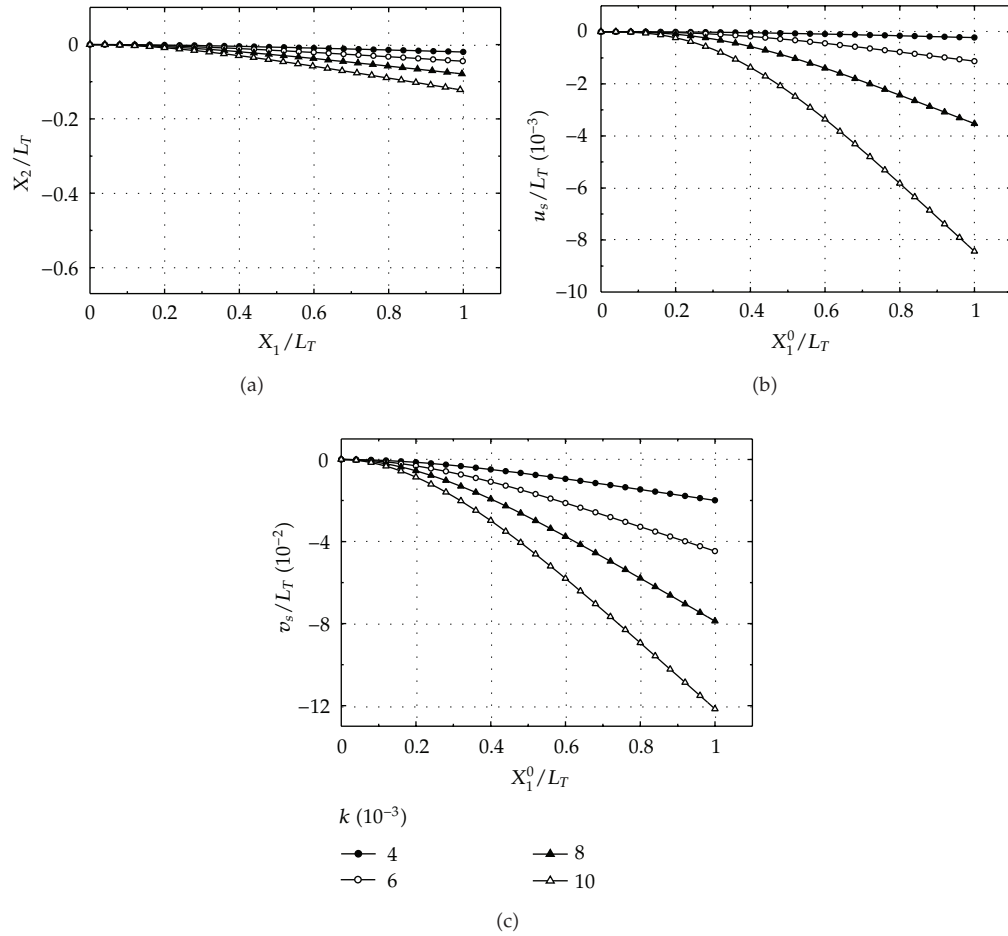


**Figure 4:** The steady-state deformation of rotating beam, (a) deformed configuration, (b) axial displacement, and (c) lateral displacement ( $\eta = 100$ ,  $\bar{R} = 1$ ,  $\alpha = 90^\circ$ ).

vibration at  $k = 0$ , except the fourth and the sixth vibration modes of  $\eta = 39$ . Mode 3 is the third bending vibration mode, and mode 4 is the first axial vibration mode for  $\eta = 39$ . Figure 11 shows the third and the fourth dimensionless natural frequencies for the rotating beam with  $\eta = 39$  at different dimensionless angular velocities. Because the third and the fourth natural frequencies are relatively close, frequency veering phenomenon [24] induced by the Coriolis force and the centrifugal force is observed in Figure 11. It can be seen from Figures 7 and 8 that the coupling of the axial and lateral vibration modes is very significant. Due to the effect of Coriolis force and the lateral steady-state deformation, the axial and lateral vibrations of rotating beam should be coupled. However, from the numerical results of this study, it is found that the coupling is negligible for rotating beam with small slenderness ratio if the corresponding natural frequencies of the axial and lateral vibrations are not close. Due to the steady-state lateral deformation, it can be seen from Figures 9 and 10 that when  $k \neq 0$ , all vibration modes consist of the  $X_1$  and  $X_2$  components. The difference between the vibration modes of rotating beam at different  $k$  is very significant for  $\eta = 1000$ .



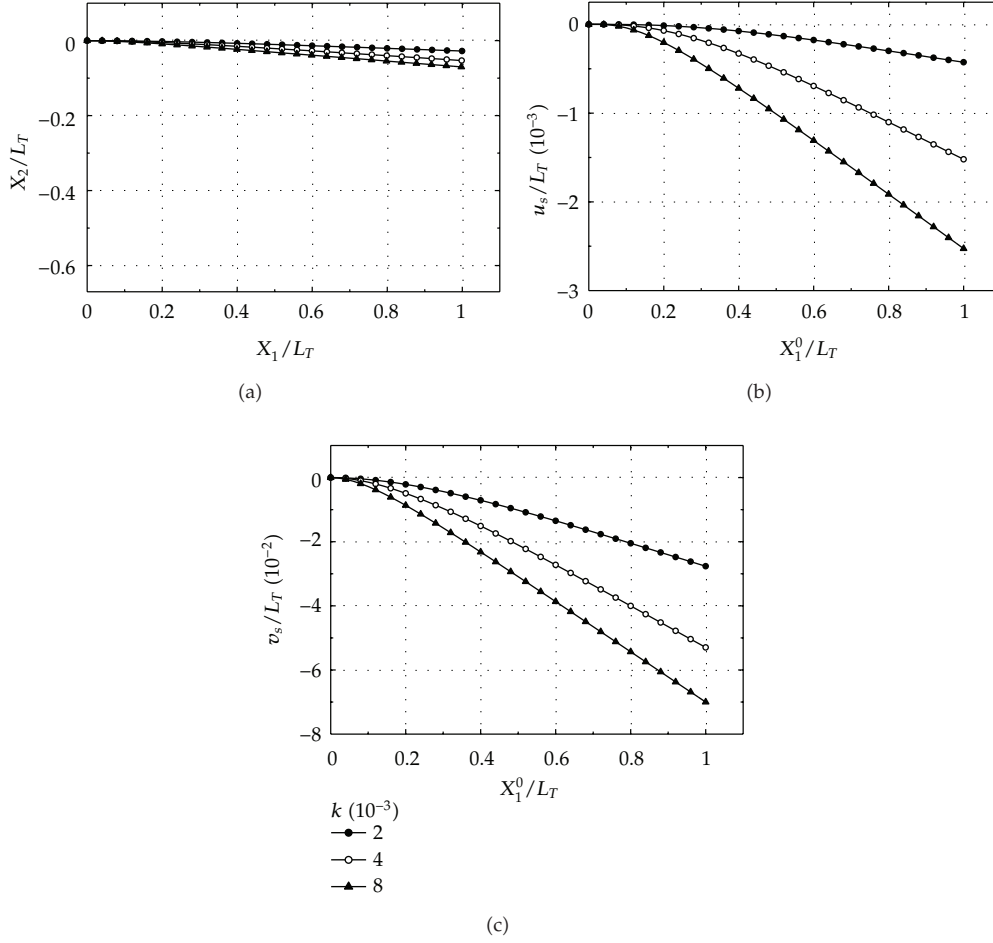


**Figure 5:** The steady-state deformation of rotating beam, (a) deformed configuration, (b) axial displacement, and (c) lateral displacement ( $\eta = 1000$ ,  $\bar{R} = 1$ ,  $\alpha = 5^\circ$ ).

#### 4. Conclusions

In this paper, a corotational finite element formulation combined with the rotating frame method and numerical procedure are proposed to derive the equations of motion for a rotating-inclined Euler beam at constant angular velocity. The element deformation and inertia nodal forces are systematically derived by the virtual work principle, the d'Alembert principle, and consistent second-order linearization of the fully geometrically nonlinear beam theory in the current element coordinates. The equations of motion of the system are defined in terms of an inertia global coordinate system which is coincident with a rotating global coordinate system rigidly tied to the rotating hub, while the total strains in the beam element are measured in an inertia element coordinate system which is coincident with a rotating element coordinate system constructed at the current configuration of the beam element. The rotating element coordinates rotate about the hub axis at the angular speed of the hub. The steady-state deformation and the natural frequency of infinitesimal-free vibration measured from the position of the corresponding steady-state deformation are

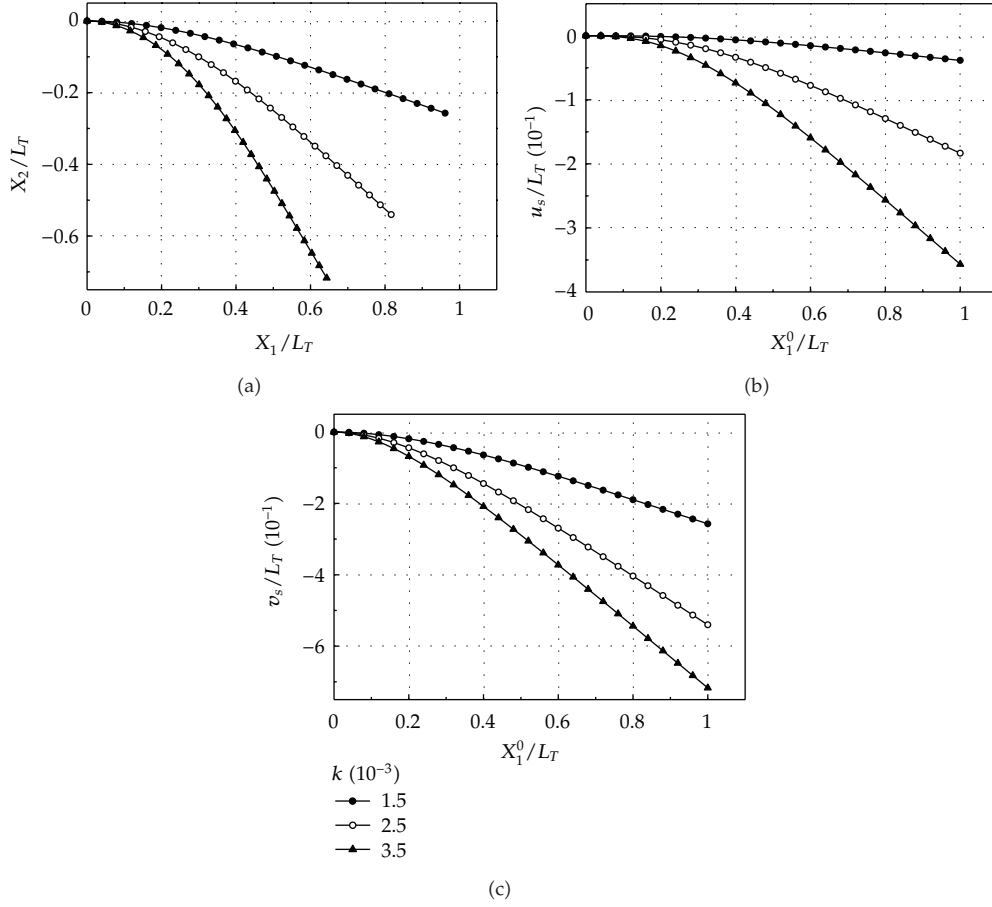


**Figure 6:** The steady-state deformation of rotating beam, (a) deformed configuration, (b) axial displacement, (c) lateral displacement ( $\eta = 1000$ ,  $\bar{R} = 1$ ,  $\alpha = 90^\circ$ ).

investigated for rotating-inclined Euler beams with different inclination angles, slenderness ratios, and angular speeds of the hub.

The results of dimensionless numerical examples demonstrate the accuracy and efficiency of the proposed method. The present results show that the geometrical nonlinearities that arise due to steady-state lateral and axial deformations should be considered for the natural frequencies of the inclined-rotating beams. Due to the effect of the centrifugal stiffening, the lower dimensionless natural frequencies of lateral vibration increase remarked with increase of the dimensionless angular speed for slender beam. The decrease of the centrifugal stiffening effect of the rotating inclined beam caused by the increase of the inclination angle is alleviated by the increase of lateral deflection induced by the lateral centrifugal force. Due to effect of the Coriolis force and centrifugal stiffening, frequency veering phenomenon is observed when inclination angle  $\alpha = 0^\circ$ , and two natural frequencies corresponding to axial vibration and lateral vibration are close.

Finally, it may be emphasized that, although the proposed method is only applied to the two dimensional rotating cantilever beams with inclination angle here, the present method can be easily extended to three dimensional rotating beams with precone and setting angle.

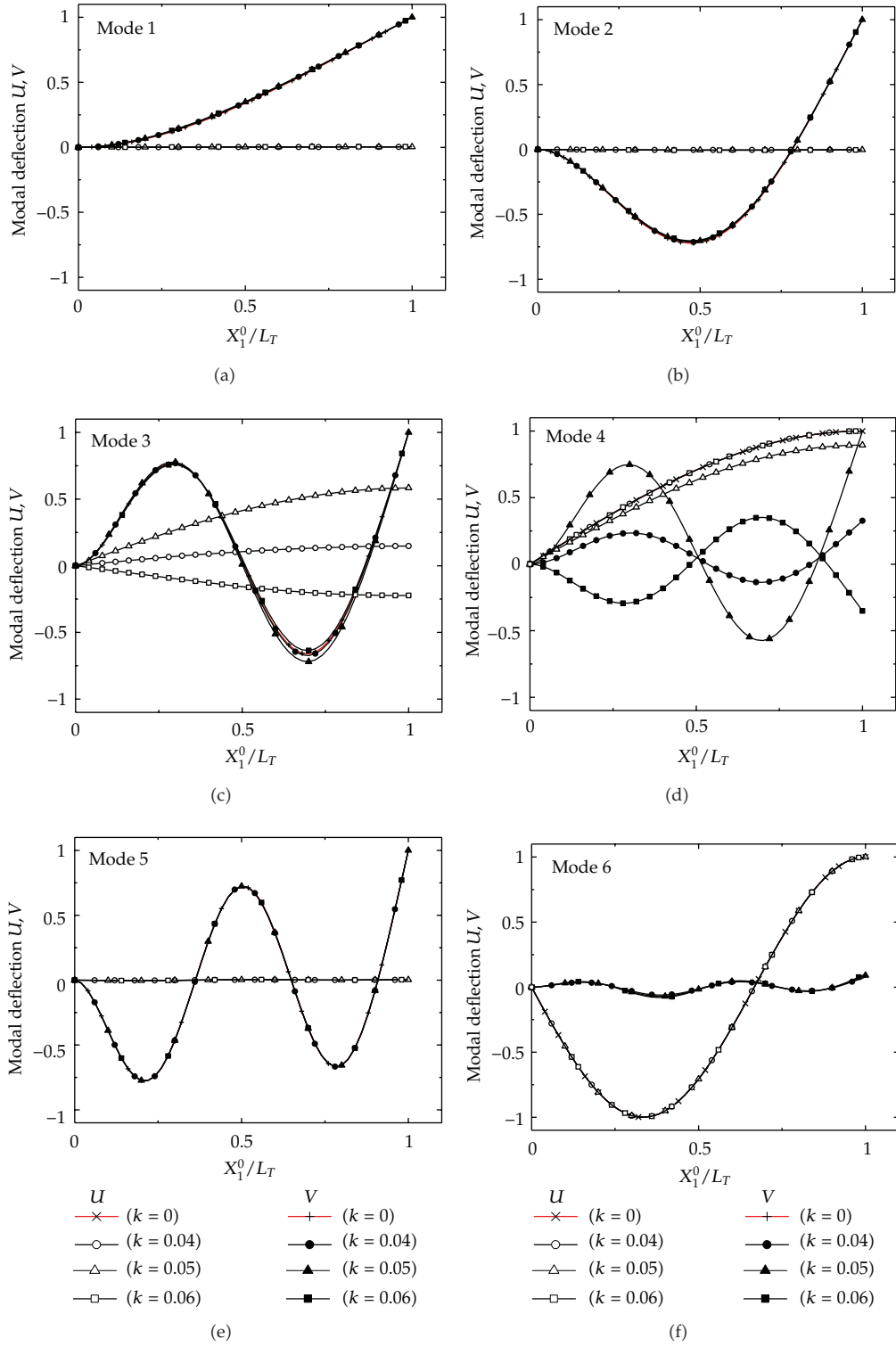


**Figure 7:** The first six vibration mode shapes of a rotating beam ( $\eta = 39$ ,  $\bar{R} = 1$ ,  $\alpha = 0^\circ$ ).

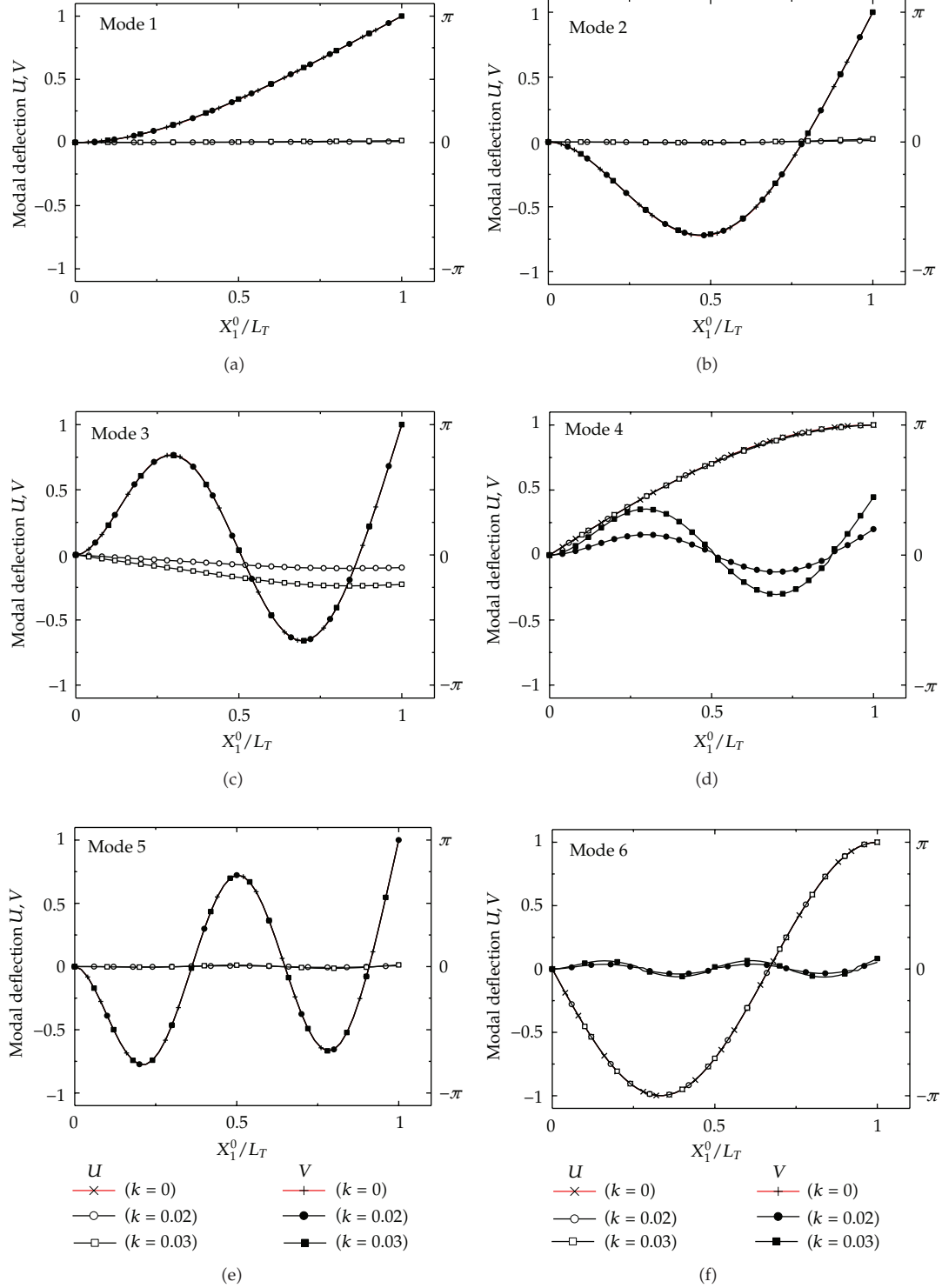
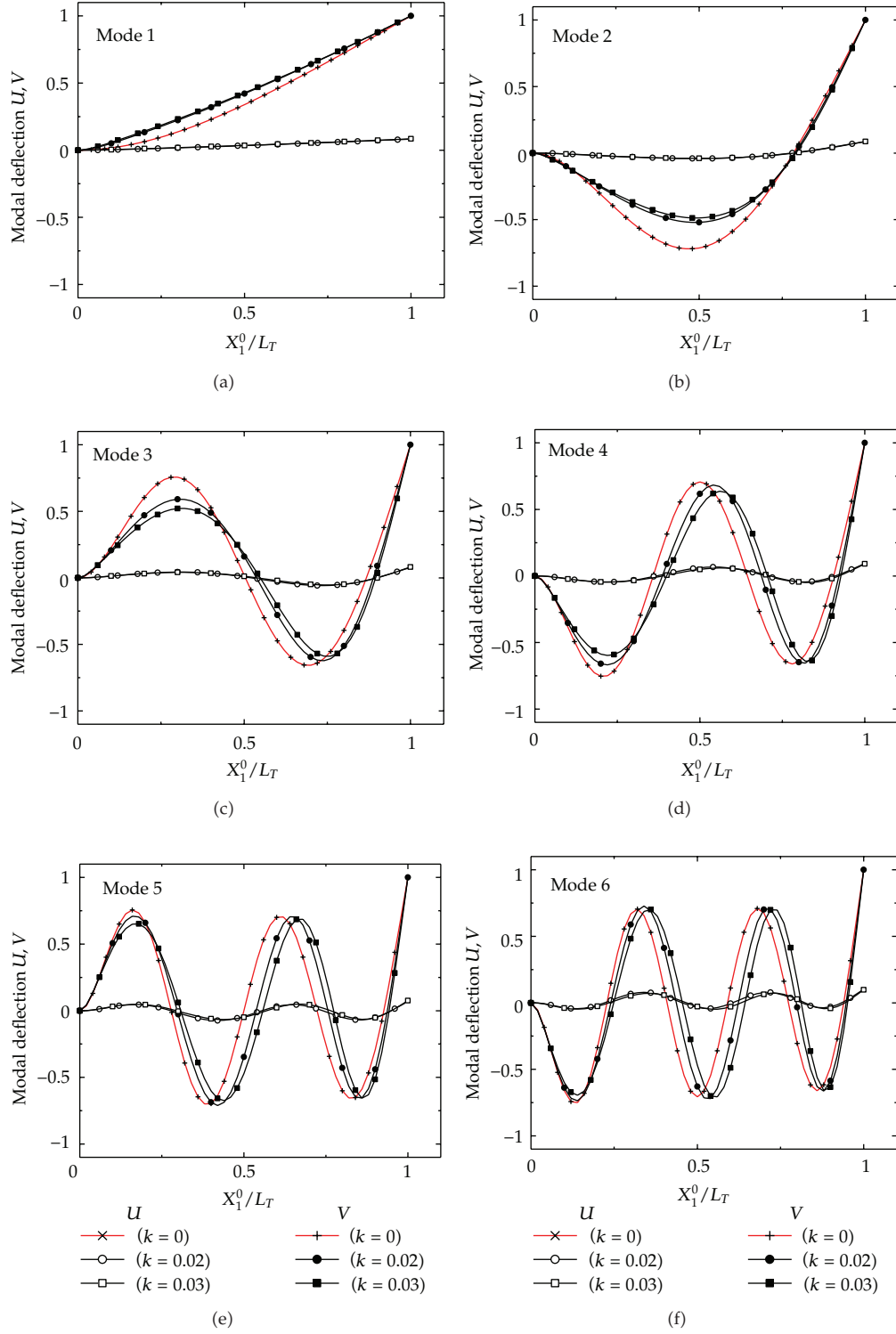
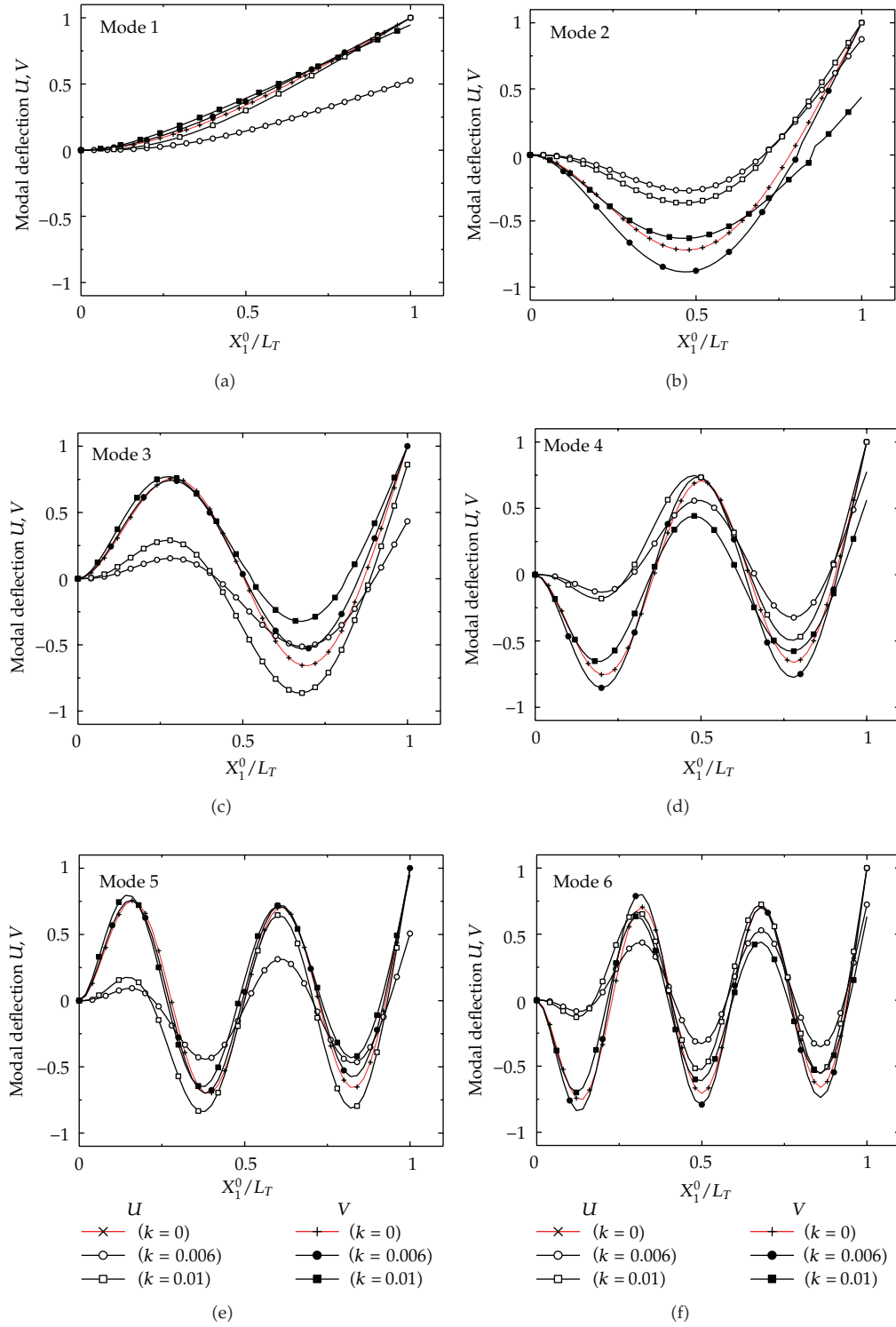


Figure 8: The first six vibration mode shapes of a rotating beam ( $\eta = 39$ ,  $\bar{R} = 1$ ,  $\alpha = 5^\circ$ ).



**Figure 9:** The first six vibration mode shapes of a rotating beam ( $\eta = 1000$ ,  $\bar{R} = 1$ ,  $\alpha = 5^\circ$ ).



**Figure 10:** The first six vibration mode shapes of a rotating beam ( $\eta = 1000$ ,  $\bar{R} = 1$ ,  $\alpha = 90^\circ$ ).

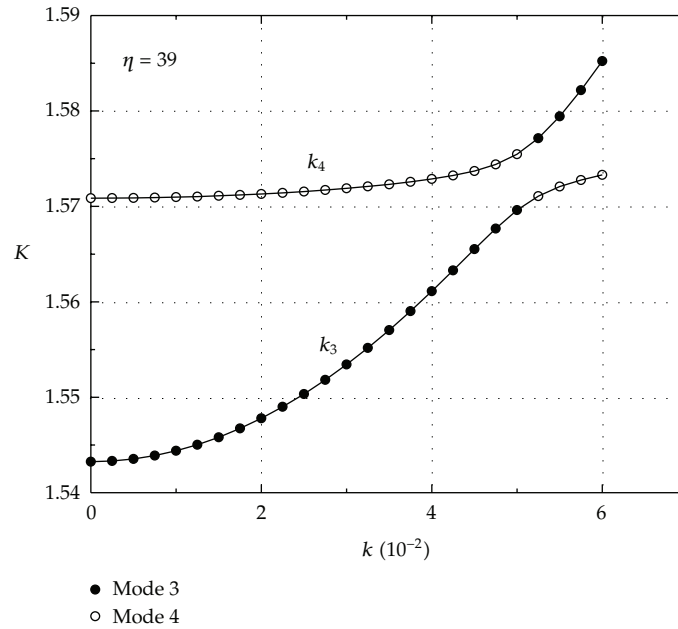


**Figure 11:** The third and fourth natural frequencies verse the dimensionless angular velocity ( $\alpha = 0^\circ$ ,  $r = 1$ ,  $\eta = 39$ ).

## Acknowledgment

The research was sponsored by the National Science Council, ROC, Taiwan, under contract NSC 98-2221-E-009-099-MY2.

## References

- [1] M. J. Schilhansl, "Bending frequency of a rotating cantilever beam," *Journal of Applied Mechanics*, vol. 25, pp. 28–30, 1958.
- [2] R. O. Stafford and V. Giurgiutiu, "Semi-analytic methods for rotating Timoshenko beams," *International Journal of Mechanical Sciences*, vol. 17, no. 11-12, pp. 719–727, 1975.
- [3] A. Leissa, "Vibrational aspects of rotating turbomachinery blades," *Applied Mechanics Reviews*, vol. 34, no. 5, pp. 629–635, 1981.
- [4] D. H. Hodges and M. J. Rutkowski, "Free-vibration analysis of rotating beams by a variable-order finite-element method," *AIAA Journal*, vol. 19, no. 11, pp. 1459–1466, 1981.
- [5] A. D. Wright, C. E. Smith, R. W. Thresher, and J. L. C. Wang, "Vibration modes of centrifugally stiffened beams," *Journal of Applied Mechanics*, vol. 49, no. 1, pp. 197–202, 1982.
- [6] K. B. Subrahmanyam and K. R. V. Kaza, "Non-linear flap-lag-extensional vibrations of rotating, pretwisted, preconed beams including Coriolis effects," *International Journal of Mechanical Sciences*, vol. 29, no. 1, pp. 29–43, 1987.
- [7] T. Yokoyama, "Free vibration characteristics of rotating Timoshenko beams," *International Journal of Mechanical Sciences*, vol. 30, no. 10, pp. 743–755, 1988.
- [8] M. R. M. da Silva, C. L. Zaretzky, and D. H. Hodges, "Effects of approximations on the static and dynamic response of a cantilever with a tip mass," *International Journal of Solids and Structures*, vol. 27, no. 5, pp. 565–583, 1991.
- [9] S. Y. Lee and Y. H. Kuo, "Bending frequency of a rotating beam with an elastically restrained root," *Journal of Applied Mechanics*, vol. 58, no. 1, pp. 209–214, 1991.

- [10] H. P. Lee, "Vibration on an inclined rotating cantilever beam with tip mass," *Journal of Vibration and Acoustics*, vol. 115, pp. 241–245, 1993.
- [11] S. Naguleswaran, "Lateral Vibration of a centrifugally tensioned uniform Euler-Bernoulli beam," *Journal of Sound and Vibration*, vol. 176, no. 5, pp. 613–624, 1994.
- [12] M. R. M. Crespo Da Silva, "A comprehensive analysis of the dynamics of a helicopter rotor blade," *International Journal of Solids and Structures*, vol. 35, no. 7-8, pp. 619–635, 1998.
- [13] H. H. Yoo and S. H. Shin, "Vibration analysis of rotating cantilever beams," *Journal of Sound and Vibration*, vol. 212, no. 5, pp. 807–828, 1998.
- [14] A. Bazoune, Y. A. Khulief, N. G. Stephen, and M. A. Mohiuddin, "Dynamic response of spinning tapered Timoshenko beams using modal reduction," *Finite Elements in Analysis and Design*, vol. 37, no. 3, pp. 199–219, 2001.
- [15] S. C. Lin and K. M. Hsiao, "Vibration analysis of a rotating Timoshenko beam," *Journal of Sound and Vibration*, vol. 240, no. 2, pp. 303–322, 2001.
- [16] P. Marugabandhu and J. H. Griffin, "A reduced-order model for evaluating the effect of rotational speed on the natural frequencies and mode shapes of blades," *Journal of Engineering for Gas Turbines and Power*, vol. 125, no. 3, pp. 772–776, 2003.
- [17] J. R. Banerjee and H. Su, "Development of a dynamic stiffness matrix for free vibration analysis of spinning beams," *Computers and Structures*, vol. 82, no. 23–26, pp. 2189–2197, 2004.
- [18] G. Wang and N. M. Wereley, "Free vibration analysis of rotating blades with uniform tapers," *AIAA Journal*, vol. 42, no. 12, pp. 2429–2437, 2004.
- [19] A. A. Al-Qaisia, "Non-linear dynamics of a rotating beam clamped with an attachment angle and carrying an inertia element," *Arabian Journal for Science and Engineering*, vol. 29, no. 1, pp. 81–98, 2004.
- [20] M. Sabuncu and K. Evran, "The dynamic stability of a rotating asymmetric cross-section Timoshenko beam subjected to lateral parametric excitation," *Finite Elements in Analysis and Design*, vol. 42, no. 5, pp. 454–469, 2006.
- [21] S. Y. Lee and J. J. Sheu, "Free vibrations of a rotating inclined beam," *Journal of Applied Mechanics*, vol. 74, no. 3, pp. 406–414, 2007.
- [22] S. Y. Lee and J. J. Sheu, "Free vibration of an extensible rotating inclined Timoshenko beam," *Journal of Sound and Vibration*, vol. 304, no. 3–5, pp. 606–624, 2007.
- [23] W. R. Chen, "On the vibration and stability of spinning axially loaded pre-twisted Timoshenko beams," *Finite Elements in Analysis and Design*, vol. 46, no. 11, pp. 1037–1047, 2010.
- [24] C. L. Huang, W. Y. Lin, and K. M. Hsiao, "Free vibration analysis of rotating Euler beams at high angular velocity," *Computers and Structures*, vol. 88, no. 17-18, pp. 991–1001, 2010.
- [25] B. Yardimoglu, "A novel finite element model for vibration analysis of rotating tapered Timoshenko beam of equal strength," *Finite Elements in Analysis and Design*, vol. 46, no. 10, pp. 838–842, 2010.
- [26] P. W. Likins, "Mathematical modeling of spinning elastic bodies for modal analysis," *AIAA Journal*, vol. 11, no. 9, pp. 1251–1258, 1973.
- [27] J. C. Simo and L. Vu-Quoc, "The role of non-linear theories in transient dynamic analysis of flexible structures," *Journal of Sound and Vibration*, vol. 119, no. 3, pp. 487–508, 1987.
- [28] K. M. Hsiao, "Corotational total Lagrangian formulation for three-dimensional beam element," *AIAA journal*, vol. 30, no. 3, pp. 797–804, 1992.
- [29] K. M. Hsiao, R. T. Yang, and A. C. Lee, "Consistent finite element formulation for non-linear dynamic analysis of planar beam," *International Journal for Numerical Methods in Engineering*, vol. 37, no. 1, pp. 75–89, 1994.
- [30] A. A. Shabana, H. A. Hussien, and J. L. Escalona, "Application of the absolute nodal coordinate formulation to large rotation and large deformation problems," *Journal of Mechanical Design*, vol. 120, no. 2, pp. 188–195, 1998.
- [31] J. L. Escalona, H. A. Hussien, and A. A. Shabana, "Application of the absolute nodal co-ordinate formulation to multibody system dynamics," *Journal of Sound and Vibration*, vol. 214, no. 5, pp. 833–850, 1998.
- [32] T. J. Chung, *Continuum Mechanics*, Prentice Hall, Englewood Cliffs, NJ, USA, 1988.
- [33] D. J. Malvern, *Introduction to the Mechanics of the Continuous Medium*, Prentice Hall, Englewood Cliffs, NJ, USA, 1969.
- [34] S. S. Rao, *Mechanical Vibrations*, Addison-Wesley, 1986.